MASARYK UNIVERSITY
FACULTY OF SCIENCE

NEXT-GENERATION SEQUENCING BIOINFORMATICS FOR PRECISION ONCOLOGY: FROM IMMUNOGENETICS TO MULTI-OMICS

HABILITATION THESIS

Mgr. Vojtěch Bystrý, Ph.D.

BRNO 2026

ABSTRACT

This habilitation thesis is a commented collection of 19 peer-reviewed publications focused on the development and application of bioinformatics approaches for next-generation sequencing (NGS) data analysis in cancer diagnostics and research. The work spans from foundational contributions to immunogenetics and clonality assessment in hematological malignancies, through the development of bioinformatics tools and platforms, to comprehensive multi-omics integration for precision oncology.

The first part describes the development of the ARResT platform for immunoglobulin and T-cell receptor (IG/TR) repertoire analysis, which became a standard tool within the EuroClonality-NGS consortium for clonality assessment and minimal residual disease (MRD) marker identification. The second part focuses on complementary bioinformatics tools developed to address the growing need for high-sensitivity mutation detection and variant calling optimization, as well as whole transcriptome analysis pipelines for structural variant detection. The final part demonstrates the evolution toward comprehensive cancer genomics—from fusion gene detection through somatic mutation analysis and epigenomics to multi-omics integration and the emerging field of radiogenomics.

The presented body of work represents a progression from specialized immunogenetics applications to broadly applicable multi-omics frameworks, contributing to the translation of NGS technologies into clinical practice for cancer patient management and laying the foundation for European-scale infrastructure development in precision oncology.

ACKNOWLEDGEMENTS

First and foremost, I would like to thank my wife Lenka for her unwavering love, partnership, and encouragement throughout this journey.

I am deeply grateful to my parents for their steadfast support throughout my scientific career, and for instilling in me the values that have guided my path.

Finally, I wish to express my appreciation to all the brilliant colleagues, collaborators, and friends with whom I have had the privilege and pleasure to work. Your insights, dedication, and camaraderie have enriched both this research and my professional life immeasurably.

ABBREVIATIONS

ALCL	Anaplastic Large Cell Lymphoma
ALL	Acute Lymphoblastic Leukemia
BCR	B-Cell Receptor
CLL	Chronic Lymphocytic Leukemia
DNA	Deoxyribonucleic Acid
ERIC	European Research Initiative on CLL
GvL	Graft-versus-Leukemia
IG	Immunoglobulin
MPN	Myeloproliferative Neoplasms
MRD	Minimal Residual Disease
NGS	Next-Generation Sequencing
RNA	Ribonucleic Acid
SASP	Senescence-Associated Secretory Phenotype
TCR	T-Cell Receptor
T-PLL	T-cell Prolymphocytic Leukemia
TR	T-cell Receptor
WTS	Whole Transcriptome Sequencing

CONTENT

1 INTRODUCTION

The advent of next-generation sequencing (NGS) technologies has fundamentally transformed our understanding of cancer biology and revolutionized approaches to cancer diagnosis, prognosis, and treatment [1–4]. Since the completion of the Human Genome Project in 2003 and the subsequent development of high-throughput sequencing platforms, the cost of genome sequencing has decreased by several orders of magnitude, making comprehensive genomic analysis accessible for both research and clinical applications. This technological revolution has created an unprecedented demand for sophisticated bioinformatics solutions capable of processing, analyzing, and interpreting the massive volumes of data generated by modern sequencing platforms.

Cancer, as a fundamentally genomic disease, represents an ideal application for NGS technologies [5,6]. The genetic and epigenetic alterations that drive malignant transformation, progression, and treatment resistance can now be comprehensively characterized at unprecedented resolution. Furthermore, the unique ability of NGS to detect rare variants within heterogeneous cell populations has enabled applications such as minimal residual disease (MRD) monitoring, where the detection of one cancer cell among thousands of normal cells can guide treatment decisions and predict patient outcomes [11,13].

This thesis presents my contributions to the field of NGS bioinformatics for cancer applications, spanning from my doctoral work on immunogenetics and clonality assessment to more recent contributions in multi-omics integration for precision oncology. The work is organized thematically, reflecting the evolution of the field and my own scientific trajectory over the past decade.

1.1 Structure of the Thesis

This thesis presents a collection of 19 peer-reviewed publications related to NGS data analysis for cancer applications. The publications are organized into three thematic areas, reflecting both the chronological development of the work and the logical progression from specialized to comprehensive approaches:

Part I: Immunogenetics Using NGS in Hematology-Oncology – Development of the ARResT platform for IG/TR repertoire analysis, its adoption as a standard within the EuroClonality-NGS consortium, and clinical applications in MRD detection

Part II: Bioinformatics Tools and Platforms – Complementary tools for variant calling optimization, standardized sequence assessment, and whole transcriptome analysis pipelines for structural variant detection

Part III: Cancer Genomics and Multi-omics Integration – Applications spanning genomics (fusion genes, somatic mutations), epigenomics, multi-omics integration in solid tumors, and the emerging field of radiogenomics

1.2 My Contribution to NGS Bioinformatics in Cancer

Currently, I have co-authored over 38 peer-reviewed journal articles, with the majority focusing on NGS data analysis for hematological malignancies and solid tumors. I have selected 19 publications that best represent my contributions to the development of bioinformatics methods for cancer diagnostics. My contributions to these publications are summarized in the tables below, with attention to experimental bioinformatics work, supervision, manuscript preparation, and research direction.

Part I: Immunogenetics Using NGS in Hematology-Oncology

1) Bystry, V. et al. ARResT/AssignSubsets. Bioinformatics 2015, 31(23), 3844–3846. (IF=4.98)

Experimental work (%)	Supervision (%)	Manuscript (%)	Research direction (%)
80	—	70	60

2) Bystry, V. et al. ARResT/Interrogate. Bioinformatics 2017, 33(3), 435–437. (IF=5.61)

Experimental work (%)	Supervision (%)	Manuscript (%)	Research direction (%)
70	30	60	50

3) Roy, A.; Bystry, V. et al. High Resolution IgH Repertoire Analysis. Clinical Immunology 2017, 183, 8–16. (IF=3.99)

Experimental work (%)	Supervision (%)	Manuscript (%)	Research direction (%)
40	—	20	20

4) Brüggemann, M.; … Bystry, V. et al. EuroClonality-NGS Validation Study. Leukemia 2019, 33(9), 2241–2253. (IF=11.53)

Experimental work (%)	Supervision (%)	Manuscript (%)	Research direction (%)
30	—	20	20

5) Knecht, H.; … Bystry, V. et al. Quality Control and Quantification in IG/TR NGS. Leukemia 2019, 33(9), 2254–2265. (IF=11.53)

Experimental work (%)	Supervision (%)	Manuscript (%)	Research direction (%)
40	—	25	25

6) Sellner, L.; … Bystry, V. et al. GvL Effects in T-PLL. Bone Marrow Transplant 2017, 52(4), 544–551. (IF=4.67)

Experimental work (%)	Supervision (%)	Manuscript (%)	Research direction (%)
30	—	15	15

Part II: Bioinformatics Tools and Platforms

7) Pal, K.; Bystry, V. et al. GLASS. Bioinformatics 2017, 33(23), 3802–3804. (IF=5.61)

Experimental work (%)	Supervision (%)	Manuscript (%)	Research direction (%)
40	30	30	40

8) Tom, N.; … Bystry, V. et al. ToTem. BMC Bioinformatics 2018, 19(1), 243. (IF=2.21)

Experimental work (%)	Supervision (%)	Manuscript (%)	Research direction (%)
30	40	20	30

9) Hynst, J.; … Bystry, V. et al. WTS Pipelines for Structural Variants. PeerJ 2019, 7, e7071. (IF=2.38)

Experimental work (%)	Supervision (%)	Manuscript (%)	Research direction (%)
20	50	30	40

Part III: Cancer Genomics and Multi-omics Integration

10) Grioni, A.; … Bystry, V. et al. RNA Capture NGS for Fusion Genes in B-ALL. HemaSphere 2019, 3(3), e250.

Experimental work (%)	Supervision (%)	Manuscript (%)	Research direction (%)
30	40	20	20

11) Kubesova, B.; … Bystry, V. et al. TP53 Mutations in MPN. Leukemia 2018, 32(2), 450–461. (IF=11.53)

Experimental work (%)	Supervision (%)	Manuscript (%)	Research direction (%)
25	—	15	15

12) Lobello, C.; … Bystry, V. et al. STAT3/TP53 in ALCL. Leukemia 2021, 35(5), 1500–1505. (IF=12.53)

Experimental work (%)	Supervision (%)	Manuscript (%)	Research direction (%)
30	—	15	15

13) Poppova, L.; … Bystry, V. et al. WNT5A Methylation in CLL. Epigenetics 2022, 17(12), 1628–1635. (IF=4.10)

Experimental work (%)	Supervision (%)	Manuscript (%)	Research direction (%)
25	—	15	15

14) Limberger, T.; … Bystry, V. et al. KMT2C in Prostate Cancer Metastasis. Mol Cancer 2022, 21(1), 89. (IF=37.30)

Experimental work (%)	Supervision (%)	Manuscript (%)	Research direction (%)
25	—	10	10

15) Redmer, T.; … Bystry, V. et al. JUN Mediates SASP in Prostate Cancer. Mol Cancer 2024, 23(1), 114. (IF=37.30)

Experimental work (%)	Supervision (%)	Manuscript (%)	Research direction (%)
20	—	10	10

16) Sternberg, C.; … Bystry, V. et al. IL6ST in Prostate Cancer. Mol Cancer 2024, 23(1), 245. (IF=37.30)

Experimental work (%)	Supervision (%)	Manuscript (%)	Research direction (%)
20	—	10	10

17) Ning, J.; … Bystry, V. et al. Machine Learning Multiomics for Prostate Cancer. Theranostics 2024, 14(12), 4570–4581. (IF=12.40)

Experimental work (%)	Supervision (%)	Manuscript (%)	Research direction (%)
30	20	15	20

18) Spielvogel, C.P.; … Bystry, V. et al. Radiogenomics in Head and Neck Cancer. Eur J Nucl Med Mol Imaging 2023, 50(2), 546–558. (IF=9.10)

Experimental work (%)	Supervision (%)	Manuscript (%)	Research direction (%)
30	20	15	20

19) Pokorna, P.; … Bystry, V. et al. Integrative Clinical Genomics in Pediatric Precision Oncology. Laboratory Investigation 2024, 104(12), 102161. (IF=5.10)

Experimental work (%)	Supervision (%)	Manuscript (%)	Research direction (%)
40	30	25	30

2 IMMUNOGENETICS USING NGS IN HEMATOLOGY-ONCOLOGY

The adaptive immune system generates an enormous diversity of immunoglobulin (IG) and T-cell receptor (TR) molecules through V(D)J recombination, creating unique "molecular fingerprints" for each lymphocyte clone [7]. In lymphoid malignancies, this clonal rearrangement serves as a powerful biomarker for disease detection, classification, and monitoring [8,12]. The application of NGS to IG/TR analysis has dramatically expanded both the depth and breadth of possible analyses, enabling simultaneous profiling of millions of rearrangements with unprecedented sensitivity [10].

Tool Development and Repertoire Analysis. My entry into this field began with the development of the ARResT (Antigen Receptor Rearrangement Software for T- and B-cell analysis) platform, which provides a comprehensive suite of tools for IG/TR sequence analysis. The first component, **ARResT/AssignSubsets** (Publication 1), addressed the challenge of chronic lymphocytic leukemia (CLL) subclassification based on B-cell receptor stereotypy. CLL is characterized by subsets of patients whose leukemic cells express quasi-identical ("stereotyped") BCRs, with important clinical implications as these subsets are associated with distinct biological characteristics and outcomes [9].

Building on this foundation, we developed **ARResT/Interrogate** (Publication 2), an interactive web-based immunoprofiler for comprehensive IG/TR NGS data analysis. This platform enables researchers to explore clonal expansions, track repertoire dynamics, and identify disease-associated patterns across large patient cohorts. Together, these tools became the standard for NGS-based immune repertoire analysis within the European research community, particularly for clonality assessment and MRD detection purposes. The biological power of high-resolution repertoire analysis was demonstrated in collaboration with researchers at Imperial College London, where we showed that the fetal liver is likely the origin of life-long innate B lymphopoiesis in humans (Publication 3), challenging existing paradigms about B-cell repertoire establishment.

Multicentric Standardization. The translation of NGS-based IG/TR analysis from research to clinical diagnostics requires rigorous standardization and validation [8]. The availability of the ARResT platform enabled the EuroClonality-NGS consortium to establish standardized protocols for clonality assessment and MRD marker identification across leading European laboratories. As a core member of the bioinformatics team, I contributed to both methodological development and multi-center validation of these approaches. Publication 4 describes the standardized approach for NGS-based MRD marker identification in acute lymphoblastic leukemia, demonstrating that NGS can reliably identify patient-specific IG/TR rearrangements with performance characteristics comparable to or exceeding traditional methods [11,13]. Publication 5 provides the complementary quality control and quantification framework essential for clinical implementation, establishing the bioinformatic protocols required for robust, reproducible results across different laboratories.

Clinical Applications. The tools and analytical framework developed within the ARResT platform enabled specific clinical research applications. Publication 6 demonstrates the application of TCR repertoire analysis and MRD monitoring in T-cell prolymphocytic leukemia (T-PLL), a rare but aggressive T-cell neoplasm. This work revealed evidence for graft-versus-leukemia effects following allogeneic stem cell transplantation, with MRD kinetics providing insights into the dynamics of immunological tumor control. The ability to track both the malignant clone and the reconstituting immune repertoire represents a powerful application of NGS-based immunoprofiling in the transplant setting.

3 BIOINFORMATICS TOOLS AND PLATFORMS

While developing the comprehensive ARResT platform for IG/TR repertoire analysis within the EuroClonality-NGS consortium, the need for complementary analytical tools became apparent. Beyond repertoire analysis, clinical and research laboratories required solutions for the detection and characterization of somatic mutations in cancer-associated genes such as TP53 and targeted gene panels, with a focus on achieving extremely high specificity and sensitivity [15,16].

Variant Detection and Pipeline Optimization. Despite the NGS revolution, Sanger sequencing remains important for variant confirmation in clinical settings. However, the interpretation of Sanger sequence traces involves subjective judgment, leading to variability between analysts and laboratories. **GLASS** (Gene Variation Assessment, Publication 7) was developed within the ERIC (European Research Initiative on CLL) TP53 Network to standardize the assessment of gene variations from Sanger sequence trace data. The tool provides assisted and reproducible variant calling, addressing the variability inherent in manual trace interpretation, and has been widely adopted within the CLL research community and beyond.

ToTem (Tool for Variant Calling Pipeline Optimization, Publication 8) addresses a fundamental challenge in NGS data analysis: the selection and configuration of analysis pipelines [15]. NGS variant calling involves numerous algorithmic choices—aligners, variant callers, quality filters—each with multiple parameter options. The optimal combination depends on the specific application, sequencing technology, and sample characteristics. ToTem enables systematic evaluation of pipeline configurations against gold-standard datasets, identifying optimal combinations for specific applications and contributing to more rigorous and reproducible NGS analysis across diverse research and clinical applications.

Whole Transcriptome Analysis for Structural Variants. As NGS implementation progressed and the scope of analysis expanded from targeted gene panels to genome-wide approaches, the need for comprehensive transcriptome analysis became evident [14,17]. Publication 9 describes bioinformatics pipelines for whole transcriptome sequencing (WTS) data analysis in leukemia patients with complex structural variants. The detection and characterization of chromosomal rearrangements, including fusion genes and complex genomic alterations, requires specialized analytical approaches that can identify novel junction sequences while discriminating true structural variants from artifacts. The developed pipelines enable comprehensive characterization of gene expression, alternative splicing, and fusion transcripts, providing a multi-layered view of the transcriptional landscape in cancer. This work marked a transition in my research trajectory from focused immunogenetics toward broader cancer genomics, setting the stage for the multi-omics approaches described in the following chapter.

4 CANCER GENOMICS AND MULTI-OMICS INTEGRATION

The comprehensive characterization of cancer requires integration of multiple data types, including DNA sequencing for mutation detection, RNA sequencing for expression and fusion gene analysis, epigenomic profiling for methylation patterns, and increasingly, imaging-derived features [23,24]. This chapter describes the evolution of my work from specialized immunogenetics toward comprehensive cancer genomics approaches, progressing through genomics, epigenomics, multi-omics integration in solid tumors, and the emerging field of radiogenomics.

Genomics: Fusion Genes and Somatic Mutations. Building on the expertise in rearrangement detection developed through IG/TR analysis, we applied targeted approaches to chromosomal rearrangements in hematological malignancies [14]. Publication 10 presents an RNA capture NGS strategy for fusion gene assessment in pediatric B-cell acute lymphoblastic leukemia, providing a cost-effective alternative to whole transcriptome sequencing for clinically relevant fusion detection. Beyond structural rearrangements, somatic mutation detection in cancer-associated genes has become central to cancer diagnosis, prognosis, and treatment selection [18,20]. Publication 11 describes the detection of low-burden TP53 mutations in myeloproliferative neoplasms, demonstrating the prognostic significance of subclonal mutations detectable only by deep sequencing, while Publication 12 shows the association of STAT3 and TP53 mutations with poor prognosis in anaplastic large cell lymphoma.

Epigenomics and Methylation Profiling. Moving beyond genomic sequence variants, epigenetic alterations—particularly DNA methylation changes—play crucial roles in cancer development and can provide insights into cellular origins and disease biology [21,22]. Publication 13 describes the association of specific WNT5A promoter methylation patterns with memory B-cell like CLL, demonstrating the integration of epigenomic analysis with established immunogenetic classification schemes. This work exemplifies the value of incorporating additional molecular layers beyond genomics for understanding disease biology and refining patient stratification.

Multi-omics Integration in Solid Tumors. The application of comprehensive multi-omics approaches extends beyond hematological malignancies to solid tumors [27,28]. A series of collaborative studies with the Medical University of Vienna has contributed to understanding prostate cancer biology through integrated genomic and transcriptomic analysis. Publication 14 describes the role of KMT2C methyltransferase in regulating INK4A expression and suppressing prostate cancer metastasis. Publications 15 and 16 further elucidate molecular mechanisms of tumor progression, demonstrating how JUN mediates the senescence-associated secretory phenotype to prevent disease progression, and revealing the tumor-suppressive role of IL6ST activation through STAT3/ARF/p53-driven senescence. Publication 17 represents a comprehensive multi-omics approach, combining machine learning with genomic, transcriptomic, and imaging data for improved Gleason grading assessment. The evolution from single-omics to multi-omics integration is also demonstrated in pediatric oncology—Publication 19 evaluates real-world performance of integrative clinical genomics for pediatric precision oncology, demonstrating the clinical utility of combined DNA and RNA sequencing approaches for diagnosis, risk stratification, and treatment selection [30].

Radiogenomics: Integrating Imaging and Molecular Data. An emerging frontier in precision oncology is the integration of imaging-derived features (radiomics) with molecular profiling (genomics) to create comprehensive patient characterization without requiring invasive tissue sampling [25,26]. Publication 18 demonstrates the potential of radiogenomic markers for risk stratification and inference of mutational pathway states in head and neck cancer. This work, together with the prostate cancer multiomics study (Publication 17) that incorporates imaging data alongside molecular features, represents my active involvement in establishing this new field. Radiogenomics holds particular promise for non-invasive monitoring of tumor evolution, treatment response assessment, and identification of patients who may benefit from targeted therapies based on predicted molecular profiles [19]. This is an area where I continue to be actively engaged, with ongoing collaborations aimed at further developing and validating radiogenomic approaches across multiple cancer types.

5 CONCLUSION AND OUTLOOK

The work presented in this thesis traces my contributions to the development of NGS bioinformatics for cancer applications over the past decade. From the foundational work on immunogenetics and clonality assessment that formed my doctoral research, through the international standardization efforts of EuroClonality-NGS, to comprehensive multi-omics approaches for precision oncology in both hematological malignancies and solid tumors, this body of work reflects the rapid evolution of the field and my own scientific trajectory.

Several key themes emerge from this collection. First, the importance of standardization and validation for clinical translation—the ARResT platform's adoption as a standard within EuroClonality demonstrates how robust tools enable multi-center efforts that accelerate methodological development while ensuring reproducibility across laboratories. Second, the value of developing complementary tools alongside specialized applications—GLASS and ToTem address fundamental challenges that span diverse NGS applications, while WTS pipelines bridged the transition from targeted to genome-wide analysis. Third, the progression toward integration—comprehensive cancer characterization increasingly requires the combination of multiple data types, as exemplified by the multi-omics and radiogenomics applications that now form a significant part of my research portfolio.

Looking forward, my current research focus has evolved to address what I see as the critical next challenge in the field: building infrastructure for high-quality analysis and data sharing across Europe. The transition from single-center studies to truly pan-European precision medicine initiatives requires not only analytical tools but also robust infrastructure for standardized multi-omics data analysis, quality assurance, and secure data sharing [27]. The experience gained through EuroClonality—developing standardized protocols, harmonizing analysis across laboratories, and ensuring reproducibility—has proven invaluable for this new direction.

The need for European-scale infrastructure for genomics and multi-omics analysis in precision medicine has become increasingly apparent. Individual research groups and clinical centers generate valuable molecular data, but the full potential of this information can only be realized through integration across institutions and countries [28,30]. This requires standardized analytical pipelines, interoperable data formats, federated analysis approaches that respect data sovereignty, and quality metrics that ensure comparability of results. My career trajectory—from developing specialized immunogenetics tools to participating in international standardization efforts to implementing multi-omics integration frameworks—has provided the foundation for contributing to this infrastructure development.

The emerging field of radiogenomics represents another area of active development, where non-invasive imaging can be combined with molecular profiling to provide comprehensive patient characterization [25,26]. The continued reduction in sequencing costs, advances in long-read technologies for structural variant detection, single-cell approaches for tumor heterogeneity analysis [29], and integration of artificial intelligence for complex data interpretation will all shape the future of the field. I believe that the bioinformatics frameworks, tools, and collaborative networks developed through this work provide a foundation for continued contributions to these emerging frontiers, with the ultimate goal of improving outcomes for patients with cancer through precision medicine approaches implemented at the European scale.

REFERENCES

[1] Lander, E.S. et al. Initial sequencing and analysis of the human genome. Nature 2001, 409(6822), 860–921.

[2] Metzker, M.L. Sequencing technologies — the next generation. Nature Reviews Genetics 2010, 11(1), 31–46.

[3] Mardis, E.R. Next-generation sequencing platforms. Annual Review of Analytical Chemistry 2013, 6, 287–303.

[4] Goodwin, S.; McPherson, J.D.; McCombie, W.R. Coming of age: ten years of next-generation sequencing technologies. Nature Reviews Genetics 2016, 17(6), 333–351.

[5] Vogelstein, B. et al. Cancer genome landscapes. Science 2013, 339(6127), 1546–1558.

[6] Stratton, M.R.; Campbell, P.J.; Futreal, P.A. The cancer genome. Nature 2009, 458(7239), 719–724.

[7] Tonegawa, S. Somatic generation of antibody diversity. Nature 1983, 302(5909), 575–581.

[8] Langerak, A.W. et al. EuroClonality/BIOMED-2 guidelines for interpretation and reporting of Ig/TCR clonality testing in suspected lymphoproliferations. Leukemia 2012, 26(10), 2159–2171.

[9] Stamatopolous, K. et al. Over 20% of patients with chronic lymphocytic leukemia carry stereotyped receptors: pathogenetic implications and clinical correlations. Blood 2007, 109(1), 259–270.

[10] Boyd, S.D. et al. Measurement and clinical monitoring of human lymphocyte clonality by massively parallel VDJ pyrosequencing. Science Translational Medicine 2009, 1(12), 12ra23.

[11] Faham, M. et al. Deep-sequencing approach for minimal residual disease detection in acute lymphoblastic leukemia. Blood 2012, 120(26), 5173–5180.

[12] van Dongen, J.J. et al. Design and standardization of PCR primers and protocols for detection of clonal immunoglobulin and T-cell receptor gene recombinations in suspect lymphoproliferations. Leukemia 2003, 17(12), 2257–2317.

[13] Kotrova, M. et al. The predictive strength of next-generation sequencing MRD detection for relapse compared with current methods in childhood ALL. Blood 2015, 126(8), 1045–1047.

[14] Fina, F. et al. Next-generation sequencing for fusion gene detection: a diagnostic tool for hematological malignancies. Journal of Molecular Diagnostics 2017, 19(5), 795–812.

[15] McKenna, A. et al. The Genome Analysis Toolkit: a MapReduce framework for analyzing next-generation DNA sequencing data. Genome Research 2010, 20(9), 1297–1303.

[16] Cibulskis, K. et al. Sensitive detection of somatic point mutations in impure and heterogeneous cancer samples. Nature Biotechnology 2013, 31(3), 213–219.

[17] Haas, B.J. et al. Accuracy assessment of fusion transcript detection via read-mapping and de novo fusion transcript assembly-based methods. Genome Biology 2019, 20(1), 213.

[18] Klco, J.M. et al. Association between mutation clearance after induction therapy and outcomes in acute myeloid leukemia. JAMA 2015, 314(8), 811–822.

[19] Zill, O.A. et al. The landscape of actionable genomic alterations in cell-free circulating tumor DNA from 21,807 advanced cancer patients. Clinical Cancer Research 2018, 24(15), 3528–3538.

[20] Sondka, Z. et al. The COSMIC Cancer Gene Census: describing genetic dysfunction across all human cancers. Nature Reviews Cancer 2018, 18(11), 696–705.

[21] Jones, P.A.; Baylin, S.B. The epigenomics of cancer. Cell 2007, 128(4), 683–692.

[22] Capper, D. et al. DNA methylation-based classification of central nervous system tumours. Nature 2018, 555(7697), 469–474.

[23] Hasin, Y.; Seldin, M.; Lusis, A. Multi-omics approaches to disease. Genome Biology 2017, 18(1), 83.

[24] Chakraborty, S.; Hosen, M.I.; Ahmed, M.; Shekhar, H.U. Onco-multi-OMICS approach: a new frontier in cancer research. BioMed Research International 2018, 2018, 9836256.

[25] Aerts, H.J. et al. Decoding tumour phenotype by noninvasive imaging using a quantitative radiomics approach. Nature Communications 2014, 5, 4006.

[26] Lambin, P. et al. Radiomics: the bridge between medical imaging and personalized medicine. Nature Reviews Clinical Oncology 2017, 14(12), 749–762.

[27] Priestley, P. et al. Pan-cancer whole-genome analyses of metastatic solid tumours. Nature 2019, 575(7781), 210–216.

[28] Rodon, J. et al. Genomic and transcriptomic profiling expands precision medicine for patients with cancer. Nature 2019, 579(7797), 259–268.

[29] Swanton, C. Intratumor heterogeneity: evolution through space and time. Cancer Research 2012, 72(19), 4875–4882.

[30] Meric-Bernstam, F. et al. Feasibility of large-scale genomic testing to facilitate enrollment onto genomically matched clinical trials. Journal of Clinical Oncology 2015, 33(25), 2753–2762.

6 SELECTED PUBLICATIONS

Publications included in this thesis are listed below. Full articles follow in Section 7.

Part I: Immunogenetics Using NGS in Hematology-Oncology

1. Bystry, V.; Agathangelidis, A.; Bikos, V.; et al. ARResT/AssignSubsets: A Novel Application for Robust Subclassification of Chronic Lymphocytic Leukemia Based on B Cell Receptor IG Stereotypy. Bioinformatics 2015, 31(23), 3844–3846. (Q1)
2. Bystry, V.; Reigl, T.; Krejci, A.; et al. ARResT/Interrogate: An Interactive Immunoprofiler for IG/TR NGS Data. Bioinformatics 2017, 33(3), 435–437. (Q1)
3. Roy, A.; Bystry, V.; et al. High Resolution IgH Repertoire Analysis Reveals Fetal Liver as the Likely Origin of Life-Long, Innate B Lymphopoiesis in Humans. Clinical Immunology 2017, 183, 8–16. (Q2)
4. Brüggemann, M.; Kotrova, M.; Knecht, H.; Bystry, V.; et al. Standardized Next-Generation Sequencing of Immunoglobulin and T-Cell Receptor Gene Recombinations for MRD Marker Identification in Acute Lymphoblastic Leukaemia; a EuroClonality-NGS Validation Study. Leukemia 2019, 33(9), 2241–2253. (Q1)
5. Knecht, H.; Reigl, T.; Kotrova, M.; Bystry, V.; et al. Quality Control and Quantification in IG/TR Next-Generation Sequencing Marker Identification: Protocols and Bioinformatic Functionalities by EuroClonality-NGS. Leukemia 2019, 33(9), 2254–2265. (Q1)
6. Sellner, L.; Brüggemann, M.; Bystry, V.; et al. GvL Effects in T-Prolymphocytic Leukemia: Evidence from MRD Kinetics and TCR Repertoire Analyses. Bone Marrow Transplant 2017, 52(4), 544–551. (Q1)

Part II: Bioinformatics Tools and Platforms

7. Pal, K.; Bystry, V.; Reigl, T.; et al. GLASS: Assisted and Standardized Assessment of Gene Variations from Sanger Sequence Trace Data. Bioinformatics 2017, 33(23), 3802–3804. (Q1)
8. Tom, N.; Tom, O.; Bystry, V.; et al. ToTem: A Tool for Variant Calling Pipeline Optimization. BMC Bioinformatics 2018, 19(1), 243. (Q1)
9. Hynst, J.; Plevova, K.; Radova, L.; Bystry, V.; et al. Bioinformatic Pipelines for Whole Transcriptome Sequencing Data Exploitation in Leukemia Patients with Complex Structural Variants. PeerJ 2019, 7, e7071. (Q2)

Part III: Cancer Genomics and Multi-omics Integration

10. Grioni, A.; Fazio, G.; Bystry, V.; et al. A Simple RNA Target Capture NGS Strategy for Fusion Genes Assessment in the Diagnostics of Pediatric B-cell Acute Lymphoblastic Leukemia. HemaSphere 2019, 3(3), e250.
11. Kubesova, B.; Bystry, V.; et al. Low-Burden TP53 Mutations in Chronic Phase of Myeloproliferative Neoplasms: Association with Age, Hydroxyurea Administration, Disease Type and JAK2 Mutational Status. Leukemia 2018, 32(2), 450–461. (Q1)
12. Lobello, C.; Tichy, B.; Bystry, V.; et al. STAT3 and TP53 Mutations Associate with Poor Prognosis in Anaplastic Large Cell Lymphoma. Leukemia 2021, 35(5), 1500–1505. (Q1)
13. Poppova, L.; Bystry, V.; et al. Memory B-Cell like Chronic Lymphocytic Leukaemia Is Associated with Specific Methylation Profile of WNT5A Promoter and Undetectable Expression of WNT5A Gene. Epigenetics 2022, 17(12), 1628–1635.
14. Limberger, T.; Schlederer, M.; Bystry, V.; et al. KMT2C Methyltransferase Domain Regulated INK4A Expression Suppresses Prostate Cancer Metastasis. Mol Cancer 2022, 21(1), 89. (Q1)

15. Redmer, T.; Raigel, M.; Sternberg, C.; Bystry, V.; et al. JUN Mediates the Senescence Associated Secretory Phenotype and Immune Cell Recruitment to Prevent Prostate Cancer Progression. Mol Cancer 2024, 23(1), 114. (Q1)
16. Sternberg, C.; Raigel, M.; Limberger, T.; Bystry, V.; et al. Cell-Autonomous IL6ST Activation Suppresses Prostate Cancer Development via STAT3/ARF/P53-Driven Senescence and Confers an Immune-Active Tumor Microenvironment. Mol Cancer 2024, 23(1), 245. (Q1)
17. Ning, J.; Spielvogel, C.P.; Bystry, V.; et al. A Novel Assessment of Whole-Mount Gleason Grading in Prostate Cancer to Identify Candidates for Radical Prostatectomy: A Machine Learning-Based Multiomics Study. Theranostics 2024, 14(12), 4570–4581. (Q1)
18. Spielvogel, C.P.; Stoiber, S.; Bystry, V.; et al. Radiogenomic Markers Enable Risk Stratification and Inference of Mutational Pathway States in Head and Neck Cancer. Eur J Nucl Med Mol Imaging 2023, 50(2), 546–558. (Q1)
19. Pokorna, P.; Palova, H.; Bystry, V.; et al. Real-World Performance of Integrative Clinical Genomics in Pediatric Precision Oncology. Laboratory Investigation 2024, 104(12), 102161. (Q1)

7 ARTICLES

Bioinformatics, 31(23), 2015, 3844–3846
doi: 10.1093/bioinformatics/btv456
Advance Access Publication Date: 6 August 2015
Applications Note

Sequence analysis

ARResT/AssignSubsets: a novel application for robust subclassification of chronic lymphocytic leukemia based on B cell receptor IG stereotypy

Vojtech Bystry[1,†], Andreas Agathangelidis[2,†], Vasilis Bikos[1,†], Lesley Ann Sutton[3], Panagiotis Baliakas[3], Anastasia Hadzidimitriou[4,3], Kostas Stamatopoulos[4,3] and Nikos Darzentas[1,*], also on behalf of ERIC, the European Research Initiative on CLL

[1]CEITEC—Central European Institute of Technology, Masaryk University, Brno, Czech Republic, [2]Division of Molecular Oncology and Department of Onco-Hematology, IRCCS San Raffaele Scientific Institute and Università Vita-Salute San Raffaele, Milan, Italy, [3]Department of Immunology, Genetics and Pathology, Science for Life Laboratory, Uppsala University, Uppsala, Sweden and [4]Institute of Applied Biosciences, Center for Research and Technology Hellas, Thessaloniki, Greece

*To whom correspondence should be addressed.
[†]The authors wish it to be known that, in their opinion, the first three should be regarded as Joint First Authors.

Associate Editor: John Hancock

Received on April 7, 2015; revised on July 13, 2015; accepted on July 30, 2015

Abstract

Motivation: An ever-increasing body of evidence supports the importance of B cell receptor immunoglobulin (BcR IG) sequence restriction, alias stereotypy, in chronic lymphocytic leukemia (CLL). This phenomenon accounts for ~30% of studied cases, one in eight of which belong to major subsets, and extends beyond restricted sequence patterns to shared biologic and clinical characteristics and, generally, outcome. Thus, the robust assignment of new cases to major CLL subsets is a critical, and yet unmet, requirement.

Results: We introduce a novel application, ARResT/AssignSubsets, which enables the robust assignment of BcR IG sequences from CLL patients to major stereotyped subsets. ARResT/AssignSubsets uniquely combines expert immunogenetic sequence annotation from IMGT/V-QUEST with curation to safeguard quality, statistical modeling of sequence features from more than 7500 CLL patients, and results from multiple perspectives to allow for both objective and subjective assessment. We validated our approach on the learning set, and evaluated its real-world applicability on a new representative dataset comprising 459 sequences from a single institution.

Availability and implementation: ARResT/AssignSubsets is freely available on the web at http://bat.infspire.org/arrest/assignsubsets/

Contact: nikos.darzentas@gmail.com

Supplementary information: Supplementary data are available at *Bioinformatics* online.

1 Introduction

Research into the immune pathogenesis of lymphomas and leukemias over the last three decades has highlighted the important role of antigen recognition by lymphocyte receptors, by uncovering restrictions in their immunogenetic makeup. Such research in large cohorts of cases of chronic lymphocytic leukemia (CLL), the most common leukemia in an ageing Western population, revealed that subsets of patients with stereotyped, or quasi-identical, B cell receptor immunoglobulin (BcR IG, or antibody) collectively account for ~30% of cases (Agathangelidis *et al.*, 2012; Darzentas *et al.*, 2010), and represent disease sub-entities with shared biologic and clinical profiles, including outcome (Baliakas *et al.*, 2014; Rossi *et al.*, 2009; Stamatopoulos *et al.*, 2007). Intriguingly, in the latest and largest such study of over 7500 patients, 19 major subsets, each with at least 20 cases, accounted for 12% of the cohort and 41% of all stereotyped cases (Agathangelidis *et al.*, 2012). This is remarkable given the negligible chance, in the range of $1{:}10^{12}$, of finding two B cell clones with stereotyped BcR IG. Thus, major stereotyped subsets have attracted great interest.

To date, assignment of new cases to these major subsets has been based on the *ad hoc* application of published criteria (Darzentas and Stamatopoulos, 2013), mostly by groups with advanced knowledge in immunogenetics, and thus with limited applicability, and arguably reliability, in routine practice. We therefore introduce a novel application, ARResT/AssignSubsets, which enables the robust assignment of submitted BcR IG sequences from CLL patients to the existing 19 major stereotyped subsets.

2 Methods

All sequence datasets used in this work are available through IMGT/CLL-DB [imgt.org/CLLDBInterface/] in accordance with its bylaws.

Sequence annotation and curation: Immunogenetic annotations are obtained from IMGT/V-QUEST (Giudicelli *et al.*, 2011), the widely accepted reference for antigen receptor sequence analysis (Lefranc, 2014). These annotations are used to extract sequence features (e.g. the variable heavy complementarity determining region 3, or VH CDR3) for the learning and assignment phases below, but also for the sequences to be validated by ARResT/SeqCure [bat.infspire.org/arrest/seqcure/], developed to systematically report compromising issues based on expert in-house rules applied on the annotations. Such issues include non-ACGT characters or short sequence length, both of which compromise sequence annotation; out-of-frame VH CDR3 with or without stop codons, which implies an unproductive chain; or absence of a gene rearrangement altogether.

At the center of ARResT/AssignSubsets lies a set of rules captured in a probabilistic model, a Bayes classifier implemented in R [r-project.org].

Learning phase: Learning of the model to be later used for assignment was based on a positive set of 929 major subset members, and a negative set ('pool' cohort) of 6 667 sequences belonging to minor subsets as well as non-subset, heterogeneous cases (Agathangelidis *et al.*, 2012).

The learning phase evaluates sequence features of these two sets divided into two groups: core and secondary. Core features are based on the latest accepted stringent criteria for subset discovery (Agathangelidis *et al.*, 2012), and if the value of a core feature of a new sequence is not shared among the members of a subset, then the sequence cannot be assigned to that subset. Currently, the three core features are: (i) VH CDR3 length, a critical determinant of the structure of the antigen recognition loop (Barrios *et al.*, 2004); (ii) immunoglobulin heavy variable (IGHV) gene phylogenetic clan, implying meaningful sequence similarity through common ancestry (Kirkham *et al.*, 1992) and (iii) mutational status of the rearrangement, with 'mutated' for <98% nucleotide identity to germline and 'unmutated' otherwise, an important prognostic indicator in patients with CLL (Damle *et al.*, 1999; Hamblin *et al.*, 1999). Secondary features are less strictly controlled for, i.e. unobserved values are accepted (but scored negatively)—these are: (i) rearranged IGHV and immunoglobulin heavy joining genes; and (ii) the VH CDR3 amino acid sequence through amino acid frequencies at any given sequence position.

To keep the model robust and avoid overfitting, the Bayesian network topology is kept as simple as possible, with only obvious dependencies captured: VH CDR3 amino acid frequencies at any position, and relative frequencies of rearranged IGHV genes of the same phylogenetic clan. To avoid creating unrealistically stringent criteria, we include a 'relaxation' coefficient to the probability calculation of the observed frequency of each feature in all available sequences. Finally, to reduce the 'noise' created by relatively less frequent values, we apply the power function on the probability distribution of each feature.

Assignment phase: Assignment is based on evaluating submitted sequence features with the learned Bayesian model. Each sequence first acquires an absolute score for each major subset of the positive set and for the negative set or 'pool' cohort. The absolute score is the minus logarithm of the exact probability of assigning to a set, with '−Inf' (minus infinity) meaning that the sequence core features did not match the subset core features. The difference between the absolute score of each major subset and that of the 'pool' cohort is then calculated as a relative score, with positive numbers for submitted sequences closer to subsets than to the 'pool' cohort. Assignment to the best-scoring subset uses a per-subset threshold, based on the range of scores achieved by existing members of that subset. The difference between the relative score and the subset threshold is 'translated' to confidence, ranging from 'borderline' to 'extreme', to further assist the user.

Output: Real-time output consists of progress reports, links, information and help, results and tables. These include the detailed ARResT/SeqCure report on the 'health' of the submitted sequences; absolute and relative frequencies of assignment to each of the 19 major CLL subsets; and an assignment report for each submitted sequence, including its 'health', the confidence of the assignment, and, when possible, heat maps of core and secondary features with their significance with respect to the submitted sequence and the best-scoring, but not necessarily assigned, subset. Additional information can be found in the Supplementary data and on the home page of ARResT/AssignSubsets.

3 Results

To validate ARResT/AssignSubsets we performed 100 learning and assignment runs, each using randomly selected 80% of the 7 596 sequences of our full cohort for learning, and the remaining 20% as 'new' sequences for assigning. False-positives (i.e. of the 'pool' cohort but assigned to a subset, or falsely assigned) and false-negatives (i.e. of a subset but assigned to the 'pool' cohort, or falsely unassigned) were closely inspected. We confirm high levels of average specificity (99.7%), sensitivity (95.2%) and overall accuracy (99.2%). Favoring specificity is by design, due to the potentially important clinical implications of the assignment results.

To evaluate the applicability and robustness of ARResT/AssignSubsets to a real-world situation, we analyzed 459 new sequences from the University of Athens, Greece (now also in IMGT/CLL-DB), a cohort representative of our larger cohort in terms of IGHV gene repertoire and mutational status. Our results confirmed the published incidence of major subsets (~12%), with 48/459 (10.5%) sequences assigned to 15/19 major subsets. Subsets 1 and 4 acquired almost half of the new assignments (13 and 10 cases, respectively), as expected, while subset 2 was under-represented in this Mediterranean population, confirming geographic biases (Ghia *et al.*, 2005).

4 Conclusions

CLL is clinically and biologically heterogeneous, and still incurable, and could benefit from accurate prognostic markers and classifiers, in an effort to implement rationally designed treatment(s). Indeed, studies focusing on major CLL subsets, which, remarkably, describe one in eight CLL patients, have revealed subset-biased biologic and clinical behaviors (Baliakas *et al.*, 2014; Rossi *et al.*, 2009; Stamatopoulos *et al.*, 2007). ARResT/AssignSubsets is an important step towards enabling scientists to tap into this expanding knowledge in a robust and standardized way.

Acknowledgements

We thank the IgCLL group [igcll.org], the IMGT® [imgt.org], the IMGT/CLL-DB initiative, and Prof. P. Panagiotidis, University of Athens.

Funding

V.Bystry, V. Bikos and N.D. by CEITEC MU, SuPReMMe, SYLICA, ESHLO::EuroClonality, FP7 NGS-PTL/2012-2015/no.306242, Czech Ministry of Education, Youth and Sports (2013–2015, no.7E13008); A.A. by Associazione Italiana per la Ricerca sul Cancro AIRC (Triennial fellowship ‘Guglielmina Lucatello é Gino Mazzega’); A.H. and K.S. by ENosAI (code 09SYN-13-880, co-funded by the EU and the Hellenic GSRT); P.B. by The Swedish Cancer Society, the Swedish Research Council, Uppsala University Hospital, and Lion’s Cancer Research Foundation, Uppsala.

Conflict of Interest: none declared.

References

Agathangelidis,A. *et al.* (2012) Stereotyped B-cell receptors in one-third of chronic lymphocytic leukemia: a molecular classification with implications for targeted therapies. *Blood*, **119**, 4467–4475.

Baliakas,P. *et al.* (2014) Clinical effect of stereotyped B-cell receptor immunoglobulins in chronic lymphocytic leukaemia: a retrospective multicentre study. *Lancet Haematol.*, **1**, e74–e84.

Barrios,Y. *et al.* (2004) Length of the antibody heavy chain complementarity determining region 3 as a specificity-determining factor. *J. Mol. Recogn.*, **17**, 332–338.

Damle,R.N. *et al.* (1999) Ig V gene mutation status and CD38 expression as novel prognostic indicators in chronic lymphocytic leukemia. *Blood*, **94**, 1840–1847.

Darzentas,N. and Stamatopoulos,K. (2013) Stereotyped B cell receptors in B cell leukemias and lymphomas. *Methods Mol. Biol.*, **971**, 135–148.

Darzentas,N. *et al.* (2010) A different ontogenesis for chronic lymphocytic leukemia cases carrying stereotyped antigen receptors: molecular and computational evidence. *Leukemia*, **24**, 125–132.

Ghia,P. *et al.* (2005) Geographic patterns and pathogenetic implications of IGHV gene usage in chronic lymphocytic leukemia: the lesson of the IGHV3-21 gene. *Blood*, **105**, 1678–1685.

Giudicelli,V. *et al.* (2011) IMGT/V-QUEST: IMGT standardized analysis of the immunoglobulin (IG) and T cell receptor (TR) nucleotide sequences. *Cold Spring Harbor Protoc.*, **2011**, 695–715.

Hamblin,T.J. *et al.* (1999) Unmutated Ig V(H) genes are associated with a more aggressive form of chronic lymphocytic leukemia. *Blood*, **94**, 1848–1854.

Kirkham,P.M. *et al.* (1992) Immunoglobulin VH clan and family identity predicts variable domain structure and may influence antigen binding. *EMBO J.*, **11**, 603–609.

Lefranc,M.P. (2014) Immunoglobulin and T cell receptor genes: IMGT((R)) and the birth and rise of immunoinformatics. *Front. Immunol.*, **5**, 22.

Rossi,D. *et al.* (2009) Stereotyped B-cell receptor is an independent risk factor of chronic lymphocytic leukemia transformation to Richter syndrome. *Clin. Cancer Res.*, **15**, 4415–4422.

Stamatopoulos,K. *et al.* (2007) Over 20% of patients with chronic lymphocytic leukemia carry stereotyped receptors: pathogenetic implications and clinical correlations. *Blood*, **109**, 259–270.

Bioinformatics, 33(3), 2017, 435–437
doi: 10.1093/bioinformatics/btw634
Advance Access Publication Date: 13 October 2016
Applications Note

Sequence analysis

ARResT/Interrogate: an interactive immunoprofiler for IG/TR NGS data

Vojtech Bystry[1,†], Tomas Reigl[1,†], Adam Krejci[1,2,†], Martin Demko[1], Barbora Hanakova[1], Andrea Grioni[1,3], Henrik Knecht[4], Max Schlitt[4], Peter Dreger[5], Leopold Sellner[5], Dietrich Herrmann[4], Marine Pingeon[6], Myriam Boudjoghra[6], Jos Rijntjes[7], Christiane Pott[4], Anton W. Langerak[8], Patricia J. T.A. Groenen[7], Frederic Davi[6], Monika Brüggemann[4] and Nikos Darzentas[1,]* also on Behalf of EuroClonality-NGS

[1]CEITEC – Central European Institute of Technology, Masaryk University, Brno, Czech Republic, [2]RECAMO, Masaryk Memorial Cancer Institute, Brno, Czech Republic, [3]Centro Ricerca Tettamanti, Clinica Pediatrica, Università di Milano-Bicocca, Ospedale San Gerardo/Fondazione MBBM, Monza, Italy, [4]Department of Hematology, University Hospital Schleswig-Holstein, Campus Kiel, Kiel, Germany, [5]Department of Medicine V, University Hospital Heidelberg, Heidelberg, Germany, [6]Department of Hematology, Hopital Pitié-Salpêtrière and Pierre et Marie Curie University, Paris, France, [7]Department of Pathology, Radboud University Nijmegen Medical Center, Nijmegen, The Netherlands and [8]Department of Immunology, Erasmus MC, University Medical Center, Rotterdam, The Netherlands

*To whom correspondence should be addressed.

[†]The authors wish it to be known that, in their opinion, the first three authors should be regarded as Joint First Authors.

Associate Editor: Inanc Birol

Received on January 28, 2016; revised on September 9, 2016; accepted on September 29, 2016

Abstract

Motivation: The study of immunoglobulins and T cell receptors using next-generation sequencing has finally allowed exploring immune repertoires and responses in their immense variability and complexity. Unsurprisingly, their analysis and interpretation is a highly convoluted task.

Results: We thus implemented ARResT/Interrogate, a web-based, interactive application. It can organize and filter large amounts of immunogenetic data by numerous criteria, calculate several relevant statistics, and present results in the form of multiple interconnected visualizations.

Availability and Implementation: ARResT/Interrogate is implemented primarily in R, and is freely available at http://bat.infspire.org/arrest/interrogate/

Contact: nikos.darzentas@gmail.com

Supplementary information: Supplementary data are available at *Bioinformatics* online.

1 Introduction

Immunoglobulins (IG) and T cell receptors (TR) are highly adaptive molecular receptors responsible for antigen recognition in immunological responses. Fundamental to their adaptiveness is their enormous inherent variability, achieved through stochastic processes during B and T cell maturation. The advent of high-throughput profiling of IG and TR repertoires (Benichou *et al.*, 2012) has been instrumental for understanding normal and pathologic immune responses, which include a wide range of diseases with an underlying immune cause. This unprecedented capability has also brought along novel and unique challenges.

The first task of immunoprofiling is sequence annotation, such as which variable (V), diversity (D) and joining (J) genes have been rearranged, or what is the sequence of the hypervariable complementarity-determining region 3 (CDR3). IMGT® (Lefranc *et al.*, 2015) is the global reference in the field of antigen receptor sequence analysis and immunogenetic annotation.

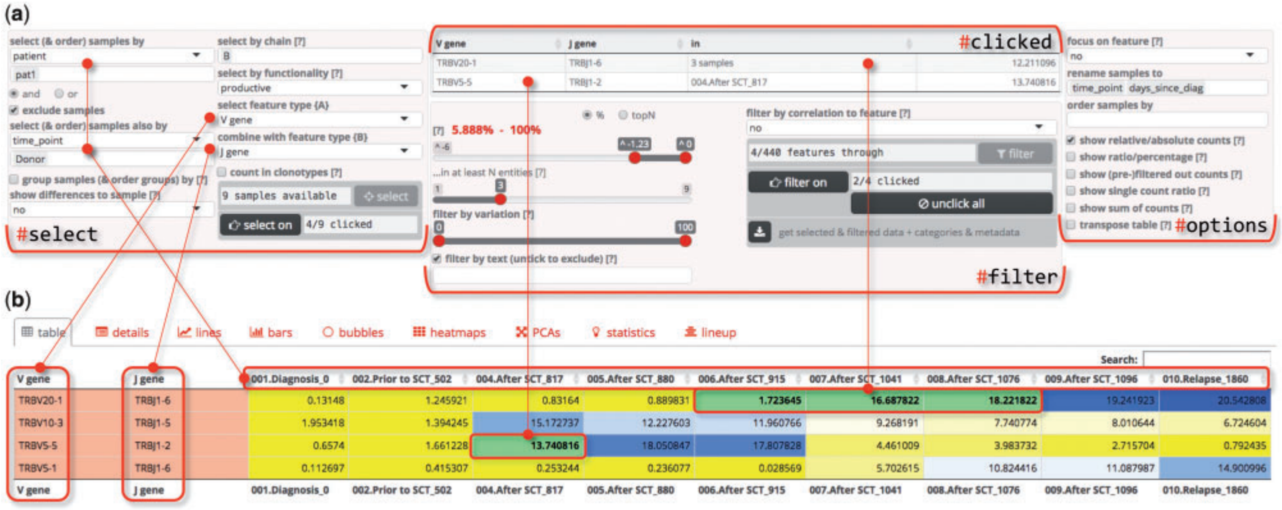

select (& order) samples by: patient
pat1
● and ○ or
☑ exclude samples
select (& order) samples also by: time_point
Donor
☐ group samples (& order groups) by [?]
show differences to sample [?]: no
select by chain [?]: B
select by functionality [?]: productive
select feature type {A}: V gene
combine with feature type {B}: J gene
☐ count in clonotypes [?]
9 samples available
select
select on 4/9 clicked

V gene	J gene	in	
TRBV20-1	TRBJ1-6	3 samples	12.211096
TRBV5-5	TRBJ1-2	004.After SCT_817	13.740816

● % ○ topN
[?] 5.888% - 100%
^-6 ^-1.23 ^0
...in at least N entities [?]: 1 3 9
filter by variation [?]: 0 100
☑ filter by text (untick to exclude) [?]
filter by correlation to feature [?]: no
4/440 features through
filter
filter on 2/4 clicked
unclick all
get selected & filtered data + categories & metadata

focus on feature [?]: no
rename samples to: time_point days_since_diag
order samples by
☑ show relative/absolute counts [?]
☐ show ratio/percentage [?]
☐ show (pre-)filtered out counts [?]
☐ show single count ratio [?]
☐ show sum of counts [?]
☐ transpose table [?]

V gene	J gene	001.Diagnosis_0	002.Prior to SCT_502	004.After SCT_817	005.After SCT_880	006.After SCT_915	007.After SCT_1041	008.After SCT_1076	009.After SCT_1096	010.Relapse_1860
TRBV20-1	TRBJ1-6	0.13148	1.245921	0.83164	0.889831	1.723645	16.687822	18.221822	19.241923	20.542808
TRBV10-3	TRBJ1-5	1.953418	1.394245	15.172737	12.227603	11.960766	9.268191	7.740774	8.010644	6.724604
TRBV5-5	TRBJ1-2	0.6574	1.661228	13.740816	18.050847	17.807828	4.461009	3.983732	2.715704	0.792435
TRBV5-1	TRBJ1-6	0.112697	0.415307	0.253244	0.236077	0.028569	5.702615	10.824416	11.087987	14.900996
V gene	J gene	001.Diagnosis_0	002.Prior to SCT_502	004.After SCT_817	005.After SCT_880	006.After SCT_915	007.After SCT_1041	008.After SCT_1076	009.After SCT_1096	010.Relapse_1860

Fig. 1. The controls panel (**a**) with the table view (**b**). (a) The controls panel is divided into 3 parts: select, filter and options. The former two are common for all the visualizations, while options change depending on which visualization view is currently selected. The table ('#clicked') above the filters shows features and samples currently highlighted in the visualizations and it is updated on the fly as the user clicks in the visualizations. (b) In the table, for each feature in a row, abundance values are shown in columns of samples. Cells with features are colored in groups (in this case by receptor and chain i.e. 'TRB'), cells with abundance values are colored in a heatmap-like fashion (Color version of this figure is available at *Bioinformatics* online.)

Mining these inherently complex immunogenetic annotations of usually millions of reads and tens to hundreds of samples for biologically relevant information is a non-trivial task. There is an increasing number of published software applications to tackle this challenge, all with their unique features and advantages, but also limitations like limited interactivity (Alamyar *et al.*, 2012; Shugay, 2015) or scope restricted to repertoire studies (Moorhouse *et al.*, 2014) or minimal residual disease (MRD) monitoring (Giraud *et al.*, 2014).

In this work, we put together in one application features and functionalities we believe are needed for wide-ranging *in silico* immunoprofiling. These insights are a result of collaborative efforts within the EuroClonality-NGS consortium, which strives to develop, standardize and validate *in vitro* assays and bioinformatics for IG/TR NGS analysis.

2 Methods

ARResT/Interrogate is primarily based on R and Shiny, a framework for user interactivity and web-based accessibility. The analytical core relies on the 'data.table' R package for efficient data handling based on advanced indexing techniques. Therefore, ARResT/Interrogate is able to maintain sufficient responsiveness even with datasets of tens of thousands of clonotypes from millions of reads and dozens of samples.

ARResT/Interrogate has four step-wise functions: input processing, data selection and filtering, comparative calculations and visualization.

2.1 Input processing

An integrated parser processes multiple IMGT/HighV-QUEST runs and their major immunogenetic annotations. Of these, the V, D and J genes and alleles are combined with the amino acid sequence of the junction (which encompasses the CDR3) to construct IMGT-like clonotypes (Li *et al.*, 2013). These annotations are referred to as 'feature types' and their corresponding individual values as 'features'; for example, feature type 'V gene' contains feature 'TRBV20-1' (Fig. 1).

2.2 Data selection and filtering

Users can annotate samples with arbitrary metadata (e.g. patient data, sampling dates) and use these to select and group samples of interest. The next necessary step is to select feature types to focus on. This creates a table of abundance per feature per sample, with abundance expressed as relative or absolute count of reads or clonotypes. Individual features can be filtered in or out using a combination of four filters: abundance, variation across samples, correlation of abundance profiles across samples, and text regular expression (see Supplementary Section S2.1).

2.3 Comparative calculations

ARResT/Interrogate can calculate and visualize differences between samples and features. Samples are compared on the basis of the abundance of a single feature (e.g. TRBV20-1), or an entire feature type (e.g. V gene). Features are compared on the basis of their abundance distributions across samples. Groups of samples can also be statistically compared, for example, to assess immunogenetic differences before and after therapy (S2.3). ARResT/Interrogate can also perform principal component analyses (PCA) of samples and features.

2.4 Visualization

Interactive views include tables; line charts, suitable for time-series analyses of clonal kinetics including MRD monitoring; bar charts, popular in clonality testing for lymphoma diagnostics; bubble charts; heatmaps, for sample-sample distance and sample-feature distributions; PCA scatterplots; statistical plots; and multiple sequence alignments. Customizing the visualizations (Fig. 1a, #options) includes changing axis properties like values, labels, scales, orientation; and using extra virtual features such as sums of abundances. Interactivity includes zooming, feature highlighting or hiding, and tooltips with detailed information on any data point. Finally, visualizations are interconnected, with features selected in one automatically highlighted in others.

3 Results

Results from the validation and the expert evaluation of ARResT/Interrogate based on actual research data, as well as a running example, are available in the Supplementary Material.

4 Conclusions

We presented ARResT/Interrogate, an interactive data manipulation and visualization application for NGS-based immunoprofiling. It offers a wide variety of options and aims to serve as a user-friendly platform with flexible and powerful analytical capabilities.

Acknowledgements

Computational resources in CEITEC MU were provided by MetaCentrum (LM2010005), and CERIT-SC (CERIT Scientific Cloud, Operational Program Research and Development for Innovations, Reg. no. CZ.1.05/3.2.00/08.0144).

Funding

Authors from CEITEC MU were supported by research grant AZV-MZ-CR 16-34272A-4/2016, project CEITEC 2020 (LQ1601) and ESLHO::EuroClonality, and an OVC Pet Trust Research Grant with the University of Guelph (051699); A.K. was additionally supported by project MEYS-NPS I-LO1413.

Conflict of Interest: none declared.

References

Alamyar,E. *et al*. (2012) IMGT/HighV-QUEST: the IMGT® web portal for immunoglobulin (IG) or antibody and T cell receptor (TR) analysis from NGS high throughput and deep sequencing. *Immunome Res*., **8**, 26.

Benichou,J. *et al*. (2012) Rep-Seq: uncovering the immunological repertoire through next-generation sequencing. *Immunology*, **135**, 183–191.

Giraud,M. *et al*. (2014) Fast multiclonal clusterization of V(D)J recombinations from high-throughput sequencing. *BMC Genomics*, **15**, 409.

Lefranc,M.P. *et al*. (2015) IMGT®, the international ImMunoGeneTics information system® 25 years on. *Nucleic Acids Res*., **43**, D413–D422.

Li,S. *et al*. (2013) IMGT/HighV QUEST paradigm for T cell receptor IMGT clonotype diversity and next generation repertoire immunoprofiling. *Nat. Commun*., **4**, 2333.

Moorhouse,M. *et al*. (2014) ImmunoGlobulin galaxy (IGGalaxy) for simple determination and quantitation of immunoglobulin heavy chain rearrangements from NGS. *BMC Immunology*, **15**.

Shugay,M. 2015. VDJtools: a framework for post-analysis of repertoire sequencing data. Release 1.0.4

Clinical Immunology 183 (2017) 8–16

Contents lists available at ScienceDirect

Clinical Immunology

journal homepage: www.elsevier.com/locate/yclim

High resolution IgH repertoire analysis reveals fetal liver as the likely origin of life-long, innate B lymphopoiesis in humans

Anindita Roy [a,1], Vojtech Bystry [b,1], Georg Bohn [c], Katerina Goudevenou [c], Tomas Reigl [b], Maria Papaioannou [c], Adam Krejci [c,d], Sorcha O'Byrne [a], Aristeidis Chaidos [c], Andrea Grioni [a,e], Nikos Darzentas [b], Irene A.G. Roberts [a,f,**,1], Anastasios Karadimitris [c,*,1]

[a] *Department of Paediatrics, University of Oxford, Brno, Czech Republic*
[b] *CEITEC - Central European Institute of Technology, Masaryk University, Brno, Czech Republic*
[c] *Centre for Haematology, Department of Medicine, Imperial College London, Imperial College Healthcare NHS Trust, Hammersmith Hospital, London, UK*
[d] *RECAMO, Masaryk Memorial Cancer Institute, Brno, Czech Republic*
[e] *Centro Ricerca Tettamanti, Clinica Pediatrica, Università di Milano-Bicocca, Ospedale San Gerardo/Fondazione MBBM, Monza, Italy*
[f] *MRC Molecular Haematology Unit, Weatherall Institute of Molecular Medicine, University of Oxford and BRC Blood Theme, NIHR Oxford Biomedical Centre, Oxford, UK*

ARTICLE INFO

Article history:
Received 15 May 2017
Received in revised form 16 June 2017
Accepted with revision 16 June 2017
Available online 20 June 2017

Keywords:
Human
Fetal
IgH repertoire

ABSTRACT

The ontogeny of the natural, public IgM repertoire remains incompletely explored. Here, high-resolution immunogenetic analysis of B cells from (unrelated) fetal, child, and adult samples, shows that although fetal liver (FL) and bone marrow (FBM) IgM repertoires are equally diversified, FL is the main source of IgM natural immunity during the 2nd trimester. Strikingly, 0.25% of all prenatal clonotypes, comprising 18.7% of the expressed repertoire, are shared with the postnatal samples, consistent with persisting fetal IgM+ B cells being a source of natural IgM repertoire in adult life. Further, the origins of specific stereotypic IgM+ B cell receptors associated with chronic lymphocytic leukemia, can be traced back to fetal B cell lymphopoiesis, suggesting that persisting fetal B cells can be subject to malignant transformation late in life. Overall, these novel data provide unique insights into the ontogeny of physiological and malignant B lymphopoiesis that spans the human lifetime.

1. Introduction

Mature B-cell development in humans starts in the fetal liver (FL) in early fetal life, and becomes well established at this site by the start of the second trimester [1,2]. Subsequently, during the second trimester, bone marrow (BM) becomes the main site of B lymphopoiesis [3] and remains so throughout post-natal life.

Development of mature B-cells depends upon, and proceeds commensurately with expression of a functional B-cell receptor (BCR) and of its constituent immunoglobulin (Ig) heavy(H) and light(L) chains. The molecular hallmark of B-cell development, somatic recombination of the genes that encode the IGH(V, D and J) and IGL(V and J) chains, takes place in early B-cell progenitors in primary B lymphopoiesis sites (i.e. FL, FBM and adult BM). This ensures the first wave of Ig repertoire diversification, with antigen specificity primarily encoded by the complementarity determining region 3 (CDR3). This process is a pre-requisite for efficient humoral immunity, even early in fetal life [4]. The first mature B-cells that emerge from FL and FBM are transitional B-cells that co-express IgM, IgD and CD10 [5,6]. Transitional B-cells mature into CD10neg naïve B-cells that express less IgM. In postnatal life, but not fetal life, naïve B-cells enter a germinal centre reaction in secondary lymphoid organs, undergoing isotype class switch to IgG/IgA and somatic hypermutation, a process that ensures the second wave of Ig repertoire diversification and the production of high affinity soluble antibodies. By contrast, the majority of the fetal life IgM repertoire comprises antibodies that are self- and poly-reactive [7]. This so called ‘natural’ IgM antibody repertoire is public, i.e., shared by different individuals at birth and is present in adult life as part of the normal, non-pathogenic innate Ig repertoire, albeit at lower frequencies than in the newborn [8,9]. Self-reactive and poly-reactive IgM antibodies, and in particular those using the IGHV6-1 gene, are dominant in FL B-cells [10]. In adult life, self-reactive IgM antibodies may play a role in protection from pathogens and autoimmunity [11]. In mice, the natural IgM repertoire is largely linked to B-1a cells which once developed and selected in FL, persist for the animal's lifespan through their ability for self-renewal rather than iterative development and selection [12].

---

* Correspondence to: Anastasios Karadimitris, Centre for Haematology, Imperial College London, 4th Floor, Commonwealth Building, Hammersmith Hospital Campus, Du Cane Road, London W12 0NN, UK.

** Correspondence to: Irene AG Roberts, Department of Paediatrics, University of Oxford, Brno, Czech Republic.

E-mail addresses: irene.roberts@paediatrics.ox.ac.uk (I.A.G. Roberts), a.karadimitris@imperial.ac.uk (A. Karadimitris).

[1] These authors contributed equally.

http://dx.doi.org/10.1016/j.clim.2017.06.005
1521-6616/

Recent evidence suggests that B-1a-like cells also exist in humans and may contribute to the development of the natural IgM repertoire [13].

Profiling of the expressed IgH gene repertoire at mRNA level has helped to understand the dynamics of humoral immunity development. However, the relationship of the fetal B-cell IgM repertoire to post-natal child and adult B-cells is incompletely understood and has mostly been approached by low-throughput analyses [14, 15]. A recent high-throughput study of the IgH repertoire of circulating fetal blood B-cells provided some insights into Ig repertoire ontogeny [16]. However, the spatiotemporal relationship between the IgH repertoire in FL with that in FBM, and the impact of the fetal Ig repertoire on the long-term repertoire present in post-natal life, as well as the link between this and the development of disease, are unknown.

Here, to address these issues and to gain insights into the ontogeny of the human innate B-cell repertoire, we take advantage of a high-resolution analysis of the IgH-Cmu repertoire of normal human FL, FBM and post-natal B-cells from healthy infants, young children and adults.

2. Materials and methods

2.1. Samples

Human FL and BM cells (Table S1) were provided by the Human Developmental Biology Resource (www.hdbr.org). Surplus blood from samples collected from healthy children was obtained under national ethics committee approval (MREC12/LO/0425). For each sample, CD34-CD19 + mature B-cells (Table S1) were FACS sorted on BD FACSAriaII (Becton Dickinson, Oxford, UK) for BCR repertoire analysis by 454 sequencing.

2.2. Bioinformatics

To reduce repertoire sampling biases, we included in the analysis only samples with a comparable number of B-cells when possible (Table S1). The raw NGS data were processed, annotated with germline sequences from IMGT® and/or using IMGT/V-QUEST and IMGT/HighV-QUEST (http://www.imgt.org), and analysed through ARResT/Interrogate [17]. As part of ARResT/Interrogate, and with the use of the R language for statistical computing [www.R-project.org]: the Jensen-Shannon divergence was used to compute repertoire similarity between pairs of samples; the inverse Simpson concentration [18], which favors abundant clonotypes over rare ones, was used on vectors of clonotype abundances to calculate clonotypic diversity. Sequences were assigned to the 19 major subsets of stereotyped B-cell receptors in chronic lymphocytic leukemia (CLL) using ARResT/AssignSubsets [19].

Further methodological details are provided in Supplementary methods.

3. Results

3.1. High-resolution analysis of fetal and postnatal IgHmu repertoires

For initial assessment of the IgM repertoire ontogeny in FL and FBM B-cells, we analysed flow-sorted CD34-CD19 + B-cells. These express cytoplasmic IgM(mu) and/or surface (s)IgM and comprise pre-B-cells, immature, transitional and naïve B-cells [5,20]. Spectratyping of IGVH-Cmu mRNA IGHV1-IGHV6 amplicons from a 2nd trimester FL sample (gestational age [GA], 15^{+3} weeks), a 2nd trimester FBM sample of the same GA(15^{+3} weeks) and B-cells from healthy children and adults revealed a polyclonal repertoire in both FL and FBM that was comparable to the postnatal samples (Fig. 1a)

To gain further insights into the ontogeny of IgH diversification, we sequenced the IGVH-Cmu mRNA IGHV1-IGHV7 family amplicons from FL, FBM and postnatal samples using next-generation sequencing (NGS) and the 454 technology. In total, 20 libraries generated from 17 individual, flow-sorted CD34-CD19 + B-cell samples were sequenced: 5 FL (4 performed in independent duplicate libraries; GA 14–18 weeks), 3 FBM (GA 13–17 weeks; different fetuses from the FL samples), 3 child peripheral blood (cPB) and 5 adult PB (aPB) B-cell samples. We obtained 117,757 unique clonotypes of which 76%(90,238) were productive, with the remainder representing unproductive rearrangements (Table S1).

Reproducibility was tested by comparing the duplicate libraries from the 4 FL B-cell samples generated and sequenced in 2 independent experiments. Principal component analysis of different combinations of immunogenetic features demonstrated clear demarcation and tight clustering of duplicate pairs (Fig. S1), showing the high degree of accuracy and reproducibility of the assay.

3.2. Diversification of the fetal IGHV, IGHD and IGHJ repertoires

Further dissection of the complexity of IgM repertoire development showed that all 52 member genes of the IGHV1-IGHV7 families were used at varying and often significantly different frequencies in all 4 developmental stages (Fig. 1b and Table S2). In line with previous reports [14–16], the most notable difference in IGHD genes usage frequency was the >10 fold higher IGHD7-27 frequency in fetal compared to postnatal samples (Fig. 1c). The pattern of IGHJ repertoire usage was nearly identical between FL and FBM, and between cPB and aPB B-cells. IGHJ4 was the most frequently used J gene in all developmental stages (Fig. 1d) and, consistent with previous reports [15,16], there was reciprocal presence of 4 IGHJ genes: IGHJ6 and IGHJ2 were significantly over-represented in postnatal B-cells ($p < 0.001$), while IGHJ3 and IGHJ5 were significantly over-represented in fetal B-cells ($p < 0.001$; Fig. 1d). Finally, as previously described [15,16], average CDR3 length was significantly shorter in fetal than postnatal B-cells, 14.8 amino acids (aa) vs. 17.3aa ($p = 0.001$; Fig. 1e)

These data show the molecular mechanisms responsible for VDJ recombination-dependent repertoire diversification are active and efficient early in B-cell development in both FL and FBM and that on a qualitative level, comparably diversified B-cell lymphopoiesis exists contemporaneously in FL and FBM.

3.3. Evidence of antigen-driven clonotypic expansions in FL B-cells

Antibodies produced by the fetus are mostly IgM and are self- and poly-reactive; however, the source of fetal IgM in FL or FBM B-cells is not known. Hypothesising that B-cells producing IgM would have undergone clonotypic expansion in response to self-antigenic stimulus, we sought to identify such expansions by studying the 100 most abundant clonotypes in each stage. Mean clonotype abundance of the top 100 most abundant clonotypes in each of the 4 stages, was 10-fold lower in FBM B-cells (0.12%) than in FL B-cells (1.2%, $p < 0.0001$), while corresponding abundances in postnatal PB B-cells were intermediate (cPB: 0.54%; aPB: 0.41%; Fig. 2a). Reflecting the paucity of expanded clonotypes amongst FBM B-cells, analysis of the 100 most abundant clonotypes from across all 4 stages (i.e., 100 of 90,238 clonotypes, Table S1) showed that none were present in FBM, compared to 65 in FL, 23 in cPB, and 12 in aPB B-cells (Fig. 2b)

To assess clonotypic expansion and diversity in individual stages, we estimated the inverse Simpson concentration of the clonotypic repertoires [18]. We found that FL clonotypes are the least diverse, followed by cPB and aPB, while FBM showed significantly higher clonotypic diversity compared to the other groups ($p < 0.001$; Fig. 2c).

Together these results are consistent with robust IgM B-cell clonotypic expansions being prominent in FL and nearly absent in FBM of the same GA, and support the notion that the FL B-cells are the main source of fetal IgM production during the 2nd trimester.

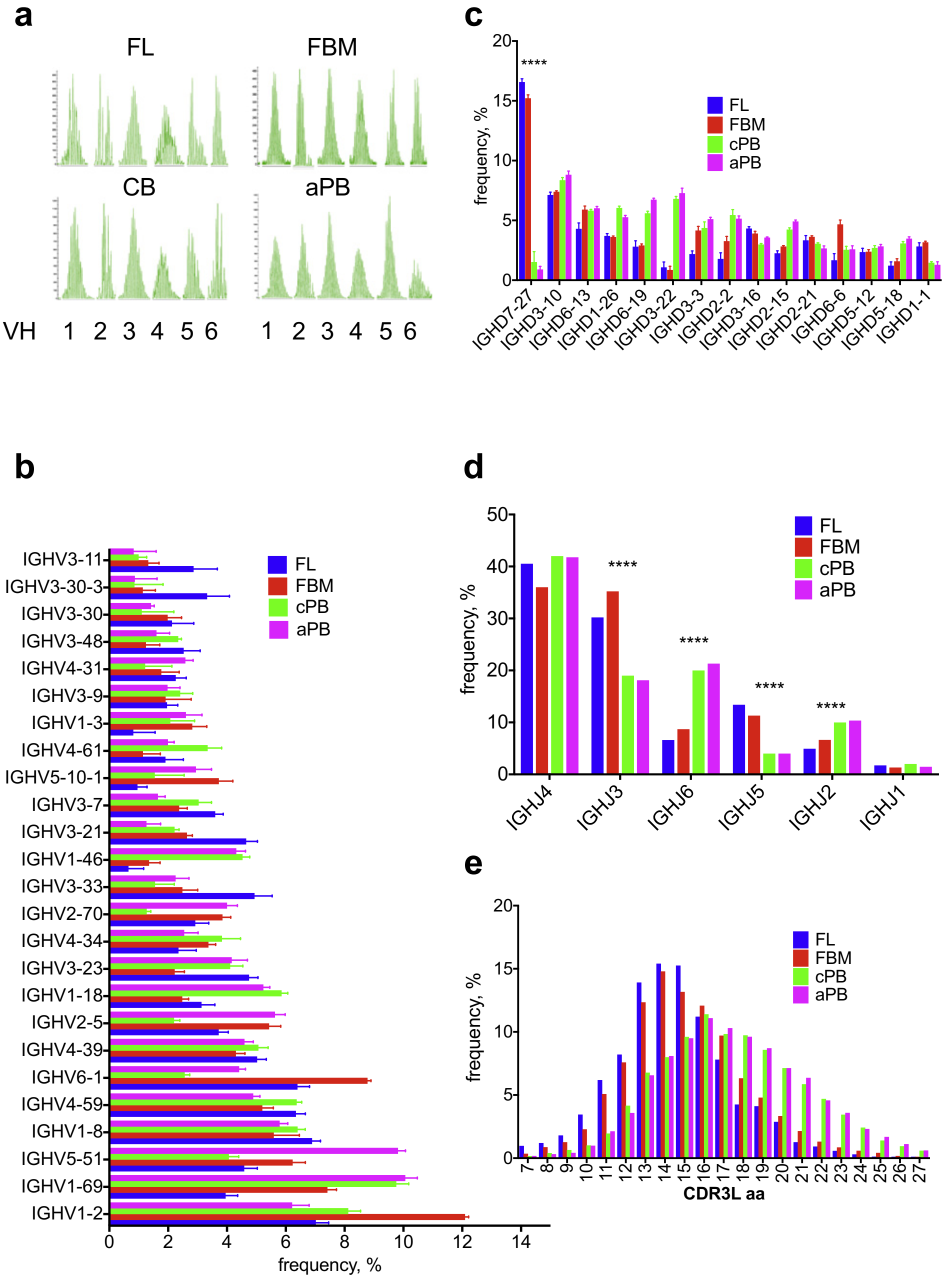

Fig. 1. Diversification features of fetal B cell repertoire. a. Spectratyping analysis of IGHV1-6 families in fetal liver (FL) GA 15^{+3} weeks, fetal bone marrow (FBM) GA 15^{+3} weeks, cord blood (CB) and adult peripheral blood (aPB) B-cells. b. IGHV gene (the top 25 out of 52 VH genes are shown) c. IGHD gene (the top 15 out of total 25 JH genes are shown) d. IGHJ gene and e. CDR3 aa length repertoires counted in unique clonotypes in the 4 different fetal and postnatal developmental stages (cPB: child peripheral blood). b–e: mean values with SD are shown, except in d & e where error bars are omitted for simplicity. (***$p < 0.001$, ****$p < 0.0001$).

3.4. Convergent recombination in fetal B-cells

We sought further evidence of antigen-driven responses amongst fetal B-cells by studying their clonotypes in detail, focusing first on clonotypes shared between the duplicate FL libraries to mitigate against possible PCR/sequencing artefacts. All 4 duplicate FL libraries showed evidence of distinct VDJ rearrangements encoding identical CDR3 peptide regions, involving 95–185 clonotypes (1.9–9.3% of all unique clonotypes per library; Table S3). Notably, these CDR3 regions were identical both at the aa and nucleotide level using either different IGHV or IGHD genes, but always the same IGHJ gene (Tables S4 & S5). This strikingly precise selection of CDR3 regions, previously termed convergent recombination, has been described for T-cell receptor repertoire [21,22] and recently in murine B-1a cells [23]. We investigated this further by systematically searching for multiple IGHV genes recombined to an identical CDR3 aa sequence in all samples. Across all stages we found evidence of hundreds of CDR3 sequences recombined with 2–4 different IGHV genes, with up to 9 different IGHV genes identified (Fig. 2d); in nearly all cases this involved genes of the same IGHV family. Detailed sequence analysis (Table S5) highlights the unambiguous assignment of respective germline sequences with no signs of PCR hybrids. Importantly, CDR3 sequences involved in convergent recombinations were most abundant in FL and cPB (Fig. 2d) in line with their increased incidence of prominent clonotypic expansions (Fig. 2a–c)

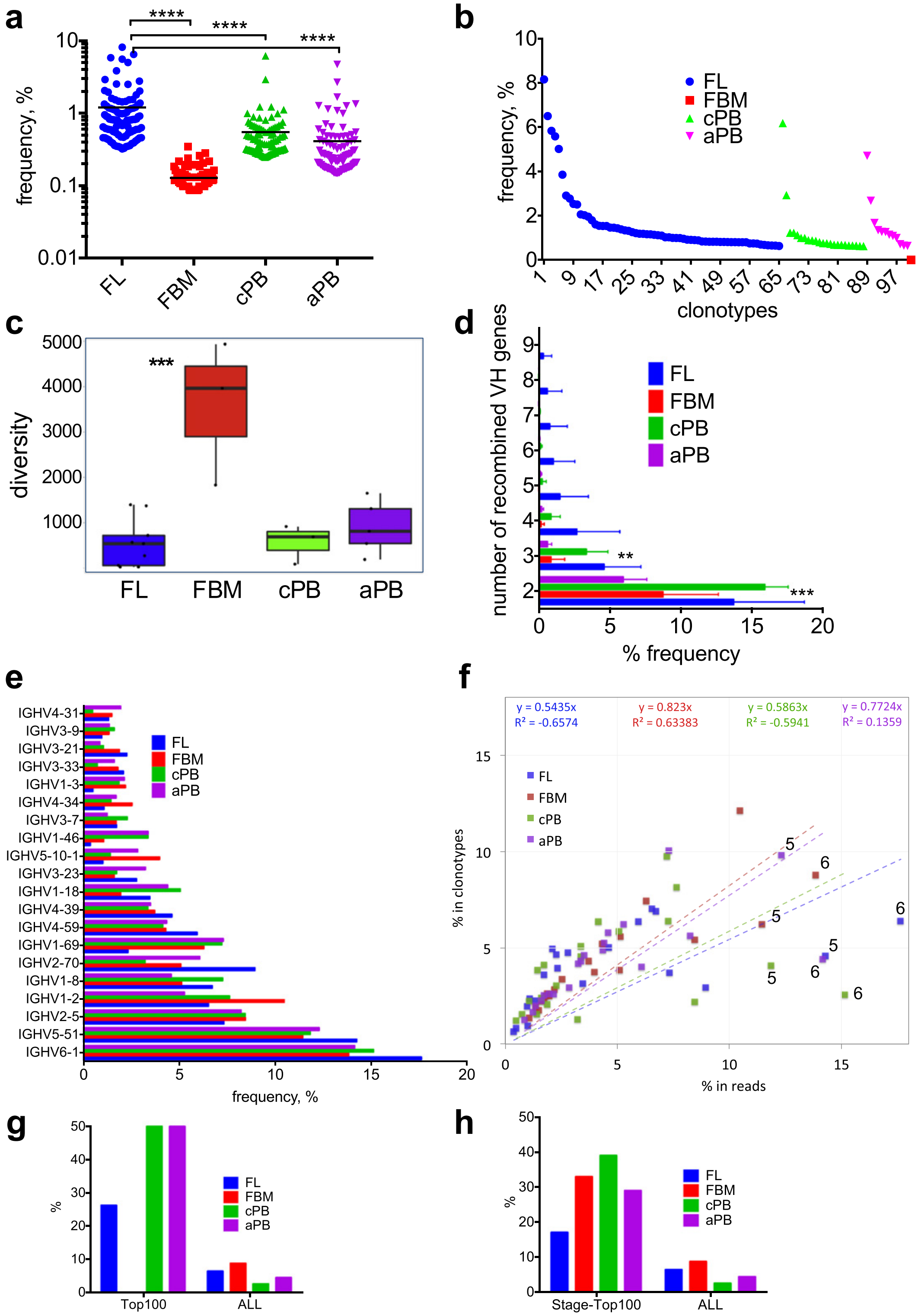

Fig. 2. Clonotypic abundance and diversity in fetal and post-natal B-cells. a. Frequency (abundance counted in reads) of the 100 most abundant clonotypes in each developmental stage (horizontal lines indicate mean values, ****$p < 0.0001$). b. Distribution of the 100 most abundant clonotypes across the 4 developmental stages. c. Clonotypic diversity in each developmental stage as assessed by the inverse Simpson concentration (see Methods). ***$p < 0.001$ for FBM as the most diverse. d. Frequency of CDR3 peptides generated by convergent recombination of 2–9 different IGHV genes in each developmental stage. ** and *** for $p < 0.01$ and $p < 0.001$ respectively for FL and cPB vs. FBM and aPB. e. IGHV gene repertoire counted in reads in fetal and postnatal B-cells. Mean values are shown (error bars omitted for simplicity). f. Correlation of the relative clonotype abundances of the 20 most popular IGHV genes across developmental stages with their corresponding relative read counts. Lower slopes (as indicated by 'y' values in respective colors) of the regression lines for FL and cPB indicate the predominance of high abundance clonotypes in these developmental stages. '5' and '6': outlying and highly expressed IGHV5-51 and IGHV6-1 respectively. g & h. IGHV6-1 usage in the 100 most abundant clonotypes across developmental stages (g), and in the 100 most abundant clonotypes in each developmental stage (h); these "Top100" frequencies are compared to those of IGHV6-1 usage in all clonotypes ("ALL").

Therefore, convergent recombination, a process that ensures generation of a high abundance public immune repertoire in T-cells [21,24], also appears to shape the early fetal B-cell repertoire.

3.5. Abundant IGHV6-1 repertoire across developmental stages

To investigate whether repertoire complexity is influenced by biases in specific IGHV family member usage, we compared the rankings of IGHV genes by their frequency of unique clonotypes (i.e. counting in unique clonotypes; Fig. 1b) and abundance (i.e. counting in sequence reads; Fig. 2e). IGHV6-1 and IGHV5-51 were the 1st and 2nd most expressed genes across all 4 developmental stages; however, both genes ranked lower when counted in unique clonotypes, especially in postnatal samples. Fig. 2f correlates relative clonotype abundances of the 20 most popular IGHV genes across developmental stages with their corresponding relative read counts. Expecting these two measures to be linearly correlated, outliers should highlight IGHV genes with highly/lowly-expressed clonotypes. We found that in all 4 developments stages, IGHV6-1 and IGHV5-51 are placed the furthest from their projected linear distribution and strongly biased towards high expression. Therefore, although IGHV6-1 and IGHV5-51 genes did not have the most associated clonotypes, they are the most likely to participate in high abundance, expanded clonotypes. At a global level, the lower slopes of the regression lines for FL and cPB are also consistent with the higher frequency of high abundance clonotypes in those samples

We then focused on IGHV6-1 as this has previously been shown to be over-represented in fetal B-cells beyond its expected frequency of ~1.9% (i.e., 1/52) [25–27]. Fetal IGHV6-1 IgM BCRs have been reported to react against ssDNA and cardiolipin autoantigens, and are thus important sources of natural IgM [10]. We confirmed that although the relative frequency of IGHV6-1 in unique clonotypes was not higher than the expected 1.9% in FL and FBM (Fig. 1b), its abundance was indeed significantly higher (18% and 14% respectively; $p = 0.002$; Fig. 2e) with similar trends in cPB and aPB. Supporting this, IGHV6-1 was identified in 17/65(26.2%) FL, 11/23(50%) cPB and 6/12(50%) aPB of the 100 most expanded clonotypes across all 4 stages (Fig. 2g). Similarly, within each developmental stage, IGHV6-1 comprised 17, 33, 39 and 29 of the 100 most abundant clonotypes respectively (Fig. 2h), significantly higher frequencies ($p < 0.01$) than their respective average unique clonotype frequencies (6.4, 8.7, 2.5 and 4.4%). Thus, IGHV6-1 clonotypic expansions are dominant in all developmental stages, highlighting an important role of IGHV6-1 IgM in innate humoral immunity throughout life.

3.6. Presence of antigen response-competent mature B-cells in FL but not FBM

The high frequency of expanded clonotypes in FL but not FBM suggests that in fetal life it is the FL rather than FBM B-cells that mount (auto-)antigen-driven responses, despite being equally diversified by VDJ recombination. To investigate this further, we compared the frequencies of B-cell sub-populations within the CD34-CD19+ compartment in FL and FBM using previously described markers especially those defining fetal B cell subsets where available [5,6,20,28,29] (see Supplementary methods). While pre-B-cells lack (s)IgM expression, immature B-cells, transitional and naïve B-cells express (s)IgM (Fig. 3a, b). Compared to FL, the FBM CD34-CD19+ compartment had a higher frequency of pre-B-cells (FL: 52.7 ± 5.4% vs. FBM: 69.2 ± 1.5%, $p < 0.01$) but a similar frequency of immature B-cells (30.7 ± 4.6% vs. 21.0 ± 1.6%), while transitional and naïve B-cells were significantly decreased in FBM (FL: 4.2 ± 0.8% vs. FBM: 1.5 ± 0.4%, $p < 0.01$; and FL: 2.8 ± 0.9% vs. FBM: 0.7 ± 0.2%, $p < 0.05$; Fig. 3c). This lack of developed mature B-cells explains, at least in part, the paucity of clonotypic expansions in 2nd trimester FBM. Of the three sIgM+ B-cell populations (immature, transitional and naïve) we used for IgHmu repertoire profiling, only the transitional B-cell subset was previously shown to expand in response to antigen in a T-cell-independent fashion. Indeed, transitional B-cells are enriched in autoreactive B-cells in normal individuals and more so in patients with systemic lupus erythematosus [30]. Thus, we speculate that transitional B-cells are likely to be the main source of the FL IgM clonotypic expansions and, in contrast to previous reports [4,31], we found a very low frequency of CD34-CD19+CD27+ B-cells in 2nd trimester FL and FBM (range 0–1.9% of total CD34-CD19+ B-cells, median 0.06%). (Fig. 3b & c).

3.7. High abundance FL clonotypes shared across developmental stages

To explore continuity in IgM B-cell immunity between fetal and adult life, we searched for clonotypes shared within and between developmental stages. Overall 0.13% (122/90,238) of productive clonotypes were shared, with none shared by >2 developmental stages (Fig. 4a); 15 were shared between FL and FBM (expressed as 0.37% and 0.22% of reads respectively) (Fig. 4b and Table S6), suggesting selection of B-cells by the same antigen can occur independently in FL or FBM, or possibly migration of B-cells between sites; 2 clonotypes were shared between cPB and aPB B-cells (not shown); 22 of the total FL IgH expressed repertoire (Table S7) were shared between FL (16.3% of reads) and postnatal B-cells (0.92% of reads; Fig. 4c); and 83 were shared between FBM (2.3% of reads) and either cPB (59; 0.85% of reads) or aPB (24; 1.13% of reads; Fig. 4d, Table S8).

Reflecting the high abundance clonotypes in FL, the mean abundance of clonotypes shared between FL and postnatal B-cells was 38-fold higher than FBM (0.77% vs. 0.02%, $p = 0.001$; Fig. 4e), highlighting sharing of only high abundance clonotypes between FL and postnatal B-cells (Fig. 4e). Indeed, 10/22 clonotypes shared between FL and postnatal B-cells were also amongst the 100 most abundant clonotypes across all developmental stages (Fig. 2b, Table S7) and 16/22 shared clonotypes were 41-fold more abundant in FL B-cells than in postnatal B-cells (median 0.36% vs. 0.005%, $p < 0.0001$; Fig. 4f). Notably, 5/22 FL-postnatal shared clonotypes, corresponding to 2 individual CDR3 sequences, had evidence of convergent recombination (Table S7), supporting the notion that clonotypic expansions shared between fetal and post-natal IgM B-cell repertoires are antigen-driven.

Together, these observations are consistent with a fully functional FL IgM repertoire in which B-cell clonotypic expansions are robust and likely to be antigen-driven. The presence of identical clonotypes in fetal and postnatal B-cells might be the result of independent selection at different developmental stages in different individuals or, more likely, selection during fetal life and subsequent persistence in postnatal life. Further, the higher abundance of some shared clonotypes in postnatal compared to FL B-cells indicates that IgM-producing B-cells of FL origin remain functional in postnatal life and retain their ability to expand in response to recurrent antigenic stimulation. Finally, the unexpected degree of clonotype sharing (0.25% of the entire fetal IgM repertoire) between fetal and postnatal B-cells derived from samples that are HLA-disparate suggests that the selection of these shared (public) clonotypes occurs in an HLA- and thus T-cell-independent manner consistent with IgM innate humoral immune responses.

3.8. Fetal BCR repertoire and malignancy-associated stereotypic receptors

Our results so far suggest that fetal IgM-producing B-cells may persist into adult life and remain under antigenic stimulation throughout life, potentially increasing their risk of neoplastic transformation. Stereotypic (or quasi-identical) IgM BCR are known to be part of the normal adult B-cell repertoire (enriched in IgM+CD5+ B-cells in particular [32]) and, importantly, they have also been demonstrated in ~30% of patients with chronic lymphocytic leukemia (CLL), one of the most common IgM+ mature B cell malignancies in humans [33–36]. Nevertheless, their developmental origins and ontogeny have not

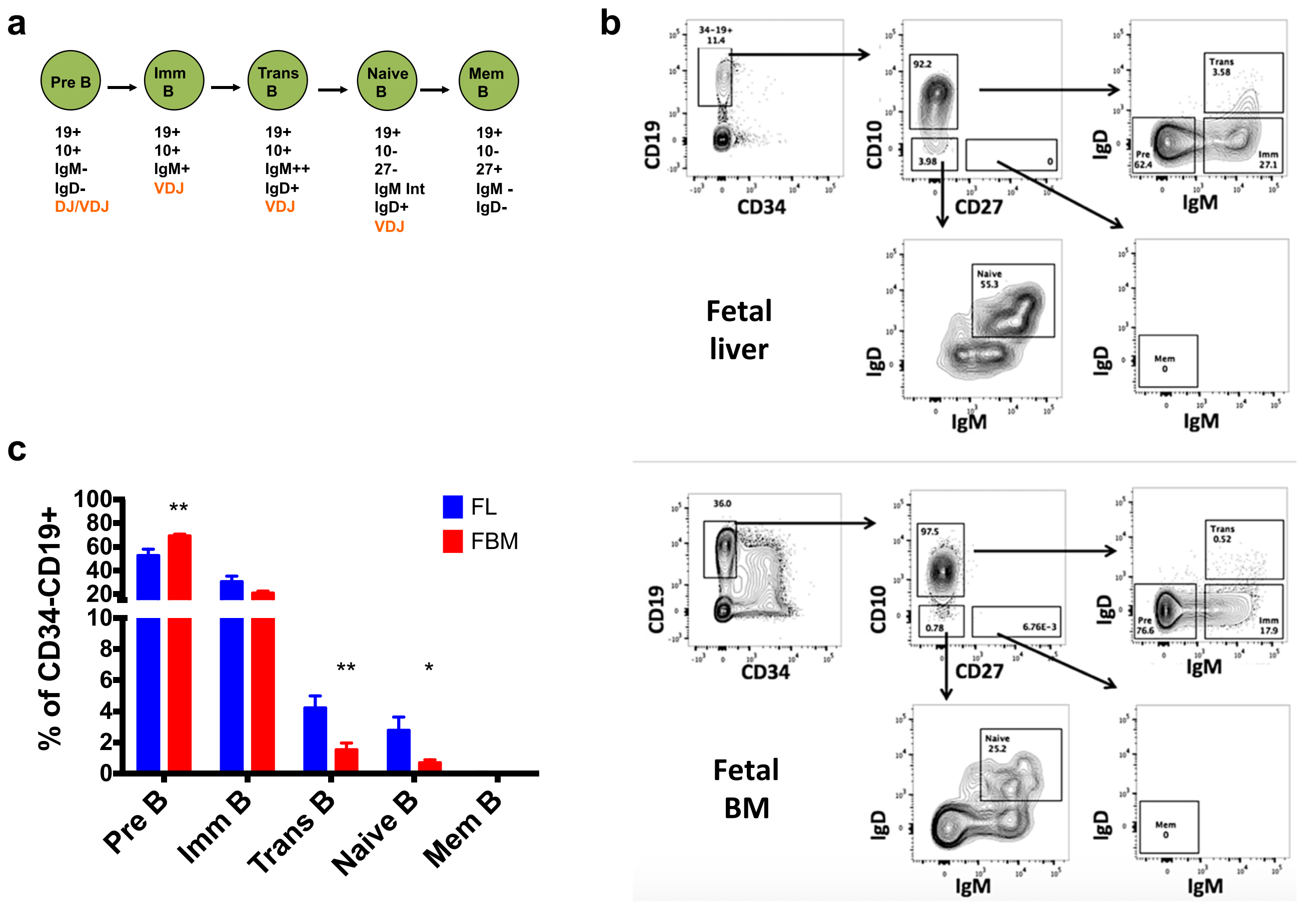

Fig. 3. B cell development in FL and FBM. a. Schematic representation of proposed fetal B cell maturation according to immunophenotypic markers and stages of VDJ recombination (using human fetal B cell development data where available) [5,6,29] that was studied in 2nd trimester FL and FBM. b. Representative flow-cytometric analysis of FL and FBM of the same fetus (GA 17 weeks) showing the gating strategy used to identify the various stages of B cell maturation as described in (a). Data are from viable CD34 negative cells for the FL sample and viable mononuclear cells for the FBM sample. c. Frequencies of the B cell stages, expressed as % of CD34-CD19+ cells, are shown in the bar graph with data represented as mean ± SEM from FL ($n = 13$) and FBM ($n = 12$) samples. (Imm: immature, Trans: transitional, Mem: memory B-cells; $^{*}p < 0.05$, $^{**}p < 0.01$).

been defined. We therefore searched for evidence in our fetal and postnatal IgM-producing B-cell samples, for the 19 major stereotypic CLL IgH receptors, or major CLL subsets, previously reported in a large study of >7500 CLL patients [33]. Overall, we found evidence of stereotypic IgH receptors corresponding to one or more of the 16 major CLL subsets in 3/5 FL B-cell samples and in all FBM and postnatal samples (Fig. 4g and not shown): 14/16 subsets were found in postnatal samples, with CLL#1, CLL#5, and CLL#28A the most prevalent but strikingly, 11/16 stereotypical subsets were also present in fetal B-cells, with 2 subsets in fetal B-cells only (Fig. 4g, Table S9). CLL#1, CLL#5 and CLL#28A subsets were again the most prevalent in FL and FBM B-cells (Fig. 4g). Importantly CLL#1, CLL#5 and CLL#28A are amongst the 10 most common CLL subsets, and CLL#1 and #5 are associated with aggressive disease [36]. These findings may provide clues into the ontogenesis of CLL and indicate that for a substantial proportion of stereotypy-associated CLL, the IgM+ B-cell that undergoes malignant transformation in adult life may originally be selected during fetal life and persist throughout adulthood.

4. Discussion

Here we present a comparative, high-resolution dissection of the human IgHmu repertoire from early fetal to adult life. This is the first such analysis to include FBM and FL, the primary sites of fetal B-cell development thus allowing ontogenic and anatomical mapping of the human natural IgM repertoire.

The IgHmu repertoire in prenatal life is responsible for development of the so-called natural antibody immunity. Work in mice has shown that development of B-cells secreting natural IgM is instructed by non-protein, lipid, phospholipid and glycan antigens often from cells undergoing apoptosis [37–39]. In this respect natural IgM are low affinity auto-reactive antibodies perhaps triggered by inadequately cleared apoptotic cells during fetal development [40]. In postnatal life, the natural IgM repertoire is further enriched with specificities against commensal flora or pathogen-derived non-protein antigens [40]. In mice, the main cellular source of natural IgM are B-1a cells that develop in FL but not FBM. After their selection and clonal expansion by auto-antigens, they persist throughout life by self-renewal.

Our analysis of the ontogeny of the corresponding human IgHmu repertoire, not previously characterised, reveals many features analogous to mice. We find that while comparably diversified B-cell lymphopoiesis exists contemporaneously in FL and FBM, the robust IgM-producing B-cell clonotypic expansions prominent in FL are virtually absent in FBM of the same GA, thus identifying human FL as the likely main source of the natural IgM repertoire in fetal life. The lack of clonotypic expansions in FBM reflects the paucity of late mature B-cells; these probably develop in late 3rd trimester to become the main source of adaptive B-cells in postnatal life. Given that the cord blood and early neonatal IgM repertoires are functionally autoreactive, these clonotypic expansions are likely to be auto-antigen-driven. Indeed, IGHV6-1 clonotypic expansions were dominant in FL, and human IGHV6-1+ fetal B-cells have previously been shown to be reactive against self-phospholipids such as cardiolipin [10]. The

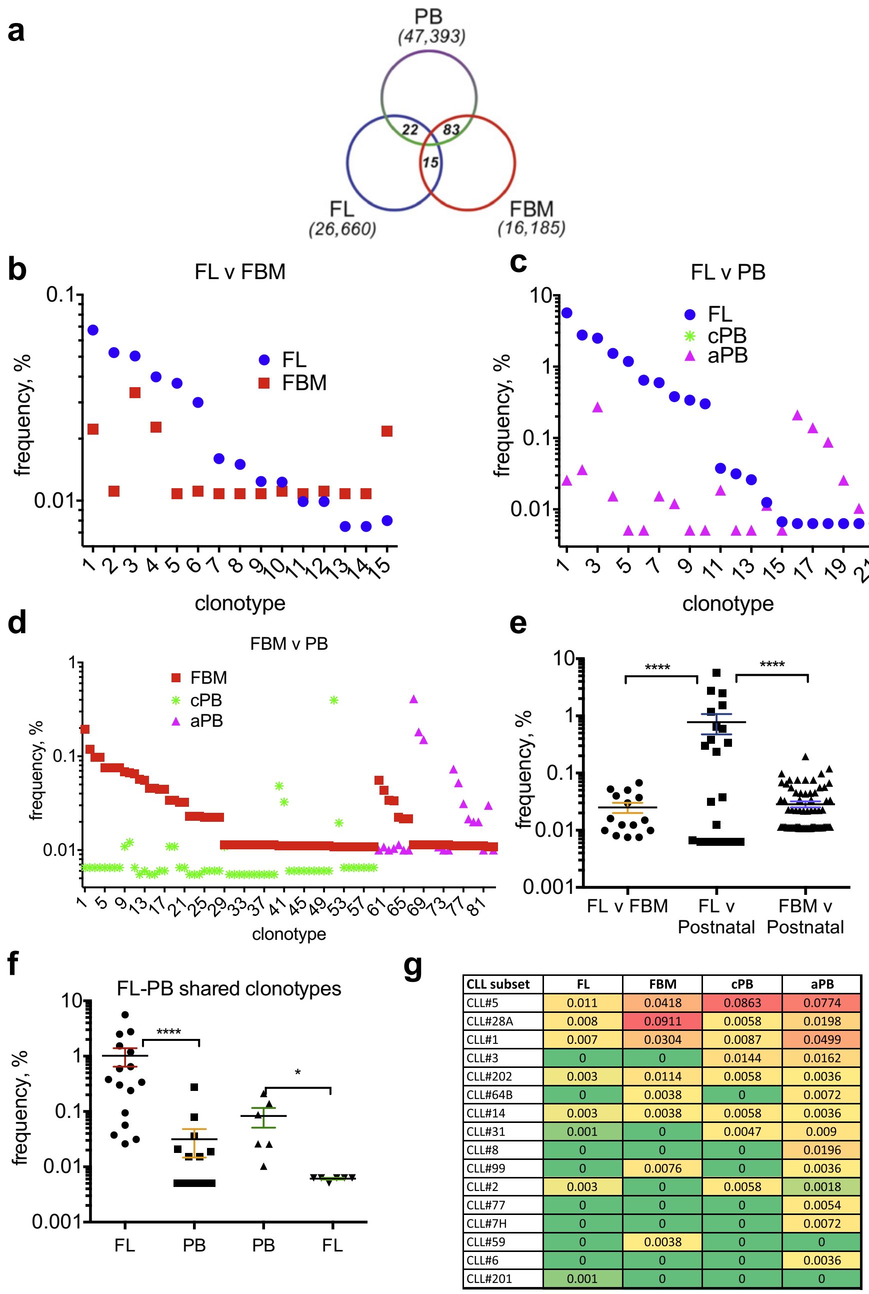

CLL subset	FL	FBM	cPB	aPB
CLL#5	0.011	0.0418	0.0863	0.0774
CLL#28A	0.008	0.0911	0.0058	0.0198
CLL#1	0.007	0.0304	0.0087	0.0499
CLL#3	0	0	0.0144	0.0162
CLL#202	0.003	0.0114	0.0058	0.0036
CLL#64B	0	0.0038	0	0.0072
CLL#14	0.003	0.0038	0.0058	0.0036
CLL#31	0.001	0	0.0047	0.009
CLL#8	0	0	0	0.0196
CLL#99	0	0.0076	0	0.0036
CLL#2	0.003	0	0.0058	0.0018
CLL#77	0	0	0	0.0054
CLL#7H	0	0	0	0.0072
CLL#59	0	0.0038	0	0
CLL#6	0	0	0	0.0036
CLL#201	0.001	0	0	0

Fig. 4. Sharing of clonotypes across developmental stages. a. Venn diagram showing the distribution of the 120 shared clonotypes between FL, FBM and post-natal PB cells. b, c & d. Sharing of clonotypes between FL and FBM, FL and post-natal, and FBM and post-natal B-cells, respectively. None of the clonotypes was shared by >2 developmental stages. Details of the clonotypes shown in b, c & d are shown in Tables S6, S7 & S8 respectively. e. Abundance of clonotypes shared between FL and FBM, FL and post-natal, and FBM and postnatal B-cells. f. Abundance of FL-PB shared clonotypes. Two left columns show shared clonotypes whose abundance is higher in FL rather than in PB, the two right-most columns show shared clonotypes with abundance higher in PB rather than in FL. g. Abundance (%) and sharing of stereotypic IgH receptors associated with CLL in fetal and postnatal B-cells showing 11 subsets shared between FL and FBM, 13 subsets shared between child and adult PB B-cells and 3 subsets shared across all 4 stages (see Table S9; *$p < 0.05$, ****$p < 0.0001$).

corresponding orthologous VH7183.1 is also dominant in murine FL [41] revealing remarkable and refined evolutionary conservation.

As in mice, the human natural IgM repertoire is also public, comprising identical/near-identical clonotypes shared by different individuals. Our data provide the first evidence of considerable sharing of IgM clonotypes that originate in human FL amongst different fetuses. For some FL clonotypes, we documented stringent (even at the nucleotide level) convergent recombination underpinning public IgM repertoire generation. While convergent recombination occurring at the aa level has been described in the adult Ig repertoire [42–44], nucleotide-level convergent recombination was recently described in murine B1 cells [23], providing further parallels between human and murine natural IgM ontogeny.

Another distinct contribution of our work to the delineation of the ontogeny of the postnatal 'public' IgM repertoire is the finding that FL expanded clonotypes, including those with IGHV6-1, are also found clonally expanded in postnatal life. This most likely reflects auto-reactive IgM-producing B-cells, clonotypically expanded in FL, persisting throughout life perhaps bypassing FBM. Whether their postnatal persistence and expansion is the result of continuous antigenic stimulation (e.g., by apoptotic cells) or of their ability to self-new (analogous to murine B-1a cells) remains to be determined.

Recent IgH repertoire analysis of fetal B cell progenitors at a single cell level, demonstrated that the distinct immunogenetic features of fetal IgH repertoire are determined, at least in part, by a fetal-specific pattern of VDJ recombination process which may be driven by differences in Tdt expression in fetal life [29].

While analysis of the human fetal IgM repertoire has revealed high concordance with the corresponding murine repertoire, our analysis of the cellular correlate of the pre-immune repertoire, i.e., of B-1a cells, has not. The existence of human counterparts of murine B-1a cells has been contentious. Recent work identified a rare IgM + CD20 + CD27 + CD43 + B-cell population in human cord blood and PB with several functional features akin to murine B-1a cells [13,31]. However, despite strict gating and use of two different anti-CD27 mAb clones (data not shown), the frequency of CD19 + CD27 + cells in the FL and FBM samples we analysed was consistently <1% with most samples having no CD19 + CD27 + cells (Fig. 3). Instead, we found FL but not FBM enriched in immunophenotypically-defined transitional B-cells, a population that in humans has also been linked with production of autoreactive IgM, autoimmune disease and a CD27-CD5 + phenotype [30,45]. This raises the possibility that in humans the B-cell subset responsible for FL IgM clonotypic expansions has features that at least in part overlap with transitional B-cells. In future work, functional characterization and high resolution analysis of the IgHmu repertoire in purified FL and FBM B-cell subsets (Fig. 3) would be required to address this question.

Another novel insight from our work is the demonstration that stereotypic, autoreactive BCR with innate function that are associated with CLL, a malignancy of older adults, may be selected during fetal life. We find that the frequencies of these stereotypic receptors in both FL and FBM are overall very low (<0.01%; Fig. 4g) and nowhere near the frequencies of expanded clonotypes in FL (up to 8%; Fig. 2b) implying that auto-antigens driving their expansion in late adult life may not present in fetal life.

Notwithstanding the very low frequency of CD27 + mature B-cells we observed in FL and FBM, this would support the notion that CD5 + B-cell CLL with unmutated BCR might have its origin in FL B-1a-like B-cells, which also express CD5 and although they are selected once during fetal life they persist long-term in postnatal life [46,47]. Alternatively, and more consistent with our immunophenotyping findings (Fig. 3), unmutated CLL has been mooted to originate from autoreactive transitional IgM + CD5 + B-cells [48]. Previous gene expression profiling of PB human B-cells identified CD27-CD5 + cells as the likely physiologic counterpart of the unmutated CLL B-cells [32]. We speculate that ongoing and life-long antigenic stimulation of these innate B-cells with stereotypic BCR originating in FL renders them susceptible to malignant transformation resulting in CLL.

In conclusion, comparative analysis of IgM repertoire development from fetal to adult IgM B-cells reveals that B-cell repertoire diversification during the 2nd trimester takes place in parallel in FL and FBM. However, since we have shown that mature B-cells capable of antigenic responses are present in FL but not in FBM, this suggests that the liver is the dominant site of likely self-antigen-driven B-cell clonotypic expansions during the 2nd trimester of fetal life. Such FL-derived expanded IgM + B-cells, including those of the IGHV6-1 gene, may persist into adult life and contribute to the auto- and poly-reactive public IgM repertoire and even become targets of malignant transformation.

Supplementary data to this article can be found online at http://dx.doi.org/10.1016/j.clim.2017.06.005.

Authorship contributions

I.R and A.K designed and supervised the study. A.R, G.B, K.G, M.P, S.OB and A.C performed the experiments and did the data collection. V.B, T.R, A.K, A.G and N.D did the data analysis and interpretation of statistical data. A.R, I.R, N.D and A.K. wrote the paper and created the figures. All authors reviewed the drafts of the paper and gave final approval of the version to be published.

Conflict of interest

The authors declare no conflict of interest.

Acknowledgments

A.R. is supported by a Bloodwise Clinician Scientist Fellowship (grant no. 14041) and an EHA-ASH Translational Research Training in Hematology Fellowship. G.B. and K.G. were supported by a Leukaemia Lymphoma Research (Bloodwise) Lectureship. This work was supported by Oxford NIHR Biomedical Centre based at Oxford University Hospitals NHS Trust and University of Oxford and NIHR Biomedical Centre based at Imperial College London. The views expressed are those of the author(s) and not necessarily those of the NHS, the NIHR or the Department of Health. The human embryonic and fetal material was provided by the Joint MRC/Wellcome Trust (grant # 099175/Z/12/Z) Human Developmental Biology Resource (www.hdbr.org). Authors from CEITEC MU were supported by Ministry of Health of the Czech Republic grant nr. 16-34272A, project CEITEC 2020 (LQ1601), and ESLHO::EuroClonality; A.K. was additionally supported by project MEYS - NPS I - LO1413; computational resources were provided by MetaCentrum (LM2010005) and CERIT-SC (CERIT Scientific Cloud, Operational Program Research and Development for Innovations, Reg. no. CZ.1.05/3.2.00/08.0144).

References

[1] C. Nunez, N. Nishimoto, G.L. Gartland, et al., B cells are generated throughout life in humans, J. Immunol. 156 (1996) 866–872.
[2] A. Roy, G. Cowan, A.J. Mead, et al., Perturbation of hematopoietic stem and progenitor cell development by trisomy 21, Proc. Natl. Acad. Sci. U. S. A. 109 (2012) 17579–17584.
[3] M. Tavian, K. Biasch, L. Sinka, J. Vallet, B. Peault, Embryonic origin of human hematopoiesis, Int. J. Dev. Biol. 54 (2010) 1061–1065.
[4] F.A. Scheeren, M. Nagasawa, K. Weijer, et al., T cell-independent development and induction of somatic hypermutation in human IgM+ IgD+ CD27+ B cells, J. Exp. Med. 205 (2008) 2033–2042.
[5] S. Agrawal, S.A. Smith, S.G. Tangye, W.A. Sewell, Transitional B cell subsets in human bone marrow, Clin. Exp. Immunol. 174 (2013) 53–59.
[6] L. McWilliams, K.Y. Su, X. Liang, et al., The human fetal lymphocyte lineage: identification by CD27 and LIN28B expression in B cell progenitors, J. Leukoc. Biol. 94 (2013) 991–1001.
[7] H. Wardemann, S. Yurasov, A. Schaefer, J.W. Young, E. Meffre, M.C. Nussenzweig, Predominant autoantibody production by early human B cell precursors, Science 301 (2003) 1374–1377.
[8] E. Meffre, J.E. Salmon, Autoantibody selection and production in early human life, J. Clin. Invest. 117 (2007) 598–601.
[9] Y. Merbl, M. Zucker-Toledano, F.J. Quintana, I.R. Cohen, Newborn humans manifest autoantibodies to defined self molecules detected by antigen microarray informatics, J. Clin. Invest. 117 (2007) 712–718.
[10] T. Logtenberg, F.M. Young, J.H. Van Es, F.H. Gmelig-Meyling, F.W. Alt, Autoantibodies encoded by the most Jh-proximal human immunoglobulin heavy chain variable region gene, J. Exp. Med. 170 (1989) 1347–1355.
[11] R. Ubelhart, H. Jumaa, Autoreactivity and the positive selection of B cells, Eur. J. Immunol. 45 (2015) 2971–2977.
[12] N. Baumgarth, The double life of a B-1 cell: self-reactivity selects for protective effector functions, Nat. Rev. Immunol. 11 (2011) 34–46.
[13] D.O. Griffin, N.E. Holodick, T.L. Rothstein, Human B1 cells in umbilical cord and adult peripheral blood express the novel phenotype CD20+ CD27+ CD43+ CD70, J. Exp. Med. 208 (2011) 67–80.
[14] V. Pascual, L. Verkruyse, M.L. Casey, J.D. Capra, Analysis of Ig H chain gene segment utilization in human fetal liver. Revisiting the "proximal utilization hypothesis", J. Immunol. 151 (1993) 4164–4172.
[15] M.M. Souto-Carneiro, G.P. Sims, H. Girschik, J. Lee, P.E. Lipsky, Developmental changes in the human heavy chain CDR3, J. Immunol. 175 (2005) 7425–7436.
[16] E. Rechavi, A. Lev, Y.N. Lee, et al., Timely and spatially regulated maturation of B and T cell repertoire during human fetal development, Sci. Transl. Med. 7 (2015) 276ra25.
[17] V. Bystry, T. Reigl, A. Krejci, et al., ARResT/Interrogate: an interactive immunoprofiler for IG/TR NGS data, Bioinformatics (2016).
[18] L. Jost, Entropy and diversity, Oikos 113 (2006) 363–375.
[19] V. Bystry, A. Agathangelidis, V. Bikos, et al., ARResT/AssignSubsets: a novel application for robust subclassification of chronic lymphocytic leukemia based on B cell receptor IG stereotypy, Bioinformatics 31 (2015) 3844–3846.
[20] M. Perez-Andres, B. Paiva, W.G. Nieto, et al., Human peripheral blood B-cell compartments: a crossroad in B-cell traffic, Cytometry B Clin. Cytom. 78 (Suppl. 1) (2010) S47–S60.

[21] V. Venturi, K. Kedzierska, D.A. Price, et al., Sharing of T cell receptors in antigen-specific responses is driven by convergent recombination, Proc. Natl. Acad. Sci. U. S. A. 103 (2006) 18691–18696.
[22] V. Venturi, D.A. Price, D.C. Douek, M.P. Davenport, The molecular basis for public T-cell responses? Nat. Rev. Immunol. 8 (2008) 231–238.
[23] Y. Yang, C. Wang, Q. Yang, et al., Distinct mechanisms define murine B cell lineage immunoglobulin heavy chain (IgH) repertoires, elife 4 (2015) e09083.
[24] V. Venturi, M.F. Quigley, H.Y. Greenaway, et al., A mechanism for TCR sharing between T cell subsets and individuals revealed by pyrosequencing, J. Immunol. 186 (2011) 4285–4294.
[25] J.E. Berman, K.G. Nickerson, R.R. Pollock, et al., VH gene usage in humans: biased usage of the VH6 gene in immature B lymphoid cells, Eur. J. Immunol. 21 (1991) 1311–1314.
[26] J.H. Van Es, F.M. Raaphorst, M.J. van Tol, F.H. Meyling, T. Logtenberg, Expression pattern of the most JH-proximal human VH gene segment (VH6) in the B cell and antibody repertoire suggests a role of VH6-encoded IgM antibodies in early ontogeny, J. Immunol. 150 (1993) 161–168.
[27] H.W. Schroeder Jr., J.Y. Wang, Preferential utilization of conserved immunoglobulin heavy chain variable gene segments during human fetal life, Proc. Natl. Acad. Sci. U. S. A. 87 (1990) 6146–6150.
[28] T.W. LeBien, Fates of human B-cell precursors, Blood 96 (2000) 9–23.
[29] M.B. Rother, K. Jensen, M. van der Burg, et al., Decreased IL7Ralpha and TdT expression underlie the skewed immunoglobulin repertoire of human B-cell precursors from fetal origin, Sci Rep 6 (2016) 33924.
[30] A. Vossenkamper, P.M. Lutalo, J. Spencer, Translational mini-review series on B cell subsets in disease. Transitional B cells in systemic lupus erythematosus and Sjogren's syndrome: clinical implications and effects of B cell-targeted therapies, Clin. Exp. Immunol. 167 (2012) 7–14.
[31] C. Bueno, E.H. van Roon, A. Munoz-Lopez, et al., Immunophenotypic analysis and quantification of B-1 and B-2 B cells during human fetal hematopoietic development, Leukemia 30 (2016) 1603–1606.
[32] M. Seifert, L. Sellmann, J. Bloehdorn, et al., Cellular origin and pathophysiology of chronic lymphocytic leukemia, J. Exp. Med. 209 (2012) 2183–2198.
[33] A. Agathangelidis, N. Darzentas, A. Hadzidimitriou, et al., Stereotyped B-cell receptors in one-third of chronic lymphocytic leukemia: a molecular classification with implications for targeted therapies, Blood 119 (2012) 4467–4475.
[34] P. Baliakas, A. Hadzidimitriou, L.A. Sutton, et al., Clinical effect of stereotyped B-cell receptor immunoglobulins in chronic lymphocytic leukaemia: a retrospective multicentre study, Lancet Haematol. 1 (2014) e74–e84.
[35] J.A. Burger, N. Chiorazzi, B cell receptor signaling in chronic lymphocytic leukemia, Trends Immunol. 34 (2013) 592–601.
[36] N. Darzentas, K. Stamatopoulos, The significance of stereotyped B-cell receptors in chronic lymphocytic leukemia, Hematol. Oncol. Clin. North Am. 27 (2013) 237–250.
[37] M.Y. Chou, L. Fogelstrand, K. Hartvigsen, et al., Oxidation-specific epitopes are dominant targets of innate natural antibodies in mice and humans, J. Clin. Invest. 119 (2009) 1335–1349.
[38] J. Kim, Identification of a human monoclonal natural IgM antibody that recognizes early apoptotic cells and promotes phagocytosis, Hybridoma (Larchmt) 29 (2010) 275–281.
[39] Y. Chen, Y.B. Park, E. Patel, G.J. Silverman, IgM antibodies to apoptosis-associated determinants recruit C1q and enhance dendritic cell phagocytosis of apoptotic cells, J. Immunol. 182 (2009) 6031–6043.
[40] P.I. Lobo, Role of natural autoantibodies and natural IgM anti-leucocyte autoantibodies in Health and disease, Front. Immunol. 7 (2016) 198.
[41] R.L. Schelonka, E. Szymanska, A.M. Vale, Y. Zhuang, G.L. Gartland, H.W. Schroeder Jr., DH and JH usage in murine fetal liver mirrors that of human fetal liver, Immunogenetics 62 (2010) 653–666.
[42] K.J. Jackson, Y. Liu, K.M. Roskin, et al., Human responses to influenza vaccination show seroconversion signatures and convergent antibody rearrangements, Cell Host Microbe 16 (2014) 105–114.
[43] J. Wrammert, D. Koutsonanos, G.M. Li, et al., Broadly cross-reactive antibodies dominate the human B cell response against 2009 pandemic H1N1 influenza virus infection, J. Exp. Med. 208 (2011) 181–193.
[44] J.C. Krause, T. Tsibane, T.M. Tumpey, et al., Epitope-specific human influenza antibody repertoires diversify by B cell intraclonal sequence divergence and interclonal convergence, J. Immunol. 187 (2011) 3704–3711.
[45] J. Lee, S. Kuchen, R. Fischer, S. Chang, P.E. Lipsky, Identification and characterization of a human CD5+ pre-naive B cell population, J. Immunol. 182 (2009) 4116–4126.
[46] R.R. Hardy, B-1 B cells: development, selection, natural autoantibody and leukemia, Curr. Opin. Immunol. 18 (2006) 547–555.
[47] N. Darzentas, A. Hadzidimitriou, F. Murray, et al., A different ontogenesis for chronic lymphocytic leukemia cases carrying stereotyped antigen receptors: molecular and computational evidence, Leukemia 24 (2010) 125–132.
[48] R. Garcia-Munoz, L. Llorente, Chronic lymphocytic leukaemia: could immunological tolerance mechanisms be the origin of lymphoid neoplasms? Immunology 142 (2014) 536–550.

Leukemia (2019) 33:2241–2253
https://doi.org/10.1038/s41375-019-0496-7

ARTICLE

Minimal resdiual disease

Standardized next-generation sequencing of immunoglobulin and T-cell receptor gene recombinations for MRD marker identification in acute lymphoblastic leukaemia; a EuroClonality-NGS validation study

Monika Brüggemann[1] · Michaela Kotrová[1,2] · Henrik Knecht[1] · Jack Bartram[3] · Myriam Boudjogrha[4] · Vojtech Bystry[5] · Grazia Fazio[6] · Eva Froňková[2] · Mathieu Giraud[7] · Andrea Grioni[6] · Jeremy Hancock[8] · Dietrich Herrmann[1] · Cristina Jiménez[9] · Adam Krejci[5] · John Moppett[10] · Tomas Reigl[5] · Mikael Salson[7] · Blanca Scheijen[11] · Martin Schwarz[1] · Simona Songia[6] · Michael Svaton[2] · Jacques J. M. van Dongen[12] · Patrick Villarese[13] · Stephanie Wakeman[8] · Gary Wright[3] · Giovanni Cazzaniga[6] · Frédéric Davi[4] · Ramón García-Sanz[9] · David Gonzalez[14] · Patricia J. T. A. Groenen[11] · Michael Hummel[15] · Elizabeth A. Macintyre[13] · Kostas Stamatopoulos[16] · Christiane Pott[1] · Jan Trka[2] · Nikos Darzentas[1,5] · Anton W. Langerak[17] · on behalf of the EuroClonality-NGS working group

Received: 15 January 2019 / Accepted: 20 February 2019 / Published online: 26 June 2019

Abstract

Amplicon-based next-generation sequencing (NGS) of immunoglobulin (IG) and T-cell receptor (TR) gene rearrangements for clonality assessment, marker identification and quantification of minimal residual disease (MRD) in lymphoid neoplasms has been the focus of intense research, development and application. However, standardization and validation in a scientifically controlled multicentre setting is still lacking. Therefore, IG/TR assay development and design, including bioinformatics, was performed within the EuroClonality-NGS working group and validated for MRD marker identification in acute lymphoblastic leukaemia (ALL). Five EuroMRD ALL reference laboratories performed IG/TR NGS in 50 diagnostic ALL samples, and compared results with those generated through routine IG/TR Sanger sequencing. A central polytarget quality control (cPT-QC) was used to monitor primer performance, and a central in-tube quality control (cIT-QC) was spiked into each sample as a library-specific quality control and calibrator. NGS identified 259 (average 5.2/sample, range 0–14) clonal sequences vs. Sanger-sequencing 248 (average 5.0/sample, range 0–14). NGS primers covered possible IG/TR rearrangement types more completely compared with local multiplex PCR sets and enabled sequencing of bi-allelic rearrangements and weak PCR products. The cPT-QC showed high reproducibility across all laboratories. These validated and reproducible quality-controlled EuroClonality-NGS assays can be used for standardized NGS-based identification of IG/TR markers in lymphoid malignancies.

Introduction

Specific antigen recognition by cells of the adaptive immune system (B cells, T cells) is mediated through receptors (immunoglobulin, IG, and T-cell receptor, TR) that are uniquely formed during immune development in bone marrow and thymus, respectively. Through recombination of IG/TR loci a diverse (polyclonal) repertoire of unique IG/TR receptors is created. In certain autoimmune diseases this repertoire is skewed (oligoclonal), whereas in lymphoid malignancies receptors are largely identical (monoclonal) [1–7]. IG/TR rearrangements thus form

---

These authors contributed equally: Monika Brüggemann, Michaela Kotrová

Supplementary information The online version of this article (https://doi.org/10.1038/s41375-019-0496-7) contains supplementary material, which is available to authorized users.

✉ Anton W. Langerak
a.langerak@erasmusmc.nl

Extended author information available on the last page of the article.

unique genetic biomarkers (molecular signatures) for studying immune cells for clinical, diagnostic and research applications [8–11]. Classically, methods for immunogenetic analysis mostly concern fragment analysis and Sanger-based sequencing. The introduction of NGS makes deeper analysis of IG/TR rearrangements possible, with impact on the main immunogenetic applications: clonality assessment, MRD detection, repertoire analysis [12–29].

The EuroClonality-NGS working group (euroclonalityngs.org; Supplementary Figure 1) has ample expertise in development, standardization and validation of IG/TR assays, to address the challenges in the translational research towards clinical application.

Here we report on the development and standardization (see also accompanying manuscript by Knecht et al. [30]) of novel amplicon-based IG/TR NGS assays between September 2012 and October 2017, via a total of 14 international coordination and evaluation meetings (Supplementary Table 1). This study focuses on IG/TR marker identification in lymphoid malignancies for subsequent MRD analysis, and their multicentre validation in acute lymphoblastic leukaemia (ALL). Assay optimizations and modifications for other applications of IG/TR NGS are partly still ongoing and will be reported in separate publications.

Materials and methods

General concept of assay design

With the objective of developing a universal amplicon-based NGS approach for IG/TR sequence analysis at the DNA level, applicable in all lymphoid malignancies, assays for multiple IG/TR loci were designed: IG heavy (IGH), IG kappa (IGK), TR beta (TRB), TR gamma (TRG) and TR delta (TRD), including complete and incomplete rearrangements whenever applicable. IG lambda (IGL) was excluded due to its limited complementarity to other IG loci and its reduced diversity. TR alpha (TRA) was excluded due to its high complexity, severely hampering a reasonable multiplex PCR approach at the DNA level.

The IGH locus is rearranged in two steps. After initial coupling of a single IGHD gene to an IGHJ gene, an IGHV gene is joined to the incomplete IGHD–IGHJ rearrangement, resulting in a complete IGHV–IGHJ rearrangement. For amplification of complete IGH rearrangements, primers located in the FR1, FR2 and FR3 regions were designed, but here we only discuss the FR1 assay for marker identification in ALL (for application of IGH-VJ-FR3 assay in clonality testing see accompanying manuscript by Scheijen et al. [31]). IGHD–IGHJ rearrangements were amplified in a separate multiplex PCR reaction. The IGK light chain locus is composed of functional IGKV and IGKJ genes, as well as the so-called kappa deleting element (Kde) that can rearrange to IGKV genes, or to a recombination signal sequence (RSS) in the IGKJ–IGKC intron, leading to functional inactivation of the IGK allele. The IGKV forward primers were designed to be used in combination with IGKJ and Kde reverse primers in one multiplex reaction, whereas a second PCR was developed for the forward intron RSS and reverse Kde primers.

The TRB locus also features a two-step process with initial formation of incomplete TRBD–TRBJ rearrangements followed by complete TRBV–TRBJ rearrangements. Incomplete and complete TRB rearrangements are detected in two separate multiplex PCR reactions. As TRG locus rearrangements are one-step VJ recombinations involving a limited number of TRGV and TRGJ genes, a single multiplex assay could be developed. Finally, in the TRD locus, complete VJ rearrangements are preceded by DD, VD and DJ rearrangements. In addition, certain TRAV genes can rearrange to both TRDJ and TRAJ, whereas TRDV–TRAJ rearrangements, usually involving TRAJ29, can also occur. All of these rearrangements were designed to be amplified in one multiplex PCR assay.

Both the design and further testing were coordinated by the respective ‘Target’ network leaders: IGH-VJ by C. Pott, Kiel and R. Garcia Sanz, Salamanca; IGH-DJ by F. Davi, Paris and K. Stamatopoulos, Thessaloniki; IGK-V/intron-IGKJ/Kde by P.J.T.A. Groenen, Nijmegen and A.W. Langerak, Rotterdam; TRB by M. Brüggemann, Kiel and M. Hummel, Berlin; TRG by G. Cazzaniga, Monza and J.J.M. van Dongen, Leiden; and TRD by E. Macintyre, Paris. Initial testing of each assay was performed by 2–3 experienced laboratories per target and final assays were validated for IG/TR marker identification in ALL in a multicentre setting. In addition, central quality control procedures were developed to monitor assay performance.

The bioinformatic platform ARResT/Interrogate [32], developed from the ground-up within the EuroClonality-NGS to assist with its multi-faceted activities, was further adapted for this study as described below.

Primer design and technical validation of primer performance

Primers were designed to be gene-specific, but in case of allelic variants, degenerate primers were designed to avoid differential annealing in individuals with different allelic variants. For the same reason, single mismatches in the middle or at the 5′-end of the primer were accepted.

Primer3 [33], Primer Digital (PrimerDigital Ltd, Helsinki, Finland) MFEprimer-2.0 [34] and Oligo (Molecular Biology Insights, Inc., Colorado, USA) were used for checking primer specificity and multiplexing. Common primer design criteria were followed for all loci:

primer melting temperature 57–63 °C; comparable size of final amplicon; primer length 20–24 nt; avoidance of primer dimers; minimal distance of 3′ primer end to the junctional region of, preferably, >10–15 bp to avoid false-negativity for rearrangements with larger nucleotide deletions from the germline sequence; avoidance of regions with known single nucleotide polymorphisms to allow identical primer annealing for all alleles of the respective V, D or J genes; targeting of, preferably, all V, D and J genes known to be rearranged plus the intronRSS and Kde regions for IGK.

Following in silico design, primers were first tested in monoplex and multiplex reactions using primary patient samples or cell lines with defined rearrangements. In occasional cases where no such samples were available, healthy tonsil or mononuclear DNA samples were employed. Oligoclonal template pools were then created from mixtures of rearranged cell lines and diagnostic samples with defined rearrangements covering many different V, D and/or J genes. Alternatively, for some loci, plasmid pools were produced, covering as many different rearrangements as possible. These multi-target pools allowed fine-tuning of reaction conditions and/or primer concentrations to assess comparable amplification efficiencies. This iterative process of testing also led to a reduction of primers if these appeared redundant. Further multicentre testing was performed with a limited number of monoclonal and poly/oligoclonal samples on different sequencing platforms, which allowed assessment of robustness of the primer mixes and protocols.

As assays were designed with the aim to be platform-independent, a two-step PCR was employed, that enabled switching of sequencing adaptors and to reduce the total number of primers even if many barcodes are necessary. Also, maximal amplicon lengths were defined with respect to the possible maximal sequencing read lengths of current sequencers. PCR conditions were optimized with the aim to find optimal conditions common for all reactions, thus allowing for parallel library preparation. Various numbers of PCR cycles in 1st and 2nd PCR, different polymerases and several library purification methods were tested and compared.

Multicentre validation of assays for MRD marker identification in ALL

Five experienced laboratories tested the robustness and applicability of the optimized assays for NGS-based IG/TR marker identification in ALL in comparison to standard techniques. All laboratories (Bristol/London, Paris, Monza, Prague and Kiel) are members of the EuroMRD consortium and reference laboratories for ALL MRD analysis. Each of them performed NGS-based IG/TR MRD marker identification in 10 patients with B- or T-lineage ALL. A central standard operating procedure was strictly followed. The study was executed using the Illumina MiSeq (2 × 250 bp v2 kit). NGS analyses were performed fully in parallel to conventional PCR plus Sanger sequencing of clonal products following standard guidelines [11]. For a part of the cases with unexplained discrepant results between the two methods, allele-specific PCR assays (either for digital droplet PCR or real-time quantitative PCR) were designed to clarify if the respective clonal rearrangement represented the leukaemic bulk. EuroMRD guidelines were used to design and interpret allele-specific PCR assays [35, 36].

Results

Primer design and technical validation of primer performance

Based on the results of the testing and validation phases (Supplementary Table 2), the final IG/TR primer mixes consisted of eight tubes with 92 forward and 30 reverse primers, 15 of the latter being used in pairs of different tubes (Supplementary Table 3). Primer positions and sequences are presented in Fig. 1.

Implementation of quality control procedures

Quality control of robust amplification, library preparation and sequencing are of utmost importance for these complex assays. Different primers need to work under the same reaction conditions, while additional variability can be introduced by sample characteristics and sequencing. Primer performance must be monitored longitudinally, and for the exact estimation of clonal abundance it is important to correct for the number of sequencing reads per input molecule.

To address these issues, we established and validated two types of quality control procedures: (i) a ‘central in-tube quality control’ (cIT-QC) spiked to each tube as library control and calibrator, and (ii) a ‘central poly-target quality control’ (cPT-QC), or run control, to monitor general primer performance and sequencing.

To compose the cIT-QC, IG/TR rearrangements of many human lymphoid cell lines were comprehensively characterized by amplicon- and capture-based NGS and Sanger sequencing. Nine cell lines were selected to form the cIT-QC with at least three different clonal rearrangements for each of the eight PCR tubes, totalling 24 rearrangements. The current design requires an equal number of cell line DNA copies to be spiked into each tube, as described below.

For the cPT-QC a mixture of different lymphoid specimens was considered to cover the whole IG/TR repertoire

IGH-V-FR1-A-1	(IGHV1-2*01)	(-277)	CTGGGGCTGAGGTGAAGAAG
IGH-V-FR1-B-1	(IGHV5-51*01)	(-282)	GCAGTCTGGAGCAGAGGTGAAAA
IGH-V-FR1-C-1	(IGHV2-5*01)	(-297)	TCACCTTGAAGGAGTCTGGTCC
IGH-V-FR1-D-1	(IGHV3-7*01)	(-295)	AGGTGCAGCTGGTGGAGTC
IGH-V-FR1-E-1	(IGHV3-23*01)	(-296)	GAGGTGCAGCTGTTGGAGTC
IGH-V-FR1-F-1	(IGHV4-4*01)	(-272)	CCAGGACTGGTGAAGCCTTC
IGH-V-FR1-G-1	(IGHV4-34*01)	(-278)	CAGTGGGGCGCAGGACTGTT
IGH-V-FR1-H-1	(IGHV4-4*01)	(-272)	CCAGGACTGGTGAAGCCTCC
IGH-V-FR1-I-1	(IGHV6-1*01)	(-302)	GTACAGCTGCAGCAGTCAGG
IGH-V-FR1-J-1	(IGHV7-4-1*01)	(-286)	GCTGGTGCAATCTGGGTCTG
IGH-V-FR1-K-1	(IGHV1-45*01)	(-250)	CCTCAGTGAAGGTTTCCTGCAAGG
IGH-V-FR1-L-1	(IGHV2-26*01)	(-265)	AAACCCACAGAGACCCTCACGCTGAC
IGH-V-FR1-M-1	(IGHV3-16*01)	(-256)	CTGGGGGGTCCCTGAGACTCTCCTG
IGH-V-FR1-N-1	(IGHV4-31*01)	(-259)	CTTCACAGACCCTGTCCCTCACCTG
IGH-V-FR1-O-1	(IGHV6-1*01)	(-263)	TCGCAGACCCTCTCACTCACCTGTG

CTTACCTGAGGAGACGGTGACC	(+68)	(IGHJ6*01)	IGH-J-A-1
CTCACCTGAGGAGACAGTGACC	(+58)	(IGHJ2*01)	IGH-J-B-1

IGH-D-A-1	(IGHD1-1*01)	(-44)	GATTCYGAACAGCCCCGAGTCA
IGH-D-B-1	(IGHD2-2*01)	(-58)	GATTTTGTGGGGGYTCGTGTC
IGH-D-C-1	(IGHD3-3*01)	(-58)	GTTTGRRGTGAGGTCTGTGTCA
IGH-D-D-1	(IGHD3-3*01)	(-58)	GTTTRGRRTGAGGTCTGTGTCACT
IGH-D-E-1	(IGHD4-4*01)	(-43)	CTTTTTGTGAAGGSCCCTCCTR
IGH-D-F-1	(IGHD5-5*01)	(-47)	GTTATTGTCAGGSGRTGTCAGAC
IGH-D-G-1	(IGHD5-5*01)	(-47)	GTTATTGTCAGGGGGTGYCAGRC
IGH-D-H-1	(IGHD6-6*01)	(-45)	GTTTCTGAAGSTGTCTGTRTCAC

CTTACCTGAGGAGACGGTGACC	(+68)	(IGHJ6*01)	IGH-J-A-1

IGK-V-A-1	(IGKV1-12*01)	(-123)	AAGTGGGGTCCCATCAAGGTTCAG
IGK-V-B-1	(IGKV1-37*01)	(-117)	AGTCCCATCTCGGTTCAGTGGCAG
IGK-V-C-1	(IGKV1-33*01)	(-125)	GAAACAGGGGTCCCATCAAGGTTC
IGK-V-D-1	(IGKV2-24*01)	(-115)	TCCCAGACAGATTCAGTGGCAGTG
IGK-V-E-1	(IGKV2-29*01)	(-121)	CTGGAGTGCCAGATAGGTTCAGTG
IGK-V-F-1	(IGKV2-40*01)	(-123)	CCCTGGAGTCCCAGACAGGTTCAG
IGK-V-G-1	(IGKV3-11*01)	(-118)	GCATCCCAGCCAGGTTCAGTG
IGK-V-H-1	(IGKV4-1*01)	(-116)	GTCCCTGACCGATTCAGTGGCA
IGK-V-I-1	(IGKV5-2*01)	(-117)	AATCCCACCTCGATTCAGTGGC
IGK-V-J-1	(IGKV6-21*01)	(-123)	CTCAGGGGTCCCCTCGAGGTT
IGK-V-K-1	(IGKV7-3*01)	(-126)	AGACACTGGGGTCCCAGCCA

ACGTTTGATCTCCACCTTGGTCCC	(+40)	(IGKJ4*01)	IGK-J-A-1
ACGTTTGATATCCACTTTGGTCCC	(+40)	(IGKJ3*01)	IGK-J-B-1
ACGTTTAATCTCCAGTCGTGTCCC	(+40)	(IGKJ5*01)	IGK-J-C-1

GCAGCTGCAGACTCATGAGGAG	(+48)	(IGKDE)	IGK-DE-A-1

IGK-INTR-A-1	(Intron)	(-111)	GAGTGGCTTTGGTGGCCATGC

TRB-V-A-1	(TRBV2*01)	(-96)	CTCAGTTGAAAGGCCTGATGGA
TRB-V-B-1	(TRBV3-1*01)	(-111)	AGTTCCAAATCGCTTCTCACCT
TRB-V-C-1	(TRBV4-1*01)	(-102)	TCGCTTCTCACCTGAATGCCC
TRB-V-D-1	(TRBV5-1*01)	(-115)	GGAAACTTCCCTGGTCGATTC
TRB-V-E-1	(TRBV5-5*01)	(-111)	ACTTCCCTGATCGATTCTCAGC
TRB-V-F-1	(TRBV5-3*01)	(-109)	TTCCCTAATCGATTCTCAGGGC
TRB-V-G-1	(TRBV5-4*01)	(-99)	GATTCTCAGGTCTCCAGTTCCC
TRB-V-H-1	(TRBV5-6*01)	(-95)	CTCAGGTCACCAGTTCCCTAAC
TRB-V-I-1	(TRBV5-8*01)	(-103)	CCTAGATTTTCAGGTCGCCAGT
TRB-V-J-1	(TRBV6-2*01)	(-129)	TACAACTGCCAAAGGAGAGGTC
TRB-V-K-1	(TRBV6-4*01)	(-129)	TACCACTGGCAAAGGAGAAGTC
TRB-V-L-1	(TRBV6-6*01)	(-120)	TAAAGGAGAAGTCCCGAATGGC
TRB-V-M-1	(TRBV6-7*01)	(-116)	GGAGAAGTTCCCAATGGCTACA
TRB-V-N-1	(TRBV7-3*01)	(-108)	CAACGATCGGTTCTTTGCAGTC
TRB-V-O-1	(TRBV7-5*01)	(-121)	TAAATCAGGGCTGCTCAGTGAT
TRB-V-P-1	(TRBV7-7*01)	(-108)	CAGTGATCGGTTCTCTGCAGAG
TRB-V-Q-1	(TRBV7-8*01)	(-133)	CTCAACTAGACAAATCGGGGCT
TRB-V-R-1	(TRBV9*01)	(-106)	CTTGAACGATTCTCCGCACAAC
TRB-V-S-1	(TRBV10-2*01)	(-121)	ATAAAGGAGAAGTCCCCGATGG
TRB-V-T-1	(TRBV10-3*01)	(-120)	CAAAGGAGAAGTCTCAGATGGC
TRB-V-U-1	(TRBV11-1*01)	(-103)	ATCGATTTTCTGCAGAGAGGCT
TRB-V-V-1	(TRBV12-3*01)	(-109)	CCGAGGATCGATTCTCAGCTAA
TRB-V-W-1	(TRBV12-5*01)	(-130)	CTCTAGATGATTCGGGGATGCC
TRB-V-X-1	(TRBV13*01)	(-116)	GGAAGCATCCCTGATCGATTCT
TRB-V-Y-1	(TRBV14*01)	(-117)	CGGTATGCCCAACAATCGATTC
TRB-V-Z-1	(TRBV15*01)	(-120)	TGAAGCAGACACCCCTGATAAC
TRB-V-AA-1	(TRBV16*01)	(-95)	TCAGCTAAGTGCCTCCCAAATT
TRB-V-AB-1	(TRBV18*01)	(-111)	GCCAAAGGAACGATTTTCTGCT
TRB-V-AC-1	(TRBV19*01)	(-106)	CTGAAGGGTACAGCGTCTCTC
TRB-V-AD-1	(TRBV20-1*01)	(-95)	TTTCTCATCAACCATGCAAGCC
TRB-V-AE-1	(TRBV21-1*01)	(-105)	TGAGCGATTTTTAGCCCAATGC
TRB-V-AF-1	(TRBV23-1*01)	(-117)	GGAGATGCACAAGAAGCGATTC
TRB-V-AG-1	(TRBV24-1*01)	(-122)	ACAAAGGAGAGATCTCTGATGGA
TRB-V-AH-1	(TRBV25-1*01)	(-107)	TCCTCTGAGTCAACAGTCTCCA
TRB-V-AI-1	(TRBV27*01)	(-118)	AGGGAGATGTTCCTGAAGGGTA
TRB-V-AJ-1	(TRBV28*01)	(-107)	CCTGAGGGGTACAGTGTCTCTA
TRB-V-AK-1	(TRBV29-1*01)	(-133)	CTGAGGCCACATATGAGAGTGG
TRB-V-AL-1	(TRBV30*01)	(-101)	CAGAATCTCTCAGCCTCCAGAC

CTACAACTGTGAGTCTGGTGCC	(+48)	(TRBJ1-1*01)	TRB-J-A-1
CTACAACGGTTAACCTGGTCC	(+48)	(TRBJ1-2*01)	TRB-J-B-1
TACAACAGTGAGCCAACTTCCC	(+49)	(TRBJ1-3*01)	TRB-J-C-1
CAAGACAGAGAGCTGGGTTCC	(+50)	(TRBJ1-4*01)	TRB-J-D-1
CTAGGATGGAGAGTCGAGTCCC	(+50)	(TRBJ1-5*01)	TRB-J-E-1
CTGTCACAGTGAGCCTGGTC	(+53)	(TRBJ1-6*01)	TRB-J-F-1
CCTTCTTACCTAGCACGGTGAG	(+59)	(TRBJ2-1*01)	TRB-J-G-1
TTACCCAGTACGGTCAGCCTAG	(+55)	(TRBJ2-2*01)	TRB-J-H-1
CTTACCGAGCACTGTCAGCC	(+54)	(TRBJ2-3*01)	TRB-J-I-1
CTTACCCAGCACTGAGAGCC	(+55)	(TRBJ2-4*01)	TRB-J-J-1
TCACCGAGCACCAGGAGCC	(+52)	(TRBJ2-5*01)	TRB-J-K-1
GAAAACTCACCCAGCACGGTC	(+63)	(TRBJ2-6*01)	TRB-J-L-1
TCACCCAGCACGGTCAGCC	(+57)	(TRBJ2-6*01)	TRB-J-M-1
GAATCTCACCTGTGACCGTGAG	(+56)	(TRBJ2-7*01)	TRB-J-N-1

TRD-D-A-1	(TRBD1*01)	(-114)	CCTCCACTCCCCTCAAAGGA
TRD-D-B-1	(TRBD2*01)	(-117)	CAGACTAACCTCTGCCACCTG

TRG-V-A-1	(TRGV2*01)	(-83)	GCACAAGGAACAACTTGAGATTG
TRG-V-B-1	(TRGV4*01)	(-88)	TGGAAGCACAAGGAAGAACTTGAGAA
TRG-V-C-1	(TRGV8*01)	(-83)	GCACAGGGAAGAGCCTTAAATT
TRG-V-D-1	(TRGV3*01)	(-82)	CAGGAGGTGGAGCTGGATATT
TRG-V-E-1	(TRGV7)	(-85)	CAAGCATGAGGAGGAGCTGGAAATTG
TRG-V-F-1	(TRGV9*01)	(-78)	ACGTCTACATCCACTCTCACC
TRG-V-G-1	(TRGV10*01)	(-79)	CTCTCACTTCAATCCTTACCATCAA
TRG-V-H-1	(TRGV11*01)	(-80)	CTTCCACTTCCACTTTGAAAATAAAGT

AGTGTTGTTCCACTGCCAAAG	(+39)	(TRGJ1*01)	TRG-J-A-1
GTTCCGGGACCAAATACCTTG	(+45)	(TRGJP*01)	TRG-J-B-1
GAGCTTAGTCCCTTCAGCAAATA	(+44)	(TRGJP1*01)	TRG-J-C-1
CCTAGTCCCTTTTGCAAACG	(+41)	(TRGJP2*01)	TRG-J-D-1

TRD-V-A-1	(TRDV1*01)	(-120)	GAATGCAAAAAGTGGTCGCTATTC
TRD-V-B-1	(TRDV2*01)	(-79)	TGCAAAGAACCTGGCTGTACT
TRD-V-C-1	(TRDV3*01)	(-117)	TGCAGATTTTACTCAAGGACGG
TRD-V-D-1	(TRAV14/DV4*01)	(-123)	GCAAAATGCAACAGAAGGTCG
TRD-V-E-1	(TRAV29/DV5*01)	(-118)	GATAAAAATGAAGATGGAAGATTCACTGT
TRD-V-F-1	(TRAV23/DV6*01)	(-89)	CTCCTTCAATAAAAGTGCCAAGC
TRD-V-G-1	(TRAV36/DV7*01)	(-118)	ATTGAAAAGAAGTCAGGAAGACTAAGT
TRD-V-H-1	(TRAV38-2/DV8*01)	(-87)	TCCAGAAAGCAGCCAAATCC

TTCCACAGTCACACGGGT	(+47)	(TRDJ1*01)	TRD-J-A-1
GGTTCCACGATGAGTTGTGTT	(+52)	(TRDJ2*01)	TRD-J-B-1
CACGAAGAGTTTGATGCCAGT	(+52)	(TRDJ3*01)	TRD-J-C-1
GTTGTTGTACCTCCAGATAGGTT	(+48)	(TRDJ4*01)	TRD-J-D-1
TGGCTAGAAACACTTACTTGCA	(+77)	(TRAJ29*01)	TRD-J-E-1

TRD-D-A-1	(TRDD2*01)	(-104)	AGGGGTATTGTGGATGGCAG

CCCAGGGAAATGGCACTTTTG	(+80)	(TRDD3*01)	TRD-D-B-1

Fig. 1 Schematic diagrams of rearrangements and primer sets. **a** Schematic diagrams of IGHV-IGHJ and IGHD-IGHJ rearrangements. The relative position of the VH family primers, DH family primers and consensus JH primers is given according to their most 5′ nucleotide upstream (−) or downstream (+) of the involved RSS. **b** Schematic diagrams of IGKV-IGKJ rearrangement and the two types of Kde rearrangements (V-Kde and intronRSS–Kde). The relative position of the IGKV, IGKJ, Kde, and intronRSS (INTR) primers is given according to their most 5′ nucleotide upstream (−) or downstream (+) of the involved RSS. **c** Schematic diagrams of TRBV-TRBJ rearrangement and TRBD-TRBJ rearrangement. The relative position of the TRBV family primers, TRBD primers and the TRBJ primers is given according to their most 5′nucleotide upstream (−) or downstream (+) of the involved RSS. **d** Schematic diagrams of TRGV–TRGJ rearrangement and the relative position of the TRGV and TRGJ primers. The relative position of the TRGV primers and the TRGJ primers is given according to their most 5′ nucleotide upstream (−) or downstream (+) of the involved RSS. **e** Schematic diagram of TRDV–TRDJ,TRDD–TRDJ, TRDD–TRDD, and TRDV–TRDD, TRDV-TRAJ29 rearrangements, showing the positioning of TRDV, TRDJ, TRDD, and TRAJ29 primers, all combined in a single tube. The relative position of the TRDV, TRDD, and TRDJ primers is indicated according to their most 50 nucleotides upstream (−) or downstream (+) of the involved RSS

more comprehensively. To this end we produced material consisting of equal ratios of DNA from peripheral blood mononuclear cells (MNCs), thymus and tonsil. For more details see accompanying manuscript by Knecht et al. [30].

Laboratory protocol

Primers were tailed with universal and T7-linker sequences, and divided over eight tubes (IGH-VJ, IGH-DJ, IGK-VJ-Kde, intron-Kde, TRB-VJ, TRB-DJ, TRG, TRD). The PCR protocol is summarized in Table 1. Sequencing libraries were prepared via a two-step PCR, each using a final reaction volume of 50 µl with 100 ng diagnostic DNA and 10 ng of polyclonal DNA. For the cIT-QC, 40 cell equivalents of the nine different cell lines were spiked into all samples (see accompanying manuscript by Knecht et al. [30]). $MgCl_2$ was intended to be used at a final concentration of 1.5 mM, but needed optimization for some tubes. Therefore, master-mixes for the 1st PCR were tube-specific, but the temperature profile was uniform for all tubes.

Table 1 Standardized PCR protocol

(a) Reaction conditions of 1st and 2nd PCR

1st PCR

	Stock concentration	IGH V-J		IGH D-J		IGK-VJ-Kde, intron-Kde		TRB V-J, D-J		TRG		TRD	
		Final concentration	µl/library	Final concentration	µl/library	Final concentration	µl/library	Final concentration	µl/library	Final concentration	µl/library	Final concentration	µl/library
PCR Buffer II	10×	1×	5	1×	5	1×	5	1×	5	1×	5	1×	5
$MgCl_2$	25 mM	2.5 mM	5	3 mM	6	1.5 mM	3	4 mM	8	4 mM	8	2 mM	4
dNTP-Mix	10 mM	0.2 mM	1	0.4 mM	2.0	0.2 mM	1	0.2 mM	1	0.2 mM	1	0.2 mM	1
EagleTaq/ AmpliTaq Gold	5 U/µl	1 U/rxn	0.2	1.5 U/rxn	0.3	1 U/rxn	0.2	1 U/rxn	0.2	1 U/rxn	0.2	1 U/rxn	0.2

2nd PCR

	Stock concentration	all tubes	
		Final concentration	µl/sample
PCR buffer with $MgCl_2$	10×	1×	5
	18 mM	1.8 mM	0
dNTP-Mix	10 mM	0.2 mM	1
Fast Start High Fidelity polymerase	5 U/µl	2.5 U/rxn	0.5

(b) Cycling conditions

1st PCR				2nd PCR			
1 cycle	Initial denaturation	94 °C	10 min	1 cycle	Initial denaturation	95 °C	2 min
35 cycles	Denaturation	94 °C	1 min	20 cycles	Denaturation	94 °C	30 s
	Annealing	63 °C	1 min		Annealing	63 °C	30 s
	Extension	72 °C	30 s		Extension	72 °C	30 s
1 cycle	Final extension	72 °C	30 min	1 cycle	Final extension	72 °C	5 min
		12 °C	∞			12 °C	∞

Reaction volume: 50 µl

Table 2 Mean size of PCR products after the 2nd PCR (containing the Illumina sequencing adaptors and barcodes)

Gene	Amplicon length (bp)
TRB-VJ	309–407
TRB-DJ	300–408
TRG	256–360
TRD	309–450
IGH-VJ	484–681
IGH-DJ	266–358
IGK-VJ-Kde	296–384
intron-Kde	309–382

Concentrations of all primers are shown in Supplementary Table 3. After 1st PCR, gel electrophoresis was performed to check for successful amplification of all targets. For TRB, gel extraction of the specific PCR products was performed prior to the 2nd PCR.

All 1st round PCR products, except TRB PCR products, were diluted 1:50 unless amplicons were very weak. TRB PCR products and PCR products with weak amplicons were used undiluted. Master-mixes for the 2nd PCR and the temperature profiles were identical for all tubes (Table 1). Primers for the 2nd PCR contained sequencing adaptors and sequencing indexes (barcodes). Unique combination of forward and reverse indexes was used for each library. Three microlitres of undiluted TRB PCR products and 1 µl of 1:50-diluted IGH, IGK, TRG and TRD PCR products were amplified in the 2nd PCR.

Following 2nd PCR, products from all samples of a run were pooled in equimolar ratios into eight tube-wise subpools and purified by gel extraction (see Table 2 for the amplicon lengths). Finally, the subpools were pooled equimolarly into one final pool. Sequencing was performed on Illumina MiSeq sequencers, using 2 × 250 bp v2 chemistry with a final concentration of 7 pM for the amplicon library and 10% PhiX control added to avoid low-complexity library issues. The detailed standard operating procedure is provided as supplementary information.

Bioinformatic protocol

ARResT/Interrogate [32] was the main bioinformatics platform used in this study. Both Vidjil [37] and IMGT [38] resources are available through ARResT/Interrogate as built-in tools and were employed for specific aspects of this work, mainly analysis of rearrangements with unclear annotation. Data are deposited at EMBL/EBI European Nucleotide Archive (ENA), accession code PRJEB32668.

Demultiplexing was performed accepting no mismatches. Reads were annotated with EuroClonality-NGS primer sequences (to trim non-amplicon sequences, and for the cPT-QC-based quality control), paired-end joined, dereplicated, immunogenetically annotated [39], and eventually classified into rearrangement types (complete and incomplete, and other special types like intron-Kde rearrangements), or 'junction classes'. Reads without rearrangement were excluded from the total read count used for relative abundances.

cIT-QC sequences described above and elsewhere (see accompanying manuscript by Knecht et al. [30]), were identified in the data through their immunogenetic annotation. Their counts served both as 'in-tube' control and for normalization per primer set: total cIT-QC cells are divided by cIT-QC total reads, the resulting factor used to convert rearrangement reads to cells, and those cells then further divided by total input cells (15,000 in this study). Identified IG/TR sequences were defined as index sequences if their abundance after cIT-QC normalisation exceeded 5%.

ARResT/Interrogate can track the DNJ 3′ stem of a junction, the sequence remaining stable during IGH or TRB clonal evolution in case of V replacement or ongoing V to DJ rearrangements. The stem consists of the last ≤ 3nt of D (or of the NDN if no D is identifiable), any and all of N2 nucleotides, and the J nucleotides of the junction. This stem is available as a separate immunogenetic feature across all samples and thus can be linked to other features, e.g. clonotypes.

Multicentre validation of assays for MRD marker identification in ALL

Next, 50 ALL diagnostic samples (29 BCP-ALL and 21 T-ALL; Supplementary Table 4) were analysed for the multicentre validation study. Each of the five participating laboratories received preconfigured 96-well plates containing the different multiplexed NGS primer combinations per target (Fig. 2).

In total, 96 libraries were generated per lab (total of 480 libraries), and sequenced with a collective output of 47M reads (⌀ 9.2 M/lab). Centralised analysis was performed with ARResT/Interrogate [32] using IMGT germline sequences [39]—further analyses and verifications were performed with Vidjil [37] and IMGT/V-QUEST [38].

Overall, 311 clonal IG/TR rearrangements (clonotypes) were identified, with a mean of 5.2 (0–14)/sample by NGS (a 5% threshold was applied for NGS after cIT-QC-based normalization) vs. 5.0 (0–14)/sample by Sanger, while 217 (45%) libraries demonstrated no clonotypes above threshold by either method. A total of 196/311 (63%) clonotypes were fully concordant between NGS and Sanger (Fig. 3). NGS exclusively identified 63/311 (20%) index sequences, whereas 52/311 (17%) IG/TR Sanger sequences were not assigned as NGS index sequence by ARResT/Interrogate. 26/63 NGS positive/Sanger negative cases showed a clonal PCR product

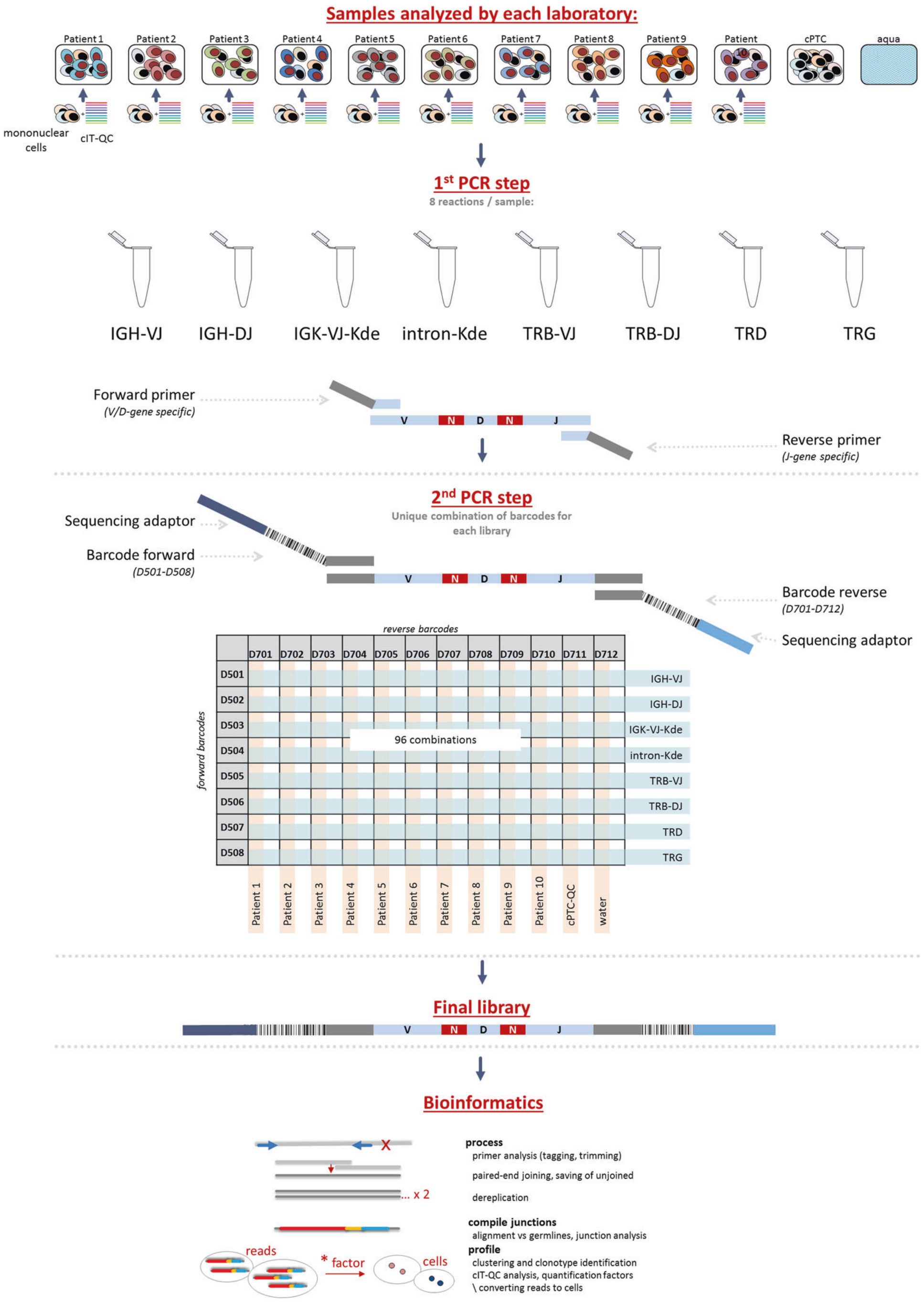

Fig. 2 Schematic overview of the workflow for multicentre validation of IG/TR NGS assays for MRD marker identification in ALL. The IG and TR gene rearrangements are amplified in a two-step approach using multiplex PCR assays. Each of the participating laboratories performed NGS-based IG/TR MRD marker identification in 10 patients with ALL. A central polytarget control (cPT-QC) was used to monitor primer performance, and central in-tube controls (cIT-QC) were spiked to each sample as library-specific quality control and calibrator. Pipetting was performed in a 96-well format. The data analysis was performed using ARResT/Interrogate

also in the respective low-throughput approach but subsequent Sanger sequencing failed due to polyclonal background, mixed sequences or weak PCR products. In an additional 6/63 NGS positive/Sanger negative cases the respective primer was missing in the low-throughput approach. For the remaining 31/63 discrepancies no technical explanation for Sanger failure could be found. In 16/19 q/ddPCR evaluated cases the rearrangement was confirmed by ASO-PCR, in three of these on a subclonal level.

Conversely, 52/311 clonal IG/TR rearrangements were detected by Sanger sequencing only, when applying the 5% NGS threshold: for 5/52 sequences (1 TRG, 2 TRB-VJ and

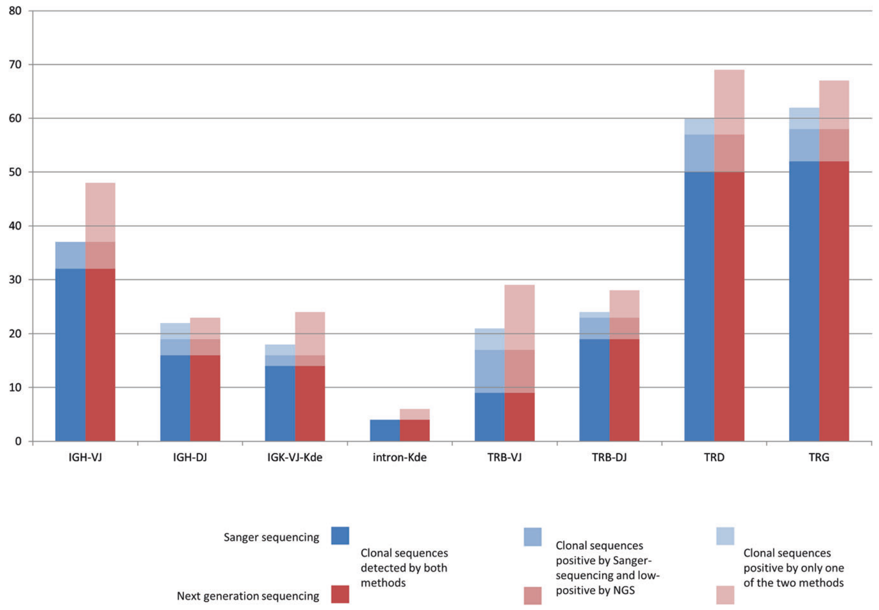

Fig. 3 Results of multicentre validation of assays for MRD marker identification in ALL. Blue: Index sequences identified by Sanger sequencing. Red: Index sequences identified by NGS. Darkest blue/red are clonal sequences identified by both methods; lightest blue/red are sequences identified only by the respective method. Median blue/red are clonal sequences identified by both methods, but by NGS with an abundance of <5% after normalization

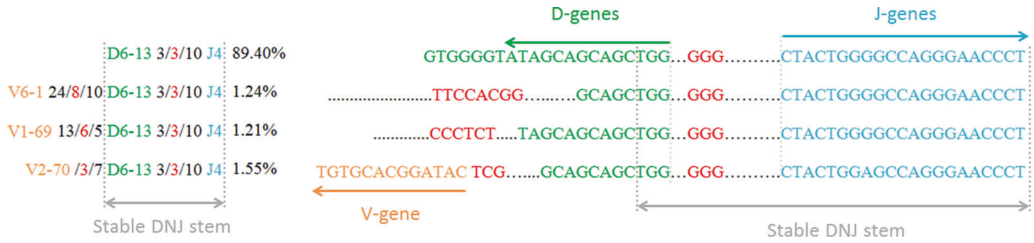

Fig. 4 Clonal evolution in a BCP-ALL patient. The dominant incomplete IGH rearrangement (IGHD6-13 - IGHJ4) was identified with an abundance of 89.4% together with three additional complete IGH rearrangements with lower abundance (1.21–1.55%) and the same DNJ sequence. Only the CDR3 region is shown for each sequence

2 IGH-DJ) the relevant primer was not present in the NGS primer set, in 12/52 cases no explanation was found for the discrepancy. However, in most discordant cases (35/52) the Sanger identified sequences (7 TRD, 8 TRB-VJ, 6 TRG, 4 TRB-DJ, 2 IGK-VJ-Kde, 5 IGH-VJ and 3 IGH-DJ) that were also detectable by NGS, but with an abundance below 5%. In 36/39 q/ddPCR evaluated cases the rearrangement was confirmed by ASO-PCR (including all low NGS positive sequences), in 14 of these on a subclonal level. The overall concordance between Sanger and NGS, including negative libraries, was 78%.

Interestingly, in 12/29 B-lineage ALL samples the evolution of the dominant clonal IGH sequence was identified employing a special tool in ARResT/Interrogate. The evolved clonotypes shared the DNJ stem with the dominant one, but the VND part of the rearrangement differed (example in Fig. 4).

Assay performance was also analysed by standardized evaluation of QC samples (cIT-QC and cPT-QC, see accompanying manuscript by Knecht et al. [30]) and showed high intra- and inter-lab consistency without statistically significant differences between the five labs.

Modifications of the central SOP

During the process of multicentre validation, modifications of the SOP were tested in particular laboratories as parallel projects.

One-step versus two-step PCR

It was decided to use two-step PCR to enable switching of sequencing adaptors and to limit the total number of required primer batches even if a large number of barcodes is required. As first round PCR products are not barcoded, identification of contamination phenomena is hampered in this approach. Therefore, a one-step PCR was tested in a single centre (Paris). The one-step approach reduces the risk of contamination and thus favours use of NGS not only for marker identification, but also for MRD assessment. The standard operating procedure is shown in Supplementary information.

Use of Ion Torrent platform

Ion Torrent platform was tested in a single-centre setting (Prague) and showed a very good concordance ($R^2 = 0.89$) with the standard approach. The standard operating procedure is shown in Supplementary information.

Removal of polyclonal DNA from reaction mix

Polyclonal DNA was added to each reaction in order to prevent excessive primer dimer formation in samples lacking particular rearrangements. The addition of polyclonal DNA, however, alters the composition of polyclonal background of the samples and hampers the analysis of the immune repertoire. We therefore performed testing on four samples with B- and four samples with T-cell aplasia and showed that addition of cIT-QC is sufficient to prevent the excessive formation of unspecific PCR products (see Supplementary information).

Bead extraction

During the single target evaluation and validation phase, gel extraction of the specific TRB amplicons turned out to lead to more specific libraries compared with bead extraction. However, gel extraction is not used in all laboratories, therefore, in a later phase of the study bead purification of all libraries was also tested. Optimization of the purification processes led to comparable ratios of specific reads irrespective of the type of library purification (Supplementary Table 5).

Discussion

Amplicon-based IG/TR NGS provides an elegant method to detect clonality, identify MRD markers and monitor MRD in lymphoid malignancies. However, comprehensive SOPs for all relevant IG/TR targets, applicable QC procedures, suitable bioinformatic tools, and validation of the technology in a scientifically controlled, multicentre setting are still lacking [19].

Here we describe an in vitro and in silico protocol for the diagnostic identification of IG/TR MRD markers in ALL, and demonstrate its robustness and applicability across five European laboratories. EuroClonality-NGS primer sets were successfully used with high reproducibility and good concordance to Sanger sequencing, identifying on average 4% more markers per patient than classical low-throughput methods. NGS was particularly successful in correctly identifying bi-allelic rearrangements, which are technically challenging for Sanger sequencing because this requires prior separation of the respective clonal PCR products. NGS also performs better in the presence of a background of polyclonal rearrangements. Besides, it allows a more comprehensive coverage of rearrangement types. The EuroClonality-NGS TRD assay for example not only detects all types of complete and incomplete TRD gene rearrangements but also VD-JA29 recombinations [40], present in about 20% of all B-cell precursor (BCP) ALLs. In our current series, these TRDV2-JA29 rearrangements were detected in 7/29 BCP-ALL patients (24%), providing an attractive target for MRD monitoring. Notably, rearrangement coverage is not complete. The IGH-DJ tube lacks an IGHD7 primer because that would predominantly amplify the germline-configured IGH-IGHD7-IGHJ1.

Low-throughput sequencing of clonal IG/TR gene rearrangements is often cumbersome. This particularly holds true for TRB, where Sanger sequencing of clonal TRB BIOMED-2 amplicons requires a multistep approach: first with the complete set of primers to identify the rearranged genes, and second, a repetition of the sequencing reaction with gene-specific primers. In contrast, the EuroClonality-NGS assays do not require specific workflows for particular targets, thus enormously streamlining the process of MRD marker identification. This becomes increasingly important in times of MRD-based treatment requiring early patient assignment to the respective MRD risk group.

Critically, our assays provide ways to evaluate primer performance and overall quality of the whole NGS run (primers in the cPT-QC) and of each tube (spike-ins in the cIT-QC, see accompanying manuscript by Knecht et al. [30]). Such functionalities are embedded in the ARResT/Interrogate pipeline, further standardizing the whole workflow. A challenge for correct MRD marker identification in NGS data is the phenomenon of accompanying lymphoid clones that might be mixed up with the leukaemia-specific ones. Therefore, information regarding blast infiltration of the analysed sample must be related to the combined abundance information of the clonal rearrangement, the polyclonal background and the cIT-QC sequences. The integration of all this information allows for a more specific assignment compared with published approaches that define an index sequence simply as sequence with an abundance of >5% [16]. This is particularly necessary for tubes that exclusively cover rearrangements being present only in a minority of lymphoid cells (especially the TRD and intron-Kde tubes). TRD genes are not rearranged in normal B cells and are deleted in most TRγδ cells [41]. Therefore, oligoclonal TCRγδ T cells might give rise to dominant clonotypes in TRD NGS assay, in particular as the normal TCRγδ T-cell repertoire is strikingly skewed during childhood.

Here the cIT-QC-based abundance correction is of utmost importance to avoid miss-assignment of (minor) clonal TRD rearrangements from minor TCRγδ cell populations as leukaemic rearrangements. Also, knowledge on rearrangement patterns in ALL is important. BCP-ALL features neither complete TRD, nor TRBJ1 gene rearrangements, T-ALL in contrast generally does not harbour complete IGH or IGK gene rearrangements [42]. Hence, identification of such rearrangements would actually reflect more the presence of accompanying T- and B-cell clones, respectively. This immunogenetic knowledge is of particular importance if marker identification is performed, e.g. at relapse after stem cell transplantation, when patients often harbour a restricted B- and T-cell repertoire. The EuroClonality-NGS approach allows for the bioinformatic identification and correction of this phenomenon, whereas conventional low-throughput approaches do not harbour correction mechanisms. Nevertheless, we urge caution in assignment of minor clones to the ALL. Although smaller subclones might be missed based on an abundance threshold (which largely explains discrepancies between Sanger sequencing and NGS in our study), decreasing the threshold would be at the expense of specificity.

Oligoclonality is a well-known phenomenon in ALL that hampers conventional IG/TR MRD [43] assessment, but this can be better identified by NGS. Multiple IG/TR gene rearrangements in ALL result from both continuing rearrangement processes (e.g. continuing IGHV to DJ joining) and from secondary rearrangements (e.g. IGH-DJ replacements, V replacement in a complete IGH rearrangement) [23, 44–49]. In 12 of 29 (41.4%) patients with B-lineage ALL, a dominant clonal IGH rearrangement was subjected to clonal evolution, resulting in the presence of smaller subclones with the same D-J stem, but different V-genes. D-J replacements are also an evolutionary possibility but cannot be unambiguously discriminated from unrelated lymphoid clones even with sophisticated bioinformatic tools.

Modifications to the here described EuroClonality-NGS assays would be possible, and have actually been tested and approved to be suitable within the working group. In particular, a one-step instead of the two-step PCR presented here might be a reasonable alternative for sites that would apply NGS not only for marker identification but also for MRD assessment. Finally, the Ion Torrent platform was successfully tested as a replacement for the Illumina MiSeq used in this study, and has subsequently also been applied more extensively for clonality assessment in formalin-fixed paraffin-embedded tissue (see accompanying manuscript by Scheijen et al. [31]).

In summary, the EuroClonality-NGS developed an IG/TR marker identification protocol, which was validated across many expert European laboratories. It covers in vitro and in silico requirements and allows for quality-controlled, streamlined, comprehensive detection of clonal IG/TR rearrangements in ALL. Compared with low-throughput methods, more MRD markers are identified, sensitivity is increased, processing time is reduced and labour-intensive conventional methods to resolve mixed sequences in case of bi-allelic rearrangements or background are avoided. In parallel, the ARResT/Interrogate bioinformatic platform has been developed with specific functionalities addressing potential pitfalls of IG/TR marker identification in ALL, thus enabling a standardized workflow. In addition, the presented approach forms the basis for future applications in clonality assessment, repertoire analysis and MRD quantification in a quality-controlled and accreditable assay with the potential to meet the upcoming European criteria (EU Regulation 2017/746) for in vitro diagnostics.

Acknowledgements Analyses in Brno were supported by Ministry of Health of the Czech Republic, grant no. 16-34272A. Computational resources by the CESNET LM2015042 and the CERIT Scientific Cloud LM2015085, under the programme “Projects of Large Research, Development, and Innovations Infrastructures”. Analyses in the Monza (Centro Ricerca Tettamanti, SS, AG, GF and GC) laboratory were supported by the Italian Association for Cancer Research (AIRC) and Comitato Maria Letizia Verga. Analyses in the Paris (Necker, AP-HP) laboratory were supported by the Ile de France CancéroPôle. Analyses in Prague were supported by AZV 16-32568A, and PRIMUS/17/MED/11. Design of IGK assays and analyses in Nijmegen and Rotterdam laboratories were supported by an Innovation project granted by the Zorgverzekeraars Nederland (number 2017-3442). This publication presents independent research commissioned by the Health Innovation Challenge Fund R9-486, a parallel funding partnership between the Department of Health & Social Care and Wellcome Trust. The views expressed in this publication are those of the author(s) and not necessarily those of the Department of Health & Social Care or Wellcome Trust.

Compliance with ethical standards

Conflict of interest The EuroClonality-NGS Working Group is an independent scientific subdivision of EuroClonality that aims at innovation, standardization and education in the field of diagnostic clonality analysis. The revenues of the previously obtained patent (PCT/NL2003/000690), which is collectively owned by the EuroClonality Foundation and licensed to InVivoScribe, are exclusively used for EuroClonality activities, such as for covering costs of the Working Group meetings, collective WorkPackages and the EuroClonality Educational Workshops. The EuroClonality consortium operates under an umbrella of ESLHO, which is an official EHA Scientific Working Group. MB: contract research for Affimed, Amgen, Regeneron, advisory board of Amgen, Incyte, Speaker bureau of Janssen, Pfizer, Roche. AWL: contract research for Roche-Genentech, research support from Gilead, advisory board for AbbVie, speaker for Gilead, Janssen. RG-S: research grants from Gilead, Takeda, Amgen, and the Spanish government; and reports consulting fees from Janssen, Takeda, Incyte, and BMS. KS: research support from Janssen, Abbvie, Gilead; speaker for Janssen, Abbvie, Gilead; advisory board for Janssen, Abbvie, Gilead. PG: speaker for Gilead.

References

1. Tonegawa S. Somatic generation of antibody diversity. Nature. 1983;302:575–81.
2. Davis MM, Bjorkman PJ. T-cell antigen receptor genes and T-cell recognition. Nature. 1988;334:395–402.
3. Schlissel MS. Regulating antigen-receptor gene assembly. Nat Rev Immunol. 2003;3:890–9.
4. Lefranc M-P, Lefranc G. The T cell receptor factsbook. Academic Press; 2001. https://www.sciencedirect.com/science/book/9780124413528. Accessed 22 Mar 2018.
5. Lefranc M-P, Lefranc G The immunoglobulin factsbook. Academic Press; 2001.
6. Monroe JG, Dorshkind K. Fate decisions regulating bone marrow and peripheral B lymphocyte development. Adv Immunol. 2007;95:1–50.
7. von Boehmer H, Melchers F. Checkpoints in lymphocyte development and autoimmune disease. Nat Immunol. 2010;11:14–20.
8. Evans PAS, Pott C, Groenen PJTA, Salles G, Davi F, Berger F, et al. Significantly improved PCR-based clonality testing in B-cell malignancies by use of multiple immunoglobulin gene targets. Report of the BIOMED-2 Concerted Action BHM4-CT98-3936. Leukemia. 2007;21:207–14.
9. Brüggemann M, White H, Gaulard P, Garcia-Sanz R, Gameiro P, Oeschger S, et al. Powerful strategy for polymerase chain reaction-based clonality assessment in T-cell malignancies Report of the BIOMED-2 Concerted Action BHM4 CT98-3936. Leukemia. 2007;21:215–21.
10. Langerak AW, Groenen PJTA, Brüggemann M, Beldjord K, Bellan C, Bonello L, et al. EuroClonality/BIOMED-2 guidelines for interpretation and reporting of Ig/TCR clonality testing in suspected lymphoproliferations. Leukemia. 2012;26:2159–71.
11. van Dongen JJM, Langerak AW, Brüggemann M, Evans PAS, Hummel M, Lavender FL, et al. Design and standardization of PCR primers and protocols for detection of clonal immunoglobulin and T-cell receptor gene recombinations in suspect lymphoproliferations: report of the BIOMED-2 Concerted Action BMH4-CT98-3936. Leukemia. 2003;17:2257–317.
12. Boyd SD, Marshall EL, Merker JD, Maniar JM, Zhang LN, Sahaf B, et al. Measurement and clinical monitoring of human lymphocyte clonality by massively parallel VDJ pyrosequencing. Sci Transl Med. 2009;1:12ra23.
13. DeKosky BJ, Ippolito GC, Deschner RP, Lavinder JJ, Wine Y, Rawlings BM, et al. High-throughput sequencing of the paired human immunoglobulin heavy and light chain repertoire. Nat Biotechnol. 2013;31:166–9.
14. Bartram J, Goulden N, Wright G, Adams S, Brooks T, Edwards D, et al. High throughput sequencing in acute lymphoblastic leukemia reveals clonal architecture of central nervous system and bone marrow compartments. Haematologica. 2018;103:e110–e114.
15. Faham M, Zheng J, Moorhead M, Carlton VE, Stow P, Coustan-Smith E, et al. Deep-sequencing approach for minimal residual disease detection in acute lymphoblastic leukemia. Blood. 2012;120:5173–80.
16. Ladetto M, Bruggemann M, Monitillo L, Ferrero S, Pepin F, Drandi D, et al. Next-generation sequencing and real-time quantitative PCR for minimal residual disease detection in B-cell disorders. Leukemia. 2014;28:1299–307.
17. Pulsipher MA, Carlson C, Langholz B, Wall DA, Schultz KR, Bunin N, et al. IgH-V(D)J NGS-MRD measurement pre- and early post- allo-transplant defines very low and very high risk ALL patients. Blood. 2015;125:3501–8.
18. Kotrova M, Muzikova K, Mejstrikova E, Novakova M, Bakardjieva-Mihaylova V, Fiser K, et al. The predictive strength of next-generation sequencing MRD detection for relapse compared with current methods in childhood ALL. Blood. 2015;126:1045–7.
19. Langerak AW, Brüggemann M, Davi F, Darzentas N, Gonzalez D, Cazzaniga G, et al. High throughput immunogenetics for clinical and research applications in immunohematology: potential and challenges. J Immunol. 2017;198:3765–74.
20. Kotrova M, van der Velden VHJ, van Dongen JJM, Formankova R, Sedlacek P, Brüggemann M, et al. Next-generation sequencing indicates false-positive MRD results and better predicts prognosis after SCT in patients with childhood ALL. Bone Marrow Transpl. 2017;52:962–8.
21. Kotrova M, Trka J, Kneba M, Brüggemann M. Is next-generation sequencing the way to go for residual disease monitoring in acute lymphoblastic leukemia? Mol Diagn Ther. 2017. https://doi.org/10.1007/s40291-017-0277-9.
22. Freeman JD, Warren RL, Webb JR, Nelson BH, Holt RA. Profiling the T-cell receptor beta-chain repertoire by massively parallel sequencing. Genome Res. 2009;19:1817–24.
23. Gawad C, Pepin F, Carlton VEH, Klinger M, Logan AC, Miklos DB, et al. Massive evolution of the immunoglobulin heavy chain locus in children with B precursor acute lymphoblastic leukemia. Blood. 2012;120:4407–17.
24. Logan AC, Gao H, Wang C, Sahaf B, Jones CD, Marshall EL, et al. High-throughput VDJ sequencing for quantification of minimal residual disease in chronic lymphocytic leukemia and immune reconstitution assessment. Proc Natl Acad Sci USA. 2011;108:21194–9.
25. Logan AC, Zhang B, Narasimhan B, Carlton V, Zheng J, Moorhead M, et al. Minimal residual disease quantification using consensus primers and high-throughput IGH sequencing predicts post-transplant relapse in chronic lymphocytic leukemia. Leukemia. 2013;27:1659–65.
26. Robins HS, Srivastava SK, Campregher PV, Turtle CJ, Andriesen J, Riddell SR, et al. Overlap and effective size of the human CD8+ T cell receptor repertoire. Sci Transl Med. 2010;2:47ra64–47ra64.
27. Wang C, Sanders CM, Yang Q, Schroeder HW, Wang E, Babrzadeh F, et al. High throughput sequencing reveals a complex pattern of dynamic interrelationships among human T cell subsets. Proc Natl Acad Sci. 2010;107:1518–23.
28. Wu D, Sherwood A, Fromm JR, Winter SS, Dunsmore KP, Loh ML, et al. High-throughput sequencing detects minimal residual disease in acute T lymphoblastic leukemia. Sci Transl Med. 2012;4:134ra63–134ra63.
29. Wu Y-C, Kipling D, Leong HS, Martin V, Ademokun AA, Dunn-Walters DK. High-throughput immunoglobulin repertoire analysis distinguishes between human IgM memory and switched memory B-cell populations. Blood. 2010;116:1070–8.
30. Knecht H, Reigl T, Kotrová M, Appelt F, Stewart P, Bystry V, et al. Quality control and quantification in IG/TR next-generation sequencing marker identification: protocols and bioinformatic

functionalities by EuroClonality-NGS. Leukemia; revision. [Epub ahead of print]

31. Scheijen B, Meijers R, Rijntjes J, van der Klift M, Möbs M, Steinhilber J, et al. Next-generation sequencing of immunoglobulin gene rearrangements for clonality assessment: a technical feasibility study by EuroClonality-NGS. Leukemia; revision. [Epub ahead of print]
32. Bystry V, Reigl T, Krejci A, Demko M, Hanakova B, Grioni A, et al. ARResT/Interrogate: an interactive immunoprofiler for IG/TR NGS data. Bioinformatics. 2016;33:btw634.
33. Rozen S, Skaletsky H. Primer3 on the WWW for general users and for biologist programmers. Methods Mol Biol. 2000;132:365–86.
34. Qu W, Zhou Y, Zhang Y, Lu Y, Wang X, Zhao D, et al. MFEprimer-2.0: a fast thermodynamics-based program for checking PCR primer specificity. Nucleic Acids Res. 2012;40:W205–8.
35. van der Velden VHJ, Cazzaniga G, Schrauder A, Hancock J, Bader P, Panzer-Grumayer ER, et al. Analysis of minimal residual disease by Ig/TCR gene rearrangements: guidelines for interpretation of real-time quantitative PCR data. Leukemia. 2007;21:604–11.
36. Pongers-Willemse MJ, Seriu T, Stolz F, D'Aniello E, Gameiro P, Pisa P, et al. Primers and protocols for standardized detection of minimal residual disease in acute lymphoblastic leukemia using immunoglobulin and T cell receptor gene rearrangements and TAL1 deletions as PCR targets: report of the BIOMED-1 CONCERTED ACTION. Leukemia. 1999;13:110–8.
37. Duez M, Giraud M, Herbert R, Rocher T, Salson M, Thonier F, et al. Vidjil: a web platform for analysis of high-throughput repertoire sequencing. PLoS ONE. 2016;11:e0166126.
38. Giudicelli V, Brochet X, Lefranc M-P. IMGT/V-QUEST: IMGT standardized analysis of the immunoglobulin (IG) and T cell. Recept (TR) Nucleotide Seq Cold Spring Harb Protoc. 2011;2011:695–715.
39. Giudicelli V, Chaume D, Lefranc MP. IMGT/GENE-DB: a comprehensive database for human and mouse immunoglobulin and T cell receptor genes. Nucleic Acids Res. 2005;33:D256–61.
40. Szczepanski T, Van Der Velden VHJ, Hoogeveen PG, De Bie M, Jacobs CH, Van Wering ER, et al. Vdelta2-Jalpha rearrangements are frequent in precursor-B-acute lymphoblastic leukemia but rare in normal lymphoid cells. Blood. 2004;103:3798–804.
41. Lefranc MP, Rabbitts TH. Genetic organization of the human T-cell receptor gamma and delta loci. Res Immunol. 1990;141:565–77.
42. Dongen J van, Szczepanski T, Adriaansen H. Immunobiology of leukemia. 7th edn. WB Saudners Company: Philadelphia; 2002.
43. van Dongen JJ, Seriu T, Panzer-Grumayer ER, Biondi A, Pongers-Willemse MJ, Corral L, et al. Prognostic value of minimal residual disease in acute lymphoblastic leukaemia in childhood. Lancet. 1998;352:1731–8.
44. Kitchingman GR. Immunoglobulin heavy chain gene VH-D junctional diversity at diagnosis in patients with acute lymphoblastic leukemia. Blood. 1993;81:775–82.
45. Steenbergen EJ, Verhagen OJ, van Leeuwen EF, von dem Borne AE, van der Schoot CE. Distinct ongoing Ig heavy chain rearrangement processes in childhood B-precursor acute lymphoblastic leukemia. Blood. 1993;82:581–9.
46. Szczepański T, Willemse MJ, Brinkhof B, van Wering ER, van der Burg M, van Dongen JJM. Comparative analysis of Ig and TCR gene rearrangements at diagnosis and at relapse of childhood precursor-B-ALL provides improved strategies for selection of stable PCR targets for monitoring of minimal residual disease. Blood. 2002;99:2315–23.
47. de Haas V, Verhagen OJ, von dem Borne AE, Kroes W, van den Berg H, van der Schoot CE. Quantification of minimal residual disease in children with oligoclonal B-precursor acute lymphoblastic leukemia indicates that the clones that grow out during relapse already have the slowest rate of reduction during induction therapy. Leukemia. 2001;15:134–40.
48. Germano G, del Giudice L, Palatron S, Giarin E, Cazzaniga G, Biondi A, et al. Clonality profile in relapsed precursor-B-ALL children by GeneScan and sequencing analyses. Consequences on minimal residual disease monitoring. Leukemia. 2003;17:1573–82.
49. Theunissen PMJ, van Zessen D, Stubbs AP, Faham M, Zwaan CM, van Dongen JJM, et al. Antigen receptor sequencing of paired bone marrow samples shows homogeneous distribution of acute lymphoblastic leukemia subclones. Haematologica. 2017;102:1869–77.

Affiliations

Monika Brüggemann[1] · Michaela Kotrová[1,2] · Henrik Knecht[1] · Jack Bartram[3] · Myriam Boudjogrha[4] · Vojtech Bystry[5] · Grazia Fazio[6] · Eva Froňková[2] · Mathieu Giraud[7] · Andrea Grioni[6] · Jeremy Hancock[8] · Dietrich Herrmann[1] · Cristina Jiménez[9] · Adam Krejci[5] · John Moppett[10] · Tomas Reigl[5] · Mikael Salson[7] · Blanca Scheijen[11] · Martin Schwarz[1] · Simona Songia[6] · Michael Svaton[2] · Jacques J. M. van Dongen[12] · Patrick Villarese[13] · Stephanie Wakeman[8] · Gary Wright[3] · Giovanni Cazzaniga[6] · Frédéric Davi[4] · Ramón García-Sanz[9] · David Gonzalez[14] · Patricia J. T. A. Groenen[11] · Michael Hummel[15] · Elizabeth A. Macintyre[13] · Kostas Stamatopoulos[16] · Christiane Pott[1] · Jan Trka[2] · Nikos Darzentas[1,5] · Anton W. Langerak[17] · on behalf of the EuroClonality-NGS working group

[1] Department of Hematology, University Hospital Schleswig-Holstein, Kiel, Germany

[2] CLIP - Childhood Leukaemia Investigation Prague, Department of Paediatric Haematology and Oncology, Second Faculty of Medicine, Charles University, University Hospital Motol, Prague, Czech Republic

[3] Department of Paediatric Haematology, Great Ormond Street Hospital, London, UK

[4] Department of Hematology, Hopital Pitié-Salpêtrière, Paris, France

[5] Central European Institute of Technology, Masaryk University, Brno, Czech Republic

[6] Centro Ricerca Tettamanti, University of Milano Bicocca, Monza, Italy

[7] CNRS, CRIStAL, Université Lille, Inria Lille, France

[8] Bristol Genetics Laboratory, Southmead Hospital, Bristol, UK

[9] Hospital Universitario de Salamanca-IBSAL, Salamanca, Spain

[10] Department of Pediatric Haematology, Bristol Royal Hospital for Children, Bristol, UK

[11] Department of Pathology, Radboud University Medical Center, Nijmegen, The Netherlands

[12] Department of Immunohematology and Blood Transfusion (IHB), Leiden University Medical Center, Leiden, The Netherlands

[13] Department of Hematology, APHP Necker-Enfants Malades and Paris Descartes University, Paris, France

[14] Centre for Cancer Research and Cell Biology, Queen's University Belfast, Belfast, UK

[15] Insititute of Pathology, Charité – Universitätsmedizin Berlin, Berlin, Germany

[16] Institute of Applied Biosciences, Thessaloniki, Greece

[17] Department of Immunology, Laboratory Medical Immunology, Erasmus MC, University Medical Center, Rotterdam, The Netherlands

Leukemia (2019) 33:2254–2265
https://doi.org/10.1038/s41375-019-0499-4

ARTICLE

Minimal residual disease

Quality control and quantification in IG/TR next-generation sequencing marker identification: protocols and bioinformatic functionalities by EuroClonality-NGS

Henrik Knecht[1] · Tomas Reigl[2] · Michaela Kotrová[1] · Franziska Appelt[1] · Peter Stewart[3] · Vojtech Bystry[2] · Adam Krejci[2] · Andrea Grioni[4] · Karol Pal[2] · Kamila Stranska[2,5] · Karla Plevova[2,5] · Jos Rijntjes[6] · Simona Songia[4] · Michael Svatoň[7] · Eva Froňková[7] · Jack Bartram[8] · Blanca Scheijen[6] · Dietrich Herrmann[1] · Ramón García-Sanz[9] · Jeremy Hancock[10] · John Moppett[11] · Jacques J. M. van Dongen[12] · Giovanni Cazzaniga[4] · Frédéric Davi[13] · Patricia J. T. A. Groenen[6] · Michael Hummel[14] · Elizabeth A. Macintyre[15] · Kostas Stamatopoulos[16] · Jan Trka[7] · Anton W. Langerak[17] · David Gonzalez[3] · Christiane Pott[1] · Monika Brüggemann[1] · Nikos Darzentas[1,2] · on behalf of the EuroClonality-NGS Working Group

Received: 15 January 2019 / Revised: 23 March 2019 / Accepted: 23 April 2019 / Published online: 21 June 2019

Abstract

Assessment of clonality, marker identification and measurement of minimal residual disease (MRD) of immunoglobulin (IG) and T cell receptor (TR) gene rearrangements in lymphoid neoplasms using next-generation sequencing (NGS) is currently under intensive development for use in clinical diagnostics. So far, however, there is a lack of suitable quality control (QC) options with regard to standardisation and quality metrics to ensure robust clinical application of such approaches. The EuroClonality-NGS Working Group has therefore established two types of QCs to accompany the NGS-based IG/TR assays. First, a central polytarget QC (cPT-QC) is used to monitor the primer performance of each of the EuroClonality multiplex NGS assays; second, a standardised human cell line-based DNA control is spiked into each patient DNA sample to work as a central in-tube QC and calibrator for MRD quantification (cIT-QC). Having integrated those two reference standards in the ARResT/Interrogate bioinformatic platform, EuroClonality-NGS provides a complete protocol for standardised IG/TR gene rearrangement analysis by NGS with high reproducibility, accuracy and precision for valid marker identification and quantification in diagnostics of lymphoid malignancies.

Introduction

Identification and assessment of clonal immunoglobulin (IG) and T cell receptor (TR) gene rearrangements is a widely used tool for the diagnosis of lymphoid malignancies, and is also essential for monitoring minimal residual disease (MRD) [1–6].

Next-generation sequencing (NGS) of IG/TR gene rearrangements is gaining popularity in clinical laboratories, as it avoids laborious design of patient-specific real-time quantitative (RQ)-PCR assays and provides the capability to sequence multiple rearrangements and rearrangement types within a single sequencing run. It also allows detection of MRD with a more specific readout than RQ-PCR [7]. Hence, several methods have already been described for high-throughput profiling of IG/TR rearrangements at diagnosis and follow-up in acute lymphoblastic leukaemia (ALL), chronic lymphocytic leukaemia (CLL) and other lymphoid malignancies [8–13].

NGS assays, especially those based on amplicons, pose major challenges, as multiple primers need to anneal under the same reaction conditions, while many technical variables may be introduced by library preparation, sequencing and bioinformatics, potentially leading to inaccurate results [14]. Particularly in a clinical context, strategies for standardisation of laboratory protocols and quality control (QC) of each component of an NGS assay are highly desirable, if not required.

Supplementary information The online version of this article (https://doi.org/10.1038/s41375-019-0499-4) contains supplementary material, which is available to authorized users.

✉ Anton W. Langerak
a.langerak@erasmusmc.nl

Extended author information available on the last page of the article.

Reference standards are essential for the evaluation of wet-lab and in silico NGS processes to ensure the analytical validity of test results prior to implementation of an NGS technology into clinical practice [15–17]. Reference DNA materials should be stable sources of rearrangements that can be sequenced and used for measuring qualitative and quantitative properties. However, previously published standards have a limited scope and utility, since they (1) do not cover all relevant IG/TR loci, (2) do not report on the quality of the sequencing run or the performance of samples and primers and/or (3) are synthetic constructs that may not reflect the complexity of native genomic DNA [9, 18, 19].

The EuroClonality-NGS Working Group was initiated to develop, standardise and validate protocols for IG/TR NGS applications, as introduced in Langerak et al. [20] and described in the accompanying manuscripts by Brüggemann et al. [21] and Scheijen et al. [22]. Innovatively, the EuroClonality-NGS assays include two types of QCs, both based on basic assay components, and both fully integrated in ARResT/Interrogate [23], the interactive bioinformatics platform developed within the Working Group:

1. A central polytarget QC (cPT-QC) consisting of a standardised mixture of lymphoid specimens, representing a full repertoire of IG/TR genes. It serves to assess performance biases or unusual amplification shifts in a sequencing run by tracking primer usage and comparison with stored reference profiles.
2. A central in-tube quality/quantification control (cIT-QC) consisting of human B and T cell lines with well-defined IG/TR rearrangements. The cIT-QC is directly added to a sample to undergo concurrent library preparation and sequencing, acting as in-tube qualitative and quantitative standard that is subjected to the same technical downstream variables.

Here we describe, evaluate and showcase these concepts and functionalities. We tested the developed protocol on a dataset of polyclonal samples, B-ALL and T-ALL diagnostic materials and follow-ups of patients with substantial treatment-induced shifts in IG/TR repertoires. We show its successful application and robustness for clinical laboratories that want to implement the EuroClonality-NGS assays for marker identification and quantification. Figure 1 provides an overview of the study.

Materials and methods

EuroClonality-NGS assay

The EuroClonality-NGS assay for marker identification used herein is the two-step PCR protocol with eight primer sets (IGH-VJ, IGH-DJ, IGK-VJ-Kde, intron-Kde, TRB-VJ, TRB-DJ, TRG, TRD)—hereafter termed ‘tubes’—per sample, as described in the accompanying manuscript by Brüggemann et al. [21].

ARResT/Interrogate

ARResT/Interrogate uses a web browser-based interface to (1) run an analytical pipeline to identify different types of rearrangements—‘junction classes’—across all IG/TR loci (Supplementary Table S1), (2) store, retrieve and report on runs, (3) allow highly varied analyses and visualisations and (4) enable purpose-built meta-analyses and applications. Bioinformatic analyses were performed with ARResT/Interrogate and purpose-built tools unless otherwise stated. Further implementation details are provided below and as Supplementary Information. The platform is currently freely available at arrest.tools/interrogate, hosted at the MetaCentrum and CERIT-SC centres in the Czech Republic.

Implementation of the cPT-QC

Sources and methods

The cPT-QC consists of genomic DNA isolated from healthy human thymus, tonsil and peripheral blood mononuclear cells (MNCs) in a 1:1:1 ratio (see Supplementary Information). The cPT-QC undergoes library preparation alongside the investigated samples (Figs. 1 and 2).

Implementation

Primers are bioinformatically identified in the reads of each of the eight cPT-QC tubes of the run and their abundances compared to stored cPT-QC reference results using the test of proportions.

Stored reference results are the output of ARResT/Interrogate from the analysis of a cPT-QC sample. These results should be confirmed through replicate runs over time in each lab to accommodate for technical variability (see Discussion). The results (and not the raw NGS data) are stored to ensure that the bioinformatic analysis is not compromised inadvertently by the user; this means that the results are updated with every major release of ARResT/Interrogate to ensure compatibility with new runs.

Issues with abundances of primers of a specific primer set are used to tag the corresponding cPT-QC samples and all user samples of the same primer set as ‘QC-failed’.

Replicates

As reproducibility is important for a QC of this type, we performed replicate runs of cPT-QC and also of MNC (four

Fig. 1 Study design: components and steps of development (in blue), application (in green) and testing for the central polytarget quality control (cPT-QC) and central in-tube quality/quantification control (cIT-QC), including a schematic overview of the test dataset based on a 96-well plate. Text boxes are either shared across cPT-QC and cIT-QC or describing equivalent steps if on same row. MNC = mononuclear cells, QC = quality control, ref. = reference, w/o = without

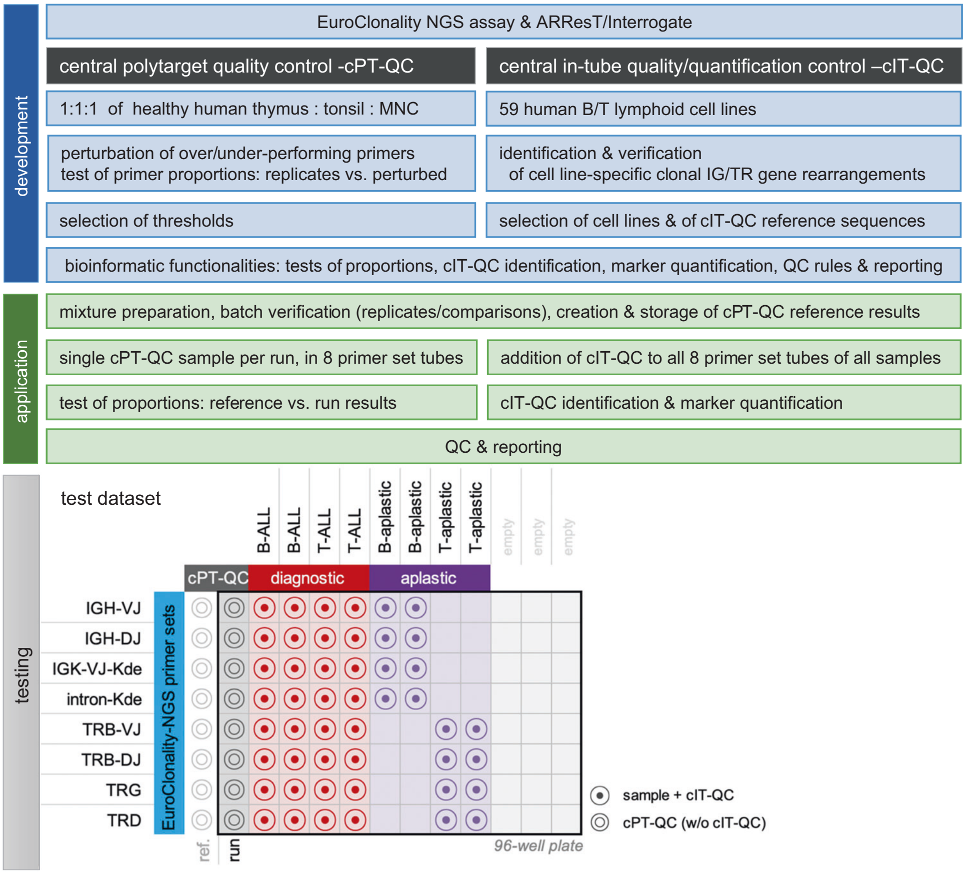

libraries in total); MNCs are regularly used and could serve as an alternative. Relative abundances of 5′ primers were compared employing the test of proportions.

Primer perturbations

To investigate whether and how the cPT-QC can be used to detect issues with primer performance, artificial perturbations of primer concentrations were created to simulate missing pipetting a primer or pipetting the wrong primer concentration.

First, 5′ primer usage was analysed in a cPT-QC sample. Two primers of differing abundances were selected from each primer set, skipping intron-Kde that only has two primers: IGH-VJ-FR1-M-1, IGHV-FR1-O-1; IGHD-B-1, IGHD-E-1; IGK-V-G-1, IGK-V-I-1; TRB-V-AD-1, TRB-V-G-1; TRB-D-A-1, TRB-D-B-1; TRG-V-F-1, TRG-V-E-1; TRD-D-A-1, TRD-V-B-1. Second, these primers were perturbed by fully excluding them from the primer pool (0%) and by changing their concentration by reduction to 10% and by increase to 200%. Replicate runs of these three primer-perturbed cPT-QC libraries (six in total) were performed; however, since the replicates were consistent (data not shown), only the first replicate of each is shown in Results. Finally, relative abundances of 5′ primers were compared between normal replicates and between normal replicates and the perturbed libraries using the test of proportions.

Design and validation of the cIT-QC

Sources and methods

In total, 59 human B ($n = 30$) and T ($n = 29$) lymphoid cell lines were obtained from the American Type Culture Collection (ATCC, Manassas, VA, USA; www.lgcpromochem-atcc.com) and the German Collection of Microorganisms and Cell Cultures GmbH (DSMZ, Braunschweig, Germany; www.dsmz.de), or were derived from internal cell line banks. Supplementary Table S2 gives an overview of the cell lines. DNA from cultured cell lines was isolated using a phenol–chloroform extraction protocol, followed by ethanol precipitation and elution in Tris ethylenediaminetetra-acetic acid buffer. Alternatively, DNA was isolated with the GenElute Mammalian Genomic DNA Miniprep Kit (Sigma-Aldrich, St. Louis, MO, USA) according to the manufacturer's protocol.

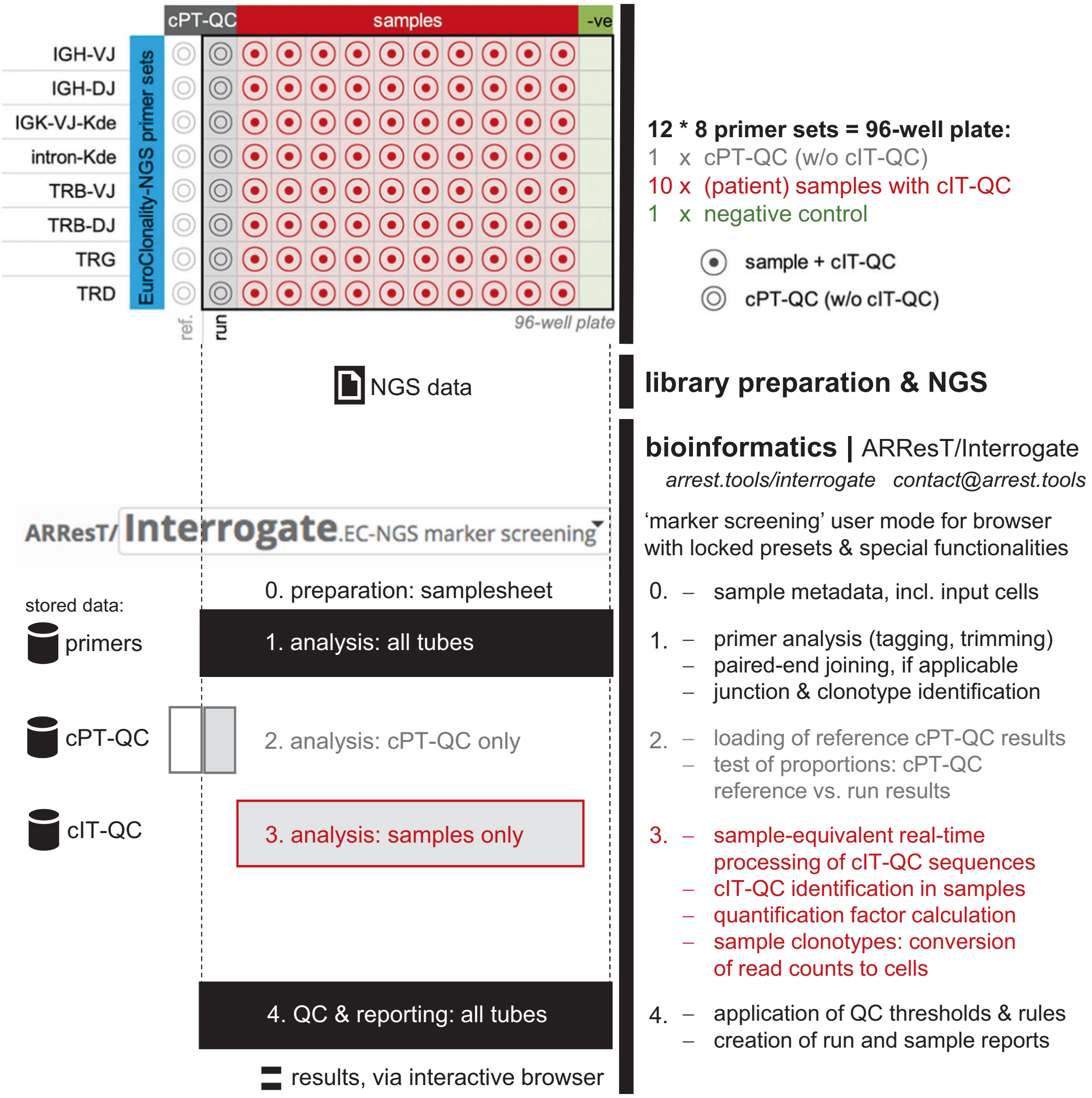

Fig. 2 EuroClonality-NGS (next-generation sequencing) protocol for quality control and quantification in marker identification: 96-well plate set-up, including central polytarget quality control (cPT-QC) and central in-tube quality/quantification control (cIT-QC), library preparation and NGS, bioinformatics with ARResT/Interrogate. The bioinformatics are additionally organised per sample type to showcase distinct steps and functionalities listed on the right: all tubes (1 and 4, in black), cPT-QC (2, in grey), (patient) samples (3, in red)—these colours are shared with the well plate. ref. = reference, QC = quality control, w/o = without

Identification of cell line-specific clonal IG/TR gene rearrangements

Each of the 59 cell lines was screened for clonal IG/TR gene rearrangements using the EuroClonality-NGS assay with 100 ng of DNA (quantified with Qubit 3.0, Thermo Fisher Scientific) from each cell line, without the addition of MNC. Paired-end sequencing (2 × 250 bp) was performed on Illumina MiSeq (Illumina, San Diego, CA, USA) with a final concentration of 7 pM per library aiming for at least 2000 reads per sample. To avoid low-complexity issues, 10% PhiX control was added to each sequencing run.

Verification of cell line-specific clonal IG/TR gene rearrangements

Additional methods were used to verify the NGS amplicon-identified cell line rearrangements:

1. A capture-based protocol, established within EuroClonality-NGS Working Group and covering the coding V, D and J genes of IG/TR loci [13]: in short, cell line DNA was fragmented and processed with the KAPA Hyperplus Kit with Library Amplification (Roche Sequencing Solutions, Pleasanton, CA, USA); hybridisation of libraries was performed

with customised SeqCap EZ Choice Probes (Roche Sequencing Solutions, Pleasanton, CA, USA), developed based on Wren et al. [13] 2 × 150 bp paired-end sequencing was performed on Illumina NextSeq.
2. Multiplex amplification and Sanger sequencing according to the BIOMED-2 protocol: PCR products were checked for fragment sizes and clonality in the QIAXCEL Advanced System [24, 25]. Clonal PCR products were subjected to heteroduplex analysis and sequenced on either an ABI 3130 or ABI 3500 platform (Applied Biosystems, Foster City, CA, USA).

IG/TR rearrangement profiles of all cell lines were compared between the different methods.

For cases with discrepant results between the three methods, IG/TR allele-specific PCR assays were designed for digital droplet PCR (ddPCR) (QX200TM Droplet DigitalTM PCR System, Bio-Rad) to verify the respective rearrangement. Absolute quantification of IG/TR gene rearrangements by ddPCR was performed using two different genomic DNA amounts (50 ng, 100 ng) (Supplementary Information). Each experiment included a polyclonal MNC control and a no-template control.

Cell line selection criteria

For establishment of the cIT-QC from the spectrum of IG/TR gene rearrangements of the 59 cell lines, the following selection criteria were defined:

1. The final set should consist of as few cell lines as possible, while covering each primer set by at least three different rearrangements, hence aiming for ALL cell lines harbouring not only lineage characteristic but also cross-lineage rearrangements.
2. The rearrangements should be unambiguously detectable with Sanger sequencing and amplicon-based NGS.
3. The variable region of IGHV-(IGHD)-IGHJ gene rearrangements should preferably be unmutated in order to avoid issues with primer annealing.

Implementation

For cIT-QC mixture preparation see Supplementary Information.

Bioinformatically, cIT-QC reads are identified using an immunogenetic annotation-based approach that is extremely fast while allowing for variations in sequence, avoiding compute-intensive and potentially inaccurate alignment.

For QC, we expect identification of at least one read per cIT-QC rearrangement and of at least as many total cIT-QC reads as total cIT-QC cells, otherwise the tube is tagged as 'QC-failed' (see below for how this is used in ARResT/Interrogate).

Quantification applies the quantification factor—calculated per primer set by dividing total cIT-QC cells by total cIT-QC reads—to convert read counts of a clonotype to cell counts, and then calculate its relative abundance against the total sample input cells.

Creation of a test dataset

To evaluate and showcase the aforementioned concepts and functionalities, we compiled a test dataset with:

1. Four diagnostic bone marrow B-/T-ALL samples with high leukaemic infiltration (assessed by routine cytomorphology to be 60–80%).
2. Four samples of patients with B/T cell aplasia after antibody treatment. The two samples with B cell aplasia were CLL samples after Rituximab (anti-CD20) treatment and the two samples with T cell aplasia were T cell prolymphocytic leukaemia samples after Alemtuzumab (anti-CD52) treatment. In all these samples lineage-specific aplasia was confirmed by flow cytometry.
3. cPT-QC for all primer sets, but with the TRB-VJ primer set results swapped with perturbed results from experiments outlined above. To showcase generic QC functionalities, one diagnostic sample was subsampled to <1000 random reads.

The diagnostic samples and the cPT-QC were run with all primer sets as described in the accompanying manuscript by Brüggemann et al. [21], while the aplastic follow-up samples only with the corresponding primer sets, that is, the IG sets for samples with B cell aplasia, and the TR sets for samples with T cell aplasia. Figure 1 includes a schematic of the test dataset. Finally, the follow-up samples were run without the addition of MNC to test that the addition of cIT-QC is sufficient to stabilise the samples for sequencing without compromising their immunogenetic profile.

Results

The resulting protocol and functionalities for QC and quantification in IG/TR NGS marker identification are depicted in Fig. 2. We present and further discuss the underlying results below.

Table 1 cPT-QC: replicates and primer perturbations. Relative abundances (%) of selected 5′ primers across all primer sets. Top group of primers were perturbed as described in Materials and methods; bottom group is a selection of primers that were left un-perturbed: one per primer set selected alphabetically, plus two examples where the primer behaviour is of interest to the discussion (see text). Results are shown from two cPT-QC replicates (blue column) and from replicate 1 of the blue column ("rep1") vs. cPT-QC libraries where primers were excluded (0%, orange column), reduced to 10% (yellow column) and increased to 200% (green column). Changes in abundance compared to cPT-QC rep1 are shown separately (column "% or rep1", in italics) and coloured from red (0%) to white (100%, i.e. no change) to green (200%). Actual primer abundances are coloured based on the p value from the test of proportions, with grey indicating a noticeable change according to our threshold of 1e−200 (p value <1e−199 highlighted in dark grey, and <1e−99 in light grey, otherwise in white)

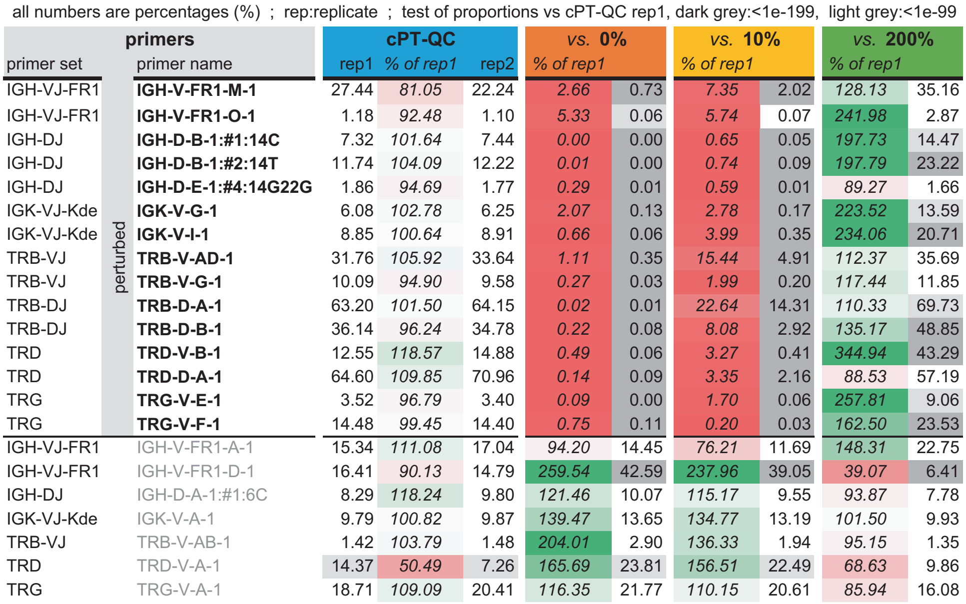

all numbers are percentages (%) ; rep:replicate ; test of proportions vs cPT-QC rep1, dark grey:<1e-199, light grey:<1e-99

primers			**cPT-QC**			*vs.* **0%**		*vs.* **10%**		*vs.* **200%**	
primer set		primer name	rep1	*% of rep1*	rep2	*% of rep1*		*% of rep1*		*% of rep1*	
IGH-VJ-FR1	perturbed	**IGH-V-FR1-M-1**	27.44	*81.05*	22.24	*2.66*	0.73	*7.35*	2.02	*128.13*	35.16
IGH-VJ-FR1		**IGH-V-FR1-O-1**	1.18	*92.48*	1.10	*5.33*	0.06	*5.74*	0.07	*241.98*	2.87
IGH-DJ		**IGH-D-B-1:#1:14C**	7.32	*101.64*	7.44	*0.00*	0.00	*0.65*	0.05	*197.73*	14.47
IGH-DJ		**IGH-D-B-1:#2:14T**	11.74	*104.09*	12.22	*0.01*	0.00	*0.74*	0.09	*197.79*	23.22
IGH-DJ		**IGH-D-E-1:#4:14G22G**	1.86	*94.69*	1.77	*0.29*	0.01	*0.59*	0.01	*89.27*	1.66
IGK-VJ-Kde		**IGK-V-G-1**	6.08	*102.78*	6.25	*2.07*	0.13	*2.78*	0.17	*223.52*	13.59
IGK-VJ-Kde		**IGK-V-I-1**	8.85	*100.64*	8.91	*0.66*	0.06	*3.99*	0.35	*234.06*	20.71
TRB-VJ		**TRB-V-AD-1**	31.76	*105.92*	33.64	*1.11*	0.35	*15.44*	4.91	*112.37*	35.69
TRB-VJ		**TRB-V-G-1**	10.09	*94.90*	9.58	*0.27*	0.03	*1.99*	0.20	*117.44*	11.85
TRB-DJ		**TRB-D-A-1**	63.20	*101.50*	64.15	*0.02*	0.01	*22.64*	14.31	*110.33*	69.73
TRB-DJ		**TRB-D-B-1**	36.14	*96.24*	34.78	*0.22*	0.08	*8.08*	2.92	*135.17*	48.85
TRD		**TRD-V-B-1**	12.55	*118.57*	14.88	*0.49*	0.06	*3.27*	0.41	*344.94*	43.29
TRD		**TRD-D-A-1**	64.60	*109.85*	70.96	*0.14*	0.09	*3.35*	2.16	*88.53*	57.19
TRG		**TRG-V-E-1**	3.52	*96.79*	3.40	*0.09*	0.00	*1.70*	0.06	*257.81*	9.06
TRG		**TRG-V-F-1**	14.48	*99.45*	14.40	*0.75*	0.11	*0.20*	0.03	*162.50*	23.53
IGH-VJ-FR1		IGH-V-FR1-A-1	15.34	*111.08*	17.04	*94.20*	14.45	*76.21*	11.69	*148.31*	22.75
IGH-VJ-FR1		IGH-V-FR1-D-1	16.41	*90.13*	14.79	*259.54*	42.59	*237.96*	39.05	*39.07*	6.41
IGH-DJ		IGH-D-A-1:#1:6C	8.29	*118.24*	9.80	*121.46*	10.07	*115.17*	9.55	*93.87*	7.78
IGK-VJ-Kde		IGK-V-A-1	9.79	*100.82*	9.87	*139.47*	13.65	*134.77*	13.19	*101.50*	9.93
TRB-VJ		TRB-V-AB-1	1.42	*103.79*	1.48	*204.01*	2.90	*136.33*	1.94	*95.15*	1.35
TRD		TRD-V-A-1	14.37	*50.49*	7.26	*165.69*	23.81	*156.51*	22.49	*68.63*	9.86
TRG		TRG-V-A-1	18.71	*109.09*	20.41	*116.35*	21.77	*110.15*	20.61	*85.94*	16.08

cPT-QC allows to assess primer performance

We compared normal cPT-QC and MNC replicate libraries and primer-perturbed cPT-QC replicate libraries (10 libraries in total) to investigate the use of cPT-QC in assessing primer performance. We applied the test of proportions on 5′ primer relative abundances in those libraries, which showed that there is a clear difference in p values between un-perturbed (high p values indicating insignificant changes) and perturbed (low p values) primers. In other words, p values of the differences in abundance of the perturbed primers are noticeably lower, an observation we can use to highlight such cases.

Table 1 presents a simplified view of the results, focusing on perturbed primers plus at least one other un-perturbed primer per primer set, either to show their normal behaviour or discuss their abnormal behaviour. At a p value threshold of $1e^{-200}$ none of the primers are flagged in the cPT-QC (white cells), which highlights the reproducibility of the assay, while all the perturbed primers are flagged in the perturbed libraries (light/dark grey cells). Significant changes in abundance are also visible in other cells, with the most likely explanation that those primers were indirectly affected by perturbations of other primers. That is, a primer 'taking over' when an initially abundant primer was excluded, such as IGHV-FR1-D-1 when IGH-VJ-FR1-M-1 is perturbed either way, especially since these primers amplify partially overlapping lists of genes. Supplementary Table S3 presents the full set of results, including the actual p values and results from the replicate MNC libraries.

Composing the cIT-QC sample from human B and T cell lines

Following the criteria outlined above, we selected six B cell lines: ALL/MIK (ALL), Raji (Burkitt lymphoma), REH (B cell precursor ALL), TMM (CML-BC/EBV + B-LCL), TOM-1 (ALL) and WSU-NHL (B cell lymphoma, histiocytic lymphoma); and three T cell lines: JB6 (ALCL), Karpas299 (ALCL) and MOLT-13 (ALL). The nine cell lines featured a total of 46 rearrangements, all of which are used as part of the cIT-QC. All but two rearrangements that were not detected by capture NGS were detected by all three sequencing methods. Also, another two were of very low abundance and/or trimmed in the capture NGS data, but since the junction segmentation was clearly the same, they were still tagged as confirmed. Table 2 presents the full list of the 46 rearrangements, with the NGS amplicon-based reference nucleotide sequences in Supplementary Table S4.

QC aspects can be evaluated in ARResT/Interrogate

Information on the in silico QC based on both the cPT-QC and cIT-QC is available in ARResT/Interrogate (Supplementary Figure S1). Generic QC is also performed on samples, specifically to check for low number of raw reads and low percentage of reads with an identified junction. Such samples are tagged as 'QC-failed' and excluded by default to prevent the user from their unintended use. However, the user is notified and has the option to include them back in the analysis.

Marker identification and quantification

Abundances of lymphocyte subpopulations are frequently not available for samples of patients with lymphoid malignancies. Furthermore, as IG/TR NGS only reflects relative representation of the rearrangements, it was important to establish a calibrator that would allow us to normalise sequencing reads to input DNA cells.

Analysis of our test dataset showed the utility of the cIT-QC in marker identification and quantification. Excluding cIT-QC reads, both diagnostic and aplastic samples seem to harbour few highly abundant clones if simply based on the number of reads (Fig. 3, Supplementary Table S5). However, the very high number of reads from only a very limited number of cIT-QC cells (120–440, dependent on the number of cIT-QC rearrangements per primer set), in all aplastic and a few of the diagnostic samples, are an indirect yet clear indication of the restricted numbers of patient cells harbouring rearrangements in those samples. From another perspective, the total percentage of reads of cIT-QC is much greater than that of patient rearrangements in those samples, suggesting that also cIT-QC cells are more numerous than patient cells with rearrangements. Consequently, after quantification with the cIT-QC, marker abundances fall well below the threshold indicating clonality. On the other hand, and as expected, in most diagnostic samples cIT-QC reads constitute a minority, indicating the true abundant presence of patient cells with clonal rearrangements. Hence, using the cIT-QC, a marker can be more accurately quantified and identified.

ARResT/Interrogate user mode for marker identification

A critical aspect of bioinformatic-based protocols is their standardisation and usability, as evident from our experiences within EuroClonality-NGS and EuroMRD. We have thus designed ARResT/Interrogate to be flexible but also 'lockable'. Flexibility comes from a deep parameterisation of many aspects of the pipeline and the browser. At the same time, we can lock down important parameters so that users cannot inadvertently compromise the analysis. This concept is called 'user mode' in ARResT/Interrogate, and as a result of this study we have created a marker identification user mode.

In this user mode, EuroClonality-NGS primer sets and cIT-QC sequences are pre-selected and locked, as are other pipeline options. A special samplesheet is available to annotate samples with metadata, including providing numbers of sample input cells for quantification. The user interface is simplified, with many non-essential functionalities (including many of the visualisations normally available) hidden from view, and with less user actions required to load results. The minimum read-based percentage abundance for a clonotype is pre-set to 5% for marker identification.

Discussion

In this study, we introduce protocols developed within the EuroClonality-NGS Working Group for QC and quantification in NGS-based IG/TR marker identification. Both laboratory and bioinformatic protocols are presented and showcased on clinically relevant data.

The cPT-QC is used to monitor the primer performance of each of the EuroClonality multiplex NGS assays; the cIT-QC is spiked into each patient DNA sample for QC and quantification. The use of 'central' highlights that these controls should be as stable as possible and thus centrally available at an applicable level (minimum at an intra-laboratory level)—this is further discussed below in the context of the cPT-QC.

Our experiments show that the cPT-QC is a valuable tool to monitor reproducibility of results and to identify primer perturbations and other deviations in the wet-lab protocol, as they introduce detectable changes to the sequencing profile. The addition of cPT-QC to each analysis allows to check the primer and assay performance after sequencing. Accidental deviations in the concentrations of single primers within the multiplexed IG/TR primer sets can be detected, performance failures of single primers can be traced and consequences for the IG/TR analysis can be estimated by analysis of cPT-QC data.

In our study, replicates of cPT-QC demonstrated high reproducibility. Nevertheless, we are aware that reproducibility across labs may be affected by a large number of other variables, from consumables and equipment to users. Only centralised access to consumables, for example, in the form of a kit, and a comprehensive protocol, including the

Table 2 cIT-QC: full list of gene rearrangements per primer set and human B/T cell line, with notes on their verification and clonotype annotation

Primer set	Cell line	Notes	Clonotype (see Supplementary Information—Materials and methods)
TRB-VJ	JB6		VJ:Vb-(Db)-Jb V12–3 = V12–4 6/14/4 J2–3 CASRLAGGPDTQYF pro
TRB-DJ	JB6		DJ:Db-Jb D1 7/6/4 J2–2 VGTEITGELFF pop
TRG	JB6		VJ:Vg-Jg V10 7/12/12 J1 = J2 CAAWS*GW#KLF unp
TRG	JB6		VJ:Vg-Jg V2 5/13/ J1 = J2 CATWGSI*VNYYKKLF unp
TRB-VJ	Karpas299		VJ:Vb-(Db)-Jb V20–1 1/22/6 J2–7 CSARAQIGSSPLEQYF pro
TRB-DJ	Karpas299		DJ:Db-Jb D1 /2/6 J1–6 VGTGGLNSPLHF pop
TRG	Karpas299		VJ:Vg-Jg V2 /13/4 JP2 CATWDGG*VP#SDWIKTF unp
TRG	Karpas299		VJ:Vg-Jg V8 /2/5 J1 = J2 CATWDR##YKKLF unp
IGH-VJ-FR1	ALL/MIK		VJ:Vh-(Dh)-Jh V3–72 16/24/ J4 SPCPPRKN#YFDYW unp
IGH-VJ-FR1	ALL/MIK		VJ:Vh-(Dh)-Jh V7–4–1 11/40/27 J4 TPYYYDSSGY*VP unp
IGK-VJ-Kde	ALL/MIK		Vk-Kde V2–24 = V2D-24 26/6/20 Kde LGGR unk
IGK-VJ-Kde	ALL/MIK		VJ:Vk-Jk V1–39 = V1D-39 6/7/5 J3 CQQSYSTGA#F unp
intron-Kde	ALL/MIK		Intron-Kde intron 4/2/ Kde PCVCPIDAAVASFP##SPSGSPGR unk
Intron-Kde	ALL/MIK	Capture: low%	Intron-Kde intron 4/6/1 Kde PCVCPIDAAVASFPSL#SPSGSPGR unk
TRD	ALL/MIK		VJ:Vd-(Dd)-Ja V2 5/21/4 J29 CACAQGGPRS#SGNTPLVF unp
TRG	ALL/MIK		VJ:Vg-Jg V2 /5/8 JP1 CATWDGP#GWFKIF unp
TRG	ALL/MIK		VJ:Vg-Jg V5 2/3/ JP1 CATWDTYTTGWFKIF pro
TRB-VJ	MOLT-13		VJ:Vb-(Db)-Jb V10–1 6/18/1 J1–1 CASRRVRRDRNTEAFF unp
TRB-DJ	MOLT-13		DJ:Db-Jb D1 //6 J1–5 VGTGG#QPQHF pop
TRB-DJ	MOLT-13		DJ:Db-Jb D2 /4/3 J2–3 VGTSGRA#TDTQYF pop
TRD	MOLT-13		VJ:Vd-(Dd)-Jd V1 1/9/ J1 CALGEPGGYTDKLIF pro
TRG	MOLT-13		VJ:Vg-Jg V3 /8/9 J1 = J2 CATWDRPRLKKLF pro
TRG	MOLT-13		VJ:Vg-Jg V8 3//3 JP1 CATWD#TGWFKIF unp
IGH-VJ-FR1	Raji	Capture: low%	VJ:Vh-(Dh)-Jh V3–11 = V3–21 = V3–48 2/40/3 J4 CARQRNDFSDNNSYYSNFDFW pro
IGH-DJ	Raji		DJ:Dh-Jh D6–13 8/12/6 J1 VGYSSIPPP#YFQHW pop
IGK-VJ-Kde	Raji		Vk-Kde V1–8 2/2/4 Kde CQQYYSYSVPSGSPGR unk
IGH-VJ-FR1	REH		VJ:Vh-(Dh)-Jh V3–15 1/21/5 J6 CTTGMVRGVI#YYYYGMDVW unp
IGK-VJ-Kde	REH		VJ:Vk-Jk V2–29 5/4/ J4 *MQGIHLS#LTF unp
IGK-VJ-Kde	REH		Vk-Kde V3–20 = V3D-20 4/1/ Kde CQQYGSS##SPSGSPGR unk
Intron-Kde	REH		Intron-Kde intron 5// Kde PCVCPINAAVASF##SPSGSPGR unk
TRB-VJ	REH		VJ:Vb-(Db)-Jb V20–1 1/2/26 J2–7 CSARG unp
TRD	REH		VD:Vd-Dd3 V2 7/3/ D3 CACLLGDTH unk
TRD	REH		VJ:Vd-(Dd)-Ja V2 3/22/5 J29 CACDPYGGGSP#SGNTPLVF unp
TRG	REH		VJ:Vg-Jg V9 1/2/3 J1 = J2 CALWEV#YYKKLF unp
TRG	REH		VJ:Vg-Jg V4 10/14/3 J1 = J2 CATLF*R#YYKKLF unp
IGH-VJ-FR1	TMM		VJ:Vh-(Dh)-Jh V1–24 /28/8 J5 CATDQAISGVVKSFDPW pro

Table 2 (continued)

Primer set	Cell line	Notes	Clonotype (see Supplementary Information—Materials and methods)
IGH-DJ	TMM		DJ:Dh-Jh D2–2 3/13/ J3 VRIL**YQLLLNSANDAFDIW pop
IGK-VJ-Kde	TMM		Vk-Kde V2–30 = V2D-30 /7/3 Kde CMQGTHWRPGR#PSGSPGR unk
IGH-VJ-FR1	TOM-1		VJ:Vh-(Dh)-Jh V4–55 1/17/10 J6 CARWAGTTG#YYGMDVW unp
TRD	TOM-1		VD:Vd-Dd3 V2 3/3/2 D3 CACDL#GDTH unk
TRD	TOM-1		VD:Vd-Dd3 V2 8/4/ D3 CAFLLGDTH unk
TRG	TOM-1		VJ:Vg-Jg V5 8//18 J1 = J2 CAT#F unp
IGH-VJ-FR1	WSU-NHL		VJ:Vh-(Dh)-Jh V6–1 1/22/19 J6 CARGTYAAKASMDVW pro
IGH-DJ	WSU-NHL		DJ:Dh-Jh D2–2 1/1/8 J4 VRIL**YQLLY#DYW pop
IGK-VJ-Kde	WSU-NHL	Not in capture	VJ:Vk-Jk V1–17 = V1D-17 1//4 J4 CLQHNSYP#TF unp
Intron-Kde	WSU-NHL	Not in capture	Intron-Kde intron 2//3 Kde PCVCPIDAAVASFP##PSGSPGR unk

See Supplementary Table S4 for NGS amplicon-based full nucleotide reference sequences. *cIT-QC* central in-tube quality/quantification control

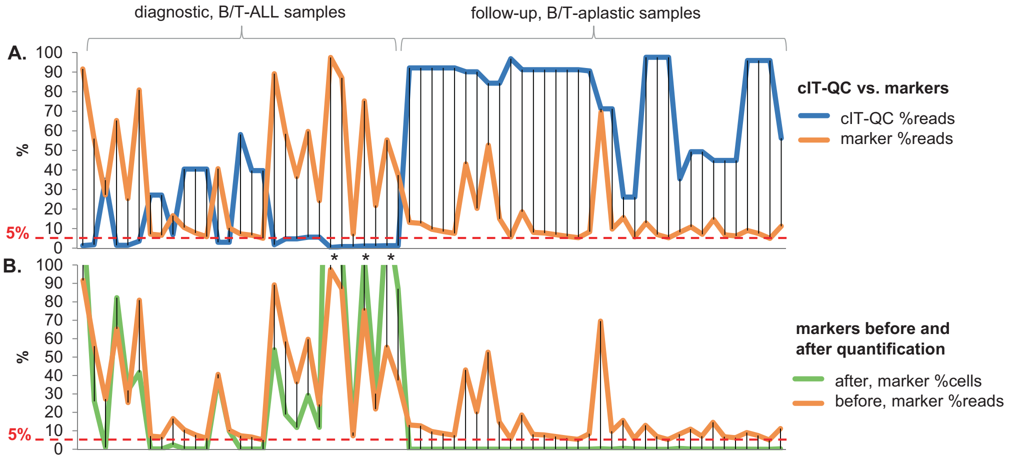

Fig. 3 Abundances of central in-tube quality/quantification control (cIT-QC) and of markers before and after quantification, in the test dataset. The line of marker abundances before quantification (in orange) is shared in both plots for reference. The 5% threshold used for marker identification is shown in both plots. **a** Abundance in percentage of reads ("%reads") of cIT-QC (in blue) and of markers before quantification (in orange), in diagnostic (left half) and follow-up aplastic (right half) samples. As expected because of the nature of the samples, the cIT-QC is generally most abundant where patient cells with clonal rearrangements are not, and vice versa. Note: For cIT-QC (in blue), the denominator is all reads with junction; for markers (in orange), it is what we term 'usable' reads with junction, which excludes cIT-QC reads; this may lead to sums of those two numbers that exceed 100% per sample. **b** Abundance of markers before (in orange) and after (in green) cIT-QC-based quantification to percentage of patient input cells ("%cells"). Quantification of markers in the aplastic samples places their abundances below the 5% threshold routinely used in marker identification and in the EuroClonality-NGS protocols. Note: When cIT-QC read counts are very low, indicating clonality, quantification factors may lead %cells to exceed 100%; three such cases in the test dataset are indicated by an asterisk (" * ")

equipment used, will further improve inter-laboratory comparability of results. Besides, activities such as the QC rounds organised bi-annually by ESLHO (eslho.org) are an opportunity to gather data and experience, compare assay performance and identify relevant factors introducing variations. Until full inter-laboratory standardisation is guaranteed, the implementation of the cPT-QC will require that the reference samples are analysed in each laboratory separately, and updated with every new batch of reagents, while keeping track of equipment and users. These reference data can then be stored in ARResT/Interrogate, which has the ability to store as many different such sets of reference data as needed, for example, linking a specific set to a specific user if necessary.

In this study we also highlighted a number of unique and advantageous properties of the cIT-QC. In contrast to plasmids or synthetic reference templates, cIT-QC cell lines are particularly well suited to be used as control because they are sources of large quantities of genomic DNA. Second, the nine cell lines with a total of 46 rearrangements represent as few cell lines as possible while covering each primer set by at least three different rearrangements, taking advantage of ALL cell lines harbouring not only lineage-associated but also cross-lineage rearrangements. Third, the rearrangements are unambiguously detectable with amplicon-based NGS. Fourth, the variable region of IGHV-(IGHD)-IGHJ gene rearrangements are not/lowly mutated and therefore minimise issues with primer annealing. Fifth, cIT-QC rearrangements represent 2/3 of the amplifiable junction classes (in italics in Supplementary Table S1) over all eight primer sets, and thus offer an opportunity to highlight a number of issues, most obviously over-/under-amplification, but also bioinformatic misidentification. Additionally, cIT-QC rearrangements can replace MNC for PCR stability without influencing the patient immune repertoire (since cIT-QC rearrangements are identified and by default excluded from the results).

Our cIT-QC enables the conversion from reads to cells, which is of utmost importance for clinical use. Diagnostic material being analysed for MRD marker identification can show abundances of particular clonotypes that do not reflect the clonal composition of the sample. For example, if the diagnostic sample is highly infiltrated by a lymphoid malignancy that does not harbour a targetable rearrangement, the (few) residual lymphoid cells would generate the whole spectrum of detectable rearrangements; in such situations minor accompanying physiological B or T cell clones could be misassigned as clones with leukaemic markers. In the accompanying study by Brüggemann et al. [21], where 134 clonal signals with abundance >5% were detected by NGS but not by Sanger sequencing, cIT-QC quantification reduced the abundances of 71 (53%) of them below the 5% threshold.

In addition to its use in marker identification, and as exemplarily shown for B and T cell depletion in aplastic follow-up samples, the cIT-QC is of utmost relevance for MRD quantification in samples on or after treatment, in particular if B or T cell-directed therapy was applied, which minimises the background of polyclonal gene rearrangements. If the relative tumour burden is calculated by the ratio of leukaemia-specific reads to all annotated reads without any quantification, the quotient reflects the marker frequency only among cells carrying a particular type of rearrangement (e.g. IG rearrangements in B cells) and might thus heavily overestimate the tumour load [26].

Quantification values over 100% (examples in Fig. 3b and Supplementary Table S5) show that using the cIT-QC is still a semi-quantitative approach, potentially affected by amplification biases. However, there is to date no other scientific or commercial solution available that exceeds our methodology in its broad applicability (universal IG/TR approach) and/or allows precise absolute quantification [12, 27–29].

Finally, the QC protocols are embedded in ARResT/Interrogate, which informs users with reports and messages and allows them, for example, to include the QC-failed samples back into the analysis. The logic behind this is that the 'fail' flag simply indicates that our pre-defined QC criteria were not met, and not that the data are corrupt beyond use. Nevertheless, flagged data should always be used with caution, and dependent on the application or question.

In summary, our study showcases the applicability of two reference standards, developed by the EuroClonality-NGS Working Group, which allow standardised analysis of IG/TR NGS data (using the EuroClonality-NGS primer sets) with high reproducibility, accuracy and precision in marker identification. With ARResT/Interrogate, a complete in silico solution accompanying the in vitro assays was built, enabling an analysis of IG/TR sequences including all quality criteria and quantification concepts necessary for valid marker identification in lymphoid malignancies.

Acknowledgements This work was supported by Ministry of Health of the Czech Republic, grant no. 16-34272A; computational resources were provided by the CESNET LM2015042 and the CERIT Scientific Cloud LM2015085, provided under the programme "Projects of Large Research, Development, and Innovations Infrastructures". Analyses in Prague (JT, EF and MS) were supported by Ministry of Health, Czech Republic, grant no. 00064203, and by PRIMUS/17/MED/11. Analyses in the Monza (Centro Ricerca Tettamanti, SS, AG and GC) laboratory were supported by the Italian Association for Cancer Research (AIRC) and Comitato Maria Letizia Verga.

Compliance with ethical standards

Conflict of interest The EuroClonality-NGS Working Group is an independent scientific subdivision of EuroClonality that aims at innovation, standardisation and education in the field of diagnostic clonality analysis. The revenues of the previously obtained patent (PCT/NL2003/000690), which is collectively owned by the EuroClonality Foundation and licensed to InVivoScribe, are exclusively used for EuroClonality activities, such as for covering costs of the Working Group meetings, collective WorkPackages and the EuroClonality Educational Workshops. MB: contract research for Affimed, Amgen, Regeneron, advisory board of Amgen, Incyte, Speaker bureau of Janssen, Pfizer, Roche; AWL: contract research for Roche-Genentech, research support from Gilead, advisory board for AbbVie, speaker for Gilead, Janssen; RG-S: research grants from Gilead, Takeda, Amgen and the Spanish government; and reports consulting fees from Janssen, Takeda, Incyte and BMS; KS: research support from Janssen, Abbvie, Gilead; speaker for Janssen, Abbvie, Gilead;

advisory board for Janssen, Abbvie, Gilead; PG: speaker for Gilead. The other authors declare that they have no conflict of interest.

References

1. Pott C. Minimal residual disease detection in mantle cell lymphoma: technical aspects and clinical relevance. Semin Hematol. 2011;48:172–84.
2. Ferrero S, Drandi D, Mantoan B, Ghione P, Omedè P, Ladetto M. Minimal residual disease detection in lymphoma and multiple myeloma: Impact on therapeutic paradigms. Hematol Oncol. 2011;29:167–76.
3. Brüggemann M, Gökbuget N, Kneba M. Acute lymphoblastic leukemia: monitoring minimal residual disease as a therapeutic principle. Semin Oncol. 2012;39:47–57.
4. Brüggemann M, Raff T, Kneba M. Has MRD monitoring superseded other prognostic factors in adult ALL? Blood. 2012;120:4470–81.
5. Van Dongen JJM, Seriu T, Panzer-Grümayer ER, Biondi A, Pongers-Willemse MJ, Corral L, et al. Prognostic value of minimal residual disease in acute lymphoblastic leukaemia in childhood. Lancet. 1998;352:1731–8.
6. Brüggemann M, Kotrova M. Minimal residual disease in adult ALL: technical aspects and implications for correct clinical interpretation. Hematol Am Soc Hematol Educ Progr. 2017;2017 (1):13–21.
7. Kotrova M, Van Der Velden VHJ, Van Dongen JJM, Formankova R, Sedlacek P, Brüggemann M, et al. Next-generation sequencing indicates false-positive MRD results and better predicts prognosis after SCT in patients with childhood ALL. Bone Marrow Transplant. 2017;52:962–8.
8. Logan AC, Vashi N, Faham M, Carlton V, Kong K, Buño I, et al. Immunoglobulin and t cell receptor gene high-throughput sequencing quantifies minimal residual disease in acute lymphoblastic leukemia and predicts post-transplantation relapse and survival. Biol Blood Marrow Transplant. 2014;20:1307–13.
9. Faham M, Zheng J, Moorhead M, Carlton VEH, Stow P, Coustan-Smith E, et al. Deep-sequencing approach for minimal residual disease detection in acute lymphoblastic leukemia. Blood. 2012;120:5173–80.
10. Logan AC, Zhang B, Narasimhan B, Carlton V, Zheng J, Moorhead M, et al. Minimal residual disease quantification using consensus primers and high-throughput IGH sequencing predicts post-transplant relapse in chronic lymphocytic leukemia. Leukemia. 2013;27:1659–65.
11. Logan AC, Gao H, Wang C, Sahaf B, Jones CD, Marshall EL, et al. High-throughput VDJ sequencing for quantification of minimal residual disease in chronic lymphocytic leukemia and immune reconstitution assessment. Proc Natl Acad Sci USA. 2011;108:21194–9.
12. Ladetto M, Brüggemann M, Monitillo L, Ferrero S, Pepin F, Drandi D, et al. Next-generation sequencing and real-time quantitative PCR for minimal residual disease detection in B-cell disorders. Leukemia. 2014;28:1299–307.
13. Wren D, Walker BA, Brüggemann M, Catherwood MA, Pott C, Stamatopoulos K, et al. Comprehensive translocation and clonality detection in lymphoproliferative disorders by next-generation sequencing. Haematologica. 2017;102:e57–e60.
14. Hardwick SA, Deveson IW, Mercer TR. Reference standards for next-generation sequencing. Nat Rev Genet. 2017;18:473–84.
15. Gargis AS, Kalman L, Lubin IM. Assuring the quality of next-generation sequencing in clinical microbiology and public health laboratories. J Clin Microbiol. 2016;54:2857–65.
16. Endrullat C, Glökler J, Franke P, Frohme M. Standardization and quality management in next-generation sequencing. Appl Transl Genom. 2016;10:2–9.
17. Kotrova M, Trka J, Kneba M, Brüggemann M. Is next-generation sequencing the way to go for residual disease monitoring in acute lymphoblastic leukemia? Mol Diagn Ther. 2017;21:481–92.
18. Kurtz DM, Green MR, Bratman SV, Scherer F, Liu CL, Kunder CA, et al. Noninvasive monitoring of diffuse large B-cell lymphoma by immunoglobulin high-throughput sequencing. Blood. 2015;125:3679–87.
19. Pulsipher Ma, Carlson C, Langholz B, Wall Da, Schultz KR, Bunin N, et al. IgH-V (D) J NGS-MRD measurement pre- and early post-allotransplant de fi nes very low- and very high-risk ALL patients. Blood. 2015;125:3501–9.
20. Langerak AW, Brüggemann M, Davi F, Darzentas N, van Dongen JJM, Gonzalez D, et al. High-throughput immunogenetics for clinical and research applications in immunohematology: potential and challenges. J Immunol. 2017;198:3765–4.
21. Brüggemann M, Kotrova M, Knecht H, Bartram J, Boudjoghra M, Bystry, V et al. Next-generation sequencing of immunoglobulin and T-cell receptor gene rearrangements for MRD marker identification in acute lymphoblastic leukemia: a validation study by EuroClonality-NGS. Leukemia. 2019. In press.
22. Scheijen B, Meijers RW, Rijntjes J, van der Klift MY, Möbs M, Steinhilber J et al. Next-generation sequencing of immunoglobulin gene rearrangements for clonality assessment: a technical feasibility study by EuroClonality-NGS. Leukemia. 2019. In press.
23. Bystry V, Reigl T, Krejci A, Demko M, Hanakova B, Grioni A, et al. ARResT/Interrogate: an interactive immunoprofiler for IG/TR NGS data. Bioinformatics. 2017;33:435–7.
24. van Dongen JJM, Langerak AW, Brüggemann M, Evans PAS, Hummel M, Lavender FL, et al. Design and standardization of PCR primers and protocols for detection of clonal immunoglobulin and T-cell receptor gene recombinations in suspect lymphoproliferations: Report of the BIOMED-2 concerted action BMH4-CT98-3936. Leukemia. 2003;17:2257–317.
25. Langerak a W, Szczepański T, Van Der Burg M, ILM Wolvers-Tettero, JJM VanDongen. Heteroduplex PCR analysis of rearranged T cell receptor genes for clonality assessment in suspect T cell proliferations. Leukemia. 1997;11:2192–9.
26. Grupp SA, Kalos M, Barrett D, Aplenc R, Porter DL, Rheingold SR, et al. Chimeric antigen receptor-modified T cells for acute lymphoid leukemia. N Engl J Med. 2013;368:1509–18.
27. Salson M, Giraud M, Caillault A, Grardel N, Duployez N, Ferret Y, et al. High-throughput sequencing in acute lymphoblastic leukemia: follow-up of minimal residual disease and emergence of new clones. Leuk Res. 2017;53:1–7.

28. Takamatsu H, Wee RK, Zaimoku Y, Murata R, Zheng J, Moorhead M, et al. A comparison of minimal residual disease detection in autografts among ASO-qPCR, droplet digital PCR, and next-generation sequencing in patients with multiple myeloma who underwent autologous stem cell transplantation. Br J Haematol. 2017. https://doi.org/10.1111/bjh.15002.

29. Wood B, Wu D, Crossley B, Dai Y, Williamson D, Gawad C, et al. Measurable residual disease detection by high-throughput sequencing improves risk stratification for pediatric B-ALL. Blood. 2018;131:1350–9.

Affiliations

Henrik Knecht[1] · Tomas Reigl[2] · Michaela Kotrová[1] · Franziska Appelt[1] · Peter Stewart[3] · Vojtech Bystry[2] · Adam Krejci[2] · Andrea Grioni[4] · Karol Pal[2] · Kamila Stranska[2,5] · Karla Plevova[2,5] · Jos Rijntjes[6] · Simona Songia[4] · Michael Svatoň[7] · Eva Froňková[7] · Jack Bartram[8] · Blanca Scheijen[6] · Dietrich Herrmann[1] · Ramón García-Sanz[9] · Jeremy Hancock[10] · John Moppett[11] · Jacques J. M. van Dongen[12] · Giovanni Cazzaniga[4] · Frédéric Davi[13] · Patricia J. T. A. Groenen[6] · Michael Hummel[14] · Elizabeth A. Macintyre[15] · Kostas Stamatopoulos[16] · Jan Trka[7] · Anton W. Langerak[17] · David Gonzalez[3] · Christiane Pott[1] · Monika Brüggemann[1] · Nikos Darzentas[1,2] on behalf of the EuroClonality-NGS Working Group

[1] Department of Hematology, University Hospital Schleswig-Holstein, Kiel, Germany

[2] Central European Institute of Technology, Masaryk University, Brno, Czech Republic

[3] Centre for Cancer Research and Cell Biology, Queen's University Belfast, Belfast, UK

[4] Centro Ricerca Tettamanti, University of Milano Bicocca, Monza, Italy

[5] Department of Internal Medicine – Hematology and Oncology, University Hospital Brno and Faculty of Medicine, Masaryk University, Brno, Czech Republic

[6] Department of Pathology, Radboud University Medical Center, Nijmegen, The Netherlands

[7] CLIP – Childhood Leukaemia Investigation Prague, Department of Paediatric Haematology and Oncology, Second Faculty of Medicine, Charles University, University Hospital Motol, Prague, Czech Republic

[8] Department of Paediatric Haematology, Great Ormond Street Hospital, London, UK

[9] IBMCC-CSIC, Hospital Universitario de Salamanca-IBSAL, Salamanca, Spain

[10] Bristol Genetics Laboratory, Southmead Hospital, Bristol, UK

[11] Department of Pediatric Haematology, Bristol Royal Hospital for Children, Bristol, UK

[12] Department of Immunohematology and Blood Transfusion (IHB), Leiden University Medical Center, Leiden, The Netherlands

[13] Department of Hematology, Hopital Pitié-Salpêtrière, Paris, France

[14] Insititute of Pathology, Charité – Universitätsmedizin Berlin, Berlin, Germany

[15] Department of Hematology, APHP Necker-Enfants Malades and Paris Descartes University, Paris, France

[16] Institute of Applied Biosciences, Centre for Research and Technology Hellas, Thessaloniki, Greece

[17] Department of Immunology, Laboratory Medical Immunology, Erasmus MC, University Medical Center, Rotterdam, The Netherlands

Bone Marrow Transplantation (2017) **52,** 544–551

www.nature.com/bmt

ORIGINAL ARTICLE

GvL effects in T-prolymphocytic leukemia: evidence from MRD kinetics and TCR repertoire analyses

This article has been corrected since Advance Online Publication and a corrigendum is also printed in this issue.

L Sellner[1], M Brüggemann[2], M Schlitt[2], H Knecht[2], D Herrmann[2], T Reigl[3], A Krejci[3], V Bystry[3], N Darzentas[3], M Rieger[1,4], S Dietrich[1,5], T Luft[1], AD Ho[1], M Kneba[2] and P Dreger[1]

Allogeneic stem cell transplantation (alloSCT) is used for treating patients with T-prolymphocytic leukemia (T-PLL). However, direct evidence of GvL activity in T-PLL is lacking. We correlated minimal residual disease (MRD) kinetics with immune interventions and T-cell receptor (TCR) repertoire diversity alterations in patients after alloSCT for T-PLL. Longitudinal quantitative MRD monitoring was performed by clone-specific real-time PCR of TCR rearrangements ($n=7$), and TCR repertoire diversity assessment by next-generation sequencing (NGS; $n=3$) Although post-transplant immunomodulation (immunosuppression tapering or donor lymphocyte infusions) resulted in significant reduction (>1 log) of MRD levels in 7 of 10 occasions, durable MRD clearance was observed in only two patients. In all three patients analyzed by TCR-NGS, MRD responses were reproducibly associated with a shift from a clonal, T-PLL-driven profile to a polyclonal signature. Novel clonotypes that could explain a clonal GvL effect did not emerge. In conclusion, TCR-based MRD quantification appears to be a suitable tool for monitoring and guiding treatment interventions in T-PLL. The MRD responses to immune modulation observed here provide first molecular evidence for GvL activity in T-PLL which, however, may be often only transient and reliant on a poly-/oligoclonal rather than a monoclonal T-cell response.

Bone Marrow Transplantation (2017) **52,** 544–551; doi:10.1038/bmt.2016.305; published online 12 December 2016

INTRODUCTION

T-prolymphocytic leukemia (T-PLL) is a rare T-cell malignancy. It has an aggressive clinical course resistant to chemotherapy. Preliminary clinical data suggest that cellular immunotherapy conferred with allogeneic stem cell transplantation (alloSCT) may provide long-term disease control in a proportion of patients.[1–5] However, direct evidence that GvL activity is indeed effective in T-PLL is lacking.[6]

While circumstantial evidence for GvL in hematological malignancies could be derived from the correlation with immune-modulating events such as chronic GvHD (cGvHD), donor lymphocyte infusion, immunosuppression withdrawal, and higher relapse rates with T-cell-depleted alloSCT, the most compelling evidence for GvL may be provided by investigating the effects of immune modulation on minimal residual disease (MRD) kinetics as demonstrated in CLL.[7–11]

Clone-specific rearrangements of the T-cell receptor (TCR) genes are present in virtually all T-PLL cases. Therefore, identification and quantification of clonal T cells by PCR can be a valuable tool to monitor MRD in T-PLL and other T-cell malignancies after alloSCT.[12] In addition to measuring MRD kinetics, comprehensive longitudinal TCR repertoire analysis by next-generation sequencing (NGS) may help to dissect the anatomy of GvL activity in T-PLL by delineating TCR diversity in relation to GvL responses.[13–15]

In this study we sought to investigate MRD kinetics and TCR repertoire diversity alterations after alloSCT as tools for proving and modulating GvL activity in T-PLL. The results suggest that TCR-based MRD quantification is possible. GvL is effective in T-PLL but often only limited or transient, and is driven by poly- or oligoclonal T-cell responses rather than single dominant T-cell clones.

METHODS

Patients

The study sample consisted of consecutive 10 patients diagnosed with T-PLL who received alloSCT at the University of Heidelberg between August 2007 and March 2015. The median age at alloSCT was 59 years (range 43–72) with the majority of patients (80%) being male. Eight patients proceeded to transplant in first CR (7) or PR (1) after first-line alemtuzumab monotherapy, one patient was in CR subsequent to salvage chemotherapy upon alemtuzumab failure, and one patient was in PR subsequent to salvage alemtuzumab after chemotherapy failure. A minimum wash-out time of 6 weeks (median 12 weeks, range 6–22 weeks) between the last alemtuzumab dose and alloSCT had been observed in all patients. Five patients were transplanted with an unrelated donor, four patients with a related donor and one patient received haploidentical alloSCT. Conditioning was fludarabine with cyclophosphamide and/or TBI-based, with all regimens to be considered as reduced-intensity (4) or non-myeloablative (6). Patient and transplant characteristics are detailed in Table 1. Informed consent for transplantation, data collection and scientific evaluation of blood and marrow samples was obtained from every patient in accordance with the Declaration of Helsinki. The research was approved by the Ethics Committee of the University of Heidelberg (S-120/2002).

---

[1]Department of Medicine V, University Hospital Heidelberg, Heidelberg, Germany; [2]Department of Hematology, University Hospital Schleswig-Holstein, Kiel, Germany; [3]Central European Institute of Technology, Masaryk University, Brno, Czech Republic; [4]Oncology Practice Darmstadt, Darmstadt, Germany and [5]Genome Biology Unit, European Molecular Biology Laboratory, Heidelberg, Germany. Correspondence: Dr L Sellner, Department of Medicine V, University Hospital Heidelberg, Im Neuenheimer Feld 410, Heidelberg 69120, Germany.
E-mail: leopold.sellner@med.uni-heidelberg.de

Presented in part in abstract form at the 57th Annual Meeting of the American Society of Hematology (ASH; December 5–8, 2015, Orlando, FL, USA) and the 42nd Annual Meeting of the European Society for Blood and Marrow Transplantation (EBMT; April 3–6, 2016, Valencia, Spain).
Received 30 August 2016; revised 9 October 2016; accepted 18 October 2016; published online 12 December 2016

Table 1. Patient and transplant characteristics

Patient	Year of alloSCT	Age at alloSCT/ sex	Regimens before alloSCT	Disease status at alloSCT	Conditioning regimen	Donor	Graft source	DLI	Chronic GvHD	MRD response to	Chim day 100 (% donor)	Best chim (% donor) (months after alloSCT)	Relapse (month after alloSCT)	Alive	Follow-up (month after alloSCT)	Cause of death
1	2007	58/M	Cam s.c.	CR1	FC	MRD	PB	Y	limited	IS taper	95	100 (5)	Y (70)	N	83	Relapse
2	2008	61/F	Cam s.c.	CR1	FC/ATG	MUD	PB	Y	limited	DLI	80	100 (17)	Y (40)	N	45	Relapse
3	2008	60/M	Cam s.c.	CR1	FC	MRD	PB	N	n.a.	n.a.	95	100 (5)	N	N	6	aGvHD
4	2008	43/M	Cam s.c.	CR1	FC/ATG	MUD	PB	Y	limited	IS taper, DLI	70	100 (48)	N	Y	92+	
5	2012	72/M	Cam i.v.	CR1	F/TBI2	MRD	PB	N	none	N	98	98 (3)	Y (6)	N	15	Relapse
6	2013	64/M	FMC+Cam s.c.; Cam i.v.	PR after PIF	F/TBI6/ATG	MUD	PB	Y	extensive	IS taper, DLI	100	100 (3)	Y (19)	N	39	Relapse
7	2014	57/F	Cam i.v.; FMC	CR after PIF	F/TBI6/ATG	MUD	PB	N	none	N	100	100 (1)	Y (17)	N	21	Relapse
8	2014	45/M	Cam i.v.	CR1	F/TBI8	MRD	PB	N	limited	IS taper	100	100 (1)	N	Y	24+	
9	2014	68/M	Cam i.v.	PR1	F/TBI8/ATG	MMUD	PB	N	n.a.	n.a.	n.a.	100 (1)	N	N	3	aGvHD
10	2015	58/M	Cam i.v.	CR1	FC/TBI2/ ptCY	Haplo	BM	N	n.a.	n.a.	50	92 (1)	N	N	7	aGvHD

Abbreviations: aGvHD = acute GvHD; alloSCT = allogeneic stem cell transplantation; ATG = anti thymocyte globulin; BM = bone marrow; Cam = alemtuzumab; Chim = chimerism; CR1 = CR after first therapy; DLI = donor lymphocyte infusion; F (sex) = female; F (conditioning) = fludarabine; FC = fludarabine+cyclophosphamide; FMC = fludarabine+mitoxantrone+cyclophosphamide; haplo = haploidentical donor; IS = immunosuppression; M = male, MMUD = mismatched unrelated donor; MRD = minimal residual disease; MRD (donor) = matched related donor; MUR = matched unrelated donor; N = no, n.a. = not applicable; PB = peripheral blood; PIF = primary induction failure; PR1 PR after first therapy; ptCY = post-transplant cyclophosphamide; TBI2 = TBI2 Gray, TBI6 = TBI6 Gray, TBI8 = TBI8 Gray, Y = yes.

Quantitative MRD monitoring

Quantitative MRD monitoring was performed using clone-specific real-time quantitative PCR (RQ-PCR) of clonal TCR beta (TRB) and/or gamma gene rearrangements.[12,16,17] Data interpretation followed EuroMRD guidelines.[18]

Next-generation sequencing of the TCR repertoire

TCR repertoire diversity was analyzed longitudinally by NGS. TRBV-TRBD-TRBJ gene rearrangements were amplified according to BIOMED2 protocol on genomic DNA.[19] Paired-end libraries with individual barcoded samples were prepared and sequenced on Illumina's MiSeq platform. Raw NGS data were processed, annotated with germline sequences from IMGT[20] and analyzed through an R-based (www.R-project.org) purpose-built bioinformatics immunoprofiling platform (ARResT/Interrogate, bat.infspire.org; manuscript in preparation). First, pairs of raw paired-end reads were joined into one longer sequence using a sensitive iterative approach: overlapping regions of at least 10 nucleotides with up to 2 and then 4 mismatches were allowed. Consequently, short (<60 nucleotides) and low quality (>5 expected errors, based on Phred quality scores) sequences were filtered out. Next, TRBV and TRBJ genes were identified and the position of the junctional region was determined. An iterative sequence curation approach was employed to correct low-frequency base calls in strict junction-aware clusters of sequences. Finally, sequences without the junctional region identified were filtered out. The quality of sequences in all the analyzed samples was high, with the average number of reads passing all the filters over 90% (Supplementary Table 1). Unique clonotypes were defined as clusters of sequences having at least 96% similarity of the junctional nucleotide sequence and identical TRBV and TRBJ genes. For repertoire analyses, the abundances of features (for example, TRBV) were counted in clonotypes rather than in reads in order to alleviate the effects of technical and biological biases.

Statistical analysis

Kaplan–Meier product-limit estimates were used for calculating survival. Events for overall survival were defined as death from any cause. Events for PFS were defined as relapse, progression or death from any cause, whatever came first. Survival time calculations were performed using GraphPad Prism software (release 5.0; San Diego, CA, USA). Data were analyzed as of 31 July 2016.

In ARResT/Interrogate, Jensen–Shannon divergence was used to compute repertoire similarity between pairs of samples visualized within heatmaps; principal component analysis was conducted to evaluate the effect of repertoire components on sample relationships; Shannon entropy was used to estimate the alpha diversity of rearrangements of individual samples.

RESULTS

Correlation of MRD kinetics with immune events and the clinical course

All patients were in clinical CR immediately after hematological reconstitution from alloSCT. Patients #3 and #9 died early (day +93 and +211 post transplant) because of severe acute GvHD, and for patient #5 no MRD marker could be established, leaving seven patients for whom at least one clone-specific MRD marker was available; these MRD markers and their sensitivity levels are shown in Table 2. Of the seven patients with MRD markers, two (patients #7 and #10) were MRD negative immediately (<50 days) after alloSCT. Whereas patient #10 died early (day +241 post transplant) from severe acute GvHD without measurable MRD, patient #7 subsequently showed increasing MRD levels, which responded to immunosuppressant tapering but—in the absence of cGvHD—reappeared from month +16 onwards, followed by fatal clinical relapse. Five patients (#1, #2, #4, #6, #8) were MRD positive early (<100 days) after alloSCT. In all of these five patients, immunosuppressant tapering (four out of five) and/or DLI (three out of four) resulted in significant reduction of MRD levels (>1 log) and was accompanied by cGvHD in three patients. However, durable MRD negativity was obtained in only two patients (#4, #8; alive and free of disease 92+ and 24+ months after alloSCT). MRD re-increased in the remaining three patients

Table 2. MRD markers and sensitivity of related clone-specific RQ-PCR assays

Patient	*Marker 1*	*Sensitivity*	*Marker 2*	*Sensitivity*
1	TRBV27-TRBJ2.2	5E-04	TRBV6.6-TRBJ1.3	1E-05
2	TRBV5-4-TRBJ1.4	1E-05	TRBV11-2-TRBJ2.5	5E-05
4	TRGV8-TRBJ1/2	5E-04	TRBV19-TRBJ2.7	5E-05
6	TRBD1-TRBJ1.3	1E-04		
7	TRBV27-TRBJ2.1	5E-04	TRBV5.1-TRBJ2.7	5E-04
8	TRBV20-1-TRBD1-TRBJ1.2	1E-05		
10	TRGV2-TRGJ1	5E-04		

Abbreviations: MRD = minimal residual disease; RQ-PCR = real-time quantitative PCR; TRB = T-cell receptor beta (β); TRG = T-cell receptor gamma (ɣ); V = variable/D = diversity/J = joining genes.

after 5–28 months despite ongoing cGvHD in one of them. Table 3 shows MRD kinetics of all patients by certain clinical landmarks. In addition, Figure 1a-c delineates the MRD kinetics of three patients with the longest follow-up in correlation to immune interventions and the clinical course.

With a 3-year PFS and overall survival of 41% and 50%, the clinical outcome was in the range of published data[2–5] (Supplementary Figure 1).

Correlation of TCR repertoire diversity with immune interventions and clinical course

The TRB repertoire of the three patients with the longest follow-up was interrogated longitudinally before and after alloSCT using NGS. In total, 104 samples (patient blood ($n = 91$) and bone marrow ($n = 10$) plus donor blood samples ($n = 3$)) were analyzed (Figure 2a). Overall, 10 697 556 reads were obtained (median 78 659; range 1114–236 806 reads/sample). Sequence numbers were remarkably low in samples after alemtuzumab treatment (pre-alloSCT; Supplementary Table 1). The diagnostic sample in all three analyzed patients predominantly showed one or two major clonotypes (Figure 2b). Kinetics of these leukemic clonotypes closely followed kinetics of RQ-PCR-quantified MRD (Figure 1a-c and Table 2b). In all three patients, MRD decline was reproducibly associated with a shift from a clonal, T-PLL-driven profile to a polyclonal signature that largely corresponded to the donor TCR repertoire and receded with increasing MRD levels. Immediately after alemtuzumab treatment and alloSCT, the TRB repertoire was heavily skewed in all three patients but recovered over time (Figures 2c and 3). In each of the samples after alloSCT, several expanded non-leukemic clonotypes were observed at a maximum frequency of 3% to 54% of total TRB sequences. Notably, there was no obvious correlation of GvL-induced MRD decline with emergence of particular dominant T-cell clonotypes that could explain a clonal GvL effect. Expanded clonotypes were most dominant in one patient who received a transplant of his brother, who in turn already exhibited the same clonotypes with a frequency of up to 15%. There were no CMV reactivations in the analyzed patients. Therefore, it was not possible to correlate known viral reactivations with clonal expansions following diminution of the viral load. There was no obvious correlation of GvL-induced MRD decline or GvHD with emergence of dominant T-cell clonotypes. Clonal expansions were observed only in the context of T-PLL relapse, reflecting the malignant clone.

DISCUSSION

T-PLL is an aggressive disease with poor outcome. In the absence of effective chemotherapeutic or targeted treatment options, alloSCT may be a potent therapeutic tool. However, it is still uncertain to what extent GvL is indeed active in this lymphoproliferative disorder. To this end, delineation of MRD kinetics in relation to immune events might help to characterize potential GvL activity in T-PLL, and how it might be exploited to optimize treatment of the disease.

TCR-based RQ-PCR is an established tool for monitoring MRD kinetics in certain lymphoid malignancies. For example, in ALL, MRD levels at different time points not only predict outcome but also indicate the need for salvage therapy as well as direct the type of optimal treatment such as alloSCT.[21–25] So far, MRD monitoring is not established in T-PLL. This study shows for the first time that in T-PLL immunomodulation can decrease the MRD load up to complete MRD clearance. This finding is the clearest evidence to date that GvL is indeed effective in this entity. However, unlike similar observations in CLL[7–11] the GvL effect in T-PLL appears to be often only limited or transient, failing to provide long-term disease control (although only a single patient had severe cGvHD, indicating a strong anti-host immune effect). Nevertheless, MRD assessment by clone-specific TCR-based RQ-PCR is a useful tool for monitoring MRD kinetics in T-PLL after alloSCT. Therefore, regular monitoring of MRD in T-PLL after alloSCT to identify early the need for immune interventions seems to be recommendable. Although basically mixed chimerism would also have been a trigger for immunomodulation as per institutional routine, we never observed mixed chimerism in the absence of detectable MRD in any of these seven patients.

Determination of MRD levels by NGS has been successfully used to efficiently predict the risk of relapse in different hematological malignancies such as adult and childhood ALL,[26,27] CLL[28,29] as well as cutaneous T-cell lymphoma.[15] Multiplexed PCR followed by NGS has the benefit of being applicable to all patients without prior allele-specific customization necessary in RQ-PCR-based techniques, whereas having the potential to offer higher sensitivity. In our study, NGS-based MRD assessment in T-PLL was feasible and reflected MRD kinetics determined by RQ-PCR, despite not being designed specifically for MRD sensitivity (input DNA amount only 100 ng, limited number of readings obtained per sample, conservative definition of MRD positivity). Another point is that TRB-based NGS analysis quantifies MRD in relation to all T cells because these are the only cells harboring TRB rearrangements. In contrast, RQ-PCR quantifies MRD in relation to total DNA. In general, results from the two techniques are highly correlated, but in case of T-cell lymphopenia NGS-based MRD levels can be markedly overestimated, as seen in patient 2. This however might be overcome by additional sequencing-based calibrations. Our study clearly demonstrates the feasibility of NGS-based MRD analysis in T-PLL. Standardization, quality control and validation of this technology in a multicenter, scientifically controlled and independent setting is warranted and currently the focus of an European network, the EuroClonality-NGS Consortium (coordinated by AW Langerak).

Besides MRD monitoring, TCR repertoire analysis by NGS provides high-resolution information on immune reconstitution and emergence of dominant clones after alloSCT, for example, in response to infection, GvHD or GvL. It has been shown that the physiological hierarchy of the TCR repertoire is heavily skewed

Table 3. A: RQ-PCR-based MRD kinetics by landmark. B: NGS-based MRD kinetics

a

Landmark	*Diagnosis*	*Pre-conditioning (d −28… −7)*	*Early after alloSCT (d +28…+56)*	*Before IS taper*	*Best response after IS taper*	*Before DLI*	*Best response after DLI*	*At clinical relapse*	*At last follow-up (month after alloSCT)*
Patient									
1	100	0.06	2	2	Neg <0.001	0.06	0.04	20	40 (80)
2	100	0.005	–	0.1	0.06	0.08	0.005	5	5 (40)
3	–	–	–	–	–	–	–	–	–
4	100	Neg <0.005	0.7	4	0.03	0.2	Neg <0.005	-	Neg <0.005 (92+)
5	–	–	–	–	–	–	–	–	–
6	100	–	0.05	0.05	Neg <0.01	0.06	Neg <0.01	10	10 (29)
7	100	10	Neg <0.05	0.5	Neg <0.05	–	–	–	0.2 (15)
8	100	0.005	0.005	0.005	Neg <0.001	–	–	–	Neg <0.001 (24+)
9	–	–	–	–	–	–	–	–	–
10	100	Neg <0.05	Neg <0.05	Neg <0.05	–	–	–	–	Neg <0.05 (4)

b

Patient	*Landmark*	*Diagnosis*	*Pre-conditioning (d −28… −7)*	*Early after alloSCT (d +28…+56)*	*Before IS taper*	*Best response after IS taper*	*Before DLI*	*Best response after DLI*	*At clinical relapse*	*At last follow-up (month after alloSCT)*
1	Reads/sample	173 280	2002	92 815	92 815	103 892	184 493	76 370	103 432	109 944
	NGS-MRD (%)	48/46	1/0.4	4/4	4/4	Neg <0.01	Neg <0.01	Neg <0.01	15/12	44/6
	RQ-PCR MRD (%)	100	0.06	2	2	Neg <0.001	0.06	0.04	20	10 (70)
2	Reads/sample	111 955	11 744	–	48 162	21 363	41 361	37 214	89 065	89 065
	NGS-MRD (%)	90	2	–	2	8	3	Neg <0.01	27	27
	RQ-PCR MRD (%)	100	0.005	–	0.1	0.06	0.08	0.005	5	5 (40)
4	Reads/sample	35 301	2575	100 486	85 855	43 702	4513	82 737	–	72 679
	NGS-MRD (%)	87	Neg <0.01	0.6	4	Neg <0.01	Neg <0.01	Neg <0.01	–	Neg <0.01
	RQ-PCR MRD (%)	100	Neg <0.005	0.8	4	0.03	0.2	0.03[a]	–	0.03 (59)[a]

A: MRD values are given as percent clone-specific copies of total copies in the sample. B: Total TRB reads per sample, NGS-based MRD percentage with a detection limit of 0.01% and RQ-PCR based MRD are given per landmark. For Patient 1, two dominant clones were present. NGS-based MRD was not assessed for all time points. This panel is only showing time points where results were available for both NGS and RQ-PCR. Therefore, there are slight differences between results from panel A and B. Abbreviations: DLI = donor lymphocyte infusion; IS = immunosuppression; MRD = minimal residual disease; Neg = negative; NGS = next-generation sequencing; RQ-PCR = real-time quantitative PCR; alloSCT = allogeneic stem cell transplantation; TRB = T-cell receptor beta. [a]Sample obtained after DLI 1. This patient subsequently became MRD- by RQ-PCR after DLI 2 when material for NGS was not available.

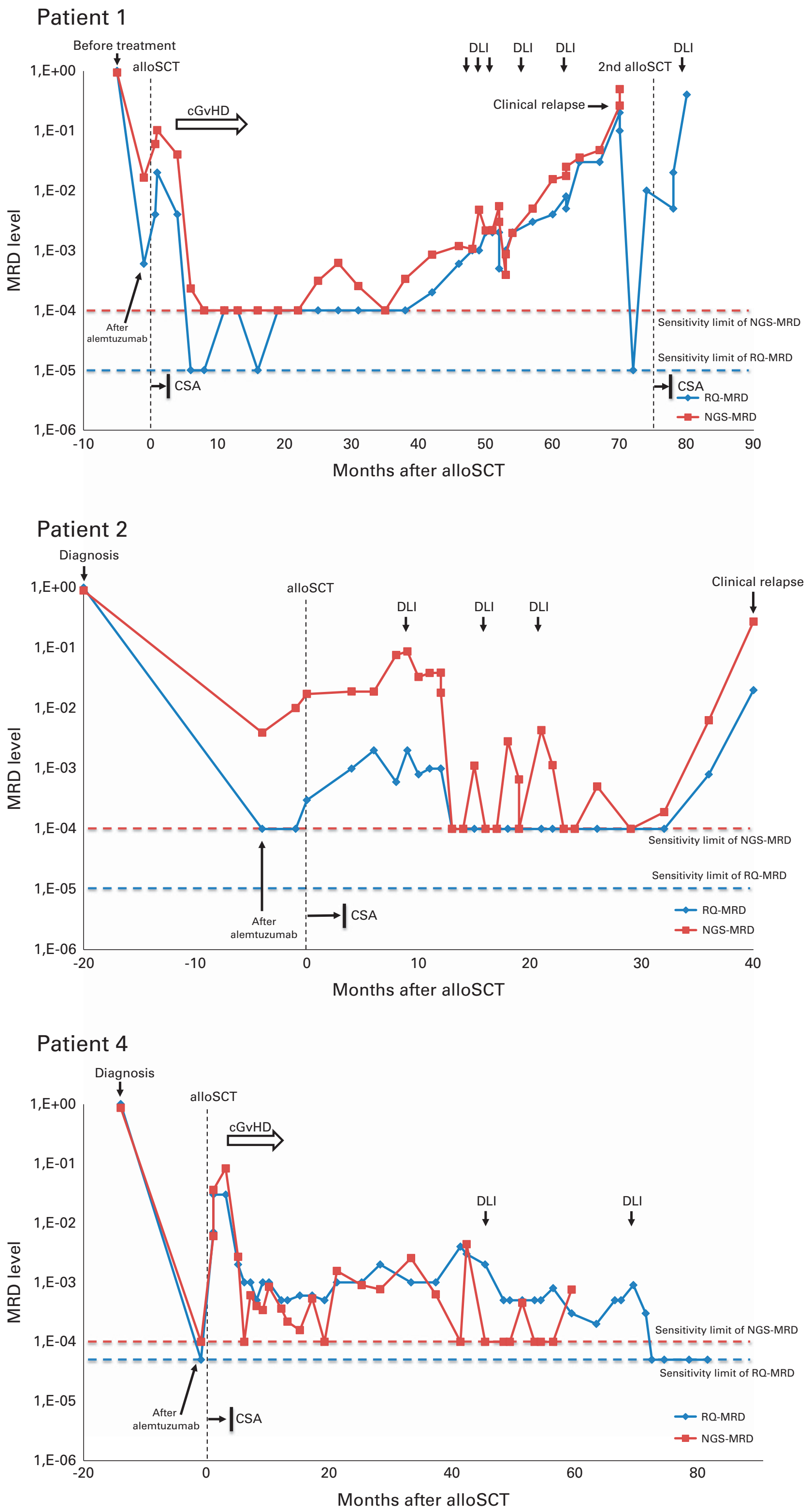

Figure 1. Minimal residual disease (MRD) course of the three T-PLL patients with the longest follow-up. Blue lines show the MRD course determined by real-time quantitative PCR (RQ-PCR), red lines show MRD course determined by next-generation sequencing (NGS). In NGS-MRD, sensitivity level was set to 1E-4 based on input DNA amount and sequencing depth (red dashed line). MRD level was calculated as number of T-PLL associated sequences divided by total number of sequences. For definition of MRD positivity, the T-PLL associated clonotype had to be identified at least 10 times. Sensitivity limit of RQ-based MRD according to EuroMRD guidelines was 1E-5 in patient 1 and 2, and 5E-05 in patient 4 (blue dashed line). MRD level at the sensitivity limit means MRD negativity. The follow-up by NGS is shorter than by RQ-PCR in patients 1 and 4. Abbreviations: alloSCT = allogeneic stem cell transplantation, cGVHD = chronic graft versus host disease, CSA = cyclosporine A, DLI = donor lymphocyte infusion.

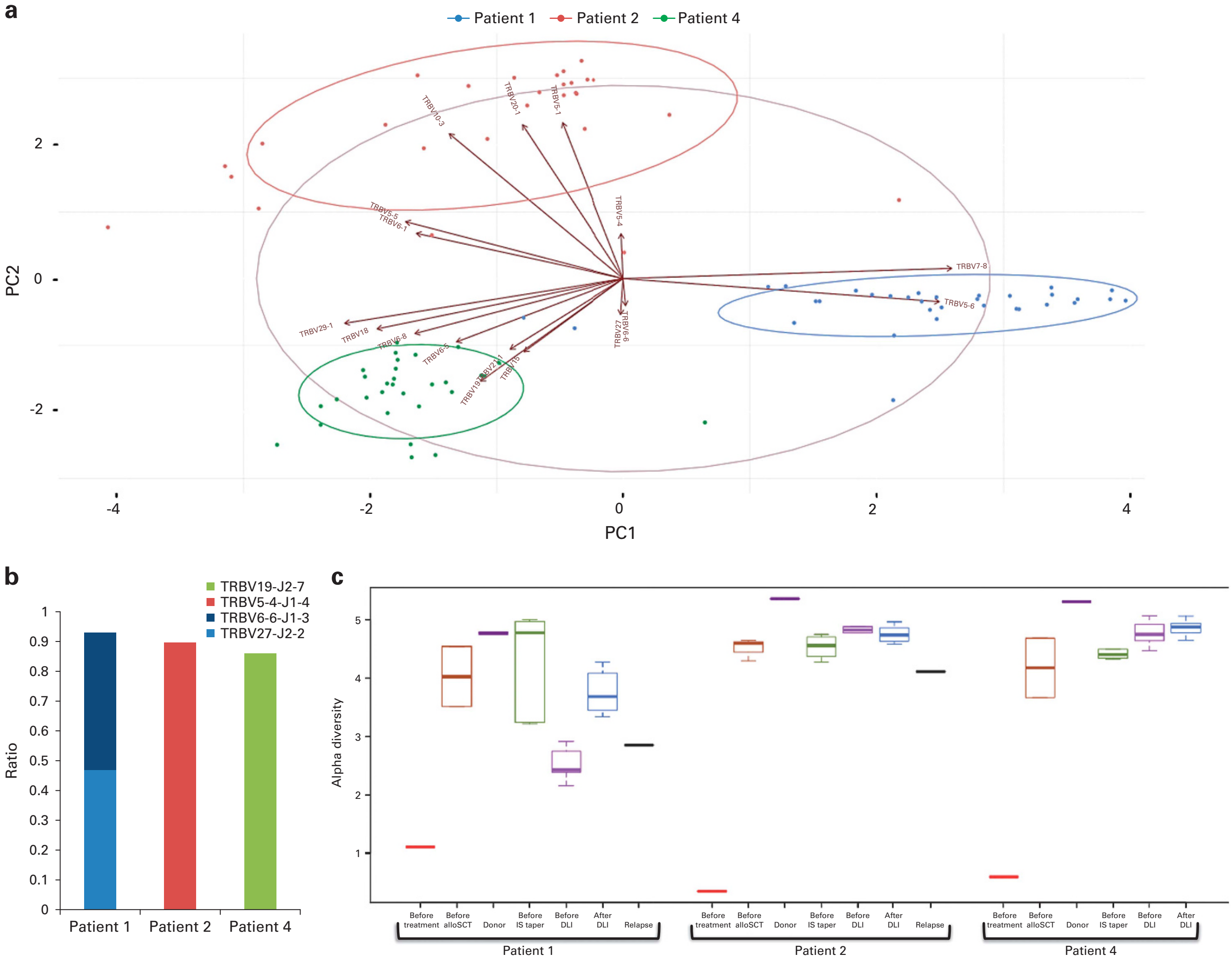

Figure 2. Next-generation sequencing (NGS) of the T-cell receptor (TCR) repertoire. (**a**) Biplot of a Principal Component Analysis (PCA) showing the V gene usage in samples of individual patients (color coded) with the main V genes contributing to the resulting separation. (**b**) Ratios (reads to total number of reads) of dominant TCR beta (TRB) sequence(s) in diagnostic samples: patient 1 showed a biallelic, patients 2 and 4 one dominant complete TRB rearrangement. In patient 2, Sanger sequencing detected a second clonal TRB gene rearrangement in the diagnostic sample (TRBV11-2-TRBJ2-5). However, in NGS this clonotype only accounted for 3.8% of all reads. (**c**) The alpha diversity of TRBV and TRBJ combinations usage at different landmarks for the three analyzed patients and their donors. Abbreviations: alloSCT = allogeneic stem cell transplantation, DLI = donor lymphocyte infusion, IS = immunosuppression tapering.

after alloSCT.[30] In addition, limited TCR diversity after alloSCT has been linked to higher susceptibility to leukemic relapse,[31,32] infection[31] and the development of GvHD.[32] However, to the best of our knowledge, there are currently no comprehensive longitudinal studies available investigating the composition of the T-cell repertoire after immune interventions in the alloSCT context. Here, we show for the first time that GvL activity in a hematological malignancy is rather relying on a polyclonal T-cell response than on the emergence of novel dominant T-cell clones with antileukemic activity. Further studies are necessary to prove if this pattern also accounts for other neoplastic alloSCT indications, such as acute leukemia and lymphoma.

In this context it has to be considered that all patients received alemtuzumab for induction therapy. Although a minimum wash-out time of 6 weeks between the last alemtuzumab dose and alloSCT had been observed, it cannot be excluded that effective alemtuzumab serum levels were present at the day of allograft infusion with implications for the integrity of the transplanted cell product. However, it is unlikely that this has interfered with donor lymphocyte infusion effects during longer follow-up or with the overall TCR repertoire pattern during GvHD/GvL episodes.

A limitation of this study is its small sample size. However, as the purpose of this analysis is not to investigate the impact of alloSCT on the clinical outcome of T-PLL, but to provide proof-of-principle evidence both for GvL and for the suitability of MRD quantification by RQ-PCR and NGS, the sample numbers investigated appear to be clearly informative.

In conclusion, this study provides the clearest evidence to date for GvL activity in T-PLL, even though it appears to be often only limited or transient. Moreover, GvL in T-PLL does not seem to be driven by the emergence of novel dominant T-cell clones but is rather relying on poly- or oligoclonal T-cell responses. Nonetheless, further evaluation of MRD monitoring might help to optimize alloSCT-based immunotherapeutic strategies in T-PLL. To this end, TRB-based NGS could not only serve as an effective tool for dissecting post-transplant immune reconstitution and GvL activity, but also emerge as an interesting alternative for MRD quantification in T-cell malignancies.

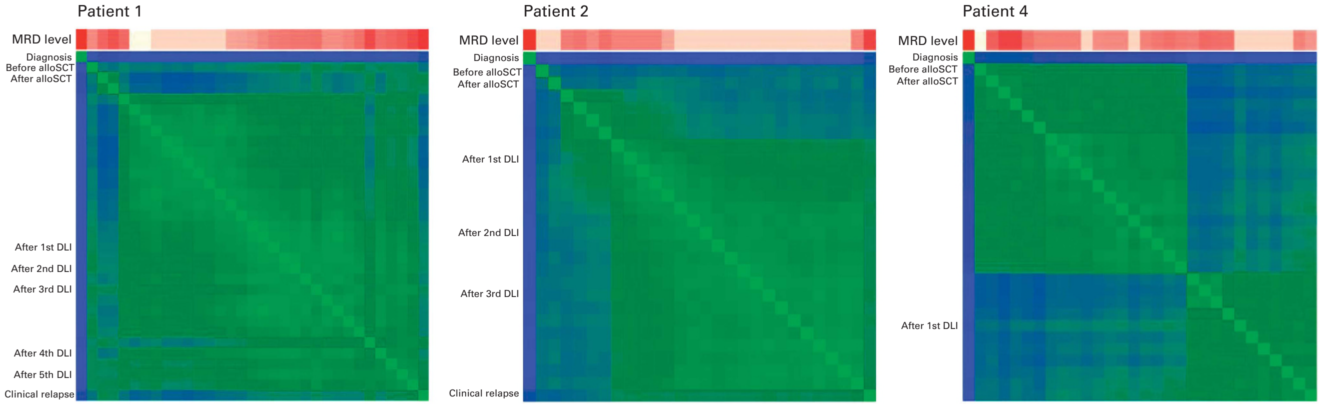

Figure 3. Heatmaps showing V gene diversity-based sample similarity in chronological order (sample before treatment on the left/top; green = similar, blue = different, *x* axis is mirrored to the *y* axis). Bars over the heatmaps show minimal residual disease (MRD) levels determined by real-time quantitative PCR (RQ-PCR; red = MRD 100%, white = MRD negative). MRD response was associated with a shift from a clonal T-PLL-driven profile to a polyclonal signature. Change of the clustering after allogeneic stem cell transplantation (alloSCT) in patients 1 and 2 could be explained by the decrease of the MRD level, the accompanied increased diversity of the TRB repertoire and the emergence of novel clones. In Patient 4, novel clonotypes emerged late after alloSCT (37 months after transplant) accompanied by psoriasis-like skin lesions —a prior infection with fever could have triggered the emergence of these clonotypes. The follow-up by NGS is shorter than by RQ-PCR in patients 1 and 4. Abbreviations: alloSCT = allogeneic stem cell transplantation, DLI = donor lymphocyte infusion, MRD = minimal residual disease.

CONFLICT OF INTEREST

The authors declare no conflict of interest.

ACKNOWLEDGEMENTS

We thank all our patients for their kind willingness to contribute clinical data and biological samples to make this study possible. TR, AK, VB, ND funded by CEITEC MU (CZ.1.05/1.1.00/02.0068) and EuroClonality, with computational resources provided by MetaCentrum under program LM2010005, and CERIT-SC under program Centre CERIT Scientific Cloud, part of the Operational Program Research and Development for Innovations, CZ.1.05/3.2.00/08.0144.

REFERENCES

1 Dearden C. How I treat prolymphocytic leukemia. *Blood* 2012; **120**: 538–551.
2 Guillaume T, Beguin Y, Tabrizi R, Nguyen S, Blaise D, Deconinck E *et al.* Allogeneic hematopoietic stem cell transplantation for T-prolymphocytic leukemia: a report from the French society for stem cell transplantation (SFGM-TC). *Eur J Haematol* 2015; **94**: 265–269.
3 Kalaycio ME, Kukreja M, Woolfrey AE, Szer J, Cortes J, Maziarz RT *et al.* Allogeneic hematopoietic stem cell transplant for prolymphocytic leukemia. *Biol Blood Marrow Transplant* 2010; **16**: 543–547.
4 Krishnan B, Else M, Tjonnfjord GE, Cazin B, Carney D, Carter J *et al.* Stem cell transplantation after alemtuzumab in T-cell prolymphocytic leukaemia results in longer survival than after alemtuzumab alone: a multicentre retrospective study. *Br J Haematol* 2010; **149**: 907–910.
5 Wiktor-Jedrzejczak W, Dearden C, de Wreede L, van Biezen A, Brinch L, Leblond V *et al.* Hematopoietic stem cell transplantation in T-prolymphocytic leukemia: a retrospective study from the European Group for Blood and Marrow Transplantation and the Royal Marsden Consortium. *Leukemia* 2012; **26**: 972–976.
6 de Lavallade H, Faucher C, Furst S, El-Cheikh J, Vey N, Coso D *et al.* Allogeneic stem cell transplantation after reduced-intensity conditioning in a patient with T-cell prolymphocytic leukemia: graft-versus-tumor effect and long-term remission. *Bone Marrow Transplant* 2006; **37**: 709–710.
7 Dreger P, Dohner H, Ritgen M, Bottcher S, Busch R, Dietrich S *et al.* Allogeneic stem cell transplantation provides durable disease control in poor-risk chronic lymphocytic leukemia: long-term clinical and MRD results of the German CLL Study Group CLL3X trial. *Blood* 2010; **116**: 2438–2447.
8 Farina L, Carniti C, Dodero A, Vendramin A, Raganato A, Spina F *et al.* Qualitative and quantitative polymerase chain reaction monitoring of minimal residual disease in relapsed chronic lymphocytic leukemia: early assessment can predict long-term outcome after reduced intensity allogeneic transplantation. *Haematologica* 2009; **94**: 654–662.
9 Hahn M, Bottcher S, Dietrich S, Hegenbart U, Rieger M, Stadtherr P *et al.* Allogeneic hematopoietic stem cell transplantation for poor-risk CLL: dissecting immune-modulating strategies for disease eradication and treatment of relapse. *Bone Marrow Transplant* 2015; **50**: 12–79-1285.
10 Moreno C, Villamor N, Colomer D, Esteve J, Gine E, Muntanola A *et al.* Clinical significance of minimal residual disease, as assessed by different techniques, after stem cell transplantation for chronic lymphocytic leukemia. *Blood* 2006; **107**: 4563–4569.
11 Ritgen M, Bottcher S, Stilgenbauer S, Bunjes D, Schubert J, Cohen S *et al.* Quantitative MRD monitoring identifies distinct GVL response patterns after allogeneic stem cell transplantation for chronic lymphocytic leukemia: results from the GCLLSG CLL3X trial. *Leukemia* 2008; **22**: 1377–1386.
12 Brüggemann M, White H, Gaulard P, Garcia-Sanz R, Gameiro P, Oeschger S *et al.* Powerful strategy for polymerase chain reaction-based clonality assessment in T-cell malignancies Report of the BIOMED-2 Concerted Action BHM4 CT98-3936. *Leukemia* 2007; **21**: 215–221.
13 Chapman M, Warren EH 3rd, Wu CJ. Applications of next-generation sequencing to blood and marrow transplantation. *Biol Blood Marrow Transplant* 2012; **18**: S151–S160.
14 Freeman JD, Warren RL, Webb JR, Nelson BH, Holt RA. Profiling the T-cell receptor beta-chain repertoire by massively parallel sequencing. *Genome Res* 2009; **19**: 1817–1824.
15 Weng WK, Armstrong R, Arai S, Desmarais C, Hoppe R, Kim YH. Minimal residual disease monitoring with high-throughput sequencing of T cell receptors in cutaneous T cell lymphoma. *Sci Transl Med* 2013; **5**: 214ra171.
16 Brüggemann M, van der Velden VH, Raff T, Droese J, Ritgen M, Pott C *et al.* Rearranged T-cell receptor beta genes represent powerful targets for quantification of minimal residual disease in childhood and adult T-cell acute lymphoblastic leukemia. *Leukemia* 2004; **18**: 709–719.
17 van der Velden VH, Wijkhuijs JM, Jacobs DC, van Wering ER, van Dongen JJ. T cell receptor gamma gene rearrangements as targets for detection of minimal residual disease in acute lymphoblastic leukemia by real-time quantitative PCR analysis. *Leukemia* 2002; **16**: 1372–1380.
18 van der Velden VH, Cazzaniga G, Schrauder A, Hancock J, Bader P, Panzer-Grumayer ER *et al.* Analysis of minimal residual disease by Ig/TCR gene rearrangements: guidelines for interpretation of real-time quantitative PCR data. *Leukemia* 2007; **21**: 604–611.
19 van Dongen JJ, Langerak AW, Brüggemann M, Evans PA, Hummel M, Lavender FL *et al.* Design and standardization of PCR primers and protocols for detection of clonal immunoglobulin and T-cell receptor gene recombinations in suspect lymphoproliferations: report of the BIOMED-2 Concerted Action BMH4-CT98-3936. *Leukemia* 2003; **17**: 2257–2317.
20 Lefranc MP, Giudicelli V, Duroux P, Jabado-Michaloud J, Folch G, Aouinti S *et al.* IMGT(R), the international ImMunoGeneTics information system(R) 25 years on. *Nucleic Acids Res* 2015; **43**: D413–D422.
21 Bassan R, Spinelli O, Oldani E, Intermesoli T, Tosi M, Peruta B *et al.* Improved risk classification for risk-specific therapy based on the molecular study of minimal

residual disease (MRD) in adult acute lymphoblastic leukemia (ALL). *Blood* 2009; **113**: 4153–4162.

22 Brüggemann M, Raff T, Flohr T, Gokbuget N, Nakao M, Droese J *et al*. Clinical significance of minimal residual disease quantification in adult patients with standard-risk acute lymphoblastic leukemia. *Blood* 2006; **107**: 1116–1123.

23 Gökbuget N, Kneba M, Raff T, Trautmann H, Bartram CR, Arnold R *et al*. Adult patients with acute lymphoblastic leukemia and molecular failure display a poor prognosis and are candidates for stem cell transplantation and targeted therapies. *Blood* 2012; **120**: 1868–1876.

24 Patel B, Rai L, Buck G, Richards SM, Mortuza Y, Mitchell W *et al*. Minimal residual disease is a significant predictor of treatment failure in non T-lineage adult acute lymphoblastic leukaemia: final results of the international trial UKALL XII/ECOG2993. *Br J Haematol* 2010; **148**: 80–89.

25 Raff T, Gökbuget N, Lüschen S, Reutzel R, Ritgen M, Irmer S *et al*. Molecular relapse in adult standard-risk ALL patients detected by prospective MRD monitoring during and after maintenance treatment: data from the GMALL 06/99 and 07/03 trials. *Blood* 2007; **109**: 910–915.

26 Logan AC, Vashi N, Faham M, Carlton V, Kong K, Buno I *et al*. Immunoglobulin and T cell receptor gene high-throughput sequencing quantifies minimal residual disease in acute lymphoblastic leukemia and predicts post-transplantation relapse and survival. *Biol Blood Marrow Transplant* 2014; **20**: 1307–1313.

27 Wu D, Sherwood A, Fromm JR, Winter SS, Dunsmore KP, Loh ML *et al*. High-throughput sequencing detects minimal residual disease in acute T lymphoblastic leukemia. *Sci Transl Med* 2012; **4**: 134ra63.

28 Logan AC, Gao H, Wang C, Sahaf B, Jones CD, Marshall EL *et al*. High-throughput VDJ sequencing for quantification of minimal residual disease in chronic lymphocytic leukemia and immune reconstitution assessment. *Proc Natl Acad Sci USA* 2011; **108**: 21194–21199.

29 Logan AC, Zhang B, Narasimhan B, Carlton V, Zheng J, Moorhead M *et al*. Minimal residual disease quantification using consensus primers and high-throughput IGH sequencing predicts post-transplant relapse in chronic lymphocytic leukemia. *Leukemia* 2013; **27**: 1659–1665.

30 Meier J, Roberts C, Avent K, Hazlett A, Berrie J, Payne K *et al*. Fractal organization of the human T cell repertoire in health and after stem cell transplantation. *Biol Blood Marrow Transplant* 2013; **19**: 366–377.

31 van Heijst JW, Ceberio I, Lipuma LB, Samilo DW, Wasilewski GD, Gonzales AM *et al*. Quantitative assessment of T cell repertoire recovery after hematopoietic stem cell transplantation. *Nat Med* 2013; **19**: 372–377.

32 Yew PY, Alachkar H, Yamaguchi R, Kiyotani K, Fang H, Yap KL *et al*. Quantitative characterization of T-cell repertoire in allogeneic hematopoietic stem cell transplant recipients. *Bone Marrow Transplant* 2015; **50**: 1227–1234.

Supplementary Information accompanies this paper on Bone Marrow Transplantation website (http://www.nature.com/bmt)

Bioinformatics, 33(23), 2017, 3802–3804
doi: 10.1093/bioinformatics/btx423
Advance Access Publication Date: 13 July 2017
Applications Note

Sequence analysis

GLASS: assisted and standardized assessment of gene variations from Sanger sequence trace data

Karol Pal[1], Vojtech Bystry[1], Tomas Reigl[1], Martin Demko[1], Adam Krejci[1], Tasoula Touloumenidou[2], Evangelia Stalika[3], Boris Tichy[1], Paolo Ghia[4], Kostas Stamatopoulos[3], Sarka Pospisilova[1,5], Jitka Malcikova[1,5,]* and Nikos Darzentas[1,]* also on behalf of the European Research Initiative on CLL (ERIC)—TP53 Network

[1]CEITEC—Central European Institute of Technology, Masaryk University, Brno, Czech Republic, [2]Hematology Department and HCT Unit, G. Papanicolaou Hospital, [3]Institute of Applied Biosciences, Center for Research and Technology Hellas, Thessaloniki, Greece, [4]Division of Molecular Oncology, Department of Onco-Hematology, IRCCS San Raffaele Scientific Institute, Università Vita-Salute San Raffaele, Milan, Italy and [5]Department of Internal Medicine–Hematology and Oncology, University Hospital Brno, Brno, Czech Republic

*To whom correspondence should be addressed.

Associate Editor: John Hancock

Received on November 21, 2016; revised on April 4, 2017; editorial decision on June 23, 2017; accepted on July 12, 2017

Abstract

Motivation: Sanger sequencing is still being employed for sequence variant detection by many laboratories, especially in a clinical setting. However, chromatogram interpretation often requires manual inspection and in some cases, considerable expertise.

Results: We present GLASS, a web-based Sanger sequence trace viewer, editor, aligner and variant caller, built to assist with the assessment of variations in 'curated' or user-provided genes. Critically, it produces a standardized variant output as recommended by the Human Genome Variation Society.

Availability and implementation: GLASS is freely available at http://bat.infspire.org/genomepd/glass/ with source code at https://github.com/infspiredBAT/GLASS.

Contact: nikos.darzentas@gmail.com or malcikova.jitka@fnbrno.cz

Supplementary information: Supplementary data are available at *Bioinformatics* online.

1 Introduction

Despite great advances in next-generation sequencing, Sanger sequencing still represents a widely used tool for variant detection and validation in both research and clinical applications. Moreover, for the majority of diagnostic laboratories, it remains the most applicable approach considering the cost and the number of samples analyzed.

The analysis of Sanger sequence trace data is also still a laborious task and, most importantly, it can be compromised by a lack of expertise and experience. Several software tools exist to ease this analysis (Supplementary Table S1), and they can be helpful, but also detrimental. Naïve trace viewers for manual inspection can be cumbersome and ultimately error-prone, while commercial solutions can be prohibitively expensive and their advanced features may prove too complex and even discouraging. Often, different users use different solutions, which lead to further complications with regard to the consistency of the reported results.

The need to harmonize and improve *TP53* gene mutational analysis in European hematological centers has led to the establishment of the TP53 Network within the European Research Initiative on Chronic Lymphocytic Leukemia (CLL)/ERIC. One of the priorities identified within this network was standardization of variant detection and description. In this context, we developed GLASS for both novice and experienced practitioners to discover and assess gene variations from Sanger sequence trace data for research, as well as diagnostic purposes. GLASS partially automates the process of comparing Sanger sequencing data to a reference sequence and identifying and reporting nucleotide differences. GLASS handles homozygous and heterozygous variants in germline, as well as somatic context, and is particularly useful in assessing low-frequency somatic variants present at the threshold of Sanger sequencing detection limit. Apart from single nucleotide variants, it also facilitates the correct description of heterozygous and somatic insertions/deletions (indels) by aligning the secondary sequence to the reference. Importantly, GLASS reports sequence variants in a standardized way, as recommended by the Human Genome Variation Society (HGVS, varnomen.hgvs.org), so that users can be valid and consistent in their clinical and research activities and collaborations.

2 Methods

Implementation: GLASS is written in R and uses Shiny (Chang *et al.*, 2016, R package) for its interface. A custom D3-based (Bostock *et al.*, 2011) JavaScript library was developed for rendering chromatograms.

Reference genes: To achieve standardization and consistency, we primarily make available a 'curated' list of genes with reference sequences expertly verified to work with GLASS. Genes can be added to this list on request and after verification. GLASS can also be used with a user-provided GenBank reference, or as a trace viewer without one.

Input files: GLASS works on processed ABI files through the 'samples' panel (Supplementary Fig. S1). It can automatically detect the reference gene and the orientation of the sequence, however, users can override these.

Variant calling: Germline variants appear as a single peak (homozygous) or as two peaks of lower but similar height (heterozygous) and are easily identifiable. For the more challenging somatic variants, GLASS estimates local background noise and calculates the signal to noise ratio for the second highest peak. If this ratio and the secondary peak (second highest peak) are above user-settable thresholds, the variant is reported.

Homozygous indels are recognized as alignment gaps either in the base calls (deletion) or the reference sequence (insertion). Heterozygous and somatic indels manifest as series of minor (secondary) peaks after the indel site on the forward strand and before the site on the reverse strand. GLASS can automatically detect such secondary sequences, realign them and identify a candidate indel, in which case it alerts the user to consider the suggested alignment correction (Supplementary Fig. S2).

GLASS can also identify alternative splicing, e.g. the *TP53* beta-variant (Flaman *et al.*, 1996) (Supplementary Fig. S3), and aberrant transcripts. This is relevant for cDNA data analysis and especially important for the functional analysis of separated alleles in yeast (FASAY; Flaman *et al.*, 1995), where whole introns and exons may 'drop in' or 'fall out'.

A diagram of the basic work flow and data structures used in GLASS is available in the Supplementary Material (Supplementary Fig. S4).

3 Results

GLASS is thus a web-based Sanger sequence trace viewer, editor, aligner and variant caller. We present core interface components that access these functionalities and introduce our validation/evaluation results.

Controls: These include changing base calls and setting parameters, e.g. the sensitivity at which somatic mutations are detected. The 'general infobox' shows details on selected chromatogram positions. Information on heterozygous indels is displayed in the 'hetero indels infobox'.

Minimap: The 'minimap' presents an overview of aligned exons and introns of the reference gene, which can also be highlighted in the case of splice variants (Supplementary Fig. S3). Candidate sequence variants appear with an intuitive structure and color code representing the reference base and the primary and secondary peaks (Fig. 1).

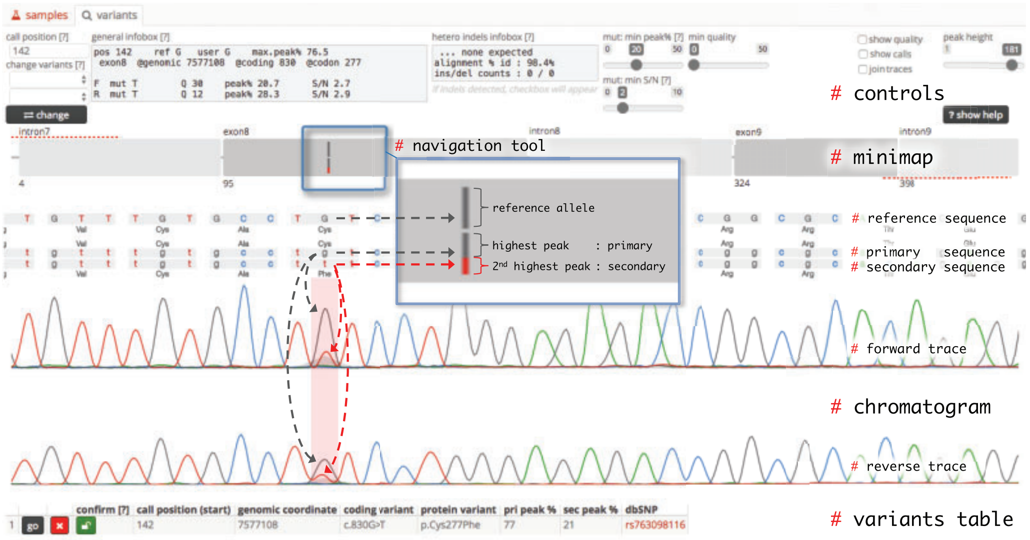

```
pos 142     ref G    user G      max.peak% 76.5
 exon8   @genomic 7577108   @coding 830   @codon 277
F  mut T          Q 30    peak% 20.7     S/N 2.7
R  mut T          Q 12    peak% 28.3     S/N 2.9
```

```
... none expected
alignment % id : 98.4%
ins/del counts : 0 / 0
```

If indels detected, checkbox will appear

			confirm [?]	call position (start)	genomic coordinate	coding variant	protein variant	pri peak %	sec peak %	dbSNP
1	go	✕	🔓	142	7577108	c.830G>T	p.Cys277Phe	77	21	rs763098116

Fig. 1. The 'variants' panel, with labels tagged with a hash (#), dashed arrows, zoomed-in inset manually added for presentation. The 'minimap' shows the alignment to the reference gene (in this case a *TP53* gene region spanning introns 7–9) and the detected variant. The 'navigation tool' (blue rectangle, also as zoomed-in inset) selects the region to display in the 'chromatogram'. In the 'chromatogram', the detected variant is highlighted with a pink vertical bar and the exportable information is printed in the 'variants table' below. Gray/red dashed arrows added to show the link between primary/secondary peaks, primary/secondary sequences and the minimap variant representation (Color version of this figure is available at *Bioinformatics* online.)

Chromatogram: The 'chromatogram' plots the sequence traces, with peak widths normalized for better forward and reverse strand alignment. Each peak is annotated with the reference sequence, the primary and secondary sequences, cDNA and genomic coordinates, call qualities and amino acid translations in the case of exons.

Variants table: All candidate variants appear in detail in the 'variants table', with emphasis on proper nomenclature and presentation according to HGVS. Upon inspection, the user can 'lock' the variant, which will then appear in the 'samples' panel and become available for export.

Validation and evaluation: GLASS is continuously validated against a growing set of manually analyzed samples with confirmed mutations. Many samples come from the official certification activities of ERIC (Supplementary Table S2), with others originating from collaborating laboratories. As showcased in the Supplementary Material, GLASS could identify correctly and name properly all the mutations in the TP53 Analysis Certification set. It is important to note that user interaction is necessary in some cases, since GLASS is built to assist and not fully automate this process.

4 Conclusions

GLASS is a bioinformatic implementation of best practices of labs with published know-how in the analysis of *TP53* and other clinically relevant genes. It was specifically developed in the context of and for the educational and certification activities of the ERIC TP53 Network, but it can already be used with other 'curated' and user-provided reference genes of diagnostic or research interest. We therefore hope and believe that GLASS will be useful to researchers and clinical practitioners as an intuitive tool for standardized Sanger trace data analysis.

Future plans include the ability to resume and share analyses; the concatenation of multiple files/amplicons from the same patient to cover the complete reference sequence; the ability to load annotations, e.g. known mutations or hotspots, for visualizations and variant calling.

Funding

This work was supported by Faculty of Medicine, Masaryk University MUNI/A//1106/2016; CEITEC 2020 (LQ1601); TEO2000058/2014-2019; EU's Horizon 2020 No. 692298 (MEDGENET); Ministry of Health of the Czech Republic grant nr. 16-34272A; MEYS—NPS I—LO1413; NCMG research infrastructure (LM2015091, MEYS CR). Computational resources by MetaCentrum (LM2010005) and CERIT-SC (CERIT Scientific Cloud, Operational Program Research and Development for Innovations, Reg. no. CZ.1.05/3.2.00/08.0144).

Conflict of Interest: none declared.

References

Bostock,M. *et al.* (2011) D3: Data-Driven Documents. *IEEE Trans Vis. Comp. Graph. Proc. InfoVis*, **17**, 2301–2309.

Flaman,J.M. *et al.* (1995) A simple p53 functional assay for screening cell lines, blood, and tumors. *Proc. Natl. Acad. Sci. USA*, **92**, 3963–3967.

Flaman,J.M. *et al.* (1996) The human tumour suppressor gene p53 is alternatively spliced in normal cells. *Oncogene*, **12**, 813–818.

Tom *et al. BMC Bioinformatics* (2018) 19:243
https://doi.org/10.1186/s12859-018-2227-x

BMC Bioinformatics

SOFTWARE Open Access

ToTem: a tool for variant calling pipeline optimization

Nikola Tom[1,2†], Ondrej Tom[3†], Jitka Malcikova[1,2], Sarka Pavlova[1,2], Blanka Kubesova[2], Tobias Rausch[4], Miroslav Kolarik[3], Vladimir Benes[4], Vojtech Bystry[1*] and Sarka Pospisilova[1,2*]

Abstract

Background: High-throughput bioinformatics analyses of next generation sequencing (NGS) data often require challenging pipeline optimization. The key problem is choosing appropriate tools and selecting the best parameters for optimal precision and recall.

Results: Here we introduce ToTem, a tool for automated pipeline optimization. ToTem is a stand-alone web application with a comprehensive graphical user interface (GUI). ToTem is written in Java and PHP with an underlying connection to a MySQL database. Its primary role is to automatically generate, execute and benchmark different variant calling pipeline settings. Our tool allows an analysis to be started from any level of the process and with the possibility of plugging almost any tool or code. To prevent an over-fitting of pipeline parameters, ToTem ensures the reproducibility of these by using cross validation techniques that penalize the final precision, recall and F-measure. The results are interpreted as interactive graphs and tables allowing an optimal pipeline to be selected, based on the user's priorities. Using ToTem, we were able to optimize somatic variant calling from ultra-deep targeted gene sequencing (TGS) data and germline variant detection in whole genome sequencing (WGS) data.

Conclusions: ToTem is a tool for automated pipeline optimization which is freely available as a web application at https://totem.software.

Keywords: Variant calling, Benchmarking, Next generation sequencing, Parameter optimization

Background

NGS is becoming the method of choice for an ever-growing number of applications in both research and clinics [1]. However, obtaining unbiased and accurate NGS analysis results usually requires a complex multi-step processing pipeline, specifically tailored to the data and experimental design. In the case of variant detection from DNA sequencing data, the analytical pipeline includes pre-processing, read alignment and variant calling. Multiple tools are available for each of these steps, each using its own set of modifiable parameters, creating a vast amount of possible distinct pipelines which vary greatly in the resulting called variants [2]. Selecting an adequate pipeline is a daunting task for a non-professional, and even an experienced bioinformatician needs to test many configurations in order to optimize the analysis.

To resolve this complexity, modern variant calling approaches utilize machine learning algorithms to automatically tune the analysis. However, the machine learning approaches often require a large number of samples. According to GATK Best practices, Variant Quality Score Recalibration (VQSR) [3, 4], which is widely used for variant filtration, requires > 30 whole exomes and at least basic parameter optimization. Variant calling on small scale data, e.g. gene panels which are very often used in diagnostics, still needs to be done with fixed thresholds, reiterating the aforementioned problem of an optimal workflow configuration.

The evaluation of current variant calling pipelines [5, 6] and the development of benchmarking toolkits [7, 8] have helped to resolve this task, but to the best of our knowledge, there is no tool enabling automated pipeline parameter configuration using a ground truth data set.

---

* Correspondence: vojtech.bystry@ceitec.muni.cz; pospisilova.sarka@fnbrno.cz
†Nikola Tom and Ondrej Tom contributed equally to this work.
[1]Center of Molecular Medicine, Central European Institute of Technology, Masaryk University, Brno, Czech Republic
Full list of author information is available at the end of the article

In this paper, we present ToTem, a method for pipeline optimization which can automatically configure and benchmark individual tools or entire workflows, based on a set of validated ground truth variants. In this way, ToTem helps to choose the optimal pipeline for specific needs. The applicability of ToTem was demonstrated using two common NGS variant calling tasks: (1) Optimal somatic variant calling using ultra-deep TGS data and (2) optimal germline variant calling using WGS data. In both scenarios, we were able to significantly improve the variant calling performance in comparison to the tools' default settings.

Implementation

ToTem is a stand-alone web application with a comprehensive GUI which allows ToTem to be used even by non-bioinformaticians, and for advanced users it features a convenient pipeline editor which takes care of parallelization and process control. The server backend is implemented in Java and PHP with an underlying connection to the MySQL database. All communication with the server is encrypted.

ToTem is primarily intended for testing variant calling pipelines with the ability to start an analysis from any level of the process. This allows testing either whole pipelines starting from raw sequencing data or focussing only on the final variant filtering phases. The results are visualized as interactive graphs and tables. ToTem also provides several convenient auxiliary tools that facilitate maintenance, backup and input data source handling.

Pipeline configuration and execution

The core principle of pipeline optimization in ToTem is to automatically test pipeline performance for all the parameter combinations in a user defined range. Pipelines are defined through consecutively linked "processes", where each process can execute one or more tools, functions or code. ToTem is optimized to test the pipelines represented as linear sequences of commands, but also supports branching at the level of tested processes, e.g. to simultaneously optimize two variant callers in one pipeline. To facilitate pipeline definition, common steps shared by multiple pipelines can be easily copied or moved using drag and drop function.

Processes are constructed from template scripts that use bash script code with special syntax to include placeholders for automatic testing. From ToTem's pipeline optimization concept's point of view, the most important placeholder, called "params", is dedicated to inserting the tested parameters to be optimized. Each parameter can be represented simply by their presence or absence, one value, more values, intervals or even mathematical functions. Parameter ranges can be easily set through GUI without the necessity to scan or modify a code. Therefore, with prepared templates, the scope and focus of the optimization can easily be changed without informatics proficiency. ToTem provides predefined templates for the tools most commonly used in variant-calling pipelines.

When a pipeline framework for testing is prepared, input data can be uploaded to the attached storage via GUI, where they are accessible through several placeholders designed for particular data types. When the analysis is started, ToTem creates all possible pipelines within the preset parameter ranges and executes them on the attached computational server. All the processes for combined settings are executed in parallel, limited by a defined maximal number of threads. The parallelization, resource control and asynchronous communication with the application server are managed by ToTem's backend. The results are imported into ToTem's internal database for final evaluation and benchmarking. The analysis time depends on the available computational power, the level of parallelization, performance of the particular tool, the number of tested configurations and the size and nature of the input data. For technical details and practical examples, see Additional file 1 and watch step-by-step tutorial on totem.software web pages.

Pipeline benchmarking

The benchmarking of each pipeline is done using ground truth data and is based on an evaluation of true positives, false positives, false negative rates and performance quality metrics derived from them. Ground truth data generally consists of raw sequencing data or alignments and an associated set of validated variants [9, 10].

ToTem provides two benchmarking approaches, with each focusing on different applications and having different advantages:

- The first approach is using ToTem's filtering tool to filter (stratified) performance reports generated by external benchmarking tools, which are incorporated as a final part of tested analytical pipelines. This allows an evaluation of many parameter combinations and simple setting selection that produce the best results considering e.g. quality metrics, variant type and region of interest (variables depend on the report). This approach is particularly useful for optimizing the pipeline for WGS or whole exome sequencing (WES) and also TGS.
- Little Profet (LP) is ToTem's genuine benchmarking method, which compares variant calls generated by tested pipelines to the gold standard variant call set. LP calculates standard quality metrics (precision, recall and F-measure) and most importantly – the reproducibility of each quality metric, which is the main advantage over the standard Genome in a Bottle (GIAB) approach. ToTem thus allows the best pipelines to be selected considering the selected

quality metrics and its consistency over multiple data subsets. The LP approach is designed primarily for TGS data harbouring a limited number of sequence variants and suffering from high a risk of pipeline over-fitting.

ToTem's filtering tool for Genome in a Bottle benchmarking approach

The GIAB benchmarking approach, which combines RTG Tools [11, 12] and hap.py [13], is best suited to variant calling pipelines designed for the data which might harbour complex variants and require variant and region stratification, e. g. WGS data. RTG Tools use complex matching algorithms and standardized counting applied for variant normalization and comparison to the ground truth. Hap.py is applied for variant and region annotation/stratification [14]. These tools serve as reference implementations of the benchmarking standards agreed upon by the ga4gh data working group [15]. Regarding ToTem's pipeline optimization concept, RTG Tools and hap.py are used to be a final part of the pipeline providing, as a result, a regionally stratified performance (precision, recall, F-measure, etc.) report for several variant types.

The reports from all pipeline configurations are imported into the internal database and processed by ToTem's filtering tool, allowing easy selection of an optimal pipeline based on the user's needs and priorities. This could be extremely useful while ranking the pipelines for a specific variant type, e.g. single nucleotide variant (SNV) versus insertion or deletion (InDel), variant calling filters and/or specific regions of the genome such as low-mappability regions, low-complexity regions, AT-rich regions, homopolymers, etc. described as significantly influencing variant calling performance [16–18]. The complete list of filtered results describing the performance qualities for the selected variant type and region for all the pipelines can be exported into a csv table for deeper evaluation.

ToTem's filtering tool utility is not only restricted to the GIAB approach but can also be applied to other table formats describing pipeline performance. The specific format, e.g. column names, column separator, needs to be set through the ToTem GUI before importing pipeline results into the database. ToTem's fitering workflow is described in Fig. 1, part A. For technical details and practical examples, see Additional file 1 and watch step-by-step tutorial on totem.software web pages.

Benchmarking by Little Profet

The weakness of pipeline optimization using a ground truth data set is that it may lead to an over-fit of the parameters causing inaccuracies when analyzing a different dataset. This negative effect is even more pronounced when using small scale data like TGS, usually harboring a relatively small number of ground truth variants.

To address this task, ToTem proposes its genuine benchmarking algorithm, LP, which prevents over-fitting and ensures the pipeline reproducibility. LP therefore represents an alternative to the GIAB approach with the added value of taking additional measures to guarantee robust results.

The LP benchmarking is based on the comparison of the normalized variants detected by each pipeline to the ground truth reference variants in the regions of interest and the inferred precision, recall and F-measure.

The over-fitting correction utilizes cross validation approaches that penalize the precision, recall and F-measure scores based on the result variation over different data subsets. The assumption is that the pipelines showing the least variability of results among data subsets will also prove to be more robust when applied to unknown data.

The reproducibility is calculated from all the samples (> 3) going into the analysis, while a repeated (number of repeats = ½ of samples) random sub-sampling (number of samples in one sampling group = ½ of samples) validation is performed to estimate the sub-sampling standard deviation (SMSD) of the validation results for individual performance quality metrics (precision, recall and F-measure). The reproducibility may also be inferred from the min/max values for a given performance quality measure calculated for each sub-sampling group. If multiple distinct data sets are provided (at least 2), standard deviation between the selected data set results (DSD) can be used to assess reproducibility as well.

Additionally, to improve the precision and consistency of variant detection [19], the intersection of the results from each pair of 10 best performing pipelines (5 pipelines with higher precision, 5 with higher recall) is done by default. The detailed information about pipeline performance including over-fitting correction can be exported to excel file for further evaluations. Little Profet workflow is described in Fig. 1, part B. To better understand LP method, pseudo code is provided in Additional file 2. For other technical details and practical examples, see Additional file 1 and watch step-by-step tutorial on totem.software web pages.

Results

To showcase the advantages and versatility of ToTem, we performed the optimization test of variant calling pipelines for two very diverse experimental settings:

- somatic variant calling on ultra-deep TGS data
- germline variant calling on WGS data.

In the first setting, we used ultra-deep targeted gene sequencing data from the *TP53* gene (exons 2–11) from 220 patient samples divided into 3 data sets based on differences in diagnosis, verification status and mutation load. A combination of three datasets was used in the context of

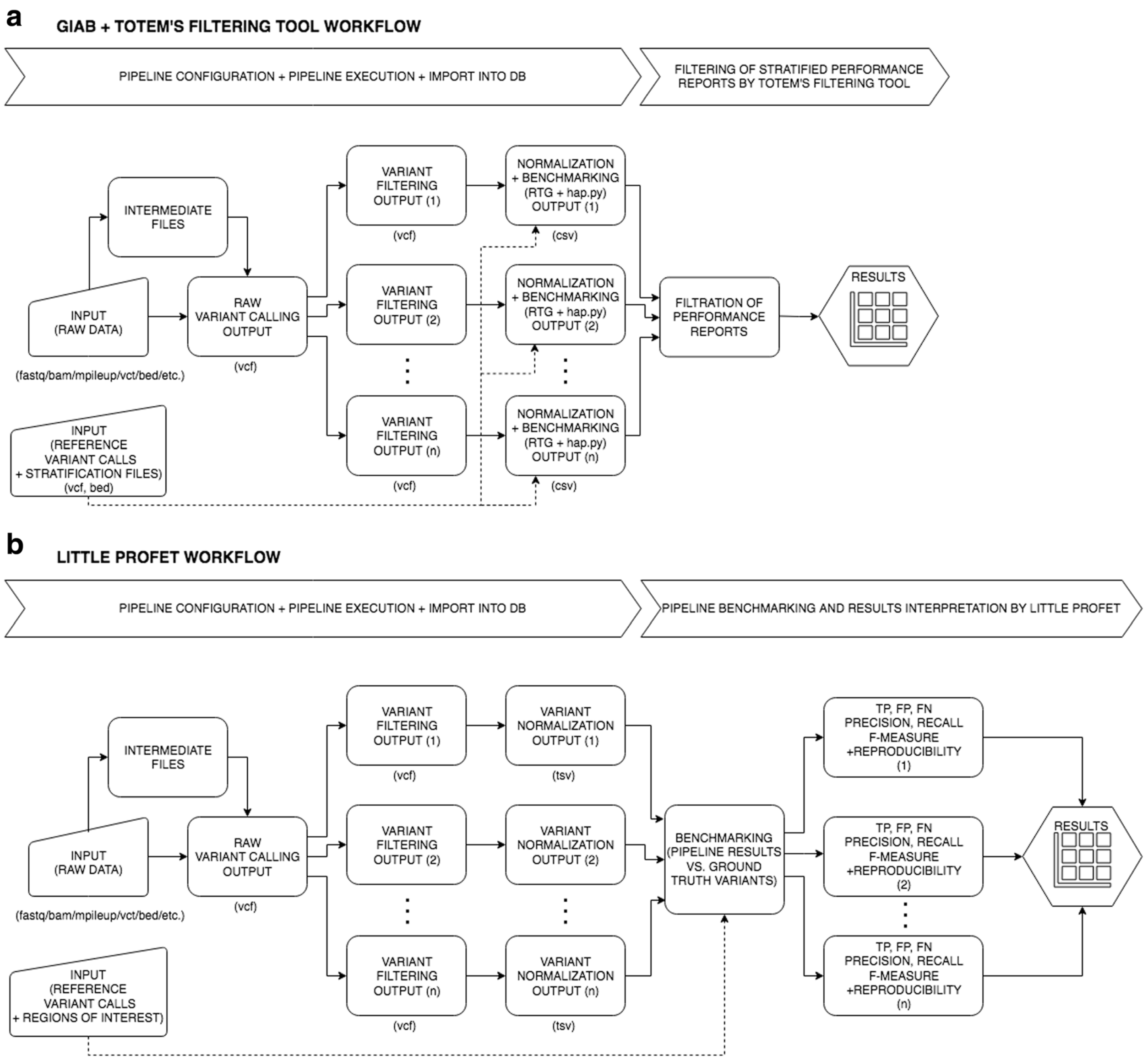

Fig. 1 **a** Once the pipeline is set up for the optimization, all the configurations are run in parallel using raw input data. In this particular example, the emphasis is placed on optimizing the variant calling filters, however, the pipeline design depends on the user's needs. In the case of the GIAB approach, the benchmarking step is part of the pipeline done by RTG Tools and hap.py. The pipeline results in the form of the stratified performance reports (csv) provided by hap.py are imported into ToTem's internal database and filtered using ToTem's filtering tool. This allows the best performing pipeline to be selected based on the chosen quality metrics, variant type and genomic region. **b** Similar to the previous diagram, the optimization is focused on tuning the variant filtering. Contrary to the previous case, Little Profet requires the pipeline results to be represented as tables of normalized variants with mandatory headers (CHROM, POS, REF, ALT). Such data are imported into ToTem's internal database for pipeline benchmarking by the Little Profet method. Benchmarking is done by comparing the results of each pipeline to the ground truth reference variant calls in the given regions of interest and by estimating TP, FP, FN; and quality metrics derived from them - precision, recall and F-measure. To prevent overfitting of the pipelines, Little Profet also calculates the reproducibility of each quality metric over different data subsets. The results are provided in the form of interactive graphs and tables

the Little Profet over-fitting control capability, ensuring the robustness of the particular pipeline settings applied to a slightly different type of data. One thousand twelve manually curated variants with a variant allele frequency (VAF) ranging from 0.1 to 100% were used as ground truth variant calls for pipeline benchmarking [20, 21].

All DNA samples were sequenced with ultra-high coverage (min. coverage depth > 5000×, average depth of coverage approx. 35 000×) using Nextera XT DNA Sample Preparation Kit and MiSeq Reagent Kit v2 (300 cycles) (Illumina, San Diego, CA, USA) on a MiSeq instrument, as described previously [20]. Reads' quality trimming, merging and mapping onto the reference genome (GRCh37) as well as variant calling, was done using CLC Genomic Workbench. The Shearwater algorithm from the R-package DeepSNV, computing a Bayes classifier based on a beta-binomial model for variant calling with multiple samples to precisely estimate model parameters - such as local error rates and dispersion, [22] was used as the second variant calling approach. The minimum variant read count was set to 10. Only variants detected either by both variant calling algorithms or confirmed by a technical or biological replicate were added to the list of candidate ground truth variants. To remove remaining FP, filtering was applied according to VAF present in an in-house database containing all the samples processed in our laboratory. Because an in-house database accumulates false-positive variants specific for the used sequencing platform, sequencer and analysis pipeline, it could be used to identify and remove these FP. All computationally predicted variants were manually checked by expert users and confirmed by biological findings [20, 21]. This approach allowed us to detect variants down to 0.1% VAF.

Only SNV were considered during the analysis. Short InDels were not included in the ground truth set due to their insufficient quantity.

Dataset TGS 1 was represented by 355 SNVs detected in 103 samples from patients diagnosed with chronic lymphocytic leukemia (CLL). The dataset represented variants detected in VAF ranging from 0.1–100%. Variant calling was done by CLC Genomic Workbench and Shearwater algorithm. Only variants confirmed by both algorithms or by a biological/technical replicate were taken into account. The dataset should not contain any false positive variants.

Dataset TGS 2 consisted of 248 SNVs present in 77 patient samples with myeloproliferative neoplasm (MPN). With the exception of known germline polymorphisms, variants representing low burden sub-clones up to 10% VAF prevailed, as fully expanded (> 20%VAF) *TP53* mutations are rare in MPN [21]. Only variants detected by CLC Genomic Workbench, confirmed by technical replicates or by independent sampling were used. The dataset should not contain any false positives variants.

Dataset TGS 3 was represented by 409 SNVs detected in 40 patient samples with CLL with VAF 0.1–100%. Variant calling was done using CLC Genomic Workbench only and false positive variants may rarely occur as some of the low frequency variants were not confirmed by a technical replicate, for more details see Additional file 3.

In the first experiment, three variant callers were optimized: Mutect2 [3, 4], VarDict [23] and VarScan2 [24, 25], using all 3 TGS datasets. Aligned reads generated outside of ToTem with the BWA-MEM algorithm [26] were used as input data for the pipeline optimization, which was focused on tuning the variant callers' hard filters. As part of the optimized pipeline, variants passing filters were normalized by vcflib [27], imported into the internal database and processed using Little Profet. The pipelines' performance was sorted by F-measure corrected by SMSD. A detailed description of the pipelines including their configurations can be found in Additional file 3.

The best results were achieved using optimized VarScan2, specifically by intersecting the results generated by two different settings, reaching a precision of 0.8833, recall of 0.8903 and an F-measure of 0.8868. This precision is high considering the tested datasets contained 624 variants with very low VAF (< 1%), which are generally problematic to identify because of sequencing errors. The importance of ToTem is even more pronounced when compared to the median scoring pipeline, which had a precision of 0.5405, a recall of 0.7527 and an F-measure of 0.6292, and compared to the baseline VarScan2 pipeline using its default parameters, which had a precision of 0.9916, recall of 0.2312 and an F-measure of 0.3763. The best-scoring pipeline thus identified 3.84-fold more true positive variants and showed only an 11% lower precision than the VarScan2 pipeline using default parameters.

The input mpileup files were generated using very sensitive settings allowing the optimization of 4 parameters in 54 different combinations including their default values, for details, see Additional file 3. Compared to the default settings, the detection quality of the best scoring pipeline was affected by tuning all 4 parameters. Higher recall was caused by lowering the parameters for *the minimum variant allele frequency* and *p-value*. High precision was maintained by increasing the parameter values for *the minimum base quality* and *the minimum number of variant supporting reads*.

The second best performing variant caller in our test was VarDict. VarDict parameter optimization was, in principle, similar to VarScan2 – raw variant calling was done using very sensitive settings allowing the testing of hard filter parameters.

The optimized settings achieved a precision of 0.8903, recall of 7468 and an F-measure of 0.8123. Compared to the default settings (a precision of 0.9483, recall of 0.3083 and an F-measure of 0.4653), the quality of detection (F-measure) was improved by 42.7%.

In total, 7 parameters were optimized by assessing 192 of their combinations, including the default values, for details, see Additional file 3. Compared to the default settings, the optimized caller had a decreased parameter for *the minimum allele frequency*, which led to its higher recall. This setting was apparently balanced by increasing *the minimum high quality variant depth*, which works towards a higher precision. The parameters for *the maximal distance for proximity filter*, the *minimum mean base quality* and *the maximum mean mismatches* performed best with their default values. The other parameters had no impact on the analysis results in the tested ranges.

Mutect2 variant calling optimization was done without applying the “FilterMutectCalls” function, because testing several of this function’s parameters, including the default settings, led in our case to rapidly decreased recall and thus to decreased overall performance. Some of the parameters from the “FilterMutectCalls” function are also available as a part of the Mutect2 raw variant calling and were the subject of testing. The best optimized settings thus reached a precision of 0.8397, recall of 0.7567 and an F-measure of 0.7960, whereas the default settings offered a precision of 0.4826, recall of 0.7714 and an F-measure of 0.5937, which was the highest recall and F-measure of all the default settings for all the tested variant callers.

The variant calling optimization tested 36 combinations of 4 parameters including their default values. For details, see Additional file 3. The best Mutect2 pipeline was very similar to the default settings with only one parameter value increased (*the minimum base quality required to consider a base for calling*) towards higher precision. The values of the other parameters remained unchanged or had no effect on the results.

The graphical interpretation for different pipeline configuration performance for all 3 variant callers and the demonstration of the optimization effect is visualized in Fig. 2; for a detailed performance report exported from LP, see Additional file 4.

In the second experiment, we tested pipeline optimization for germline variant calling using GATK HaplotypeCaller followed by VQSR and VarDict on 2 whole genomes. As reference samples with high-confident variant calls were used NA12878 and HG002 genomes analyzed by GIAB, hosted by the National Institute of Standards and Technology (NIST) which creates reference materials and data for human genome sequencing [10].

As an input for the WGS analysis, BAM files downloaded from the GIAB ftp server were used. Alignments were preprocessed using GATK best practices (removing duplicates, adding read groups, base quality score recalibration) and downsampled to 30× coverage, for details see Additional file 3.

Raw variant calling was done by each variant caller to produce intermediate results representing an input for variant filtering optimization in ToTem, considering both, SNV and InDels. In the case of GATK HaplotypeCaller, the emphasis was placed on tuning the VQSR using machine learning algorithms. In the case of VarDict, hard filters were tuned, for details see Additional file 3.

The filtered variants were compared to the ground truth variant calls by RTG Tools in given high confidence

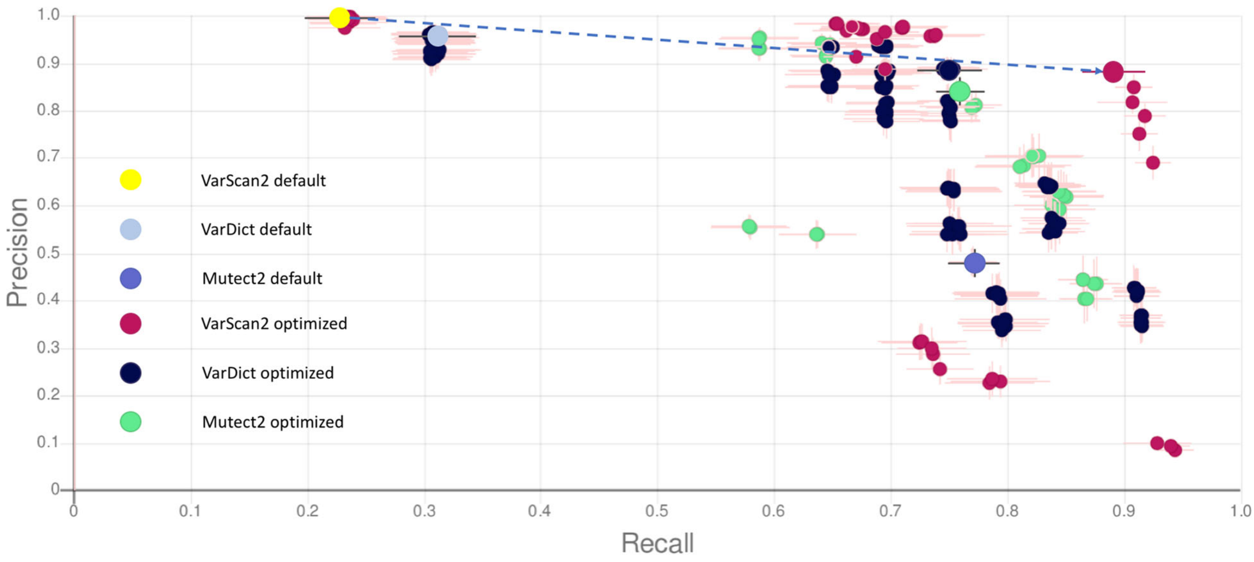

Fig. 2 Each dot represents an arithmetic mean of recall (X-axis) and precision (Y-axis) for one pipeline configuration calculated based on repeated random sub-sampling of 3 input datasets (220 samples). The crosshair lines show the standard deviation of the respective results across the sub-sampled sets. Individual variant callers (Mutect2, VarDict and VarScan2) are colour coded with a distinguished default setting for each. The default settings and the best performing configurations for each variant caller are also enlarged. Based on our experiment, the largest variant calling improvement (2.36× higher F-measure compared to default settings, highlighted by an arrow) and also the highest overall recall, precision, precision-recall, and F-measure were registered for VarScan2. In case of VarDict, a significant improvement in variant detection, mainly for recall (2.42×) was observed. The optimization effect on Mutect2 had a great effect on increasing the precision (1.74×). Although the F-measure after optimization did not reach as high values as VarScan2 and VarDict, Mutect2’s default setting provided the best results, mainly in a sense of recall

regions. Information about the pipelines' performance (precision, recall, F-measure, etc.) was stratified into variant sub-types and genomic regions by hap.py. The results in the form of a quality report for each pipeline were imported into ToTem's internal database and filtered using ToTem's filtering tool, which allows the best performing pipeline to be selected based on region, variant type and quality metrics.

The best results were achieved by GATK HaplotypeCaller, with a precision of 0.9993, recall of 0.9989 and F-measure of 0.9991 for SNV, and 0.9867, 0.9816 and 0.9842 for InDels, respectively. In comparison to the default settings, a total of 123,716 more TP and 1889 less FP were registered after the optimization by ToTem, where 40 combinations of 2 parameters were tested for both variant types, for details, see Additional file 3. An evident impact on the results' quality was proven by both of them. Increased values of the parameter for *the truth sensitivity level* influenced the detection of SNP and InDels towards higher recall. The parameter for *the maximal number of Gaussians* only needed to be optimised for InDel detection towards the lower values, otherwise the first VQSR step would not finish successfully for the NA12878 sample.

In the case of VarDict, the best pipeline setting reached a precision of 0.9977, a recall of 0.8597 and F-measure of 0.9236 for SNP; and 0.8859, 0.8697 and 0.8778 for InDels, respectively. Compared to the default settings, the results were improved by identifying 17,985 more TP and 183,850 less FP. In total, 6 parameters were tested in 216 combinations. For details, see Additional file 3.

The improved variant quality detection was affected mainly by the increasing *the minimum allele frequency values*, leading towards higher precision while increasing *the maximum mean mismatches* was responsible for higher recall in SNP detection. InDels calling was also improved by increasing *the minimum mean position of the variants in the read*, which supported higher pipeline precision. The other parameters remained unchanged for the best performing pipeline. The difference between the best pipeline for every tool and the baseline for that tool using default parameters is described in Additional file 5.

The TGS experiment optimizing 3 variant callers was run in parallel by 15 threads (15 parameter combinations running simultaneously) and was completed in approximately 60 h; WGS experiment optimizing 2 variant callers was run using 5 threads and lasted approximately 30 h. The experiments were performed separately on a server with 100 CPU cores and 216 GB RAM memory available, however the server was not used to its full capacity.

Discussion

ToTem is a web application with an intuitive GUI primarily designed for automated configuration and evaluation of variant calling pipeline performance using validated ground truth material. Once the pipeline is optimized for specific data, project, kit or diagnosis, it can be effortlessly run through ToTem for routine data analysis with no additional need for ground truth material. From this perspective, ToTem represents a unique hybrid between a workflow manager like bcbio [28], SeqMule [19] or Galaxy [29] and a pipeline benchmarking tool like SMaSH [7], with the added value of an automated pipeline generator.

To meet the latest best practices in variant calling benchmarking, ToTem is perfectly suited and fully compatible with the current GIAB approach using RTG Tools and hap.py. This allows comfortable automated parameter optimization, benchmarking and selection of the best pipeline based on variant type, region stratification and preferred performance quality metrics.

The Little Profet benchmarking approach introduces novel estimates of pipeline reproducibility based on a cross validation technique allowing the selection of a robust pipeline that will be less susceptible to over-fitting.

ToTem is also very robust in terms of implementing various tools by its "template approach" allowing the integration and running of any tool or even more importantly, custom or novel code without having to create a special wrapper. These properties enable automatic and significantly less biased testing for new or existing variant calling pipelines than standard procedures, testing only the default or just a few alternative settings [5, 6].

The results are visualized through several interactive graphs and tables enabling users to easily choose the best pipeline or to help adapt and optimize the parametrization of the tested pipelines.

At the moment, ToTem's core function is to efficiently trigger many pipeline configurations and streamline their benchmarking. However, the optimization process itself is not fully automated. Selecting tools and their parameter ranges needs to be done manually, according to the particular data type and thus, this task relies mostly on the knowhow of an experienced user. The primary objective for future development is to provide the option of optimizing the pipeline settings automatically using more complex machine learning algorithms. Implementation will be based on the results collection, mainly from the optimization of pipelines for a specific data type, which can be detected based on their quality control. The data will be anonymized and transformed for the purposes of machine learning applications, which will both select candidates for optimization settings and also select configurations suitable for a specific data type's routine analysis. Routine analysis results could eventually be used for benchmarking if the user provides feedback. We are also considering installing ToTem using a docker image.

Conclusion

NGS data analysis workflow quality is significantly affected by the selection of tools and their respective parameters. In this study we present ToTem, a tool enabling the integration of a broad variety of tools and pipelines and their automatic optimization based on benchmarking results controlled through efficient analysis management.

We demonstrated ToTem's usefulness in increasing the performance of variant calling in two distinct NGS experiments. In the case of somatic variant detection on ultra-deep TGS data, we reached a 2.36-fold improvement in F-measure compared to best performing variant caller's default settings. In the case of germline variant calling using WGS data, we were able to discover 123,716 additional true positive variants than GATK HaplotypeCaller's default settings, among those 147 were coding and 70 non-synonymous and of likely functional importance.

Availability and requirements

Project name: ToTem

Project home page: https://totem.software

Operating system(s): Platform independent

Programming language: Java, PHP, MySQL

Other requirements: No

License: Free for academic use.

Any restrictions to use by non-academics: License needed.

Additional files

Additional file 1: ToTem's technical documentation. ToTem's technical documentation describes the technical details of ToTem. (PDF 1464 kb)

Additional file 2: Pseudo code for the Little profet algorithm. The pseudo code describes the general principles of Little Profet algorithm. (TXT 9 kb)

Additional file 3: Material and details of pipeline configurations. The document describes in detail the material and pipeline configurations used in the study. (DOCX 48 kb)

Additional file 4: Detailed performance report generated by Little Profet. The detailed report describing pipeline performance including different over-fitting correction metrics generated by LP. These data were generated as a part of TGS experiment. (XLS 90 kb)

Additional file 5: Performance comparison of 2 variant callers with default and optimized pipelines applied on WGS dataset. The difference between the best pipeline for every tool and the default settings. These data were generated as a part of WGS experiment. (XLSX 14 kb)

Abbreviations

CLL: Chronic lymphocytic leukemia; CPU: Central processing unit; DSD: Dataset standard deviation; FN: False negative; FP: False positive; GIAB: Genome in a Bottle; GUI: Graphical user interface; HC: High confidence; InDel: Insertion or deletion; LP: Little Profet; MPN: Myeloproliferative neoplasm; NGS: Next generation sequencing; NIST: The National Institute of Standards and Technology; RAM: Random-access memory; SMSD: Sample mix standard deviation; SNV: Single nucleotide variant; TGS: Targeted gene; TP: True positive; UG: GATK UnifiedGenotyper; VAF: Variant allele frequency; VQSR: Variant Quality Score Recalibration; WES: Whole exome sequencing; WGS: Whole genome sequencing

Acknowledgements

We acknowledge the CEITEC Genomics CF supported by the NCLG research infrastructure (LM2015091 funded by MEYS CR) for their support with obtaining the scientific data presented in this paper.

Funding

This work was supported by the Ministry of Education, Youth and Sports of the Czech Republic project CEITEC2020 (LQ1601), European Union's Horizon 2020 research and innovation programme under grant agreement No 692298 (MEDGENET), the Ministry of Health of the Czech Republic research grants AZV-MZ-CR 15-30015A and 15-31834A, the Medical Faculty of Masaryk University grant no. MUNI/A/0968/2017, the European Regional Development Fund-Project "EATRIS-CZ" No. CZ.02.1.01/0.0/0.0/16_013/0001818, the research grant TACR (TEO2000058/2014-2019) and by research infrastructure EATRIS-CZ, ID number LM2015064, funded by MEYS CR. This article reflects only the author's view and the Research Executive Agency is not responsible for any use that may be made of the information it contains. The funding body did not affect the design of the study and collection, analysis, and interpretation of data and in writing the manuscript.

Availability of data and materials

The TGS datasets used and/or analysed during the current study are available from the corresponding author on reasonable request.
The WGS datasets analysed during the current study are available in the GIAB repository [ftp://ftp-trace.ncbi.nlm.nih.gov/giab/ftp/].

Authors' contributions

NT conceived the software, designed the algorithmic solutions, tested the functions and wrote the manuscript. OT designed the algorithmic solutions and wrote the code. JM participated on the creation of ground truth data. SP participated on the creation of ground truth data. BK participated on the creation of ground truth data. TR designed the algorithmic solutions. MK supervised the project. VB supervised the project. VB designed the algorithmic solutions and wrote the manuscript. SP supervised the project. All authors drafted the manuscript. All authors have read and approved the manuscript.

Ethics approval and consent to participate

The whole study and written informed consent obtained from all patients analysed for variant discovery in the *TP53* were approved by the Ethical Committee of University Hospital Brno in concordance with the Declaration of Helsinki.
For GIAB data, ethics approval is not required as the human data were publicly available on the GIAB website.

Competing interests

The authors declare that they have no competing interests.

Publisher's Note

Author details

[1]Center of Molecular Medicine, Central European Institute of Technology, Masaryk University, Brno, Czech Republic. [2]Department of Internal Medicine - Hematology and Oncology, Medical Faculty, Masaryk University and University Hospital Brno, Brno, Czech Republic. [3]Department of Computer Science, Faculty of Science, Palacky University, Olomouc, Czech Republic. [4]Genomics Core Facility, European Molecular Biology Laboratory, Heidelberg, Germany.

Received: 3 January 2018 Accepted: 31 May 2018

References

1. Park JY, Kricka LJ, Fortina P. Next-generation sequencing in the clinic. Nat Biotechnol. 2013;31:990–2.
2. Pabinger S, Dander A, Fischer M, Snajder R, Sperk M, Efremova M, et al. A survey of tools for variant analysis of next-generation genome sequencing data. Brief Bioinform. 2014;15:256–78.

3. DePristo MA, Banks E, Poplin RE, Garimella KV, Maguire JR, Hartl C, et al. A framework for variation discovery and genotyping using next-generation DNA sequencing data. Nat Genet. 2011;43:491–8.
4. Van der Auwera GA, Carneiro MO, Hartl C, Poplin R, del Angel G, Levy-Moonshine A, et al. From FastQ data to high confidence variant calls: the Genome Analysis Toolkit best practices pipeline. Curr Protoc Bioinforma Ed Board Andreas Baxevanis Al. 2013;43:11. https://doi.org/10.1002/0471250953.bi1110s43.
5. Hwang S, Kim E, Lee I, Marcotte EM. Systematic comparison of variant calling pipelines using gold standard personal exome variants. Sci Rep. 2015;5:srep17875.
6. Sandmann S, de Graaf AO, Karimi M, van der Reijden BA, Hellström-Lindberg E, Jansen JH, et al. Evaluating variant calling tools for non-matched next-generation sequencing data. Sci Rep. 2017;7:srep43169.
7. Talwalkar A, Liptrap J, Newcomb J, Hartl C, Terhorst J, Curtis K, et al. SMaSH: a benchmarking toolkit for human genome variant calling. Bioinformatics. 2014;30:2787–95.
8. Bahcall OG. Genomics: Benchmarking genome analysis pipelines. Nat Rev Genet. 2015;16:194.
9. Zook JM, Chapman B, Wang J, Mittelman D, Hofmann O, Hide W, et al. Integrating human sequence data sets provides a resource of benchmark SNP and indel genotype calls. Nat Biotechnol. 2014;32:246–51.
10. Zook JM, Catoe D, McDaniel J, Vang L, Spies N, Sidow A, et al. Extensive sequencing of seven human genomes to characterize benchmark reference materials. Sci Data. 2016;3:sdata201625.
11. rtg-tools: RTG tools: utilities for accurate VCF comparison and manipulation. Java. Real time genomics; 2017. https://github.com/RealTimeGenomics/rtg-tools. Accessed 18 Dec 2017.
12. Cleary JG, Braithwaite R, Gaastra K, Hilbush BS, Inglis S, Irvine SA, et al. Comparing Variant Call Files for Performance Benchmarking of Next-Generation Sequencing Variant Calling Pipelines. bioRxiv. 2015:023754. https://doi.org/10.1101/023754.
13. hap.py: Haplotype VCF comparison tools. C++. Illumina; 2017. https://github.com/Illumina/hap.py. Accessed 18 Dec 2017.
14. GIAB General Group. The Joint Initiative for Metrology in Biology. http://jimb.stanford.edu/giab-general-group/. Accessed 19 Dec 2017.
15. Contribute to benchmarking-tools development by creating an account on GitHub. HTML. Global alliance for genomics and health; 2017. https://github.com/ga4gh/benchmarking-tools. Accessed 19 Dec 2017.
16. Popitsch N, WGS500 Consortium, Schuh A, Taylor JC. ReliableGenome: annotation of genomic regions with high/low variant calling concordance. Bioinforma Oxf Engl. 2017;33:155–60.
17. Goldfeder RL, Priest JR, Zook JM, Grove ME, Waggott D, Wheeler MT, et al. Medical implications of technical accuracy in genome sequencing. Genome Med. 2016;8:24.
18. Li H. Toward better understanding of artifacts in variant calling from high-coverage samples. Bioinformatics. 2014;30:2843–51.
19. Guo Y, Ding X, Shen Y, Lyon GJ, Wang K. SeqMule: automated pipeline for analysis of human exome/genome sequencing data. Sci Rep. 2015;5:14283.
20. Malcikova J, Stano-Kozubik K, Tichy B, Kantorova B, Pavlova S, Tom N, et al. Detailed analysis of therapy-driven clonal evolution of TP53 mutations in chronic lymphocytic leukemia. Leukemia. 2015;29:877–85.
21. Kubesova B, Pavlova S, Malcikova J, Kabathova J, Radova L, Tom N, et al. Low-burden TP53 mutations in chronic phase of myeloproliferative neoplasms: association with age, hydroxyurea administration, disease type and JAK2 mutational status. Leukemia. 2017; https://doi.org/10.1038/leu.2017.230
22. Gerstung M, Papaemmanuil E, Campbell PJ. Subclonal variant calling with multiple samples and prior knowledge. Bioinforma Oxf Engl. 2014; 30:1198–204.
23. Lai Z, Markovets A, Ahdesmaki M, Chapman B, Hofmann O, McEwen R, et al. VarDict: a novel and versatile variant caller for next-generation sequencing in cancer research. Nucleic Acids Res. 2016;44:e108.
24. Koboldt DC, Chen K, Wylie T, Larson DE, McLellan MD, Mardis ER, et al. VarScan: variant detection in massively parallel sequencing of individual and pooled samples. Bioinforma Oxf Engl. 2009;25:2283–5.
25. Koboldt DC, Zhang Q, Larson DE, Shen D, McLellan MD, Lin L, et al. VarScan 2: somatic mutation and copy number alteration discovery in cancer by exome sequencing. Genome Res. 2012;22:568–76.
26. Li H, Durbin R. Fast and accurate short read alignment with Burrows–Wheeler transform. Bioinformatics. 2009;25:1754–60.
27. vcflib: a simple C++ library for parsing and manipulating VCF files, + many command-line utilities. C++. vcflib; 2017. https://github.com/vcflib/vcflib. Accessed 22 Dec 2017.
28. Chapman B. bcbio-nextgen: Validated, scalable, community developed variant calling, RNA-seq and small RNA analysis. Python. 2017. https://github.com/bcbio/bcbio-nextgen. Accessed 19 Dec 2017.
29. Afgan E, Baker D, van den Beek M, Blankenberg D, Bouvier D, Čech M, et al. The galaxy platform for accessible, reproducible and collaborative biomedical analyses: 2016 update. Nucleic Acids Res. 2016;44:W3–10.

Bioinformatic pipelines for whole transcriptome sequencing data exploitation in leukemia patients with complex structural variants

Jakub Hynst[1,2], Karla Plevova[1,2,3], Lenka Radova[1], Vojtech Bystry[1], Karol Pal[1,2] and Sarka Pospisilova[1,2,3]

[1] Central European Institute of Technology, Masaryk University, Brno, Czech Republic
[2] Department of Internal Medicine—Hematology and Oncology, Faculty of Medicine, Masaryk University, Brno, Czech Republic
[3] Department of Internal Medicine—Hematology and Oncology, University Hospital Brno, Brno, Czech Republic

ABSTRACT

Background. Extensive genome rearrangements, known as chromothripsis, have been recently identified in several cancer types. Chromothripsis leads to complex structural variants (cSVs) causing aberrant gene expression and the formation of *de novo* fusion genes, which can trigger cancer development, or worsen its clinical course. The functional impact of cSVs can be studied at the RNA level using whole transcriptome sequencing (total RNA-Seq). It represents a powerful tool for discovering, profiling, and quantifying changes of gene expression in the overall genomic context. However, bioinformatic analysis of transcriptomic data, especially in cases with cSVs, is a complex and challenging task, and the development of proper bioinformatic tools for transcriptome studies is necessary.

Methods. We designed a bioinformatic workflow for the analysis of total RNA-Seq data consisting of two separate parts (pipelines): The first pipeline incorporates a statistical solution for differential gene expression analysis in a biologically heterogeneous sample set. We utilized results from transcriptomic arrays which were carried out in parallel to increase the precision of the analysis. The second pipeline is used for the identification of *de novo* fusion genes. Special attention was given to the filtering of false positives (FPs), which was achieved through consensus fusion calling with several fusion gene callers. We applied the workflow to the data obtained from ten patients with chronic lymphocytic leukemia (CLL) to describe the consequences of their cSVs in detail. The fusion genes identified by our pipeline were correlated with genomic break-points detected by genomic arrays.

Results. We set up a novel solution for differential gene expression analysis of individual samples and *de novo* fusion gene detection from total RNA-Seq data. The results of the differential gene expression analysis were concordant with results obtained by transcriptomic arrays, which demonstrates the analytical capabilities of our method. We also showed that the consensus fusion gene detection approach was able to identify true positives (TPs) efficiently. Detected coordinates of fusion gene junctions were in concordance with genomic breakpoints assessed using genomic arrays.

Submitted 30 December 2018
Accepted 6 May 2019
Published 12 June 2019

Corresponding authors
Karla Plevova,
karla.plevova@mail.muni.cz,
karla.plevova@gmail.com
Sarka Pospisilova,
sarka.pospisilova@ceitec.muni.cz

Academic editor
Enza Lonardo

Additional Information and Declarations can be found on page 13

DOI **10.7717/peerj.7071**

How to cite this article Hynst J, Plevova K, Radova L, Bystry V, Pal K, Pospisilova S. 2019. Bioinformatic pipelines for whole transcriptome sequencing data exploitation in leukemia patients with complex structural variants. *PeerJ* **7**:e7071 http://doi.org/10.7717/peerj.7071

Discussion. By applying our methods to real clinical samples, we proved that our approach for total RNA-Seq data analysis generates results consistent with other genomic analytical techniques. The data obtained by our analyses provided clues for the study of the biological consequences of cSVs with far-reaching implications for clinical outcome and management of cancer patients. The bioinformatic workflow is also widely applicable for addressing other research questions in different contexts, for which transcriptomic data are generated.

Subjects Bioinformatics, Genomics, Hematology, Oncology
Keywords Chromothripsis, Complex structural variants, Fusion gene, Gene expression, Bioinformatic pipeline, Next-generation sequencing, Leukemia, Transcriptomics, Chronic lymphocytic leukemia, Statistics

INTRODUCTION

Whole-genome sequencing of cancer samples has enabled the identification and detailed description of complex structural variants (cSVs) with chromothripsis being their prime example (*Stephens et al., 2011*; *Rausch et al., 2012*). Chromothripsis is characterized by tens to hundreds of clustered genomic rearrangements accompanied by extensive losses of genetic information and arises as a consequence of genomic instability. Approximately 2–3% of tumors bear chromosomes featuring the hallmarks of chromothripsis (*Stephens et al., 2011*; *Kinsella, Patel & Bafna, 2014*). Its incidence is variable among tumor types and peaks in brain and bone tumors (*Stephens et al., 2011*). There is also strong evidence for the presence of chromothripsis and related cSVs in hematological malignancies including chronic lymphocytic leukemia (CLL), the most common leukemia of adults in the Western world.

In contrast to the concept of gradual accumulation of chromosomal defects in the cancer genome, it has been assumed that chromothripsis arises in a single catastrophic event. The most widely accepted explanation of chromothripsis origin is based on aberrant mitosis, which is accompanied by physical separation of certain chromosomes in nuclear structures called micronuclei (*Zhang et al., 2015*; *Ly & Cleveland, 2017*). Another possible mechanism involved in chromothripsis formation revolves around the generation of so-called breakage-fusion-bridge cycles (*Lo et al., 2002*) leading to the occurrence of dicentric chromosomes that are disrupted during cell division. This is related to telomere shortening and, consequently, to the absence of telomeres at chromosome ends which enables chromosome fusion (*Maciejowski et al., 2015*; *Ernst et al., 2016*). All these events lead to multiple clustered chromosomal aberrations that feature a unique pattern in every affected case and alter the expression of genes in an impaired cell (Fig. 1).

Next-generation sequencing (NGS) serves as a powerful tool for describing any abnormalities occurring in the genome and has also been instrumental in discovering and describing cSVs. However, in many NGS experiments, consequent bioinformatic analysis remains challenging. Publicly available tools are often developed for a specific purpose with limitations in different experimental settings and do not take into account all genomic

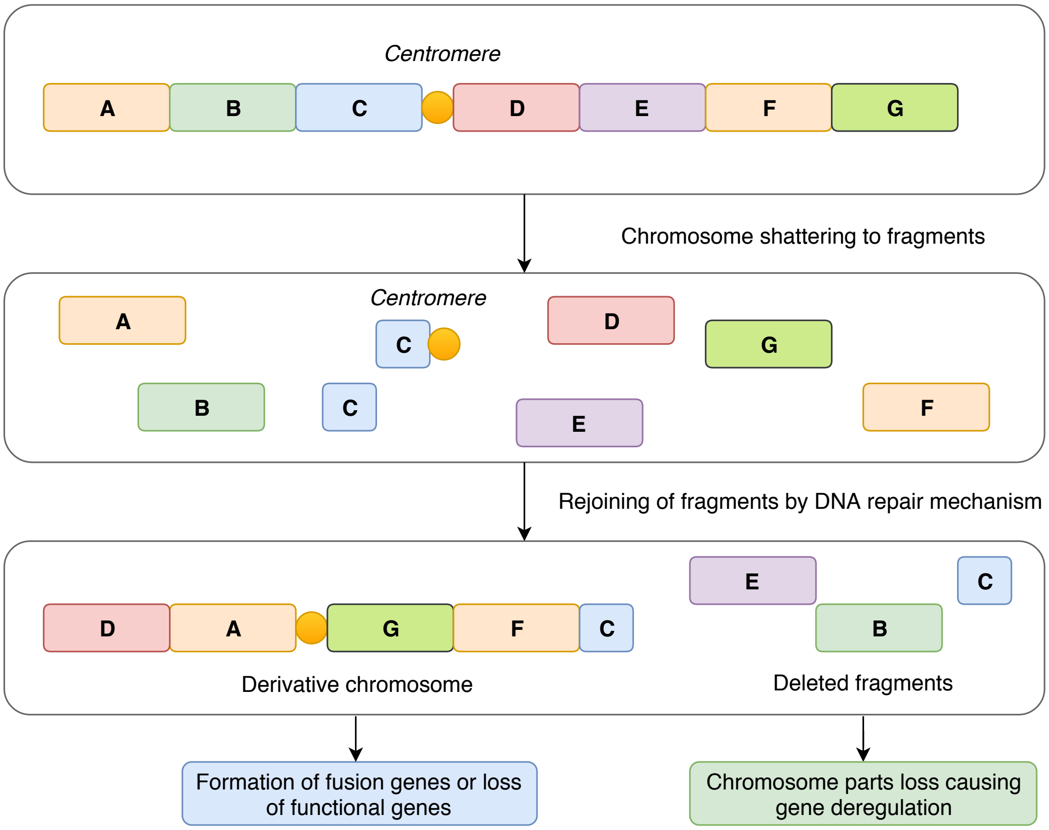

Figure 1 **Schematic representation of the mechanism of chromothripsis.** During chromothripsis, chromosomes are scattered into hundreds of fragments that persist as intermediates and eventually rejoin together via error-prone DNA repair mechanisms. Such an event can lead to the loss of functional genes and directly or indirectly influence gene expression in affected regions. Another common and frequently observed feature is the formation of aberrant fusion genes, which leads to a change in gene expression and production of fusion proteins with novel structure and functions.

Full-size DOI: 10.7717/peerj.7071/fig-1

rearrangements that might be present in a sample. Moreover, when attempting to describe the impact of cSVs on cell phenotype, each case should be considered independently. The reason for such an approach is that, although there are a limited number of processes causing cSVs among individual cases, they affect different genomic loci with different impact. Thus, we developed a statistical approach for differential gene expression analysis from total RNA-Seq data, which is based on the comparison of individual cases within a tested dataset. Applying the method on a set of ten CLL samples, our strategy provided highly convincing gene candidates. In the next step, we focused on the identification of fusion genes and their stemming breakpoints from total RNA-Seq data. Due to the high rate of FP results of different methods, we developed a pipeline combining available analytic tools to maximize TP rate in dataset. Results were then cross-checked with data from genomic arrays in order to assess the sensitivity and specificity of our method.

MATERIALS & METHODS

Data generation and preprocessing

Our pipelines were developed and tested on total RNA-Seq data generated from ten CLL cases (T1-T10) with cSVs that were previously detected using genomic CytoScan^{TM} HD Arrays and analyzed with Chromosome Analysis Suite (Thermo Fisher Scientific). These cases were identified during the long-term clinical research at the University Hospital Brno and were classified as chromothripsis as they showed clustered copy number alterations on a limited number of chromosomes. Genomic breakpoint localization was extracted for all detected copy number variants and losses of heterozygosity. Total RNA-Seq libraries were prepared with TruSeq® Stranded Total RNA kit (Illumina) with Ribo-Zero ribosomal RNA depletion and sequenced using an Illumina HiSeq 2500 machine producing 125bp long pair-end reads. Sequencing read quality was evaluated in FastQC software. Adapter sequences were trimmed from raw reads using Trimmomatic software (*Bolger, Lohse & Usadel, 2014*) (version 0.32) according to sequencing facility standards. In parallel, we performed GeneChip® Human Transcriptome Arrays 2.0 (Thermo Fisher Scientific) to complement expression data from the RNA-Seq experiment. These data were then analyzed by the Transcriptome Analysis Console (Thermo Fisher Scientific) by comparing each consecutive sample to all other samples using a one-way ANOVA statistical test to identify a unique expression pattern in each sample. Identified fusion gene junctions and their respective sequencing reads were visualized in the Integrative Genomic Viewer (*Thorvaldsdottir, Robinson & Mesirov, 2013*).

The study was approved by the Ethical Committee of the University Hospital Brno under the ref. no. 15-31834A. All patients involved in the study provided their written informed consent to the research use of their samples.

RNA-Seq data processing for differential genes expression analysis

Processed reads were mapped to the hg38 human genome reference using STAR, a splice-aware aligner (*Dobin et al., 2013*). We chose the genome reference over the transcriptome as recommended by best practices for RNA-Seq data when non-canonical junctions and fusion transcripts are of interest (*Conesa et al., 2016*). The parameters of the STAR aligner were set to default settings according to best practices.

Gene expression analysis from RNA-Seq data is based on counting reads covering gene regions (defined by reference relative GTF file) and statistical analysis of these read counts. In the first step, we used an htseq-count script (*Anders, Pyl & Huber, 2015*), which efficiently counts reads that align to or overlap with more than one gene. For this purpose, the software parameter *union* was applied. The reads were then assigned to gene regions irrespective of DNA strand orientation. A read count table was used as an input for consequent statistical analysis of differential gene expression; low-expressed genes were filtered out from the dataset to decrease dataset complexity and avoid FP. Of the ten CLL cases in our cohort, we expected at least six samples to be covered by at least one read. However, these criteria can be modified in the pipeline according to the actual dataset analyzed. Pre-filtered read count table was then normalized using the *rpkm()* function from edgeR Bioconductor package (*Robinson, McCarthy & Smyth, 2010*). The function applies the RPKM (reads per kilobase per million mapped reads) method, which performs data normalization based on a read length and a total number of sequencing reads with respect to gene length. Obtained $\log_2$ scale normalized expressions were subjected to further computational steps, for which we developed a novel statistical pairwise comparison (PComp) approach that allows obtaining a gene expression profile of individual samples.

Design and evaluation of novel statistical approach PComp

For the read count (expression) table resulting from RNA-Seq data processing steps, linear regression model with confidence bands containing expression values for all possible sample combinations (i.e., T1–T2, …, T1–T10) was applied to identify gene outliers in particular sample. Only genes constantly lying outside these bands in all possible sample combination were stored. In the next step, one sample t-test was applied to assess the p.value to every single gene outlier in a given sample according to the gene expression in the rest of the samples. All gene candidates with significant p.value that can be specified manually (default 0.05) were considered as differentially expressed. Graphical representation of PComp algorithm is depicted in Fig. 2 with artificial expression values. Obtained results were compared to the transcriptomic array results representing a gold standard for gene expression analysis.

RNA-Seq data were also subjected to a differential gene expression analysis using widely used and well-established algorithm *limma* (*Ritchie et al., 2015*) to gain an insight on overall performance of our PComp tool. Using *limma* we compared gene expression in a single sample (group 1) with all other samples (group 2) in all possible combinations and correlated the results to the PComp output.

Identification of gene fusions in cSVs cases from RNA-Seq

Based on a literature search (*Liu et al., 2016*), four state of the art tools for gene fusion detection—EricScript (*Benelli et al., 2012*), JAFFA (*Davidson, Majewski & Oshlack, 2015*), FusionCatcher (*Nicorici et al., 2014*), and TopHat-fusion (*Kim & Salzberg, 2011*)—were tested in our approach. TopHat-fusion was excluded due to a high rate of FP results and time-consuming computation in comparison to other methods. Thus, three tools—EricScript, JAFFA, and FusionCatcher—were run in parallel in our bioinformatic workflow for fusion gene identification; default settings were used for all of them. Although read alignment algorithms differ among the selected tools (*Kent, 2002*; *Li & Durbin, 2009*; *Langmead & Salzberg, 2012*; *Dobin et al., 2013*), the utilized computational algorithms follow similar concept (*Kumar et al., 2016*). In general, the mapping step consists of two alignments, one to the hg38 reference and the other to putative junction reference for each potential fusion. During these steps, unmapped and discordant pair-end reads that were mapped uniquely to different loci of the genome were identified, and a library of putative fusion junctions was derived. Reads were then realigned to the putative fusion junction sequences and annotated, a split-read signature (reads spanning fusion junctions) was recognized, and potential fusion genes were reported.

For efficient fusion gene detection, we developed an in-house meta-caller, which combines results from the selected tools into a consensus call. Each piece of software

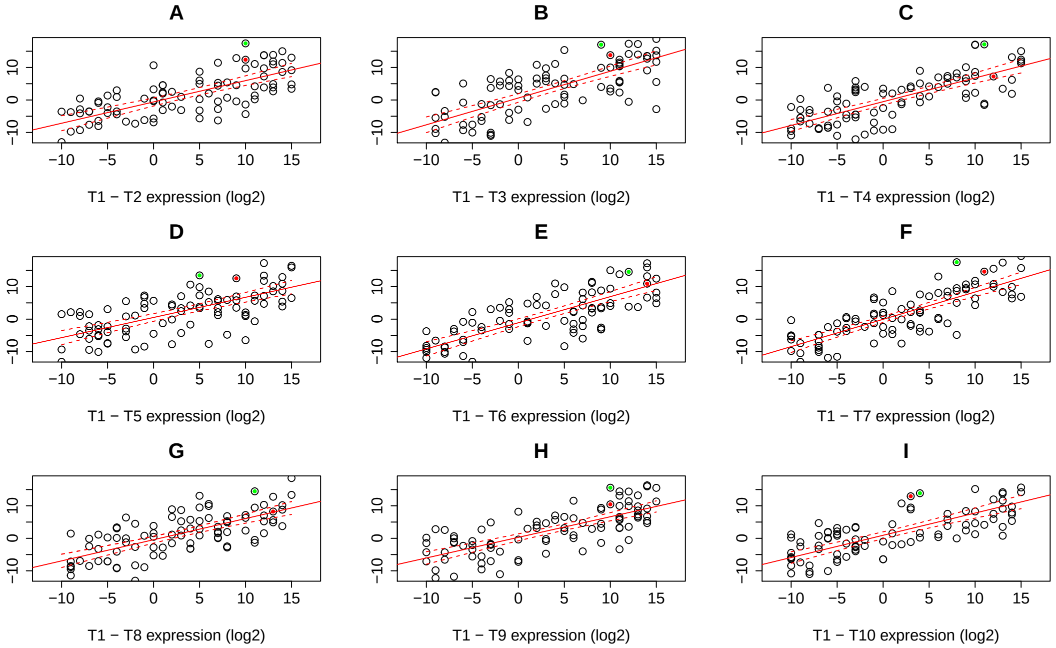

Figure 2 Expression data plots demonstrating our statistical algorithm PComp for differential gene expression assessment. A solid red line represents the linear regression line, while dashed red curves delimit 99.9% confidence bands (A–I). Selected expressed genes identified in an RNA-Seq experiment for sample T1 are highlighted as green and red dots. The green dots represent a gene that is considered significantly differentially expressed in all sample pair combinations, i.e., the gene is outside the confidence band with $p < 0.001$ for all pairs. The gene highlighted as red dots is not significantly differentially expressed when comparing T1 sample to T4, T6, and T8 (C, E, G), thus not differentially expressed as a whole. Down/up-regulation was taken into account.

Full-size DOI: 10.7717/peerj.7071/fig-2

applies various metrics enabling classification of fusions to confidence subsets. In the first meta-caller step, detected fusions were filtered in individual callers as follows: for EricScript fusions with an Eric score (ES) of over 0.90, for JAFFA only fusions with the "HighConfidence" tag, and for FusionCatcher only high confidence fusions. In the consequent consensus call only fusions that passed at least two callers were kept which allowed increasing TP fusion rate and removal of FP fusions arising as specific artifacts of an individual caller algorithm (i.e., read alignments errors). The whole fusion gene detection pipeline is schematically visualized in the Fig. 3.

Validation of gene fusions by overlap with genomic arrays

Finally, to estimate TP and FP rates of the individual callers and the meta-caller, coordinates of fusions detected in RNA-Seq data were compared with the coordinates of genomic breakpoints detected by the genomic arrays. The interval of ± 100 kb around the breakpoints was applied in order to adjust to the array resolution and to the fact that the breakpoints can be located in introns, whereas fusions in RNA-Seq data appear in exon-exon boundaries. All potentially TP fusions identified by this approach were inspected visually in the array results.

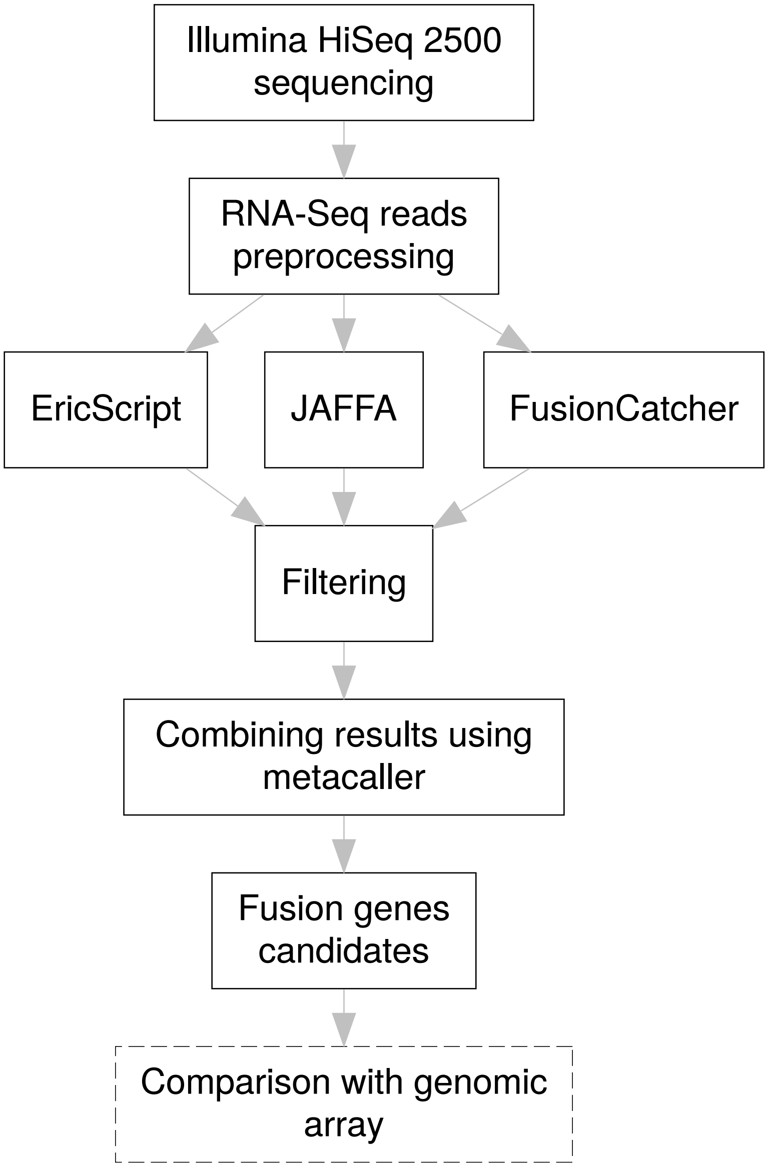

Figure 3 Pipeline design for fusion gene identification. Schematic overview of RNA-Seq fusion gene identification pipeline summarizes all steps of the procedure. Comparison with results of the genomic arrays is an optional manual step, independent on the pipeline, which can serve as a secondary confirmation of the results.

Full-size DOI: 10.7717/peerj.7071/fig-3

Implementation of analytical algorithms

Algorithms and procedures of our novel solution were implemented in the R programming language. The meta-caller and the tool for differential expression are both freely available at GitHub (https://github.com/Hynst/WTS_cSVs_analysis), where the source codes are accessible for download. No installation is needed, as all dependencies (i.e., R packages and libraries) are installed automatically to the R environment.

Table 1 Differentially expressed genes identified by PComp in RNA-Seq data and transcriptomic array analyses. For RNA-Seq data pairwise comparison (PComp) analysis was applied to identify deregulated genes. Numbers in parentheses represent deregulated genes including also unannotated transcripts.

Sample	RNA-Seq Expression Analysis (PComp)			GeneChip Human Transcriptome Array 2.0			Method overlap		
	up	down	total	up	down	total	up	down	total
T1	1,534	552	2,086	707 (956)	399 (909)	1,106	351	29	380
T2	539	66	605	253 (660)	83 (191)	336	54	1	55
T3	314	82	396	124 (293)	92 (188)	216	22	3	25
T4	1,768	657	2,425	482 (882)	154 (197)	636	207	66	273
T5	1,572	355	1,927	567 (1,268)	77 (127)	644	78	21	99
T6	1,346	258	1,604	644 (1,405)	134 (178)	778	178	38	216
T7	1,865	245	2,110	423 (804)	186 (439)	609	164	15	179
T8	1,855	419	2,274	1,446 (2,173)	428 (821)	1,874	682	55	737
T9	544	96	640	124 (384)	92 (110)	216	27	3	30
T10	968	165	1,133	213 (418)	50 (89)	263	45	5	50
TOTAL	12,305	2,895	15,200	4,983	1,695	6,678	1,808	236	2,044

RESULTS

PComp performance in differential gene expression analysis

We used PComp approach to identify differentially expressed genes on the level of individual samples. We followed a linear regression model and estimated a linear regression line with 99.9% confidence bands ($1-p=0.999$, i.e., $p=0.001$) for each pair of samples. All genes lying outside the confidence bands were suggested as potentially differentially expressed candidates. We repeated this procedure for each sample pair combination and obtained nine sets of potential candidates per sample. Genes occurring in all nine sets were considered as differentially expressed for a given sample. By applying one sample t-test we assessed the differential expression of a given gene in a given sample according to the rest of the samples. We considered all gene candidates in particular sample with a $p < 0.001$ by one sample t-test to be differentially expressed. Using this approach, we found 15,200 differentially expressed genes in total (Table 1).

We inspected the results from RNA-Seq obtained using the PComp method and compared them to the results of transcriptomic arrays analyzed by one-way ANOVA. In the ten CLL samples tested, we identified 12,492 deregulated transcripts (including also unannotated ones) using transcriptomics arrays and extracted only annotated gene transcripts which resulted in 6,678 deregulated genes. We created an overlap between PComp and transcriptomic array results and found 1,808 significantly upregulated and 236 significantly downregulated gene candidates (Table 1). We also studied whether the results were concordant between the methods in terms of assigning genes as up-/downregulated and observed good concordance of the methods ranging 97.44–100% for individual samples (Table S1).

Similarly, in RNA-Seq data we identified 14,803 deregulated genes using *limma*. When we overlapped array data with *limma* results we found 1168 upregulated and 414 downregulated genes (Table S2). We compared the overlap rate of transcriptomic

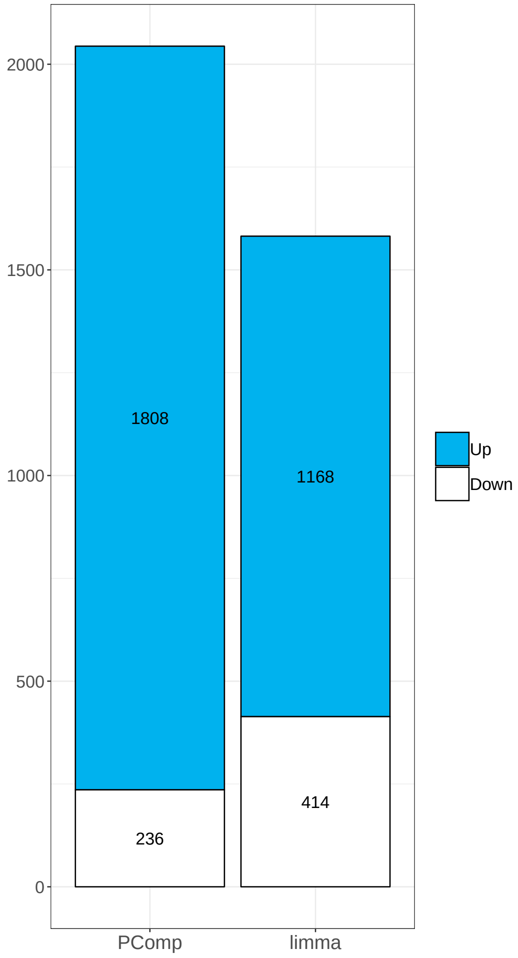

Figure 4 **Comparison of PComp vs. *limma* statistical analysis of RNA-Seq data overlapped with results of the transcriptomic arrays.** Graphical representation of upregulated (blue) and downregulated (white) genes as identified by PComp and *limma* after overlapping the data with transcriptomic array outputs. PComp was capable of identifying higher number of differentially expressed genes concordant with transcriptomic arrays.

Full-size DOI: 10.7717/peerj.7071/fig-4

array with PComp and *limma* data, respectively, in terms of up-/downregulated genes. Both methods performed differently, we observed 14.7% and 28.9% upregulated genes, and 8.2% and 4.1% downregulated genes using PComp and limma, respectively. Finally, we observed larger overlap between transcriptomic array and PComp approach (Fig. 4), where 2044 deregulated genes were identified in total (compared to 1,585 identified by *limma*).

Meta-caller approach efficiency of fusion gene identification

In RNA-Seq data, we pre-filtered results of the individual pieces of software in the first meta-caller step to create a fusion gene subset with high confidence. No explicit pre-filtering of lowly expressed fusions was done in order to allow for the capture of lowly expressed fusion genes (i.e., the number of reads spanning fusion junction ≥ 1). In the next step of the meta-caller, results obtained by ≥2 callers were combined into a consensus call. Following these steps, our pipeline was capable of identifying 40 fusion genes which were potentially TP with high confidence across the ten samples (Table S3). Further, we used breakpoint coordinates generated using genomic arrays and compared them with those identified by RNA-Seq to test TP rates of our pipeline. Only fusions where at least one fusion gene partner was located in a genomic breakpoint were considered as potentially TP. Genomic array data corresponded to RNA-Seq breakpoints in 19 of the 40 cases. These uniquely expressed TP fusions were identified in eight of the ten CLL patients with 1 to 7 fusions per patient.

Considering candidates that were not supported by genomic arrays (21 of 40 features), potential fusions ZMYM5-PSPC1, HACL1-COLQ, MFSD7-ATP5I, and CYTIP-ERMN, occurring recurrently in six, three, three and two instances, respectively, were considered FP because they represented neighboring genes (read-through). Similarly, YWHAZ-ZNF706, LINCPINT-MKLN1, and NFATC3-PLA2G15 were also considered FP due to their adjacent localization in the genome, although not observed recurrently. Altogether, 17 of 21 fusions were considered FP. The remaining four fusions were not confirmed by the independent method; in all of them, at least one fusion partner appeared recurrently in the data, however, with a different partner. All of the four fusions could still represent TP resulting from balanced translocations or inversions that were not detectable by genomic arrays.

To assess the ability of the meta-caller to increase TP rate, we inspected overlap between individual callers and genomic arrays (Table 2). The meta-caller was superior to a single caller approach with the overall 47.5% TP rate, while JAFFA, FusionCatcher, and EricScript showed 9.4%, 8.2%, and 0.5% TP rate, respectively. Still individual callers identified TP fusions (as designated based on the overlap with genomic array results) which were missed by the meta-caller because they were supported only by one caller. Altogether 29 TP fusions were detected by all callers and meta-caller with the highest number of 22 TP fusions by FusionCatcher (Table S4). FusionCatcher and the meta-caller did not show any FP when overlapped with genomic arrays. Detailed results of this comparison are depicted in Table 3. Taking overall TP rates of the callers into account, the meta-caller appears as an efficient tool for fusion gene detection.

DISCUSSION

Several mechanisms of the influence of cSVs on cancer development have been suggested. NGS techniques provide an opportunity to unravel them by focusing on changes occurring at both the DNA and the RNA level. However, there still is a need for designing efficient pipelines and algorithms for consequent bioinformatic analyses. In this article, we introduce our approach for RNA-Seq data analysis in cases with cSVs. We tested the proposed workflow on a set of ten CLL patients with chromothripsis to validate the efficiency of our method.

Although cSVs reminiscent of chromothripsis likely share a common mechanism of origin across cSV cases, they appear in various genomic loci and, consequently, they lead to diverse expression profiles which makes it very difficult to select an appropriate biological

Table 2 True positive rate of fusion genes identified using the individual pieces of software and the meta-caller.

Sample	EricScript			JAFFA			FusionCatcher			meta-caller		
	fusions overall	TP	TP rate (%)	fusions overall	TP	TP rate (%)	fusions overall	TP	TP rate (%)	fusions overall	TP	TP rate (%)
T1	207	3	1.45	37	5	13.51	48	4	8.33	9	3	33.33
T2	275	0	0	22	1	4.55	19	2	10.53	2	1	50.00
T3	180	0	0	13	0	0	18	0	0	1	0	0
T4	188	1	0.53	20	0	0	7	1	14.29	2	1	50.00
T5	211	2	0.95	8	2	25.00	10	1	10.00	3	2	66.67
T6	165	0	0	16	1	6.25	14	1	7.14	1	1	100.00
T7	182	0	0	15	3	20.00	31	4	12.90	6	3	50.00
T8	133	0	0	12	0	0	39	1	2.56	1	0	0
T9	336	0	0	30	1	3.33	29	1	3.45	4	1	25.00
T10	189	4	2.12	29	6	20.69	53	7	13.21	11	7	63.64
TOTAL	**2,066**	**10**	**0.48**	**202**	**19**	**9.41**	**268**	**22**	**8.21**	**40**	**19**	**47.50**

group as a control. Unfortunately, the majority of conventional tools for differential gene expression (*Robinson, McCarthy & Smyth, 2010*; *Love, Huber & Anders, 2014*) are designed to distinguish two (or more) biological groups (i.e., treated vs. untreated), with each of them bearing uniform expression profiles. To the best of our knowledge there is no well-established tool for individual sample expression analysis. Thus, we developed PComp, a statistical framework for RNA-Seq differential gene expression analysis, that allows us to describe the impact of genomic changes through identification of exclusive features related to an actual cSV pattern in a given case. We believe this is the first approach developed and fully dedicated to address this challenge. A set of significantly deregulated genes, according to the regression model and one sample t-test, is the output of the analysis. PComp provides solid results comparable with transcriptomic array analysis and in our comparison performed better than *limma* tool, which is used widely for RNA-Seq data analysis. Although in our experimental setup we expected unique expression profiles for individual samples of our sample set, it is possible to specify the number of samples that can share expression similarities within the tool. We believe that the PComp approach is versatile and applicable to various RNA-Seq experimental designs and biological questions where a single sample expression profile is desired. Last but not least, the PComp tool is freely available on GitHub and easy to use by the potential users on their own data.

Another common feature of cSV case is the formation of fusion genes originating in chromosome shattering and consequent segment rejoining. Approximately 20% of fusion genes are expressed (*Boeva et al., 2013*), which in theory leads to the assembly of *de novo* proteins with aberrant structure and function. Aberrant protein products of fusion genes can influence important biological processes through direct or indirect regulation of expression of various genes which can eventually be reflected in the overall expression profile. Effective screening for such events in various diagnoses could help with identifying specific, potentially targetable disease markers (*Holderfield et al., 2014*).

Table 3 Overlap between gene fusions identified by RNA-Seq and genomic breakpoints detected by genomic arrays. Numbers of true positive (TP), false positive (FP) and false negative (FN) results evaluated using the individual callers and the meta-caller in a set of total 29 fusion genes overlapping with genomic breakpoints.

Software	Fusions identified by overlap between RNA-Seq and arrays	TP	FP	FN
EricScript	17	10	7	19
FusionCatcher	22	22	0	7
JAFFA	21	19	2	10
meta-caller	19	19	0	10

Current approaches for fusion gene identification have many limitations. Among them, a high FP rate represents a significant obstacle, often hindering proper analysis (*Boeva et al., 2013*). Apart from that, in cSV cases, one must also deal with fundamental structural complexity. Thus, a need for the development of new software and tools to address these challenges is obvious. In our test cohort, we tested four state-of-the-art tools for fusion gene identification; from which we selected EricScript, JAFFA, and FusionCatcher based on their performance. To increase the precision of fusion gene identification and to overcome possible technical issues potentially resulting in FPs, we applied a method of consensus fusion gene calling where we combined results filtered to confidence subsets from the selected methods (*Liu et al., 2016*) in our in-house meta-caller. Consensus calling improves the precision of results, increases overall TP rate and significantly saves time, which needs to be dedicated to manual inspection of the results. In the consensus calling approach, a low rate of FP results is the biggest advantage, on the other hand, some TPs can be lost due to their detection by a single caller. Notwithstanding, there has not been a tool providing an optimal solution for handling potential TPs and FPs and considering the overall TP rates of the tested callers, our meta-caller appears as a good solution for fusion gene detection.

Our analytical procedure was able to detect 40 fusion genes from RNA-Seq data of the ten CLL cases. We localized genomic breakpoints, compared the data with coordinates assessed by genomic arrays and found high overlap between the methods. We have also found cases where no TP fusions were identified; we hypothesize that in these cases fusion genes were either not present, transcribed or were below the detection limit of RNA-Seq experiment. We identified several FPs in our RNA-Seq results. The most common reason for their detection was adjacent localization of the partners in the genome leading to their coupled transcription. Some of them occurred in the dataset recurrently, which is highly unlikely in cases with cSVs differing considerably among the samples. However, we have also noted genes recurring in fusions but with different partners localized even on different chromosomes. We did not consider these directly as FPs though they were not confirmed by other methods, since genomic arrays may produce false negative results due to balanced translocations or inversions.

CONCLUSIONS

Complex structural variants, such as chromothripsis, have a significant impact on cellular physiology and thus also dramatically influence the biological features of a cell. Advanced experimental approaches, e.g., total RNA-Seq, has enabled the study of the causes and consequences of chromosomal shattering in detail, however, the bioinformatic component of the analysis still needs improvement. We developed bioinformatic pipelines for differential gene expression analysis and fusion gene identification in RNA-Seq data. We applied the pipelines to the set of CLL cases with chromothripsis and obtained results highly consistent with other experimental approaches (transcriptomic and genomic arrays). In our test dataset, the PComp tool outperformed well-established *limma* approach and the meta-caller dramatically increased overall TP rate of fusion gene detection and allowed for effective FP filtering. The general algorithm and the steps of our pipelines are broadly applicable in many experimental setups.

ACKNOWLEDGEMENTS

JH is involved in the Specific University Research program for students of the Medical Faculty, Masaryk University. We thank the staff of the Fasteris facility for generating sequencing data and Francesco Daniel Muto for language editing.

ADDITIONAL INFORMATION AND DECLARATIONS

Funding

The present work was financially supported exclusively by Ministry of Health of the Czech Republic, grant nr. AVR 15-31834A. The funders had no role in study design, data collection and analysis, decision to publish, or preparation of the manuscript.

Grant Disclosures

The following grant information was disclosed by the authors:
Ministry of Health of the Czech Republic: AVR 15-31834A.

Competing Interests

The authors declare there are no competing interests.

Author Contributions

- Jakub Hynst conceived and designed the experiments, analyzed the data, contributed reagents/materials/analysis tools, prepared figures and/or tables, authored or reviewed drafts of the paper, approved the final draft.
- Karla Plevova conceived and designed the experiments, performed the experiments, analyzed the data, contributed reagents/materials/analysis tools, prepared figures and/or tables, authored or reviewed drafts of the paper, approved the final draft.
- Lenka Radova conceived and designed the experiments, analyzed the data, contributed reagents/materials/analysis tools, authored or reviewed drafts of the paper, approved the final draft.

- Vojtech Bystry and Karol Pal contributed reagents/materials/analysis tools, authored or reviewed drafts of the paper, approved the final draft.
- Sarka Pospisilova conceived and designed the experiments, authored or reviewed drafts of the paper, approved the final draft.

Human Ethics

The following information was supplied relating to ethical approvals (i.e., approving body and any reference numbers):

The study was approved by the Ethical Committee of the University Hospital Brno, Brno, Czech Republic (15-31834A).

DNA Deposition

The following information was supplied regarding the deposition of DNA sequences:

The data are available at the GEO database: GSE128668.

Microarray Data Deposition

The following information was supplied regarding the deposition of microarray data:

The respective data were uploaded to the GEO database under accession numbers GSE124329 and GSE124330.

Data Availability

The following information was supplied regarding data availability:

Data is available at GitHub:

https://github.com/Hynst/WTS_cSVs_analysis.

Supplemental Information

Supplemental information for this article can be found online at http://dx.doi.org/10.7717/peerj.7071#supplemental-information.

REFERENCES

Anders S, Pyl PT, Huber W. 2015. HTSeq—a Python framework to work with high-throughput sequencing data. *Bioinformatics* **31**:166–169 DOI 10.1093/bioinformatics/btu638.

Benelli M, Pescucci C, Marseglia G, Severgnini M, Torricelli F, Magi A. 2012. Discovering chimeric transcripts in paired-end RNA-seq data by using EricScript. *Bioinformatics* **28**:3232–3239 DOI 10.1093/bioinformatics/bts617.

Boeva V, Jouannet S, Daveau R, Combaret V, Pierre-Eugène C, Cazes A, Louis-Brennetot C, Schleiermacher G, Ferrand S, Pierron G, Lermine A, Frio TR, Raynal V, Vassal G, Barillot E, Delattre O, Janoueix-Lerosey I. 2013. Breakpoint features of genomic rearrangements in neuroblastoma with unbalanced translocations and chromothripsis. *PLOS ONE* **8**:e72182 DOI 10.1371/journal.pone.0072182.

Bolger AM, Lohse M, Usadel B. 2014. Trimmomatic: a flexible trimmer for Illumina sequence data. *Bioinformatics* **30**:2114–2120 DOI 10.1093/bioinformatics/btu170.

Conesa A, Madrigal P, Tarazona S, Gomez-Cabrero D, Cervera A, McPherson A, Szcześniak MW, Gaffney DJ, Elo LL, Zhang X, Mortazavi A. 2016. A survey of best practices for RNA-seq data analysis. *Genome Biology* **17(13)** DOI 10.1186/s13059-016-0881-8.

Davidson NM, Majewski IJ, Oshlack A. 2015. JAFFA: high sensitivity transcriptome-focused fusion gene detection. *Genome Medicine* **7**:43 DOI 10.1186/s13073-015-0167-x.

Dobin A, Davis CA, Schlesinger F, Drenkow J, Zaleski C, Jha S, Batut P, Chaisson M, Gingeras TR. 2013. STAR: ultrafast universal RNA-seq aligner. *Bioinformatics* **29**:15–21 DOI 10.1093/bioinformatics/bts635.

Ernst A, Jones DTW, Maass KK, Rode A, Deeg KI, Jebaraj BMC, Korshunov A, Hovestadt V, Tainsky MA, Pajtler KW, Bender S, Brabetz S, Gröbner S, Kool M, Devens F, Edelmann J, Zhang C, Castelo-Branco P, Tabori U, Malkin D, Rippe K, Stilgenbauer S, Pfister SM, Zapatka M, Lichter P. 2016. Telomere dysfunction and chromothripsis. *International Journal of Cancer* **138**:2905–2914 DOI 10.1002/ijc.30033.

Holderfield M, Deuker MM, McCormick F, McMahon M. 2014. Targeting RAF kinases for cancer therapy: BRAF-mutated melanoma and beyond. *Nature Reviews. Cancer* **14**:455–467 DOI 10.1038/nrc3760.

Kent WJ. 2002. BLAT—the BLAST-like alignment tool. *Genome Research* **12**:656–664 DOI 10.1101/gr.229202.

Kim D, Salzberg SL. 2011. TopHat-Fusion: an algorithm for discovery of novel fusion transcripts. *Genome Biology* **12**:R72 DOI 10.1186/gb-2011-12-8-r72.

Kinsella M, Patel A, Bafna V. 2014. The elusive evidence for chromothripsis. *Nucleic Acids Research* **42**:8231–8242 DOI 10.1093/nar/gku525.

Kumar S, Vo AD, Qin F, Li H. 2016. Comparative assessment of methods for the fusion transcripts detection from RNA-Seq data. *Scientific Reports* **6**: Article 21597 DOI 10.1038/srep21597.

Lo AW l, Sabatier L, Fouladi B, Pottier G, Ricoul M, Mumane JP. 2002. DNA amplification by breakage/fusion/bridge cycles initiated by spontaneous telomere loss in a human cancer cell line. *Neoplasia* **4**:531–538 DOI 10.1038/sj.neo.7900267.

Langmead B, Salzberg SL. 2012. Fast gapped-read alignment with Bowtie 2. *Nature Methods* **9**:357–359 DOI 10.1038/nmeth.1923.

Li H, Durbin R. 2009. Fast and accurate short read alignment with Burrows-Wheeler transform. *Bioinformatics* **25**:1754–1760 DOI 10.1093/bioinformatics/btp324.

Liu S, Tsai W-H, Ding Y, Chen R, Fang Z, Huo Z, Kim S, Ma T, Chang T-Y, Priedigkeit NM, Lee AV, Luo J, Wang H-W, Chung I-F, Tseng GC. 2016. Comprehensive evaluation of fusion transcript detection algorithms and a meta-caller to combine top performing methods in paired-end RNA-seq data. *Nucleic Acids Research* **44**:e47-e47 DOI 10.1093/nar/gkv1234.

Love MI, Huber W, Anders S. 2014. Moderated estimation of fold change and dispersion for RNA-seq data with DESeq2. *Genome Biology* **15**:550 DOI 10.1186/s13059-014-0550-8.

Ly P, Cleveland DW. 2017. Rebuilding Chromosomes After Catastrophe: emerging Mechanisms of Chromothripsis. *Trends in Cell Biology* DOI 10.1016/j.tcb.2017.08.005.

Maciejowski J, Li Y, Bosco N, Campbell PJ, De Lange T. 2015. Chromothripsis and kataegis induced by telomere crisis. *Cell* **163**:1641–1654 DOI 10.1016/j.cell.2015.11.054.

Nicorici D, Satalan M, Edgren H, Kangaspeska S, Murumagi A, Kallioniemi O, Virtanen S, Kilkku O. 2014. FusionCatcher—a tool for finding somatic fusion genes in paired-end RNA-sequencing data. *bioRxiv* DOI 10.1101/011650.

Rausch T, Jones DTW, Zapatka M, Stütz AM, Zichner T, Weischenfeldt J, Jäger N, Remke M, Shih D, Northcott PA, Pfaff E, Tica J, Wang Q, Massimi L, Witt H, Bender S, Pleier S, Cin H, Hawkins C, Beck C, Von Deimling A, Hans V, Brors B, Eils R, Scheurlen W, Blake J, Benes V, Kulozik AE, Witt O, Martin D, Zhang C, Porat R, Merino DM, Wasserman J, Jabado N, Fontebasso A, Bullinger L, Rücker FG, Döhner K, Döhner H, Koster J, Molenaar JJ, Versteeg R, Kool M, Tabori U, Malkin D, Korshunov A, Taylor MD, Lichter P, Pfister SM, Korbel JO. 2012. Genome sequencing of pediatric medulloblastoma links catastrophic DNA rearrangements with TP53 mutations. *Cell* **148**:59–71 DOI 10.1016/j.cell.2011.12.013.

Ritchie ME, Phipson B, Wu D, Hu Y, Law CW, Shi W, Smyth GK. 2015. limma powers differential expression analyses for RNA-sequencing and microarray studies. *Nucleic Acids Research* **43**:e47-e47 DOI 10.1093/nar/gkv007.

Robinson MD, McCarthy DJ, Smyth GK. 2010. edgeR: a Bioconductor package for differential expression analysis of digital gene expression data. *Bioinformatics* **26**:139–140 DOI 10.1093/bioinformatics/btp616.

Stephens PJ, Greenman CD, Fu B, Yang F, Bignell GR, Mudie LJ, Pleasance ED, Lau KW, Beare D, Stebbings LA, McLaren S, Lin M-L, McBride DJ, Varela I, Nik-Zainal S, Leroy C, Jia M, Menzies A, Butler AP, Teague JW, Quail MA, Burton J, Swerdlow H, Carter NP, Morsberger LA, Iacobuzio-Donahue C, Follows GA, Green AR, Flanagan AM, Stratton MR, Futreal PA, Campbell PJ. 2011. Massive genomic rearrangement acquired in a single catastrophic event during cancer development. *Cell* **144**:27–40 DOI 10.1016/j.cell.2010.11.055.

Thorvaldsdottir H, Robinson JT, Mesirov JP. 2013. Integrative Genomics Viewer (IGV): high-performance genomics data visualization and exploration. *Briefings in Bioinformatics* **14**:178–192 DOI 10.1093/bib/bbs017.

Zhang C-Z, Spektor A, Cornils H, Francis JM, Jackson EK, Liu S, Meyerson M, Pellman D. 2015. Chromothripsis from DNA damage in micronuclei. *Nature* **522**:179–184 DOI 10.1038/nature14493.

HemaSphere
Powered by EHA

EUROPEAN HEMATOLOGY ASSOCIATION

Article
OPEN ACCESS

A Simple RNA Target Capture NGS Strategy for Fusion Genes Assessment in the Diagnostics of Pediatric B-cell Acute Lymphoblastic Leukemia

Andrea Grioni[1,2], Grazia Fazio[1], Silvia Rigamonti[1], Vojtech Bystry[2], Giulia Daniele[3], Zuzana Dostalova[2], Manuel Quadri[1], Claudia Saitta[1,6], Daniela Silvestri[7,8], Simona Songia[1], Clelia T. Storlazzi[3], Andrea Biondi[1,5], Nikos Darzentas[2,4], Giovanni Cazzaniga[1]

Correspondence: Giovanni Cazzaniga (e-mail: gianni.cazzaniga@hsgerardo.org).

Abstract

Acute lymphoblastic leukemia (ALL) is the most frequent pediatric cancer. Fusion genes are hallmarks of ALL, and they are used as biomarkers for risk stratification as well as targets for precision medicine. Hence, clinical diagnostics pursues broad and comprehensive strategies for accurate discovery of fusion genes. Currently, the gold standard methodologies for fusion gene detection are fluorescence in situ hybridization and polymerase chain reaction; these, however, lack sensitivity for the identification of new fusion genes and breakpoints. In this study, we implemented a simple operating procedure (OP) for detecting fusion genes. The OP employs RNA CaptureSeq, a versatile and effortless next-generation sequencing assay, and an in-house as well as a purpose-built bioinformatics pipeline for the subsequent data analysis. The OP was evaluated on a cohort of 89 B-cell precursor ALL (BCP-ALL) pediatric samples annotated as negative for fusion genes by the standard techniques. The OP confirmed 51 samples as negative for fusion genes, and, more importantly, it identified known (*KMT2A* rearrangements) as well as new fusion events (*JAK2* rearrangements) in the remaining 38 investigated samples, of which 16 fusion genes had prognostic significance. Herein, we describe the OP and its deployment into routine ALL diagnostics, which will allow substantial improvements in both patient risk stratification and precision medicine.

Introduction

Acute lymphoblastic leukemia (ALL) is the most common pediatric cancer.[1] The 5-year survival rate exceeds 85% in children, but the survival following relapse is poor.[2] Analysis of paired diagnosis/relapse ALL samples shows clonal diversity that arises from the accumulation of new deletions and mutations over time. Despite that, the founding fusion genes are usually conserved from diagnosis to relapse, indicating that the predominant clones observed at diagnosis and relapse are clones derived from a common ‘preleukemic’ clone.[3] Fusion genes arise from chromosomal translocations and intrachromosomal

---

This work was partially supported by the program ‘Passaporto genetico’ of the Parents Committee ‘Comitato Maria Letizia Verga ONLUS’, as well as by the IG17593 and IG20564 Grants of the Associazione Italiana per la Ricerca sul Cancro (AIRC) to GC and AB, respectively; the IG2014 grant no. 15413 to CTS; the fellowship program Brno PhD talent 2017 as well as fellowship AIRC 2018 no. 22620 to AG; by the DIMET PhD program - University of Milano-Bicocca to CS. Bioinformatics of CEITEC Masaryk University is gratefully acknowledged for the obtaining of the scientific data presented in this paper

AG, ND and VB contributed new analytic tools, and participated in the data analysis and writing of the paper. AB, AG, GF and GC participated in research design and writing of the paper. GF, SR, GD and CTS participated in the performance of the research. CS and MQ performed PCR validations. DS provided samples information. ZD participated in the writing and correction of the paper.

The authors declare no conflicts of interest.

[1] *Centro Ricerca Tettamanti, Clinica Pediatrica, Università degli Studi di Milano-Bicocca, Fondazione MBBM/Ospedale S. Gerardo, Monza, Italy*
[2] *Central European Institute of Technology, Masaryk University, Brno, Czech Republic*
[3] *Department of Biology, University of Bari “Aldo Moro”, Bari, Italy*
[4] *Department of Hematology, University Hospital Schleswig-Holstein, Kiel, Germany*
[5] *Clinica Pediatrica, Università degli Studi di Milano-Bicocca, Fondazione MBBM/Ospedale S. Gerardo, Monza, Italy*
[6] *Cancer Center, Humanitas Research Hospital, Humanitas University, Rozzano, Milan, Italy*
[7] *Center of Biostatistics for Clinical Epidemiology, Department of Health Science, University of Milano-Bicocca, Milan, Italy*
[8] *Pediatric Hematology-Oncology Unit, Department of Pediatrics, University of Milano-Bicocca, MBBM Foundation/ASST Monza, Monza, Italy.*

HemaSphere (2019) 3:3(e250)
Received: 27 December 2018 / Received in final form: 4 April 2019 / Accepted: 4 April 2019
Citation: Grioni A, Fazio G, Rigamonti S, Bystry V, Daniele G, Dostalova Z, Quadri M, Saitta C, Silvestri D, Songia S, Storlazzi CT, Biondi A, Darzentas N, Cazzaniga G. A Simple RNA Target Capture NGS Strategy for Fusion Genes Assessment in the Diagnostics of Pediatric B-cell Acute Lymphoblastic Leukemia. *HemaSphere*, 2019;3:3. http://dx.doi.org/10.1097/HS9.0000000000000250

rearrangements that mainly disrupt genetic regulators of normal hematopoiesis as well as lymphoid development (e.g., those involving *RUNX1* and *ETV6*) and constitutively activate tyrosine kinases[4] (e.g., *ABL1* chimeras). Thus, fusion genes are hallmarks of ALL that play a pivotal role in leukemogenesis, and their identification is crucial for patient risk stratification.[5]

Common fusion genes in B-lineage ALL are: t(12;21)(p13;q22), encoding ETV6-RUNX1 (TEL-AML); t(1;19)(q23;p13), encoding TCF3-PBX1 (E2A-PBX1)[6]; t(9;22)(q34;q11.2), resulting in formation of the "Philadelphia" chromosome, encoding BCR-ABL1; rearrangements of *KMT2A* (*MLL*) at 11q23 to a range of fusion partners[7]; and rearrangements of the cytokine receptor gene *CRLF2* at the pseudo autosomal region 1 (PAR1) at Xp22.3/Yp11.3.[8,9] Fusion genes correlate with the clinical outcome, and they are used as biomarkers for patient risk stratification[10]: for example, patients positive for t(12;21)/ETV6-RUNX1 have the most favorable prognosis, whereas t(9;22)/BCR-ABL1, t(1;19)/TCF3-PBX1, and KMT2A-AFF1 correlate with a brief disease latency and have a poor prognosis.[10,11] Moreover, specific drug inhibitors antagonizing the fusion proteins provide a more efficient and less toxic tool for disease eradication (precision medicine): for example, the imatinib tyrosine kinase inhibitor inhibits the oncogenic deregulation caused by the (9;22)/BCR-ABL1 fusion protein.[12]

Before the next generation sequencing (NGS) era, elaborate and extensive cytogenetic studies lead to the description of few recurrent and highly expressed fusion genes,[13] such as BCR-ABL1 and ETV6-RUNX1. The characterization of their breakpoint coordinates enabled the design of diagnostic screening by both quantitative multiplex polymerase chain reaction (qPCR) and fluorescence in situ hybridization (FISH).[14] The recent introduction of NGS allowed a fast and accurate screening of the patient's genome at the nucleotide level, which lead to the discovery of a broad array of previously unknown fusion genes.[15] This reflects the increased capability of NGS to recognize subtle chromosomal rearrangements. On the contrary, FISH may only detect exchanges of considerably larger chromosome segments, without nucleotide precision, while qPCR screenings can identify already known fusion gene breakpoints only.[16]

Whole transcriptome sequencing (RNAseq), together with open-source bioinformatics tools, has already been applied to identifying fusion genes.[17] Whole RNAseq performs well in the detection and quantification of highly and medium abundant transcripts, but it may fail in cases of low abundance transcripts.[18] The RNA capture sequencing (RNA CaptureSeq) is a probe-based assay for capturing, amplifying, and sequencing genomic regions of interest only (targets). The RNA CaptureSeq generates libraries of small fragments (250–300 bp) in a short time (2.5 days) compared to whole RNAseq, and it is compatible with the well-known MiSeq and NextSeq Illumina NGS platforms. RNA CaptureSeq is sensitive to low abundance transcript variants of targeted genes[19]; however, the detection of fusion transcripts may be compromised when the fusion partner gene is not part of the capture procedure (unknown partner). This scenario reduces discoverability of fusion transcripts to only those fragments that span the target gene breakpoint.

We have developed and herein present a simple, efficient, and ready-to-use operating procedure (OP) for the clinical identification of fusion genes in B-cell ALL. The OP is based on RNA CaptureSeq, and it is supported by an in-house bioinformatics pipeline that is purpose-built to detect and extend fragments spanning the fusion gene breakpoint. We applied the OP to a cohort of 89 B-cell ALL pediatric patients enrolled in the AIEOP-BFM ALL clinical protocol[20] that were annotated as negative to fusion genes by the standard screening methods. This paper summarizes the results of the OP applied to clinical diagnostics and discusses its implications for patient risk stratification.

Results

Comparison of available bioinformatics pipelines

We developed a bioinformatic method for fusion gene assessment from RNA CaptureSeq datasets and evaluated it on a training dataset composed of 23 samples evaluated as positive to 6 different fusion genes, namely t(9;22)/BCR-ABL1, t(12;21)/ETV6-RUNX1, t(4;11)/KMT2A-AFF1, del(X)/P2RY8-CRLF2, t(1;19)/TCF3-PBX, and t(9;11)/KMT2A-MLLT3, by standard methods. Our method distinguished all 6 sample-specific fusion genes within the dataset. In addition, we analyzed the same training dataset through Illumina BaseSpace, STAR-Fusion,[21] and the customized pipeline described by Jennifer L. Winters et al.[22] The STAR-Fusion tool did not detected 1 out of 6 fusion genes (del(X)/P2RY8-CRLF2), while the Illumina BaseSpace did not detect 2 out of 6 fusion genes (t (9;11)/KMT2A-MLLT3 and t(4;11)/ KMT2A- AFF1). The method described by Jennifer L. Winters et al. did not detect 3 out of 6 fusion genes (t(1;19)/TCF3-PBX, t(9;11)/KMT2A-MLLT3, and del(X)/P2RY8-CRLF2) (Table 1).

The ability of our procedure to detect all fusion transcripts derives from the fine-tuning of the bioinformatics pipeline to cover the specific RNA target–capture scenario, where both genes involved in the fusion are not always captured (see Material and Methods and Fig. 1). For these reasons, we applied only our method in the subsequent analyses.

Evaluation of the OP in clinical diagnosis

RNA material obtained from patient bone marrow mononuclear cells at the onset or relapse of the disease was sequenced using the RNA PanCancer (Illumina, San Diego, CA). Raw FASTQ files underwent quality control and were afterwards analyzed through our system. A detailed description of the OP strategy is available in the Materials and Methods section. The time required for the procedure from library preparation to obtaining results was 2.5 days.

We screened a cohort of 89 samples of B-cell ALL leukemia (test set) for positivity to fusion genes. All samples were negative for the fusion genes t(12;21)/ETV6-RUNX1, t(9;22)/BCR-ABL1, t(4;11)/KMT2A-AFF1, and t(1;19)/TCF3-PBX1 by the standard screening methods. The test set was divided into 3 groups: frontline high-risk (HR), relapse (RL), and patients with a high value of minimal residual disease (MRD) at day 33 of chemotherapy induction (TP1 +). Overall, the OP identified 26 different fusion genes in 38 out of the 89 investigated samples, with the transcripts of 16 of them being of prognostic value (Table 2 and Suppl. Table 1, Supplemental Digital Content, http://links.lww.com/HS/A34). New fusion genes in B-cell ALL and not recorded in public databases were validated through reverse transcription PCR (RT-PCR) or FISH to discern between false and true positives (Supplementary Table 2, Supplemental Digital Content, http://links.lww.com/HS/A34).

OP applied to the frontline HR group

Seven out of 16 samples (43%) resulted as positive for fusion genes (Fig. 2a). Four samples carried fusion genes recurrently associated to B-cell ALL: t(5;5)/EBF1-PDGFRB (n=2), t(9;9)/PAX5-JAK2 (n=1), and t(12;19)/ZNF384-TCF3 (n=1) and 3 samples were positive for t(19;19)/TCF3-OAZ1 (n=1), t(7;7)/IKZF1-DDC (n=1), t(2;9)/ZEB2-JAK2 (n=1), and t(9;17)/MPRIP-JAK2 (n=1)

Table 1

Comparison of available bioinformatics pipelines.

		Metadata					Bioinformatics Pipeline		
Sample	**Blast%**	**Fusion gene**	**Raw-reads**	**FASTQC**	**Probes**	**Internal**	**BaseSpace**	**TopHat**	**Star-Fusion**
KN1	90	t(9;22) BCR-ABL1	3.22E+06	+	t/p	+	+	+	+
KN2	90	t(12;21) ETV6-RUNX1	5.19E+06	+	t/p	+	+	ND	+
KN3	92	t(4;11) KMT2A-AFF1	5.60E+06	+	t/p	+	+	ND	+
KN4	90	t(9;22) BCR-ABL1	4.76E+06	+	t/p	+	+	ND	+
KN5	93	t(9;22) BCR-ABL1	6.06E+06	+	t/p	+	+	ND	+
KN5	93	t(12;21) ETV6-RUNX1	6.06E+06	+	t/p	+	+	ND	+
KN6	98	del(X) P2RY8-CRLF2	3.81E+06	+	t/p	+	+	ND	ND
KN7	NA	t(9;22) BCR-ABL1	2.41E+06	+	t/p	+	+	ND	+
KN8	NA	t(4;11) KMT2A-AFF1	2.57E+06	+	t/p	+	+	ND	+
KN9	91	t(1;19) TCF3-PBX	2.46E+06	+	t/p	+	+	ND	+
KN10	64	t(12;21) ETV6-RUNX1	2.30E+06	+	t/p	+	+	ND	+
KN11	NA	t(9;11) KMT2A-MLLT3	2.50E+06	+	t/p	+	+	ND	+
KN12	NA	t(9;22) BCR-ABL1	1.62E+06	+	t/p	+	+	+	+
KN13	NA	t(4;11) KMT2A-AFF1	2.40E+06	+	t/p	+	+	+	+
KN14	91	t(1;19) TCF3-PBX	6.53E+05	+	t/p	+	+	ND	+
KN15	64	t(12;21) ETV6-RUNX1	2.47E+06	+	t/p	+	+	ND	+
KN16	NA	t(9;11) KMT2A-MLLT3	6.21E+06	+	t/p	+	ND	ND	+
KN17	NA	t(9;22) BCR-ABL1	5.29E+06	+	t/p	+	+	ND	+
KN18	93	t(4;11) KMT2A-AFF1	3.17E+06	+	t/p	+	ND	ND	+
KN19	90	t(4;11) KMT2A-AFF1	6.56E+06	+	t/p	+	+	+	+
KN20	93	t(1;19) TCF3-PBX	6.73E+06	+	t/p	+	+	ND	+
KN21	94	t(4;11) KMT2A-AFF1	4.50E+06	+	t/p	+	+	ND	+
KN22	70	t(12;21) ETV6-RUNX1	4.66E+06	+	t/p	+	+	+	+
KN23	97	t(9;22) BCR-ABL1	5.44E+06	+	t/p	+	+	+	+

fusion genes. All fusion transcripts were confirmed by RT-PCR, while the novel fusion genes t(2;9)/ZEB2-JAK2 (n = 1) and t(9;17)/MPRIP-JAK2 were validated through FISH (Suppl. Fig. 1, Supplemental Digital Content, http://links.lww.com/HS/A34).

OP applied to the TP1+ group

The OP identified fusion genes in 19 out of 49 samples (38.8%) (Fig. 2b). Nine samples were evaluated as positive for fusion genes that are frequent in B-cell ALL: t(17;19)/TCF3-HLF (n = 2), del(X)/P2RY8-CRLF2 (n = 3), t(5;5)/EBF1-PDGFRB (N = 2), t(12;19)/ETV6-JAK3 (n = 1), t(12;22)/ZNF384-EP300 (n = 1). We also identified a novel inter-chromosomal rearrangement, t(9;20)/PAX5-C20orf112 (n = 1), and a variety of intra-chromosomal fusion genes (n = 9) that were already annotated in public databases, and we validated them by RT-PCR (Suppl. Table 1, Supplemental Digital Content, http://links.lww.com/HS/A34).

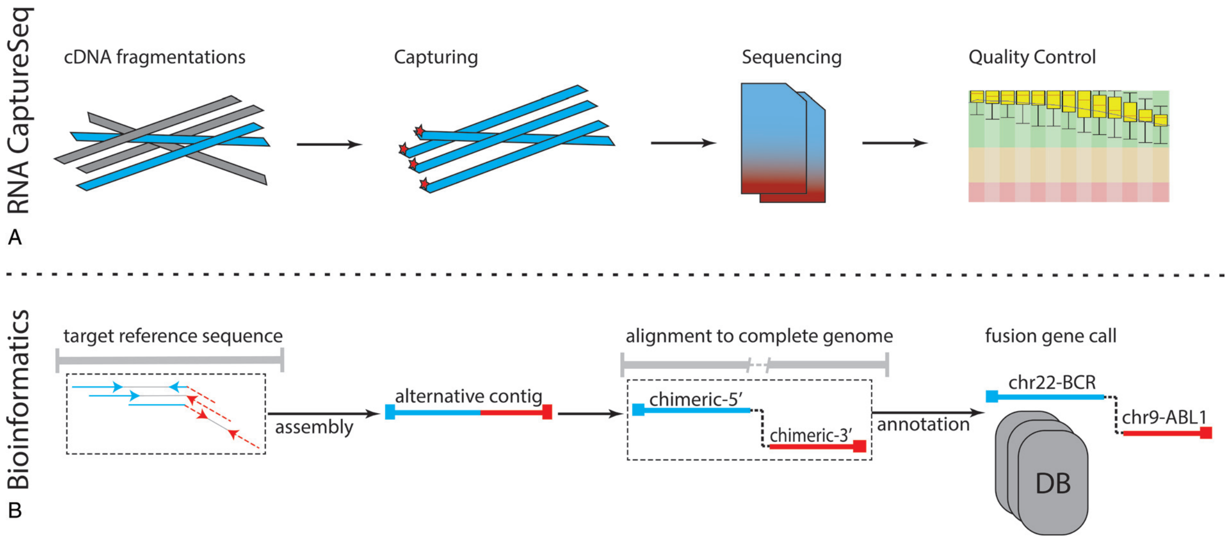

FIGURE 1. The standard operating procedure: (A) RNA CaptureSeq protocol allows the isolation of specific genomic regions (targets) through complementary probes; then, the captured fragments are sequenced, and the FASTQ file quality is evaluated. (B) The bioinformatics pipeline includes four sequential steps, which allows the identification of fusion genes through the identification of putative break-points on the genomic sequences of targeted genes.

Table 2

RNAseq Fusion transcripts identified by our OP.

fz	Fusion gene	Probes	Progn.	PCR	FusionHub
6	t(8;8) NDRG1-ST3GAL1	t	–	+	[’CHIMERSEQ’, ’Tumor_Fusion_GDP’,’HPA’,’Banned_dataset’,’Known_Fusions’]
5	t(5;5) CAMK2A-CD74	t/p	–	+	[’Known_Fusions’]
5	del(X) P2RY8-CRLF2	t/p	+	+	[’CHIMERPUB’, ’FARE-CAFE’, ’TICDB’]
4	t(5;5) PDGFRB-EBF1	t/p	+	+	[’CHIMERSEQ’, ’CHITARS’, ’Known_Fusions’]
3	t(13;13) PSPC1-ZMYM2	p	–	+	[’Banned_Dataset’,’GTEx’]
3	t(19;19) DOT1L-OAZ1	t	–	+	[’HPA’, ’Banned_Dataset’]
2	t(10;10) PTEN-RNLS	t	–	+	[’Tumor_Fusion_GDP’]
2	5(13;13) RB1-RCBTB2	t	–	+	[’GTEx’]
2	t(17;19) TCF3-HLF	t/p	+	+	[’CHIMERKB’, ’CHIMERPUB’, ’FARE-CAFE’,’TICDB’]
2	t(19;19) TCF3-OAZ1	t	–	+	NOVEL
2	t(5;5) ARHGAP26-NR3C1	t/p	–	+	[’HPA’, ’Banned_Dataset’,’GTEx’]
1	t(10;11) MLLT10-KMT2A	t/p	+	+	[’CHIMERKB’, ’CHIMERPUB’]
1	5(11;11) KMT2A-USP2	t/p	+	+	[’Known_Fusions’]
1	t(12;12) BCL7A-NCOR2	t/p	–	+	[’Known_Fusions’]
1	t(12;19) ETV6-JAK3	t/p	+	+	NOVEL
1	t(12;19) ZNF384-TCF3	t/p	+	+	[’CHIMERSEQ’, ’CHITARS’, ’FARE-CAFE’, ’TICDB’, ’Known_Fusions’]
1	t(12;22) ZNF384-EP300	t/p	+	+	[’CHIMERPUB’]
1	t(17;17) SUZ12P1-CRLF3	t	–	+	[’18_Cancers’]
1	t(9;17) MPRIP-JAK2	p	+	+	NOVEL
1	t(21;21) RUNX1-DYRK1A	t	+	+	[’GTEx’]
1	t(2;9) ZEB2-JAK2	p	+	+	NOVEL
1	t(3;9) MBNL1-PAX5	t/p	+	+	[’Known_Fusions’]
1	t(7;7) IKZF1-DDC	t	–	+	NOVEL
1	t(9;20) PAX5-C20orf112	t	+	+	[’CHIMERSEQ’, ’CHITARS’, ’FARE-CAFE’, ’TICDB’]
1	t(9;9) NUP214-ABL1	t/p	+	+	[’COSMIC’,’CHIMERAKB’,’CHIMERPUB’,’CHIMERSEQ’, ’FARE-CAFE’, ’ TICDB’,’TUMOR_Fusion_GDP’,’Oesophagus_Dataset]
1	t(9;9) PAX5-JAK2	t/p	+	+	[’COSMIC’, ’CHIMERKB’, ’FARE-CAFE’, ’TICDB’]

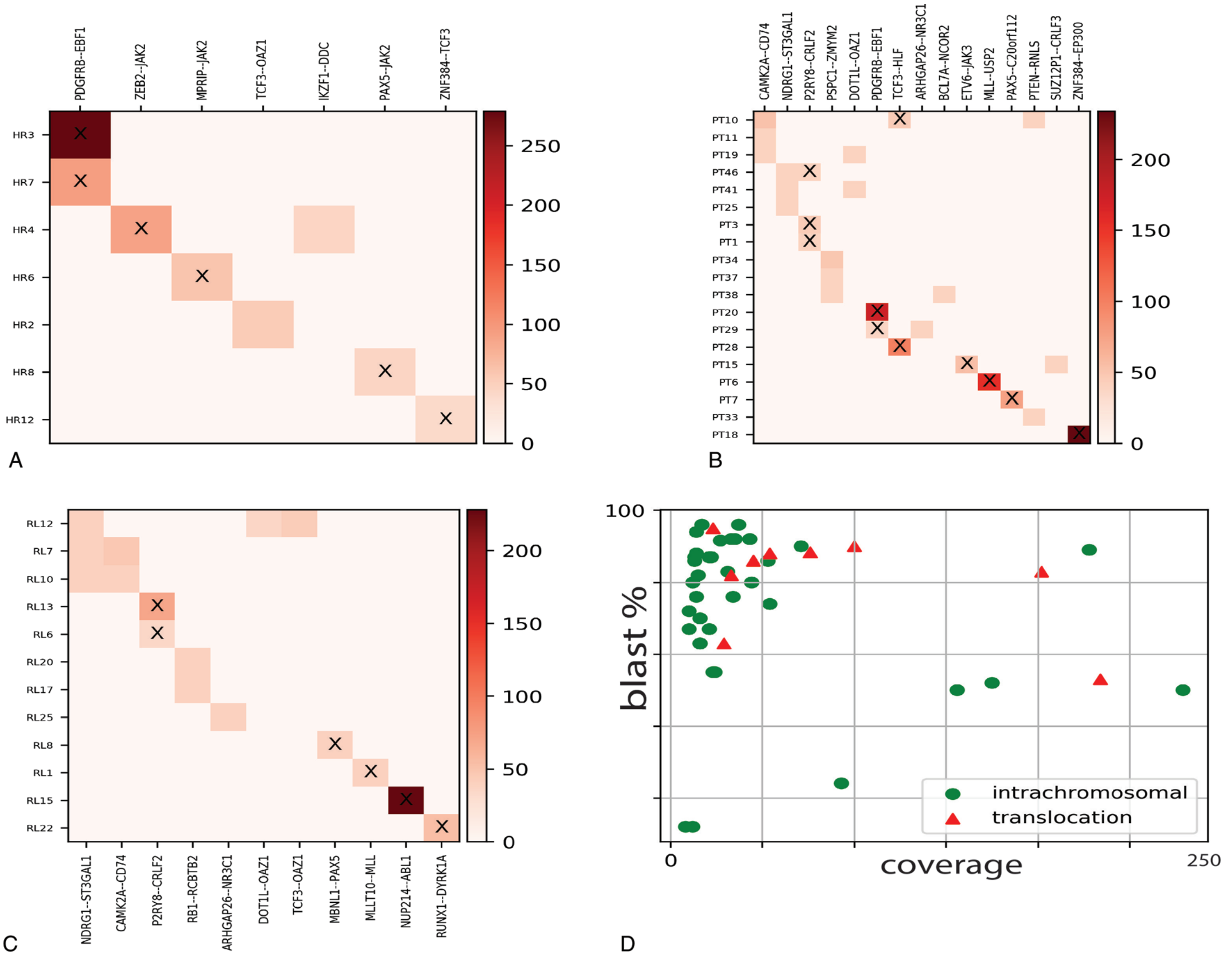

FIGURE 2. (A), (B), and (C) Heatmaps of detected fusion genes among different risk groups. The axes correspond to the detected fusion genes (X) and sample names (Y). The color code represents the coverage on the fusion gene breakpoint as reported by the scale on the right. The ‘X’ tag highlights fusion genes of prognostics relevance. (D) Fusion genes distribution in terms of intrachromosomal (green dots) or interchromosomal translocations (red triangles) in relations to the breakpoint read coverage and percentage of blast cells.

OP applied to the RL group

The OP identified fusion genes in 12 out of 24 samples of the RL group (~50%) (Fig. 2c): t(9;9)/NUP214-ABL1 (n=1), del(X)/P2RY8-CRLF2 (n=2), t(10;11)/MLLT10-KMT2A (n=1), t(21;21)/RUNX1-DYRK1A (n=1), and t(3;9)/PAX5-MBLN1 (n=1) fusion genes were associated with ALL and of clinical relevance for the patients and were hence immediately validated by RT-PCR. On the other hand, the OP identified additional fusion genes derived from intra-chromosomal rearrangements, such as t(8;8)/NDRG1-ST3GAL1 (n=3), t(13;13)/RB1-RCBTB2 (n=2), t(19;19)/DOT1L-OAZ1 (n=1), t(19;19)/TCF3-OAZ1 (n=1), t(5;5)/ARHGAP26-NR3C1 (n=1), and t(5;5)/CAMK2A-CD74 (n=2), which were already annotated in public databases.

Enrichment of intra-chromosomal fusion genes

The OP identified 26 fusion genes in 38 investigated patients (HR, RL, and TP1+ groups). Among them, 17 (65%) fusion genes derived from intra-chromosomal rearrangements and were supported by a low read coverage (~20× to ~50×) in coexistence with high levels of blast cells in the BM (~70% to ~96%) (Fig. 2d). We did not observe a correlation between intra-chromosomal fusion genes associated with recurrent chromosomal translocations in B-cell ALL (Table 3). RT-PCR confirmed frequent B-cell ALL intra-chromosomal fusion genes, such as PDGFRB-EBF1, NUP214-ABL1, and PAX5-JAK2 (Suppl. Table 2, Supplemental Digital Content, http://links.lww.com/HS/A34). P2RY8-CRLF2 fusions were not confirmed by RT-PCR since those samples correlated with del(X)(p22p22) detected by multiplex ligation-dependent probe amplification and highly expressed CRLF2 detected by gene expression profile (data not presented). We further investigated gene expression levels in healthy whole-blood samples for genes involved in intra-chromosomic fusions as well as those not known in B-cell ALL (n=21, gene set) through the GTEx portal.[23] Sixteen genes had transcript per million (TPM) expression levels from medium to high (TPM greater than 5.4), while 5 of them had low levels (TPM between 1 and 5.4) (Fig. 3). Also, some intra-chromosome fusion transcripts involved genes spatially close, within a range of

Table 3

Sample-specific fusion transcripts.

Sample	Fusion gene	Chromosome	% Leukemic cell in BM	Sex	Karyotype
HR2	TCF3-OAZ1	t(19;19)	98	F	
HR3	PDGFRB-EBF1	t(5;5)	60	M	
HR4	ZEB2-JAK2|IKZF1-DDC	t(2;9)|t(7;7)	NA	M	
HR6	MPRIP-JAK2	t(9;17)	NA	M	
HR7	PDGFRB-EBF1	t(5;5)	53	M	46,XY,der(1)inv(1)(q21q31)dup(1)(q31q32)[8]/46,XY[14]
HR8	PAX5-JAK2	t(9;9)	NA	M	
HR12	ZNF384-TCF3	t(12;19)	90	F	
PT1	P2RY8-CRLF2	del(X)	91	M	46,XY, der(9)T(9;?)(p13;?), -13, add(13)(q34), +21 [10]/47,XY,+21[4]
PT3	P2RY8-CRLF2	del(X)	95	M	
PT6	KMT2A-USP2	t(11;11)	NA	M	
PT7	PAX5-C20orf112	t(9;20)	NA	M	
PT10	TCF3-HLF|CAMK2A-CD74|PTEN-RNLS	t(17;19)|t(5;5)|t(10;10)	NA	F	
PT11	CAMK2A-CD74	t(5;5)	90	M	
PT15	ETV6-JAK3|SUZ12P1-CRLF3	t(12;19)|t(17;17)	90	F	
PT18	ZNF384-EP300	chr12-chr22	85	M	
PT19	CAMK2A-CD74|DOT1L-OAZ1	t(5;5)|t(19;19)	NA	M	
PT20	PDGFRB-EBF1	t(5;5)	80	F	
PT25	NDRG1-ST3GAL1	t(8;8)	NA	F	
PT28	TCF3-HLF	t(17;19)	95	F	
PT29	PDGFRB-EBF1|ARHGAP26-NR3C1	t(5;5)|t(5;5)	98	F	
PT33	PTEN-RNLS	t(10;10)	NA	M	
PT34	PSPC1-ZMYM2	t(13;13)	NA	F	
PT37	PSPC1-ZMYM2	t(13;13)	80	M	
PT38	BCL7A-NCOR2|PSPC1-ZMYM2	t(12;12)|t(13;13)	NA	F	
PT41	DOT1L-OAZ1|NDRG1-ST3GAL1	t(19;19)|t(8;8)	NA	M	
PT46	P2RY8-CRLF2|NDRG1-ST3GAL1	del(X)|t(8;8)	NA	F	
RL1	MLLT10-KMT2A	t(10;11)	90	M	
RL6	P2RY8-CRLF2	del(X)	76	M	
RL7	CAMK2A-CD74|NDRG1-ST3GAL1	t(5;5)|t(8;8)	70	M	
RL8	MBNL1-PAX5	t(3;9)	NA	M	
RL10	CAMK2A-CD74|NDRG1-ST3GAL1	t(5;5)|t(8;8)	NA	M	
RL12	NDRG1-ST3GAL1|TCF3-OAZ1|DOT1L-OAZ1	t(8;8)|t(19;19)|t(19;19)	97	M	
RL13	P2RY8-CRLF2	del(X)	98	F	47,XX,+21c[14]
RL15	NUP214-ABL1	t(9;9)	92	F	
RL17	RB1-RCBTB2	t(13;13)	40	M	
RL20	RB1-RCBTB2	t(13;13)	NA	M	
RL22	RUNX1-DYRK1A	t(21;21)	NA	M	
RL25	ARHGAP26-NR3C1	t(5;5)	99	F	

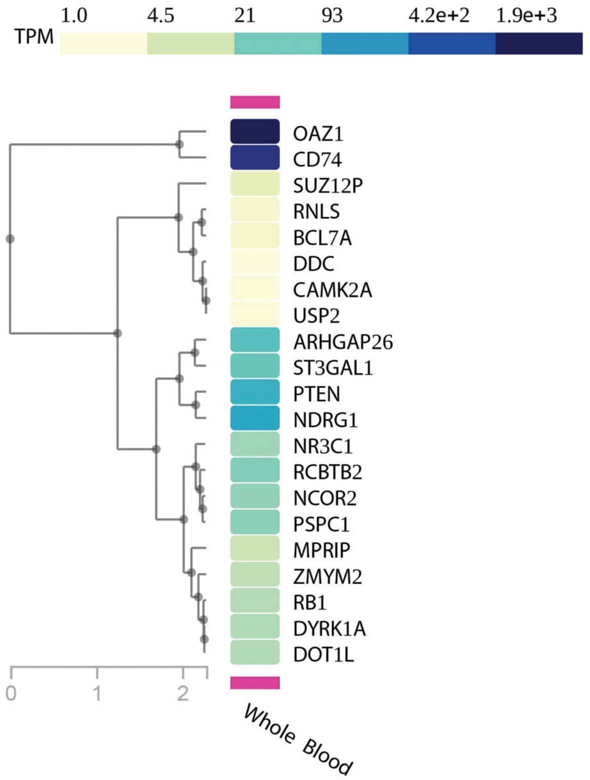

FIGURE 3. Gene expression profile of genes involved in intra-chromosomal fusion genes but not associated to ALL.

150 to 250 kb, and annotated as conjoined genes. Indeed, we validated those fusion gene events by RT-PCR and confirmed their nucleotide sequences by Sanger sequencing (Suppl. Table 2, Supplemental Digital Content, http://links.lww.com/HS/A34).

Discussion

Fusion genes are hallmarks of ALL both in pediatric and adult patients; their identification is crucial to design a risk-reducing-driven chemotherapy treatment (precision medicine). Precision medicine allows either very low-risk patients to proceed with standard therapy or very high-risk patients to be candidates for experimental and/or targeted therapies. For this purpose, sensitive, specific, and comprehensive screening of selected genomic regions prone to chromosomic breaks are needed in routine diagnostics to identify the increasing variety of fusion genes.

We built a versatile and straightforward OP to recognize fusion genes at nucleotide resolution without any a priori knowledge, which overcomes the limitations of qPCR and FISH. The OP employs an RNA CaptureSeq panel that allows targeted transcriptome sequencing through a simple library preparation protocol. For the subsequent data analysis, we fine-tuned a bioinformatics pipeline that deploys robust and stable tools, which can be easily set up on any operative system through the Anaconda Platform. Our bioinformatics pipeline recognized all fusion genes harbored by samples within the training dataset, while the Star-Fusion, Illumina BaseSpace, and the strategy proposed by Winter et al reached 83%, 66%, and 50% success in fusion transcripts identification, respectively. Prognostically significant and frequent B-cell precursor ALL fusion genes such as *KMT2A* rearrangements and P2RY8-CRLF2 were not fully detected by the external tools. Patients harboring *KMT2A* rearrangements have a particularly unfavorable prognosis.[10,24,25] *KMT2A* is prone to breaks in various genomic location with several partners, thus making the detection of its resulting fusion genes challenging. On the other hand, the repetitive nature of the chromosome X may compromise read alignment and the identification of the P2RY8-CRLF2 fusion gene. Our results indicated that our purpose-built, disease- and NGS-strategy specific bioinformatics pipeline is required for covering many possible scenarios causing fusion genes. The evaluation of the OP through the analysis of 89 pediatric B-cell precursor ALL samples identified 26 different fusion genes among 38 samples that were undetectable by the standard routine diagnostics. Sixteen of those fusion transcripts have prognostic value since they involved rearrangements in genes driving leukemogenesis (*KMT2A*, *JAK2*, and *PAX5*). Moreover, the newly identified fusion genes t(2;9)/ZEB2-JAK2 and t(9;17)/MPRIP-JAK2, which are possibly targetable by JAK/STAT inhibitors, highlight the potential of our OP for precision medicine and biomarker discovery. Additionally, we detected a case of NUP214/ABL1 fusion genes in B-cell ALL, which only 2 cases were previously reported.[26] We confirmed the increased capability provided by RNA CaptureSeq to detect small local structural variants through the identification of a variety of intra-chromosomal fusion genes (n = 17). Multiple intra-chromosomal fusion genes were the only detected in the sample within our set of genes (n = 1385); hence, it is not possible to state any functional correlation between those rearrangements and the recurrent fusion genes (such as BCR-ABL1, ETV6-RUNX1, and *KMT2A* rearrangements). Some intra-chromosomal fusion transcripts, namely PSPC1-ZMYM2, DOT1L-OAZ1, RB1-RCBTB2, ARHGAP26-NR3C1, were also observed in NGS studies[27,28,29] of healthy populations (e.g., GTEx, Banned_dataset, and HPA), or annotated as conjoined genes.[30,31] We also detected intra-chromosomal fusion transcripts involving recurrent leukemogenic genes (IKZF1-DDC, P2RY8-CRLF2, KMT2A-UPS2, MLLT10-KMT2A) that are prone to deletions and with a prognostic value (such as IKZF1,[32] and KMT2A[33]). Despite RNA CaptureSeq cannot discerns between inter- and intra- chromosome fusion genes when the same chromosomes are involved, these previous studies suggested an intra-chromosome origin.

In conclusion, herein we have described an NGS-based approach suitable for the detection of fusion genes, regardless of their expression levels, that may be incorporated into routine ALL diagnostics, with the advantage of a substantial improvement of precision medicine. Despite the OP lacks ISO certification, our finding highlights its potential and the need to develop bioinformatics tools addressing fusion genes detections from the RNA CaptureSeq scenario with precision. For this purpose, our OP may offer an idea for their implementation. Nonetheless, further studies are required to understand the biological significance and the potential therapeutic implication of the additional discoveries allowed by this tool.

Materials and methods

Patient cohort

A cohort of 89 B-cell precursor (BCP) ALL patients enrolled in the AIEOP-BFM ALL2009 protocol in Italy was sequenced by Illumina RNA CaptureSeq PanCancer to discern prognostic fusion genes. The cohort was composed of: 16 patients from the frontline HR group, with a level of MRD above 5×10^{-4} at day +78 (TP2), who were shown as fusion gene-negative during the screening; 49 patients TP1+, that is, with a high level of PCR-MRD ($>5 \times 10^{-4}$ compared to diagnostic value) at day +33 from the start of the induction therapy; and 24 patients from the RL (defined as having at least 5×10^{-2} blast cells after complete remission, CR). See Suppl. Table 3 (Supplemental Digital Content, http://links.lww.com/HS/A34).

Training dataset

A subgroup of 23 pediatric ALL patients enrolled in the AIEOP-BFM ALL2009 protocol, who were positive for fusion genes by standard clinical diagnosis, were selected. We used this subgroup as a training dataset for the development and evaluation of our bioinformatics pipeline of analysis for the assessment of fusion genes.

FISH analysis for validating the identified fusion genes

The experiments were performed on BM metaphases from archival methanol:acetic acid-fixed chromosome suspensions, as previously described.[17] Bacterial Artificial Chromosome (BAC) clones were opportunely selected according to the NGS data from the University of California Santa Cruz (UCSC) database (release of December 2013, GRCh38/hg38) and previously tested on normal human metaphases. Briefly, chromosome preparations from BM cells were hybridized in situ with 1 μg of each BAC probe labeled by nick translation. Hybridization was performed at 37°C in 2× saline–sodium citrate (SSC), 50% (vol/vol) formamide, 10% (w/vol) dextran sulfate, 5 μg Cot-1 DNA (Bethesda Research Laboratories, Gaithersburg, MD, USA), and 3 μg sonicated salmon sperm DNA in a volume of 10 μL. Post-hybridization washings were performed at 60°C in 0.1× SSC (3 times). In co-hybridization experiments, the probes were directly labeled with fluorescein, Cy3, and Cy5 or indirectly with biotin–dUTP and subsequently detected by 7-(diethylamino)coumarin-3-carboxylic acid *N*-succinimidyl ester-conjugated streptavidin. Chromosomes were identified by DAPI staining. Digital images were obtained using a Leica DMRXA epifluorescence microscope equipped with a cooled CCD camera (Princeton Instruments, Boston, MA). All fluorescence signals that were detected using specific filters were recorded separately as gray-scale images. Pseudo-coloring and merging of images were performed with Adobe Photoshop software.

Enrichment analysis

Ensembl gene IDs were extracted through the BioMart API (https://www.ensembl.org/biomart). Gene expression profile data from non-diseased samples were obtained from the GTEx portal through submission of the corresponding ENSEMBL gene ID (https://gtexportal.org/home/).

External tools for fusion gene assessment

The Illumina BaseSpace pipeline for the identification of fusion genes first aligns filtered FASTQ files to the reference human genome through the TopHat[34] (v. 2.1.0) or STAR[35] aligner (v. 2.5.0a). Then, the STAR aligner supports Manta-fusion and the TopHat aligner supports the TopHat-fusion[36] to identify candidate fusion genes. For the purpose of our analysis, we required the Illumina BaseSpace to recognize the sample-specific fusion gene by at least one application. The STAR-Fusion tool, v. 1.5.0, was utilized with standard parameters on the GRCh38.p12 genome reference and the corresponding Gencode[37] annotation set. We simulated the customized pipeline described by Jennifer L. Winters et al by deploying TopHat v. 2.1.1, which included TopHat-Fusion, and running the TopHat-Fusion pipeline with the Bowtie1[38] flag activated.

Operating procedure

The OP consists of a laboratory and a bioinformatics module that has been built to both maximize the efficiency and minimize the time of ALL clinical diagnostics. Each element of the laboratory module is fully customizable and commercially available, whereas each tool deployed for the bioinformatics module is freely available through the Anaconda Platform (https://www.anaconda.com/).

Laboratory module

RNA extraction protocol. Total RNA was extracted during diagnosis from bone marrow mononuclear cells by the guanidinium thiocyanate–phenol–chloroform method. Guanidine methods were used for total RNA preparation, as described by Sacchi et al.[39]

RNA CaptureSeq and sample sequencing. The RNA CaptureSeq 'TruSight RNA PanCancer' (Illumina), which includes 57,010 probes complementary to 21,043 coding regions for a total of 1385 cancer-related RNA transcripts, was applied (Fig. 1a). The protocol required 2.5 days, from library preparation to NGS sequencing. The sample libraries were prepared per the manufacturer's protocol using 10 ng of total RNA. Batches of 8 samples per run were sequenced through cartridge V3 on the Illumina MiSeq platform in a 75 bp paired-end setting for a total of 25 million paired-end reads (PE reads). The cost per sample was about 250 USD. A detailed list of targeted regions can be obtained from Illumina (https://support.illumina.com/sequencing/sequencing_kits/trusight-rna-pan-cancer-panel/downloads.html).

Bioinformatics module

FASTQ file quality control. The raw FASTQ quality control was performed using the FASTQC tool (https://www.bioinformatics.babraham.ac.uk/), which provided information on reads in terms of sequence duplication levels, per base and per sequence average quality score, sequence length distribution, and adapter content.

Fusion gene assessment. A purpose-built bioinformatics pipeline was developed to detect fusion genes from RNA CaptureSeq datasets. The pipeline deploys stable and open-source bioinformatics tools in a sequential mode (Fig. 1b):

- *Alignment to targets*. BWA-MEM[40] v. 0.7.15-r1140 aligned PE reads to the genomic sequences of the targeted genes. The PE reads that did not map entirely on the reference genome through SAMTOOLS[41] v. 1.8 were isolated; these PE reads (informative) may derive from fragments of the fusion gene breakpoint.
- *Assembly*. The informative reads are assembled into longer sequences (contigs) through the SPAdes[42] v. 3.12.0 tool.

SPAdes was run with 3 different settings of k-mer size (25, 31, and 51) to cover any possible contig scenarios, thus maximizing the sensitivity of our strategy. This step is critical since more extended sequences have a higher chance of correctly aligning on the fusion gene partner at the genomic level.

- *Alignment to the complete genome*. BWA-MEM aligned contig sequences to the complete human genome (GRCh38.p12). SAMTOOLS then retrieved contig sequences that showed chimeric features, thus mapping the 5′- and 3′-sides of different genomic locations.
- *Gene annotation and fusion gene assessment*. The chimeric sequences were annotated with BEDTOOLS[43] v. 2.27.0 and GENCODE[37] release 29 (GRCh38.p12) annotation. Any chimeric sequence with different gene annotation between the 5′- and 3′-side were termed fusion genes. These were queried to the web-application FusionHub[44] to highlight fusion genes already described in other studies.
- Description of public databases is provided by the FusionHub's authors (https://www.ncbi.nlm.nih.gov/pmc/articles/PMC5929557/table/pone.0196588.t001/?report=objectonly).

REFERENCES

1. Inaba H, Greaves M, Mullighan CG. Acute lymphoblastic leukaemia. *Lancet.* 2013;381:1943–1955. doi:10.1016/S0140-6736(12)62187-4.
2. Nguyen K, Devidas M, Cheng S-C, et al. Factors influencing survival after relapse from acute lymphoblastic leukemia: a Children's Oncology Group study. *Leukemia.* 2008;22:2142–2150. doi:10.1038/leu.2008.251.
3. Hunger SP, Mullighan CG. Redefining ALL classification: toward detecting high-risk ALL and implementing precision medicine. *Blood.* 2015;125:3977–3987. doi:10.1182/blood -2015- 02-580043.
4. Iacobucci I, Mullighan CG. Genetic basis of acute lymphoblastic leukemia. *J Clin Oncol.* 2017;35:975–983. doi:10.1200/JCO.2016.70.7836.
5. Harrison CJ. Cytogenetics of paediatric and adolescent acute lymphoblastic leukaemia. *Br J Haematol.* 2009;144:147–156. doi:10.1111/j.1365-2141.2008.07417.x.
6. Felice MS, Gallego MS, Alonso CN, et al. Prognostic impact of t(1;19)/TCF3-PBX1 in childhood acute lymphoblastic leukemia in the context of Berlin-Frankfurt-Münster-based protocols. *Leuk Lymphoma.* 2011;52:1215–1221. doi:10.3109/10428194.2011.565436.
7. Winters AC, Bernt KM. MLL-rearranged leukemias-an update on science and clinical approaches. *Front Pediatr.* 2017;5:4doi:10.3389/fped.2017.00004.
8. Harvey RC, Mullighan CG, Chen I-M, et al. Rearrangement of CRLF2 is associated with mutation of JAK kinases, alteration of IKZF1, Hispanic/Latino ethnicity, and a poor outcome in pediatric B-progenitor acute lymphoblastic leukemia. *Blood.* 2010;115:5312–5321. doi:10.1182/blood -2009- 09-245944.
9. Russell LJ, Capasso M, Vater I, et al. Deregulated expression of cytokine receptor gene, CRLF2, is involved in lymphoid transformation in B-cell precursor acute lymphoblastic leukemia. *Blood.* 2009;114:2688–2698. doi:10.1182/blood-2009-03-208397.
10. Pui C-H, Robison LL, Look AT. Acute lymphoblastic leukaemia. *Lancet.* 2008;371:1030–1043. doi:10.1016/S0140-6736(08)60457-2.
11. Stam RW. MLL-AF4 driven leukemogenesis: what are we missing? *Cell Res.* 2012;22:948–949. doi:10.1038/cr.2012.16.
12. Iqbal N, Iqbal N. Imatinib: a breakthrough of targeted therapy in cancer. *Chemother Res Pract.* 2014;2014:357027doi:10.1155/2014/357027.
13. Nowell PC, Hungerford DA. Chromosome studies on normal and leukemic human leukocytes. *J Natl Cancer Inst.* 1960;25:85–109. http://www.ncbi.nlm.nih.gov/pubmed/14427847. Accessed February 19, 2019.
14. Iijima-Yamashita Y, Matsuo H, Yamada M, et al. Multiplex fusion gene testing in pediatric acute myeloid leukemia. *Pediatr Int.* 2018;60:47–51. doi:10.1111/ped.13451.
15. Mertens F, Johansson B, Fioretos T, et al. The emerging complexity of gene fusions in cancer. *Nat Rev Cancer.* 2015;15:371–381. doi:10.1038/nrc3947.
16. Bacher U, Shumilov E, Flach J, et al. Challenges in the introduction of next-generation sequencing (NGS) for diagnostics of myeloid malignancies into clinical routine use. *Blood Cancer J.* 2018;8:113doi:10.1038/s41408-018-0148-6.
17. Kumar S, Vo AD, Qin F, et al. Comparative assessment of methods for the fusion transcripts detection from RNA-Seq data. *Sci Rep.* 2016;6:21597doi:10.1038/srep21597.
18. Mercer TR, Clark MB, Crawford J, et al. Targeted sequencing for gene discovery and quantification using RNA CaptureSeq. *Nat Protoc.* 2014;9:989–1009. doi:10.1038/nprot.2014.058.
19. Clark MB, Mercer TR, Bussotti G, et al. Quantitative gene profiling of long noncoding RNAs with targeted RNA sequencing. *Nat Methods.* 2015;12:339–342. doi:10.1038/nmeth.3321.
20. Conter V, Bartram CR, Valsecchi MG, et al. Molecular response to treatment redefines all prognostic factors in children and adolescents with B-cell precursor acute lymphoblastic leukemia: results in 3184 patients of the AIEOP-BFM ALL 2000 study. *Blood.* 2010;115:3206–3214. doi:10.1182/blood -2009- 10-248146.
21. Haas B, Dobin A, Stransky N, et al. STAR-fusion: fast and accurate fusion transcript detection from RNA-seq. *bioRxiv.* 2017;120295. doi: https://doi.org/10.1101/120295.
22. Winters JL, Davila JI, McDonald AM, et al. Development and verification of an RNA sequencing (RNA-Seq) assay for the detection of gene fusions in tumors. *J Mol Diagn.* 2018;20:495–511. doi:10.1016/J.JMOLDX.2018.03.007.
23. GTEx Consortium TGteThe genotype-tissue expression (GTEx) project. *Nat Genet.* 2013;45:580–585. doi:10.1038/ng.2653.
24. van der Linden MH, Valsecchi MG, De Lorenzo P, et al. Outcome of congenital acute lymphoblastic leukemia treated on the Interfant-99 protocol. *Blood.* 2009;114:3764–3768. doi:10.1182/blood -2009- 02-204214.
25. Pieters R, Schrappe M, De Lorenzo P, et al. A treatment protocol for infants younger than 1 year with acute lymphoblastic leukaemia (Interfant-99): an observational study and a multicentre randomised trial. *Lancet.* 2007;370:240–250. doi:10.1016/S0140-6736(07)61126-X.
26. Roberts KG, Morin RD, Zhang J, et al. Genetic alterations activating kinase and cytokine receptor signaling in high-risk acute lymphoblastic leukemia. *Cancer Cell.* 2012;22:153–166. doi:10.1016/j.ccr.2012.06.005.
27. Puig-Oliveras A, Revilla M, Castelló A, et al. Expression-based GWAS identifies variants, gene interactions and key regulators affecting intramuscular fatty acid content and composition in porcine meat. *Sci Rep.* 2016;6:31803doi:10.1038/srep31803.
28. Babiceanu M, Qin F, Xie Z, et al. Recurrent chimeric fusion RNAs in non-cancer tissues and cells. *Nucleic Acids Res.* 2016;44:2859–2872. doi:10.1093/nar/gkw032.
29. Nicorici D, Şatalan M, Edgren H, et al. FusionCatcher – a tool for finding somatic fusion genes in paired-end RNA-sequencing data. *bioRxiv.* 2014;011650. doi:10.1101/011650.
30. Kim RN, Kim A, Choi S-H, et al. Novel mechanism of conjoined gene formation in the human genome. *Funct Integr Genomics.* 2012;12:45–61. doi:10.1007/s10142-011-0260-1.
31. Prakash T, Sharma VK, Adati N, et al. Expression of conjoined genes: another mechanism for gene regulation in eukaryotes. *PLoS One.* 2010;5:e13284doi:10.1371/journal.pone.0013284.
32. Mullighan CG, Su X, Zhang J, et al. Deletion of IKZF1 and prognosis in acute lymphoblastic leukemia. *N Engl J Med.* 2009;360:470–480. doi:10.1056/NEJMoa0808253.
33. Sevov M, Bunikis I, Häggqvist S, et al. Targeted RNA sequencing assay efficiently identifies cryptic KMT2A (MLL)-fusions in acute leukemia patients. *Blood.* 2014;124: http://www.bloodjournal.org/content/124/21/2406?sso-checked=true. Accessed March 2, 2019.
34. Trapnell C, Pachter L, Salzberg SL. TopHat: discovering splice junctions with RNA-Seq. *Bioinformatics.* 2009;25:1105–1111. doi:10.1093/bioinformatics/btp120.
35. Dobin A, Davis CA, Schlesinger F, et al. STAR: ultrafast universal RNA-seq aligner. *Bioinformatics.* 2013;29:15–21. doi:10.1093/bioinformatics/bts635.
36. Kim D, Salzberg SL. TopHat-Fusion: an algorithm for discovery of novel fusion transcripts. *Genome Biol.* 2011;12:R72doi:10.1186/gb -2011-12-8-r72.
37. Harrow J, Frankish A, Gonzalez JM, et al. GENCODE: The reference human genome annotation for The ENCODE Project. *Genome Res.* 2012;22:1760–1774. doi:10.1101/gr.135350.111.
38. Langmead B, Trapnell C, Pop M, et al. Ultrafast and memory-efficient alignment of short DNA sequences to the human genome. *Genome Biol.* 2009;10:R25doi:10.1186/gb-2009-10-3-r25.

39. Chomzynski P, Sacchi N. Single-step method of RNA isolation by acid guanidinium thiocyanate–phenol–chloroform extraction. *Anal Biochem.* 1987;162:156–159. doi:10.1006/abio.1987.9999.
40. Li H, Durbin R. Fast and accurate long-read alignment with Burrows–Wheeler transform. *Bioinformatics.* 2010;26:589–595. doi:10.1093/bioinformatics/btp698.
41. Li H, Handsaker B, Wysoker A, et al. The sequence alignment/map format and SAMtools. *Bioinformatics.* 2009;25:2078–2079. doi:10.1093/bioinformatics/btp352.
42. Bankevich A, Nurk S, Antipov D, et al. SPAdes: a new genome assembly algorithm and its applications to single-cell sequencing. *J Comput Biol.* 2012;19:455–477. doi:10.1089/cmb.2012.0021.
43. Quinlan AR, Hall IM. BEDTools: a flexible suite of utilities for comparing genomic features. *Bioinformatics.* 2010;26:841–842. doi:10.1093/bioinformatics/btq033.
44. Panigrahi P, Jere A, Anamika K. FusionHub: a unified web platform for annotation and visualization of gene fusion events in human cancer. Kumar-Sinha C, ed. *PLoS One.* 2018;13:e0196588doi:10.1371/journal.pone.0196588.

Leukemia (2018) **32**, 450–461

www.nature.com/leu

ORIGINAL ARTICLE

Low-burden *TP53* mutations in chronic phase of myeloproliferative neoplasms: association with age, hydroxyurea administration, disease type and *JAK2* mutational status

B Kubesova[1,6], S Pavlova[1,2,6], J Malcikova[1,2], J Kabathova[1], L Radova[2], N Tom[2], B Tichy[2], K Plevova[1,2], B Kantorova[1,2], K Fiedorova[2], M Slavikova[2], V Bystry[2], J Kissova[3], B Gisslinger[4], H Gisslinger[4], M Penka[3], J Mayer[1,2], R Kralovics[5], S Pospisilova[1,2] and M Doubek[1,2]

The multistep process of *TP53* mutation expansion during myeloproliferative neoplasm (MPN) transformation into acute myeloid leukemia (AML) has been documented retrospectively. It is currently unknown how common *TP53* mutations with low variant allele frequency (VAF) are, whether they are linked to hydroxyurea (HU) cytoreduction, and what disease progression risk they carry. Using ultra-deep next-generation sequencing, we examined 254 MPN patients treated with HU, interferon alpha-2a or anagrelide and 85 untreated patients. We found *TP53* mutations in 50 cases (0.2–16.3% VAF), regardless of disease subtype, driver gene status and cytoreduction. Both therapy and *TP53* mutations were strongly associated with older age. Over-time analysis showed that the mutations may be undetectable at diagnosis and slowly increase during disease course. Although three patients with *TP53* mutations progressed to *TP53*-mutated or *TP53*-wild-type AML, we did not observe a significant age-independent impact on overall survival during the follow-up. Further, we showed that complete p53 inactivation alone led to neither blast transformation nor HU resistance. Altogether, we revealed patient`s age as the strongest factor affecting low-burden *TP53* mutation incidence in MPN and found no significant age-independent association between *TP53* mutations and hydroxyurea. Mutations may persist at low levels for years without an immediate risk of progression.

Leukemia (2018) **32,** 450–461; doi:10.1038/leu.2017.230

INTRODUCTION

Leukemic transformation of Ph-negative myeloproliferative neoplasms (MPN; polycythemia vera, PV; essential thrombocythemia, ET; primary myelofibrosis, PMF) is a relatively rare but fatal event. Several intrinsic risk factors have been suggested involving MPN phenotype (PMF > PV > ET), abnormal karyotype and higher age.[1] The effect of MPN therapy has been widely discussed and alkylating agents, pipobroman and ^{32}P were shown to be leukemogenic.[1–3] Possible negative impacts of hydroxyurea (HU) remain controversial,[1,2,4–9] as summarized in.[10] Great effort has been invested into the search for genetic changes predicting and/or triggering MPN transformation to AML and MDS.[11–16]

Eliminating tumor suppressor *TP53* during myelopoiesis helps escape from control mechanisms preventing differentiation loss, aberrant self-renewal, and large genome rearrangements.[17,18] In chronic MPN phase, *TP53* gene defects have been extremely rarely detected using Sanger sequencing or cytogenetic analysis; on the contrary, they were shown to be common in post-MPN acute myeloid leukemia (AML).[19–21] This pronounced difference is indicative of *TP53* role in the transformation process. Retrospective analysis of individual cases of *TP53*-mutated post-MPN AML showed that *TP53* mutations can be traced months or even years before leukemic transformation.[11,19,22,23] The level of mutation burden was shown to remain low until complete p53 inactivation by losing the second allele (17p defects or second mutation), followed by rapid clonal expansion.[11,22]

TP53 mutations occurring at a level above detection limit of Sanger sequencing (10–20% variant allelic frequency; VAF) show negative prognostic and/or predictive impact in some types of cancer, especially in hematological malignancies.[24,25] Small *TP53*-mutated subclones below this sensitivity threshold were described to drive relapse or disease progression in many cases of chronic hematological malignancies,[26–29] but their impact is less clear in prospective setting.[30] Cytotoxic agents support a minor *TP53*-mutated subclone overgrowth.[26,31–33] Previous therapy with hydroxyurea (HU), a ribonucleotide reductase inhibitor activating p53 response via replication stress,[34,35] has been associated with *TP53*/17p defects in post-MPN AML;[4,12,22,36] however, this observation has not been confirmed in a large unbiased study.

While minor *TP53* mutations in MPN have been tracked retrospectively in individual cases and have been suggested as carrying an increased risk of leukemic transformation,[11] the occurrence of low-burden *TP53* mutations (< 5%) has not been

---

[1]Department of Internal Medicine—Hematology and Oncology, Faculty of Medicine, Masaryk University Brno, Czech Republic; [2]Central European Institute of Technology, Masaryk University, Brno, Czech Republic; [3]Department of Clinical Hematology, Faculty of Medicine, Masaryk University Brno, Czech Republic; [4]Department of Internal Medicine I, Division of Hematology and Blood Coagulation, Medical University of Vienna, Austria and [5]CeMM Research Center for Molecular Medicine of Austrian Academy of Sciences, Vienna, Austria. Correspondence: Dr S Pavlova, Department of Internal Medicine—Hematology and Oncology, University Hospital and Medical Faculty of Masaryk University, Cernopolni 9, Brno 61300, Czech Republic.
E-mail: pavlova.sarka@fnbrno.cz

[6]These authors contributed equally to this work.

Received 30 November 2016; revised 30 June 2017; accepted 5 July 2017; accepted article preview online 24 July 2017; advance online publication, 15 August 2017

analyzed so far. Whether therapy or other factors affect their origin and outgrowth is unknown. To map *TP53*-mutated subclones' presence in MPN patients treated with cytoreductive drugs and study their evolution over time, we used an ultra-deep next-generation sequencing (NGS) approach.

PATIENTS AND METHODS

Patients and samples

Peripheral blood (PB) samples and clinical and routine laboratory data from MPN patients were collected from Czech hospitals (University Hospital Brno and local hospitals) and Vienna General Hospital, Austria. The study was approved by the Ethical Committee of University Hospital Brno. For all samples, written informed consent approved by the Ethics Committees of the respective institutions were available in accordance with the Declaration of Helsinki. Patients were diagnosed according to the revised World Health Organization criteria.[37]

In total, 339 MPN patients were included (Supplementary Table S1). Treated patients ($N=254$) were having or had discontinued cytoreductive therapy–HU, interferon alpha-2a (IFN) or anagrelide (ANG)—and had been diagnosed ⩾4 years (y) before sampling. To assess the effect of therapy, the treated patients were categorized as follows: (1) by administration of HU, IFN or ANG at any time during disease course (referred to as HU-yes/HU-no, IFN-yes/IFN-no, ANG-yes/ANG-no); (2) more strictly, in the HU-yes group, only patients fulfilling a criterion of HU treatment for ⩾4y were kept. This group was compared to HU-no patients. Besides these, 85 samples from patients with no cytoreductive therapy before sampling were analyzed. Retrospective and prospective samples from 31/50 patients with detected *TP53* mutations were analyzed to describe mutation development.

Ultra-deep next-generation sequencing of *TP53* amplicons

NGS analysis was performed as described previously[26] with minor modifications. Briefly, 30 ng of leukocyte or granulocyte DNA was amplified with high-fidelity Q5 Polymerase (New England Biolabs, Ipswich, MA, USA) using primers specific for the *TP53* exons 4–10. The indexed library was prepared with Nextera XT DNA Sample Preparation Kit (Illumina, San Diego, CA, USA) and sequenced using MiSeq Reagent Kit v2 (300 cycles; Illumina, San Diego, CA, USA) on a MiSeq instrument according to manufacturer recommendations. The coverage per base exceeded 5000 (⩾10 000 in 82% of exons); mean coverage reached 39535. For variant detection we used bioinformatics pipeline (Supplementary Figure S1) combining CLC Genomic Workbench version 7.5 (Qiagen, Hilden, Germany) and the deepSNV R-package.[38–42] Samples containing variants above 0.2% VAF by either approach were subjected to validation from independent sampling and/or PCR amplification (Supplementary Table S2). For over-time monitoring and validation of previously identified mutation, cutoff 0.1% was applied (minimal coverage per base ⩾10 000).

Statistical analysis

Statistical analyses were performed within the R environment.[42] The distribution normality was tested using the Kolmogorov-Smirnov normality test. Non-parametric tests were applied because of normality violation in most clinical variables (for example, age distribution). To analyze the relationship between the variables, the Spearman correlation test, Mann–Whitney test, Kruskal–Wallis test and Fisher's exact test with simulated *P*-value (Monte-Carlo simulation) were used. Data sets were described with median and s.d. and/or range as indicated in the legends. The comparison of patients' survival was performed by log-rank test and visualized using Kaplan–Meier curves; Cox proportional hazards regression was used to model the effect of multiple predictor variables. Logistic regression models were applied to assess the significance of age and therapy in *TP53* mutational status. Age adjustment was performed by adding the age covariate into the logistic model. Finally, the age-adjusted models were compared with a model with age parameter only by anova chi-square tests. The level of statistical significance was set $P \leqslant 0.05$. All statistical tests were performed as two-sided. Plots were created with the GraphPad Prism version 5.00 for Windows (GraphPad Software, La Jolla, CA, USA).

Single-nucleotide polymorphism arrays

Genome-wide analysis was performed on CytoScan HD arrays (Affymetrix, Santa Clara, CA, USA) according to the manufacturer's instructions. CEL files were analyzed using the Chromosome Analysis Suite software, v3.1.0.15 (Affymetrix, Santa Clara, CA, USA) and annotated using NetAffx 33.1 annotation data set.

For details on methods see Supplementary Material.

RESULTS

Ultra-deep NGS analysis of *TP53* gene in treated MPN patients

To screen for *TP53* mutations and assess the effect of therapy, we analyzed 254 chronic-phase MPN patients using ultra-deep NGS. All patients were treated with one or more cytoreductive drugs (hydroxyurea, HU; interferon alpha-2a, IFN; anagrelide, ANG) and diagnosed ⩾4y before sampling (4.2–29.5; median 9.2y; Supplementary Table S1). *TP53* mutations were identified in 41 patients (41/254; 16.1%; Table 1) with VAF for the most abundant variant ranging between 0.2 and 11.6%. In a pronounced proportion of patients, more than one mutation was present (11/41; 26.8%). Colony-forming assay[43,44] performed in 3 patients confirmed the presence of *TP53*-mutated subclones within *JAK2* or *CALR*-mutated populations (Supplementary Figure S2). To verify the mutations' presence in myeloid lineage in patients examined from leukocyte DNA, the granulocyte sample was analyzed where available. No evident discrepancy was found (Supplementary Table S3).

TP53 mutations in MPN are strongly associated with higher age

TP53 mutations were found in all disease subtypes, regardless of driver gene status and even if no HU had been administered (Figure 1; Table 2). Further, we performed thorough analysis of relationships between *TP53* mutational status and disease parameters (Supplementary Table S4). The comparison of patients carrying *TP53* mutation (*TP53*-mut) to patients without *TP53* mutation (*TP53*-wt) revealed a highly significant association between *TP53* mutations and higher age ($P=5.54\times10^{-5}$; median age at sampling 69.3 for *TP53*-mut and 62.4 for *TP53*-wt; Figure 2a). *TP53* mutations were less frequent in patients who obtained ANG during disease course (9/104, 8.7% in ANG-no vs 32/150, 21.3% in ANG-yes; $P=0.0087$). Patients receiving HU at sampling carried the *TP53* mutation more frequently (HU at sampling, 28/125, 22.4% vs without HU at sampling, 13/128, 10.2%; $P=0.0205$) but associating the *TP53* mutation with HU administration anytime during disease course did not reach significance (31/164; 18.9% in HU-yes vs 10/90; 11.1% in HU-no). As expected, the age at sampling was significantly associated to multiple therapy parameters, partially due to the frequent use of HU in older patients (Figure 2b, Supplementary Figure S3).

As the patient cohort was compiled of several hospitals' contributions, which may have introduced bias, we limited the analysis to University Hospital Brno patients ($N=169$; $N_{TP53\text{-mut}}=22$), which lead to similar results (data not shown).

Some of the patients received HU for a short time period and were switched to other therapy or vice versa. Thus, to further disclose the relationship between *TP53* mutations, HU, and age, we eliminated these patients from the analysis, using more stringent criteria to categorize patient therapy (Figure 2c; Supplementary Table S5): (1) patients who had obtained HU for at least 48 months ($N=122$) and (2) patients treated with IFN and/or ANG only (HU-no; $N=90$). Also in this subset, patient age was the most significant predictor of *TP53* mutation (Supplementary Figure S4A; *TP53*-mut 69.5y vs *TP53*-wt 63.4y; $P=0.0009$) and *TP53* mutations were more frequent in patients in the HU subgroup (HU⩾4y, 28/122, 22.9% vs HU-no, 10/90, 11.1%; $P=0.03$). In parallel, the therapy category was strongly associated to age (Supplementary Figure S4B). To eliminate the influence of age, we applied a logistic regression model with the age adjustment (Supplementary Table S6); using this approach, the *TP53* mutation frequency was not found to be significantly different in patients treated with various cytoreductive drugs. This

Table 1. Clinical and laboratory data of patients treated with cytoreductive drugs and carrying *TP53* mutations

		Disease type and course					*Therapy*						*Mutations*		*Follow-up*	
Therapy group	*Sample*	*Driver mutation* [a]	*Sex*	*Disease phenotype*	*Age at sampling*	*Time from dg to study enrollment (mo)*	*Total therapy length (mo)*	*Therapy at sampling*	*HU therapy (mo)*	*IFN therapy (mo)*	*ANG therapy (mo)*	*Busulfan or chemo/radio therapy*	*Most abundant mutation (VAF %)*	*TP53 mutations (VAF %)*	*Follow-up from study enrollment (mo)*	*Outcome*
no HU	MP315	JAK2	M	PV	62	109	89	I	0	0	0	no	0.8	p.Y126D 0.79	39	Alive
	048C	JAK2	M	PV	73	145	96	I	0	96	0	no	0.8	p.E285K 0.82	41	Alive
	JAK1716	JAK2	F	PV	63	111	110	I	0	110	0	no	0.2	p.C238S 0.20	83	Alive
	MP189	CALR +JAK2	F	ET	67	138	112	A	0	0	112	no	2.9	p.P58A 2.90	51	Alive
	MP247	CALR	F	PMF	56	122	119	A	0	5	115	no	0.3	p.Y220C 0.26	48	Alive
	MP155	CALR	F	PMF	61	122	121	A	0	0	121	no	0.2	p.V143E 0.21	52	Alive
	227A	CALR	M	PMF	72	154	123	I	0	123	0	CH	0.3	p.A138V 0.26	10	Dead
	65A	CALR	F	ET	70	158	152	IA	0	152	11	no	1.7	c.376-2A > G 1.71; p.R273H 0.2	121	Alive
	186A	JAK2	F	ET	80	180	175	I	0	175	0	no	8.3	c.454dupC 8.27	37	Dead-AML[b]
	221A	CALR	M	ET	69	180	179	I	0	179	0	no	2.2	p.I162S 2.24	118	Alive
HU < 4y	MP15	JAK2	M	PV	66	84	84	I	17	77	0	no	4.4	p.Y220C 4.4	62	Alive
	MP160	JAK2	M	ET	69	61	18	H	18	0	0	no	0.2	p.P142R 0.23	52	Alive
	MP68	JAK2	F	MPN	70	58	56	H	47	0	9	no	6.9	p.R248Q 6.90; p.A159V 6.40; p.P151R 1.73; p.I195S 0.24; p.R273H 0.23	44	Dead-AML[c]
HU ⩾ 4y	MP326	JAK2	F	PV	58	80	48	H	48	0	0	no	0.6	p.Y220C 0.55	39	Alive
	MP345	JAK2	M	PV	68	50	48	H	48	0	0	no	1.1	p.S215R 1.10	38	Alive
	MP302	JAK2	F	PV	71	231	65	H	56	0	0	B	0.4	p.G199E 0.44	29	Alive
	MP319	JAK2	M	PV	61	62	57	HA	57	0	32	no	0.4	p.R273H 0.37	28	Alive
	MP168	JAK2	F	PV	68	86	57	H	57	0	0	no	1.0	p.H179R 0.95	49	Alive
	MP153	JAK2	M	PV	63	62	61	HA	60	0	61	no	0.2	p.R213G 0.23	51	Alive
	MP96	JAK2	F	PV	55	64	62	H	62	0	0	no	0.5	p.I195T 0.51; p.R282W 0.20	54	Alive
	MP327	JAK2	F	ET	73	125	64	H	64	0	0	no	0.5	p.R273H 0.47	39	Alive
	MP317	CALR	M	PMF	81	65	65	H	65	0	0	no	0.8	p.V216M 0.83; p.H179R 0.25	17	Dead
	MP63	JAK2	F	ET	68	79	69	H	69	0	0	no	0.2	p.M246V 0.20	53	Alive
	MP5	JAK2	M	PV	68	70	70	H	70	0	0	no	0.3	p.I195T 0.26	64	Alive
	MP10	JAK2	M	PMF	79	77	76	H	76	0	0	no	10.5	p.G245S 10.50; p.R158H 0.54; p.H168R 0.29; p.F134L 0.23; p.Y234H 0.21	46	Dead-expansion[d]
	MP307	MPL	F	PV	82	103	76	H	76	0	0	no	0.2	c.572_574del 0.21	40	Alive
	MP369	JAK2	F	PV	73	84	81	H	81	0	0	no	1.4	p.T170M 1.39	35	Alive
	MP246	JAK2	F	ET	71	108	103	A	82	0	30	no	0.2	p.D259H 0.2; p.G245S 0.2	48	Alive
	MP314	JAK2	F	PV	69	233	92	H	86	0	0	B	1.3	p.C242Y 1.26; p.G245D 0.35	39	Alive
	MP8	JAK2	M	PV	82	92	90	H	90	0	0	no	0.2	p.R175H 0.24	49	Dead

Table 1. (Continued)

		Disease type and course					Therapy						Mutations		Follow-up	
Therapy group	*Sample*	*Driver mutation* [a]	*Sex*	*Disease phenotype*	*Age at sampling*	*Time from dg to study enrollment (mo)*	*Total therapy length (mo)*	*Therapy at sampling*	*HU therapy (mo)*	*IFN therapy (mo)*	*ANG therapy (mo)*	*Busulfan or chemo/radio therapy*	*Most abundant mutation (VAF %)*	*TP53 mutations (VAF %)*	*Follow-up from study enrollment (mo)*	*Outcome*
	MP356	JAK2	F	ET	69	109	91	H	91	0	0	no	1.6	p.R248Q 1.64	37	Alive
	MP230	JAK2	M	MPN	70	96	96	H	96	0	0	no	0.5	p.R248Q 0.50; c.512_514dup 0.22; p.V274G 0.20	22	Dead
	MP289	JAK2	F	PV	61	265	140	no	98	42	0	no	3.3	p.R213* 3.29; p.I251T 0.93; p.Y234H 0.67	39	Alive
	MP273	JAK2	F	ET	75	111	111	H	111	0	0	no	0.3	p.C176S 0.31; p.S240G 0.22	47	Alive
	MP229	JAK2	F	PMF	85	112	112	H	112	0	0	no	1.0	c.376-1G>A 0.95	49	Alive
	MP363	JAK2	M	ET	87	117	112	H	112	0	0	no	0.3	p.R248Q 0.29	37	Alive
	MP7	JAK2	F	PV	69	133	130	H	121	9	0	no	0.5	p.I255T 0.46	64	Alive
	MP329	JAK2	F	ET	73	162	142	H	142	0	0	no	2.6	p.R248W 2.61	27	Alive
	MP250	JAK2	F	PV	74	152	152	H	152	0	0	no	0.4	p.W91* 0.36	11	Dead
	MP2	CALR	F	ET	68	195	186	HA	169	11	110	no	11.6	p.E286K 11.60; p.R248Q 0.45	67	Alive
	MP324	JAK2	M	PV	72	255	255	H	255	0	0	no	0.3	p.T253A 0.26	15	Dead

Abbreviations: A/ANG, anagrelide; B, busulphan; CH, chemotherapy; ET, essencial thrombocythemia; F, female; H/HU, hydroxyurea; I/IFN, interferon alpha; M, male; mo, months; PMF, primary myelofibrosis; PV, polycythemia vera; R, radiotherapy; y, years. [a]All three driver genes (*JAK2* V617F+exon 12, *CALR* exon 9 and *MPL* exon 10) were sequenced in all patients with *TP53* mutation. [b]Sample from leukemic transformation not available. [c]sAML *JAK2*-wt/*TP53*-wt. [d]Clonal expansion without leukemic transformation.

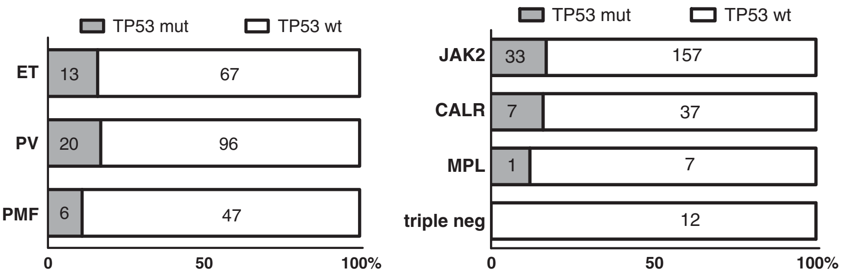

Figure 1. Disease type and driver gene mutation status stratified according to *TP53* mutation presence in patients treated with cytoreductive drugs (NS; Fisher exact test). Driver gene mutations examined in order of *JAK2* > *CALR* > *MPL*.

Table 2. Clinical characteristics of patients according to *TP53* mutational status

	Treated (N = *254)*					*Untreated* (N = *85)*				
	TP53 wt	%	*TP53 mut*	%	P	*TP53 wt*	%	*TP53 mut*	%	P
N	213	100	41	100		76	100	9	100	
Sex (male)	91	43	16	39	NS	36	47	5	56	NS
Age at study enrollment (median, range, s.d.)	62 (25–90, 13.2)		69 (55–87, 7.4)		0.0002	70 (19–89, 13.8)		70 (66–82, 5.4)		NS
Time from diagnosis (mo; median, range, s.d.)	109 (50–354, 54.9)		111 (50–265, 54.5)		NS	0 (0–255, 52.9)		4 (0–53, 17.2)		NS
Disease subtype										
ET	67	31	13	32	NS	21	28	1	11	NS
PV	96	45	20	49		20	26	2	22	
PMF	47	22	6	15		30	39	6	67	
unclassified MPN	3	1	2	5		5	7	0	0	
JAK2-mutated	157	74	33	80	NS	54	72	8	89	NS
JAK2-wt	56	26	8	20		22	29	1	11	
CALR-mut	37	17	7	17		13	17	1	11	
MPL-mut	7	3	1	2		4	5	0	0	
Triple negative	12	6	0	0		3	4	0	0	
Therapetutic history										
Total therapy length (mo; median, range, s.d.)	87 (24–265, 44.7)		92 (18–255, 45.4)		NS	0		0		
HU yes	133	62	31	76	NS	0	0	0	0	
Length of HU in HU yes (mo; median, range, s.d.)	65 (2–265, 53.9)		76 (17–255, 46.1)		0.0343	0		0		
HU at study enrollment	97	46	28	68	0.0120	0	0	0	0	
HU ⩾ 48 months	94	44	28	68	0.0060	0	0	0	0	
ANG yes	95	45	9	22	0.0392	0	0	0	0	
IFN yes	72	34	12	29	NS	0	0	0	0	
Busulfan/chemo-/radiotherapy	9	4	3	7	NS	2	3	1	11	NS

Abbreviations: %, percentage of patients with given parameter in *TP53*-wt or *TP53*-mut group; mo, months; driver gene status considered in order *JAK2* > *CALR* > *MPL*; PMF, primary myelofibrosis; PV, polycythemia vera; ET, essential thrombocythemia; post-PV MF was grouped to PV, no post-PV patient carried TP53 mutation. *MPL* status was unknown in one untreated *JAK2*-wt/*CALR*-wt/*TP53*-wt patient

is in agreement with the observation that in patients over 65y, the difference in proportion of *TP53* mutation between HU ⩾ 4y and HU-no therapy groups was much lower (23/75, 30.6% vs 6/30, 20.0%; n.s.) even though the HU-no group was significantly younger ($P = 0.026$; Supplementary Figure S5).

To further explore whether minor *TP53* mutations occur independently of the therapy, we examined a set of 85 patients with no cytoreductive treatment (Supplementary Table S1) and found *TP53* mutations in 9 of them (10.6%; Supplementary Table S7, Supplementary Figure S6).

TP53 mutations in HU-treated and other patients

We did not see any difference in mutation spectra between patients treated with HU and the others (Supplementary Figure S7). Neither the VAF of the most abundant variant nor the cumulative size of the mutated population significantly differed between the therapy groups (Figure 3). Nevertheless, we observed a trend towards the presence of more than one mutation (⩾ 0.2% VAF) in HU-treated patients (10/31) compared to patients treated with non-HU drugs (1/10) and untreated patients (2/9) (n.s.). The mutations showed typical distribution, the vast majority of them were located within the DNA-binding domain and they clustered within characteristic hot-spot sites (Supplementary Figure S8, Supplementary Table S8). All but one patient carried mutations which have been described as non-functional or, rarely, partially functional. The exception was the mutation p.P58A (MP189; VAF 2.9%) which displays no significant loss of transactivation activity.[45,46] The mutation remained stable in all three samplings (7.7y). We have not excluded the mutation

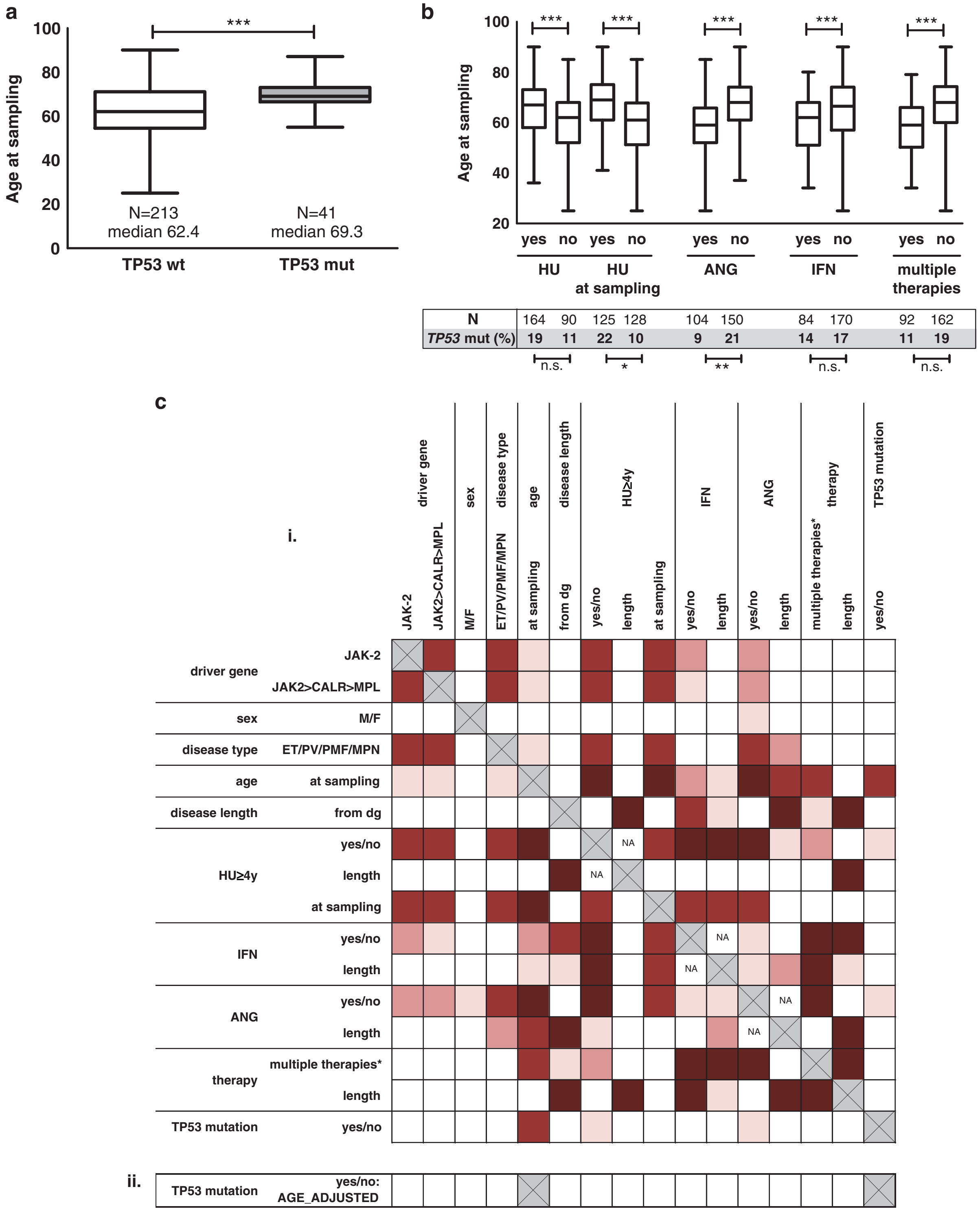

Figure 2. TP53 mutations: age and treatment in patients treated with cytoreductive drugs. (**a**) Age at sampling in *TP53*-mut and *TP53*-wt patients ($P = 5.54 \times 10^{-5}$; Kruskal–Wallis test). (**b**) Age at sampling and *TP53* mutation frequency according to therapy parameters (Kruskal–Wallis and Fisher exact test, respectively; age: HU-yes/no $P = 0.0007$; HU at sampling yes/no $P = 3.96 \times 10^{-7}$; ANG-yes/no $P = 1.32 \times 10^{-8}$; IFN-yes/no $P = 0.0006$; multiple therapies during disease course yes/no $P = 8.7 \times 10^{-8}$). Lines within boxes indicate median, box limits—25th and 75th percentiles, whiskers—minimum and maximum. (**c**) Comparison of patients treated with HU for ⩾ 4y and patients treated with IFN or/and ANG only. (i) Relationship between clinical and laboratory parameters. Red boxes: significant, scaled from $P \leqslant 0.0001$ (dark red) to $0.05 \geqslant P > 0.01$ (light red). Statistical tests used for combinations of variables: continuous—Spearman correlation test, continuous vs categorical—Kruskal–Wallis test; categorical–Fisher's exact test. (ii) Logistic regression model with the age adjustment did not reveal any age-independent significant difference. *Multiple therapies = more types of cytoreductive therapy during disease course. Length of the therapy = restricted to patients positive for given therapy type.

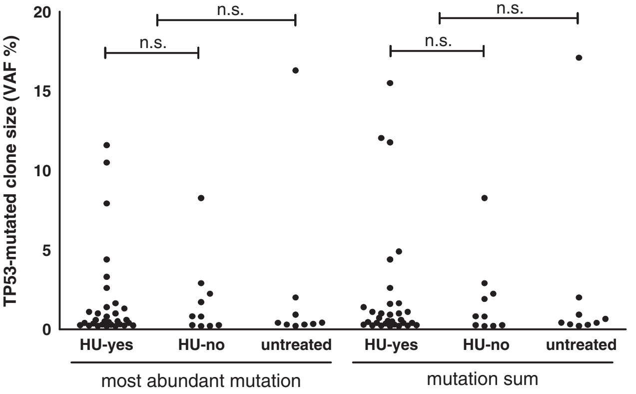

Figure 3. Mutated clone size. VAFs of most abundant mutation and VAF sums do not significantly differ between therapy groups (Mann–Whitney test).

from the analysis as we could not rule out other effects on p53 function.

TP53 mutations may escape detection if examined at diagnosis

Since the majority of mutations we describe were identified in samples taken later during the disease course, we raised the question whether the mutations can be detected earlier, or even at diagnosis. Out of 50 patients with a mutated clone, at least one retrospective sample was available in 20 (Table 2). A later identified mutation was traceable in at least one sample in 14 patients. The sample from the time of diagnosis was available in 10 patients; no *TP53* mutation was detected in 5 (50%; VAF ⩾ 0.1%) of them. Correspondingly, the mutation was detectable at diagnosis in only one of two patients who later developed *TP53*^{mut} sAML (JAK22 and JAK453; Figure 4). In conclusion, despite some *TP53* mutations being found at diagnosis with VAF ⩾ 10% (JAK646: 16.3%, Supplementary Table S7; 221A: 10.2%; Table 3), mutations frequently appear later in the disease course and may be undetectable (⩾ 0.1%) at diagnosis.

Monitoring patients with *TP53* mutations – dynamic behavior of mutated clones

To explore *TP53* mutation evolution in MPN prospectively, disease course was monitored and serial samples were collected. Prospective samples were available in 30 of 50 MPN patients with *TP53*^{mut}-subclones (median between study enrollment and the last serial sample 2.8y; 0.5–9.6y; Table 3). *TP53* mutations remained present in all but three serial samples (MP63, MP160 and MP307) in which mutations originally identified and confirmed in 0.2% were not detected 3.4, 2 and 1.6 years later, respectively.

TP53 mutation expanded and became predominant tumor cell population in 2/30 patients. The expansion was accompanied by the second allele inactivation in both cases. While the JAK22 patient progressed to AML carrying biallelic *TP53* inactivation (VAF 46%), the clonal biallelic expansion in patient MP10 (VAF 86%) did not result in leukemic transformation; this case is described further in detail (Figure 4; Supplementary Table S9).

When we considered all samples tested during the disease course, that is, retrospective as well as prospective samples, median interval between first and last sample was 7.1y (0.5–24.6; 31 patients). During this time, a slow mutation burden increase was the most frequent scenario (14 patients). We saw no clear association between the mutation burden changes and the VAF at study enrollment, therapy, other clinical data or mutation localization (Table 3, Supplementary Figure S8B and S10).

Impact of *TP53* mutations on overall survival or leukemic transformation

TP53 mutation with VAF < 5% did not impact overall survival (OS) during the follow-up when tested either from diagnosis or study enrollment (Supplementary Figure S9). The patients carrying *TP53* mutations above 5% VAF at study enrollment had significantly shorter OS ($P = 0.0064$ OS from sampling, $P = 0.0185$ OS from diagnosis). However, the impact on OS was lost when adjusted for age (Cox proportional hazard regression model for both age and mutation: $P = 1.01 \times 10^{-10}$ for age; $P = 0.121$ for *TP53* mutation > 5%). Besides, their shortened survival was not attributed to *TP53*-mut AML (Supplementary Figure S9G).

In total, AML developed in three patients with *TP53* mutation (3/50; 6%; Figure 4). Patient JAK22 (p.289fs 2%) was diagnosed with PV 4y after chemo/radiotherapy for B-cell lymphoma. The patient was treated with HU and progressed to *TP53*^{mut}-AML 5y later. On the contrary, patient MP68 (p.R248Q 6.9%) treated with HU developed *JAK2*^{wt}*TP53*^{wt}-AML outside multiple *JAK2*^{mut}*TP53*^{mut}-clones 3.5y from study enrollment (8.3y from diagnosis). Patient 186A (p.P153fs 8.27%) treated with IFN progressed to AML 2.9y after mutation detection (17.9y from diagnosis). The patient was switched to HU soon after study enrollment and an AML sample was not available, thus we cannot confirm the clonal expansion of *TP53* mutation or the effect of the therapy.

Rapid *TP53*-mutated clone expansion accompanied by cn-LOH but no other karyotype changes resulted neither in AML transformation nor HU resistance

In the *JAK2*^{mut}-PMF patient MP10, multiple *TP53* low-burden mutations were present at study enrollment. Among them, a hotspot *TP53*^{G245S} mutation grew rapidly during prospective monitoring up to 95% in granulocytes (Figure 4), reflecting the loss of heterozygosity (LOH). Since complex karyotype changes have been described as very common in AML with mutated *TP53*,[18] we analyzed the karyotype changes using CytoScan HD arrays. Only copy-neutral LOH (cn-LOH) in 17p13, including *TP53* gene, and chromosome Y loss were detected in the expanded clone. To further examine the time course of allelic changes, we analyzed myeloid progenitors. CFC assay indicated that second allele inactivation occurred intra-clonally in the clone carrying monoallelic p.G245S mutation (Supplementary Figure S2). Interestingly, despite complete p53 inactivation and clonal expansion, the patient remained clinically stable without signs of blast transformation for next 23 months, showed no signs of HU resistance and died 10.2y from diagnosis.

DISCUSSION

Previously published retrospectively analyzed cases showed that the development of *TP53*-mutated post-MPN AML is a multistep process. It likely involves mutation origin in the HSPC pool, mutated subclone propagation to level exceeding detection limit and persistence at low levels for an extended time period. Second allele inactivation was described as resulting in rapid clonal expansion and leukemic transformation.

We focused on the early phase of this process, that is, occurrence of low-burden *TP53* mutations which, in theory, may carry increased risk of leukemic transformation. Using highly sensitive and previously verified methods enabled us to detect mutations as low as 0.2%.[26] In total, we found mutations in 50 patients (14.7%). This is the first study using ultra-deep NGS to search for *TP53* mutations in MPN at a level ⩽ 1%. Lundberg et al.[11] found mutations in 5/197 (2.5%) patients using NGS with sensitivity of 5%, which roughly corresponds to our data (5 patients with mutations > 5% out of all 339 examined, 1.5%). As our study aimed to compare patients on HU and non-HU

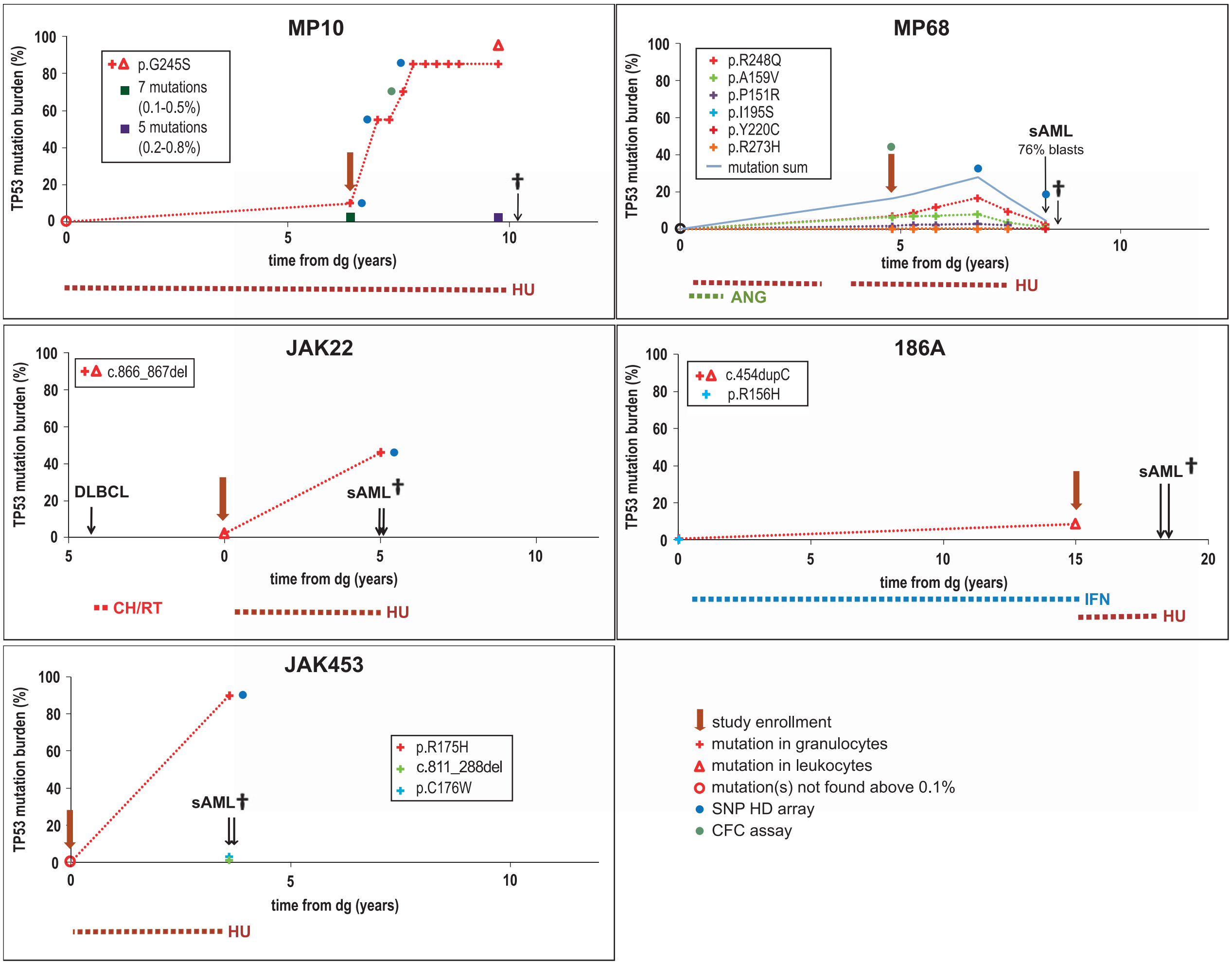

Figure 4. Selected cases of leukemic transformation or clonal expansion in patients with *TP53* mutations**.** Details on cytogenetic analysis using Single-nucleotide polymorphism (SNP) HD Array are shown in Supplementary Table S9. MP10: *TP53*^{G245S} clonal expansion without leukemic transformation in PMF. *TP53*^{G245S} development was monitored by Sanger sequencing. Diagnostic sample and two other samples (green and purple mark) were analyzed by NGS, for detail see Supplementary Table 1. Chromosome 17 analysis: cn-LOH(17)(p13.3p11.2) in 2nd and 3rd SNP array. MP68: *JAK2*^{wt}*TP53*^{wt}-AML outside multiple *JAK2*^{V617F}*TP53*^{mut}-clones. After transient increase of *JAK2*$^{V617F/wt}$*TP53*^{R248Q} subclone from 8 to 16%, all *TP53*^{mut} clones decreased accompanied by *JAK2*^{V617F} burden drop and transformation to sAML 3.5y from study enrollment. SNP array showed no aberrations on chromosome 17. JAK22: *JAK2*^{V617F}*TP53*$^{L289fs/L289fs}$ sAML with complex karyotype changes including cn-LOH (17)(p13.3p11.2) developed from PV secondary to diffuse large B-cell lymphoma (DLBCL). Single mutation *TP53*^{L289fs} was present at PV diagnosis (2%) and expanded in blast transformation. 186A: sAML with unknown *TP53* status developed in *JAK2*^{mut} ET 2.9y after study enrollment when *TP53* mutation was present with VAF 8.3%. JAK453: *JAK2*^{V617F}*TP53*$^{R175H/-}$ sAML with complex karyotype changes including del (17p) developed 3.6y after study enrollment at PMF diagnosis when no *TP53* mutation and karyotype changes were found.

therapies, the frequency in the general MPN cohort was out of the scope. However, some information may be gained from our analysis of 48 consecutive newly diagnosed MPNs examined partially within the untreated cohort and partially as retrospective samples (data not shown): only one mutation ⩾0.2% was found (2.1%). This observation, together with the slow increase in mutation load during disease course and strong age bias, points to the fact that *TP53* mutations are probably rare in general cohorts at diagnosis.

We detected no mutation ⩾0.2% in 70 patients below 55y. In contrast, 41/179 (22.9%) patients above 65y carried *TP53* mutation. This agrees with the hypothesis that *TP53* mutations arose spontaneously and accumulate with age, as described in the elderly population without hematological abnormalities.[47] Higher age brings inherent risks of MPN transformation[1] and less vital progenitor pools in the elderly may favor cells carrying oncogenic mutations both under DNA-damaging and normal conditions.[48] On the other hand, younger patients are a subgroup with the perspective of decades living with clonally shifted hematopoiesis and using cytoreductive drugs and should be examined in detail.

It has been described that not only single accidentally arising *TP53*-mutated clones but several coexisting in parallel may be present in myeloid precursors before expansion.[49] We detected more than one mutation in one third of cases. This phenomenon, described as ‘convergence’,[50] occurs for example, in chronic lymphocytic leukemia (CLL)[51] and points to a selective pressure favoring the mutations in some but not all patients. In MPN, one may consider either the pressure of cytoreductive therapy, since multiple mutations tended to be more frequent in HU-treated patients, or, possibly, the effort of non-vital HPSC to survive and proliferate. The clonal competition among individual *TP53*-mutated subclones is difficult to foresee and likely depends on accompanying defects; hot-spot mutations with documented oncogenic properties may be overgrown by subclones carrying variants with lower oncogenic potential (for example, loss-of function mutations).[25,26]

Table 3. Monitoring *TP53* mutations over time

Sample ID	*Retrospective (R) /prospective (P) analysis*	*First available sample: time from dg (y)*	*Study enrollment: time from dg (years)*	*Last available sample: time from dg (years)*	*Total follow-up (years)*	*MPN therapy before study enrollment*	*Therapy after study enrollment*	*Mutation ⩾0.1% in dg sample*	*The development of most abundant mutation (%)* [a]	*Mutation development during follow-up*
186A	R	0.0	15.0	15.0	15.0	IFN	HU[b]	yes	0.4-**8.3**-NA	Increase
MP15	P/R	0.2	7.0	11.9	11.5	HU, IFN	IFN	no	0-0.8-2.1-2.6-3.8-**4.4**-10.7-11.3-11.2(W) 13.8(G)	
MP10	P/R	0.0	6.4	9.8	9.8	HU	HU	no	0-**10.1**-85.5	
JAK1716	P/R	6.0	9.3	16.2	10.2	IFN	IFN → HU	NA	0-0.1-0.1-**0.2**-0.7-2.2-2-2.2	
MP326	P/R	0.0	6.7	9.1	9.1	HU	HU	no	0-**0.6**-0.5-0.5	
MP96	P/R	0.0	5.4	8.8	8.8	HU	HU	no	0-**0.5**-0.6	
MP168	P/R	2.4	7.1	10.5	8.1	HU	HU	NA	0.1-**1**-0.5-0.6	
MP319	P/R	0.0	5.2	7.5	7.5	HU, ANA	HU, ANA	yes	0.1-**0.4**-0.4-0.8	
MP369	P	0.0	0.0	7.0	7.0	none[c]	HU	NA	NA-**0.13**-1.4	
65A	P	13.2	13.2	19.6	6.5	IFN, ANA	IFN, ANA	NA	NA-**1.7**-5.4	
MP327	P/R	4.9	10.4	11.2	6.3	HU	HU	NA	0-0.1-**0.5**-0.5	
JAK22	P	0.0	0.0	5.0	5.0	none[c]	HU	yes	NA-**2.0**-46.1	
MP273	P	9.3	9.3	12.0	2.8	HU	HU	NA	NA-**0.3/0**-0.3/1.7	
MP317	P	5.5	5.5	6.0	0.5	HU	HU	NA	NA-**0.8**-1.9	
MP289	P/R	15.2	22.1	24.6	9.3	HU, IFN	none	NA	0.2/1.4-**3.3/0.7**-4.4/0.4-6.3/0.6-3.5/0.4[d]	Increase/decrease
MP68	P/R	0.0	4.8	8.3	8.3	HU, ANA	HU → none	no	0-**6.9**-8.8-10.7-11.7-16.9-9.6-2.7	
MP315	P/R	4.6	9.1	11.5	6.9	IFN	IFN	NA	0.2-**0.8**-0.4-0.2	
MP230	P	8.0	8.0	9.2	1.2	HU	HU	NA	NA-**0.5**-2.3-1.3	
MP189	P/R	6.9	11.5	14.6	7.7	ANA	HU, ANA	NA	3.9-2.8-2.5	Stable
MP155	P/R	5.7	10.2	13.0	7.3	ANA	ANA	NA	0.4-**0.2**-0.2	
MP229	P	9.4	9.4	12.4	3.0	HU	HU, ANA	NA	NA-**1**-0.5-0.6	
MP302	P	19.3	19.3	21.7	2.4	busulfan → HU	HU	NA	NA-**0.4**-0.4-0.7	
MP329	P	13.5	13.5	15.7	2.2	HU	HU, ANA	NA	NA-**2.6**-1.9-3.1/3.0	
MP324	P	21.2	21.2	22.0	0.7	HU	HU	NA	NA-0.3-0.4	
221A	P/R	0.0	15.0	24.6	24.6	IFN	IFN	yes	10.2/ND-**2.2/0.6**-0.7/2.0[d]	Decrease
MP2	P/R	12.1	16.3	21.7	9.6	HU, IFN, ANA	HU, ANA	NA	11.5-**10.6**-11.6-2.9-2.2-1.9-2.1	
MP63	P/R	1.5	6.6	10.0	8.5	HU	HU	NA	0-**0.2/0.1**-0.1/0.2-0/0[d]	
MP160	P/R	1.2	5.1	7.1	5.8	HU	HU	NA	0.5-**0.2**-0	
MP307	P	8.6	8.6	10.2	1.6	HU	HU	NA	**0.2**-0	
MP314	P/R	14.8	19.4	21.9	7.1	busulfan → HU	HU	NA	3.3/0.2-**1.3/0.4**-0.6/0.9-0.2/0.2[d]	
MP345	P/R	0.0	4.2	6.3	6.3	HU	HU	yes	0.1-**1.1**-0.9-0.5-0.6	

Abbreviations: G, granulocytes; *NA*, not available; W, leukocytes. Mutations with highest VAF are shown. "Study enrollment" describes the sampling from which the mutation was identified. For over-time monitoring and validation of previously identified mutation, cut-off 0.1% was applied (minimal coverage per base ⩾10000). VAF bellow 0.1% considered as a background (0%). Development was cathegorised as follows: increase—VAF twofold increase between first and last sample or no mutation at diagnosis; decrease—VAF decrease in VAF to half between first and last sample or no mutation at last sampling; increase/decrease—increase followed by decrease; stable—other. *y*, years; *NA*, not available; G, granulocytes; W, leukocytes. [a]Result from study enrollment is highlighted. [b]Samples not available. [c]Mutation identified at diagnosis. [d]Two mutations with the highest VAFs in distinct samplings.

The murine model and clinical observations pointed to the leukemogenic potential of *JAK2*^{V617F} overexpression in *TP53*-null background;[23,52] *JAK2*^{wt}*TP53*^{mut} AML following *JAK2*^{mut}-MPN is however not exceptional.[22] We observed no clear evidence supporting the leukemogenic potential of *TP53*^{mut} and *JAK2*^{V617F} combination. Admittedly, the *JAK2* mutation was homozygous neither in patient MP68 developing *JAK2*^{wt}-AML alongside multiple *JAK2*^{mut}*TP53*^{mut} subclones nor patient MP10 with complete *TP53* loss within the *JAK2*^{V617F} population.

TP53/17p-aberrant post-MPN AML has been repeatedly suggested - but never independently proven - to be associated with HU therapy.[4,12,22,36] Several findings support possible *TP53*^{mut}-subclone selection by HU: (1) HU blocks cell division via ribonucleotide reductase inhibition, resulting in dNTP depletion.[34] Replication stress then activates p53 and cell cycle arrest although these processes' p53 dependence is controversial and dose-dependent.[35,53,54] (2) The expansion of low-burden *TP53*^{mut}-subclones under *TP53*-triggering therapy was shown in CLL,[26–28] myelodysplastic syndrome[29] and secondary AML.[32] Further, HSPC competition triggered by low-level DNA damage in the murine model led to *TP53*$^{+/+}$ being outcompeted by *TP53*$^{+/-}$ cells via senescence-like changes.[33] Similarly, clinically relevant low- (but not high) level replication stress induced p53-dependent senescence-like arrest in fibroblasts and led to *TP53*-aberrant subpopulation selection.[53] We suppose that if there was a proliferative and/or survival advantage favoring *TP53*^{mut}-subclones during HU treatment in MPN, we would have observed a pronounced difference in the abundance and incidence of low-burden *TP53* mutations after several years of therapy. Contrary to this assumption and observations from *in vitro* and *in vivo* models, we saw no significant age-independent difference between patients treated with HU and non-HU therapies; moreover, the mutations were present even if no cytoreductive therapy was given. Although long-term prospective monitoring of patients with *TP53* mutations on various therapies is necessary to fully exclude any HU impact on the second allele loss and clonal expansion, the case of patient MP10 further weakens the advantage of MPN cells with aberrant p53 during HU therapy. While the *TP53*$^{G245S/G245S}$ clone replaced *TP53*^{wt} myelopoiesis, the patient did not show any signs of HU resistance, blood counts remained unchanged and no disease progression was observed for next 2y, despite the patient being treated with a constant HU dose. The clonal competition in MPN both under and without HU treatment may differ from experimental data for several reasons: (1) chronic low-level replication stress may affect HPSC compartment differently to single dose DNA damage; (2) in highly sensitive myeloid cells, threshold for p53-dependent selection induced by low-level replication stress[55] may be shifted; (3) competition may be affected by presence of oncogenic mutations; (4) p53 activity in MPN cells may not fully correspond to that of artificially manipulated p53 in murine and cell line models. In contrast, there seems to be a difference between subclones with monoallelic and biallelic p53 defects, first increasing slowly with the latter expanding rapidly.[11]

We showed that relatively high proportion of older-age MPN patients carry low-burden *TP53* mutations. In contrast to retrospective reports, we did not observe correlation with disease progression accompanied with *TP53* mutation clonal expansion. However, our study was not designed with the primary goal to assess the prognostic impact of low-burden *TP53* mutations as we were aware that larger cohorts and long follow-up is definitely required to address this issue completely.

The competition between an in-theory-adverse minor subclone and a major population may be more complex than one may assume from the retrospective studies. Observations on minor *TP53* mutations in CLL, another non-acute hematological malignancy, show that the mutation does not have to expand despite several specific therapy lines in some patients.[26] Further, a *TP53*-mutated subclone outgrowth occurs very rarely in patients that remain untreated, that is, strong selection pressure in the form of chemotherapy dramatically changes the *TP53*-wt vs *TP53*-mut clonal competition.[26,28] Apparently, cytoreduction regimens currently used in MPN do not create such strong pressure. More likely, other intrinsic factors (genomic instability, hematopoiesis exhaustion) lead to disease progression only in a proportion of patients carrying minor *TP53*-mutated clone.

Importantly, 3 out of 4 patients with clonal evolution (blast transformation or mut-*TP53* clonal expansion) carried *TP53* mutation(s) with VAF ⩾ 5%. This indicates that *TP53* mutations increased to a certain level may be the marker of clonal instability or even a poor prognosis, as demonstrated by shorter OS in patients with mutations ⩾ 5% VAF in our study which however cannot be attributed to *TP53* mutation expansion followed by leukemic transformation. Of note, we recorded 6 patients whose prospective samples were available and VAF exceeded 5% at some point, but none developed *TP53*-mutated sAML during the follow-up. Moreover, one patient with no mutations ⩾ 0.1% VAF developed *TP53*-mutated sAML within 3.6y.

To conclude, we show that minor *TP53* mutations are present in a significant proportion of MPN patients and their presence is strongly associated with age. We did not see any significant age-independent association with hydroxyurea therapy, disease type or MPN driver gene mutations. We also show that even a fully expanded biallelic hotspot mutation, leading to complete loss of *TP53* transactivation activity,[45,46] does not *a priori* lead to leukemic transformation. Despite our findings do not support the assumption that there is unequivocal relation between *TP53*-mutated subclones, HU cytoreduction and leukemic transformation in MPN, larger sample sizes are warranted to definitively address this. *TP53* minor mutations in MPN undoubtedly represent a pool for further clonal evolution; however their prognostic and predictive utilization requires further investigation to identify which patients are at risk and whether any risk factors are preventable.

CONFLICT OF INTEREST

HG: AOP Orphan, Calgene, Novartis—Consultancy, Honoraria, Research Funding and Speakers Bureau; JC: Honoraria and Speakers Bureau; Baxalta-Consultancy and Honoraria. MJ: Research Funding from AOP Orphan and Novartis. KR: Research Funding from AOP Orphan, a member on an entity's Board of Directors or advisory committees in Qiagen. PM: AOP Orphan and Novartis—Consultancy, Honoraria, Research Funding and Speakers Bureau. DM: AOP Orphan, Novartis—Consultancy and Honoraria. The remaining authors declare no conflict of interest.

ACKNOWLEDGEMENTS

We kindly thank the staff of local hospitals in Kromeriz, Znojmo, Breclav, Boskovice, Kyjov, Uherske Hradiste, Ostrava, Hodonin, Trebic, Nove Mesto na Morave for providing samples and clinical data, Hana Skabrahova for organizing blood collections, Jan Palecek for providing us methodical help and Matthew Smith for language editing. Supported by projects of Faculty of Medicine, Masaryk University MUNI/A/1106/2016 and ROZV/24/LF/2016 (SPav and JMal), by projects of MH CR 16-29447A, MEYS CR LM2015064 EATRIS, CEITEC 2020 (LQ1601) and TACR TE02000058. Also supported by Czech Leukemia Study Group for Life (CELL) and Genomics Core Facility CEITEC under MEYS CR project LM2011020.

REFERENCES

1 Finazzi G, Caruso V, Marchioli R, Capnist G, Chisesi T, Finelli C *et al.* Acute leukemia in polycythemia vera: an analysis of 1638 patients enrolled in a prospective observational study. *Blood* 2005; **105**: 2664–2670.

2 Kiladjian JJ, Chevret S, Dosquet C, Chomienne C, Rain JD. Treatment of polycythemia vera with hydroxyurea and pipobroman: final results of a randomized trial initiated in 1980. *J Clin Oncol* 2011; **29**: 3907–3913.

3 Berk PD, Goldberg JD, Silverstein MN, Weinfeld A, Donovan PB, Ellis JT *et al.* Increased incidence of acute leukemia in polycythemia vera associated with chlorambucil therapy. *N Engl J Med* 1981; **304**: 441–447.

4 Sterkers Y, Preudhomme C, Laï JL, Demory JL, Caulier MT, Wattel E *et al.* Acute myeloid leukemia and myelodysplastic syndromes following essential thrombocythemia treated with hydroxyurea: high proportion of cases with 17p deletion. *Blood* 1998; **91**: 616–622.

5 Björkholm M, Derolf AR, Hultcrantz M, Kristinsson SY, Ekstrand C, Goldin LR *et al.* Treatment-related risk factors for transformation to acute myeloid leukemia and myelodysplastic syndromes in myeloproliferative neoplasms. *J Clin Oncol* 2011; **29**: 2410–2415.

6 Tefferi A. Is hydroxyurea leukemogenic in essential thrombocythemia? *Blood* 1998; **92**: 1459–1460, author reply 1460–1451.

7 Nand S, Stock W, Godwin J, Fisher SG. Leukemogenic risk of hydroxyurea therapy in polycythemia vera, essential thrombocythemia, and myeloid metaplasia with myelofibrosis. *Am J Hematol* 1996; **52**: 42–46.

8 Liozon E, Brigaudeau C, Trimoreau F, Desangles F, Fermeaux V, Praloran V *et al.* Is treatment with hydroxyurea leukemogenic in patients with essential thrombocythemia? An analysis of three new cases of leukaemic transformation and review of the literature. *Hematol Cell Ther* 1997; **39**: 11–18.

9 Baz W, Najfeld V, Yotsuya M, Talwar J, Terjanian T, Forte F. Development of myelodysplastic syndrome and acute myeloid leukemia 15 years after hydroxyurea use in a patient with sickle cell anemia. *Clin Med Insights Oncol* 2012; **6**: 149–152.

10 Björkholm M, Hultcrantz M, Derolf Å. Leukemic transformation in myeloproliferative neoplasms: therapy-related or unrelated? *Best Pract Res Clin Haematol* 2014; **27**: 141–153.

11 Lundberg P, Karow A, Nienhold R, Looser R, Hao-Shen H, Nissen I *et al.* Clonal evolution and clinical correlates of somatic mutations in myeloproliferative neoplasms. *Blood* 2014; **123**: 2220–2228.

12 Thoennissen NH, Krug UO, Lee DH, Kawamata N, Iwanski GB, Lasho T *et al.* Prevalence and prognostic impact of allelic imbalances associated with leukemic transformation of Philadelphia chromosome-negative myeloproliferative neoplasms. *Blood* 2010; **115**: 2882–2890.

13 Abdel-Wahab O, Manshouri T, Patel J, Harris K, Yao J, Hedvat C *et al.* Genetic analysis of transforming events that convert chronic myeloproliferative neoplasms to leukemias. *Cancer Res* 2010; **70**: 447–452.

14 Zhang SJ, Rampal R, Manshouri T, Patel J, Mensah N, Kayserian A *et al.* Genetic analysis of patients with leukemic transformation of myeloproliferative neoplasms shows recurrent SRSF2 mutations that are associated with adverse outcome. *Blood* 2012; **119**: 4480–4485.

15 Ding Y, Harada Y, Imagawa J, Kimura A, Harada H. AML1/RUNX1 point mutation possibly promotes leukemic transformation in myeloproliferative neoplasms. *Blood* 2009; **114**: 5201–5205.

16 Green A, Beer P. Somatic mutations of IDH1 and IDH2 in the leukemic transformation of myeloproliferative neoplasms. *N Engl J Med* 2010; **362**: 369–370.

17 Zhao Z, Zuber J, Diaz-Flores E, Lintault L, Kogan SC, Shannon K *et al.* p53 loss promotes acute myeloid leukemia by enabling aberrant self-renewal. *Genes Dev* 2010; **24**: 1389–1402.

18 Haferlach C, Dicker F, Herholz H, Schnittger S, Kern W, Haferlach T. Mutations of the TP53 gene in acute myeloid leukemia are strongly associated with a complex aberrant karyotype. *Leukemia* 2008; **22**: 1539–1541.

19 Harutyunyan A, Klampfl T, Cazzola M, Kralovics R. p53 lesions in leukemic transformation. *N Engl J Med* 2011; **364**: 488–490.

20 Neri A, Fracchiolla NS, Radaelli F, Boletini A, Ribera S, Migliorini C *et al.* p53 tumour suppressor gene and RAS oncogenes: molecular analysis in the chronic and leukaemic phases of essential thrombocythaemia. *Br J Haematol* 1996; **93**: 670–673.

21 Gaidano G, Guerrasio A, Serra A, Carozzi F, Cambrin GR, Petroni D *et al.* Mutations in the P53 and RAS family genes are associated with tumor progression of BCR/ABL negative chronic myeloproliferative disorders. *Leukemia* 1993; **7**: 946–953.

22 Beer PA, Delhommeau F, LeCouédic JP, Dawson MA, Chen E, Bareford D *et al.* Two routes to leukemic transformation after a JAK2 mutation-positive myeloproliferative neoplasm. *Blood* 2010; **115**: 2891–2900.

23 Rampal R, Ahn J, Abdel-Wahab O, Nahas M, Wang K, Lipson D *et al.* Genomic and functional analysis of leukemic transformation of myeloproliferative neoplasms. *Proc Natl Acad Sci USA* 2014; **111**: E5401–5410.

24 Robles A, Harris C. Clinical outcomes and correlates of TP53 mutations and cancer. *Cold Spring Harb Perspect Biol* 2010; **2**: a001016.

25 Malcikova J, Pavlova S, Kozubik KS, Pospisilova S. TP53 mutation analysis in clinical practice: lessons from chronic lymphocytic leukemia. *Human Mutation* 2014; **35**: 663–671.

26 Malcikova J, Stano-Kozubik K, Tichy B, Kantorova B, Pavlova S, Tom N *et al.* Detailed analysis of therapy-driven clonal evolution of TP53 mutations in chronic lymphocytic leukemia. *Leukemia* 2015; **29**: 877–885.

27 Zenz T, Krober A, Scherer K, Habe S, Buhler A, Benner A *et al.* Monoallelic TP53 inactivation is associated with poor prognosis in chronic lymphocytic leukemia: results from a detailed genetic characterization with long-term follow-up. *Blood* 2008; **112**: 3322–3329.

28 Rossi D, Khiabanian H, Spina V, Ciardullo C, Bruscaggin A, Famà R *et al.* Clinical impact of small TP53 mutated subclones in chronic lymphocytic leukemia. *Blood* 2014; **123**: 2139–2147.

29 Jädersten M, Saft L, Pellagatti A, Göhring G, Wainscoat JS, Boultwood J *et al.* Clonal heterogeneity in the 5q- syndrome: p53 expressing progenitors prevail during lenalidomide treatment and expand at disease progression. *Haematologica* 2009; **94**: 1762–1766.

30 Belickova M, Vesela J, Jonasova A, Pejsova B, Votavova H, Merkerova MD *et al.* TP53 mutation variant allele frequency is a potential predictor for clinical outcome of patients with lower-risk myelodysplastic syndromes. *Oncotarget* 2016; **7**: 36266–36279.

31 Marusyk A, Porter CC, Zaberezhnyy V, DeGregori J. Irradiation selects for p53-deficient hematopoietic progenitors. *PLoS Biol* 2010; **8**: e1000324.

32 Wong TN, Ramsingh G, Young AL, Miller CA, Touma W, Welch JS *et al.* Role of TP53 mutations in the origin and evolution of therapy-related acute myeloid leukaemia. *Nature* 2015; **518**: 552–555.

33 Bondar T, Medzhitov R. p53-mediated hematopoietic stem and progenitor cell competition. *Cell Stem Cell* 2010; **6**: 309–322.

34 Krakoff IH, Brown NC, Reichard P. Inhibition of ribonucleoside diphosphate reductase by hydroxyurea. *Cancer Res* 1968; **28**: 1559–1565.

35 Nayak BK, Das GM. Stabilization of p53 and transactivation of its target genes in response to replication blockade. *Oncogene* 2002; **21**: 7226–7229.

36 Furgerson JL, Vukelja SJ, Baker WJ, O'Rourke TJ. Acute myeloid leukemia evolving from essential thrombocythemia in two patients treated with hydroxyurea. *Am J Hematol* 1996; **51**: 137–140.

37 Vardiman JW, Thiele J, Arber DA, Brunning RD, Borowitz MJ, Porwit A *et al.* The 2008 revision of the World Health Organization (WHO) classification of myeloid neoplasms and acute leukemia: rationale and important changes. *Blood* 2009; **114**: 937–951.

38 van Dongen JJ, Langerak AW, Brüggemann M, Evans PA, Hummel M, Lavender FL *et al.* Design and standardization of PCR primers and protocols for detection of clonal immunoglobulin and T-cell receptor gene recombinations in suspect lymphoproliferations: report of the BIOMED-2 Concerted Action BMH4-CT98-3936. *Leukemia* 2003; **17**: 2257–2317.

39 Vandenbroucke I, Van Marck H, Verhasselt P, Thys K, Mostmans W, Dumont S *et al.* Minor variant detection in amplicons using 454 massive parallel pyrosequencing: experiences and considerations for successful applications. *Biotechniques* 2011; **51**: 167–177.

40 Varley JM. Germline TP53 mutations and Li-Fraumeni syndrome. *Hum Mutat* 2003; **21**: 313–320.

41 Forbes SA, Beare D, Gunasekaran P, Leung K, Bindal N, Boutselakis H *et al.* COSMIC: exploring the world's knowledge of somatic mutations in human cancer. *Nucleic Acids Res* 2015; **43**(Database issue): D805–811.

42 R_Core_Team. R: A Language and Environment for Statistical Computing, 2015. Available at https://www.R-project.org.

43 Olcaydu D, Harutyunyan A, Jäger R, Berg T, Gisslinger B, Pabinger I *et al.* A common JAK2 haplotype confers susceptibility to myeloproliferative neoplasms. *Nat Genet* 2009; **41**: 450–454.

44 Klampfl T, Gisslinger H, Harutyunyan AS, Nivarthi H, Rumi E, Milosevic JD *et al.* Somatic mutations of calreticulin in myeloproliferative neoplasms. *N Engl J Med* 2013; **369**: 2379–2390.

45 Bouaoun L, Sonkin D, Ardin M, Hollstein M, Byrnes G, Zavadil J *et al.* TP53 variations in human cancers: new lessons from the IARC TP53 Database and Genomics Data. *Hum Mutat* 2016; **37**: 865–876.

46 Soussi T, Hamroun D, Hjortsberg L, Rubio-Nevado JM, Fournier JL, Béroud C. MUT-TP53 2.0: a novel versatile matrix for statistical analysis of TP53 mutations in human cancer. *Hum Mutat* 2010; **31**: 1020–1025.

47 Jaiswal S, Fontanillas P, Flannick J, Manning A, Grauman PV, Mar BG *et al.* Age-related clonal hematopoiesis associated with adverse outcomes. *N Engl J Med* 2014; **371**: 2488–2498.

48 Marusyk A, DeGregori J. Declining cellular fitness with age promotes cancer initiation by selecting for adaptive oncogenic mutations. *Biochim Biophys Acta* 2008; **1785**: 1–11.

49 Beer PA, Ortmann CA, Stegelmann F, Guglielmelli P, Reilly JT, Larsen TS *et al.* Molecular mechanisms associated with leukemic transformation of MPL-mutant myeloproliferative neoplasms. *Haematologica* 2010; **95**: 2153–2156.

50 Gerlinger M, Rowan AJ, Horswell S, Larkin J, Endesfelder D, Gronroos E *et al.* Intratumor heterogeneity and branched evolution revealed by multiregion sequencing. *N Engl J Med* 2012; **366**: 883–892.

51 Jethwa A, Hüllein J, Stolz T, Blume C, Sellner L, Jauch A *et al.* Targeted resequencing for analysis of clonal composition of recurrent gene mutations in chronic lymphocytic leukaemia. *Br J Haematol* 2013; **163**: 496–500.

52 Tsuruta-Kishino T, Koya J, Kataoka K, Narukawa K, Sumitomo Y, Kobayashi H *et al.* Loss of p53 induces leukemic transformation in a murine model of Jak2 V617F-driven polycythemia vera. *Oncogene* 2017; **36**: 3300–3311.

53 Marusyk A, Wheeler LJ, Mathews CK, DeGregori J. p53 mediates senescence-like arrest induced by chronic replicational stress. *Mol Cell Biol* 2007; **27**: 5336–5351.

54 Gottifredi V, Shieh S, Taya Y, Prives C. p53 accumulates but is functionally impaired when DNA synthesis is blocked. *Proc Natl Acad Sci USA* 2001; **98**: 1036–1041.

55 Marusyk A, DeGregori J. Replicational stress selects for p53 mutation. *Cell Cycle* 2007; **6**: 2148–2151.

Supplementary Information accompanies this paper on the Leukemia website (http://www.nature.com/leu)

Leukemia (2021) 35:1500–1505
https://doi.org/10.1038/s41375-020-01093-1

LETTER

Lymphoma

STAT3 and *TP53* mutations associate with poor prognosis in anaplastic large cell lymphoma

Cosimo Lobello[1] · Boris Tichy[1] · Vojtech Bystry[1] · Lenka Radova[1] · Daniel Filip[1,2] · Marek Mraz[1,2] · Ivonne-Aidee Montes-Mojarro[3] · Nina Prokoph[4] · Hugo Larose[4] · Huan-Chang Liang[5] · Geeta G. Sharma[6] · Luca Mologni[6] · David Belada[7] · Katerina Kamaradova[8] · Falko Fend[3] · Carlo Gambacorti-Passerini[6] · Olaf Merkel[5] · Suzanne D. Turner[1,4] · Andrea Janikova[2] · Sarka Pospisilova[1,2]

Received: 7 April 2020 / Revised: 1 October 2020 / Accepted: 9 November 2020 / Published online: 27 November 2020

To the Editor:

Systemic anaplastic large cell lymphoma (sALCL) encompasses two distinct clinical entities of T-cell non-Hodgkin lymphoma: anaplastic lymphoma kinase-positive (ALK+) ALCL and ALK-negative (ALK−) ALCL. These entities are characterized by either the presence or absence of an ALK translocation. It has been reported that ALK+ ALCL has a better prognosis compared to ALK−, with a 5-year overall survival (OS) of 70–80% versus 40–60%, respectively, [1–3]. Furthermore, more than 30% of ALK+ ALCL patients relapse [4, 5]. Despite the distinction between the two sALCL subtypes, frontline treatment for adults is similar and is based on CHOP or CHOEP, instead pediatric ALCL patients are mainly treated following the ALCL99 protocol [6–8]. Whilst high-throughput genomic studies in sALCL have shown recurrent genetic alterations, their association with outcome has not been fully investigated [9–13].

In this study, the mutational landscape of sALCL patient tumors was investigated to discover potential biomarkers that may improve risk stratification and patient management.

A cohort of 82 sALCL patient tumors (47 ALK+ and 35 ALK−) and 6 ALCL cell lines (4 ALK+, 2 ALK−) (Table S1) were subjected to deep targeted next-generation sequencing analyzing the whole coding regions of 275 cancer related genes (Table S2). The average depth achieved across all the samples sequenced was ~2000×. Sequencing data are available at Sequence Read Archive (https://www.ncbi.nlm.nih.gov/sra/, SRA identifier PRJNA602225).

Male subjects were predominant in both subgroups of our cohort, 57.4% in ALK+ versus 67.6% in ALK−. ALK+ patients were significantly younger than ALK− patients with an average age of 22.7 (3–61) and 55.2 (27–81) years, respectively. ALK+ ALCL patients had a longer survival than ALK− ALCL with a 7-year OS of 77.6% and 46.7%, respectively, and with 7-year progression free survival (PFS) being comparable at 58.7% for ALK+ and 44.1% for ALK− patients (Fig. S1). The first line of treatment for all the adult patients was systemic chemotherapy, and most of the childhood ALK+ ALCL patients (80%) were treated following the ALCL99 or ALCL98 protocols. Although ALK+ patients have a longer

---

Supplementary information The online version of this article (https://doi.org/10.1038/s41375-020-01093-1) contains supplementary material, which is available to authorized users.

✉ Sarka Pospisilova
sarka.pospisilova@ceitec.muni.cz

[1] Center of Molecular Medicine, Central European Institute of Technology (CEITEC), Masaryk University, Brno, Czech Republic

[2] Department of Internal Medicine—Hematology and Oncology, University Hospital Brno and Medical Faculty MU, Brno, Czech Republic

[3] Institute of Pathology and Neuropathology and Comprehensive Cancer Center Tübingen, Eberhard Karls University, Tübingen, Germany

[4] Division of Cellular and Molecular Pathology, Department of Pathology, University of Cambridge, Cambridge, UK

[5] Department of Pathology, Medical University of Vienna, Vienna, Austria

[6] Department of Medicine and Surgery, University of Milano-Bicocca, Monza, Italy

[7] 4th Department of Internal Medicine—Hematology, Charles University Hospital and Faculty of Medicine, Hradec Králové, Czech Republic

[8] Fingerland Department of Pathology, Charles University Hospital and Faculty of Medicine, Hradec Králové, Czech Republic

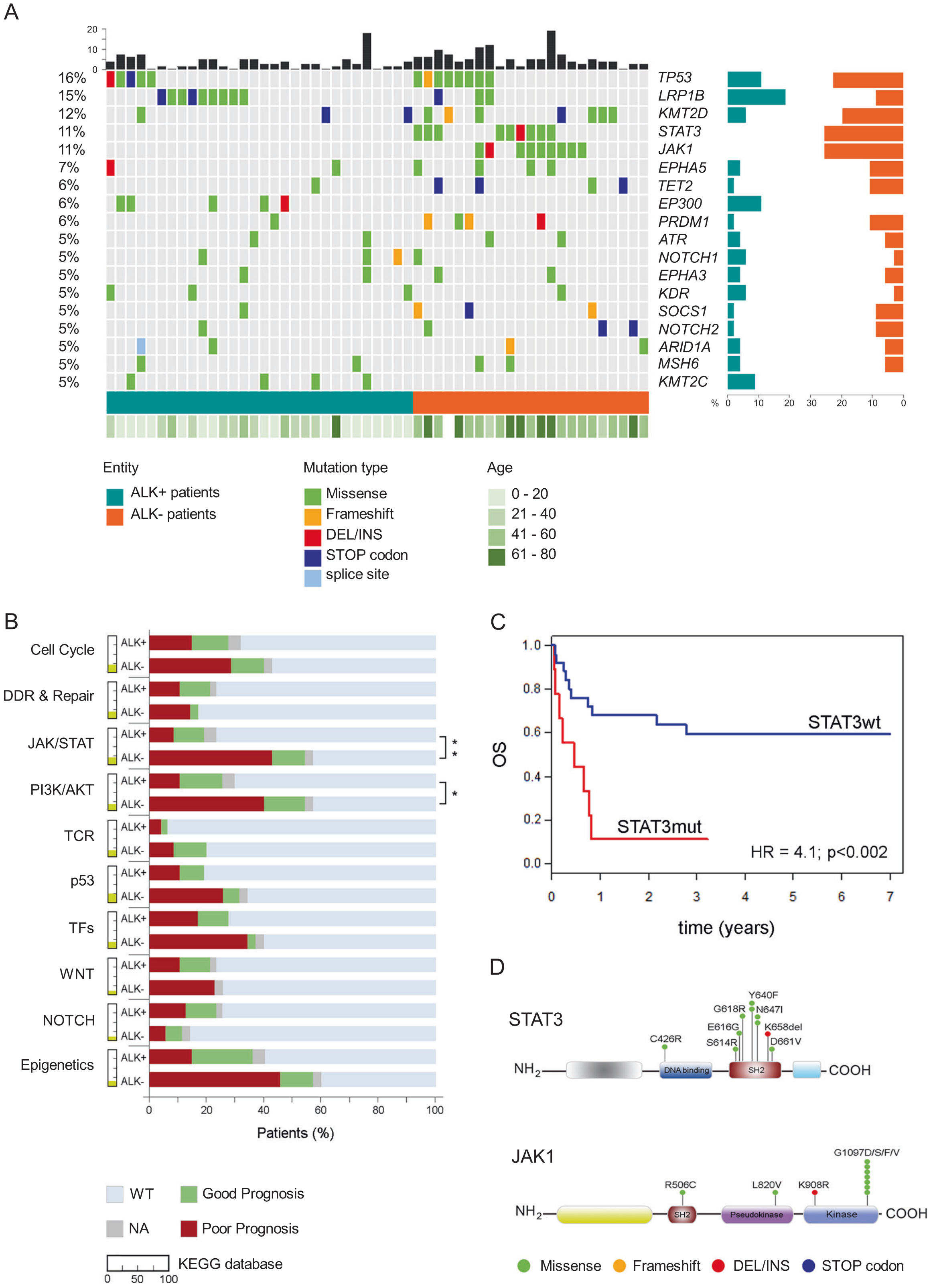

OS, more than 30% relapsed after first-line treatment. Among the 275 genes analyzed, we identified 148 (54%) genes harboring at least one mutation throughout the entire cohort; 132 genes among the patients and 43 among the cell lines, with 27 genes in common (Fig. S2, Table S3). Overall, 72 out of 82 (88%) patients carried at least one

◀ **Fig. 1** Mutational landscape in sALCL reveals prognostic biomarkers. **a** Oncoplot shows the genes mutated in at least 5% of the entire cohort. The percentage is shown on the left axis. Each column represents a patient, ALK+ in dark green and ALK− ALCL patients in dark orange. The black bars on the top represent the number of mutated genes in each patient. On the right axis, the frequency of mutated gene in ALK+ (dark green) and ALK− (dark orange) ALCL patients. The green bar on the bottom shows the age of each patient. Mutation types are represented in different colors as shown in the legend. **b** Percentage of patients harboring at least one mutated gene in ten biological pathways. The yellow colored portion next to each pathway indicates the percentage of genes present in our panel that belong to that specific pathway according to the KEGG database. For each pathway shown, the patients are divided according to prognosis; red: patients with poor prognosis; green: patients with good prognosis; gray: patients for whom clinical information is not available (NA); light blue patients wildtype (WT) that do not harbor mutated genes in that specific pathway. The patients are represented as percentage of the total. DDR and repair DNA damage response and repair pathway, TFs transcription factors. Fisher's exact test: $*p < 0.05$, $**p < 0.01$ and $***p < 0.001$. **c** 7-year OS of ALK− ALCL patients according to *STAT3* status: *STAT3* mutated (red) versus *STAT3* wt (blue). *P* values and hazard ratios (HR) shown were determined by the Cox proportional hazards model. **d** Schematic representation of STAT3 and JAK1 domains and the position of the variants.

mutation within the genes analyzed. We detected an average of 4.2 mutations per patient in ALK− ALCL and an average of 2.7 in ALK+ ALCL. The most recurrently mutated gene in the entire cohort was *TP53* found in 16% of sALCL patients (11% ALK+, 23% ALK− and in all ALK+ cell lines). Interestingly, for the ALK+ group, mutated *TP53* was more frequent in young patients ($p < 0.04$). *LRP1B* was prevalently mutated in ALK+ patients (19%) and in three cell lines. *STAT3* and *JAK1* were mutated solely in ALK− ALCL, both with a prevalence of 26%, and were the most mutated genes in this group (Fig. 1a). Recurrent mutations were detected in epigenetic modifier genes also recently reported to be frequently mutated in BIA-ALCL [14]. *KMT2D* and *TET2* were found mutated in ALCL patients regardless of ALK status and *EP300* and *KMT2C* only in ALK+ patients. Pathway enrichment analysis showed a significant enrichment in mutated genes involved in JAK/STAT ($p < 0.003$) and PI3K/AKT signaling pathways ($p < 0.02$) for ALK− ALCL compared with ALK+ ALCL (Fig. 1b). We investigated possible correlations between the existence of mutations in the most mutated genes and the clinical characteristics of our cohort. Poor prognostic outcome was defined as patients meeting at least one of the following criteria: deceased, unresponsive to treatment and/or disease relapse. The most recurrently mutated genes in the poor prognostic sub-cohort independent of ALK status were *TP53* (27%), *STAT3* (24%), *EPHA5* (16%), *JAK1* (16%), *PRDM1* (13.5%), *LRP1B* (11%) and *KMT2D* (11%). Considering only refractory/relapsed ALCL patients, mutations within *TP53* (28%) and *EPHA5* (19%) were the most common (Table S4). In relation to the prognosis, ALK+ patients did not show any significant difference in the signaling pathways affected by mutations. On the contrary, the JAK/STAT ($p < 0.005$) and PI3K/AKT pathways ($p < 0.036$) were enriched in ALK− ALCL patients with an inferior outcome (Fig. 1b). Pathogenetic variants of *STAT3* were detected in 9/35 (26%) of ALK− ALCL patients. Mutations were located mainly within the SH2 domain (S614R, E616G, Y640F, N647I, K658delinsNM and D661V) and in one case within the DNA binding domain (C426R). Mutated *JAK1* was detected in 9/35 (26%) of ALK− ALCL patients and of those, 6/9 were at the hotspot codon 1097 (G1097D/F/N/S) (Fig. 1d). For four patients, *JAK1* was mutated together with *STAT3*, thereby emphasizing the importance of the JAK/STAT signaling axis. To evaluate the prognostic value of mutations in the JAK/STAT pathway, we performed Cox regression analysis and showed that ALK− ALCL patients harboring *STAT3* and/or *JAK1* mutation have a shorter OS (hazard ratio [HR] = 2.8; 95% confidence interval [CI], 1.1–7.1, $p < 0.03$) (Fig. S3A). Furthermore, the prognostic value of the most mutated genes in ALK− ALCL: *STAT3* (9/35), *JAK1* (9/35), *TP53* (8/35) and *KMT2D* (7/35) were investigated. Cox regression analysis showed that patients with *STAT3* mutations have a significantly shorter OS compared to those with wild-type *STAT3* (HR = 4.1; 95% CI, 1.56–10.71, $p < 0.002$) (Fig. 1c). In addition, while *JAK1* and *KMT2D* mutations did not significantly correlate with OS ($p < 0.2$ and $p < 0.3$, respectively), *TP53* mutations clearly displayed the correlation ($p < 0.01$) (Fig. S3B–D). To further confirm that mutations in *STAT3* are associated with shorter OS, we applied Akaike's informative criteria model to the four aforementioned genes. *STAT3* mutations were found to be the best predictor of OS in ALK− ALCL (Table S5). Moreover, no significant differences were found between mutation status of these genes with age, gender, disease stage, eastern cooperative oncology group performance status or age-adjusted international prognostic index (AA-IPI). As expected [9, 13, 15], expression of p-STAT3 (Y705) was detected at a high level in all ALK− ALCL patients harboring *STAT3* mutations, although low/medium expression of p-STAT3 was also detected in *STAT3* wild-type patient tumors (Fig. S4, Table S6). Mutations in the *LRP1B* gene were detected in 12/82 (15%) of sALCL patients (19% ALK+ and 9% ALK−) and three cell lines. Since *LRP1B* was the most recurrently altered gene in ALK+ ALCL, we assessed its possible association with outcome, but no differences were found between mutated and nonmutated patients.

To investigate somatic mutations with a possible role in disease relapse, we sequenced paired diagnostic and relapse samples available for four patients (1 ALK+ and 3 ALK−) (Fig. 2a). Two different acquired mutations in *EPHA5* were detected in each of the two relapse samples (patient tumors

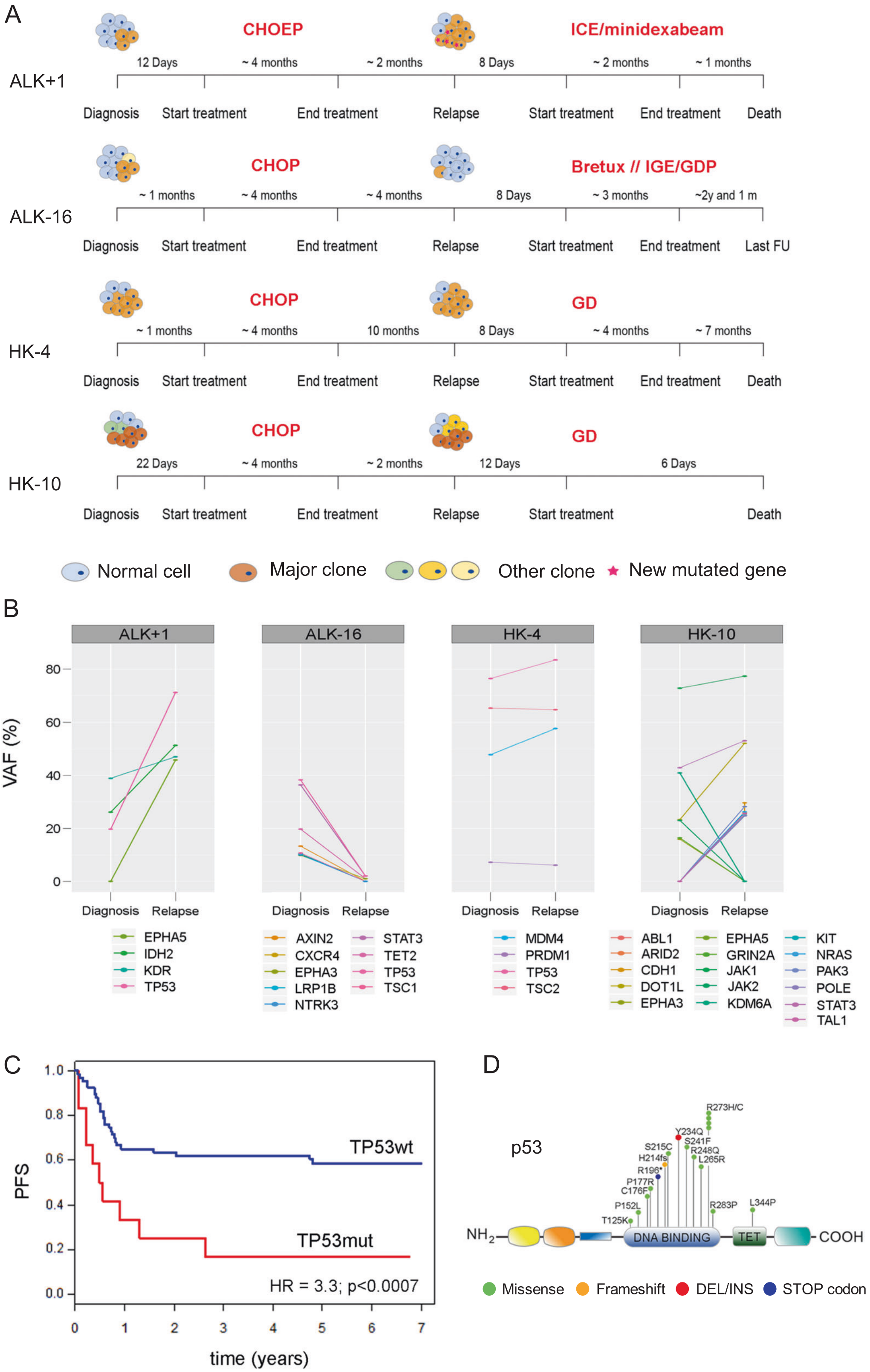

ALK+ 1R and HK-10R): a stop codon at S566 and a glycine–valine change at residue 723. In the latter patient (HK-10), identification of mutated *EPHA5* appears to be the result of the emergence of a new malignant clone, harboring novel mutations in several other genes consistently with a similar variant allele frequency (Fig. 2b). Interestingly,

◀ **Fig. 2** Diagnosis versus relapse showed mutated ***TP53*** to be associated with a shorter PFS in sALCL**. a** Schematic representation of four patients sequenced at diagnosis and at relapse highlighting their clinical path and treatment. Meaning of the color is described in the legend. CHOEP chemotherapy with cyclophosphamide, doxorubicin, etoposide, vincristine and prednisone, CHOP chemotherapy with cyclophosphamide, doxorubicin, vincristine and prednisone, ICE chemotherapy combination that includes ifosfamide, carboplatin and etoposide, bretux: brentuximab vedotin, GDP gemcitabine, dexamethasone, and cisplatin, GD gemcitabine and docetaxel, FU follow up. **b** Changes in mutational burden during tumor progression. The percentage of variant allele frequency (VAF%) for each gene is plotted at diagnosis and at relapse. The names of genes involved are reported under each plot. **c** 7-year PFS in systemic ALCL patients according to *TP53* status; red: *TP53* mutated (mut) patients; blue: *TP53* wild-type (wt) patients. *P* values and hazard ratios (HR) shown were determined by Cox proportional hazards. **d** Schematic representation of p53 domains and the variants detected.

EPHA5 was also found to be the second most mutated gene in relapsed/refractory patients in the entire cohort (Table S4B). Three out of four patients harbored mutated *TP53* both at diagnosis and at relapse (Fig. 2b). As *TP53* is the most recurrent gene mutated in our cohort and the most mutated gene in relapsed patients (Table S4B), we investigated its possible association with the treatment outcome for all ALCL patients regardless of ALK status. Nearly all mutations in *TP53* were detected in the DNA binding domain except for L344P in the TET domain for one patient (Fig. 2d). sALCL patients harboring *TP53* mutations have a shorter PFS compared to those with the wild-type gene (HR = 3.3; 95% CI, 1.59–6.87, $p < 0.0007$) (Fig. 2c). These data, together with the diagnosis versus relapse analysis, suggest that *TP53* mutations may confer resistance to chemotherapy. Moreover, mutations in *TP53* were the most common genetic events on re-analysis of publicly available datasets (Table S7) [9, 11].

Losses at the genomic regions that encompass *TP53* and *PRDM1* genes have been shown to be the most common lesions in sALCL with a clinical implication [12]. *PRDM1* mutations were detected in five patients, with three of these co-occurring with *TP53* mutations and all five patients being categorized within the poor prognostic sub-group. These data confirm the correlation between *TP53* and *PRDM1* gene mutations, thereby demonstrating either copy number loss or concomitant mutations are mechanisms which have the potential to alter p53 and PRDM1 pathways activity.

In summary, within one of the largest cohort of 82 sALCL patients, we provide robust information on the genetic spectrum of genes either solely mutated in ALK− ALCL (*STAT3*, *JAK1*) or across the whole spectrum of ALCL (*TP53*, *LRP1B*, *EPHA5*, *KMT2D*). In addition, we describe novel biomarkers for predicting treatment outcome reporting an association between mutated *STAT3* and *TP53* with an inferior outcome, in the former case in ALK− disease and in the latter case all sALCL independent of ALK status. Finally, this mutational landscape provides further candidate genes that deserve consideration for their possible role in the patient outcome, such as *EPHA5*, *KMT2D*, *PRDM1* and *SOCS1*.

Acknowledgements This project has received funding from the European Union's Horizon 2020 Marie Skłodowska-Curie Innovative Training Networks (ITN-ETN) under grant agreement no. 675712. The project was also supported by Czech Science Foundation (GACR), GA19-15737S and junior project no. 19-23424Y, the MEYS CZ project CEITEC 2020 (LQ1601) and project MH CZ-DRO (FNBr, 65269705). We acknowledge the CF Genomics CEITEC MU supported by the NCMG research infrastructure (LM2018132 funded by MEYS CR) and Core Facility Bioinformatics of CEITEC MU for their support with scientific data presented here. We thank Vasileios Bikos and Stephen Paul Ducray for the support and advice. We acknowledge the different biobanks for collecting the samples and providing access to them: the CCLG Tissue Bank and contributing CCLG Centres, members of the ECMC Paediatric Network, the Czech National Lymphoma Registry (NiHiL, NCT 03199066), University Hospital Brno (grant no. NV18-03-00054) and University Hospital Hradec Kralove (Project BBMRI-CZ, no.: EF16 013/0001674).

Author contributions Conceptualization: CL; methodology: CL and BT; performed bioinformatics and statistical analysis: VB and LR; performed and interpreted IHC data: I-AM-M and FF; investigation: CL, AJ and SP; visualization: CL, LR and VB; writing—original draft: CL; writing—review and editing: SDT and SP; funding acquisition: OM, SDT, AJ and SP; collected data and samples: CL, DF, MM, NP, HL, SDT, H-CL, OM, KK, DB, GGS, LM, CG-P and AJ and supervision: SP.

Compliance with ethical standards

Conflict of interest The authors declare that they have no conflict of interest.

References

1. Savage KJ, Harris NL, Vose JM, Ullrich F, Jaffe ES, Connors JM, et al. ALK- anaplastic large-cell lymphoma is clinically and immunophenotypically different from both ALK+ ALCL and peripheral T-cell lymphoma, not otherwise specified: report from the International Peripheral T-Cell Lymphoma Project. Blood. 2008;111:5496–504. http://www.ncbi.nlm.nih.gov/pubmed/18385450.

2. Janikova A, Chloupkova R, Campr V, Klener P, Hamouzova J, Belada D, et al. First-line therapy for T cell lymphomas: a retrospective population-based analysis of 906 T cell lymphoma patients. Ann Hematol. 2019. http://link.springer.com/10.1007/s00277-019-03694-y.
3. Hapgood G, Savage KJ. The biology and management of systemic anaplastic large cell lymphoma. Blood. 2015;2:17–25. https://pubmed.ncbi.nlm.nih.gov/25869285/.
4. Brugières L, Deley MC Le, Pacquement H, Meguerian-Bedoyan Z, Terrier-Lacombe MJ, Robert A, et al. CD30+ anaplastic large-cell lymphoma in children: analysis of 82 patients enrolled in two consecutive studies of the French Society of Pediatric Oncology. Blood. 1998;92:3591–8.
5. Mussolin L, Damm-Welk C, Pillon M, Zimmermann M, Franceschetto G, Pulford K, et al. Use of minimal disseminated disease and immunity to NPM-ALK antigen to stratify ALK-positive ALCL patients with different prognosis. Leukemia. 2013;27:416–22. http://www.ncbi.nlm.nih.gov/pubmed/22907048.
6. Morel A, Brière J, Lamant L, Loschi M, Haioun C, Delarue R, et al. Long-term outcomes of adults with first-relapsed/refractory systemic anaplastic large-cell lymphoma in the pre-brentuximab vedotin era: a LYSA/SFGM-TC study. Eur J Cancer. 2017;83:146–53.
7. Wrobel G, Mauguen A, Rosolen A, Reiter A, Williams D, Horibe K, et al. Safety assessment of intensive induction therapy in childhood anaplastic large cell lymphoma: Report of the ALCL99 randomised trial. Pediatr Blood Cancer. 2011;56:1071–7. http://www.ncbi.nlm.nih.gov/pubmed/21280197.
8. Prokoph N, Larose H, Lim MS, Burke GAA, Turner SD. Treatment options for paediatric anaplastic large cell lymphoma (ALCL): current standard and beyond. Cancers. 2018;10:1–18.
9. Crescenzo R, Abate F, Lasorsa E, Tabbo' F, Gaudiano M, Chiesa N, et al. Convergent mutations and kinase fusions lead to oncogenic STAT3 activation in anaplastic large cell lymphoma. Cancer Cell. 2015;27:516–32. https://linkinghub.elsevier.com/retrieve/pii/S153561081500094X.
10. Larose H, Prokoph N, Matthews JD, Schlederer M, Högler S, Alsulami AF, et al. Whole exome sequencing reveals NOTCH1 mutations in anaplastic large cell lymphoma and points to Notch both as a key pathway and a potential therapeutic target. Haematologica. 2020. http://www.haematologica.org/lookup/doi/10.3324/haematol.2019.238766.
11. Song TL, Nairismägi ML, Laurensia Y, Lim JQ, Tan J, Li ZM, et al. Oncogenic activation of the STAT3 pathway drives PD-L1 expression in natural killer/T-cell lymphoma. Blood. 2018;132:1146–58.
12. Boi M, Rinaldi A, Kwee I, Bonetti P, Todaro M, Tabbò F, et al. PRDM1/BLIMP1 is commonly inactivated in anaplastic large T-cell lymphoma. Blood. 2013;122:2683–93.
13. Andersson EI, Brück O, Braun T, Mannisto S, Saikko L, Lagström S, et al. STAT3 mutation is associated with STAT3 activation in CD30+ ALK− ALCL. Cancers. 2020;12:702. https://www.mdpi.com/2072-6694/12/3/702.
14. Laurent C, Nicolae A, Laurent C, Le Bras F, Haioun C, Fataccioli V, et al. Gene alterations in epigenetic modifiers and JAK-STAT signaling are frequent in breast implant–associated ALCL. Blood. 2020;135:360–70.
15. Shen J, Li S, Medeiros LJ, Lin P, Wang SA, Tang G, et al. PD-L1 expression is associated with ALK positivity and STAT3 activation, but not outcome in patients with systemic anaplastic large cell lymphoma. Mod Pathol. 2020;33:324–33. https://www.nature.com/articles/s41379-019-0336-3.

Taylor & Francis
Taylor & Francis Group

Epigenetics

ISSN: 1559-2294 (Print) 1559-2308 (Online) Journal homepage: www.tandfonline.com/journals/kepi20

Memory B-cell like chronic lymphocytic leukaemia is associated with specific methylation profile of *WNT5A* promoter and undetectable expression of *WNT5A* gene

Lucie Poppova, Sarka Pavlova, Beatriz Gonzalez, Jana Kotaskova, Karla Plevova, Gabrijela Dumbovic, Pavlina Janovska, Vojtech Bystry, Anna Panovska, Lucie Bezdekova, Stanislava Maslejova, Yvona Brychtova, Michael Doubek, Marcela Krzyzankova, Marek Borsky, Jiri Mayer, Vitezslav Bryja, Sergio Alonso & Sarka Pospisilova

To cite this article: Lucie Poppova, Sarka Pavlova, Beatriz Gonzalez, Jana Kotaskova, Karla Plevova, Gabrijela Dumbovic, Pavlina Janovska, Vojtech Bystry, Anna Panovska, Lucie Bezdekova, Stanislava Maslejova, Yvona Brychtova, Michael Doubek, Marcela Krzyzankova, Marek Borsky, Jiri Mayer, Vitezslav Bryja, Sergio Alonso & Sarka Pospisilova (2022) Memory B-cell like chronic lymphocytic leukaemia is associated with specific methylation profile of *WNT5A* promoter and undetectable expression of *WNT5A* gene, Epigenetics, 17:12, 1628-1635, DOI: 10.1080/15592294.2022.2050004

To link to this article: https://doi.org/10.1080/15592294.2022.2050004

EPIGENETICS
2022, VOL. 17, NO. 12, 1628–1635
https://doi.org/10.1080/15592294.2022.2050004

Taylor & Francis
Taylor & Francis Group

BRIEF REPORT

Memory B-cell like chronic lymphocytic leukaemia is associated with specific methylation profile of *WNT5A* promoter and undetectable expression of *WNT5A* gene

Lucie Poppova[a,b*], Sarka Pavlova[a,b*], Beatriz Gonzalez[c], Jana Kotaskova[a,b], Karla Plevova[a,b,d], Gabrijela Dumbovic[c,e], Pavlina Janovska[f], Vojtech Bystry[b], Anna Panovska[a], Lucie Bezdekova[a], Stanislava Maslejova[a], Yvona Brychtova[a], Michael Doubek[a,b,d], Marcela Krzyzankova[a,b], Marek Borsky[a], Jiri Mayer[a,b], Vitezslav Bryja[f], Sergio Alonso[c], and Sarka Pospisilova[a,b,d]

[a]Department of Internal Medicine – Hematology and Oncology, University Hospital Brno and Faculty of Medicine, Masaryk University, Brno, Czech Republic; [b]Central European Institute of Technology (CEITEC), Masaryk University, Brno, Czech Republic; [c]IGTP-PMPPC: Program of Predictive and Personalized Medicine of Cancer, Germans Trias I Pujol Research Institute, Badalona, Spain; [d]Institute of Medical Genetics and Genomics, University Hospital Brno and Faculty of Medicine, Masaryk University, Brno, Czech Republic; [e]Institute for Cardiovascular Regeneration, Center for Molecular Medicine, Goethe University Frankfurt, Frankfurt am Main, Germany; [f]Department of Experimental Biology, Faculty of Science, Masaryk University, Brno, Czech Republic

ABSTRACT
Genome methylation profiles define naïve-like (n-CLL), memory-like (m-CLL), and intermediate (i-CLL) subsets of chronic lymphocytic leukaemia (CLL). The profiles can be easily determined by the analysis of the five-CpG signature. m-CLL, i-CLL, and n-CLL with the good, intermediate, and poor prognoses, respectively, differ by the somatic hypermutation status of the immunoglobulin heavy chain variable gene (IGHV), a widely used prognostic predictor in CLL. We have previously shown that the expression of *WNT5A*, encoding a ROR1 ligand, distinguishes patients with the worse outcome within the prognostically favourable IGHV-mutated subgroup. To analyse the mechanisms controlling *WNT5A* expression, we investigated the methylation status of 54 CpG sites within the *WNT5A* promoter and its relation to the *WNT5A* gene expression. In a cohort of 59 CLL patients balanced for combinations of IGHV and *WNT5A* statuses, we identified three promoter CpG sites whose methylation level correlated with the *WNT5A* expression within the IGHV-mutated subgroup. Further, we complemented our data with the methylation status of the five-CpG signature. IGHV-mutated/*WNT5A*-negative and IGHV-mutated/*WNT5A*-positive cases overlapped with m-CLL and i-CLL methylation subgroups, respectively, while most IGHV-unmutated samples were assigned to n-CLL. Median methylation levels of all the three CpG sites in the *WNT5A* promoter were lowest in i-CLL. Finally, a detailed analysis of m-CLL and i-CLL showed that undetectable *WNT5A* expression predicts longer treatment-free survival with higher statistical significance than the classification according to the five-CpG signature. To conclude, a -favourable m-CLL subgroup is associated with mutated IGHV and undetectable *WNT5A* expression due to its promoter methylation.

ARTICLE HISTORY
Received 22 April 2021
Revised 15 February 2022
Accepted 21 February 2022

KEYWORDS
WNT5A; chronic lymphocytic leukaemia; methylation; i-CLL; m-CLL

Background

DNA methylation plays a vital role during the maturation of B-cells, and it is crucial for their normal functioning [1–3]. During the maturation process, DNA undergoes global hypomethylation with local hypermethylation, and a similarly occurring process is even more pronounced in cells of chronic lymphocytic leukaemia (CLL) [3,4]. Aberrant changes in the methylation profile of CLL cells accumulate during early leukaemogenesis; afterwards, the overall profile remains more or less stable [1,3–6]. The methylation status of the five-CpG signature was shown to divide patients into subgroups based on their similarity to B-cell developmental stages [6]: (i) Naïve-like CLL (n-CLL) with a high methylation level, associated with a poor prognosis of the patients, (ii) memory-like CLL (m-CLL) with a low methylation

CONTACT Sarka Pospisilova pospisilova.sarka@fnbrno.cz Department of Internal Medicine – Hematology and Oncology, University Hospital Brno and Faculty of Medicine, Masaryk University, Brno, Czech Republic; Central European Institute of Technology (CEITEC), Masaryk University, Brno, Czech Republic; Institute of Medical Genetics and Genomics, University Hospital Brno and Faculty of Medicine, Masaryk University, Brno, Czech Republic

*Authors contributed equally

Supplemental data for this article can be accessed here level, associated with a good prognosis, and (iii) intermediate-CLL (i-CLL) with both methylation and prognosis in-between [6,7]. These three methylation subgroups partially overlap with prognostic categories defined by the somatic hypermutation status of the immunoglobulin heavy chain variable gene (IGHV), an important prognostic predictor [8–11]. CLL patients with IGHV identity to germline ≥98% (IGHV-unmutated) have a poor prognosis. However, even within the prognostically favourable IGHV-mutated subgroup, there is a subset of patients with an aggressive disease course [12,13].

We have previously shown that the expression of *WNT5A*, a gene encoding a ligand activating WNT/Planar Cell Polarity pathway via the ROR1 receptor, varies significantly among CLL patients, from high levels in some patients to undetectable levels in 50% of IGHV-unmutated and 85% of IGHV-mutated cases (marked as *WNT5A*-negative) [13]. *WNT5A* expression is a strong and overtime-stable prognostic predictor, distinguishing cases with worse prognosis within otherwise favourable IGHV-mutated CLL better than the percentage of IGHV identity [12,13].

Considering the absence of *WNT5A* expression in more than half of tested patients [13], together with reports of a correlation between the *WNT5A* expression and its promoter methylation in other cancer types [14–16], we hypothesized that the *WNT5A* expression might be regulated by methylation also in CLL. Further, taking advantage of the current understanding of the CLL methylation profiles, we explored how methylation within the *WNT5A* promoter correlates with the global methylation profile, IGHV status, and *WNT5A* expression.

Material and methods

Patient samples

CLL cells were isolated from peripheral blood of 59 CLL patients monitored and treated at the University Hospital Brno. All samples were obtained after written informed consent in concordance with the Declaration of Helsinki, and the study was approved by the Ethical Committee of the University Hospital Brno. B-cells from patient samples were separated using B-cell Enrichment RosetteSep kits (StemCell Technologies). The original cohort consisted of 39 patients; another 20 IGHV-mutated patients were added to refine the results. The assessment of *WNT5A* expression and IGHV gene mutational status were processed as previously described [13].

DNA isolation and bisulphite conversion

DNA was isolated on QIAcube (Qiagen) and dissolved in TE buffer with 0.1 M EDTA. DNA (200 ng) was treated with an EZ DNA Methylation^{TM} kit (Zymo Research) according to the manufacturer's recommendation and eluted into 22 μl of water.

Primer design for *WNT5A* promoter analysis

The sequences of three CpG Islands (CGI1–CGI3) located within the *WNT5A* promoter (Ensembl databases, version GRCh37.p13) were used for primer design. The sequences were modified to match bisulphite-converted DNA. The Primer3 tool (http://bioinfo.ut.ee/primer3-0.4.0/) was used for primer design. The parameters of the primers were tested with OligoAnalyzer 3.1 (https://eu.idtdna.com/calc/analyser) and ePCR (http://bisearch.enzim.hu/) tools. Primers were synthesized by Generi Biotech (Table S1). The location of the examined regions is illustrated in the scheme in Figure 1a.

PCR and sequencing

Bisulphite-treated DNA was amplified with PCR using HotStarTaq DNA Polymerase (Qiagen) in reaction conditions: 5 min 95°C, (30 sec 95°C, 30 sec 60°C, 1 min 72°C) x 35 cycles, 7 min 72°C. PCR products were sequenced either by GATC Biotech or in-house using ABI PRISM® 3700 Genetic Analyser according to the manufacturer's instructions (Big Dye terminator v1.1 kit, Applied Biosystems). Primer sequences for the *WNT5A* promoter regions are listed in Table S1; primers for the five-CpG signature analysis were used as published previously [6].

Statistical analyses

The following tests were used to verify distribution normality: Kolmogorov–Smirnov test, Shapiro–

Wilk test, or D´Agostino-Pearson normality test. Parametric and non-parametric tests (for normally and non-normally distributed variables, respectively) were used to evaluate the relationships between variables (unpaired t-test and Mann Whitney test) and correlation between two variables (Pearson and Spearman correlation). Differences in survival were analysed by the log-rank test. The level of statistical significance was set to $P < 0.05$. In multiple testing, the P-value was adjusted using the Holm–Bonferroni method. All assays were performed as two-tailed using GraphPad Prism 8 (GraphPad Software Inc., La Jolla, CA, USA) and R program (http://www.r-project.org; univariate and multivariate survival analysis). Within TFS, treatment or death due to CLL was treated as an event.

Results:

Using ENSEMBL GRCh37, we identified 54 CpG sites in three regions within the *WNT5A* promoter localized in three CpG Islands (CGI1–CGI3): region 1 (R1) in CGI1, region 2 (R2) in CGI2, and region 3 (R3) in CGI3 (Figure 1a). For the initial experiment, 39 previously untreated CLL patients were classified based on IGHV status and *WNT5A* expression: IGHV-mutated/ *WNT5A*-negative (MW-), IGHV-mutated /*WNT5A*-positive (MW+), IGHV-unmutated /*WNT5A*-negative (UW-), IGHV-unmutated /*WNT5A*-positive (UW+) (Figure S1 and numbered samples in Figure 1b). In separated B-cells, we explored the methylation status of the 54 individual CpG sites using bisulphite conversion (EZ DNA Methylation kit; Zymo Research) followed by Sanger sequencing. We used a more precise approach that provides information about the methylation level of individual CpG sites compared to other studies using methylation-specific PCR, providing only the overall methylation status of the whole measured locus [14–17]. We identified three CpG sites within R1 (further indicated as R1_CpG1, R1_CpG2, and R1_CpG3), whose methylation levels negatively correlated with *WNT5A* expression within the IGHV-mutated subset. We detected high methylation levels of these three CpG sites in MW-patients, while in MW+ patients, the methylation level decreased with increasing *WNT5A* expression. We extended the cohort of IGHV-mutated patients (10 MW- and 10 MW+; Figure 1b) and confirmed significant differences in methylation of these three CpG sites (Figure 1c; R1_CpG1: $P = 0.0014$, R1_CpG2: $P = 0.0001$, R1_CpG3: $P = 0.0005$; Mann–Whitney test). We also confirmed the negative correlation between *WNT5A* methylation and expression (MW+ cohort; Figure 1d: R1_CpG1: $P = 0.001$, R1_CpG2: $P = 0.0013$, R1_CpG3: $P = 0.0028$; Spearman correlation).

We observed high methylation levels in UW-patients with a median methylation level being even higher than in MW-patients (Figure 1b and S2A). In contrast, we have not seen any specific dependency between *WNT5A* methylation and the expression levels in UW+ patients (Figure S2B). It implies that the *WNT5A* expression in the IGHV-unmutated subset is driven by different mechanisms than mere *WNT5A* promoter methylation.

Furthermore, when we compared our classification based on the combination of IGHV status and *WNT5A* expression to the classification based on the five-CpG signature described by Queirós et al. [6], we found that both largely overlapped. The two prognostically distinct IGHV-mutated subgroups, MW- and MW+ that differed by *WNT5A* promoter methylation and *WNT5A* expression, corresponded to the memory-like (m-CLL) and intermediate (i-CLL) methylation subgroups, respectively (Figure 2a). In contrast, except for two patients belonging to i-CLL, all IGHV-unmutated patients from our cohort were assigned to the naïve-like CLL methylation subgroup. In agreement with published data [6], we detected significant differences in the IGHV somatic hypermutation load. All n-CLL patients had IGHV identity above 99.1%, the two i-CLL IGHV-unmutated cases had identity below 99%, and the rest of i-CLL (18 of 20) and all m-CLL were IGHV-mutated with identity below 98%; i-CLL patients had mostly borderline IGHV identity (Figure 2b). The *WNT5A* promoter methylation levels also significantly varied among individual methylation subgroups: m-CLL vs. i-CLL ($P < 0.0001$) and m-CLL vs. n-CLL ($P = 0.0183$) (Figure 2c-e). This data suggests that hypomethylation of CpG regions in the *WNT5A* promoter largely overlaps with i-CLL.

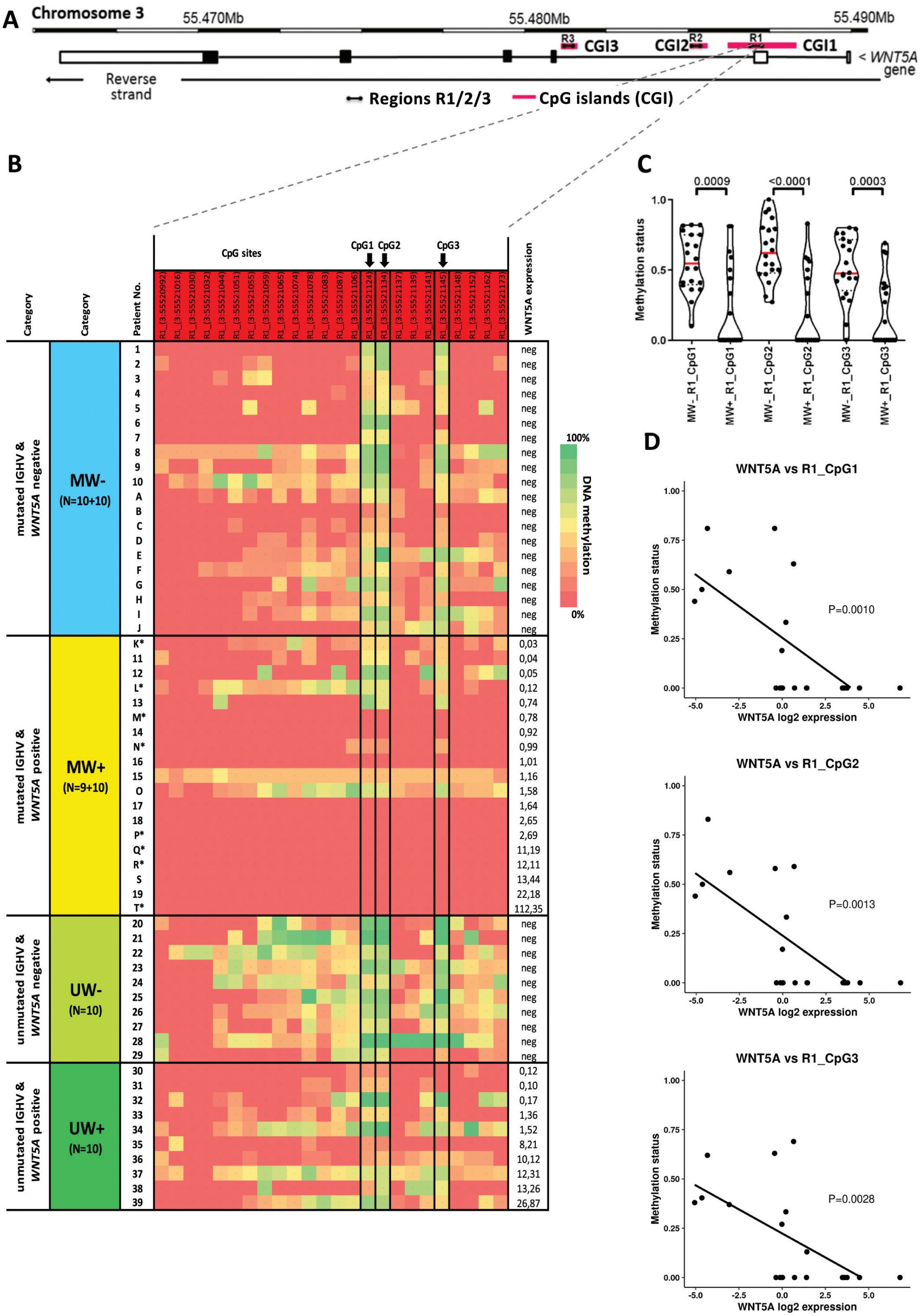

Figure 1. **Methylation analysis of *WNT5A* promoter**. (a) Schematic location of the regions R1, R2, R3 amplified with PCR within the CpG Islands CGI1/2/3 of the *WNT5A* promoter. (b) Heatmap displaying the results of the methylation analysis of the region R1 within CpG Island CGI3 in the total cohort of 59 CLL patients divided into four groups based on IGHV status and *WNT5A* expression. The initial cohort of 39 patients (described with numbers; see Figure S1 for initial analysis of regions R1, R2 and R3), was extended with 10 patients per MW- and MW+ cohorts each (described with letters). Arrows point to the three CpG sites R1_(3:55,521,124), R1_(3:55,521,134), and R1_(3:55,521,145), the methylation status of which correlated with the *WNT5A* expression in the IGHV-mutated subset. *Sample taken in relapse after treatment. (c) Comparison of the methylation level between MW- and MW+ samples for all three CpG sites (Mann–Whitney test). (d) The negative correlation between the *WNT5A* expression and methylation status of the three CpG sites (Spearman correlation) within the IGHV-mutated subset.

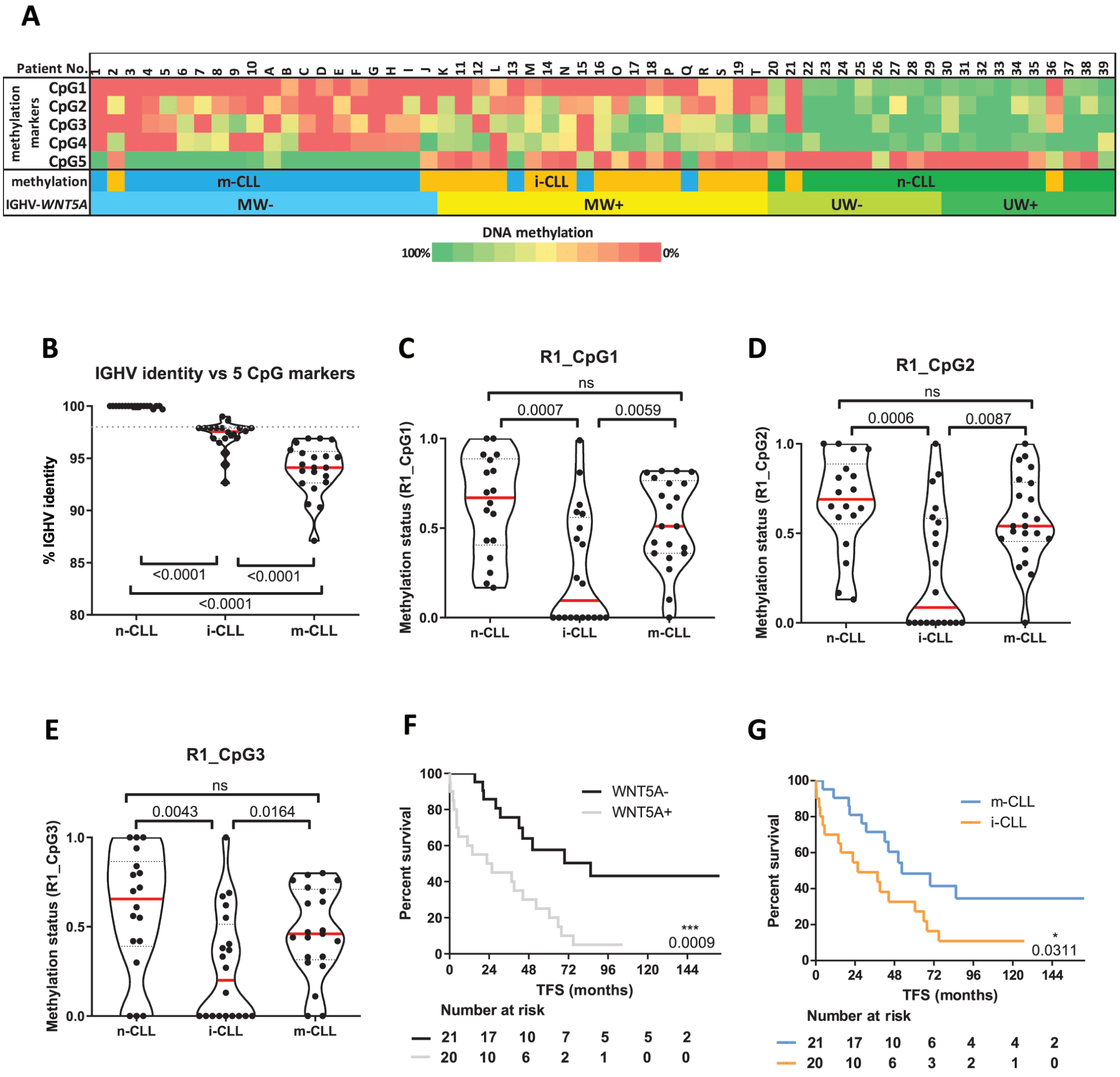

Figure 2. CLL patient classification into three methylation subgroups n-CLL, i-CLL, m-CLL, and treatment-free survival. (a) CLL patients were classified into the three subgroups based on the methylation profile of the five-CpG signature identified by Queirós et al. [6]. The three methylation subgroups were further investigated for the association with IGHV identity (b) and with the methylation levels of the three CpG sites in the *WNT5A* promoter (c-e). Treatment free-survival prediction in the cohort of m-CLL and i-CLL subgroups (N = 41 patients) according to the *WNT5A* expression (f) and the five-CpG signature (g).

Since the vast majority of m-CLL and i-CLL corresponded to IGHV-mutated CLL, we also decided to analyse treatment-free survival (TFS) and overall survival (OS) based on the *WNT5A* expression in the cohort consisting of m-CLL and i-CLL subgroups. Both the *WNT5A*-positivity (Figure 2f) and classification into i-CLL methylation subgroup (Figure 2g) distinguished patients with shorter TFS; the *WNT5A* positivity was a stronger prognostic factor than global epigenetics (i-CLL vs. m-CLL) ($P = 0.0009$ vs. $P = 0.0311$). Neither classification system showed a significant difference in OS for these subgroups of patients (Figure S3).

Discussion

The Wnt5a ligand signals via the ROR1 receptor that is highly expressed on CLL cells [18–20]. The Wnt5a/ROR1 axis has been shown to regulate multiple aspects of CLL biology – including cell survival, migration, and proliferation [13,21–25]. Importantly, a high activity of the non-canonical Wnt pathway has been connected to the poor outcome of CLL patients [13,21,26]. Following our previous work, here we verified that the *WNT5A* expression is a robust prognostic marker distinguishing CLL patients with worse prognosis within the prognostically favourable subset of IGHV-mutated patients.

In CLL, multiple epigenetic changes have been associated with the Wnt pathway (for review, see [27]). Interestingly, there is no direct evidence for epigenetic silencing of 'activators' such as WNT ligands and FZD receptors. This contrasts with Wnt pathway inhibitors such as members of the SFRP family or WIF1 that have been found methylated in CLL [28–31]. Our study thus represents the first observation of the epigenetic control of a Wnt ligand in CLL as we demonstrated that the *WNT5A* expression is associated with DNA methylation changes of *WNT5A* promoter in a significant proportion of CLL patients. The methylation status of three CpG sites within the *WNT5A* promoter correlated with *WNT5A* expression only in the IGHV-mutated but not in the IGHV-unmutated subgroup, suggesting that *WNT5A* expression in these two CLL subgroups is controlled via different mechanisms.

Furthermore, we confirmed that the five-CpG signature divides patients into the three prognostically distinct subgroups: m-CLL, i-CLL, and n-CLL [6,7]. The i-CLL epitype had been poorly characterized until recently when it was linked to specific biological and clinical features, namely the usage of IGLV3-21^{R110} [32,33], stereotyped BCR immunoglobulins (mainly of subset #2), increased frequency of *SF3B1* and *ATM* mutations, and unfavourable prognosis [34,35]. Very recently published paper recognized *WNT5A/B* overexpression as a specific signature of patients carrying IGLV3-21^{R110} [35]; this corresponds to our results and our previous work showing that among IGHV-mutated patients, the *WNT5A* expression is high in patients with borderline number of IGHV somatic hypermutations and *SF3B1* mutations and more aggressive disease compared to *WNT5A*-negative patients [13].

While the majority of patients with unmutated IGHV from our cohort were assigned to n-CLL, the *WNT5A* expression and methylation status of patients with mutated IGHV was strongly related to their distribution between the m-CLL and i-CLL subgroups. In our study, the classification based on the *WNT5A* expression distinguished patients with shorter TFS with even a higher significance than their classification into the m-CLL and i-CLL subgroups defined by the five-CpG signature.

To summarize, the level of *WNT5A* expression has been associated with CLL clinical behaviour [13,35]. Our current findings shed light on the interconnection of the varying *WNT5A* expression with the methylation profile of IGHV-mutated patients, prevalently comprising the m-CLL and i-CLL subsets as based on the five-CpG signature. While the methylated CpG sites in the *WNT5A* promoter of the m-CLL subtype patients correlated with undetectable *WNT5A* expression, the demethylation of these *WTN5A* promoter sites was shown in the i-CLL subset and associated with the high *WNT5A* expression. Together with previously published observations, our present results could serve for future designing better stratification models distinguishing patients with different prognoses.

Acknowledgments

The authors thank Francesco Muto for language editing and Lenka Radova and Karol Pal for help with figures. The internship of L.P. in Barcelona was funded by the Erasmus+ Programme of the European Union. V.B. and P.J. were supported by European Structural and Investment Funds, Operational Programme Research, Development and Education– "Preclinical Progression of New Organic Compounds with Targeted Biological Activity" (Preclinprogress) - CZ.02.1.01/0.0/0.0/16_025/0007381.

Disclosure statement

No potential conflict of interest was reported by the author(s).

Funding

This work was supported by the Ministerstvo Zdravotnictví České Republiky [MH CR - DRO (FNBr,65269705)]; Ministerstvo Školství, Mládeže a Tělovýchovy [MUNI/A/1330/2021; EATRIS-CZ research infrastructure LM2018133; CZ.02.1.01/0.0/0.0/16_025/0007381]; Instituto de Salud Carlos III, Spain [PI18/01484; PI21/01766]; Fundación Mutua Madrileña, Spain [AP174232020]; Grantová Agentura Šeské Republiky [GA19-11299S].

Data availability statement

The authors confirm that the data supporting the findings of this study are available within the article and its supplementary materials.

ORCID

Sarka Pavlova http://orcid.org/0000-0003-1528-9743
Beatriz Gonzalez http://orcid.org/0000-0002-3699-9392
Jana Kotaskova http://orcid.org/0000-0003-1672-7346
Karla Plevova http://orcid.org/0000-0002-6148-8877
Gabrijela Dumbovic http://orcid.org/0000-0002-1278-0273
Pavlina Janovska http://orcid.org/0000-0001-9871-0876
Vojtech Bystry http://orcid.org/0000-0001-5278-0801
Anna Panovska http://orcid.org/0000-0003-4955-3039
Lucie Bezdekova http://orcid.org/0000-0002-2123-5226
Yvona Brychtova http://orcid.org/0000-0003-1038-870X
Michael Doubek http://orcid.org/0000-0002-1269-6282
Marek Borsky http://orcid.org/0000-0001-5803-5941
Jiri Mayer http://orcid.org/0000-0003-0567-9887
Vitezslav Bryja http://orcid.org/0000-0002-9136-5085
Sergio Alonso http://orcid.org/0000-0001-6497-892X
Sarka Pospisilova http://orcid.org/0000-0001-7136-2680

References

[1] Oakes CC, Seifert M, Assenov Y, et al. DNA methylation dynamics during B cell maturation underlie a continuum of disease phenotypes in chronic lymphocytic leukemia. Nat Genet. 2016;48(3):253–264.
[2] Kulis M, Merkel A, Heath S, et al. Whole-genome fingerprint of the DNA methylome during human B cell differentiation. Nat Genet. 2015;47(7):746–756.
[3] Kulis M, Heath S, Bibikova M, et al. Epigenomic analysis detects widespread gene-body DNA hypomethylation in chronic lymphocytic leukemia. Nat Genet. 2012;44(11):1236–1242.
[4] Kretzmer H, Biran A, Purroy N, et al. Preneoplastic alterations define CLL DNA methylome and persist through disease progression and therapy. Blood Cancer Discov. 2021;2(1):54–69.
[5] Mansouri L, Wierzbinska JA, Plass C, et al. Epigenetic deregulation in chronic lymphocytic leukemia: clinical and biological impact. Semin Cancer Biol. 2018;51:1–11.
[6] Queirós AC, Villamor N, Clot G, et al. A B-cell epigenetic signature defines three biologic subgroups of chronic lymphocytic leukemia with clinical impact. Leukemia. 2015;29(3):598–605.
[7] Wojdacz TK, Amarasinghe HE, Kadalayil L, et al. Clinical significance of DNA methylation in chronic lymphocytic leukemia patients: results from 3 UK clinical trials. Blood Adv. 2019;3(16):2474–2481.
[8] Damle RN, Wasil T, Fais F, et al. Ig V gene mutation status and CD38 expression as novel prognostic indicators in chronic lymphocytic leukemia. Blood. 1999;94(6):1840–1847.
[9] Hamblin TJ, Davis Z, Gardiner A, et al. Unmutated Ig V(H) genes are associated with a more aggressive form of chronic lymphocytic leukemia. Blood. 1999;94(6):1848–1854.
[10] Hallek M, Cheson BD, Catovsky D, et al. iwCLL guidelines for diagnosis, indications for treatment, response assessment, and supportive management of CLL. Blood. 2018;131(25):2745–2760.
[11] Eichhorst B, Robak T, Montserrat E, et al. Chronic lymphocytic leukaemia: ESMO clinical practice guidelines for diagnosis, treatment and follow-up. Ann Oncol. 2021;32(1):23–33.
[12] Hamblin TJ, Davis ZA, Oscier DG. Determination of how many immunoglobulin variable region heavy chain mutations are allowable in unmutated chronic lymphocytic leukaemia - long-term follow up of patients with different percentages of mutations. Br J Haematol. 2008;140(3):320–323.
[13] Janovska P, Poppova L, Plevova K, et al. Autocrine signaling by Wnt-5a deregulates chemotaxis of leukemic cells and predicts clinical outcome in chronic lymphocytic leukemia. Clin Cancer Res. 2016;22(2):459–469.
[14] Roman-Gomez J, Jimenez-Velasco A, Cordeu L, et al. WNT5A, a putative tumour suppressor of lymphoid malignancies, is inactivated by aberrant methylation in acute lymphoblastic leukaemia. Eur J Cancer. 2007;43(18):2736–2746.
[15] Ying J, Li H, Yu J, et al. WNT5A exhibits tumor-suppressive activity through antagonizing the Wnt/beta-catenin signaling, and is frequently methylated in colorectal cancer. Clin Cancer Res. 2008;14(1):55–61.
[16] Martín V, Valencia A, Agirre X, et al. Epigenetic regulation of the non-canonical Wnt pathway in acute myeloid leukemia. Cancer Sci. 2010;101(2):425–432.
[17] Li J, Ying J, Fan Y, et al. WNT5A antagonizes WNT/β-catenin signaling and is frequently silenced by promoter CpG methylation in esophageal squamous cell carcinoma. Cancer Biol Ther. 2010;10(6):617–624.
[18] Baskar S, Kwong KY, Hofer T, et al. Unique cell surface expression of receptor tyrosine kinase ROR1 in human B-cell chronic lymphocytic leukemia. Clin Cancer Res. 2008;14(2):396–404.
[19] Daneshmanesh AH, Mikaelsson E, Jeddi-Tehrani M, et al. Ror1, a cell surface receptor tyrosine kinase is expressed in chronic lymphocytic leukemia and may serve as a putative target for therapy. Int J Cancer. 2008;123(5):1190–1195.
[20] Fukuda T, Chen L, Endo T, et al. Antisera induced by infusions of autologous Ad-CD154-leukemia B cells identify ROR1 as an oncofetal antigen and receptor for Wnt5a. Proc Natl Acad Sci U S A. 2008;105(8):3047–3052.

[21] Kaucká M, Plevová K, Pavlová S, et al. The planar cell polarity pathway drives pathogenesis of chronic lymphocytic leukemia by the regulation of B-lymphocyte migration. Cancer Res. 2013;73(5):1491–1501.

[22] Hasan MK, Yu J, Chen L, et al. Wnt5a induces ROR1 to complex with HS1 to enhance migration of chronic lymphocytic leukemia cells. Leukemia. 2017;31(12):2615–2622.

[23] Hasan MK, Ghia EM, Rassenti LZ, et al. Wnt5a enhances proliferation of chronic lymphocytic leukemia and ERK1/2 phosphorylation via a ROR1/DOCK2-dependent mechanism. Leukemia. 2021;35(6):1621–1630.

[24] Yu J, Chen L, Cui B, et al. Wnt5a induces ROR1/ROR2 heterooligomerization to enhance leukemia chemotaxis and proliferation. J Clin Invest. 2016;126(2):585–598.

[25] Zhang Q, Wang HY, Liu X, et al. Cutting edge: ROR1/CD19 receptor complex promotes growth of mantle cell lymphoma cells independently of the B cell receptor-BTK signaling pathway. J Immunol. 2019;203(8):2043–2048.

[26] Cui B, Ghia EM, Chen L, et al. High-level ROR1 associates with accelerated disease progression in chronic lymphocytic leukemia. Blood. 2016;128(25):2931–2940.

[27] Bennett LB, Taylor KH, Arthur GL, et al. Epigenetic regulation of WNT signaling in chronic lymphocytic leukemia. Epigenomics. 2010;2(1):53–70.

[28] Rahmatpanah FB, Carstens S, Guo J, et al. Differential DNA methylation patterns of small B-cell lymphoma subclasses with different clinical behavior. Leukemia. 2006;20(10):1855–1862.

[29] Rahmatpanah FB, Carstens S, Hooshmand SI, et al. Large-scale analysis of DNA methylation in chronic lymphocytic leukemia. Epigenomics. 2009;1(1):39–61.

[30] Liu TH, Raval A, Chen SS, et al. CpG Island methylation and expression of the secreted frizzled-related protein gene family in chronic lymphocytic leukemia. Cancer Res. 2006;66(2):653–658.

[31] Chim CS, Fung TK, Wong KF, et al. Infrequent Wnt inhibitory factor-1 (Wif-1) methylation in chronic lymphocytic leukemia. Leuk Res. 2006;30(9):1135–1139.

[32] Maity PC, Bilal M, Koning MT, et al. is an inherited risk factor for CLL through the acquisition of a single-point mutation enabling autonomous BCR signaling. Proc Natl Acad Sci U S A. 2020;117(8):4320–4327.

[33] Minici C, Gounari M, Übelhart R, et al. Distinct homotypic B-cell receptor interactions shape the outcome of chronic lymphocytic leukaemia. Nat Commun. 2017;8:15746.

[34] Giacopelli B, Zhao Q, Ruppert AS, et al. Developmental subtypes assessed by DNA methylation-iPLEX forecast the natural history of chronic lymphocytic leukemia. Blood. 2019;134(8):688–698.

[35] Nadeu F, Royo R, Clot G, et al. IGLV3-21R110 identifies an aggressive biological subtype of chronic lymphocytic leukemia with intermediate epigenetics. Blood. 2021;137(21):2935–2946.

Limberger *et al. Molecular Cancer* (2022) 21:89
https://doi.org/10.1186/s12943-022-01542-8

Molecular Cancer

RESEARCH

Open Access

KMT2C methyltransferase domain regulated INK4A expression suppresses prostate cancer metastasis

Tanja Limberger[1,2], Michaela Schlederer[1], Karolina Trachtová[3,4,5], Ines Garces de los Fayos Alonso[1,6], Jiaye Yang[1], Sandra Högler[6], Christina Sternberg[1,6,7], Vojtech Bystry[3], Jan Oppelt[3], Boris Tichý[3], Margit Schmeidl[1], Petra Kodajova[6], Anton Jäger[1], Heidi A. Neubauer[8], Monika Oberhuber[2], Belinda S. Schmalzbauer[9], Sarka Pospisilova[3], Helmut Dolznig[10], Wolfgang Wadsak[2,5], Zoran Culig[11], Suzanne D. Turner[12,13], Gerda Egger[1,14], Sabine Lagger[6†] and Lukas Kenner[1,2,5,6*†]

Abstract

Background: Frequent truncation mutations of the histone lysine N-methyltransferase *KMT2C* have been detected by whole exome sequencing studies in various cancers, including malignancies of the prostate. However, the biological consequences of these alterations in prostate cancer have not yet been elucidated.

Methods: To investigate the functional effects of these mutations, we deleted the C-terminal catalytic core motif of *Kmt2c* specifically in mouse prostate epithelium. We analysed the effect of *Kmt2c* SET domain deletion in a *Pten*-deficient PCa mouse model in vivo and of truncation mutations of *KMT2C* in a large number of prostate cancer patients.

Results: We show here for the first time that impaired KMT2C methyltransferase activity drives proliferation and PIN formation and, when combined with loss of the tumour suppressor PTEN, triggers loss of senescence, metastatic dissemination and dramatically reduces life expectancy. In *Kmt2c*-mutated tumours we show enrichment of proliferative MYC gene signatures and loss of expression of the cell cycle repressor p16$^{\mathrm{INK4A}}$. In addition, we observe a striking reduction in disease-free survival of patients with *KMT2C*-mutated prostate cancer.

Conclusions: We identified truncating events of *KMT2C* as drivers of proliferation and PIN formation. Loss of PTEN and KMT2C in prostate cancer results in loss of senescence, metastatic dissemination and reduced life expectancy. Our data demonstrate the prognostic significance of *KMT2C* mutation status in prostate cancer patients. Inhibition of the MYC signalling axis may be a viable treatment option for patients with KMT2C truncations and therefore poor prognosis.

Keywords: Prostate cancer, Senescence, Metastasis, KMT2C, MYC, p16$^{\mathrm{INK4A}}$

Introduction

Prostate cancer (PCa) ranks as the second most frequently diagnosed malignancy in men worldwide and is expected to surpass even lung cancer incidence levels within the next decade [1, 2]. Diagnosis and therapy are challenged by enormous inter-tumour heterogeneity regarding clinical, morphological, and molecular features [3]. While patients with localized or regional disease have

---

*Correspondence: lukas.kenner@meduniwien.ac.at
[†] Sabine Lagger and Lukas Kenner contributed equally to this work.
[1] Division of Experimental and Translational Pathology, Department of Pathology, Medical University of Vienna, 1090 Vienna, Austria
Full list of author information is available at the end of the article

an excellent prognosis, metastatic PCa remains largely incurable [4]. Therefore, therapeutic strategies must be tailored to the individual risk of the patient to avoid overtreatment of low-risk tumours while ensuring rapid and decisive intervention in high-risk cases. To better stratify PCa and to advance the development of new therapies, a deeper understanding of the genetic and epigenetic events responsible for the progression and metastatic spread of PCa is urgently needed.

Multiple key pathways of prostate tumorigenesis have already been identified. Inactivating mutations of the phosphatase and tensin homolog (*PTEN*) tumour suppressor gene rank among the most common alterations observed in PCa [5]. Loss of PTEN results in the aberrant activation of the phosphoinositide 3-kinase (PI3K) – AKT signalling pathway, which uncouples proliferation, survival and metabolism from external growth-stimulatory signals [6]. However, loss of PTEN has also been shown to induce cellular senescence. This form of cell cycle arrest, which can be triggered upon oncogenic stress, is usually mediated via the p16$^{\mathrm{INK4A}}$-RB and the p14$^{\mathrm{ARF}}$-p53-p21$^{\mathrm{CIP1}}$ pathways and has previously been shown to act as a barrier to metastatic transformation in PCa [7]. Besides inactivation of tumour suppressor genes, the amplification and overexpression of oncogenes is similarly known to play a crucial role in prostate tumorigenesis. The frequently altered androgen receptor (AR) signalling axis is the most well-studied pathway in the context of PCa. However, other key effectors, such as the activation of the proto-oncogene MYC, have also been found to be fundamental to PCa progression [8].

Besides genetic mutations, several epigenetic alterations, including DNA and histone modifications, have been identified in clinical PCa samples. Only recently has the pivotal importance of epigenetic reprogramming as a driver of carcinogenesis been widely recognized [9, 10]. Large cancer genome sequencing projects have revealed a substantial number of alterations in epigenetic modulators [11]. The histone lysine N-methyltransferase *KMT2C*, an enzymatically active scaffold protein within the COMPASS (Complex Proteins Associated with Set1) multi-subunit complex, is the most frequently mutated gene within this group, predominantly presenting with frameshift and nonsense mutations [12, 13]. Previous studies have shown evidence of tumour suppressive roles for KMT2C and its close paralogue KMT2D, and have proposed their involvement in cellular growth, stemness and epithelial differentiation [13, 14]. However, despite the tremendous prevalence of mutations in these genes, the molecular mechanisms contributing to carcinogenic processes are still poorly understood [13]. In PCa, alterations of epigenetic modifiers and chromatin-remodelling genes occur in about 20% of tumours with a strong overrepresentation of *KMT2C* mutations (7%), suggestive of a crucial role in carcinogenesis [15]. A substantial number of mutations detected in *KMT2C* lead to loss of function of the encoded protein, whereby the catalytic domain is lost.

In this study, we investigated the effects of loss of the catalytic domain of KMT2C on the development and progression of PCa. We established a transgenic mouse model with prostate-specific deletion of either the catalytic core motif of KMT2C alone or in combination with loss of the tumour suppressor PTEN. In these models we observed that mutant KMT2C drives proliferation in vivo and triggers PCa metastasis when co-deleted with PTEN. Our data show that loss of the KMT2C catalytic core motif, mimicking the scenario in patients, results in an enrichment of the proliferative MYC gene signature and impairs p16$^{\mathrm{INK4A}}$-mediated cell cycle arrest in both our model system and human prostate cancers. Importantly, we show that mutated KMT2C significantly correlates with reduced disease-free survival (DFS) for PCa patients. Taken together, we identify the SET domain deletion of KMT2C as a novel driver of prostate carcinogenesis in murine models and suggest that the presence of mutated forms is a biomarker for poor outcome in PCa patients. Furthermore, our data are indicative of a possible therapeutic application through blockade of the MYC pathway.

Results

KMT2C SET Domain Deletion Initiates Formation of Prostatic Intraepithelial Neoplasia In Vivo

Whole exome sequencing studies of various human cancers have identified frequent somatic mutations in the gene encoding the histone-methyltransferase KMT2C [14]. Like other KMT2 proteins, KMT2C acts as a scaffold for the multi-subunit COMPASS complex where it regulates enhancer elements mainly through monomethylation of lysine 3 on histone 4 (H3K4me1) via the enzymatically active SET domain located at the C-terminal end of the protein [13, 16] (Fig. 1a). To gain insight into the mutational spectrum of human PCa we analysed a cohort of 1013 patients with either localized or metastatic disease (MSKCC/DFCI cohort) [15] and found *KMT2C* to be the 7th most frequently mutated gene (Fig. 1b, left panel). In contrast to previously published data of the mutational pattern of *KMT2C* in different human cancers [17], *KMT2C* mutations in the analysed PCa dataset were distributed along the gene with no apparent mutational hotspot (Supplementary Fig. 1a) in keeping with the types of mutations commonly observed in tumour suppressor genes. While the functional significance of individual missense mutations is difficult to discern, truncation mutations (nonsense, frameshift, and splice mutations), which account for the majority of the changes we detected in *KMT2C* in the MSKCC/DFCI cohort, are primarily predicted to negatively impact the C-terminal SET domain, and are twice as common in metastatic samples in this dataset (Fig. 1b, right panel). Thus, we hypothesized that mutations leading to loss of the methyltransferase activity of KMT2C play a functional role in the initiation and/or progression of PCa. To investigate the impact of impaired KMT2C methyltransferase activity in vivo we established a mouse model with prostate-specific deletion of the *Kmt2c* SET domain-encoding exons (Kmt2c$^{\mathrm{SET}\Delta/\Delta}$). Specifically, we crossed mice carrying loxP sites flanking exons 57 and 58, which encode the catalytic core motif of KMT2C [18], to mice carrying the *Cre* recombinase transgene under the control of the androgen-regulated prostate-specific probasin promoter (PbCre4) [19] (Fig. 1c). Deletion of the *Kmt2c* SET domain-encoding exons was confirmed after the onset of puberty at both genetic and transcriptional levels by Polymerase Chain Reaction (PCR) and quantitative reverse transcription—PCR (RT-qPCR), respectively (Supplementary Fig. 1b-c). RT-qPCR analysis of total *Kmt2c* mRNA expression, using primers detecting a region outside of the deleted locus, revealed comparable levels of the mutated mRNA transcripts in *Kmt2c*$^{\mathrm{SET}\Delta/\Delta}$ mouse prostates to wild type *Kmt2c* expression in control animals (Supplementary Fig. 1d). Interestingly, we found no compensatory up-regulation of the closely related paralogue *Kmt2d* (Supplementary Fig. 1e). Upon macroscopic evaluation, we discovered that the total prostate weight was significantly increased in mutant animals at 19 and 90 weeks *postpartum* (p.p.) compared to wild type controls (Fig. 1d, Supplementary Fig. 1f). Analysis of haematoxylin and eosin (H&E) stained sections of mouse prostates revealed focal areas of prostatic intraepithelial neoplasia (PIN) in Kmt2c$^{\mathrm{SET}\Delta/\Delta}$ mice sacrificed as early as 19 weeks p.p. increasing to full penetrance by 90 weeks p.p. (Fig. 1e-f). Immunohistochemistry (IHC) showed a significant increase in the percentage of Ki-67 positive proliferating cells in Kmt2c$^{\mathrm{SET}\Delta/\Delta}$ prostates (Fig. 1g-h, Supplementary Fig. 1g) and clusters of cells highly positive for AR expression, the primary driver of prostate cancer initiation and progression (Fig. 1i-j). These data suggest that loss of KMT2C catalytic activity drives proliferation and initiates transcriptional programs involved in prostate tumorigenesis evidenced by increased AR expression. However, even at 90 weeks of age mice showed only PIN, but no signs of PCa, suggesting that secondary events are required for full cancer progression. Thus, similar to many other prominent genetic alterations in PCa (e.g., affecting *TP53* or *ERG*), KMT2C inactivation is insufficient to initiate malignant transformation.

Mutant KMT2C Drives Metastatic Transformation in a *Pten*-null Mouse Model of Prostate Cancer

To identify genes with a potential additive effect to *KMT2C* mutations in PCa progression, we analysed the MSKCC/DFCI PCa patient cohort and found a significant co-occurrence of alterations in *PTEN* amongst other genes (Supplementary Fig. 2a). *PTEN* is the most prominent tumour suppressor gene in PCa [20]. Deleterious alterations of this gene are found in ~ 14% of primary and over 30% of metastatic PCa [21]. Previous studies have shown that prostate-specific deletion of *Pten* is sufficient to induce tumorigenesis in mice and that disease progression closely mimics early human PCa [22–24]. Therefore, we back-crossed a mouse model in

(See figure on next page.)

Fig. 1 Mutant KMT2C induces prostate intraepithelial neoplasia. **a** Schematic representation of the multi-subunit COMPASS (Complex Proteins Associated with Set1) complex containing KMT2C. KMT2C/D acts as a scaffold to bind multiple subunits unique to KMT2C or KMT2D containing COMPASS-like complexes (PAX-interacting protein 1 (PAXIP1), PAXIP1-associated glutamate-rich protein 1 (PAGR1), nuclear receptor coactivator 6 (NCOA6), lysine specific demethylase 6A (KDM6A)) as well as proteins common to all KMT2 complexes (WD repeat-containing protein 5 (WDR5), Retinoblastoma-binding protein 5 (RBBP5), Set1/Ash2 histone methyltransferase complex subunit ASH2 (ASH2L), Protein dpy-30 homolog (DPY30)). The SET domain located at the C-terminal end of the protein confers the methyltransferase activity needed to methylate lysine 3 on histone 4 (H3K4me1) at enhancer regions. **b** Spectrum of *KMT2C* mutations in the MSKCC/DFCI patient cohort comprised of 680 primary and 333 metastatic PCa samples. Data were retrieved from cBioPortal. Left panel: Top 10 most frequently mutated genes in this cohort. Right panel: Proportion of *KMT2C* alterations found in primary and metastatic PCa samples. Values within and above bars indicate alteration frequency of the respective mutation type and total percentage of altered samples, respectively. Samples with simultaneous mutations of more than one class are depicted with alternating stripes of both respective colours. **c** Scheme of the construct allowing for the conditional deletion of exon 57 and 58 within the SET domain of *Kmt2c*, which confers the methyltransferase activity, and the mutant transcript expressed specifically in prostate epithelial cells after *Cre*-mediated recombination controlled by the androgen-dependent *probasin* promoter (hereafter Kmt2c$^{\mathrm{SET}\Delta/\Delta}$). **d** Weight of wild type and Kmt2c$^{\mathrm{SET}\Delta/\Delta}$ prostates at 19 weeks p.p. ($n = 18$) **e** Representative pictures of PIN formation in a 19-week-old Kmt2c$^{\mathrm{SET}\Delta/\Delta}$ prostate. Wild type prostate is shown as a control. Scale bars: 50 µm. **f** Percentage of wild type and Kmt2c$^{\mathrm{SET}\Delta/\Delta}$ mice presenting with PIN at 19- and 90 weeks p.p. Number above the bar indicates PIN-positive/total number of analysed mice. ($n \geq 5$) **g-h** Representative pictures of Ki-67 IHC analysis of wild type and Kmt2c$^{\mathrm{SET}\Delta/\Delta}$ mouse prostate tissue at 19 weeks p.p. ($n \geq 9$) (**g**) and associated quantification (**h**). Scale bars: 50 µm. Cells positive for Ki-67 were quantified using QuPath software. **i-j** Representative pictures of AR IHC analysis of wild type and Kmt2c$^{\mathrm{SET}\Delta/\Delta}$ mouse prostate tissue at 19 weeks p.p. ($n \geq 9$) (**i**) and associated quantification (**j**). Scale bars: 50 µm. Stains were semi-quantitatively analysed by a board-certified genitourinary pathologist. Arbitrary unit (AU) is a multiplication of percentage of positive cells and staining intensity (0, 1, 2, 3). **(d**, **h**, and **j)** Individual biological replicates are shown. Data are plotted as the mean ± standard deviation, and *P* values were determined by unpaired two-tailed Student's t-tests

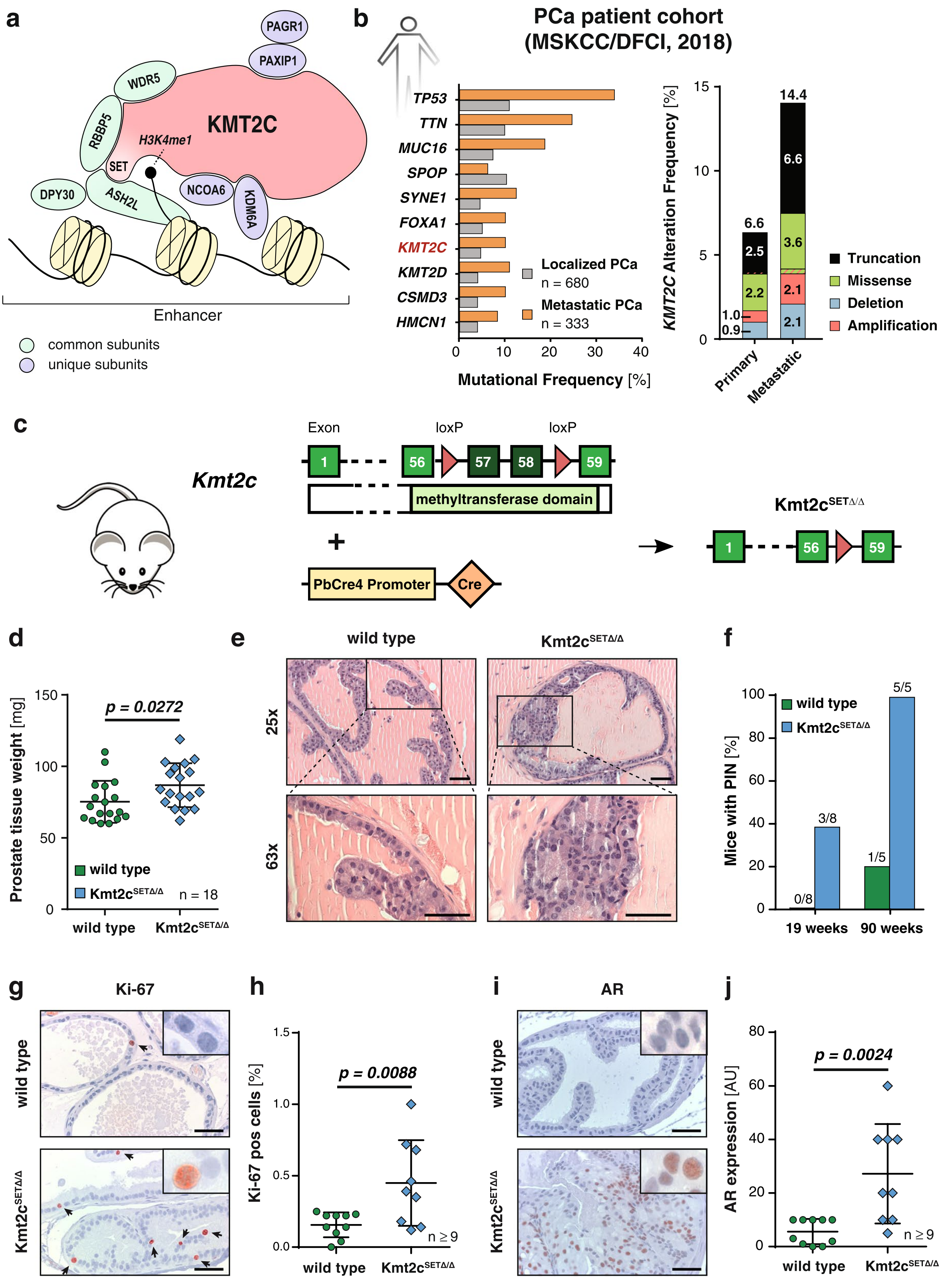

Fig. 1 (See legend on previous page.)

which conditional deletion of *Pten* is possible [24] to our Kmt2c$^{\text{SET}\Delta/\Delta}$ animals to generate a double transgenic line with prostate-specific loss of both *Kmt2c-SET* and *Pten* (Pten$^{\Delta/\Delta}$Kmt2c$^{\text{SET}\Delta/\Delta}$) (Fig. 2a).

Prostate-specific deletion of these genes was verified at the genetic level by PCR (Supplementary Fig. 2b). Efficient abrogation of *Pten* mRNA expression levels were found for both Pten$^{\Delta/\Delta}$ and Pten$^{\Delta/\Delta}$Kmt2c$^{\text{SET}\Delta/\Delta}$ prostates (Supplementary Fig. 2c). Deletion of the *Kmt2c* SET domain resulted in successful depletion of its full-length transcript. Expression levels of the mutant *Kmt2c* gene in Pten$^{\Delta/\Delta}$Kmt2c$^{\text{SET}\Delta/\Delta}$ double transgenic mice were comparable to full-length *Kmt2c* in Pten$^{\Delta/\Delta}$ mice (Supplementary Fig. 2e). We observed no compensatory upregulation of *Kmt2d* upon *Kmt2c* SET domain deletion (Supplementary Fig. 2f). In line with the H3K4 mono-methyltransferase activity of KMT2C we found a global reduction of the enhancer mark H3K4me1 but not H3K27ac in Pten$^{\Delta/\Delta}$Kmt2c$^{\text{SET}\Delta/\Delta}$ prostate tissue (Supplementary Fig. 2g-h). Prostates of mice sacrificed at 19 weeks p.p. were significantly enlarged in Pten$^{\Delta/\Delta}$Kmt2c$^{\text{SET}\Delta/\Delta}$ animals compared to Pten$^{\Delta/\Delta}$ controls (Fig. 2b-c). Interestingly, heterozygous deletion of *Kmt2c-SET* in combination with loss of *Pten* (Pten$^{\Delta/\Delta}$Kmt2c$^{\text{SET}\Delta/+}$) was sufficient to induce increased prostate weight indicative of tumour development (Fig. 2c).

We found a striking difference in the gross morphology between Pten$^{\Delta/\Delta}$Kmt2c$^{\text{SET}\Delta/\Delta}$ and Pten$^{\Delta/\Delta}$ tumours. Deletion of *Pten* alone in the prostate epithelium led to formation of cystic tumours comprised of ~ 40% fluid, while Pten$^{\Delta/\Delta}$Kmt2c$^{\text{SET}\Delta/\Delta}$ animals developed solid tumours with cyst formation observed only in a minority of mice (Fig. 2d). Histopathological analysis of the primary tumour tissue revealed locally invasive areas in Pten$^{\Delta/\Delta}$Kmt2c$^{\text{SET}\Delta/\Delta}$ animals compared to age matched Pten$^{\Delta/\Delta}$ mice. In Pten$^{\Delta/\Delta}$Kmt2c$^{\text{SET}\Delta/\Delta}$ prostates the basal cell layer was focally disrupted, and isolated tumour cells infiltrated into the surrounding stroma (Fig. 2e, Supplementary Fig. 2i). Double transgenic tumour cells infiltrating into blood vessels or nerve sheaths were observed at localised areas (Supplementary Fig. 2j). Furthermore, we found significantly more Ki-67 positive cells in Pten$^{\Delta/\Delta}$Kmt2c$^{\text{SET}\Delta/\Delta}$ tumours compared to Pten$^{\Delta/\Delta}$ controls (Fig. 2e-f). Strikingly, Pten$^{\Delta/\Delta}$Kmt2c$^{\text{SET}\Delta/\Delta}$ and even Pten$^{\Delta/\Delta}$Kmt2c$^{\text{SET}\Delta/+}$ mice showed a significant reduction in median life expectancy to 30 and 59 weeks, respectively, compared to > 80 weeks for Pten$^{\Delta/\Delta}$ animals ($p < 0.0001$; Fig. 2g). Pten$^{\Delta/\Delta}$ and Pten$^{\Delta/\Delta}$Kmt2c$^{\text{SET}\Delta/+}$ mice developed large tumours and had to be sacrificed due to tumour burden. In contrast, the general health of Pten$^{\Delta/\Delta}$Kmt2c$^{\text{SET}\Delta/\Delta}$ mice deteriorated rapidly after sudden disease onset despite significantly smaller tumour sizes. Necropsies of Pten$^{\Delta/\Delta}$Kmt2c$^{\text{SET}\Delta/\Delta}$ mice showed invasion of tumour cells into the urethra and urinary bladder, leading to severe obstructive uropathy with parenchymal reduction in the kidneys due to hydronephrosis (Fig. 3a, Supplementary Fig. 3a). This was accompanied by a sharp increase in serum creatinine levels, suggestive of renal failure (Supplementary Fig. 3b). These findings indicate a switch from organ confined PCa towards aggressive disease spreading beyond the prostate upon ablation of KMT2C activity in combination with PTEN loss.

To further investigate the invasive nature of Pten$^{\Delta/\Delta}$Kmt2c$^{\text{SET}\Delta/\Delta}$ prostate tumours we analysed draining lymph nodes and organs to identify metastatic tumour cells in mice showing clinical signs over 40 weeks of age. The prostatic origin of potential metastatic cells was determined by IHC staining of AR and keratin 8 (KRT8) (Fig. 3b). Lymph node metastases were found in more than 50% of analysed Pten$^{\Delta/\Delta}$Kmt2c$^{\text{SET}\Delta/\Delta}$ and 20% of Pten$^{\Delta/\Delta}$Kmt2c$^{\text{SET}\Delta/+}$ mice (Fig. 3b-c). Alongside lymphatic metastasis, prostatic tumour cells were detected in the blood vessels demonstrating metastatic dissemination via the circulatory system (Fig. 3b). Remarkably, 3 out of 10 Pten$^{\Delta/\Delta}$Kmt2c$^{\text{SET}\Delta/\Delta}$ mice had further progressed to develop lung metastases (Fig. 3b, d). In contrast, metastatic dissemination could not be found in lymph nodes or in distant organs in Pten$^{\Delta/\Delta}$ mice up to 90 weeks p.p., which is in agreement with previously published data [25, 26] (Fig. 3c-d). Kaplan

(See figure on next page.)

Fig. 2 Loss of the *Kmt2c* SET domain exacerbates prostate cancer tumorigenesis in *Pten*-null mice. **a** Scheme of the constructs allowing for the double deletion of *Kmt2c* (top) and *Pten* (bottom) in combination with expression of *Cre* recombinase under the control of the androgen-regulated *probasin* promoter. Mutated transcripts expressed specifically in the prostate epithelium after recombination are depicted on the right-hand side. **b** Representative pictures of prostates of wild type, Pten$^{\Delta/\Delta}$, Pten$^{\Delta/\Delta}$Kmt2c$^{\text{SET}\Delta/+}$ and Pten$^{\Delta/\Delta}$Kmt2c$^{\text{SET}\Delta/\Delta}$ mice resected at 19 weeks p.p. Scale bar: 10 mm. **c** Quantification of prostate tissue weight of wild type, Pten$^{\Delta/\Delta}$, Pten$^{\Delta/\Delta}$Kmt2c$^{\text{SET}\Delta/+}$ and Pten$^{\Delta/\Delta}$Kmt2c$^{\text{SET}\Delta/\Delta}$ prostates at 19 weeks p.p. ($n \geq 13$) **d** Percentage of cystic fluid per total tumour weight (solid tissue and fluid) of Pten$^{\Delta/\Delta}$, Pten$^{\Delta/\Delta}$Kmt2c$^{\text{SET}\Delta/+}$ and Pten$^{\Delta/\Delta}$Kmt2c$^{\text{SET}\Delta/\Delta}$ prostates at 19 weeks p.p. ($n \geq 13$) **e** Representative pictures of H&E (left panel) and Ki-67 (right panel) IHC staining of wild type, Pten$^{\Delta/\Delta}$, Pten$^{\Delta/\Delta}$Kmt2c$^{\text{SET}\Delta/+}$ and Pten$^{\Delta/\Delta}$Kmt2c$^{\text{SET}\Delta/\Delta}$ prostates at 19 weeks p.p., Scale bars: 100 µm. **f** Quantification of cells positive for Ki-67 using QuPath software. ($n \geq 8$) **g** Kaplan Meier cumulative survival analysis of wild type, Kmt2c$^{\text{SET}\Delta/\Delta}$, Pten$^{\Delta/\Delta}$, Pten$^{\Delta/\Delta}$Kmt2c$^{\text{SET}\Delta/+}$ and Pten$^{\Delta/\Delta}$Kmt2c$^{\text{SET}\Delta/\Delta}$ mice ($n \geq 5$). Values next to the dotted lines at the x-axis of the graph indicate the median life expectancy. *P* values were determined by log-rank (Mantel-Cox) tests. **(c, d, f)** Individual biological replicates are shown. Data are plotted as mean ± standard deviation, and *P* values were determined by ordinary one-way ANOVA with Tukey's multiple comparisons test

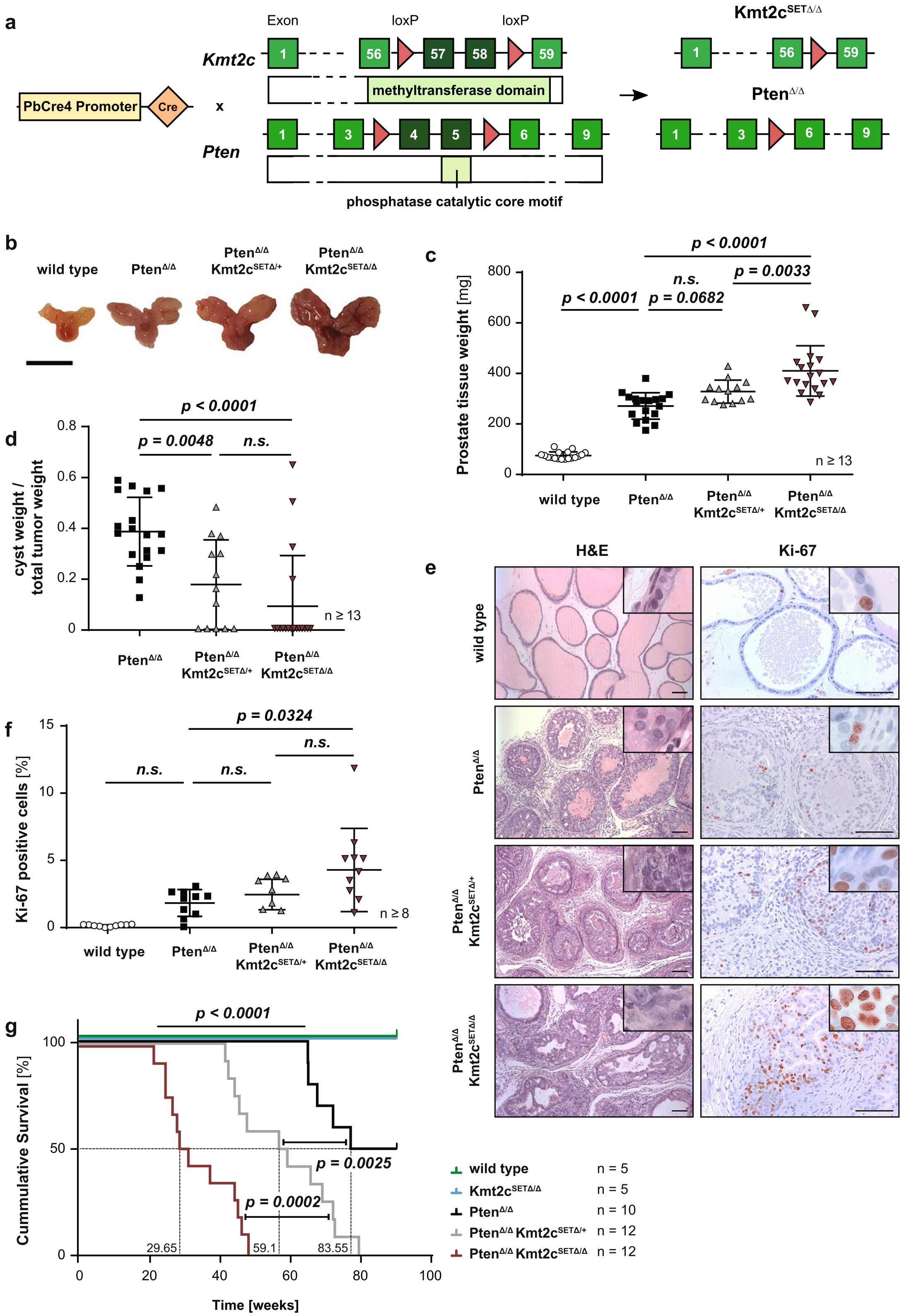

Fig. 2 (See legend on previous page.)

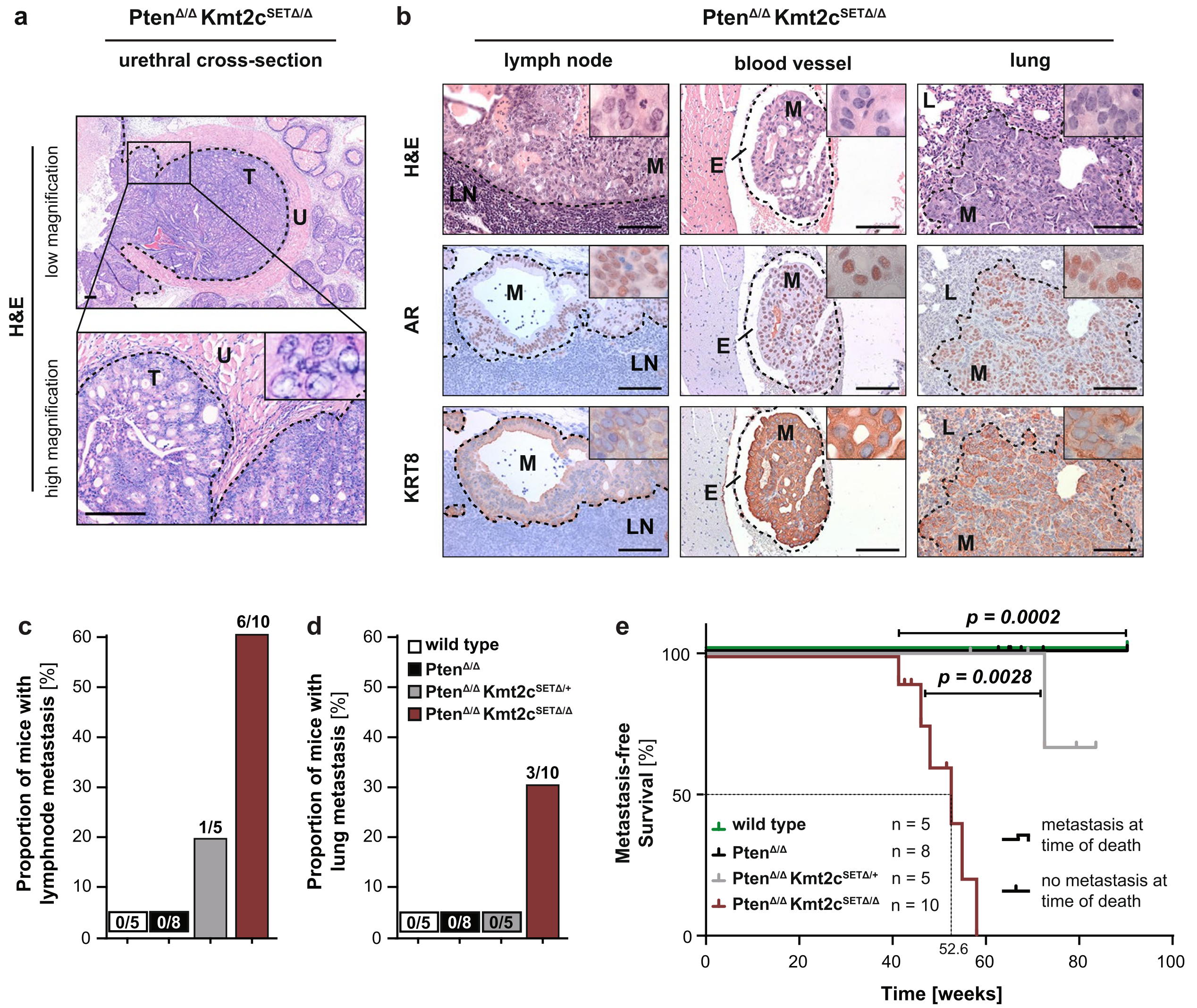

Fig. 3 KMT2C methyltransferase deficiency triggers metastatic dissemination of prostate cancer. **a** H&E stains of urinary tract obstruction by invasive PCa in a moribund Pten$^{\Delta/\Delta}$Kmt2c$^{SET\Delta/\Delta}$ mouse at 39 weeks p.p. at low (top) and high (bottom) magnification. Scale bars: 200 µm. T, tumour; U, urethra. **b** H&E-stained sections and IHC analysis of the androgen receptor (AR) and keratin 8 (KRT8) of tumour dissemination into lumbar lymph nodes, blood vasculature and lungs. Depicted material was derived from two moribund animals at 46- and 48-weeks p.p. Scale bars: 100 µm. LN, lymph node; L, lung; E, endothelial lumen; M, metastasis. **c-d** Percentage of wild type, Pten$^{\Delta/\Delta}$, Pten$^{\Delta/\Delta}$Kmt2c$^{SET\Delta/+}$ and Pten$^{\Delta/\Delta}$Kmt2c$^{SET\Delta/\Delta}$ mice presenting with lymph node (**c**) and lung (**d**) metastasis at the time of death. The number above the bar indicates metastasis-bearing/total number of analysed mice ($n \geq 5$). **e** Kaplan Meier analysis depicting wild type, Pten$^{\Delta/\Delta}$, Pten$^{\Delta/\Delta}$Kmt2c$^{SET\Delta/+}$ and Pten$^{\Delta/\Delta}$Kmt2c$^{SET\Delta/\Delta}$ mice having developed metastasis at the time of death ($n \geq 5$). Mice that did not present with metastasis at the time of death are shown as censored events. The value below the dotted line indicates the median metastasis-free survival of Pten$^{\Delta/\Delta}$Kmt2c$^{SET\Delta/\Delta}$ mice. The *P* value was determined by a log-rank (Mantel-Cox) test

Meier analysis, whereby an event is defined as the presence of metastatic disease detected on necropsy, showed a median time of metastasis-free survival of 52.6 weeks in Pten$^{\Delta/\Delta}$Kmt2c$^{SET\Delta/\Delta}$ animals (Fig. 3e). This suggests that a significant number of animals likely die due to renal failure from bladder obstruction, resulting from invasive growth of PCa into the local surrounding tissues, before distant metastases of a detectable size can form. Taken together, these data reveal that loss of KMT2C histone methyltransferase activity in *Pten*-null prostate tumours not only drives proliferation, but also confers invasive properties allowing tumour cells to invade surrounding tissues and spread to distant organs.

Transcriptional Profiling of KMT2C Mutated Prostate Epithelial Cells Reveals Enrichment of the Proliferative MYC Gene Signature

We performed RNA sequencing (RNA-Seq) of prostate tissue from wild type, Kmt2c$^{\mathrm{SET}\Delta/\Delta}$, Pten$^{\Delta/\Delta}$ and Pten$^{\Delta/\Delta}$Kmt2c$^{\mathrm{SET}\Delta/\Delta}$ mice at 19 weeks p.p. following the onset of tumour formation to gain insights into alterations in gene expression that are associated with the observed phenotypes. Cells expressing the epithelial cell adhesion molecule (EpCAM) were isolated from prostate tissue using a magnetic bead-based cell sorting approach. Successful enrichment of EpCAM$^{\mathrm{pos}}$ cells was confirmed using fluorescence activated cell sorting (FACS) (Fig. 4a) before RNA isolation and RNA-Seq was conducted. Principal component analysis revealed a clear separation of tumour samples (Pten$^{\Delta/\Delta}$ and Pten$^{\Delta/\Delta}$Kmt2c$^{\mathrm{SET}\Delta/\Delta}$) according to their genotypes. In contrast, Kmt2c$^{\mathrm{SET}\Delta/\Delta}$ samples clustered closely with wild type samples, indicating only minor changes in overall gene expression between these groups (Supplementary Fig. 4a). These results substantiate our previous data, highlighting the importance of KMT2C in tumour progression rather than initiation. Whereas differential gene expression analysis of the transcriptomes of Pten$^{\Delta/\Delta}$Kmt2c$^{\mathrm{SET}\Delta/\Delta}$ with *Pten*-null prostate epithelial cells showed significant up-regulation of 252 and down-regulation of 943 genes (Fig. 4b) the number of significantly deregulated genes between the wild type and Kmt2c$^{\mathrm{SET}\Delta/\Delta}$ cells was considerably smaller with only 5 up- and 80 downregulated transcripts in Kmt2c$^{\mathrm{SET}\Delta/\Delta}$ mice (Supplementary Fig. 4b). To gain further insight into the pathways affected by these gene expression changes, we performed fast pre-ranked gene set enrichment analysis (fGSEA) using hallmark gene sets derived from MSigDB [27, 28]. In accordance with our previous results, we found a significant enrichment for genes driving proliferation upon loss of the KMT2C methyltransferase domain (Fig. 4c, Supplementary Fig. 4c). Of note, we found the proto-oncogene *Myc*, which is a known master regulator of proliferation, and its downstream targets *Ccnd1* and *Ccnd2* to be upregulated in Pten$^{\Delta/\Delta}$Kmt2c$^{\mathrm{SET}\Delta/\Delta}$ samples (Fig. 4d, Supplementary Fig. 4d). In line with this observation, MYC target genes were overrepresented in *Kmt2c* SET domain deleted samples (Fig. 4e, Supplementary Fig. 4e). Overexpression of MYC in the progression of PCa has previously been observed [8, 29]. Additionally, MYC expression has been shown to correlate with increased disease severity and to positively regulate the well described PCa driver AR [30, 31]. In line with this dependency, we observed an upregulation of androgen response genes in Pten$^{\Delta/\Delta}$Kmt2c$^{\mathrm{SET}\Delta/\Delta}$ samples (Supplementary Fig. 4f). Besides its role in cellular proliferation, MYC has been recognized as regulating epithelial-to-mesenchymal (EMT) transition and in the general acquisition of invasive properties of cancer cells [32]. Accordingly, an enrichment of genes involved in EMT was observed upon *Kmt2c* SET domain deletion (Fig. 4f, Supplementary Fig. 4 g). To further confirm the invasive nature of Pten$^{\Delta/\Delta}$Kmt2c$^{\mathrm{SET}\Delta/\Delta}$ prostate epithelial cells we analysed two additional sets of genes described in general to be upregulated in metastatic tumours (RAMASWAMY Metastasis_UP) [33] or lymph node metastasis in PCa (PCa LN Metastasis_UP) [34] and found both signatures to be enriched in the double transgenic samples (Pten$^{\Delta/\Delta}$Kmt2c$^{\mathrm{SET}\Delta/\Delta}$) compared to controls (Fig. 4g-h). Taken together, changes in the transcriptome observed upon disruption of KMT2C methyltransferase activity verify the activation of proliferative signalling pathways and indicate alterations in processes involved in disease aggressiveness.

Mutant KMT2C Impairs Oncogene-Induced Expression of the Cell Cycle Repressor p16$^{\mathrm{INK4A}}$

While sustained growth-stimulatory signalling is a fundamental trait of cancer cells, the replicative stress induced by excessive proliferation may elicit a counteractive growth arrest. This tumour suppressive process, known as oncogene-induced senescence (OIS), can present a barrier to malignant transformation of precursor lesions and must be overcome for tumours to progress to lethal, metastatic disease [35, 36]. Elevated signalling by strong oncogenic drivers, as well as loss of potent tumour suppressors, such as PTEN, have been described to trigger OIS, highlighting the potentially crucial role of this phenomenon in our model system [35, 37]. The unrestrained proliferation and metastatic dissemination of

(See figure on next page.)

Fig. 4 Mutant KMT2C results in enrichment of the MYC gene signature in prostate epithelial cells. **a** Schematic overview of the magnetic bead-based enrichment procedure of murine prostate epithelial cells. Sequence from left to right: 19-week-old mice were sacrificed and prostates were dissected. Tissue was enzymatically and mechanically dissociated to generate single cell suspensions. Cells were labelled with biotinylated anti-EpCAM antibody and retrieved from the bulk population using streptavidin-coated magnetic beads. The sorting efficiency was verified via flow cytometry. **b** Unsupervised hierarchical clustering and heatmap of significant differentially expressed genes between Pten$^{\Delta/\Delta}$ and Pten$^{\Delta/\Delta}$Kmt2c$^{\mathrm{SET}\Delta/\Delta}$ prostate epithelial cells. 5 biological replicates were included per group. Number of genes deregulated with an adj. *P* value < 0.05 and $\log_2$FC ≥ 1 / ≤ -1 are shown on the left. **c** HALLMARK gene sets enriched in Pten$^{\Delta/\Delta}$Kmt2c$^{\mathrm{SET}\Delta/\Delta}$ versus Pten$^{\Delta/\Delta}$ groups at an FDR < 0.25. Dotted lines: adj. *P* value = -log10(0.05). **d** Gene expression levels of *Myc* based on normalized counts from RNA-Seq analysis of Pten$^{\Delta/\Delta}$ and Pten$^{\Delta/\Delta}$Kmt2c$^{\mathrm{SET}\Delta/\Delta}$ prostate epithelial cells. Individual biological replicates are shown. Data are plotted as mean ± standard deviation, and the *P* value was determined by unpaired two-tailed Student's t-test. **e–h** fGSEA plots of Pten$^{\Delta/\Delta}$Kmt2c$^{\mathrm{SET}\Delta/\Delta}$ versus Pten$^{\Delta/\Delta}$ groups showing an enrichment of MYC target genes (HALLMARK_MYC_TARGETS_V1) (**e**), genes involved in EMT (HALLMARK_EPITHELIAL_MESENCHYMAL_TRANSITION) (**f**), genes upregulated in metastasis of solid tumours (RAMASWAMY_METASTASIS_UP) (**g**) and genes upregulated in prostate cancer lymph node metastasis versus primary prostate cancer (PCa LN Metastasis UP, see also Supplementary Materials and Methods) (**h**)

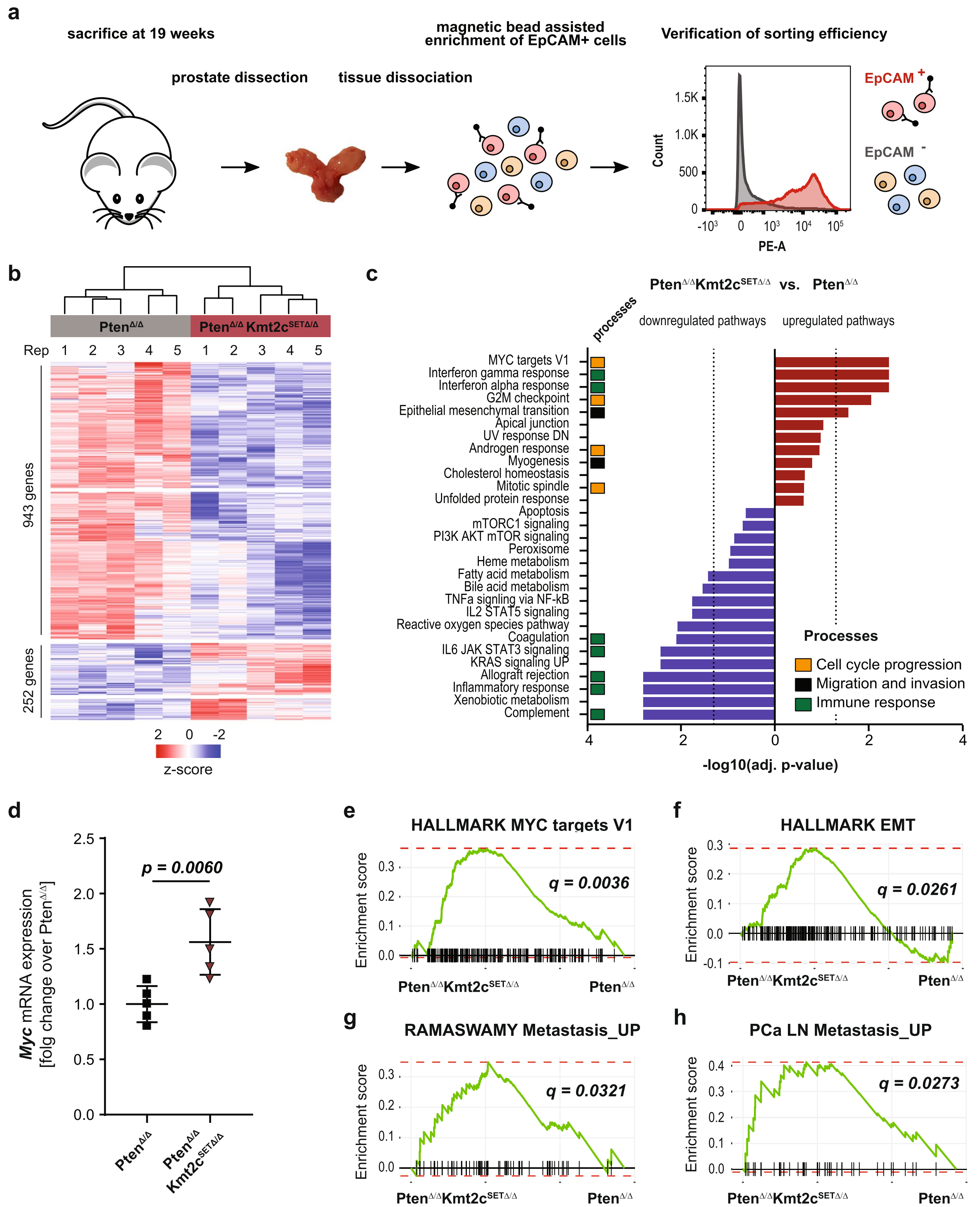

Fig. 4 (See legend on previous page.)

Pten$^{\Delta/\Delta}$Kmt2c$^{\text{SET}\Delta/\Delta}$ prostate tumour cells described so far indicate an escape from PTEN-loss induced cellular senescence (PICS) in KMT2C mutant tumours. Another key attribute of senescent cells is the extensive change in expression of inflammatory cytokines and other signalling molecules known as the senescence-associated secretory phenotype (SASP) [38]. Interestingly, analysis of the RNA-Seq data (Fig. 4) revealed a significant deregulation of immune response pathways between the transcriptomes of Pten$^{\Delta/\Delta}$ and Pten$^{\Delta/\Delta}$Kmt2c$^{\text{SET}\Delta/\Delta}$ prostate epithelial cells (Fig. 4c). This might reflect changes to the SASP as there is considerable overlap of genes involved in those processes. To further investigate potential loss of the SASP gene signature in Pten$^{\Delta/\Delta}$Kmt2c$^{\text{SET}\Delta/\Delta}$ prostate cells we performed fGSEA using a set of genes previously described to be induced upon PICS ("core SASP of PICS") [39] and found them to be strongly downregulated in the Pten$^{\Delta/\Delta}$Kmt2c$^{\text{SET}\Delta/\Delta}$ double transgenic group compared to Pten$^{\Delta/\Delta}$ mouse prostate cells (Fig. 5a). Next, we performed IHC staining of mouse prostate tissue taken from mice at 19 weeks p.p. for the senescence markers β-galactosidase (GLB1) and p16$^{\text{INK4A}}$. Pten$^{\Delta/\Delta}$ prostate cells showed an accumulation of GLB1 and pronounced induction of p16$^{\text{INK4A}}$ which corroborates previously published data describing senescence in the Pten$^{\Delta/\Delta}$ PCa mouse model [37]. In contrast, expression of both markers was lower in Pten$^{\Delta/\Delta}$Kmt2c$^{\text{SET}\Delta/\Delta}$ prostate samples (Fig. 5b-d). As senescence is known to be mediated by the two isoforms of *Cdkn2a*, p16$^{\text{INK4A}}$ and p19$^{\text{ARF}}$, and the *Cdkn1a* gene product p21$^{\text{CIP1}}$ [38] we analysed expression of these genes via RT-qPCR. In line with the induction of senescence upon loss of *Pten,* expression of *Cdkn2a* transcripts and, to a lesser extent, *Cdkn1a* was induced in Pten$^{\Delta/\Delta}$ samples. Combined loss of *Pten* with the *Kmt2c* SET domain led to the loss of p16$^{\text{INK4A}}$ expression and a similar but less pronounced effect for p19$^{\text{ARF}}$ (Fig. 5e). Western blot analysis for p16$^{\text{INK4A}}$ and the cyclin-dependent kinase CDK4, which is known to be inhibited by p16$^{\text{INK4A}}$, confirmed the loss of p16$^{\text{INK4A}}$ detected in Pten$^{\Delta/\Delta}$Kmt2c$^{\text{SET}\Delta/\Delta}$ protein lysates and an upregulation of CDK4. In addition, we analysed p53 expression, the key mediator of p19$^{\text{ARF}}$-p53-p21$^{\text{CIP1}}$-mediated senescence but did not detect a deregulation of this axis at the protein level nor at the transcript level as indicated by no significant change in p21 levels (Fig. 5e-g). We therefore conclude that mutant KMT2C impairs the induction of OIS in *Pten*-null mice by circumventing p16$^{\text{INK4A}}$-mediated cell cycle arrest.

KMT2C Truncation Mutations are Associated with Increased Proliferation and Reduced Disease-Free Survival for Prostate Cancer Patients

We have identified KMT2C SET domain deletion as a driving event of metastatic PCa in our murine model system and have observed an enrichment of the MYC gene signature accompanied by concurrent loss of p16$^{\text{INK4A}}$ as mechanistic downstream effects. Therefore, we hypothesized that *KMT2C* truncation mutations may be associated with aggressive disease and poor prognosis in PCa patients. Therefore, we stratified sample data derived from the Cancer Genome Atlas Prostate Adenocarcinoma (TCGA-PRAD) [20] patient cohort into *KMT2C* wildtype and *KMT2C* truncated tumours for further pathway analysis. Analogous to our murine data, fGSEA of hallmark gene sets revealed strong upregulation of proliferative pathways, with MYC target genes ranking as the most highly enriched gene sets (Fig. 6a-b). Furthermore, mRNA expression of *MYC* itself was upregulated in patient samples carrying *KMT2C* truncation mutations (Fig. 6c). In line with the capacity of MYC to induce transcription and enhance the stability of the AR, we detected enrichment of androgen response genes in the *KMT2C* truncated patient group (Supplementary Fig. 5a). As our murine data show that activation of proliferative signalling pathways occurs concurrently with evasion of p16$^{\text{INK4A}}$-mediated growth arrest, we performed fGSEA on the "core SASP of PICS" gene set and found a significant reduction of this transcriptional signature in *KMT2C* truncated tumours (Supplementary Fig. 5b), potentially indicating loss of senescence features. We further observed a reduction in expression of the gene encoding p16$^{\text{INK4A}}$, *CDKN2A*, in these samples

(See figure on next page.)

Fig. 5 KMT2C SET domain is crucial for oncogene-induced expression of the cell cycle repressor p16$^{\text{INK4A}}$. **a** fGSEA plot of Pten$^{\Delta/\Delta}$Kmt2c$^{\text{SET}\Delta/\Delta}$ versus Pten$^{\Delta/\Delta}$ transcriptomes showing a depletion of the core SASP gene signature previously described upon PICS in Pten$^{\Delta/\Delta}$Kmt2c$^{\text{SET}\Delta/\Delta}$ samples (core SASP of PICS, see also Supplementary Materials and Methods). **b** IHC staining for GLB1 and p16$^{\text{INK4A}}$ on prostate tissue of 19-week-old wild type, Pten$^{\Delta/\Delta}$ and Pten$^{\Delta/\Delta}$Kmt2c$^{\text{SET}\Delta/\Delta}$ mice. Scale bars: 50 µm. **c** Semi-quantitative analysis of GLB1 staining intensity performed by a board-certified pathologist. Expression was classified as low, medium, or high of 5 biological replicates analysed per group. **d** Quantification of cells positive for p16$^{\text{INK4A}}$ using QuPath software ($n=5$). **e** RT-qPCR based quantification of *Cdkn2a transcript variant 2* (*p16), Cdkn2a transcript variant 1* (*p19)* and *Cdkn1a* (*p21)* mRNA transcripts ($n \geq 5$). *P* values of statistically non-significant results are included in the graph for $P<0.1$ and are additionally labelled as non-significant (n.s.) **f** Western blot analysis showing protein levels of p16$^{\text{INK4A}}$, CDK4 and p53 for wild type, Pten$^{\Delta/\Delta}$ and Pten$^{\Delta/\Delta}$Kmt2c$^{\text{SET}\Delta/\Delta}$ prostate lysates ($n \geq 4$). β-Actin and β-Tubulin serve as loading controls. The number above the band depicts the fold change over the average expression level detected in Pten$^{\Delta/\Delta}$ samples. ǂ indicates unspecific bands. **g** Quantification of Western blots shown in Fig. 5f. (**d-e, g**) Individual biological replicates are shown. Data are plotted as mean ± standard deviation, and *P* values were determined by unpaired two-tailed Student's t-test (**d**) or ordinary one-way ANOVA with Tukey's multiple comparisons test (**e**, **g**)

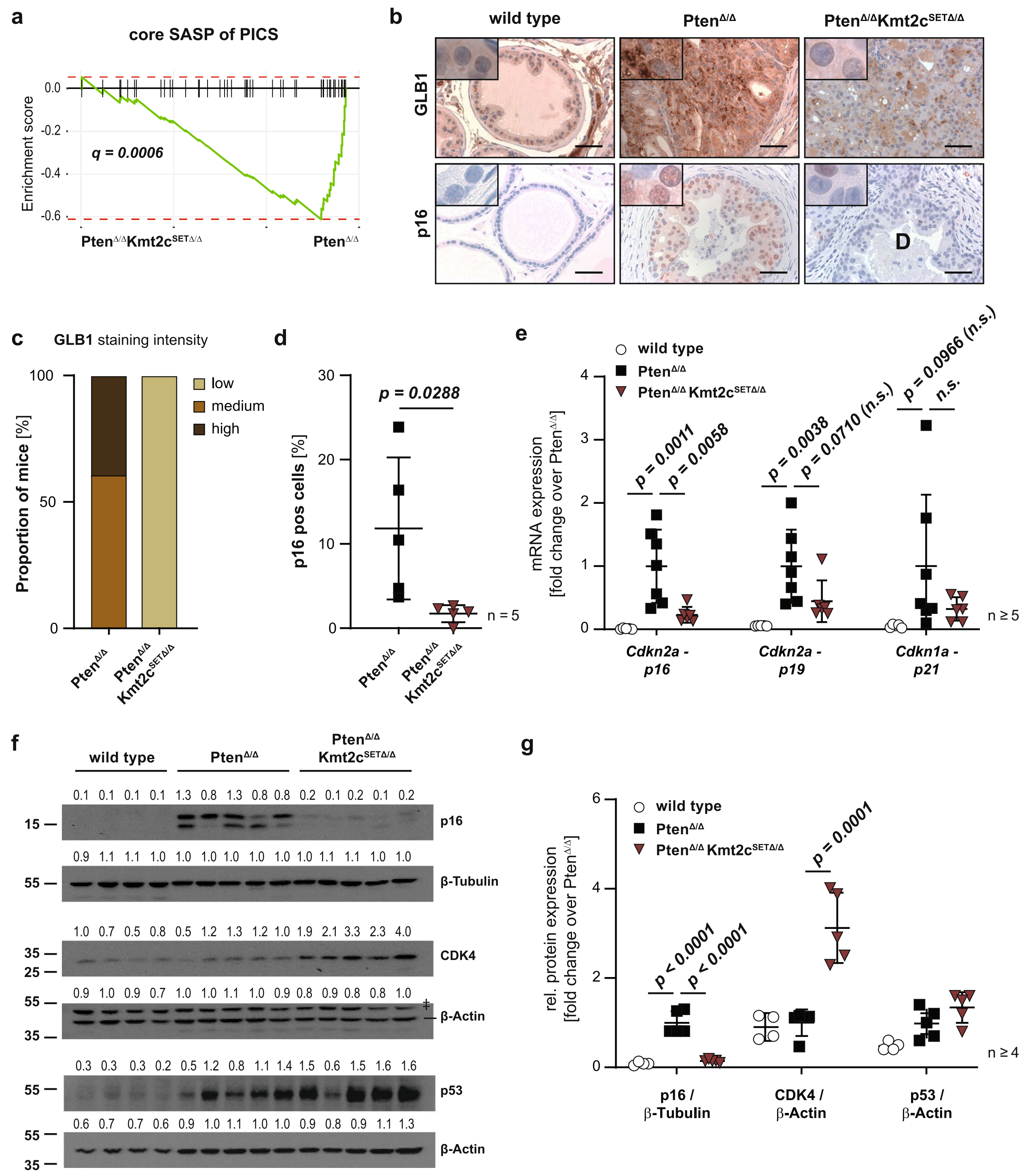

Fig. 5 (See legend on previous page.)

(Fig. 6d). As p16^{INK4A} inhibits cell cycle progression at the G1/S transition, we performed fGSEA of two sets of genes upregulated during this process (REACTOME G1/S, FISCHER G1/S) and found these to be highly enriched in the *KMT2C* truncated patient group, further highlighting the likely depletion of cell cycle repressors in this cohort (Fig. 6e). Collectively, these data indicate hyperactivation of proliferation in PCa carrying truncated forms of KMT2C, which is remarkably similar to the effect observed in our model system. Thus, we hypothesize that *KMT2C* mutations, in agreement with our murine data, also influence prognosis in PCa. Therefore, we analysed data derived from the International Cancer Genome Consortium (ICGC) [40] and found that *KMT2C* truncation mutations (nonsense and frameshift mutations) correlate with reduced disease-free survival (DFS) in PCa (Fig. 6f). Taken together our data show that KMT2C truncating events drive cancer progression by upregulating MYC target genes and circumventing p16^{INK4A}-mediated growth arrest. These effects may ultimately facilitate the formation of lethal, metastatic disease in PCa patients. Therefore, *KMT2C* truncation mutations represent a biomarker for aggressive disease and indicate that inhibitors of the MYC signalling axis might be beneficial to these patients.

Discussion

Although KMT2C is the most frequently mutated epigenetic regulator in PCa [15], and loss of histone methylation correlates with a poorer clinical outcome [41], functional studies investigating the impact of these mutations on prostate carcinogenesis are scarce. Here, we describe for the first time that loss of the KMT2C methyltransferase domain accelerates tumour growth and promotes a switch from indolent to lethal, metastatic disease in vivo when combined with other PCa associated mutational events, specifically loss of PTEN. Our study also reveals that this exacerbation of tumour progression is accompanied by an enrichment of the proliferative MYC gene signature and an escape of p16^{INK4A}-mediated oncogene-induced senescence.

Previous studies have shown correlations between expression levels of KMT2C and cancer progression, while others have instead highlighted the importance of genetic alterations affecting protein function [17, 42–44]. To date, the contribution of KMT2C to carcinogenesis has most extensively been studied in breast cancer (BCa), which is biologically similar to PCa due to its dependence on steroid hormone signalling. Reduced expression of KMT2C or KMT2D results in decreased oncogenic estrogen receptor (ER) signalling, possibly due to impaired interaction with the ER pioneer factor Forkhead box protein A1 (FOXA1) [44, 45]. In contrast, low KMT2C expression correlates with bad prognosis in BCa [43] and both truncation mutations as well as mutations in the plant homeodomain (PHD) of KMT2C have been shown to be tumour-promoting events [17, 44]. Thus, the contribution of KMT2C to carcinogenesis appears to be influenced by cellular context, alteration type, as well as hormone-dependence even within a single malignancy. Our analysis of the mutational spectrum in PCa patients showed a high prevalence of nonsense and frameshift mutations resulting in truncated forms of KMT2C, especially in metastatic samples. We therefore focused our work on the genetic loss of the C-terminal methyltransferase domain rather than the analysis of expressional changes.

To study the complex biological consequences of KMT2C alterations in vivo, we established a genetically engineered mouse model (GEMM) with a prostate epithelium specific deletion of the catalytic core motif of *Kmt2c*. *Kmt2c*-mutated animals developed PIN lesions but never progressed to develop carcinomas. This observation resembles other GEMMs modelling key alterations observed in human PCa, such as deletion of *TP53* or overexpression of ERG or AR in the prostate epithelium [25, 46, 47]. Regardless, loss of the *Kmt2c* SET domain resulted in the activation of the oncogenic AR signalling pathway and a significant increase in cellular proliferation, albeit at low levels. These data are in contrast to the ability of wildtype KMT2C/D in facilitating the closely related ER signalling axis in BCa [44, 45]. A potential difference in interaction of ER and AR with their co-regulators, including FOXA1, might result in diverging effects of KMT2C on these transcriptional programs. However, the varied effects of KMT2C observed across different BCa model systems hints at a multitude of factors capable of influencing the biological outcome of KMT2C alterations in carcinogenesis.

Previous studies have identified loss of PTEN or overexpression of MYC to be sufficient to induce carcinogenesis in vivo. However, neither alteration leads to

(See figure on next page.)

Fig. 6 KMT2C truncations enhance MYC target gene expression and correlate with reduced DFS for PCa patients. **a** HALLMARK gene sets enriched in patients with *KMT2C* truncation mutations versus wild type forms of *KMT2C*. Gene sets enriched at an FDR < 0.05 are depicted. Dotted lines: adj. *P* value = -log10(0.05). **b** fGSEA plots of *KMT2C* truncated versus *KMT2C* wild type (wt) prostate cancer patient samples showing an enrichment for MYC target genes (HALLMARK_MYC_TARGETS_V1, HALLMARK_MYC_TARGETS_V2). **c-d** *MYC* (**c**) and *CDKN2A* (**d**) mRNA expression levels in prostate cancer patients with wild type ($n = 461$) or truncated ($n = 15$) forms of *KMT2C*. Data are shown as box and whiskers (min to max) plots, and *P* values were determined by a Mann–Whitney test for non-normal distribution (**c**) or a two-tailed unpaired Student's t-test (**d**). **e** fGSEA plots of *KMT2C* truncated versus *KMT2C* wild type (wt) prostate cancer patient samples showing an enrichment of transcriptional signatures upregulated during G1/S phase transition (REACTOME_G1_S_TRANSITION, FISCHER_G1_S_CELL_CYCLE). **f** Disease free survival for prostate cancer patients dependent of the *KMT2C* mutational status. Frameshift and nonsense mutations were grouped as truncation mutations (wild type *KMT2C*: $n = 724$; truncated *KMT2C*: $n = 11$). Samples with alterations that were not classified as truncation mutations were excluded from the analysis. Data were retrieved from the ICGC Data Portal and analysed by a log-rank (Mantel-Cox) test. **(a-e)** Data were derived from the TCGA-PRAD dataset

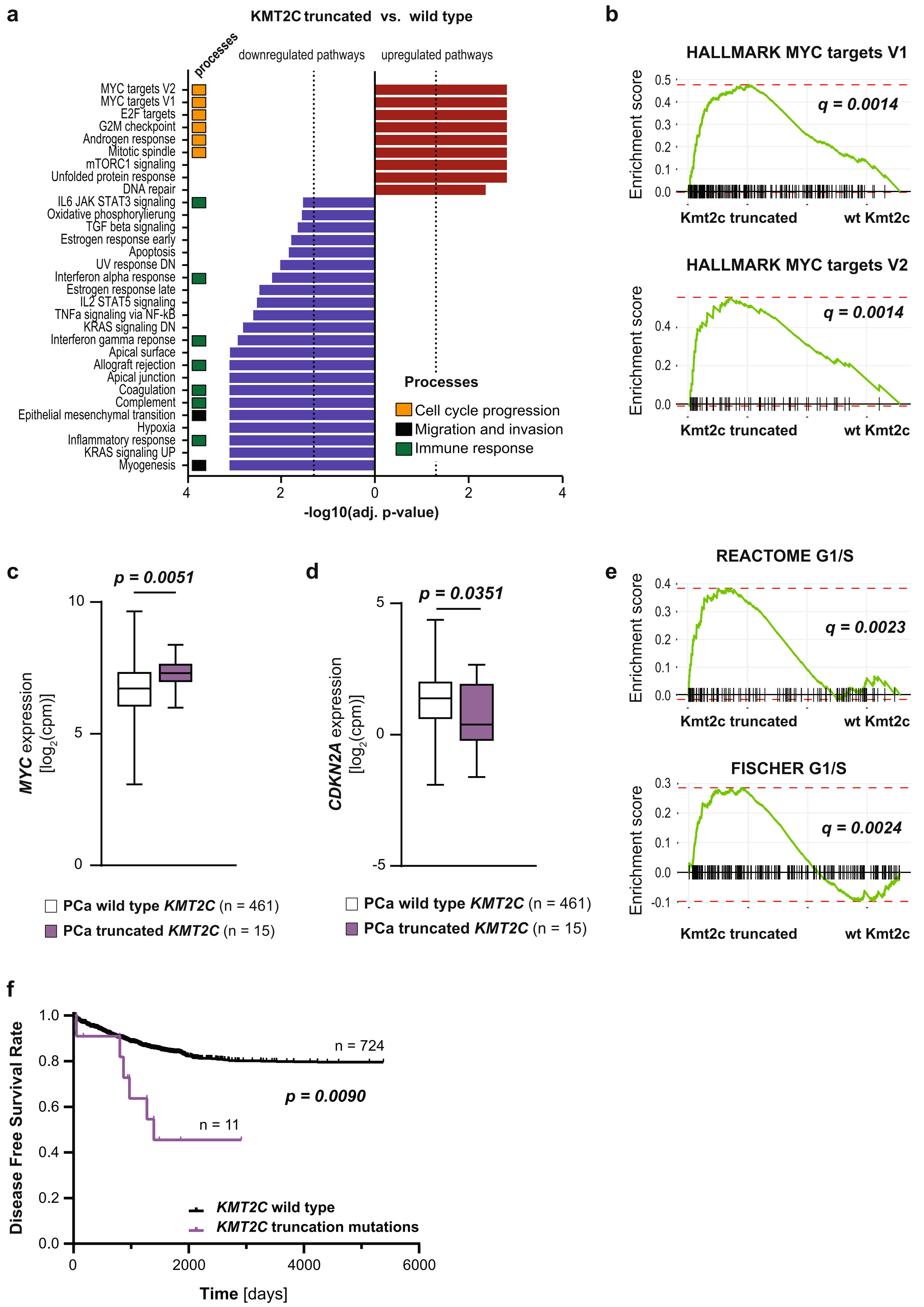

Fig. 6 (See legend on previous page.)

metastatic disease suggesting a requirement for other contributory genetic events [23, 48]. Formation of distant metastasis has previously been achieved in the *Pten*-null model in combination with select additional genetic alterations [26, 39, 49–51]. For example, it was recently shown that the combined overexpression of MYC and loss of *Pten* in prostate luminal epithelial cells can induce lethal metastatic PCa [52]. Our analysis of the mutational spectrum present in PCa patients revealed a significant co-occurrence of *PTEN* and *KMT2C* alterations, pointing towards a synergistic effect. In accordance, we demonstrate in our study that *Kmt2c* SET domain deletion represents an as-yet unknown aberration capable of initiating the important switch from localized to metastatic PCa in a *Pten*-null GEMM.

A frequent observation in relation to metastatic transformation is the circumvention of the senescent phenotype initiated upon *Pten*-deficiency [37], or upregulation of the proto-oncogene MYC [50–52]. There is ample evidence for the fundamental role of senescence as an abortive stage of cancer development. However, its impact on tumorigenesis appears to be diverse and highly dependent on the context in which it arises. A multitude of inducers of senescence have been described, yet the molecular effectors activated downstream mainly converge on two major tumour suppressive pathways: the $p16^{INK4A}$-RB and the $p14^{ARF}$-p53-$p21^{CIP1}$ signalling axes [53]. Interestingly, genetic deletion of *p19*^{Arf}, the murine homolog to *p14*^{ARF}, in *Pten*-null mice does not impact p53 expression in vivo and is not sufficient to abrogate senescence or promote tumorigenesis [54]. Furthermore, while senescent features are lost in *Pten / p53* double-knockout prostate epithelial cells in a GEMM, the formation of distant metastases was not observed [25]. These findings indicate that circumvention of OIS may be insufficient to drive metastatic transformation and needs to occur in parallel with the induction of an additional driver of cellular dissemination. In our model system, combined deletion of *Pten* and the *Kmt2c* catalytic core motif led to loss of $p16^{INK4A}$ in double transgenic mice but failed to convincingly show any change in the $p19^{ARF}$-p53-$p21^{CIP1}$ axis. Still, we observed a loss of senescence features and, more importantly, a drastic reduction in life expectancy due to obstructive tumour cell infiltration into the urethra and the development of lymph node and lung metastases. Our data additionally suggest a possible involvement of the MYC signalling axis in the switch to metastatic PCa in our model system based on increased expression of MYC target genes and an upregulation of *Myc* mRNA levels. However, as other drivers of proliferation might activate a similar set of downstream targets and MYC protein levels and activity are tightly controlled not only on transcriptional level but also through RNA stability, protein turnover and posttranslational modifications [55] the transcriptional changes observed in our model system may not exclusively point towards MYC but drivers of proliferation in general.

Based on the functional role of KMT2C as an H3K4 mono-methyltransferase, loss of $p16^{INK4A}$ might directly be regulated by impaired placement of activating H3K4me1 marks at enhancer elements associated with *Cdkn2a*. On the other hand, an upregulation of *Myc* is unlikely to be a direct effect of H3K4me1 loss and possibly mediated by the downregulation of a transcriptional inhibitor of *Myc* instead. While our data convincingly show a global deregulation of H3K4me1 upon impaired KMT2C methyltransferase activity deciphering site specific changes in the enhancer landscape in our model system and how they correlate with transcriptional changes remains to be investigated.

The relevance of our findings to human patients is supported by the fact that we observe both enrichment of the MYC gene signature and downregulation of *CDKN2A*, which encodes $p16^{INK4A}$, in PCa patients with truncation mutations of *KMT2C*. Remarkably, we found a significant correlation between DFS and truncated *KMT2C* in patients, demonstrating the prognostic significance of *KMT2C* mutation status in PCa. Based on our findings, we speculate that inhibition of MYC transcriptional activity may be a viable treatment option for patients with *KMT2C* truncation mutations. Furthermore, elucidating the complex transcriptional networks that are altered in response to *KMT2C* mutations uncovered in this study may facilitate the identification of novel pro-metastatic pathways and promote the development of new clinical therapeutics that can counteract PCa metastases.

Taken together, this work reveals new insights into the previously poorly understood transition from local to lethal metastatic PCa. Furthermore, data presented in this study provide a rationale for the inclusion of *KMT2C* mutation status in standard diagnostics of patients with suspected PCa. Based on our findings, inhibition of MYC-associated transcriptional activity could represent a strategy for treating PCa patients with deleterious *KMT2C* mutations and thus a poor prognosis. As many other human cancers also show a high *KMT2C* mutation prevalence our work may have translational relevance to an array of malignancies similarly affected.

Methods

Analysis of mutation data from publicly available datasets

Mutation data including frequency and co-occurrence of specific mutations in PCa patients were obtained from the MSKCC/DFCI dataset using http://www.cbioportal.org [15, 56, 57].

The DFS Rate of PCa patients dependent on *KMT2C* mutational status was derived from the ICGC Data Portal. For "*KMT2C* wildtype" all patients with *KMT2C* mutations of any kind, including those of unknown significance, were removed. Mutations of the consequence type "Frameshift" and "Stop Gained" were grouped as truncation mutations. Consequence type "Missense" was selected for missense mutations. All available PCa projects (PRAD-US, PRAD-CA, PRAD-UK, EOPC-DE, PRAD-CN, PRAD-FR) were included in this analysis.

Animal models

Pb-Cre4 (Tg(Pbsn-cre)4Prb, RRID: IMSR_JAX:026,662), $Pten^{flox/flox}$ ($Pten^{tm2Mak}$, RRID: IMSR_RBRC02300) and $Kmt2c^{flox/flox}$ ($Kmt2c^{tm1.2Jwle}$, RRID: MGI:4,948,101) mice have previously been described [18, 19, 24]. All animals were maintained on a C57Bl/6-Sv/129 mixed background. Male mice were allocated to experimental groups based on their genotype and sacrificed at 19 or 90 weeks of age as indicated in the individual figure legends. All animal studies were reviewed and approved by the Federal Ministry Republic of Austria for Education, Science and Research and conducted according to regulatory standards (BMBWF GZ 66.009/0135-WF/V/3b/2016).

Pathologic review

Sections were reviewed by two independent board-certified pathologists with specific expertise in laboratory animals (L.K. and S.H.). All analyses were performed blinded to genotype.

Immunohistochemistry and histological analysis

Immunohistochemistry (IHC) and haematoxylin/eosin stains (H&E) were performed with formalin-fixed paraffin-embedded (FFPE) tissue using standard protocols. The following antibodies were used for IHC: Ki67 (Cell Signaling, #12,202, 1:400), AR (Abcam, ab133273, 1:100), p16 (Abcam, ab211542, 1:500), GLB1 (Novus Biologicals, NBP2-45,731, 1:120), KRT8 (Abcam, ab53280, 1:100) and p63 (Abcam, ab735, 1:80).

All images were taken with a Zeiss AxioImager M2. Quantification was performed using QuPath 0.1.2 [58]. If automated quantification was not possible, semi-quantitative analysis was performed by a board-certified pathologist with specific expertise in mouse models of prostate cancer (L.K.). Analyses were performed blinded to genotype.

Western blot analysis

Protein extraction from frozen prostate samples for Western blot analysis has previously been described [49]. Western blots were prepared using 15–20 µg of protein lysate, blocked with 5% BSA in 1 × TBS / 0.1% Tween-20 for 1 h and incubated at 4 °C overnight with primary antibodies against AR (1:1000, ab133273, Abcam), $p16^{INK4A}$ (1:2000, ab211542, Abcam), CDK4 (1:200, sc-260, Santa Cruz), p53 (1:1000, CST#2524, Cell Signaling), β-Actin (1:1000, CST#4967, Cell Signaling) and β-Tubulin (1:2000, CST#2146, Cell Signaling). Western blots were quantified using ImageJ2.

RNA Isolation and RT-qPCR

RNA from mouse tissue was extracted using TRI Reagent (Merck) and purified using the ReliaPrep RNA Tissue Miniprep kit (Promega). DNase digestion was performed on a column. For RT-qPCR, 1 µg of total RNA was reverse transcribed to cDNA using the iScript cDNA Synthesis Kit (Bio-Rad). RT-qPCR was performed in triplicates with the Luna Universal qPCR Master Mix (NEB). All procedures were performed according to the manufacturers' instructions. Real-time monitoring of PCR amplification was performed using the CFX96 Real-Time System C1000 Thermal Cycler (Bio-Rad). mRNA levels were calculated using the Pfaffl analysis method [59] and normalized to the geometric mean of β-actin and cyclophilin A. RT-qPCR primer sequences are listed in the Supplementary Materials and Methods.

RNA-Seq of mouse prostate epithelial cells

Mice were sacrificed at 19 weeks p.p. and prostates were dissected. Prostate tissue was digested as previously described [60]. Cell suspensions were strained through a 40 µm cell strainer and washed twice using MACS buffer (1 × PBS + 2 mM EDTA + 2% FCS). The cell solution was subject to centrifugation for 5 min at 150 g, and cells were resuspended in 800 µL MACS buffer. Cells were passed 5 times through a 27G needle and counted. 1–3 * 10^7 cells were collected by centrifugation at 300 g for 5 min and resuspended in 200 µL MACS buffer. 100 ng anti-CD326-biotin (13–5791-82, eBioscience) were added to the cell solution and incubated at room temperature for 10 min. 1 mL MACS buffer was added to the solution and cells were collected by centrifugation at 300 g for 5 min. The cell pellet was resuspended in 200 µL MACS buffer and transferred to a 12 × 75 mm FACS tube. 60 µL streptavidin positive selection beads (T9424, Sigma) were added to the tubes and incubated for 10 min at room temperature. 2.5 mL MACS buffer were added to the cell-bead suspension and the tube was transferred to a magnetic stand. Beads were allowed to adhere to the magnet for 5 min at room temperature before MACS buffer was discarded. Beads were washed twice more in an identical manner using 2.5 mL MACS buffer for each wash and resuspending the cell-bead solution with a P1000 pipette between washes. The bound fraction containing CD326-positive cells was then collected in 5 mL MACS buffer and subject to centrifugation for 5 min at 150 g at 4 °C. Cells were resuspended in 200 µL MACS buffer, counted, and transferred to a fresh (RNase-free) Eppendorf tube. 5 µL of sorted prostate epithelial cells were removed for FACS analysis. The remaining cells were pelleted at 300 g for 5 min at 4 °C, supernatant was removed, and the cell pellet was snap frozen in liquid nitrogen and stored at -80 °C until further use.

RNA isolation was performed using the ReliaPrep RNA Tissue Miniprep kit (Promega). RNA quality was assessed using the 4200 TapeStation System (Agilent). For library preparation, the Ultra II Directional RNA Library Prep Kit (E7760, NEB) was used in combination with a poly(A) mRNA magnetic isolation module (E7490) and multiplex oligos for Illumina (E7600). Library preparation was performed according to the manufacturer's instructions (optimized for an insert size of 200 nt, input: 250 ng, adaptor dilution: fivefold, 11 amplification cycles). The library quality was analysed using the 4200 TapeStation System.

RNA-Seq data analysis

Raw FASTQ files from murine RNA-Seq were subject to a quality check with FastQC (v0.11.5) [61] and MultiQC (v1.4) [62]. Adapters and low-quality read ends were trimmed using Trimmomatic (v0.36) [63] and reads shorter than 35 nt were discarded. The preprocessed reads were mapped to the reference mouse genome (Ensembl GRCm38) utilizing gene annotation (Ensembl v91) with STAR [64, 65]. The quality of mapping was evaluated with RSeQC (v2.6.4) [66] and Picard (v2.10.6) [67] and rRNA content was checked with FastQ Screen (v0.13.0) [68]. Gene quantification was performed on uniquely mapped reads only, with featureCounts (v1.5.2) [69]. Differential expression analysis was carried out in R (version 3.5.1) [70] with DESeq2 package (v1.20.0) [71] and limma package (v3.38.2) [72]. Genes with a FDR-adjusted P value < 0.05 and fold change ≥ 2 or fold change ≤ 0.5 were considered significantly differentially expressed. Heatmaps of differentially expressed genes (DEG) were generated using unsupervised hierarchical clustering with the pheatmap package (v1.0.12) [73]. fGSEA of gene sets was done with the fgsea package (v1.14.0) [74]. Gene sets were derived from MSigDB (version 6.1.1) (hallmark gene sets, Ramaswamy_metastasis_up, Reactome_G1_S_transition, Fischer G1_S_cell_cycle) or previously published works (core SAPS of PICS [37], PCa LN metastasis [34]). Gene sets based on previously published works are detailed in the Supplementary Materials and Methods. Human gene symbols present in custom gene sets were converted to orthologous mouse genes using the biomaRt package (v2.44.4) [75].

TCGA data analysis

Harmonized TCGA PRAD [20] RNA-seq data were acquired as HTSeq-Counts via R package TCGAbiolinks (v2.16.4) [76]. Differentially expressed genes between patients with truncated and wild-type forms of *KMT2C* were identified with DESeq2 package (v1.20.0) [71]. fGSEA of hallmark gene sets (MSigDB version 6.1.1) and custom gene sets was performed with the fgsea package (v1.14.0) [74]. Detailed steps and parameters of the analysis are described in the Supplementary Materials and Methods.

Statistical analysis

Data in figures are plotted as individual replicates with their mean and standard deviation for analyses with $n \leq 20$ per group or as boxplots depicting the 25th to 75th percentile (box) and min to max (whiskers) for $n > 20$ per group. DFS rate for data derived from the ICGC database was calculated using the "cohort comparison" tool provided by the platform. All other statistical analyses were performed using GraphPad Prism 8. The significance level of differences between groups was determined by two-tailed unpaired Student's t-tests for 2 groups or ordinary one-way ANOVA with Tukey's multiple comparisons tests for 3 or more groups. For Kaplan–Meier analysis the log rank (Mantel-Cox) test was performed.

Abbreviations

AR: Androgen receptor; BCa: Breast cancer; COMPASS: Complex of proteins associated with Set1; DEG: Differentially expressed genes; DFS: Disease-free survival; EMT: Epithelial-to-mesenchymal transition; EpCAM: Epithelial cell adhesion molecule; FACS: Fluorescence activated cell sorting; fGSEA: Fast preranked gene set enrichment analysis; FFPE: Formalin-fixed paraffin-embedded; GEMM: Genetically engineered mouse model; GLB1: β-Galactosidase; H&E: Haematoxylin and eosin; H3K4me1: Mono-methylation of lysine 4 on histone 3; IHC: Immunohistochemistry; ICGC: International Cancer Genome Consortium; KRT8: Keratin 8; PHD: Plant homeodomain; PIN: Prostatic intraepithelial neoplasia; PICS: PTEN-loss induced cellular senescence; p.p.: Postpartum; PbCre4: Probasin Cre promoter; PCa: Prostate Cancer; PCR: Polymerase Chain Reaction; PI3K: Phosphoinositide 3-kinase; qRT-PCR: Quantitative reverse transcription-PCR; PTEN: Phosphate and Tensin Homologue; RNA-Seq: RNA sequencing; SASP: Senescence-associated secretory phenotype; TCGA-PRAD: Cancer Genome Atlas Prostate Adenocarcinoma.

Supplementary Information

The online version contains supplementary material available at https://doi.org/10.1186/s12943-022-01542-8.

Additional file 1: Supplementary Figure 1. related to Figure 1. **Supplementary Figure 2.** related to Figure 2. **Supplementary Figure 3.** related to Figure 3. **Supplementary Figure 4.** related to Figure 4. **Supplementary Figure 5.** related to Figure 6.

Additional file 2. Supplementary Methods.

Additional file 3. Supplementary Table 1. Genotyping Primers. **Supplementary Table 2.** Genotyping Protocols. Supplementary Table 3. RT-qPCR Primers. **Supplementary Table 4.** Geneset "PCa LN Metastasis UP". **Supplementary Table 5.** Geneset "core SASP of PICS".

Acknowledgements

We thank Jae W. Lee (Oregon Health and Sciences University, Portland, OR) for generously providing the Kmt2c$^{tm1.1Jwle}$ mouse strain. Core Facility Bioinformatics and Core Facility Genomics of CEITEC Masaryk University supported by the NCLG research infrastructure (LM2018132 funded by MEYS CR) is gratefully acknowledged for the obtaining of the sequencing data presented in this paper.

Authors' contributions

Conceptualization: TL, LK. Formal analysis: TL, KT, JO. Funding acquisition: LK, WW, HD. Investigation: TL, MSchl, KT, SH, CS, JY, JO, BT, IG, HAN, BS, MSchm, PK, SL. Methodology:. TL, MSchm, KT, SH, JO, VB, BT, SL. Project administration: TL, LK, WW. Resources: TL, LK, WW, SP. Supervision: LK, GE, ZC. Validation: TL, MSchl, JY, JO, VB, KT, BT. Visualization: TL, KT, AJ. Writing – original draft: TL. Writing – review & editing: TL, CS, ZC, GE, SL, SDT, LK. The author(s) read and approved the final manuscript.

Authors' information

DI Tanja Limberger (PhD student): This work is part of her PhD thesis at Medical University of Vienna (MUV), Vienna, Austria, which was done at Department of Experimental and Laboratory Animal Pathology, MUV, Vienna, Austria.
Mag. Michaela Schlederer: (MA): BMA at the at Department of Experimental and Laboratory Animal Pathology, MUV, Vienna, Austria.
Mag Karolina Trachtová (PhD student): This work is part of her PhD thesis at Medical University of Vienna (MUV), which was done at Department of Experimental and Laboratory Animal Pathology, MUV, Vienna, Austria.
Mag. Jiaye Yang (MA): BMA at the at Department of Experimental and Laboratory Animal Pathology, MUV, Vienna, Austria.
Dr. Sandra Högler (DVM): Veterinary Pathologist at the Unit of Laboratory Animal Pathology, University of Veterinary Medicine (VetMedUni), Vienna, Austria.
Dr. Christina Sternberg (PhD): PostDoc at the at the Unit of Laboratory Animal Pathology, VetMedUni, Vienna, Austria.
Dr. Vojtech Bystry (PhD): Scientific researcher at the Central European Institute of Technology (CEITEK), Masaryk University, Brno, Czech Republic.
Mag. Margit Schmeidl (MA): BMA at the at Department of Pathology, MUV, Vienna, Austria.
Anton Jäger, Scientific Researcher at Department of Pathology, MUV, Vienna, Austria.
Mag Ines Garces (PhD student): This work is part of her PhD thesis at the Unit of Laboratory Animal Pathology, University of Veterinary Medicine (VetMedUni), Vienna, Austria.
Heidi A. Neubauer (PhD): PostDoc at the at the Institute of Animal Breeding and Genetics, VetMedUni, Vienna, Austria.
Dr. Monika Oberhuber (PhD): PostDoc at CBmed-Center for Biomarker Research in Medicine GmbH, Graz, 8010, Austria.
Mag. Belinda Schmalzbauer (PhD student): PostDoc at Institute of Pharmacology and Toxicology, VetMedUni, Vienna, Austria.
Prof Dr Sarka Pospisilova (MD, PhD): Professor and Vice-Rector for Science at Masaryk University and CEITEC, Brno, Czech Republic.
Prof Dr. Helmut Dolznig (PhD): Associate Prof. at Institute of Medical Genetics, MUV, Vienna, Austria.
Prof. Dr. Wolfgang Wadsak (PhD): Associate Prof. at Division of Nuclear Medicine, Department of Biomedical Imaging and Image-Guided Therapy, MUV, Vienna, 1090, Austria.
Prof. Dr. Zoran Culig (PhD): Associate Prof. at Department of Urology, Innsbruck Medical University, Innsbruck, 6020, Austria.
Prof Dr. Suzanne D. Turner (PhD): Professor at Department of Pathology, University Cambridge, UK.
Prof. Dr. Gerda Egger (PhD): Professor at Department of Pathology, MUV.
Dr. Sabine Lagger (PhD): PostDoc at the at the Unit of Laboratory Animal Pathology, VetMedUni, Vienna, Austria.
Prof. Dr. Lukas Kenner (MD) Clinical and Laboratory Animal Pathologist, Head of Department of Experimental and Laboratory Animal Pathology, MUV and of the Unit of Laboratory Animal Pathology, VetMedUni, Vienna, Austria.

Funding

LK was supported by the BM Fonds (15142), the Margaretha Hehberger Stiftung (15142), and the Christian-Doppler Lab for Applied Metabolomics. LK and TL were supported by the Austrian Science Fund, FWF grant P 26011 and P 29251 and by the COMET Competence Center CBmed—Center for Biomarker Research in Medicine (FA791A0906.FFG). The COMET Competence Center CBmed is funded by the Austrian Federal Ministry for Transport, Innovation and Technology (BMVIT); the Austrian Federal Ministry for Digital and Economic Affairs (BMDW); Land Steiermark (Department 12, Business and Innovation); the Styrian Business Promotion Agency (SFG); and the Vienna Business Agency (WAW). The COMET program is executed by the FFG. LK was recipient of funds from a European Union Horizon 2020 Marie Sklodowska-Curie Innovative Training Network (ITNETN) grant, award n. 675712.

Availability of data and materials

The RNA-Seq dataset supporting the conclusions of this article is available in the GEO repository, GSE186413 and is publicly available as of date of publication. The following publicly available datasets were used: The Cancer Genome Atlas—Prostate Adenocarcinoma (https://portal.gdc.cancer.gov/projects/TCGA-PRAD). The long tail of oncogenic drivers in prostate cancer [15], ICGC Prostate Cancer Project (PRAD-US, PRAD-CA, PRAD-UK, EOPC-DE, PRAD-CN, PRAD-FR) [40].

Declarations

Ethics approval and consent to participate

Institutional Review Board Statement: The use of clinical material was approved by the Research Ethics Committee of the Medical University Vienna, Austria (1877/2016) and conducted in adherence to the Declaration of Helsinki protocols. Patient consent was waived due to the completely anonymized, retrospective nature of the study.
All animal studies were reviewed and approved by the Federal Ministry Republic of Austria for Education, Science and Research and conducted according to regulatory standards (BMBWF GZ 66.009/0135-WF/V/3b/2016).

Consent for publication

Not applicable.

Competing interests

The authors declare that they have no competing interests.

Author details

[1] Division of Experimental and Translational Pathology, Department of Pathology, Medical University of Vienna, 1090 Vienna, Austria. [2] CBmed-Center for Biomarker Research in Medicine GmbH, 8010 Graz, Austria. [3] Central European Institute of Technology, Masaryk University, Brno 62500, Czech Republic. [4] Christian Doppler Laboratory for Applied Metabolomics, 1090 Vienna, Austria. [5] Division of Nuclear Medicine, Department of Biomedical Imaging and Image-Guided Therapy, Medical University of Vienna, 1090 Vienna, Austria. [6] Unit of Laboratory Animal Pathology, University of Veterinary Medicine Vienna, 1210 Vienna, Austria. [7] Institute of Biochemistry, Christian-Albrechts-University Kiel, 24118 Kiel, Germany. [8] Institute of Animal Breeding and Genetics, University of Veterinary Medicine Vienna, 1210 Vienna, Austria. [9] Institute of Pharmacology and Toxicology, University of Veterinary Medicine Vienna, 1210 Vienna, Austria. [10] Institute of Medical Genetics, Medical University of Vienna, 1090 Vienna, Austria. [11] Department of Urology, Innsbruck Medical University, 6020 Innsbruck, Austria. [12] Department of Pathology, University Cambridge, Cambridge, UK. [13] CEITEC, Masaryk University, Brno, Czech Republic. [14] Ludwig Boltzmann Institute Applied Diagnostics, 1090 Vienna, Austria.

Received: 27 December 2021 Accepted: 17 February 2022

References

1. Sung H, Ferlay J, Siegel RL, Laversanne M, Soerjomataram I, Jemal A, Bray F: Global cancer statistics 2020: GLOBOCAN estimates of incidence and mortality worldwide for 36 cancers in 185 countries. CA Cancer J Clin. 2021;71:209–49.
2. Cancer Tomorrow [https://gco.iarc.fr/]
3. Haffner MC, Zwart W, Roudier MP, True LD, Nelson WG, Epstein JI, De Marzo AM, Nelson PS, Yegnasubramanian S. Genomic and phenotypic heterogeneity in prostate cancer. Nat Rev Urol. 2021;18:79–92.
4. Siegel RL, Miller KD, Fuchs HE, Jemal A. Cancer Statistics, 2021. CA Cancer J Clin. 2021;71:7–33.

5. Jamaspishvili T, Berman DM, Ross AE, Scher HI, De Marzo AM, Squire JA, Lotan TL. Clinical implications of PTEN loss in prostate cancer. Nat Rev Urol. 2018;15:222–34.
6. Hoxhaj G, Manning BD. The PI3K-AKT network at the interface of oncogenic signalling and cancer metabolism. Nat Rev Cancer. 2020;20:74–88.
7. Parisotto M, Grelet E, El Bizri R, Dai Y, Terzic J, Eckert D, Gargowitsch L, Bornert JM, Metzger D. PTEN deletion in luminal cells of mature prostate induces replication stress and senescence in vivo. J Exp Med. 2018;215:1749–63.
8. Koh CM, Bieberich CJ, Dang CV, Nelson WG, Yegnasubramanian S, De Marzo AM. MYC and prostate cancer. Genes Cancer. 2010;1:617–28.
9. Feinberg AP, Koldobskiy MA, Gondor A. Epigenetic modulators, modifiers and mediators in cancer aetiology and progression. Nat Rev Genet. 2016;17:284–99.
10. Perdigoto CN. Epigenetic cancer evolution, one cell at a time. Nat Rev Genet. 2019;20:434–5.
11. Chatterjee A, Rodger EJ, Eccles MR. Epigenetic drivers of tumourigenesis and cancer metastasis. Semin Cancer Biol. 2018;51:149–59.
12. Kandoth C, McLellan MD, Vandin F, Ye K, Niu B, Lu C, Xie M, Zhang Q, McMichael JF, Wyczalkowski MA, et al. Mutational landscape and significance across 12 major cancer types. Nature. 2013;502:333–9.
13. Rao RC, Dou Y. Hijacked in cancer: the KMT2 (MLL) family of methyltransferases. Nat Rev Cancer. 2015;15:334–46.
14. Fagan RJ, Dingwall AK. COMPASS Ascending: Emerging clues regarding the roles of MLL3/KMT2C and MLL2/KMT2D proteins in cancer. Cancer Lett. 2019;458:56–65.
15. Armenia J, Wankowicz SAM, Liu D, Gao J, Kundra R, Reznik E, Chatila WK, Chakravarty D, Han GC, Coleman I, et al. The long tail of oncogenic drivers in prostate cancer. Nat Genet. 2018;50:645–51.
16. Lavery WJ, Barski A, Wiley S, Schorry EK, Lindsley AW. KMT2C/D COMPASS complex-associated diseases [KCDCOM-ADs]: an emerging class of congenital regulopathies. Clin Epigenetics. 2020;12:10.
17. Wang L, Zhao Z, Ozark PA, Fantini D, Marshall SA, Rendleman EJ, Cozzolino KA, Louis N, He X, Morgan MA, et al. Resetting the epigenetic balance of Polycomb and COMPASS function at enhancers for cancer therapy. Nat Med. 2018;24:758–69.
18. Lee S, Lee DK, Dou Y, Lee J, Lee B, Kwak E, Kong YY, Lee SK, Roeder RG, Lee JW. Coactivator as a target gene specificity determinant for histone H3 lysine 4 methyltransferases. Proc Natl Acad Sci U S A. 2006;103:15392–7.
19. Wu X, Wu J, Huang J, Powell WC, Zhang J, Matusik RJ, Sangiorgi FO, Maxson RE, Sucov HM, Roy-Burman P. Generation of a prostate epithelial cell-specific Cre transgenic mouse model for tissue-specific gene ablation. Mech Dev. 2001;101:61–9.
20. Cancer Genome Atlas Research Network. The Molecular taxonomy of primary prostate cancer. Cell. 2015;163:1011–25.
21. Nguyen B, Mota JM, Nandakumar S, Stopsack KH, Weg E, Rathkopf D, Morris MJ, Scher HI, Kantoff PW, Gopalan A, et al. Pan-cancer analysis of CDK12 alterations identifies a subset of prostate cancers with distinct genomic and clinical characteristics. Eur Urol. 2020;78:671–9.
22. Wang S, Gao J, Lei Q, Rozengurt N, Pritchard C, Jiao J, Thomas GV, Li G, Roy-Burman P, Nelson PS, et al. Prostate-specific deletion of the murine Pten tumor suppressor gene leads to metastatic prostate cancer. Cancer Cell. 2003;4:209–21.
23. Trotman LC, Niki M, Dotan ZA, Koutcher JA, Di Cristofano A, Xiao A, Khoo AS, Roy-Burman P, Greenberg NM, Van Dyke T, et al. Pten dose dictates cancer progression in the prostate. PLoS Biol. 2003;1:E59.
24. Suzuki A, Yamaguchi MT, Ohteki T, Sasaki T, Kaisho T, Kimura Y, Yoshida R, Wakeham A, Higuchi T, Fukumoto M, et al. T cell-specific loss of Pten leads to defects in central and peripheral tolerance. Immunity. 2001;14:523–34.
25. Chen Z, Trotman LC, Shaffer D, Lin HK, Dotan ZA, Niki M, Koutcher JA, Scher HI, Ludwig T, Gerald W, et al. Crucial role of p53-dependent cellular senescence in suppression of Pten-deficient tumorigenesis. Nature. 2005;436:725–30.
26. Aytes A, Mitrofanova A, Kinkade CW, Lefebvre C, Lei M, Phelan V, LeKaye HC, Koutcher JA, Cardiff RD, Califano A, et al. ETV4 promotes metastasis in response to activation of PI3-kinase and Ras signaling in a mouse model of advanced prostate cancer. Proc Natl Acad Sci U S A. 2013;110:E3506-3515.
27 Liberzon A, Subramanian A, Pinchback R, Thorvaldsdottir H, Tamayo P, Mesirov JP. Molecular signatures database (MSigDB) 3.0. Bioinformatics. 2011;27:1739–40.
28. Liberzon A, Birger C, Thorvaldsdottir H, Ghandi M, Mesirov JP, Tamayo P. The molecular signatures database (MSigDB) hallmark gene set collection. Cell Syst. 2015;1:417–25.
29. Gurel B, Iwata T, Koh CM, Jenkins RB, Lan F, Van Dang C, Hicks JL, Morgan J, Cornish TC, Sutcliffe S, et al. Nuclear MYC protein overexpression is an early alteration in human prostate carcinogenesis. Mod Pathol. 2008;21:1156–67.
30. Hawksworth D, Ravindranath L, Chen Y, Furusato B, Sesterhenn IA, McLeod DG, Srivastava S, Petrovics G. Overexpression of C-MYC oncogene in prostate cancer predicts biochemical recurrence. Prostate Cancer Prostatic Dis. 2010;13:311–5.
31. Bai S, Cao S, Jin L, Kobelski M, Schouest B, Wang X, Ungerleider N, Baddoo M, Zhang W, Corey E, et al. A positive role of c-Myc in regulating androgen receptor and its splice variants in prostate cancer. Oncogene. 2019;38:4977–89.
32 Meskyte EM, Keskas S, Ciribilli Y. MYC as a multifaceted regulator of tumor microenvironment leading to metastasis. Int J Mol Sci. 2020;21(20):7710.
33. Ramaswamy S, Ross KN, Lander ES, Golub TR. A molecular signature of metastasis in primary solid tumors. Nat Genet. 2003;33:49–54.
34. Arias CR, Yeh HY, Soo VW. Biomarker identification for prostate cancer and lymph node metastasis from microarray data and protein interaction network using gene prioritization method. ScientificWorldJournal. 2012;2012:842727.
35. Hanahan D, Weinberg RA. Hallmarks of cancer: the next generation. Cell. 2011;144:646–74.
36. Collado M, Serrano M. Senescence in tumours: evidence from mice and humans. Nat Rev Cancer. 2010;10:51–7.
37. Alimonti A, Nardella C, Chen Z, Clohessy JG, Carracedo A, Trotman LC, Cheng K, Varmeh S, Kozma SC, Thomas G, et al. A novel type of cellular senescence that can be enhanced in mouse models and human tumor xenografts to suppress prostate tumorigenesis. J Clin Invest. 2010;120:681–93.
38. Sharpless NE, Sherr CJ. Forging a signature of in vivo senescence. Nat Rev Cancer. 2015;15:397–408.
39. Guccini I, Revandkar A, D'Ambrosio M, Colucci M, Pasquini E, Mosole S, Troiani M, Brina D, Sheibani-Tezerji R, Elia AR, et al. Senescence reprogramming by TIMP1 deficiency promotes prostate cancer metastasis. Cancer Cell. 2021;39:68-82 e69.
40. Zhang J, Bajari R, Andric D, Gerthoffert F, Lepsa A, Nahal-Bose H, Stein LD, Ferretti V. The international cancer genome consortium data portal. Nat Biotechnol. 2019;37:367–9.
41. Bianco-Miotto T, Chiam K, Buchanan G, Jindal S, Day TK, Thomas M, Pickering MA, O'Loughlin MA, Ryan NK, Raymond WA, et al. Global levels of specific histone modifications and an epigenetic gene signature predict prostate cancer progression and development. Cancer Epidemiol Biomarkers Prev. 2010;19:2611–22.
42. Dawkins JB, Wang J, Maniati E, Heward JA, Koniali L, Kocher HM, Martin SA, Chelala C, Balkwill FR, Fitzgibbon J, Grose RP. Reduced expression of histone methyltransferases KMT2C and KMT2D correlates with improved outcome in pancreatic ductal adenocarcinoma. Cancer Res. 2016;76:4861–71.
43. Sato K, Akimoto K. Expression levels of KMT2C and SLC20A1 identified by information-theoretical analysis are powerful prognostic biomarkers in estrogen receptor-positive breast cancer. Clin Breast Cancer. 2017;17:e135–42.
44. Gala K, Li Q, Sinha A, Razavi P, Dorso M, Sanchez-Vega F, Chung YR, Hendrickson R, Hsieh JJ, Berger M, et al. KMT2C mediates the estrogen dependence of breast cancer through regulation of ERalpha enhancer function. Oncogene. 2018;37:4692–710.
45. Toska E, Osmanbeyoglu HU, Castel P, Chan C, Hendrickson RC, Elkabets M, Dickler MN, Scaltriti M, Leslie CS, Armstrong SA, Baselga J. PI3K pathway regulates ER-dependent transcription in breast cancer through the epigenetic regulator KMT2D. Science. 2017;355:1324–30.
46. Carver BS, Tran J, Gopalan A, Chen Z, Shaikh S, Carracedo A, Alimonti A, Nardella C, Varmeh S, Scardino PT, et al. Aberrant ERG expression cooperates with loss of PTEN to promote cancer progression in the prostate. Nat Genet. 2009;41:619–24.
47. Stanbrough M, Leav I, Kwan PW, Bubley GJ, Balk SP. Prostatic intraepithelial neoplasia in mice expressing an androgen receptor transgene in prostate epithelium. Proc Natl Acad Sci U S A. 2001;98:10823–8.
48. Ellwood-Yen K, Graeber TG, Wongvipat J, Iruela-Arispe ML, Zhang J, Matusik R, Thomas GV, Sawyers CL. Myc-driven murine prostate cancer

shares molecular features with human prostate tumors. Cancer Cell. 2003;4:223–38.
49. Ding Z, Wu CJ, Chu GC, Xiao Y, Ho D, Zhang J, Perry SR, Labrot ES, Wu X, Lis R, et al. SMAD4-dependent barrier constrains prostate cancer growth and metastatic progression. Nature. 2011;470:269–73.
50. Wang J, Kobayashi T, Floc'h N, Kinkade CW, Aytes A, Dankort D, Lefebvre C, Mitrofanova A, Cardiff RD, McMahon M, et al. B-Raf activation cooperates with PTEN loss to drive c-Myc expression in advanced prostate cancer. Cancer Res. 2012;72:4765–76.
51. Arriaga JM, Panja S, Alshalalfa M, Zhao J, Zou M, Giacobbe A, Madubata CJ, Yeji Kim J, Rodriguez A, Coleman I, et al. A MYC and RAS co-activation signature in localized prostate cancer drives bone metastasis and castration resistance. Nat Cancer. 2020;1:1082–96.
52. Hubbard GK, Mutton LN, Khalili M, McMullin RP, Hicks JL, Bianchi-Frias D, Horn LA, Kulac I, Moubarek MS, Nelson PS, et al. Combined MYC activation and pten loss are sufficient to create genomic instability and lethal metastatic prostate cancer. Cancer Res. 2016;76:283–92.
53. Faget DV, Ren Q, Stewart SA. Unmasking senescence: context-dependent effects of SASP in cancer. Nat Rev Cancer. 2019;19:439–53.
54. Chen Z, Carracedo A, Lin HK, Koutcher JA, Behrendt N, Egia A, Alimonti A, Carver BS, Gerald W, Teruya-Feldstein J, et al. Differential p53-independent outcomes of p19(Arf) loss in oncogenesis. Sci Signal. 2009;2:ra44.
55. Madden SK, de Araujo AD, Gerhardt M, Fairlie DP, Mason JM. Taking the Myc out of cancer: toward therapeutic strategies to directly inhibit c-Myc. Mol Cancer. 2021;20:3.
56. Cerami E, Gao J, Dogrusoz U, Gross BE, Sumer SO, Aksoy BA, Jacobsen A, Byrne CJ, Heuer ML, Larsson E, et al. The cBio cancer genomics portal: an open platform for exploring multidimensional cancer genomics data. Cancer Discov. 2012;2:401–4.
57. Gao J, Aksoy BA, Dogrusoz U, Dresdner G, Gross B, Sumer SO, Sun Y, Jacobsen A, Sinha R, Larsson E, et al. Integrative analysis of complex cancer genomics and clinical profiles using the cBioPortal. Sci Signal. 2013;6:p11.
58. Bankhead P, Loughrey MB, Fernandez JA, Dombrowski Y, McArt DG, Dunne PD, McQuaid S, Gray RT, Murray LJ, Coleman HG, et al. QuPath: Open source software for digital pathology image analysis. Sci Rep. 2017;7:16878.
59 Pfaffl MW. A new mathematical model for relative quantification in real-time RT-PCR. Nucleic Acids Res. 2001;29:e45.
60. Drost J, Karthaus WR, Gao D, Driehuis E, Sawyers CL, Chen Y, Clevers H. Organoid culture systems for prostate epithelial and cancer tissue. Nat Protoc. 2016;11:347–58.
61. Babraham Bioinformatics [https://www.bioinformatics.babraham.ac.uk/projects/fastqc/]
62. Ewels P, Magnusson M, Lundin S, Kaller M. MultiQC: summarize analysis results for multiple tools and samples in a single report. Bioinformatics. 2016;32:3047–8.
63. Bolger AM, Lohse M, Usadel B. Trimmomatic: a flexible trimmer for Illumina sequence data. Bioinformatics. 2014;30:2114–20.
64. Howe KL, Achuthan P, Allen J, Allen J, Alvarez-Jarreta J, Amode MR, Armean IM, Azov AG, Bennett R, Bhai J, et al. Ensembl 2021. Nucleic Acids Res. 2021;49:D884–91.
65. Dobin A, Davis CA, Schlesinger F, Drenkow J, Zaleski C, Jha S, Batut P, Chaisson M, Gingeras TR. STAR: ultrafast universal RNA-seq aligner. Bioinformatics. 2013;29:15–21.
66. Wang L, Wang S, Li W. RSeQC: quality control of RNA-seq experiments. Bioinformatics. 2012;28:2184–5.
67. Broad Institute. [http://broadinstitute.github.io/picard/].
68 Wingett SW, Andrews S. Fast Screen: A tool for multi-genome mapping and quality control. F1000Res. 2018;7:1338.
69. Liao Y, Smyth GK, Shi W. featureCounts: an efficient general purpose program for assigning sequence reads to genomic features. Bioinformatics. 2014;30:923–30.
70. R: A language and environment for statistical computing. R Foundation for Statistical Computing [https://www.R-project.org/]
71. Love MI, Huber W, Anders S. Moderated estimation of fold change and dispersion for RNA-seq data with DESeq2. Genome Biol. 2014;15:550.
72. Ritchie ME, Phipson B, Wu D, Hu Y, Law CW, Shi W, Smyth GK. limma powers differential expression analyses for RNA-sequencing and microarray studies. Nucleic Acids Res. 2015;43:e47.
73. pheatmap: Pretty Heatmaps. R package version 1.0.12. [https://CRAN.R-project.org/package=pheatmap]
74. Gennady K. Fast gene set enrichment analysis. Biorxiv. 2021. https://doi.org/10.1101/060012.
75. Durinck S, Spellman PT, Birney E, Huber W. Mapping identifiers for the integration of genomic datasets with the R/Bioconductor package biomaRt. Nat Protoc. 2009;4:1184–91.
76. Colaprico A, Silva TC, Olsen C, Garofano L, Cava C, Garolini D, Sabedot TS, Malta TM, Pagnotta SM, Castiglioni I, et al. TCGAbiolinks: an R/Bioconductor package for integrative analysis of TCGA data. Nucleic Acids Res. 2016;44:e71.

Publisher's Note

Redmer *et al. Molecular Cancer* (2024) 23:114
https://doi.org/10.1186/s12943-024-02022-x

Molecular Cancer

RESEARCH **Open Access**

JUN mediates the senescence associated secretory phenotype and immune cell recruitment to prevent prostate cancer progression

Torben Redmer[1*†], Martin Raigel[1,2,3†], Christina Sternberg[1,2,4†], Roman Ziegler[1,21], Clara Probst[1,2,3], Desiree Lindner[1,2,3], Astrid Aufinger[2], Tanja Limberger[2,5], Karolina Trachtova[2,3,6], Petra Kodajova[1], Sandra Högler[1], Michaela Schlederer[2], Stefan Stoiber[2,3,7], Monika Oberhuber[8], Marco Bolis[9,10,11], Heidi A. Neubauer[12,22], Sara Miranda[12], Martina Tomberger[8], Nora S. Harbusch[8], Ines Garces de los Fayos Alonso[1,2], Felix Sternberg[13,23], Richard Moriggl[14], Jean-Philippe Theurillat[9], Boris Tichy[6], Vojtech Bystry[6], Jenny L. Persson[15,16], Stephan Mathas[17,18,19], Fritz Aberger[14], Birgit Strobl[12], Sarka Pospisilova[6], Olaf Merkel[2], Gerda Egger[2], Sabine Lagger[1*†] and Lukas Kenner[1,2,7,8,20*†]

Abstract

Background Prostate cancer develops through malignant transformation of the prostate epithelium in a stepwise, mutation-driven process. Although activator protein-1 transcription factors such as JUN have been implicated as potential oncogenic drivers, the molecular programs contributing to prostate cancer progression are not fully understood.

Methods We analyzed JUN expression in clinical prostate cancer samples across different stages and investigated its functional role in a *Pten*-deficient mouse model. We performed histopathological examinations, transcriptomic analyses and explored the senescence-associated secretory phenotype in the tumor microenvironment.

Results Elevated JUN levels characterized early-stage prostate cancer and predicted improved survival in human and murine samples. Immune-phenotyping of *Pten*-deficient prostates revealed high accumulation of tumor-infiltrating leukocytes, particularly innate immune cells, neutrophils and macrophages as well as high levels of STAT3 activation and IL-1β production. *Jun* depletion in a *Pten*-deficient background prevented immune cell attraction which was accompanied by significant reduction of active STAT3 and IL-1β and accelerated prostate tumor growth.

---

†Torben Redmer, Martin Raigel, Christina Sternberg, Sabine Lagger and Lukas Kenner shared contribution.

*Correspondence:
Torben Redmer
torben.redmer@vetmeduni.ac.at
Sabine Lagger
sabine.lagger@vetmeduni.ac.at
Lukas Kenner
lukas.kenner@meduniwien.ac.at
Full list of author information is available at the end of the article

Comparative transcriptome profiling of prostate epithelial cells revealed a senescence-associated gene signature, upregulation of pro-inflammatory processes involved in immune cell attraction and of chemokines such as IL-1β, TNF-α, CCL3 and CCL8 in *Pten*-deficient prostates. Strikingly, JUN depletion reversed both the senescence-associated secretory phenotype and senescence-associated immune cell infiltration but had no impact on cell cycle arrest. As a result, JUN depletion in *Pten*-deficient prostates interfered with the senescence-associated immune clearance and accelerated tumor growth.

Conclusions Our results suggest that JUN acts as tumor-suppressor and decelerates the progression of prostate cancer by transcriptional regulation of senescence- and inflammation-associated genes. This study opens avenues for novel treatment strategies that could impede disease progression and improve patient outcomes.

Keywords Prostate cancer, AP-1 transcription factors, JUN, Senescence, SASP, Immune infiltration

Graphical Abstract

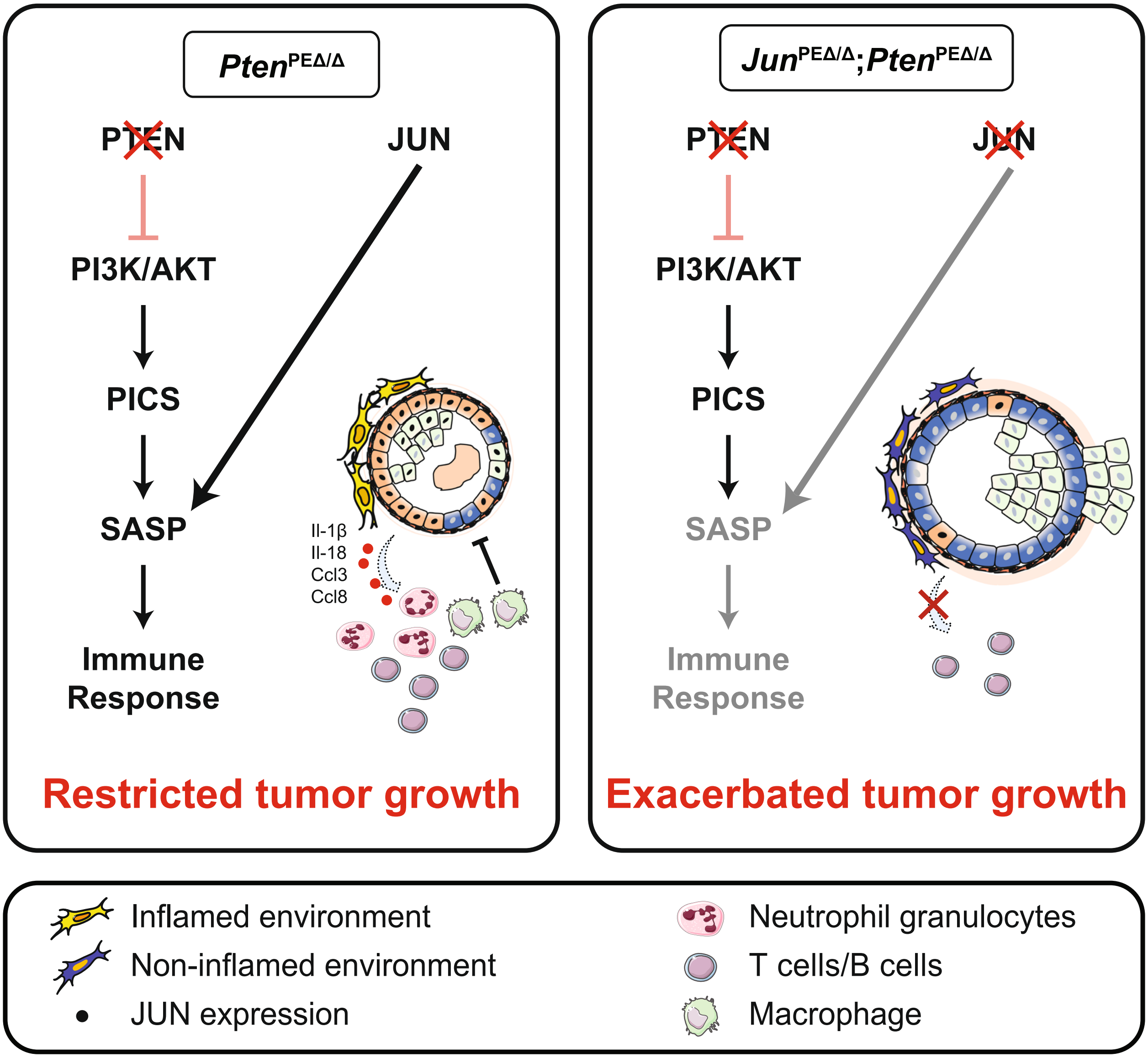

Background

Prostate cancer (PCa) is one of the most frequently diagnosed malignancies in men worldwide [1]. Its significance lies not only in its prevalence but also in the potential to progress to aggressive forms that resist conventional treatments and lead to high mortality rates [2]. The complex molecular programs that determine the routes of PCa progression are still incompletely understood. On the molecular level, the dysregulation of the phosphoinositide 3-kinase (PI3K) and androgen receptor (AR) pathways has been implicated in the pathology of PCa [3]. The constitutive activation of the PI3K cascade, which is caused by mutations in the tumor-suppressor gene and PI3K antagonist *Phosphate and tensin homologue* (*PTEN),* was identified in 20% of primary PCa tumors and represents a major oncogenic driver [4]. The current standard treatment for primary advanced-stage PCa is the administration of anti-androgens to deprive the tumor of dihydrotestosterone. PCa inevitably escapes androgen deprivation by relapsing into castration resistant PCa (CRPC), which is associated with loss of *PTEN* tumor-suppressor activity in 50% of cases. The characteristic dissemination of CRPC into local and distant regions such as bone, is correlated with poor survival [3–5].

In a previously described mouse model, the abrogation of *Pten* in prostate epithelium (PE) caused activation of a p53-mediated senescence program [6–8]. The emergence of senescence in cancer is considered a double-edged sword: it either confers anti-tumorigenic effects when originating from tumor cells or results in pro-tumorigenic outcomes when the tumor microenvironment (TME) is affected [9]. This phenomenon is mainly attributed to the induction of a senescence-associated secretory phenotype (SASP), characterized by the secretion of soluble signaling factors, proteases and extracellular matrix proteins [10]. In particular, pro-inflammatory cytokines such as IL-6, IL-1, TNF-α, CCL3 and CCL8 attract innate immune cells to the vicinity of the tumor site. As a collective, all components of SASP aid in creation of a pro-tumorigenic microenvironment and ultimately advance tumor progression depending on the tissue context. IL-6 and its downstream effector signal transducer and activator of transcription 3 (STAT3) are known to regulate apoptosis, angiogenesis, proliferation and differentiation, making them promising therapeutic targets in PCa [11]. However, our group has recently challenged active IL-6/STAT3 signaling as a tumor driver in PCa, as loss of *Stat3* unexpectedly resulted in increased tumor burden and was accompanied by a bypass of PTEN-loss induced cellular senescence (PICS) in a *Pten*-deficient PCa mouse model [12, 13].

Besides the hyperactivation of PI3K/AKT and amplification of AR signaling, other mechanisms driving the progression of PCa include the activation of activator protein-1 (AP-1) mediated gene expression [14]. AP-1 transcription factors (TF) such as JUN, were initially considered as proto-oncogenes [15] and deregulation of AP-1 family members was observed in several cancers [16]. Previous studies have suggested that JUN modulates hepatocellular tumorigenesis as a regulator of cell cycle genes and has co-activator and repressor functions in the regulation of AR in the prostate [17–19]. Recent evidence suggests tumor-suppressive functions for several members of the AP-1 TF family and their regulators [17, 20]. For example, the JUN-activating JUN N-terminal kinase (JNK) has previously been identified as a potent tumor-suppressor in a murine PCa model [21]. JUNB, which is also activated by JNK has been associated with growth limiting properties in PCa and its activation may explain the mechanism of JNK's tumor-suppression [22]. A recent study provides novel insights how the tumor-suppressive functions of AP-1 might be exerted, as JUN was particularly implicated as pioneering factor in bookmarking the enhancers of genes associated with the induction of the senescence program [23].

Here we investigated the role of *Jun* in a murine model of *Pten*-loss driven neoplasia of the PE and surveyed the consequence of JUN-deficiency in tumor development and senescence.

Methods

Mouse strains and animal work

To establish the PCa mouse model used in this study, we bred a *Pten* knockout prostate cancer mouse strain (*Pten*$^{\mathrm{PE}\Delta/\Delta}$) [24] with a *Jun*-floxed (*Jun*$^{\mathrm{fl/fl}}$) [25] mouse strain. The *Pten*$^{\mathrm{PE}\Delta/\Delta}$ mouse strain was originally established by crossing *Pten*$^{\mathrm{Ex4/Ex5}}$-floxed mice [26] and heterozygous transgenic *Probasin* (*Pb*) *Cre* mice [27]. *Pb Cre* transgenic mice express the Cre recombinase under the *Probasin* promoter restricted to PE cells of sexually mature mice [27]. To minimalize tumor burden for breeding animals, heterozygous *Pten*$^{\mathrm{PE}\Delta/+}$ males were used for breeding. The resulting genotypes of experimental animals are: *PbCre*$^{+/+}$ (*wildtype (wt)*), *PbCre*$^{\mathrm{tg}/+}$;*Jun*$^{\mathrm{fl/fl}}$ (*Jun*$^{\mathrm{PE}\Delta/\Delta}$); *PbCre*$^{\mathrm{tg}/+}$;*Pten*$^{\mathrm{fl/fl}}$ (*Pten*$^{\mathrm{PE}\Delta/\Delta}$); *PbCre*$^{\mathrm{tg}/+}$;*Jun*$^{\mathrm{fl/fl}}$;*Pten*$^{\mathrm{fl/fl}}$ (*Jun*$^{\mathrm{PE}\Delta/\Delta}$;*Pten*$^{\mathrm{PE}\Delta/\Delta}$). For all experiments, mice were sacrificed at 19-weeks of age, with the exception of animals used for the Kaplan–Meier survival analysis and for metastasis analysis (39-weeks of age).

Histological staining

Hematoxylin and eosin (H&E), immunohistochemistry (IHC) and immunofluorescence (IF) stainings were performed on 2 μm sections of formalin-fixed paraffin embedded (FFPE) tissue. H&E staining was done according to routine diagnostic protocols. Details of IHC staining for the different markers are indicated in Supplementary Table 6 and all slides were counterstained with hematoxylin.

For the EpCAM IF staining, slides were dewaxed and heated in pH 6 citrate buffer. After blocking with 2% bovine serum albumin (Roth 8076.4), the slides were incubated in primary antibody (EpCAM, Elab Science, E-AB-70132, dilution 1:300) overnight. Next, slides were incubated for 1 h at room temperature in secondary antibody (Goat anti-Rabbit IgG Alexa Fluor 488, Dilution 1:500) and stained with DAPI.

Human tissue microarray analysis

The generation of human tissue microarrays (TMAs) of healthy and tumor prostate tissues was previously described [28]. The TMAs were stained with an antibody for JUN (Supplementary Table 6) and analysed by trained pathologists. The JUN levels were determined by combining the staining intensity with the percentage of positive cells and graded into absent (0), low-grade (1), medium-grade (2) and high-grade (3). We next stratified TMA samples according to Gleason scores, resulting in three groups (healthy: no Gleason score; low Gleason: Gleason score 5–6; and high Gleason: Gleason score 7–9) and analysed JUN expression for all groups. For the Kaplan–Meier analysis, patients were grouped into absent (0) ($\text{JUN}^{\text{absent}}$) and present (1–3) ($\text{JUN}^{\text{present}}$) JUN expression and correlated with biochemical recurrence (BCR) data.

Whole slide scan analysis

Analysis of IHC staining was performed with QuPath (version 0.3.2) [29]. First, regions of interest were annotated, excluding non-prostate tissue such as urethra, seminal vesicles and ductus deferens. Cell detection was performed with the StarDist extension [30] for the NIMP-R14 staining and the built-in watershed cell detection plugin for F4/80, CD79b, JUN, Granzyme B and phosphorylated (p)STAT3. Parameters were chosen individually for each staining. Thereafter, smoothed features were calculated with a FWHM radius of 25 µm. The tissue was then classified into tumor/epithelium and stroma using an object classifier, trained individually for each staining. A threshold was set for the mean DAB optical density value, categorizing cells into positive or negative. For pSTAT3, multiple thresholds were set and cells were classified into 1*, 2* and 3* positive to calculate the H-score. The H-score was calculated by multiplying the percentage of cells by their respective intensity value and ranged from 1 to 300. Analysis was performed by a single investigator and evaluated by two independent pathologists. For quantification of Ki67 levels of tumor and non-tumor samples, we defined four circular regions of interest with a radius of 150 µm. Within each region, we manually counted the positive epithelial cells and used QuPath to detect the negative cells. Percentage of $\text{p21}^{\text{CIP1/WAF1}}$ positive epithelial cells was estimated by a blinded pathologist. For Galactosidase beta 1 (GLB1), regions of interest were annotated and categorized into positive and negative areas using a stringent pixel threshold for the DAB optical density value. The threshold was adjusted to detect the granular expression pattern. Results shown are from the anterior prostate.

Statistical analysis for immunohistochemistry

Measurements were exported as TSV files and imported into GraphPad PRISM (version 9.5.0). Significance was determined using an ordinary one-way ANOVA with Tukey's multiple comparisons tests for 3 or more groups. Graphs were created and formatted in GraphPad PRISM.

Protein extraction and immune blotting

Protein extraction from frozen prostate samples and immune blotting was performed as previously described [31]. Briefly, 15–20 µg of protein lysate was separated via SDS-PAGE, transferred onto nitrocellulose membranes (Amersham) and blocked with 5% milk in 1×TBS /0.1% Tween-20 or with 5% BSA in 1×TBS /0.1% Tween-20 for 1 h according to manufacturer's antibody datasheets. Membranes were incubated with primary antibodies against pJUN^{S73} (CST 9164), JUN (CST 9165), $\text{pAKT}^{\text{S473}}$ (CST 4060), AKT (CST 4691), EpCAM (Elab Science, E-AB-70132), β-ACTIN (CST 4967), NLRP3 (CST 15101), Pro-IL-1β (R&D Systems, AF-401-NA) and β-TUBULIN (CST 2146 and CST 2128) at 4 °C overnight. TGX stain free technology (Bio-Rad), β-ACTIN or β-TUBULIN were used as loading controls.

Magnetic cell sorting, library preparation and RNA sequencing

The preparation of sequencing libraries and subsequent RNA sequencing (RNA-seq) was performed as previously described [32]. Briefly, prostates of 19-week-old mice were dissected, processed to yield a single cell suspension and EpCAM (CD326) positive cells were isolated by magnetic cell sorting (Magnisort®, Thermo Fisher Scientific) using anti-CD326-biotin (13–5791–82, eBioscience). EpCAM positive cells were collected by centrifugation at 300 xg for 5 min at 4 °C and stored at -80 °C until further use. High-quality RNA, as assessed by 4200 TapeStation System (Agilent) was used for library preparation according to the manufacturer's instructions.

RNA sequencing data analysis

Single-end 75 bp reads sequencing of libraries was performed at CEITEC, Centre for Molecular Medicine (Brno, Czech Republic) as previously described [32]. Genes with a false discovery rate (FDR) FDR-adjusted p-value < 0.05 and log2 fold change ≥ 1 or ≤ -1 were considered significantly up- or downregulated.

Kaplan–Meier survival analyses of public datasets

To assess whether expression levels of *JUN, PTEN, IL1B, CCL3* and *CCL8* affected survival capabilities of human PCa patients, we applied the KM plotter tool (https://kmplot.com/analysis/) which computed probabilities of RFS based on the TCGA-PRAD study [33]. Output data were used for re-plotting of survival curves and performing of cox-regression analyses with R packages “Survival” and “Survminer” and R-script “ggsurvplot”. Combined KM plotter output was used for calculation of subgroups as stratified by expression levels of both genes, such as *JUN* and *PTEN*. Relapse-free survival (RFS) analysis was based on survival data of $n = 333$ PCa patients. Groups were automatically separated and the calculated, best performing and most significant threshold was used as a cut-off. Hazard ratios and *p*-values were retrieved from Cox-regression analyses.

Results

JUN levels discriminate progression states in prostate cancer dependent on *PTEN*

To clarify the role of AP-1 TFs in PCa progression, we investigated the level of the master factor JUN in tissue microarrays (TMA) of low and high progressive human prostate tumors by immunohistochemistry (IHC). We performed semi-quantitative analysis and categorized each tumor based on JUN levels from 0 (absent), 1 (low-grade), 2 (medium-grade) to 3 (high grade) (Fig. 1a). Patients were divided into present ($n = 29 + 6$ censored subjects) ($\text{JUN}^{\text{present}}$) and absent ($n = 32 + 8$ censored subjects) ($\text{JUN}^{\text{absent}}$) cohorts and correlated with biochemical recurrence (BCR) data (Supplementary Fig. 1a). PCa progression is marked by histological changes of the tumor architecture and is categorized by Gleason scoring [34]. We observed a gradual decrease of JUN protein abundance from healthy tissue to primary tumors (low Gleason; Gleason score 5–6), reaching the lowest JUN expression state in advanced tumor stages (high Gleason; Gleason score 7–9) (Fig. 1a). The correlation between JUN protein and patient BCR status revealed a significantly ($p = 1.8\text{e-}02$) diminished BCR-free survival in patients with low JUN, whereas high JUN levels were associated with increased survival probability (Supplementary Fig. 1a). We next mined a publicly available transcriptome dataset ([35]; $n = 140$) and stratified PCa patients into high-risk and low-risk groups as defined by the prognostic index and characterized by a significant difference in relapse-free survival (RFS) using the SurvExpress webtool [36] ($p = 4\text{e-}04$) (Supplementary Fig. 1b). We investigated *JUN* mRNA expression in the high- and low-risk groups and found significantly ($p = 1.3\text{e-}30$) higher *JUN* among low-risk patients compared to the high-risk group (Supplementary Fig. 1c). To explore *JUN* levels in advanced stages of PCa, we used the Taylor dataset [35], comprising primary tumors of different progression stages and Gleason scores ($n = 131$) as well as healthy prostate tissue ($n = 29$). Compared to healthy tissue, we observed higher levels of *JUN* in early disease stages with Gleason scores 5–6 and significantly decreased expression of *JUN* in high grade tumors ($p = 3\text{e-}03$; Gleason scores 7–9) (Fig. 1b). Concordantly, *JUN* was highly expressed in primary tumors ($n = 131$; $n = 65$) but significantly lower expressed in PCa metastases ($n = 19$; $n = 25$) as observed in two independent datasets (Fig. 1c-d; $p = 1.3\text{e-}02$; [35]; $p = 5.3\text{e-}09$; [37]). We next investigated levels of *JUN*, *JUNB* and *FOS* and observed a comparable regulation (Supplementary Fig. 1d-e). Metastatic CRPC and neuroendocrine PCa (NEPC) present aggressive tumor subtypes that emerge under androgen deprivation

(See figure on next page.)

Fig. 1 JUN levels are correlated with prostate cancer progression stages. **a** Left panel: Representative immunohistochemistry (IHC) images of tissue microarrays (TMAs) investigating human prostate tumors ($n = 60$) with high or low Gleason scores stained for JUN protein. Scale bars indicate 150 µm (top row) and 30 µm (bottom row), images are presented in 16.8 × (top row) and 80.0 × magnification (bottom row). The area used for the higher magnification is indicated by the rectangle. Right panel: Violin plot showing JUN expression divided in absent (0), low-grade (1), medium-grade (2) and high-grade (3) in healthy (no Gleason score), low Gleason (Gleason score 5–6) and high Gleason (Gleason score 7–9) TMA samples. **b** *JUN* mRNA levels in high (Gleason score ≥ 7) and low (Gleason score < 7) grade human prostate tumors. Data were retrieved from [35]. Significance was determined by an unpaired, two-sided t-test or one-sided Anova. **c** High and low *JUN* levels significantly ($p = 1.3\text{e-}02$) discriminate primary prostate tumors ($n = 131$) (red) and metastases ($n = 19$) (blue). Data were retrieved from [35]. **d** High and low *JUN* levels significantly ($p = 5.3\text{e-}09$) discriminate primary prostate tumors ($n = 65$) (red) and metastases ($n = 25$) (blue). Data were retrieved from [37]. Significances in c-d were determined by an unpaired, two-sided t-test. **e** Principal component analysis (PCA) of prostate tumors of different developmental stages comprising normal prostate tissue, primary tumors and primary (p) and metastatic (m) CRPC and NEPC tumors. Datasets from [38]. **f** Overlay of *JUN* expression with PCA clustering from e). *JUN* levels are color coded from high expression (yellow) to low expression (blue). **g** Kaplan–Meier survival analysis of TCGA-PRAD [33] tumors ($n = 333$) assessing levels of *JUN* and *PTEN*. Hazard ratios (HR) were determined by Cox-regression analysis: $\text{HR}(\text{JUN}^{\text{high}} \text{ vs. } \text{JUN}^{\text{low}}) = 0.461$, $p = 3.8\text{e-}02$ and $\text{HR}(\text{PTEN}^{\text{high}} \text{ vs. } \text{PTEN}^{\text{low}}) = 0.307$, $p = 1.5\text{e-}03$. Statistical testing was done with a logrank test. **h** Co-analysis between *PTEN* expression (RNA-Seq by Expectation–Maximization (RSEM) and PTEN protein level reverse-phase protein array (RPPA)). **i** Co-analysis between PTEN protein level (RRPA) and *JUN* expression (RSEM)

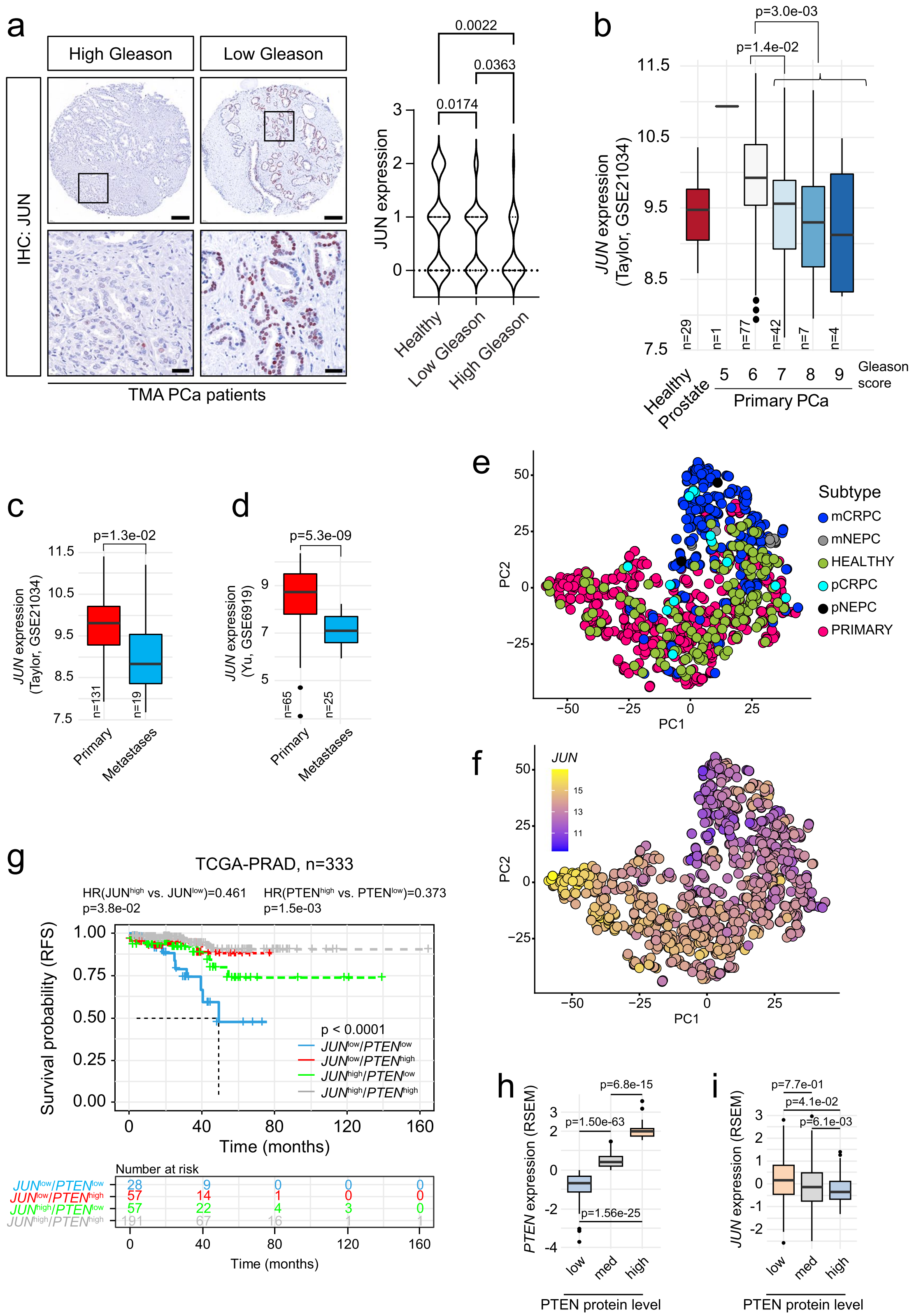

Fig. 1 (See legend on previous page.)

therapy and are associated with poor prognosis. We compared levels of *JUN* and its related TFs *FOS* and *JUNB* in primary ($n=715$) and metastatic ($n=320$) PCa [38], including CRPC and NEPC (Fig. 1e-f, Supplementary Fig. 1f). The tumor-subtype and stage-dependent expression of *JUN* was highly significant when comparing healthy and primary ($p=2.8\text{e-}05$), primary and metastatic CRPC ($p=2.6\text{e-}43$) and primary and metastatic NEPC ($p=5.3\text{e-}04$) (Supplementary Fig. 1g), suggesting JUN as a potential marker of progressive subtypes of PCa. In addition, our survey revealed higher levels of *JUN* in primary PCa associated with low Gleason scores than healthy prostates (Supplementary Fig. 1g-h), suggesting a gradual change of *JUN* levels in PCa development and progression. Our data implicate that JUN and other AP-1 factors except MAF and MAFB may act as suppressors rather than drivers of PCa which was reflected by hazard ratios (HR) calculated from RFS (Supplementary Fig. 1i).

Mutations in the tumor suppressor *PTEN* are considered as main drivers of oncogenic transformation and malignancy in PCa [4]. As PTEN loss is highly correlated with increasing Gleason score and associated with activation of several downstream processes, primarily via hyperactivation of PI3K/AKT and inactivation of AR signaling [4], we next investigated synergistic effects of additional *JUN* alterations. We applied the KMplot tool to assess RFS of PCa patients ([33]; $n=333$) that were stratified into four risk groups *JUN*$^{\mathrm{high}}$/*PTEN*$^{\mathrm{high}}$, *JUN*$^{\mathrm{high}}$/*PTEN*$^{\mathrm{low}}$, *JUN*$^{\mathrm{low}}$/*PTEN*$^{\mathrm{high}}$ and *JUN*$^{\mathrm{low}}$/*PTEN*$^{\mathrm{low}}$. We observed that patients featuring low levels of *JUN* and *PTEN* showed the lowest survival probability whereas patients with high *JUN* and *PTEN* expression presented with the most favorable prognosis. In contrast to singular *JUN* depletion, downregulation of *PTEN* alone resulted in intermediate survival probabilities confirming its role as main oncogenic driver in PCa (Fig. 1g). Finally, we surveyed reverse-phase protein array (RPPA) data of the TCGA-PRAD cohort [33] and observed that PTEN protein correlated well with *PTEN* mRNA levels whereas we identified an inverse relationship between PTEN and *JUN* levels (Fig. 1h-i). Although loss of JUN alone is not sufficient to cause significant changes in survival probability, our data suggest that the absence of PTEN promotes JUN to a survival-determining factor in PCa patients.

Genetic depletion identifies a tumor-suppressive role of JUN in prostate cancer development

As patients presenting with low expression of *JUN* and *PTEN* showed severely reduced survival rates, we next sought to elucidate the mechanistic role of JUN in the development of *PTEN*-deficient PCa and employed a *Pten* floxed murine model of PCa (Fig. 2a) [26, 39]. The homozygous deletion of murine *Pten* via the *Probasin (Pb)* Cre recombinase [27] mirrored 20% of all primary human PCa cases with homozygous loss of *PTEN* (Fig. 2a, *PbCre/Pten*). The PE of homozygous mutants developed hyperplasia that progressed into prostate adenocarcinoma between 12 and 29-weeks of age [39]. We inter-crossed a floxed *Jun* mouse strain where the sole exon is flanked by loxP sites [25] (Fig. 2a, *Jun*) to generate 4 individual genotypes. This enabled comparison of prostate tissue of *wildtype (wt)* mice to either *Jun* (*Jun*$^{\mathrm{PE}\Delta/\Delta}$), *Pten* (*Pten*$^{\mathrm{PE}\Delta/\Delta}$) or *Jun*/*Pten* (*Jun*$^{\mathrm{PE}\Delta/\Delta}$; *Pten*$^{\mathrm{PE}\Delta/\Delta}$) double knockout mice (Fig. 2a, colored F1 mice). We examined protein extracts of whole prostates and observed a significant increase in levels of phosphorylated (S73) and total JUN in *Pten*$^{\mathrm{PE}\Delta/\Delta}$, whereas notable JUN expression was absent in *wt* prostates (Fig. 2b). We also confirmed efficient Cre-mediated deletion of *Jun* alone (*Jun*$^{\mathrm{PE}\Delta/\Delta}$) and in combination with *Pten* (*Jun*$^{\mathrm{PE}\Delta/\Delta}$; *Pten*$^{\mathrm{PE}\Delta/\Delta}$) (Fig. 2b). As a verification of functional *Pten* deletion, we detected robust activation of the PI3K/AKT pathway in *Pten*$^{\mathrm{PE}\Delta/\Delta}$

(See figure on next page.)

Fig. 2 *Jun*-deficiency fosters the progression of *Pten*-loss induced tumors. **a** Top: Schematic representation of mouse models used in the study. Homozygous loss of *Pten* or *Jun* was achieved by a *Probasin* promoter-controlled Cre recombinase (*PbCre*)-mediated ablation of floxed exons 4 and 5 (*Pten*) or exon 1 (*Jun*). Bottom: established and investigated genetic models. Wildtype (*PbCre*$^{+/+}$; *wt*) and mice with single knockout of *Pten* (*PbCre*$^{\mathrm{tg}/+}$; *Pten*$^{\mathrm{PE}\Delta/\Delta}$) and *Jun* (*PbCre*$^{\mathrm{tg}/+}$; *Jun*$^{\mathrm{PE}\Delta/\Delta}$) were compared with double knockout (*PbCre*$^{\mathrm{tg}/+}$; *Jun*$^{\mathrm{PE}\Delta/\Delta}$;*Pten*$^{\mathrm{PE}\Delta/\Delta}$). PE = prostate epithelium; tg = transgene; Δ = knockout. **b** Western blot analysis of phosphorylated (pJUN$^{\mathrm{S73}}$ and pAKT$^{\mathrm{S473}}$) and total JUN and AKT. β-TUBULIN served as loading control. Protein lysates of entire organs ($n=3$ biological replicates) from 19-week-old *wt*, *Pten*$^{\mathrm{PE}\Delta/\Delta}$, *Jun*$^{\mathrm{PE}\Delta/\Delta}$ and *Jun*$^{\mathrm{PE}\Delta/\Delta}$;*Pten*$^{\mathrm{PE}\Delta/\Delta}$ were investigated. **c** Top row: H&E stainings of 19-week-old *wt*, *Pten*$^{\mathrm{PE}\Delta/\Delta}$, *Jun*$^{\mathrm{PE}\Delta/\Delta}$ and *Jun*$^{\mathrm{PE}\Delta/\Delta}$;*Pten*$^{\mathrm{PE}\Delta/\Delta}$ prostates. Scale bars indicate 60 µm (top row) and 2 µm (second row), images are presented in 40.0 × (top row) and 600.0 × magnification (second row). Black rectangles represent the area used for the zoom image below. Bottom row: IHC with an antibody against JUN in 19-week-old prostates of all four experimental groups. Scale bars indicate 30 µm; images are presented in 100.0 × magnification. **d** Macroscopic images of 19-week-old dissected prostates of *wt*, *Pten*$^{\mathrm{PE}\Delta/\Delta}$, *Jun*$^{\mathrm{PE}\Delta/\Delta}$ and *Jun*$^{\mathrm{PE}\Delta/\Delta}$;*Pten*$^{\mathrm{PE}\Delta/\Delta}$ mice. **e** Box plot showing the weights of prostates in grams between *wt*, *Pten*$^{\mathrm{PE}\Delta/\Delta}$, *Jun*$^{\mathrm{PE}\Delta/\Delta}$ and *Jun*$^{\mathrm{PE}\Delta/\Delta}$;*Pten*$^{\mathrm{PE}\Delta/\Delta}$ 19-week-old animals ($n=20$). Significance was determined with an unpaired, two-sided t-test. **f** Kaplan–Meier survival analysis of *wt*, *Pten*$^{\mathrm{PE}\Delta/\Delta}$, *Jun*$^{\mathrm{PE}\Delta/\Delta}$ and *Jun*$^{\mathrm{PE}\Delta/\Delta}$;*Pten*$^{\mathrm{PE}\Delta/\Delta}$ animals. Biological replicates are indicated and the cumulative survival (%) is shown. Statistical significance was calculated with a logrank test. **g** Organs (heart, lung, liver, spleen, kidney, lymph nodes and brain) of 39-week-old *wt*, *Pten*$^{\mathrm{PE}\Delta/\Delta}$, *Jun*$^{\mathrm{PE}\Delta/\Delta}$ and *Jun*$^{\mathrm{PE}\Delta/\Delta}$;*Pten*$^{\mathrm{PE}\Delta/\Delta}$ mice were stained with H&E and analysed for metastatic lesion formation. The number of metastases detected in each tissue are shown

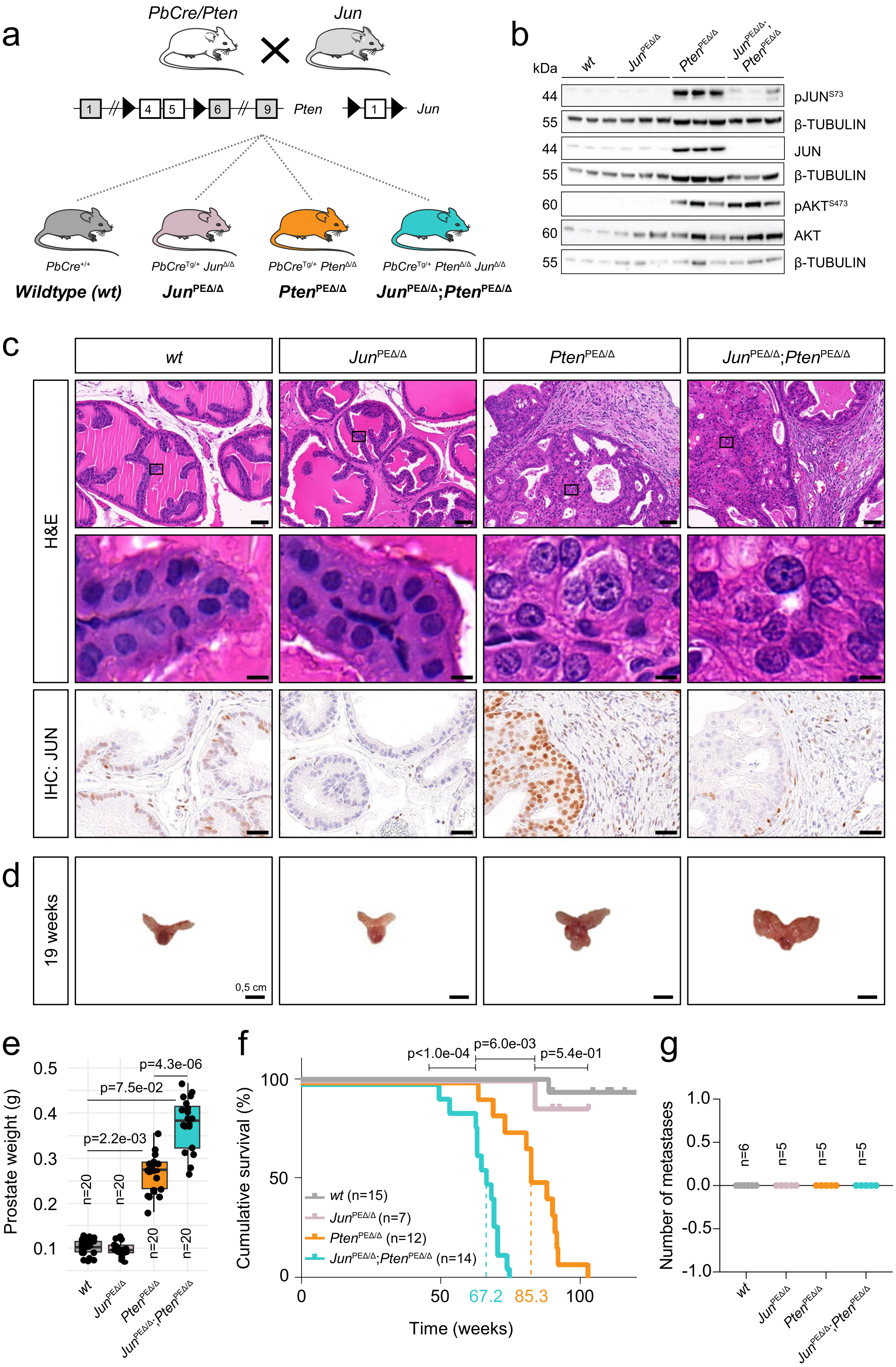

Fig. 2 (See legend on previous page.)

and *Jun*$^{\mathrm{PE}\Delta/\Delta}$; *Pten*$^{\mathrm{PE}\Delta/\Delta}$ mice as assessed by analysis of phosphorylated AKT (pAKT^{S473}) levels (Fig. 2b).

To investigate the morphological architecture of prostates upon *Jun* deletion in the PCa mouse model, we analyzed histological sections by hematoxilin and eosin (H&E) staining (Fig. 2c, top panel). Both *wt* and *Jun*$^{\mathrm{PE}\Delta/\Delta}$ animals showed physiological growth patterns and morphology, characteristic for the respective prostate lobes. In *Pten*$^{\mathrm{PE}\Delta/\Delta}$ and *Jun*$^{\mathrm{PE}\Delta/\Delta}$; *Pten*$^{\mathrm{PE}\Delta/\Delta}$ prostates, we observed hyperplastic epithelium growing in cribriform patterns into the lumen. Both groups showed anisocytosis, anisokaryosis and alterations in nucleus-to-cytoplasmic ratios, but largely without invasion of the stroma.

Next, we analyzed JUN levels in prostates of all genotypes. Supporting our immunoblot results, IHC revealed increased levels of total JUN predominantly in the PE of *Pten*$^{\mathrm{PE}\Delta/\Delta}$ mice and absence in epithelial cells of *Jun*$^{\mathrm{PE}\Delta/\Delta}$ and *Jun*$^{\mathrm{PE}\Delta/\Delta}$; *Pten*$^{\mathrm{PE}\Delta/\Delta}$ (Fig. 2c, bottom panel). We assessed the effects of *Jun* deficiency on tumor burden and survival by morphological and survival analyses. Macroscopically, prostates from *Pten*$^{\mathrm{PE}\Delta/\Delta}$ and *Jun*$^{\mathrm{PE}\Delta/\Delta}$; *Pten*$^{\mathrm{PE}\Delta/\Delta}$ mice were notably enlarged as compared to *wt* or *Jun*$^{\mathrm{PE}\Delta/\Delta}$ prostates (Fig. 2d). This finding was corroborated by prostate weight analysis (Fig. 2e). The additional deletion of *Jun* on the *Pten*-deficient background resulted in even higher prostate weights, hinting at JUN's potential function as a tumor-suppressor in murine PCa development. We performed a Kaplan–Meier survival analysis where overall survival or the occurrence of the discontinuation criteria according to the guidelines of the 3Rs principles were defined as the endpoint of the experiments (Fig. 2f) [40]. We observed comparable survival probabilities of *wt* and *Jun*$^{\mathrm{PE}\Delta/\Delta}$ mice ($p = 5.4$e-01) but a significantly decreased survival of *Pten*$^{\mathrm{PE}\Delta/\Delta}$ (mean survival 85.3 weeks, $p = 6$e-03) as compared to *wt* mice. Remarkably, the survival of *Pten*$^{\mathrm{PE}\Delta/\Delta}$ mice was significantly ($p < 1$e-04) reduced by the additional deletion of *Jun*. *Jun*$^{\mathrm{PE}\Delta/\Delta}$; *Pten*$^{\mathrm{PE}\Delta/\Delta}$ mice exhibited a mean survival of 67.2 weeks. Despite the significantly reduced survival rates in *Jun*$^{\mathrm{PE}\Delta/\Delta}$; *Pten*$^{\mathrm{PE}\Delta/\Delta}$ mice, we did not detect metastatic lesions in the analysed genotypes (Fig. 2g). We therefore conclude that *Jun*-deficiency alone is not sufficient to induce prostate tumorigenesis, but causes a significant increase in tumor burden and a significant reduction in overall survival in combination with *Pten* knockout. The results of our murine PCa model reinforce our observations from human PCa samples, suggesting that JUN acts as a tumor-suppressor in PCa.

To determine whether aberrant cellular proliferation contributes to enhanced tumor growth in *Jun*$^{\mathrm{PE}\Delta/\Delta}$; *Pten*$^{\mathrm{PE}\Delta/\Delta}$-deficient prostates, we assessed the number of Ki67^{+} epithelial cells by IHC. Although we noticed higher Ki67 levels in *Jun*$^{\mathrm{PE}\Delta/\Delta}$; *Pten*$^{\mathrm{PE}\Delta/\Delta}$ tumors by trend, the difference was not significant ($p = 1.3$e-01) when compared to *Pten*$^{\mathrm{PE}\Delta/\Delta}$ prostates (Supplementary Fig. 2a). To investigate the effects of *JUN* ablation in vitro, we utilized the CRISPR/Cas9 technology in the human PCa cell lines DU145 (*PTEN* wildtype) and PC3 (*PTEN* mutated). We designed three individual guide RNAs for the *JUN* locus (Supplementary Fig. 2b) and used lentiviral transduction of empty vector (EV) and guide RNA (G1, G12, G14) plasmids. We identified varying efficiencies of JUN knockout in bulk cultures of DU145 and PC3 cell lines (Supplementary Fig. 2c, e) and no significant differences in cellular proliferation (Supplementary Fig. 2d, f). We confirmed the results of unchanged proliferation in single clones of both cell lines which were selected according to complete loss of JUN protein (Supplementary Fig. 2g-j). The in vivo and in vitro results indicate that proliferation may not be the primary biological process influenced by JUN during PCa progression.

Transcriptome profiling reveals JUN-mediated alterations in senescence-associated secretion and immune response

To elucidate the tumor cell-specific molecular programs regulated by JUN in vivo, we performed transcriptome profiling of PE cells across all four experimental murine groups (Fig. 2a). To obtain a homogenous epithelial fraction, we enriched prostate lysates for the Epithelial cell adhesion molecule (EpCAM) showing a uniform expression in PE cells (Fig. 3a, Supplementary Fig. 3a) via magnetic cell separation [32] (Fig. 3b, Supplementary Fig. 3b). The correlation analysis revealed high congruence between *Jun*$^{\mathrm{PE}\Delta/\Delta}$; *Pten*$^{\mathrm{PE}\Delta/\Delta}$ and *Pten*$^{\mathrm{PE}\Delta/\Delta}$ tumor and *wt* and *Jun*$^{\mathrm{PE}\Delta/\Delta}$ samples (Fig. 3c).

We next performed a comparative analysis of *Jun*$^{\mathrm{PE}\Delta/\Delta}$; *Pten*$^{\mathrm{PE}\Delta/\Delta}$ and *Pten*$^{\mathrm{PE}\Delta/\Delta}$ prostate samples to discern JUN-dependent programs potentially contributing to PCa formation. Our survey revealed 1706 (p.adjust < 5e-02) differentially expressed genes (DEGs) with top 102 genes being up- (log$_2$fold change ≥ 1) and top 91 genes downregulated (log$_2$fold change $\leq$ -1; Supplementary Table 1). DAVID analysis of top genes showed increased "innate immunity" and "immune system processes" but decreased secretory-, extracellular matrix- and immune-related processes. Notably, *Jun* ranked among the top 10 downregulated genes confirming the successful knockout in epithelial cells (Supplementary Table 1). Gene set enrichment analysis (GSEA) revealed immune system-related processes, IL-6/STAT3 signaling and senescence-associated gene signatures among the most enriched processes in *Pten*$^{\mathrm{PE}\Delta/\Delta}$ prostates which were significantly depleted in *Jun*$^{\mathrm{PE}\Delta/\Delta}$; *Pten*$^{\mathrm{PE}\Delta/\Delta}$ (Fig. 3d). Our previous work suggested that activation of IL-6/STAT3 signaling and of the downstream acting p19$^{\mathrm{ARF}}$–MDM2–p53 axis contributed to senescence in *Pten*$^{\mathrm{PE}\Delta/\Delta}$ prostates [12].

We therefore investigated the enrichment level of different senescence signatures including "oncogene-induced senescence" (OIS), "SASP" signatures and the novel "SenMayo" gene signature, consisting of 125 previously identified senescence/SASP-associated factors. SenMayo genes are transcriptionally regulated by senescence and allow identification of senescent cells across tissues [41]. SenMayo genes were significantly (qval = 2.40e-02) enriched in *Pten*$^{PE\Delta/\Delta}$ prostates and depleted (qval = 2.64e-02) in *Jun*$^{PE\Delta/\Delta}$; *Pten*$^{PE\Delta/\Delta}$ tumors (Fig. 3d). Among the depleted SenMayo genes in *Jun*-deficient *Pten*$^{PE\Delta/\Delta}$ prostates, we identified chemokines such as *Ccl3, Ccl4 and Ccl8*, along with pro-inflammatory cytokines such as *Il1b* and *Tnfa* (Fig. 3e). As these secreted cytokines and chemokines represent well described SASP factors, we next investigated a SASP core gene signature previously described in a *Pten*-deficient prostate model [42]. Using GSEA, we indeed detected enrichment of the SASP core signature in *Pten*-deficient prostates which was reverted in *Jun*$^{PE\Delta/\Delta}$; *Pten*$^{PE\Delta/\Delta}$ animals (Fig. 3f). To investigate further aspects of JUN-dependent regulation of senescence in *Pten*-deficient murine prostates, we stained formalin-fixed paraffin embedded (FFPE) material with the senescence markers p16^{INK4A}, p21$^{CIP1/WAF1}$ and Galactosidase beta 1 (GLB1) (Supplementary Fig. 3c). We did not observe differences in the amount of p16^{INK4A} positive cells between *Pten*$^{PE\Delta/\Delta}$ and *Jun*$^{PE\Delta/\Delta}$; *Pten*$^{PE\Delta/\Delta}$ tumors, but found significant changes in staining patterns. While we detected prominent nuclear staining in *Pten*$^{PE\Delta/\Delta}$ samples, *Jun*$^{PE\Delta/\Delta}$; *Pten*$^{PE\Delta/\Delta}$ revealed predominantly cytoplasmic localization, hinting at a potential inactivation of p16^{INK4A} via nuclear export [43]. In *wt* and *Jun*$^{PE\Delta/\Delta}$ prostates, we observed a weak lobe-dependent expression pattern of p21$^{CIP1/WAF1}$. Conversely, in *Pten*$^{PE\Delta/\Delta}$ and *Jun*$^{PE\Delta/\Delta}$; *Pten*$^{PE\Delta/\Delta}$ samples, p21$^{CIP1/WAF1}$ was expressed in each individual epithelial cell, with no discernible difference between the two groups. GLB1 staining displayed its characteristic granular expression pattern prompting us to quantify percentage of positive area however we found no significant difference between *Pten*$^{PE\Delta/\Delta}$ and *Jun*$^{PE\Delta/\Delta}$; *Pten*$^{PE\Delta/\Delta}$ groups. Apart from changes in the p16 staining pattern, we found no significant deregulation of the classic senescence-associated cell cycle markers, implicating that JUN affects the SASP but not senescence-associated cell cycle arrest.

As our results suggest JUN-dependent activation of the IL-6/STAT3 axis and our previous study connected loss of activated STAT3 in *Pten*-deficient PCa to increased tumor burden via disruption of senescence [12], we sought to analyze STAT3 tyrosine 705 (Y705) phosphorylation (pSTAT3^{Y705}) in the *Jun*-deficient background. We indeed detected reduced levels of pSTAT3^{Y705} in both stroma ($p = 5.0e\text{-}04$) and epithelial cells ($p < 1.0e\text{-}04$) of *Jun*$^{PE\Delta/\Delta}$; *Pten*$^{PE\Delta/\Delta}$ compared to *Pten*$^{PE\Delta/\Delta}$ tumors (Supplementary Fig. 3d upper panel, Supplementary Fig. 3e) while total STAT3 levels remained constant (Supplementary Fig. 3d, lower panel). Our findings provide evidence that loss of JUN accompanied by reduced activation of STAT3 bypasses SASP and subsequently amplifies the tumor load in *Jun*$^{PE\Delta/\Delta}$; *Pten*$^{PE\Delta/\Delta}$ animals. We suggest an interplay of JUN and STAT3 mediating senescence-associated secretion of inflammatory factors in PCa in vivo, reinforcing JUN's proposed function as a pioneering factor of senescence [23].

JUN deficiency in the PCa mouse model leads to downregulated chemotaxis of innate immune cells

We next compared *Jun*$^{PE\Delta/\Delta}$; *Pten*$^{PE\Delta/\Delta}$ and *Pten*$^{PE\Delta/\Delta}$ prostate samples to uncover additional JUN-dependent biological processes involved in PCa formation. A stringent selection identified ~100 significantly deregulated genes (padj ≤ 1.0e-03, $\text{FClog}_2 \leq -1.2$; $n = 59$/ $\text{FClog}_2 \geq 1.2$;

(See figure on next page.)

Fig. 3 Transcriptome profiling of genetic models reveals a JUN-dependent regulation of innate immunity. **a** Representative immunofluorescence (IF) image of a *wt* murine prostate for the epithelial marker EpCAM (green). DAPI (blue) is shown as a nuclear stain. Top image: 40.0 × magnification, scale bar represents 60 µm; Bottom image: 147.5 × magnification, scale bar represents 20 µm. **b** Overview of sample preparation for transcriptome profiling of *wt*, *Pten*$^{PE\Delta/\Delta}$, *Jun*$^{PE\Delta/\Delta}$ and *Jun*$^{PE\Delta/\Delta}$;*Pten*$^{PE\Delta/\Delta}$ prostate samples of 19-week-old animals. An antibody against the epithelial marker EpCAM was used to separate single cell suspensions of minced and digested prostates into EpCAM positive (pos) and negative (neg) fractions by magnetic cell sorting. EpCAM^{pos} cells were used for RNA-seq expression profiling. **c** Heat map showing correlation analysis of tumor samples described in b) regarding global similarity of samples. The Pearson correlation coefficient (R) is shown (color coded). **d** Gene onthology (GO)-enrichment analysis of differentially expressed genes (DEGs) showing the top differentially regulated pathways between *Pten*$^{PE\Delta/\Delta}$ and *Jun*$^{PE\Delta/\Delta}$;*Pten*$^{PE\Delta/\Delta}$. Significance as shown by FDR is color coded, enriched (positive normalized enrichment score (NES)) or depleted (negative NES) processes are indicated. Asterisk represents non-significant pathways (ns). **e** Heat map showing SenMayo genes most significantly (p ≤ 1e-02) regulated among *Pten*$^{PE\Delta/\Delta}$ and *Jun*$^{PE\Delta/\Delta}$; *Pten*$^{PE\Delta/\Delta}$ prostates. **f** GSEA enrichment analysis using the Guccini_core_SASP gene set in *Pten*$^{PE\Delta/\Delta}$ versus *Jun*$^{PE\Delta/\Delta}$;*Pten*$^{PE\Delta/\Delta}$ and *Pten*$^{PE\Delta/\Delta}$ versus *wt* animals. **g** Heat map representation of *wt*, *Pten*$^{PE\Delta/\Delta}$, *Jun*$^{PE\Delta/\Delta}$ and *Jun*$^{PE\Delta/\Delta}$;*Pten*$^{PE\Delta/\Delta}$ samples showing DEGs. "Innate immunity", FDR = 7.64e-05; "Immune system", FDR = 2.77e-04 and "Extracellular space", FDR = 6.60e-03 related processes most discriminated the groups. Genotypes and expression levels are color coded. **h** GO-enrichment analysis of DEGs showing the regulation of innate immune cells such as neutrophil granulocytes. Significance as shown by p-value is color coded, enriched (positive NES) or depleted (negative NES) processes are indicated. Shown are the signaling pathways enriched in *Pten*$^{PE\Delta/\Delta}$ tumors compared to *wt* (left side) and *Jun*$^{PE\Delta/\Delta}$;*Pten*$^{PE\Delta/\Delta}$ tumors compared to *Pten*$^{PE\Delta/\Delta}$ (right side)

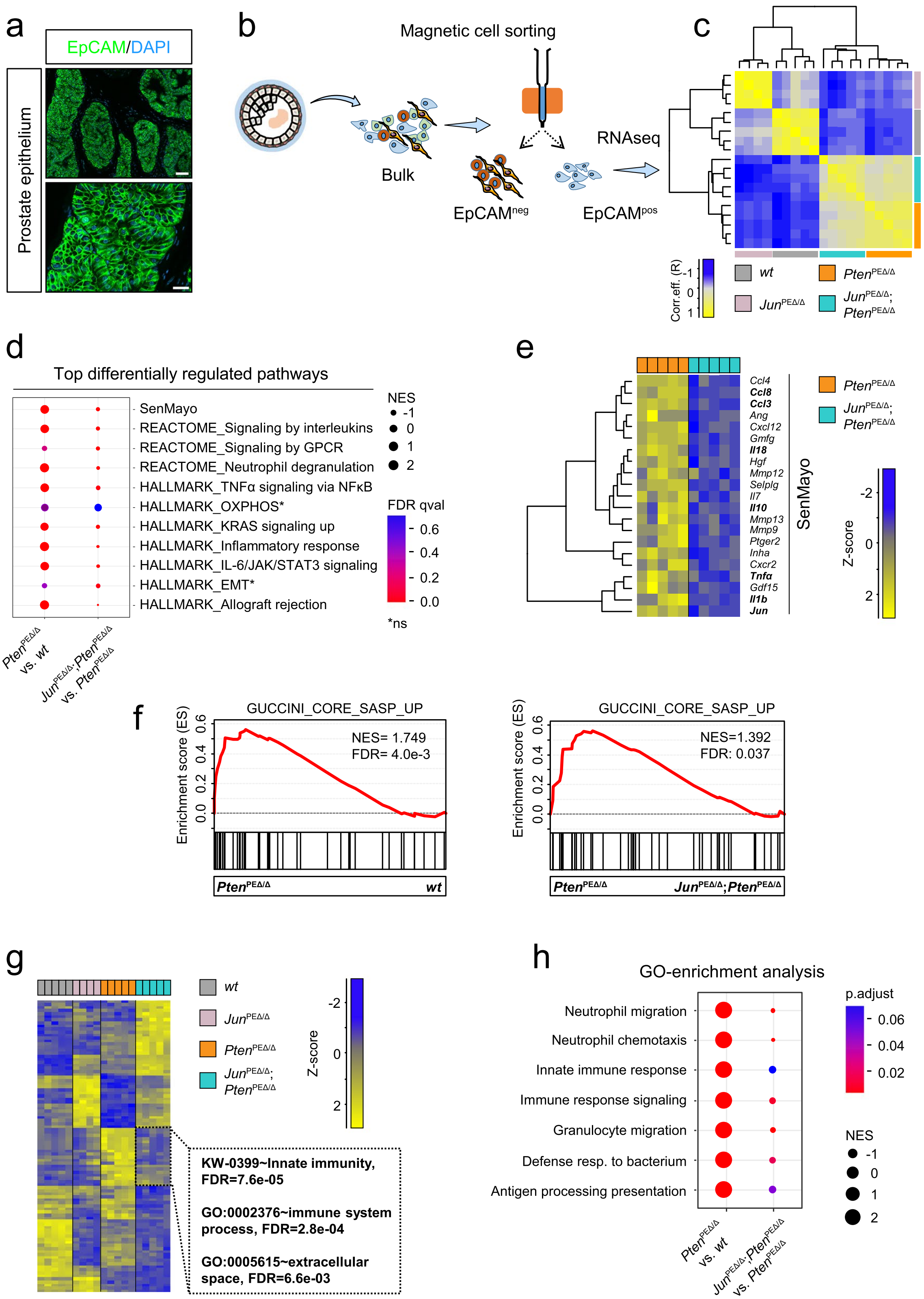

Fig. 3 (See legend on previous page.)

n = 46; Supplementary Table 3) and uncovered innate immunity and other immune system-related processes as most distinguishing between *Jun*$^{\mathrm{PE}\Delta/\Delta}$; *Pten*$^{\mathrm{PE}\Delta/\Delta}$ and *Pten*$^{\mathrm{PE}\Delta/\Delta}$ prostate tumors (Fig. 3g). Amongst the innate immunity and immune system cluster, gene onthology (GO)-enrichment analysis indeed confirmed immune system-related signatures that were activated in *Pten*$^{\mathrm{PE}\Delta/\Delta}$ and significantly reduced by *Jun*-deficiency (Fig. 3h). Innate immunity-related processes are complex and encompass more than 2000 publicly available human and mouse annotated genes [44]. We defined a core immunity-related signature by GSEA applying 645 innate immunity-related genes and investigated the enrichment specifically in *Pten*$^{\mathrm{PE}\Delta/\Delta}$ prostates. The analysis revealed 111 genes, of which 26 were significantly ($p < 1.0\text{e-}03$) differentially expressed between *Pten*$^{\mathrm{PE}\Delta/\Delta}$ and *Jun*$^{\mathrm{PE}\Delta/\Delta}$; *Pten*$^{\mathrm{PE}\Delta/\Delta}$ prostates (Fig. 4a, top panels, Supplementary Fig. 4a, Supplementary Table 4). Using the "Hallmark Inflammatory response" signature, we uncovered a similar pattern as the majority of genes from both signatures were significantly ($p < 1.0\text{e-}03$) elevated in *Pten*$^{\mathrm{PE}\Delta/\Delta}$ and depleted in *Jun*$^{\mathrm{PE}\Delta/\Delta}$; *Pten*$^{\mathrm{PE}\Delta/\Delta}$ prostates (Fig. 4a, bottom panels, Supplementary Fig. 4a). Hence, the homozygous loss of *Pten* was accompanied by inflammation and inflammatory response likely driven by increased levels of *Il1b*, *Nlrp3* and chemokines such as *Ccl5*.

Cells of the innate immune system, including neutrophil granulocytes, mast cells and macrophages serve as the primary defense against infections and consequently recruit T and B cells to infection sites [45]. Among the DEGs of *Pten*$^{\mathrm{PE}\Delta/\Delta}$ versus *Jun*$^{\mathrm{PE}\Delta/\Delta}$; *Pten*$^{\mathrm{PE}\Delta/\Delta}$ prostates, we identified neutrophil movement-specific gene signatures that play a crucial role in the recruitment of immune cells (Fig. 4b) [46]. We observed that cytokines involved in chemotaxis of immune cells such as *Ccl3*, *Ccl8* and *Il1b* were significantly deregulated between groups (Fig. 4c). To further dissect the potentially involved immune cell subsets, we conducted single sample GSEA using the M5 ontology gene sets signature from the molecular signature database (MsigDB). We identified enrichment of macrophage- and neutrophil-specific gene signatures characterized by cellular activities such as migration, activation/differentiation and enhanced expression indicating production of MIP1α/CCL3 and GM-CSF. Moreover, single sample GSEA revealed processes related to other immune cell subsets such as mast cells, myeloid cells and CD8^{+} T cells that were significantly enriched in *Pten*$^{\mathrm{PE}\Delta/\Delta}$ compared to *wt* prostates and depleted in *Jun*$^{\mathrm{PE}\Delta/\Delta}$; *Pten*$^{\mathrm{PE}\Delta/\Delta}$ (Fig. 4d). This implicates JUN in the control of inflammatory states during PCa progression. We validated the JUN-dependent regulation of IL-1β, TNF-α and NLRP3, all involved in the regulation of inflammatory response processes by immunoblot and cytokine analyses (Fig. 4e-f and Supplementary Fig. 4b).

To further examine the apparent shifts in immune system-related transcriptomic signatures, we assessed granulocytic or lymphocytic cell infiltrations based on microscopic characteristics in H&E staining of all four genotypes (Supplementary Fig. 4c). We detected no or low-grade infiltration by inflammatory cells in *wt* and *Jun*$^{\mathrm{PE}\Delta/\Delta}$ specimens. In contrast, *Pten*$^{\mathrm{PE}\Delta/\Delta}$ mouse prostates exhibited increased levels of high- and middle-grade infiltrations, which were significantly mitigated in *Jun*$^{\mathrm{PE}\Delta/\Delta}$; *Pten*$^{\mathrm{PE}\Delta/\Delta}$ prostates. Increased immune cell infiltration of *Pten*$^{\mathrm{PE}\Delta/\Delta}$ prostates as identified by histopathological analysis therefore supported the results of transcriptome profiling. This highlights the importance of JUN in the regulation of inflammation by affecting the secretion of pro-inflammatory cytokines in *Pten*-deficient PCa.

Epithelial JUN deficiency modulates the migration of innate immune cells from the periphery

To investigate the distribution and abundance of infiltrating immune cells, we performed IHC stainings. Neutrophils and inflammatory monocytes were stained using the antibody clone NIMP-R14, which targets the specific cell surface markers and differentiation antigens Ly-6G and Ly-6C (Fig. 5a). In *Pten*$^{\mathrm{PE}\Delta/\Delta}$

(See figure on next page.)

Fig. 4 JUN expression determines the level of immune cell infiltration of *Pten*-loss driven tumors. **a** Heat map showing JUN-dependent regulation of genes related to innate immunity (upper panel) and inflammatory response (lower panel) in *wt*, *Jun*$^{\mathrm{PE}\Delta/\Delta}$, *Pten*$^{\mathrm{PE}\Delta/\Delta}$ and *Jun*$^{\mathrm{PE}\Delta/\Delta}$;*Pten*$^{\mathrm{PE}\Delta/\Delta}$ prostates. JUN-dependent core factors such as *Il1b*, *Nlrp3* and *Ccl5* are highlighted. **b** Heat map presenting the JUN-dependent regulation of genes involved in migration and chemotaxis of neutrophil granulocytes in *Pten*$^{\mathrm{PE}\Delta/\Delta}$ and *Jun*$^{\mathrm{PE}\Delta/\Delta}$;*Pten*$^{\mathrm{PE}\Delta/\Delta}$ prostates. Genotypes and expression levels in **a**-**b** are color coded. **c** Expression levels (log2, FPKM) of *Ccl3, Ccl8* and *Il1b* are significantly (*Ccl3*, $p = 2.4\text{e-}04$; *Ccl8*, $p = 9.7\text{e-}05$ and *Il1b*, $p = 5.0\text{e-}03$) reduced in EpCAM^{+} cells of *Jun*$^{\mathrm{PE}\Delta/\Delta}$;*Pten*$^{\mathrm{PE}\Delta/\Delta}$ prostates. Significance was determined by an unpaired two-sided t-test. **d** Single-sample GSEA analysis using the M5 signature of Broad Institute's molecular signature database (MsigDB) revealing enrichment of macrophage- and neutrophil-associated properties in *Pten*$^{\mathrm{PE}\Delta/\Delta}$ compared to *Jun*$^{\mathrm{PE}\Delta/\Delta}$;*Pten*$^{\mathrm{PE}\Delta/\Delta}$ prostates. **e** Western blot analysis of NLRP3 and non-cleaved Pro-IL-1β in all four experimental groups in biological replicates. β-ACTIN served as loading control. **f** Multiplex immunoassay of homogenized prostate samples of 19-week-old *wt*, *Jun*$^{\mathrm{PE}\Delta/\Delta}$, *Pten*$^{\mathrm{PE}\Delta/\Delta}$ and *Jun*$^{\mathrm{PE}\Delta/\Delta}$;*Pten*$^{\mathrm{PE}\Delta/\Delta}$ animals for analysis of IL-1β levels in pico grams (pg)/ml of indicated biological replicates. Statistical testing was done with one-way Anova, significant *p*-values are indicated

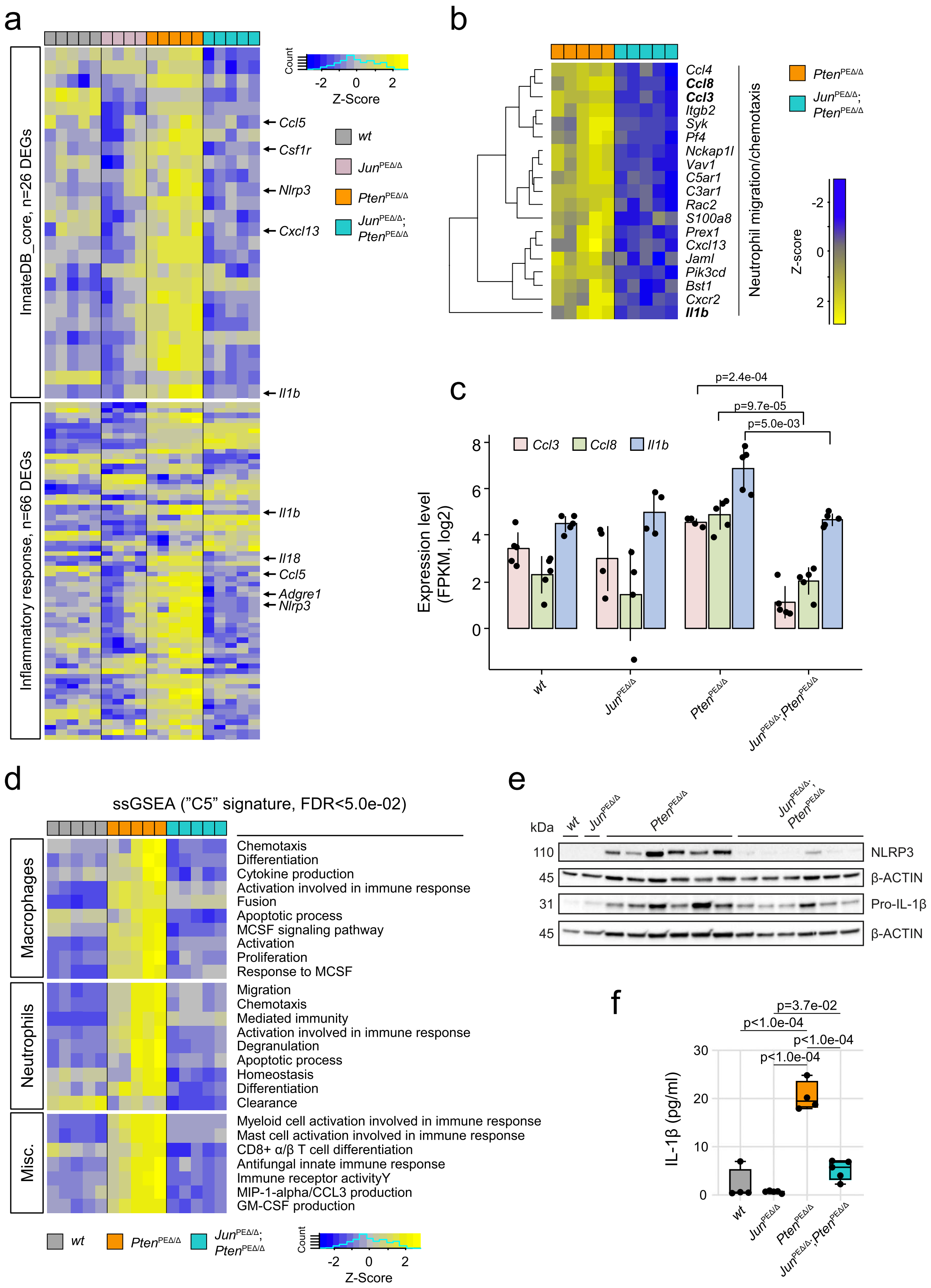

Fig. 4 (See legend on previous page.)

prostates, we observed high numbers of neutrophils migrating from the blood vessels across the stroma into the epithelium, where they predominantly accumulated, and subsequently advanced into the lumen. In *Jun*$^{PE\Delta/\Delta}$; *Pten*$^{PE\Delta/\Delta}$ prostates, we detected significantly ($p < 1.0e\text{-}04$) less neutrophils in the stroma and epithelium, but the migration patterns remained consistent with *Pten*$^{PE\Delta/\Delta}$ tumors (Fig. 5b). In contrast, macrophages, stained by the marker F4/80 were primarily located in the stroma, with no significant differences between the groups (Fig. 5c-d). We observed significantly ($p = 4.0e\text{-}04$) less macrophages infiltrating the epithelium in prostates with additional deficiency of *Jun*. In conclusion, *Pten*$^{PE\Delta/\Delta}$ displayed a highly immune infiltrated phenotype, which was substantially reverted in prostates with additional deficiency of *Jun*. This observation suggests that JUN may be essential for tumor cell recognition by innate and consequently adaptive immune cells.

Neutrophils attract T cells to the site of inflammation via secretion of chemokines such as CCL2 and CCL5 [47, 48]. We utilized multiplex IHC to discern the T cell subsets, employing a marker panel consisting of CK/CD3/CD4/CD8/CD45/PD-1/DAPI. We observed various T cell subpopulations (T helper (CD4$^+$) and cytotoxic T cells (CD8$^+$), PD-1 positive and negative) mainly in the stroma and to a lesser degree in the epithelium (Supplementary Fig. 5a-b). To further investigate active cytotoxic T cells and natural killer cells, we performed Granzyme B IHC (Supplementary Fig. 5c-d). We did not observe a significant effect of *Jun* deficiency on any of the investigated populations. Additionally, we investigated the infiltration of B cells, stained by CD79b. B cells were found almost exclusively in the stroma, with significantly less infiltration in *Jun*$^{PE\Delta/\Delta}$; *Pten*$^{PE\Delta/\Delta}$ compared to *Pten*$^{PE\Delta/\Delta}$ prostates (Fig. 5e-f). In summary, IHC validated the JUN-dependent modulation of the immune cell compartment, particularly affecting innate immune cells. This phenotype was likely provoked by a JUN-dependent regulation of neutrophil attracting chemokines such as IL-1β.

Increased expression of SASP factors is correlated with prolonged survival in prostate cancer

To translate our findings to the human disease, we investigated a potential association of JUN and SASP factors. We compared the levels of *JUN, IL1B, CCL3* and *CCL8* in patient data (TCGA-PRAD [33]) by PCA and found high *IL1B, CCL3* and *CCL8* mRNA in tumors expressing high levels of *JUN*. In contrast, tumors expressing low *JUN* levels revealed equally low amounts of *IL1B, CCL3* and *CCL8* (Fig. 6a-d). Upon separation of TCGA-PRAD tumors by using mean *JUN* expression as cut-off in *JUN* high and low expressing groups, we indeed confirmed enrichment of SASP factors and neutrophil marker *ADGRE1* in *JUN* high subgroups (Fig. 6e). We next performed a Pearson correlation analysis and detected a significant but weak positive ($R \leq 0.64$; $p \leq 0.05$) association of *IL1B, CCL3* and *CCL8* with *JUN* and additional AP-1 factors such as *JUND, JUNB, FOS* and *FOSB* (Fig. 6f).

Assuming that JUN mediates tumor-suppressor activity via positive regulation of SASP factors required for the recruitment of immune cells, we expected that high levels of SASP factors may be associated with favorable prognosis. Hence, we asked whether cytokine expression may act in concert with JUN to influence patient survival. We stratified patients according to their *PTEN, JUN* and *IL1B* (Fig. 6g) *CCL3* (Fig. 6h) or *CCL8* (Fig. 6i) levels and compared the RFS between groups. As expected, *PTEN*^{high} groups (presented in gray shades) showed overall favorable outcomes and did not significantly differ from one another. In groups where all marker genes were lowly expressed we generally detected the worst prognosis while groups with a singular lowly expressed marker showed intermediate prognosis. *CCL8* did not

(See figure on next page.)

Fig. 5 Histological analysis of infiltrating immune cells reveals downregulated innate immune response in *Jun*$^{PE\Delta/\Delta}$;*Pten*$^{PE\Delta/\Delta}$ prostates. **a** Representative images of IHC stainings of NIMP-R14, a pan-marker of neutrophil granulocytes, indicating high neutrophil infiltration of *Pten*$^{PE\Delta/\Delta}$ prostates, reverted by the additional loss of Jun in *Jun*$^{PE\Delta/\Delta}$;*Pten*$^{PE\Delta/\Delta}$ prostates. Top row: 20.0 × magnification, scale bar represents 150 µm; Bottom row: 63.0 × magnification, scale bar represents 40 µm. **b** Quantification of NIMP-R14$^+$ neutrophils in epithelium (left) and stroma (right). A significantly decreased ($p < 1e\text{-}04$) infiltration of neutrophils in tumors and adjacent stroma of *Jun*$^{PE\Delta/\Delta}$;*Pten*$^{PE\Delta/\Delta}$ prostates is evident. **c** Representative images of IHC stainings for the pan-marker of macrophages F4/80. A high infiltration of *Pten*$^{PE\Delta/\Delta}$ prostates and adjacent stroma by macrophages is evident and reverted by the additional loss of Jun in *Jun*$^{PE\Delta/\Delta}$;*Pten*$^{PE\Delta/\Delta}$ prostates. Top row: 40.0 × magnification, scale bar represents 60 µm; Bottom row: 100.0 × magnification, scale bar represents 30 µm. **d** Quantification of F4/80$^+$ macrophages in epithelium (left) and stroma (right). A significantly decreased ($p = 4e\text{-}04$) infiltration of macrophages in tumors but not adjacent stroma ($p = 8.3e\text{-}01$) of *Jun*$^{PE\Delta/\Delta}$;*Pten*$^{PE\Delta/\Delta}$ prostates is evident. **e** Representative images of IHC stainings of B cell infiltration using the pan-marker CD79b. A high infiltration of stroma adjacent to *Pten*$^{PE\Delta/\Delta}$ prostates by CD79b$^+$ B cells is evident and reverted by the additional loss of *Jun* in *Jun*$^{PE\Delta/\Delta}$;*Pten*$^{PE\Delta/\Delta}$ prostates. Top row: 40.0 × magnification, scale bar represents 60 µm; Bottom row: 100.0 × magnification, scale bar represents 30 µm. **f** Quantification of B cells in epithelium (left) and stroma (right). B cell infiltration as observed in the stroma of *Pten*$^{PE\Delta/\Delta}$ prostates was significantly decreased ($p < 1e\text{-}04$) in *Jun*$^{PE\Delta/\Delta}$;*Pten*$^{PE\Delta/\Delta}$prostates. Statistical significance between *Pten*$^{PE\Delta/\Delta}$ and *Jun*$^{PE\Delta/\Delta}$;*Pten*$^{PE\Delta/\Delta}$ groups are indicated in **b**, **d** and **f**

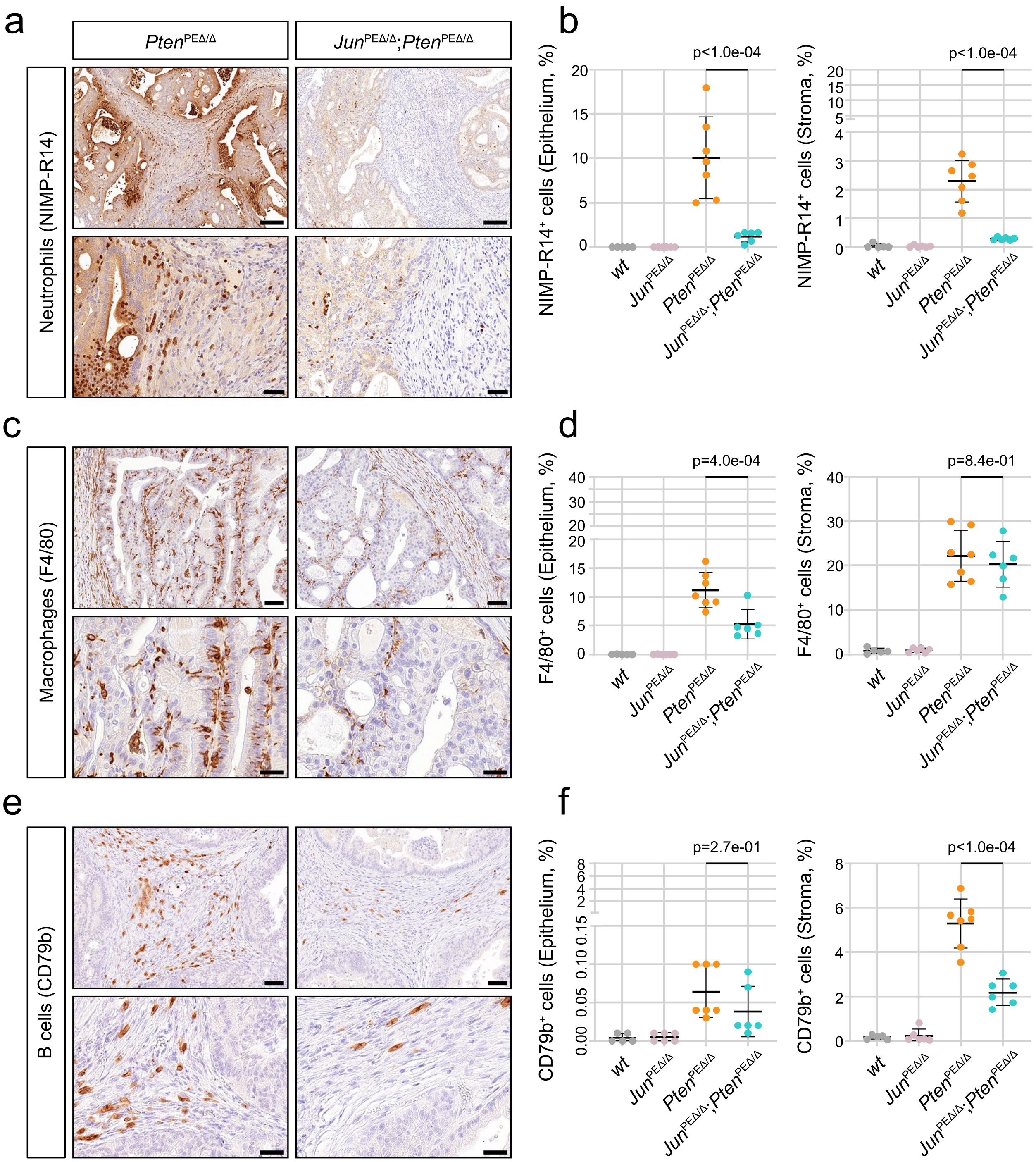

Fig. 5 (See legend on previous page.)

follow the observed *IL1B* and *CCL3* profiles suggesting that this chemokine does not act in concert with *JUN* in the absence of *PTEN*. Finally, we investigated a potential relationship between JUN and STAT3 activation and explored STAT3's role in immune modulation in TCGA-PRAD data [33]. We correlated RPPA of pSTAT3^{Y705} with levels of *JUN* and *IL1B*. We observed a weak but significant correlation of *JUN* ($R = 0.47$, $p < 2.2e\text{-}16$) and *IL1B* ($R = 0.48$, $p = 2.2e\text{-}16$) with pSTAT3^{Y705} (Fig. 6j). As observed for JUN, PCa exhibiting a high (>7) Gleason score showed reduced levels of pSTAT3^{Y705} ($p = 1.6e\text{-}02$) when compared to low risk tumors (Gleason score ≤ 7)

(Fig. 6k). To correlate the main oncogenic driver PTEN to pSTAT3^{Y705}, we grouped patients according to varying PTEN levels and observed a dose dependent decrease of pSTAT3^{Y705} (Fig. 6l). These results were analogous to our previous findings where we detected gradually reduced *JUN* expression in PTEN medium and high expressing tumors (Fig. 1i). These data might hint at interconnected mechanisms of both transcriptional regulators. In summary, we propose that levels of JUN and STAT3 potentially orchestrated via PTEN, determine progression stages of human prostate tumors by modulating the immune response through regulation of cytokines and interleukins as identified in the *Jun*-deficient murine PCa model.

Discussion

PCa is among the most frequently diagnosed malignancies in men worldwide and a significant number of patients progress to advanced and lethal stages. The mortality linked to metastatic PCa highlights the pressing need to elucidate its intricate mechanisms and pinpoint viable therapeutic interventions. Despite this urgency, the cellular mechanisms and environmental contexts that control PCa development and progression remain incompletely understood. Loss of *PTEN* is evident in 20% of primary human prostate carcinomas and escalates in 50% of metastatic CRPC [4]. Comparable to the human situation, *Pten* loss leads to the formation of precancerous lesions in PE cells in mouse models [49, 50]. Aggressive carcinomas develop only in the presence of additional mutations [51], such as abnormal expression of ERG [52], loss of IL-6/STAT3 functionality [12, 13], dysfunction of the methyltransferase Kmt2c [32] or activation of the RAS/MAPK cascade [51, 53]. While several studies indicate that augmented JUN expression drives PCa progression [14, 54], the functional role of JUN and AP-1 TFs in PCa remains controversial. Intriguingly, genetic disruption of *JunB* in vivo accelerated the progressive phenotype of *Pten*-deficient PCa [22]. A recent study using in vivo CRISPR to achieve combinatorial deletion of *Pten* and *Fos* in the PE led to increased tumorigenesis potentially via upregulation of *Jun* [55]. In contrast, we did not observe compensatory functions of other AP-1 family members in our genetically engineered mouse model or the analysis of human patient data. We therefore speculate that *Fos* deletion might be more susceptible to influencing levels of other AP-1 members than *Jun* or that the upregulation of JUN might arise due to differential CRISPR targeting efficiencies of *Pten* and *Fos* in the chosen model. An alternative explanation for the increased tumorigenesis observed upon *Fos* knockout in PCa is provided by evidence that FOS stimulates the trans-activation properties of JUN but represses its AR co-activator function [56]. Loss of *Fos* might therefore predominantly favor Jun's pro-proliferative co-activator function and weaken its anti-proliferative trans-activator function [57]. Our results similarly point towards a context dependent tumor-suppressive role, rather than a driving function of JUN in PCa progression.

In the present study, our focus was to delineate the role of JUN in PCa. We first examined JUN levels in clinical PCa samples and analyzed *JUN* patterns across varying progression stages from three publicly available datasets [35, 37, 38]. We found that *JUN* expression increased in tumors relative to normal prostates, however we did not observe the same effect when we compared healthy to low Gleason stages in the TMA data. It remains to be elucidated whether this discrepancy can be explained by differences in protein versus RNA levels or the *PTEN* mutation status in early stages of malignant transformation. Importantly, the levels of *JUN, FOS and JUNB* and the levels of JUN in the TMA dataset were all significantly decreased with progression of PCa. This suggests that high JUN levels may protect from development of progressive disease, a hypothesis further supported by the increased survival rates of patients harboring high *JUN* expressing tumors. By co-integrating the tumor suppressor *PTEN* in our survival analysis, we found that levels of *PTEN* and *JUN* determine survival probabilities of PCa and revealed the worst prognosis in *JUN*^{low}/*PTEN*^{low} PCa but highest RFS in *JUN*^{high}/*PTEN*^{high} tumors. Encouraged by these findings, we studied the functional role of JUN in a murine PCa model, characterized by homozygous loss of *Pten* (*Pten*$^{PE\Delta/\Delta}$) [26, 39]. Mirroring

(See figure on next page.)

Fig. 6 Expression of immune cell-attracting chemokines *CCL3* and *CCL8* correlates with levels of *JUN* in patient datasets. **a-d** Principal component analysis (PCA) representation of human PCa illustrating expression levels of *JUN, IL1B*, *CCL3* and *CCL8*. Expression levels are color coded from high (yellow) to low (blue). **e** Box plots indicating significant enrichment of *ADGRE1* (F4/80, $p=4.10e-02$), *CCL8* ($p=4.41e-16$), *IL1B* ($p=9.29e-21$) and *CCL3* ($p=1.35e-26$) in *JUN*^{high} and *JUN*^{low} separated groups. **f** Pearson correlation of indicated AP-1 factors, *PTEN*, *CCL3, CCL8, IL1B* and *ADGRE1*. Strength of correlation is color coded. **g-i** Kaplan–Meier survival analyses of TCGA-PRAD tumors ($n=333$) assessing the effect of *IL1B* (**g**), *CCL3* (**h**) and *CCL8* (**i**) on RFS in the context of *PTEN* and *JUN*. **j** Correlation of *JUN* (left) and *IL1B* (right) expression to amount of phosphorylated STAT3 (pSTAT3^{Y705}) in the TCGA-PRAD cohort ($n=352$). **k** Box plot of reverse-phase protein array (RPPA) data representing reduced levels of pSTAT3^{Y705} ($p=1.6e-02$) in high risk PCa of Gleason scores > 7 (range 8–10) compared to low risk (Gleason scores ≤ 7). **l** Box plot of RPPA data representing gradually decreasing levels of pSTAT3^{Y705} ($p=1.8e-02$) in PTEN low, medium and high tumors. Dataset used for Fig. 6 is TCGA-PRAD [33]

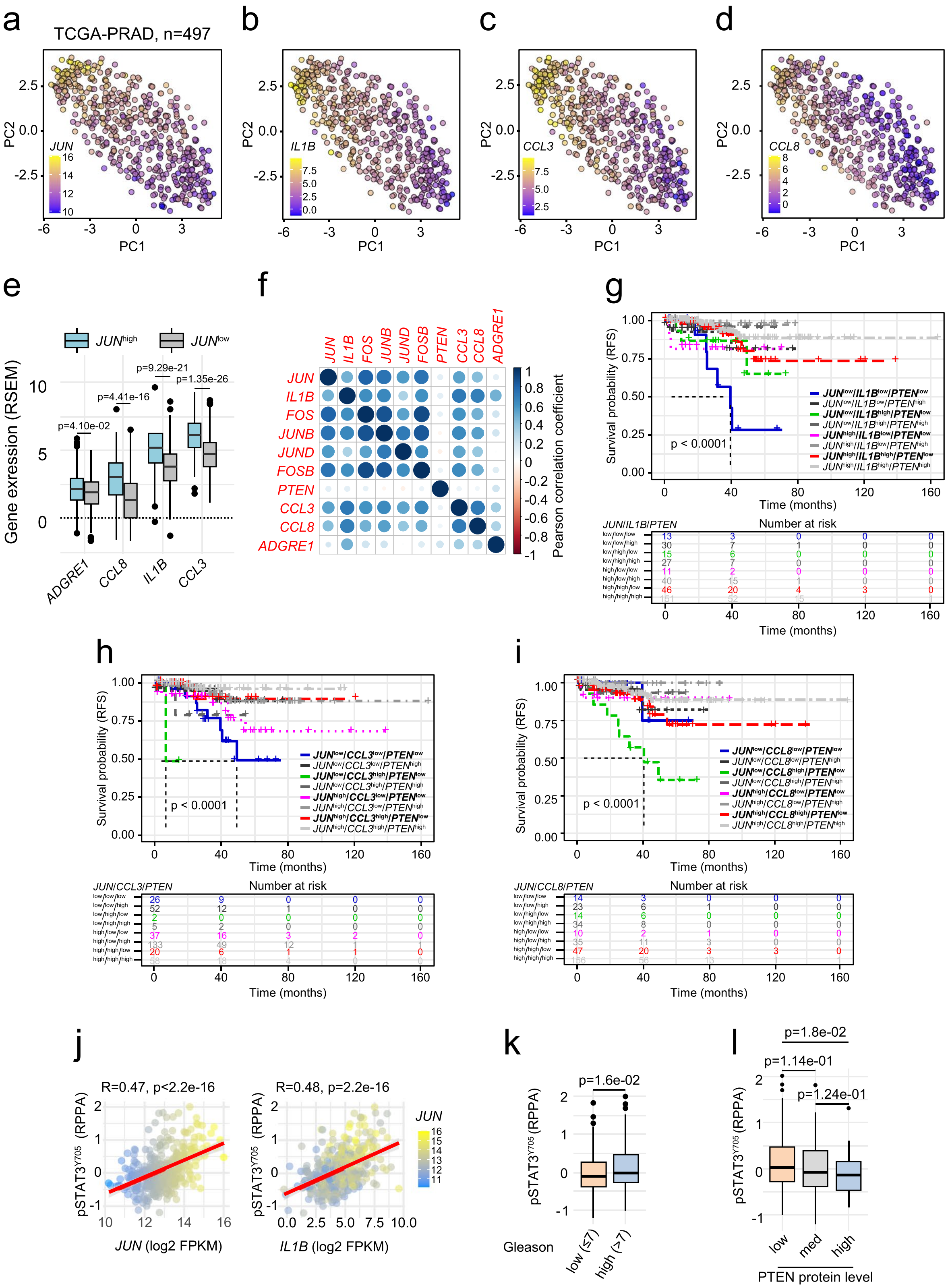

Fig. 6 (See legend on previous page.)

the early prostatic intraepithelial neoplasia (PIN) stages of human PCa, JUN was significantly upregulated in *Pten*$^{\mathrm{PE}\Delta/\Delta}$ prostates. Consistent with human patient data, depletion of *Jun* alone had no effect on the morphological architecture and growth of the prostate. Epithelial cells of *Pten*$^{\mathrm{PE}\Delta/\Delta}$ prostates developed hyperplasia, subsequently forming prostate adenocarcinoma and rapidly progressing upon additional deletion of *Jun*. The aggressive phenotype observed in *Jun*$^{\mathrm{PE}\Delta/\Delta}$; *Pten*$^{\mathrm{PE}\Delta/\Delta}$ prostates resulted in decreased survival of mice and increased prostate weight and size. We did not detect signs of severe organ dysfunction, systemic inflammation or metastatic disease (Fig. 2g).

The TME is a dynamic system characterized by chronic inflammation and participation of diverse host components, but plays a pivotal role in cancer progression [58]. Within the TME, immune cells such as tumor-associated macrophages (TAM) and tumor-associated neutrophils (TAN) both foster cancer progression or combat tumor cells, underscoring their dual roles in tumorigenesis [59–61]. Central to this environment is the SASP, where senescent cells release a plethora of inflammatory mediators. SASP-driven effects often culminate in the immune-mediated clearance of potential tumorigenic cells, a process termed “senescence surveillance” [62, 63]. Our histopathologic examination of *Pten*$^{\mathrm{PE}\Delta/\Delta}$ PCa samples revealed significant enrichment of neutrophils and macrophages that infiltrated the tumors and adjacent stroma. Concurrent deletion of *Jun* strikingly reduced tumor infiltration with neutrophils and macrophages and accelerated tumor growth. Transcriptomic analyses of *Pten*$^{\mathrm{PE}\Delta/\Delta}$ and *Jun*$^{\mathrm{PE}\Delta/\Delta}$; *Pten*$^{\mathrm{PE}\Delta/\Delta}$ prostates revealed a JUN-dependent modulation of SASP-associated genes, but we did not identify compensatory upregulation of other AP-1 members as it has been described upon inactivation of FOS [64]. To investigate further aspects of senescence and address senescence-associated cell cycle arrest, we conducted IHC stainings for p16$^{\mathrm{INK4a}}$, p21$^{\mathrm{CIP/WAF1}}$ and GLB1. We did not observe quantitative differences in expression of these classical senescence markers indicating that JUN is involved in the regulation of SASP, but not senescence-associated cell cycle arrest. The regulation of SASP without affecting cell cycle arrest has been previously demonstrated. This was evidenced by the association of the chromatin reader BRD4 with recruitment to enhancer regions activating SASP genes in senescent cells [65]. Recent findings have implicated AP-1 and in particular JUN as pioneering factors on a specific enhancer landscape essential for the execution of senescence-controlling programs [23]. In line with these results, we propose that loss of *Pten* coupled with an increase in JUN likely instigates a JUN-driven SASP phenotype.

SASP involves the expression and secretion of inflammatory cytokines such as CCL3, CCL8, IL-1β and TNF-α [32, 66] which subsequently recruit immune cells such as neutrophils, macrophages and T cells [10, 67, 68]. As we observe downregulated secretion of IL-1β and TNF-α in *Jun*$^{\mathrm{PE}\Delta/\Delta}$; *Pten*$^{\mathrm{PE}\Delta/\Delta}$ prostates, we suggest that *Jun* depletion in *Pten*-deficient prostates disrupts SASP. This impedes the recruitment of neutrophils and macrophages, as well as tumor cell clearance by macrophages and dendritic cells [9, 62]. We thus propose JUN as a key regulator of SASP. Our results support a previous study where JUN depletion was linked to diminished inflammatory responses and reverting the senescent/SASP phenotype of RAS-OIS fibroblasts to a proliferating phenotype [23]. Furthermore, GM-CSF, a direct JUN target has been shown to amplify macrophage and neutrophil immune responses [69] and modulate pro-inflammatory cytokine secretion such as TNFα and IL-6 [70].

Another intriguing mechanism of JUN-dependent modulation of the immune phenotype in PCa may depend on STAT3 levels. Our previous work identified activation of STAT3 and a p19$^{\mathrm{ARF}}$–MDM2–p53 axis to induce senescence upon *Pten* depletion [12]. Consistently, *Jun* loss was associated with decreased IL-6-JAK-STAT3 signaling, evidenced by significantly reduced pSTAT$^{\mathrm{Y705}}$ levels in *Jun*$^{\mathrm{PE}\Delta/\Delta}$; *Pten*$^{\mathrm{PE}\Delta/\Delta}$ prostates. ENCODE database exploration [71] revealed mutual promoter binding sites for JUN and STAT3 suggesting a potential JUN-STAT3 interplay in impacting senescence pathways in PCa (https://maayanlab.cloud/Harmonizome/dataset/CHEA+Transcription+Factor+Targets). This interplay is supported by results of a STAT3 binding analysis in CD4^{+} T cells, which suggests that STAT3 directly regulates the expression of *Jun* and *Fos* and may potentially function in a positive feedback loop [72]. Therefore, therapeutic activation of STAT3 potentially causes SASP factor modulation and may elevate JUN levels in tumors, thereby restricting tumor progression and enhancing PCa patient survival.

Conclusions

In summary, our data suggest that JUN functions as a pivotal regulator of SASP and survival in PTEN-deficient PCa, orchestrating the recruitment dynamics of TAMs and TANs within the TME. Given the indispensable role of robust SASP in immune surveillance of preneoplastic anomalies, its therapeutic modulation presents intricate challenges. Our recent investigations have shown the potential of the antidiabetic agent metformin, which curtails multiple pro-inflammatory SASP components by inhibiting NF-κB nuclear translocation [73]. Metformin increases STAT3 in advanced PCa cases, leading to significant tumor growth attenuation, underscored by reduced mTORC1/CREB and AR levels in a PCa murine model [13]. The interplay between JUN, STAT3 and PTEN might represent a key mechanism that could be exploited for therapeutic advances.

Abbreviations

AP-1	Activator protein-1
AR	Androgen receptor
BCR	Biochemical recurrence
BRD4	Bromodomain containing protein 4
CRPC	Castration resistant prostate cancer
DEG	Differentially expressed gene
EpCAM	Epithelial cell adhesion molecule
EV	Empty vector
FDR	False discovery rate
FFPE	Formalin-fixed paraffin embedded
GLB1	Galactosidase beta 1
GO	Gene ontology
GSEA	Gene set enrichment analysis
H&E	Hematoxylin and eosin
HR	Hazard ratio
IF	Immunofluorescence
IHC	Immunohistochemistry
JNK	JUN N-terminal kinase
MsigDB	Molecular signature database
NEPC	Neuroendocrine prostate cancer
NES	Normalized enrichment score
OIS	Oncogene induced senescence
PbCre	Probasin Cre
PCa	Prostate cancer
PCA	Principal component analysis
PE	Prostate epithelium
PI3K	Phosphoinositide 3-kinase
PICS	PTEN-loss induced cellular senescence
PIN	Prostatic intraepithelial neoplasia
PTEN	Phosphate and Tensin Homologue
RFS	Relapse-free survival
RNA-seq	RNA sequencing
RPPA	Reverse-phase protein array
SASP	Senescence-associated secretory phenotype
STAT3	Signal transducer and activator of transcription 3
TAM	Tumor-associated macrophage
TAN	Tumor-associated neutrophil
TCGA-PRAD	Cancer Genome Atlas Prostate Adenocarcinoma
TF	Transcription factor
TMA	Tissue microarray
TME	Tumor microenvironment

Supplementary Information

The online version contains supplementary material available at https://doi.org/10.1186/s12943-024-02022-x.

Supplementary Material 1.

Supplementary Material 2.

Supplementary Material 3.

Supplementary Material 4.

Authors' information

Torben Redmer, Martin Raigel and Christina Sternberg contributed equally to this work as first authors. Sabine Lagger and Lukas Kenner contributed equally to this work as last authors.

Acknowledgements

This research was supported using resources of the VetCore Facilities (VetImaging, Genomics and Transcriptomics) of the University of Veterinary Medicine Vienna. We acknowledge the Core Facility Genomics and Core Facility Bioinformatics supported by the NCMG research infrastructure (LM2023067 funded by MEYS CR) for their support with the bioinformatic analysis of scientific data presented in this paper. We would like to thank Anton Jäger, Medical University of Vienna for macroscopic image generation and support. We thank Romana Sickha for technical assistance.

Authors' contributions

Conceptualization: TR, MR, CS, SL, LK. Formal Analysis: TR, KT, MO, MB, HAN, VB. Funding Acquisition: LK, SP. Investigation: TR, MR, CS, RZ, CP, DL, AA, TL, PK, SH, MS, SS, MO, MB, HAN, IG, OM, SL. Methodology: MR, CS, RZ, CP, AA, TL, SMi, MT, NSH, BT, VB, BS, GE, SL. Project administration: TR, MR, CS, SL, LK. Resources: TR, MR, CS, RM, JT, SMa, FA, SP, JLP, GE, SL, LK. Supervision: SL, LK. Validation: TR, MR, CS, KT, PK, SH, MS, MO, FS, BT, VB, OM, GE. Visualization: TR, MR, CS, RZ, CP, AA, MB, HAN, TL. Writing – original draft: SL, TR, MR. Writing – review & editing: TR, MR, CS, TL, SS, RM, SMa, FA, BS, OM, GE, SL, LK. All authors read and approved the final manuscript.

Funding

LK acknowledges the support from MicroONE, a COMET Modul under the lead of CBmed GmbH, which is funded by the federal ministries BMK and BMDW, the provinces of Styria and Vienna, and managed by the Austrian Research Promotion Agency (FFG) within the COMET—Competence Centers for Excellent Technologies—program. Financial support was also received from the Austrian Federal Ministry of Science, Research and Economy, the National Foundation for Research, Technology and Development, and the Christian Doppler Research Association, as well as Siemens Healthineers. LK was also supported by European Union Horizon 2020 Marie Sklodowska-Curie Doctoral Network grants (ALKATRAS, n. 675712; FANTOM, n. P101072735 and eRaDicate, n. 101119427) as well as BM Fonds (n. 15142), the Margaretha Hehberger Stiftung (n. 15142), the Christian-Doppler Lab for Applied Metabolomics (CDL-AM), and the Austrian Science Fund (grants FWF: P26011, P29251, P34781 as well as the International PhD Program in Translational Oncology IPPTO 59.doc.funds). OM is supported by the Austrian Science Fund (FWF) project (P32579) and LK, OM, GE and SP European Union Horizon 2020 Marie Sklodowska-Curie Doctoral Network grants ALKATRAS, n. 675712; FANTOM, n. P101072735. Additionally, this research was funded by the Vienna Science and Technology Fund (WWTF), grant number LS19-018. LK, OM, GE and SP are members of the European Research Initiative for ALK-Related Malignancies (www.erialcl.net). SM and BS received funding from FWF DocFund DOC32-B28 and SFB F6101. CS was supported by grant Nr. 70112589 from the Deutsche Krebshilfe, Bonn, Germany. SP received funding from Next Generation EU for the project National Institute for Cancer Research (Program EXCELES, Nr. LX22NPO5102).

Availability of data and materials

The RNA-seq dataset supporting the conclusions of this article is available in the GEO repository with the accession number GSE242433.

Declarations

Ethics approval and consent to participate

Institutional Review Board Statement: The use of clinical material was approved by the Research Ethics Committee of the Medical University Vienna, Austria (1877/2016) and conducted in adherence to the Declaration of Helsinki protocols. Patient consent was waived due to the completely anonymized, retrospective nature of the study.

All animal studies were reviewed and approved by the Federal Ministry Republic of Austria for Education, Science and Research and conducted according to regulatory standards (BMWFW-66.009/0144-WF/II/3b/2014 and the amendments BMWFW-66.009/0063-WF/V/3b/2017, BMWFW-66.009/0137-WF/V/3b/2019, BMWFW-66.009/0359-V/3b/2019, 2020–0.016.881, 2020–0.659.052 and 2022–0.325.014).

Consent for publication

Not applicable.

Competing interests

The authors declare no competing interests.

Author details

[1]Unit of Laboratory Animal Pathology, University of Veterinary Medicine Vienna, Vienna 1210, Austria. [2]Department of Pathology, Medical University of Vienna, Vienna 1090, Austria. [3]Department of Biomedical Imaging and Image-Guided Therapy, Division of Nuclear Medicine, Medical University of Vienna, Vienna 1090, Austria. [4]Biochemical Institute, University of Kiel, Kiel 24098, Germany. [5]Center for Biomarker Research in Medicine (CBmed) Vienna, Core-Lab2, Medical University of Vienna, Vienna 1090, Austria. [6]CEITEC-Central European Institute of Technology, Masaryk University, Brno 625 00, Czech Republic. [7]Christian Doppler Laboratory for Applied Metabolomics, Medical University of Vienna, Vienna 1090, Austria. [8]Center for Biomarker Research in Medicine, CBmed GmbH, Graz 8010, Austria. [9]Institute of Oncology Research, Bellinzona and Faculty of Biomedical Sciences, USI, Lugano 6500, TI, Switzerland. [10]Computational Oncology Unit, Department of Oncology, Istituto di Richerche Farmacologiche 'Mario Negri' IRCCS, Milano 20156, Italy. [11]Bioinformatics Core Unit, Swiss Institute of Bioinformatics, Bellinzona 6500, TI, Switzerland. [12]Institute of Animal Breeding and Genetics, University of Veterinary Medicine Vienna, Vienna 1210, Austria. [13]Institute of Physiology, Pathophysiology and Biophysics, University of Veterinary Medicine Vienna, Vienna 1210, Austria. [14]Department of Biosciences and Medical Biology, Cancer Cluster Salzburg, Paris-Lodron University of Salzburg, Salzburg 5020, Austria. [15]Department of Molecular Biology, Umeå University, Umeå 901 87, Sweden. [16]Department of Biomedical Sciences, Malmö Universitet, Malmö 206 06, Sweden. [17]Charité—Universitätsmedizin Berlin, Hematology, Oncology and Tumor Immunology, corporate member of Freie Universität Berlin and Humboldt-Universität zu Berlin, Berlin 10117, Germany. [18]Max-Delbrück-Center for Molecular Medicine in the Helmholtz Association (MDC), Group Biology of Malignant Lymphomas, Berlin 13125, Germany. [19]Experimental and Clinical Research Center (ECRC), a cooperation between the MDC and the Charité, Berlin, Germany. [20]Comprehensive Cancer Center, Medical University Vienna, Vienna 1090, Austria. [21]Department of Cell Biology, Charles University, Prague, Czech Republic and Biotechnology and Biomedicine Centre of the Academy of Sciences and Charles University (BIOCEV), Vestec u Prahy, Czech Republic. [22]Institute of Medical Biochemistry, University of Veterinary Medicine Vienna, Vienna 1210, Austria. [23]Department of Nutritional Sciences, Faculty of Life Sciences, University of Vienna, Vienna 1090, Austria.

Received: 29 November 2023 Accepted: 10 May 2024

References

1. Gandaglia G, Leni R, Bray F, Fleshner N, Freedland SJ, Kibel A, Stattin P, Van Poppel H, La Vecchia C. Epidemiology and Prevention of Prostate Cancer. Eur Urol Oncol. 2021;4:877–92.
2. Berenguer CV, Pereira F, Câmara JS, Pereira JAM. Underlying Features of Prostate Cancer-Statistics, Risk Factors, and Emerging Methods for Its Diagnosis. Curr Oncol. 2023;30:2300–21.
3. Tan ME, Li J, Xu HE, Melcher K, Yong E. Androgen receptor: structure, role in prostate cancer and drug discovery. Acta Pharmacol Sin. 2015;36:3–23.
4. Jamaspishvili T, Berman DM, Ross AE, Scher HI, De Marzo AM, Squire JA, Lotan TL. Clinical implications of PTEN loss in prostate cancer. Nat Rev Urol. 2018;4:222–34.
5. Feldman BJ, Feldman D. The development of androgen-independent prostate cancer. Nat Rev Cancer. 2001;1:34–45.
6. Chen Z, Trotman LC, Shaffer D, et al. Crucial role of p53-dependent cellular senescence in suppression of Pten-deficient tumorigenesis. Nature. 2005;436:725–30.
7. Jung SH, Hwang HJ, Kang D, Park HA, Lee HC, Jeong D, Lee K, Park HJ, Ko YG, Lee JS. mTOR kinase leads to PTEN-loss-induced cellular senescence by phosphorylating p53. Oncogene. 2019;38:1639–50.
8. Gorgoulis V, Adams PD, Alimonti A, et al. Cellular Senescence: Defining a Path Forward. Cell. 2019;179:813–27.
9. Schosserer M, Grillari J, Breitenbach M. The Dual Role of Cellular Senescence in Developing Tumors and Their Response to Cancer Therapy. Front Oncol. 2017;7: 315584.
10. Coppé J-P, Desprez P-Y, Krtolica A, Campisi J. The senescence-associated secretory phenotype: the dark side of tumor suppression. Annu Rev Pathol. 2010;5:99–118.
11. Culig Z, Puhr M. Interleukin-6 and prostate cancer: Current developments and unsolved questions. Mol Cell Endocrinol. 2018;462:25–30.
12. Pencik J, Schlederer M, Gruber W, et al. STAT3 regulated ARF expression suppresses prostate cancer metastasis. Nat Commun. 2015;6:7736.
13. Pencik J, Philippe C, Schlederer M, et al. STAT3/LKB1 controls metastatic prostate cancer by regulating mTORC1/CREB pathway. Mol Cancer. 2023;22:133.
14. Ouyang X, Jessen WJ, Al-Ahmadie H, et al. Activator protein-1 transcription factors are associated with progression and recurrence of prostate cancer. Cancer Res. 2008. https://doi.org/10.1158/0008-5472.CAN-07-6055.
15. Vogt PK. Fortuitous convergences: the beginnings of JUN. Nat Rev Cancer. 2002;2:465–9.
16. Lopez-Bergami P, Lau E, Ronai Z. Emerging roles of ATF2 and the dynamic AP1 network in cancer. Nat Rev Cancer. 2010;10:65–76.
17. Eferl R, Wagner EF. AP-1: a double-edged sword in tumorigenesis. Nat Rev Cancer. 2003;3:859–68.
18. Cai C, Hsieh CL, Shemshedini L. c-Jun has multiple enhancing activities in the novel cross talk between the androgen receptor and Ets variant gene 1 in prostate cancer. Mol Cancer Res. 2007;5:725–35.
19. Bubulya A, Chen SY, Fisher C, Zheng Z, Shen X, Shemshedini L. c-Jun Potentiates the Functional Interaction between the Amino and Carboxyl Termini of the Androgen Receptor. J Biol Chem. 2001;276:44704–11.
20. Shaulian E. AP-1 - The Jun proteins: Oncogenes or tumor suppressors in disguise? Cell Signal. 2010;22:894–9.
21. Hübner A, Mulholland DJ, Standen CL, et al. JNK and PTEN cooperatively control the development of invasive adenocarcinoma of the prostate. Proc Natl Acad Sci. 2012;109(30):12046 LP – 12051.
22. Thomsen MK, Bakiri L, Hasenfuss SC, Wu H, Morente M, Wagner EF. Loss of JUNB/AP-1 promotes invasive prostate cancer. Cell Death Differ. 2015;22:574–82.
23. Martínez-Zamudio RI, Roux P-F, de Freitas JANLF, et al. AP-1 imprints a reversible transcriptional programme of senescent cells. Nat Cell Biol. 2020;22:842–55.
24. Birbach A, Eisenbarth D, Kozakowski N, Ladenhauf E, Schmidt-Supprian M, Schmid JA. Persistent inflammation leads to proliferative neoplasia and loss of smooth muscle cells in a prostate tumor model. Neoplasia. 2011;13:692–703.
25. Behrens A, Sibilia M, David J-P, Möhle-Steinlein U, Tronche F, Schütz G, Wagner EF. Impaired postnatal hepatocyte proliferation and liver regeneration in mice lacking c-jun in the liver. EMBO J. 2002;21:1782–90.
26. Suzuki A, Yamaguchi MT, Ohteki T, et al. T cell-specific loss of Pten leads to defects in central and peripheral tolerance. Immunity. 2001. https://doi.org/10.1016/S1074-7613(01)00134-0.
27. Wu X, Wu J, Huang J, Powell WC, Zhang J, Matusik RJ, Sangiorgi FO, Maxson RE, Sucov HM, Roy-Burman P. Generation of a prostate epithelial cell-specific Cre transgenic mouse model for tissue-specific gene ablation. Mech Dev. 2001;101:61–9.
28. Oberhuber M, Pecoraro M, Rusz M, et al. *STAT3* -dependent analysis reveals *PDK4* as independent predictor of recurrence in prostate cancer. Mol Syst Biol. 2020;16(4):e9247. https://doi.org/10.15252/msb.20199247.
29. Bankhead P, Loughrey MB, Fernández JA, et al. QuPath: Open source software for digital pathology image analysis. Sci Rep. 2017. https://doi.org/10.1038/s41598-017-17204-5.
30. Schmidt U, Weigert M, Broaddus C, Myers G. Cell Detection with Star-convex Polygons. 2018. https://doi.org/10.1007/978-3-030-00934-2_30.
31. Ding Z, Wu CJ, Chu GC, et al. SMAD4-dependent barrier constrains prostate cancer growth and metastatic progression. Nature. 2011. https://doi.org/10.1038/nature09677.
32. Limberger T, Schlederer M, Trachtová K, et al. KMT2C methyltransferase domain regulated INK4A expression suppresses prostate cancer metastasis. Mol Cancer. 2022;21:89.
33. Cancer Genome Atlas Research Network TCGAR. The Molecular Taxonomy of Primary Prostate Cancer. Cell. 2015;163:1011–25.
34. Humphrey PA. Gleason grading and prognostic factors in carcinoma of the prostate. Mod Pathol. 2004. https://doi.org/10.1038/modpathol.3800054.

35. Taylor BS, Schultz N, Hieronymus H, et al. Integrative genomic profiling of human prostate cancer. Cancer Cell. 2010;18:11–22.
36. Aguirre-Gamboa R, Gomez-Rueda H, Martínez-Ledesma E, Martínez-Torteya A, Chacolla-Huaringa R, Rodriguez-Barrientos A, Tamez-Peña JG, Treviño V. SurvExpress: An Online Biomarker Validation Tool and Database for Cancer Gene Expression Data Using Survival Analysis. PLoS ONE. 2013;8:1–9.
37. Yu YP, Landsittel D, Jing L, et al. Gene expression alterations in prostate cancer predicting tumor aggression and preceding development of malignancy. J Clin Oncol. 2004. https://doi.org/10.1200/JCO.2004.05.158.
38. Bolis M, Bossi D, Vallerga A, et al. Dynamic prostate cancer transcriptome analysis delineates the trajectory to disease progression. Nat Commun. 2021;12:7033.
39. Wang S, Gao J, Lei Q, et al. Prostate-specific deletion of the murine Pten tumor suppressor gene leads to metastatic prostate cancer. Cancer Cell. 2003;4:209–21.
40. Tannenbaum J, Bennett BT. Russell and Burch's 3Rs then and now: The need for clarity in definition and purpose. J Am Assoc Lab Anim Sci. 2015;54:120–32.
41. Saul D, Kosinsky RL, Atkinson EJ, et al. A new gene set identifies senescent cells and predicts senescence-associated pathways across tissues. Nat Commun. 2022. https://doi.org/10.1038/s41467-022-32552-1.
42. Guccini I, Revandkar A, D'Ambrosio M, et al. Senescence Reprogramming by TIMP1 Deficiency Promotes Prostate Cancer Metastasis. Cancer Cell. 2021;39:68-82.e9.
43. Nilsson K, Landberg G. Subcellular localization, modification and protein complex formation of the cdk-inhibitor p16 in Rb-functional and Rb-inactivated tumor cells. Int J Cancer. 2006;118:1120–5.
44. Breuer K, Foroushani AK, Laird MR, Chen C, Sribnaia A, Lo R, Winsor GL, Hancock REW, Brinkman FSL, Lynn DJ InnateDB: systems biology of innate immunity and beyond-recent updates and continuing curation. https://doi.org/10.1093/nar/gks1147
45. Marshall JS, Warrington R, Watson W, Kim HL. An introduction to immunology and immunopathology. Allergy, Asthma Clin Immunol. 2018;14:49.
46. Sionov RV, Fridlender ZG, Granot Z. The Multifaceted Roles Neutrophils Play in the Tumor Microenvironment. Cancer Microenviron. 2015. https://doi.org/10.1007/s12307-014-0147-5.
47. Reichel CA, Puhr-Westerheide D, Zuchtriegel G, Uhl B, Berberich N, Zahler S, Wymann MP, Luckow B, Krombach F. C-C motif chemokine CCL3 and canonical neutrophil attractants promote neutrophil extravasation through common and distinct mechanisms. Blood. 2012. https://doi.org/10.1182/blood-2012-01-402164.
48. Metzemaekers M, Gouwy M, Proost P. Neutrophil chemoattractant receptors in health and disease: double-edged swords. Cell Mol Immunol. 2020;17:433–50.
49. Wang SI, Parsons R, Ittmann M. Homozygous deletion of the PTEN tumor suppressor gene in a subset of prostate adenocarcinomas. Clin Cancer Res. 1998;4(3):811–5.
50. Wise HM, Hermida MA, Leslie NR. Prostate cancer, PI3K, PTEN and prognosis. Clin Sci. 2017;131(3):197–210. https://doi.org/10.1042/CS20160026.
51. Baker SJ, Reddy EP. Understanding the temporal sequence of genetic events that lead to prostate cancer progression and metastasis. Proc Natl Acad Sci U S A. 2013;110:14819–20.
52. Carver BS, Tran J, Gopalan A, et al. Aberrant ERG expression cooperates with loss of PTEN to promote cancer progression in the prostate. Nat Genet. 2009. https://doi.org/10.1038/ng.370.
53. Mulholland DJ, Kobayashi N, Ruscetti M, Zhi A, Tran LM, Huang J, Gleave M, Wu H. Pten loss and RAS/MAPK activation cooperate to promote EMT and metastasis initiated from prostate cancer stem/progenitor cells. Cancer Res. 2012. https://doi.org/10.1158/0008-5472.CAN-11-3132.
54. Thakur N, Gudey SK, Marcusson A, Fu JY, Bergh A, Heldin CH, Landstrom̈ M,. TGFβ-induced invasion of prostate cancer cells is promoted by c-Jun-dependent transcriptional activation of Snail1. Cell Cycle. 2014. https://doi.org/10.4161/cc.29339.
55. Udayappan UK, Casey PJ. c-Jun Contributes to Transcriptional Control of GNA12 Expression in Prostate Cancer Cells. Molecules. 2017. https://doi.org/10.3390/molecules22040612.
56. Tillman K, Oberfield JL, Shen X-Q, Bubulya A, Shemshedini L. c-Fos Dimerization with c-Jun Represses c-Jun Enhancement of Androgen Receptor Transactivation. Endocrine. 1998;9:193–200.
57. Chen S-Y, Cai C, Fisher CJ, Zheng Z, Omwancha J, Hsieh C-L, Shemshedini L. c-Jun enhancement of androgen receptor transactivation is associated with prostate cancer cell proliferation. Oncogene. 2006;25:7212–23.
58. Hanahan D, Weinberg RA. Hallmarks of cancer: the next generation. Cell. 2011;144:646–74.
59. Galdiero MR, Bonavita E, Barajon I, Garlanda C, Mantovani A, Jaillon S. Tumor associated macrophages and neutrophils in cancer. Immunobiology. 2013;218:1402–10.
60. Qian B-Z, Pollard JW. Macrophage diversity enhances tumor progression and metastasis. Cell. 2010;141:39–51.
61. Sun B, Qin W, Song M, Liu L, Yu Y, Qi X, Sun H. Neutrophil Suppresses Tumor Cell Proliferation via Fas /Fas Ligand Pathway Mediated Cell Cycle Arrested. Int J Biol Sci. 2018;14:2103–13.
62. Xue W, Zender L, Miething C, Dickins RA, Hernando E, Krizhanovsky V, Cordon-Cardo C, Lowe SW. Senescence and tumour clearance is triggered by p53 restoration in murine liver carcinomas. Nature. 2007;445:656–60.
63. Takasugi M, Yoshida Y, Ohtani N. Cellular senescence and the tumour microenvironment. Mol Oncol. 2022;16:3333–51.
64. Riedel M, Berthelsen MF, Cai H, et al. In vivo CRISPR inactivation of Fos promotes prostate cancer progression by altering the associated AP-1 subunit Jun. Oncogene. 2021;40:2437–47.
65. Tasdemir N, Banito A, Roe J-S, et al. BRD4 Connects Enhancer Remodeling to Senescence Immune Surveillance. Cancer Discov. 2016;6:612–29.
66. Muñoz-Espín D, Serrano M. Cellular senescence: From physiology to pathology. Nat Rev Mol Cell Biol. 2014;15:482–96.
67. Alexander E, Hildebrand DG, Kriebs A, Obermayer K, Manz M, Rothfuss O, Essmann F, Schulze-Osthoff K. IκBζ is a regulator for the senescence-associated secretory phenotype in DNA damage- and oncogene-induced senescence. J Cell Sci. 2013;126:3738–45.
68. Freund A, Orjalo AV, Desprez PY, Campisi J. Inflammatory networks during cellular senescence: causes and consequences. Trends Mol Med. 2010. https://doi.org/10.1016/j.molmed.2010.03.003.
69. Lotfi N, Thome R, Rezaei N, Zhang G-X, Rezaei A, Rostami A, Esmaeil N. Roles of GM-CSF in the Pathogenesis of Autoimmune Diseases: An Update. Front Immunol. 2019;10: 452989.
70. Mausberg AK, Jander S, Reichmann G. Intracerebral granulocyte-macrophage colony-stimulating factor induces functionally competent dendritic cells in the mouse brain. Glia. 2009;57:1341–50.
71. Luo Y, Hitz BC, Gabdank I, et al. New developments on the Encyclopedia of DNA Elements (ENCODE) data portal. Nucleic Acids Res. 2020;48:D882–9.
72. Durant L, Watford WT, Ramos HL, et al. Diverse targets of the transcription factor STAT3 contribute to T cell pathogenicity and homeostasis. Immunity. 2010;32:605–15.
73. Moiseeva O, Deschênes-Simard X, St-Germain E, Igelmann S, Huot G, Cadar AE, Bourdeau V, Pollak MN, Ferbeyre G. Metformin inhibits the senescence-associated secretory phenotype by interfering with IKK / NF -κ B activation. Aging Cell. 2013;12:489–98.

Publisher's Note

Sternberg *et al. Molecular Cancer* (2024) 23:245
https://doi.org/10.1186/s12943-024-02114-8

Molecular Cancer

RESEARCH

Cell-autonomous IL6ST activation suppresses prostate cancer development via STAT3/ARF/p53-driven senescence and confers an immune-active tumor microenvironment

Christina Sternberg[1,2,3*], Martin Raigel[1,3,4], Tanja Limberger[1,4,5], Karolína Trachtová[4,6], Michaela Schlederer[1], Desiree Lindner[3], Petra Kodajova[3], Jiaye Yang[1], Roman Ziegler[3,17], Jessica Kalla[1], Stefan Stoiber[1,4,7], Saptaswa Dey[8], Daniela Zwolanek[9], Heidi A. Neubauer[10,18], Monika Oberhuber[5], Torben Redmer[3], Václav Hejret[6], Boris Tichy[6], Martina Tomberger[5], Nora S. Harbusch[5], Jan Pencik[1], Simone Tangermann[3], Vojtech Bystry[6], Jenny L. Persson[11,12], Gerda Egger[1,13], Sarka Pospisilova[6], Robert Eferl[9], Peter Wolf[8,14], Felix Sternberg[15,16], Sandra Högler[3], Sabine Lagger[3], Stefan Rose-John[2*†] and Lukas Kenner[1,3,5,7,13*†]

Abstract

Background Prostate cancer ranks as the second most frequently diagnosed cancer in men worldwide. Recent research highlights the crucial roles IL6ST-mediated signaling pathways play in the development and progression of various cancers, particularly through hyperactivated STAT3 signaling. However, the molecular programs mediated by IL6ST/STAT3 in prostate cancer are poorly understood.

Methods To investigate the role of IL6ST signaling, we constitutively activated IL6ST signaling in the prostate epithelium of a *Pten*-deficient prostate cancer mouse model in vivo and examined IL6ST expression in large cohorts of prostate cancer patients. We complemented these data with in-depth transcriptomic and multiplex histopathological analyses.

Results Genetic cell-autonomous activation of the IL6ST receptor in prostate epithelial cells triggers active STAT3 signaling and significantly reduces tumor growth in vivo. Mechanistically, genetic activation of IL6ST signaling mediates senescence via the STAT3/ARF/p53 axis and recruitment of cytotoxic T-cells, ultimately impeding tumor progression. In prostate cancer patients, high *IL6ST* mRNA expression levels correlate with better recurrence-free survival, increased senescence signals and a transition from an immune-cold to an immune-hot tumor.

---

†Stefan Rose-John and Lukas Kenner co-last authors.

*Correspondence:
Christina Sternberg
christina.sternberg@meduniwien.ac.at
Stefan Rose-John
rosejohn@biochem.uni-kiel.de
Lukas Kenner
lukas.kenner@meduniwien.ac.at
Full list of author information is available at the end of the article

Conclusions Our findings demonstrate a context-dependent role of IL6ST/STAT3 in carcinogenesis and a tumor-suppressive function in prostate cancer development by inducing senescence and immune cell attraction. We challenge the prevailing concept of blocking IL6ST/STAT3 signaling as a functional prostate cancer treatment and instead propose cell-autonomous IL6ST activation as a novel therapeutic strategy.

Keywords Prostate cancer, IL6ST/STAT3 signaling, L-gp130, Senescence, Senescence-associated secretory phenotype, Tumor microenvironment, Immune cell infiltration, Cytotoxic T-cells

Background

Prostate cancer (PCa) is the second most common cancer type diagnosed in men, as reflected by 1.4 million new cases worldwide and 375,000 related deaths in 2020 alone [1]. Corresponding to the vast PCa heterogeneity regarding clinical and molecular features, a wide range of therapeutic approaches is currently in use. The accuracy of these treatments is often hampered by the lack of reliable biomarkers allowing to distinguish aggressive from non-aggressive tumors [2]. In search of such biomarkers, aberrant activity of the Interleukin-6 cytokine family signal transducer (IL6ST), also known as Glycoprotein 130 kDa (GP130), signaling axis has been identified as a crucial factor in inflammation and carcinogenesis [3, 4]. A key downstream mediator of IL6ST signaling is the transcription factor Signal transducer and activator of transcription 3 (STAT3) [3]. STAT3 signaling is aberrant in approximately 50% of PCa [5] and plays a tumor microenvironment (TME)-dependent role in cell proliferation, cell survival, angiogenesis and immune evasion [6–8]. Therefore, a further characterization of the axis connecting IL6ST and STAT3 or other potential downstream targets in PCa is important for improved treatment approaches. Other targets activated by IL6ST include the Src homology 2 domain-containing tyrosine phosphatase-2 (SHP2), Phosphatidylinositol 3-kinase (PI3K) and the Hippo/YES-associated protein (YAP) pathway [9], which have themselves been linked with PCa [10–12]. Similarly, the tumor suppressor Phosphatase and tensin homolog (PTEN) is frequently mutated or deleted in PCa [13], thereby eliciting aberrant PI3K activation, contributing to prostate carcinogenesis [14] and inducing p53-dependent cellular senescence [15]. Senescence is a state of cell cycle arrest mediated by the p19^{ARF}/p53 or p16^{INK4A}/RB pathway and has been shown to inhibit PCa progression [16]. Senescence is often accompanied by the release of inflammatory cytokines, chemokines, growth factors and proteases, referred to as the senescence-associated secretory phenotype (SASP) [17]. The SASP is a double-edged sword exerting tumor-suppressive and tumor-promoting effects. The factors modulating the balance between pro-tumorigenic and anti-tumorigenic senescence effects are likely cell type-specific and not fully understood [18].

To shed new light on the role of IL6ST signaling in PCa pathogenesis and to gain further insight into the complex downstream signaling network, we created a mouse model featuring constitutive, cell-autonomous, and prostate epithelium-specific activation of IL6ST. Utilizing this model, we aimed at identifying molecular players induced by IL6ST signaling and at determining its importance in PCa initiation and progression. Considering recent endeavors to render immune-cold PCa amenable to anti-tumor immunity [19], our study also aimed to elucidate the role of IL6ST signaling in shaping the TME, thereby providing valuable insights into its potential use for therapeutic and diagnostic strategies for PCa management.

Our data show that constitutively active IL6ST signaling in *Pten*-deficient PCa mice is associated with significantly smaller tumors compared with *Pten*-deficient mice, related with IL6ST-induced activation of the STAT3/p19^{ARF}/p53 tumor suppressor axis mediating senescence. This is accompanied by increased infiltration of cytotoxic T-cells, neutrophils, and macrophages, indicating better anti-tumor defense. These findings are supported by improved survival observed in PCa patients showing high *IL6ST* mRNA expression, active senescence patterns, and a T-cell mediated anti-tumor immune defense. Together, these results highlight a context-dependent, tumor-suppressive role of IL6ST/STAT3 signaling in prostate carcinogenesis and suggest that cell-autonomous IL6ST activation may be a promising novel therapeutic approach for the treatment of PCa.

Methods

Generation of transgenic mice

Pten$^{fl/fl}$ [20], *L-gp130*$^{fl/fl}$ [3] and PB-Cre4 [21] transgenic mice were maintained on a C57BL/6 and Sv/129 mixed genetic background. *Pten*$^{fl/fl}$ mice and/or *L-gp130*$^{fl/fl}$ mice were crossed with male PB-Cre4 transgenic mice to generate prostate-specific deletion of *Pten* and/or insertion of the *L-gp130* construct. DNA isolation was performed as previously described [22]. Mice were genotyped as previously described [3, 20, 21, 23]. Mice were housed on a 12–12 light cycle and provided food and water ad libitum. For all experiments, 19-week old male mice were used. Genotyping primer sequences and protocols are listed in Supplementary Table 1–2, Additional File 1. Formalin-fixed paraffin-embedded (FFPE) prostate tissue from *Pten*$^{\mathrm{pe}\Delta/\Delta}$;*Stat3*$^{\mathrm{pe}\Delta/\Delta}$ and respective *Pten*$^{\mathrm{pe}\Delta/\Delta}$ control mice were provided by Pencik et al. [8].

Immunohistochemistry (IHC) and hematoxylin & eosin (H&E) stains

IHC and H&E stains were performed with FFPE prostate tissue using standard protocols and antibodies listed in Supplementary Table 3, Additional File 1.

Immunofluorescence (IF) staining

Frozen tissue sections were fixed with 4% Formol for 15 min at room temperature. After washing with PBS, tissue was blocked with 2% BSA in PBS prior to overnight primary antibody incubation at 4 °C (Supplementary Table 3, Additional File 1). Secondary antibody incubation (Alexa Fluor 594 anti-rabbit, Invitrogen #A11037, 1:500; RRID:AB_2534095) was done in 2% BSA in PBS for 1 h at room temperature. Cells were counterstained with DAPI (nuclear stain) in PBS and mounted with Aqua-Poly/Mount medium (18,606–5, Polysciences).

Multiplex IHC

Multiplex IHC was performed on mouse prostate samples using the Bond RX autostainer system (Leica Biosystems Inc., Vienna, Austria; RRID:SCR_025548) and were subsequently analyzed by multispectral imaging. A panel of the following fluorescent markers plus DAPI as a nuclear stain were used to detect the following epitopes: CD3, CD4, CD8, CD45, pan Cytokeratin (Supplementary Table 3, Additional File 1). Scanning of multiplex IHC stains was done as previously described [24]. Individual cells were detected using DAPI nucleus staining by applying thresholds for nucleus size, roundness, and signal intensity. Positivity thresholds for the fluorescently labeled markers were determined based on staining intensity.

Histopathological analysis

For histopathological analysis of H&E, IHC or IF stained samples, slides were scanned using a PANNORAMIC Scan II from 3DHISTECH and quantitatively analyzed as previously described [24]. The murine prostate consists of four different lobes: the anterior, ventral, lateral, and dorsal prostate, each exhibiting distinct morphological characteristics. Due to the loss of these characteristics during tumor progression, differentiating between the lobes in tumor tissue is only feasible for the spatially separated anterior prostate. Therefore, we classified the tissue into two regions: the "anterior lobe (AL)" and the "caudal lobe (CL)", which comprises the ventral, lateral, and dorsal prostate. These stratified data are presented in Additional File 2 and Additional File 3. In the main and supplementary figures, we show analyses covering the entire prostate except for F4/80 and NimpR14 analyses. For these, only the CL was used, as the lumen of the AL contains more cellular debris, which leads to nonspecific staining and challenges analysis. Cell detection was carried out using the StarDist [25] extension for NimpR14 staining, while the built-in watershed cell detection plugin was employed for the other stainings. Parameters were tailored for each specific staining. Subsequently, smoothed features were calculated using a full width at half maximum (FWHM) radius of 25 µm. The tissue was then classified into epithelium and stroma through an object classifier, trained individually for each staining. A threshold was set for the mean DAB optical density value to categorize cells as either positive or negative. If automated quantification was not possible for IHC stainings, semi-quantitative analysis was performed by a trained pathologist, who classified the level of expression as none, mild, moderate or marked for each tissue section. A similar approach was taken for the grading of immune cell infiltration, which was classified as low or high in H&E-stained sections. Analyses were performed blinded to genotype by a single investigator and evaluated by two independent pathologists with specific expertise in mouse models of PCa. A whole slide scan of stained prostate tissue per mouse was analyzed. Representative pictures of the CL for the main and supplementary figures, as well as representative pictures of the AL (and CL) for Additional File 2 and Additional File 3 were exported from whole slide scan using the snapshot function of CaseViewer (Build 2.4.0.119028; RRID:SCR_017654).

Protein isolation and immunoblotting

Whole prostate protein lysates were extracted from snap frozen prostate samples as described [26] and 20–40 µg of protein lysate was used for Western blotting as previously described [8]. Chemiluminescent visualization was performed with a ChemiDoc™ Imaging System (Bio-Rad; RRID:SCR_019037) after incubation of the membranes with Clarity Western ECL reagent (Bio-Rad, 170–5061). Near-infrared visualization was performed using an Odyssey Classic Imaging System (LI-COR; RRID:SCR_023765) and IRDye fluorescent secondary antibodies. Quantifications were performed with Image Lab software (Bio-Rad; RRID:SCR_014210). Samples were normalized to the indicated loading controls. Applied antibodies are listed in Supplementary Table 3, Additional File 1.

RNA sequencing (RNA-Seq) and data analysis

RNA-Seq sample and library preparation was performed as described in [22]. Briefly, single cell suspension of mouse prostate tissue was done as previously described [27] and magnetic cell separation (MagniSort technology, Thermo Fisher) was performed for EpCAM positive fraction using anti-mouse CD326 (EpCAM) Biotin antibody (13–5791-82, eBioscience; RRID:AB_1659713). For higher RNA output, three wild type and three *L-gp130*$^{\mathrm{peKI/KI}}$ mouse prostates, respectively, were pooled to generate one sample. High-quality RNA was used for library preparation. Libraries were amplified with 11 PCR cycles and the library size was analyzed by Agilent Tape Station (G2938-90,014, Agilent Technologies). RNA sequencing and bioinformatic analysis of mouse prostate samples up to the differential expression was performed by Core Facility Bioinformatics of CEITEC Masaryk University as previously described [22].

The Cancer Genome Atlas (TCGA) data analysis

Clinical data for the TCGA-Prostate Adenocarcinoma (PRAD) cohort (https://portal.gdc.cancer.gov/projects/TCGA-PRAD) [28], including disease-free survival, were downloaded from the cBioPortal [29, 30] database. Raw expression counts were downloaded from TCGA with the TCGAbiolinks R package (version 2.25.3). Patients with mutation in TP53 gene (Supplementary Table 4, Additional File 1) were removed from subsequent analysis for Fig. 6b-c. Raw counts were transformed with the variance stabilizing transformation (VST). Survival analysis of TCGA-PRAD cohort was performed with the survminer R package [31] (version 0.4.9). Patients were divided into *IL6ST*$^{\mathrm{high/low}}$ expression groups based on the maximally selected rank statistics which provides a single value cutpoint that corresponds to the most significant relation with disease-free survival. Differential expression analysis between *IL6ST*$^{\mathrm{high}}$ and *IL6ST*$^{\mathrm{low}}$ group was performed with DESeq2 (version 1.36.0). Alteration data including frequency of specific mutations and correlation analysis were obtained from the cBioPortal [29, 30] database. Immune scores for TCGA-PRAD cohort from the ESTIMATE method [32] were downloaded from https://bioinformatics.mdanderson.org/estimate/. Using the Mann–Whitney test, we assessed whether there was a statistically significant difference in the immune scores between *IL6ST*^{high} and *IL6ST*^{low}.

Statistical analysis

Significant differences between two groups were determined using a two-tailed, unpaired t-test (parametric) or Mann–Whitney test (non-parametric). Significant differences between more than two groups were determined using One-way ANOVA with Tukey's multiple comparison test (parametric). Significant outliers were identified by Grubbs ' test. p values of <0.05 were assigned significance. All values are given as means ± standard deviation (SD) and were analyzed and plotted by GraphPad Prism® (version 9.5.0, GraphPad Software, San Diego, CA). Numbers of biological replicates are stated in the respective figure legends. The associations between genes/gene sets and their respective statistical significances were assessed using Spearman-correlation.

Additional methods can be found in Supplementary Methods, Additional File 4.

(See figure on next page.)

Fig. 1 Prostate epithelium-specific, cell-autonomous insertion of *L-gp130* reduces progressive prostate tumorigenesis. **a** Illustration of wild type IL6ST receptor, which can be activated by binding of the IL-6 ligand and IL-6R receptor (left panel), and Leucine-gp130 (L-gp130) construct (right panel). Wild type IL6ST consists of an extracellular domain comprising an Ig-like domain, a cytokine binding domain, three fibronectin type III-like domains, a transmembrane domain, and a cytoplasmic domain. For generating L-gp130, wild type IL6ST was truncated 15 amino acids above the transmembrane domain and replaced by the leucine zipper region of the human c-JUN gene and a FLAG-Tag. L-gp130 expression can activate downstream signaling cascades identical to stimulated wild type IL6ST. P: phosphorylation. **b** Illustration of the genetic approach for conditional deletion of *Pten* (exon 4 + 5) or/and insertion of *L-gp130-ZSGreen* in prostate epithelial cells under the control of Probasin (PB) promoter after *Cre*-mediated recombination resulting in PB-Cre4;*Pten*$^{\mathrm{fl/fl}}$;*L-gp130*$^{+/+}$ (hereafter *Pten*$^{\mathrm{pe}\Delta/\Delta}$), PB-Cre4;*Pten*$^{+/+}$;*L-gp130*$^{\mathrm{fl/fl}}$ (hereafter *L-gp130*$^{\mathrm{peKI/KI}}$) and PB-Cre4;*Pten*$^{\mathrm{fl/fl}}$;*L-gp130*$^{\mathrm{fl/fl}}$ mice (hereafter *Pten*$^{\mathrm{pe}\Delta/\Delta}$;*L-gp130*$^{\mathrm{peKI/KI}}$). pe: prostate epithelium; fl: floxed site; ex: exon; 2A: 2A peptide; CAG: CAG promoter; KI: knock in; Δ: knock out. **c** Representative immunohistochemistry (IHC) pictures of phospho-AKT (p-AKT) and immunofluorescence (IF) pictures of co-stainings of ZSGreen (red) and DAPI (blue) in mouse prostates. DAPI is used as a nuclear stain. Scale bar: 40 µm. Scale bar of inset: 10 µm. **d** Gross anatomy of representative mouse prostates. Scale bar: 0.5 cm. **e** Prostate weight of wild type ($n=10$), *L-gp130*$^{\mathrm{peKI/KI}}$ ($n=14$), *Pten*$^{\mathrm{pe}\Delta/\Delta}$ ($n=14$), and *Pten*$^{\mathrm{pe}\Delta/\Delta}$;*L-gp130*$^{\mathrm{peKI/KI}}$ ($n=14$) mice. Individual biological replicates are shown. Data are plotted as the means ± SD and p-values were determined by ordinary one-way ANOVA with Tukey's multiple comparisons test. **f** Representative pictures of hematoxylin & eosin (H&E) stains of mouse prostates at low (top) and high (bottom) magnification. Scale bar upper panel: 60 µm, scale bar lower panel: 10 µm. **g** Quantification of histopathological analysis of prostate tissue from wild type ($n=9$), *L-gp130*$^{\mathrm{peKI/KI}}$ ($n=9$), *Pten*$^{\mathrm{pe}\Delta/\Delta}$ ($n=11$), and *Pten*$^{\mathrm{pe}\Delta/\Delta}$;*L-gp130*$^{\mathrm{peKI/KI}}$ ($n=9$) mice in regards of histomorphological criteria for aggressive growth patterns: without pathological findings (white); PIN: prostate intraepithelial neoplasia (grey); PCa: prostate cancer (red)

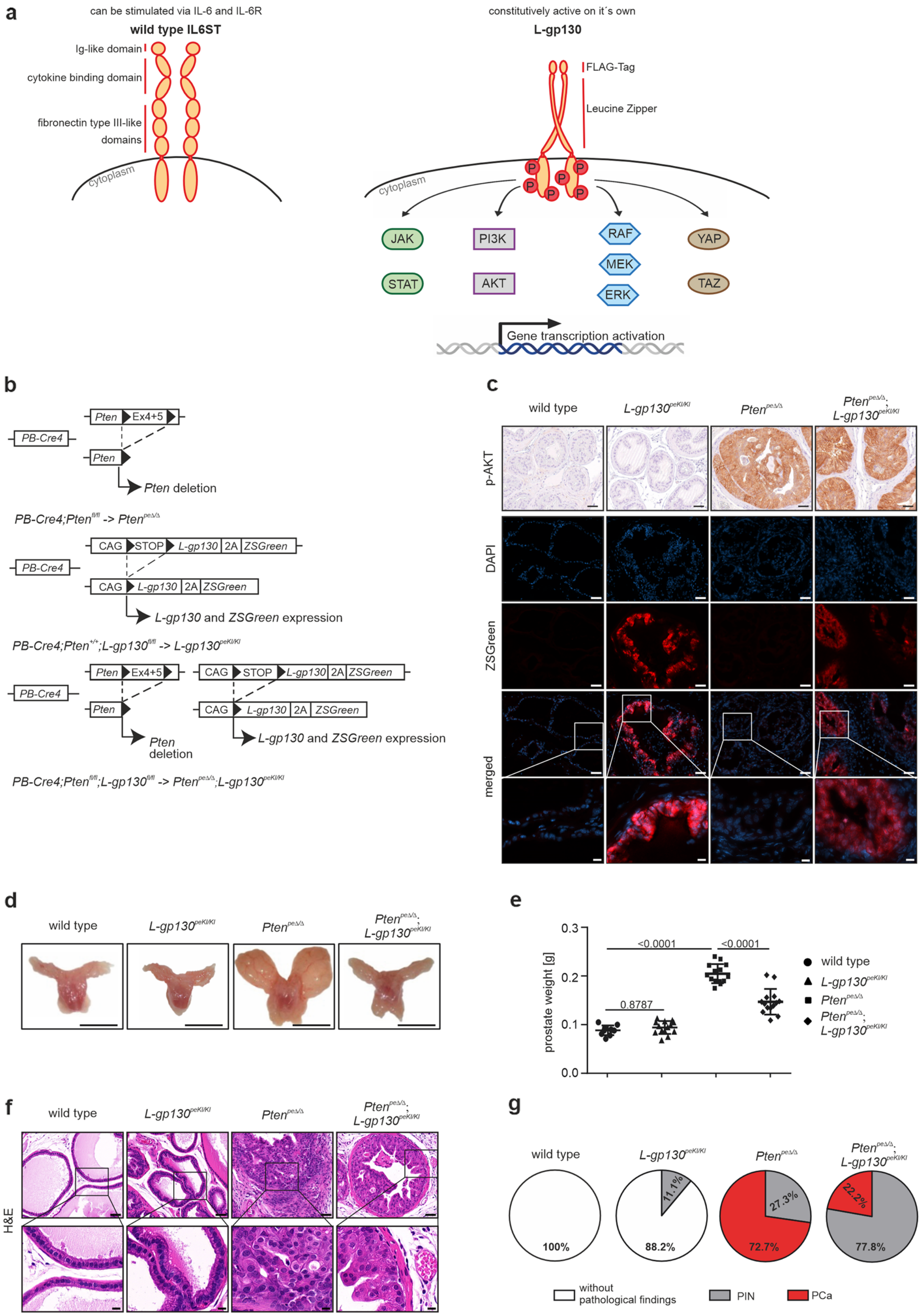

Fig. 1 (See legend on previous page.)

Results

Constitutive activation of IL6ST signaling in prostate epithelial cells

To investigate constitutively activated IL6ST signaling, we used the so-called Leucine-gp130 (L-gp130) construct introduced by Stuhlman-Laeisz et al. [33] (Fig. 1a, right panel), where the entire extracellular part of the wild type IL6ST receptor (Fig. 1a, left panel) is replaced by a leucine zipper, causing forced receptor dimerization and ligand-independent constitutive activation of downstream signaling. The wild type IL6ST receptor requires stimulation by the cytokine Interleukin-6 (IL-6) and Interleukin-6 receptor (IL-6R) for downstream signaling [9]. The downstream signaling cascades of L-gp130 include JAK/STAT, PI3K/AKT, MEK/ERK, and Hippo/YAP (Fig. 1a, right panel), which are identical to those of wild type IL6ST signaling following binding of IL-6 ligand and IL-6R. To study the role of constitutively activated IL6ST signaling in vivo and to decipher the respective downstream signaling axis involved in PCa, the *L-gp130* transgene composed of a synthetic CMV-Actin-Globin composite (CAG) promotor mediating expression of *L-gp130* and *Zoanthus sp.* green fluorescent protein (ZSGreen) was integrated into the ROSA26 locus, which can be transcriptionally activated by Cre-mediated removal of the Westphal stop sequence [3]. We introduced this construct into a conditional mouse model with prostate epithelium-specific Cre expression with sexual maturity using Probasin (PB)-Cre4 mice [21, 23]. This approach generated mice with prostate epithelium-specific constitutively active L-gp130 alleles (*L-gp130*$^{\mathrm{peKI/KI}}$; pe: prostate epithelium; KI: knock in). These *L-gp130*$^{\mathrm{peKI/KI}}$ mice were then crossed with mice in which *Pten* deletion occurs in the prostate epithelium upon PB-Cre4 expression, leading to the development of PCa (*Pten*$^{\mathrm{pe}\Delta/\Delta}$; Δ: knock out) [20]. The crossbreed resulted in PCa mice with additional prostate epithelium-specific constitutively activated IL6ST signaling (*Pten*$^{\mathrm{pe}\Delta/\Delta}$;*L-gp130*$^{\mathrm{peKI/KI}}$) (Fig. 1b).

Deletion of *Pten* and insertion of *L-gp130* were confirmed after the onset of puberty by Polymerase Chain Reaction (PCR) (Supplementary Fig. 1a, Additional File 5). In addition, prostate epithelium-specific deletion of *Pten* was assessed by IHC analysis of phospho-AKT (p-AKT) levels, as loss of PTEN leads to phosphorylation of AKT [14]. *Pten*$^{\mathrm{pe}\Delta/\Delta}$ and *Pten*$^{\mathrm{pe}\Delta/\Delta}$;*L-gp130*$^{\mathrm{peKI/KI}}$ showed elevated p-AKT expression compared to wild type and *L-gp130*$^{\mathrm{peKI/KI}}$ prostate samples (Fig. 1c, upper panel). Further confirmation of prostate-specific deletion of *Pten* was obtained by Western blot analysis and quantification of p-AKT levels. *Pten*$^{\mathrm{pe}\Delta/\Delta}$ and *Pten*$^{\mathrm{pe}\Delta/\Delta}$;*L-gp130*$^{\mathrm{peKI/KI}}$ showed significantly increased p-AKT expression compared to wild type and *L-gp130*$^{\mathrm{peKI/KI}}$ prostate samples, whereas total-AKT (t-AKT) expression was not affected between the different genotypes (Supplementary Fig. 1b-c, Additional File 5). To confirm the functional expression of the *L-gp130* construct, we examined ZSGreen expression via IF. We found ZSGreen expression in *L-gp130*$^{\mathrm{peKI/KI}}$ and *Pten*$^{\mathrm{pe}\Delta/\Delta}$;*L-gp130*$^{\mathrm{peKI/KI}}$ but not in wild type and *Pten*$^{\mathrm{pe}\Delta/\Delta}$ prostates (Fig. 1c, lower panel). Of note, endogenous wild type *Il6st* mRNA levels were not changed by *L-gp130* expression in the prostate (Supplementary Fig. 1d, Additional File 5). This is in line with previous findings revealing no impact on endogenous IL6ST expression by the introduction of the L-gp130 construct [3]. Overall, we generated a mouse model allowing us to examine the consequences of cell-autonomous, prostate epithelial cell-specific IL6ST signaling.

Constitutively active IL6ST signaling reduces *Pten*-deficient tumor growth in vivo

We next examined the impact of constitutively active IL6ST signaling in 19-week old mice and found that prostates of wild type and *L-gp130*$^{\mathrm{peKI/KI}}$ mice were macroscopically indistinguishable. As expected, *Pten*$^{\mathrm{pe}\Delta/\Delta}$ mice developed grossly visible PCa (Fig. 1d). Intriguingly, mice with concomitant activation of IL6ST signaling (*Pten*$^{\mathrm{pe}\Delta/\Delta}$;*L-gp130*$^{\mathrm{peKI/KI}}$) developed smaller prostate tumors compared to *Pten*-deficient mice, resulting in a significantly reduced prostate weight of *Pten*$^{\mathrm{pe}\Delta/\Delta}$;*L-gp130*$^{\mathrm{peKI/KI}}$ compared to *Pten*$^{\mathrm{pe}\Delta/\Delta}$ mice (Fig. 1d-e).

Assessment of H&E-stained murine prostates (Fig. 1f) revealed no pathological features in wild type and *L-gp130*$^{\mathrm{peKI/KI}}$ mice, except for one *L-gp130*$^{\mathrm{peKI/KI}}$ animal (accounting for 11.1% of analyzed mice) (Fig. 1g). This animal exhibited prostatic intraepithelial neoplasia (PIN), a precursor for PCa. The vast majority (72.7%) of the *Pten*$^{\mathrm{pe}\Delta/\Delta}$ mice showed PCa [34], whereas only 22.2% of *Pten*$^{\mathrm{pe}\Delta/\Delta}$;*L-gp130*$^{\mathrm{peKI/KI}}$ mice developed PCa. Instead, 77.8% exhibited only PIN, displaying a less aggressive morphology compared to *Pten*$^{\mathrm{pe}\Delta/\Delta}$ mice. These findings support a tumor-suppressive role of IL6ST signaling in PCa in vivo.

L-gp130 expression in prostate epithelial cells enriches STAT3 target gene expression

To unravel molecular gene expression patterns associated with the observed phenotypes and to elucidate which of the possible downstream signaling axes is activated upon *L-gp130* insertion, we performed RNA-Seq analysis of prostate tissue from wild type, *L-gp130*$^{\mathrm{peKI/KI}}$, *Pten*$^{\mathrm{pe}\Delta/\Delta}$ and *Pten*$^{\mathrm{pe}\Delta/\Delta}$;*L-gp130*$^{\mathrm{peKI/KI}}$ mice. As our mouse model allows prostate epithelium-specific modulation and to specifically isolate these prostate epithelial cells, we sorted cells obtained from prostate tissue by magnetic bead-based cell sorting for EpCAM, a marker for epithelial cells that is expressed uniformly across all four genotypes (Fig. 2a). This prostate epithelial fraction was then subjected to RNA-Seq as previously described [22] (Fig. 2b). Clustering of the samples by 3D-principal component analysis based on gene expression revealed that individual replicates clustered within the genotypes and confirmed different transcription profiles (Supplementary Fig. 2a, Additional File 5). Differential gene expression analysis of *Pten*$^{\mathrm{pe}\Delta/\Delta}$ and *Pten*$^{\mathrm{pe}\Delta/\Delta}$;*L-gp130*$^{\mathrm{peKI/KI}}$ prostate epithelial cells showed significant upregulation of 807 and downregulation of 475 genes in *Pten*$^{\mathrm{pe}\Delta/\Delta}$;*L-gp130*$^{\mathrm{peKI/KI}}$ prostates (Fig. 2c). Notably, we detected nearly twice as many upregulated genes as downregulated genes, which supports the idea that constitutively active IL6ST serves as a central receptor of signal transduction and activator of transcription. There was also a considerable, albeit smaller number of 470 genes that were significantly upregulated when comparing *L-gp130*$^{\mathrm{peKI/KI}}$ and wild type prostate epithelial cells, as well as 335 downregulated genes (Supplementary Fig. 2b, Additional File 5). Fast pre-ranked gene set enrichment analysis (fGSEA) of the “Prostate cancer” gene set from the Kyoto Encyclopedia of Genes and Genomes (KEGG) collection from the Molecular signature database (MSigDB) [35, 36] showed a significant downregulation of analyzed genes in *Pten*$^{\mathrm{pe}\Delta/\Delta}$;*L-gp130*$^{\mathrm{peKI/KI}}$ compared to *Pten*$^{\mathrm{pe}\Delta/\Delta}$ samples (Fig. 2d), which supports our mouse data showing smaller tumors in *Pten*$^{\mathrm{pe}\Delta/\Delta}$;*L-gp130*$^{\mathrm{peKI/KI}}$ mice.

To determine which downstream signaling cascade is activated by L-gp130 in PCa, we performed fGSEA of *Pten*$^{\mathrm{pe}\Delta/\Delta}$;*L-gp130*$^{\mathrm{peKI/KI}}$ compared to *Pten*$^{\mathrm{pe}\Delta/\Delta}$ samples using the REACTOME gene set collection derived from MSigDB. We detected no apparent change in the regulation of PI3K/AKT, RAS/RAF/ERK/MAPK or Hippo/YAP signaling cascades (Supplementary Fig. 2c, Additional File 5). Interestingly, we found significantly upregulated STAT3 target genes by analyzing three independent, previously described sets of STAT3 target genes [37–39]. These results imply that *L-gp130* expression correlated with STAT3 activity, which in turn acts as a transcription factor in PCa (Fig. 2e). In accordance, Western blot analysis also showed activation of STAT3, reflected in increased phosphoY705-STAT3 (pY-STAT3) levels and unaltered total-STAT3 (t-STAT3) levels in *Pten*$^{\mathrm{pe}\Delta/\Delta}$;*L-gp130*$^{\mathrm{peKI/KI}}$ compared to *Pten*$^{\mathrm{pe}\Delta/\Delta}$ prostates (Fig. 2f-g). This finding was further confirmed using IHC, which showed a nearly 50% increase in pY-Stat3 positive cells in *Pten*$^{\mathrm{pe}\Delta/\Delta}$;*L-gp130*$^{\mathrm{peKI/KI}}$ compared to *Pten*$^{\mathrm{pe}\Delta/\Delta}$ samples, while t-STAT3 levels assessed semi-quantitatively were constant in both genotypes (Fig. 2h-j). This increase in pY-STAT3^{+} epithelial cells is on top of the already nearly 60% pY-STAT3^{+} epithelial cells seen in *Pten*$^{\mathrm{pe}\Delta/\Delta}$ samples. In addition to the classical activation of STAT3 via phosphorylation of Y705 [40], transcriptional activation can be regulated by phosphorylation at Ser727 [41]. PhosphoS727-STAT3 (pS727-STAT3) levels were significantly upregulated in *Pten*$^{\mathrm{pe}\Delta/\Delta}$;*L-gp130*$^{\mathrm{peKI/KI}}$ compared to *Pten*$^{\mathrm{pe}\Delta/\Delta}$ prostates (Supplementary Fig. 2d-f, Additional File 5). In line, we observed an upregulation of STAT3 target genes (Supplementary Fig. 2g, Additional File 5) and of pY-STAT3 abundance (Supplementary Fig. 2h-l, Additional File 5) when comparing *L-gp130*$^{\mathrm{peKI/KI}}$ and wild type prostate epithelial cells. Of note, in the stromal cells of mice with *L-gp130* insertion in the prostate epithelium (*L-gp130*$^{peKI/KI}$ and *Pten*$^{pe\Delta/\Delta}$;*L-gp130*$^{peKI/KI}$ mice), we detected no increase in pY-STAT3 and

(See figure on next page.)

Fig. 2 L-gp130 leads to activation of the STAT3 transcription factor and STAT3 target gene expression. **a** Representative immunohistochemistry (IHC) pictures of mouse prostates stained for the epithelial marker EpCAM. Scale bar: 40 µm **b** RNA-Seq workflow showing processing and magnetic bead-based enrichment of EpCAM-positive (EpCAM^{+}) mouse prostate tissue. Prostates were dissected and enzymatically and mechanically dissociated to generate single cell suspensions. Cells were labeled with biotinylated anti-EpCAM antibody and enriched from the bulk population using streptavidin-coated magnetic beads. EpCAM^{+} cells were subjected to RNA-Seq analysis. **c** Heatmap and number of differentially expressed genes (log2norm) based on adj. p-value ≤ 0.05 and fold change ≥ 2 cut-off values comparing *Pten*$^{\mathrm{pe}\Delta/\Delta}$ and *Pten*$^{\mathrm{pe}\Delta/\Delta}$;*L-gp130*$^{\mathrm{peKI/KI}}$ prostate epithelial cells (n ≥ 5). blue: downregulated, red: upregulated. **d** Fast pre-ranked gene set enrichment analysis (fGSEA) of the KEGG gene set “Prostate cancer” with genes regulated in *Pten*$^{\mathrm{pe}\Delta/\Delta}$;*L-gp130*$^{\mathrm{peKI/KI}}$ compared to *Pten*$^{\mathrm{pe}\Delta/\Delta}$ prostate epithelial cells. Genes sorted based on their Wald statistics are represented as vertical lines on the x-axis. NES: normalized enrichment score. **e** fGSEA of three previously published STAT3 target signatures (“STAT3 targets (Swoboda)”, “STAT3 targets (Azare)”, “STAT3 targets (Carpenter)”) with genes regulated in *Pten*$^{\mathrm{pe}\Delta/\Delta}$;*L-gp130*$^{\mathrm{peKI/KI}}$ compared to *Pten*$^{\mathrm{pe}\Delta/\Delta}$ prostate epithelial cells. Genes sorted based on their Wald statistics are represented as vertical lines on the x-axis. NES: normalized enrichment score. **f** Western Blot analysis of prostate protein lysates for phosphoTyrosine705-STAT3 (pY-STAT3) and total-STAT3 (t-STAT3) expression in *Pten*$^{\mathrm{pe}\Delta/\Delta}$ and *Pten*$^{\mathrm{pe}\Delta/\Delta}$;*L-gp130*$^{\mathrm{peKI/KI}}$ mice ($n = 5$). β-ACTIN (β-ACT) served as loading control. **g** Quantification of pY-STAT3 protein levels relative to t-STAT3 protein levels shown in f). **h** Representative pictures of IHC staining of pY-STAT3 and t-STAT3 expression in prostate sections of *Pten*$^{\mathrm{pe}\Delta/\Delta}$ and *Pten*$^{\mathrm{pe}\Delta/\Delta}$;*L-gp130*$^{\mathrm{peKI/KI}}$ mice. Scale bar: 40 µm. **i-j** Quantitative analysis of pY-STAT3 (i) and semi-quantitative analysis of t-STAT3 (j) IHC stainings shown in h) ($n = 7$). **g**,**i-j** Individual biological replicates are shown (g,i). Data are plotted as the means ± SD and p-values were determined by unpaired two-tailed Student’s t-tests (g,i) or Mann-Whitney test (j)

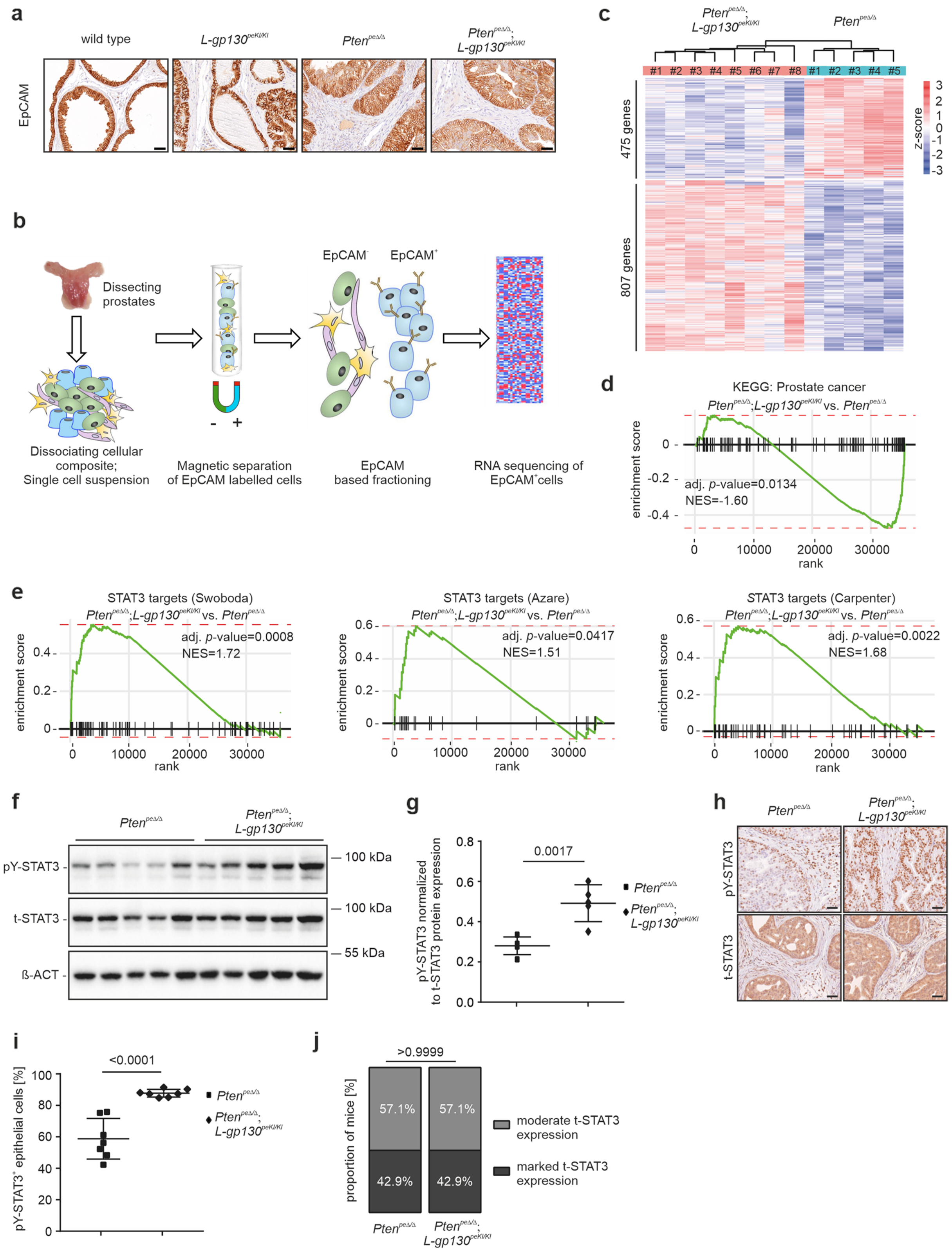

Fig. 2 (See legend on previous page.)

pS727-STAT3 levels compared to wild type and *Pten*$^{\mathrm{pe}\Delta/\Delta}$ mice, respectively (Supplementary Fig. 2m-n, Additional File 5). This underscores the prostate-epithelium specificity of our mouse model. Taken together, L-gp130 expression in prostate epithelial cells activates STAT3 signaling, as evidenced by significantly upregulated STAT3 target genes and increased pY-STAT3 and pS727-STAT3 levels.

IL6ST expression correlates with prolonged survival and STAT3 expression in PCa patients

Based on our mouse data, we hypothesized that high IL6ST expression in PCa patients would correlate with favorable clinical outcomes. To investigate the relationship between *IL6ST* mRNA expression levels and PCa, we examined the TCGA-PRAD cohort [28] comprising primary PCa patients and found a significant decrease in *IL6ST* mRNA expression in prostate tumor tissue compared to adjacent healthy tissue (Fig. 3a). We divided patients into *IL6ST* high and low expression groups using the maximally selected rank statistics method, which identifies the cutpoint with the most significant relation with disease-free survival. Stratifying patients based on their *IL6ST* mRNA demonstrated that high *IL6ST* expression is linked to a greater probability of disease-free survival compared to low *IL6ST* expression (Fig. 3b). In the TCGA-PRAD cohort, 7.2% of patients with prostate adenocarcinoma have alterations in the *IL6ST* gene, with 6.3% accounting for deep deletions and 0.9% for missense mutations of unknown significance (Fig. 3c). We therefore hypothesized that mutations leading to altered *IL6ST* expression could impact the initiation and/or progression of PCa. To test the validity of our findings, we analyzed four additional data sets from the Oncomine platform [42]. The results support a significant decrease in *IL6ST* mRNA expression in PCa compared to normal prostate glands, highlighting the potential impact of IL6ST alterations on PCa (Fig. 3d). We also observed a significant reduction in *IL6ST* expression relative to the primary PCa site during PCa progression in recurrent and advanced PCa and metastasis (Supplementary Fig. 3a, Additional File 5). Using the SurvExpress Analysis webtool [43], we next examined the MSKCC Prostate GSE21032 data set by Taylor et al. [44] in terms of survival, as it provides not only data on primary but also metastatic PCa. We assessed risk groups by a median split of samples based on their prognostic index and observed high expression of *IL6ST* in low-risk PCa patients and vice versa (Supplementary Fig. 3b, Additional File 5). In support of our previous findings from the TCGA-PRAD cohort, correlating biochemical recurrence-free survival time with *IL6ST* mRNA expression levels, we detected a significantly higher probability of biochemical recurrence-free survival associated with high as compared to low *IL6ST* levels (Supplementary Fig. 3c, Additional File 5). To further validate our findings in an independent dataset, we analyzed the SMD GSE40727 [45] cohort using the SurvExpress Analysis web tool. Survival analysis of patients expressing high and low levels of *IL6ST*, grouped according to the optimal risk split, showed a tendency for better biochemical recurrence-free survival probability in the *IL6ST*^{high} group compared to the *IL6ST*^{low} group (Supplementary Fig. 3d-e, Additional File 5). These findings corroborate a tumor suppressive role of *IL6ST* expression in PCa. Interestingly, *IL6ST* mRNA expression positively correlated with *STAT3* expression in PCa patients in both the TCGA-PRAD cohort and Taylor data set (MSKCC Prostate GSE21032), providing further evidence of the interconnected signaling between IL6ST and STAT3 in PCa (Fig. 3e and Supplementary Fig. 3f, Additional File 5). To examine the IL6ST/STAT3 signaling activation in the TCGA-PRAD data set, we correlated *IL6ST* (Supplementary Fig. 3g, Additional File 5) and *STAT3* (Supplementary Fig. 3h, Additional File 5) mRNA expression levels with three STAT3 target signatures assessed by single sample gene set variation analysis (ssGSVA). All three STAT3 target gene sets were positively correlated to *IL6ST* and *STAT3* mRNA expression levels indicating a tight association of high *IL6ST* and *STAT3* expression and active STAT3 signaling. Together, these human patient data suggest that *IL6ST* expression could serve as a useful read-out to stratify PCa cases into low- and high-risk groups.

L-gp130 promotes STAT3/p19$^{\mathrm{ARF}}$/p53-induced senescence upon *Pten*-loss

To further understand the molecular mechanisms underlying the observed reduction in tumor size in mice expressing constitutively active *Il6st* in the prostate epithelium, we investigated changes in gene expression. Performing fGSEA using the HALLMARK gene set collection from MSigDB, we identified significantly deregulated gene sets that rely on L-gp130 expression in prostate tumorigenesis. Upon *L-gp130* insertion, the “IL-6/JAK/STAT3 signaling” gene set was upregulated in *L-gp130*$^{\mathrm{peKI/KI}}$ and *Pten*$^{\mathrm{pe}\Delta/\Delta}$;*L-gp130*$^{\mathrm{peKI/KI}}$ mice, compared to wild type and *Pten*$^{\mathrm{pe}\Delta/\Delta}$ mice, respectively (Fig. 4a and Supplementary Fig. 4a, Additional File 5). This is noteworthy as IL-6 activates the Janus kinase (JAK) and subsequently STAT3 by binding to the IL6ST receptor [9], and therefore upregulated “IL-6/JAK/STAT3 signaling” aligns with our previous results on the induction of the STAT3 signaling cascade. From all HALLMARK gene sets, we found 32 being significantly deregulated when comparing *Pten*$^{\mathrm{pe}\Delta/\Delta}$;*L-gp130*$^{\mathrm{peKI/KI}}$ and *Pten*$^{\mathrm{pe}\Delta/\Delta}$ samples. Among these gene

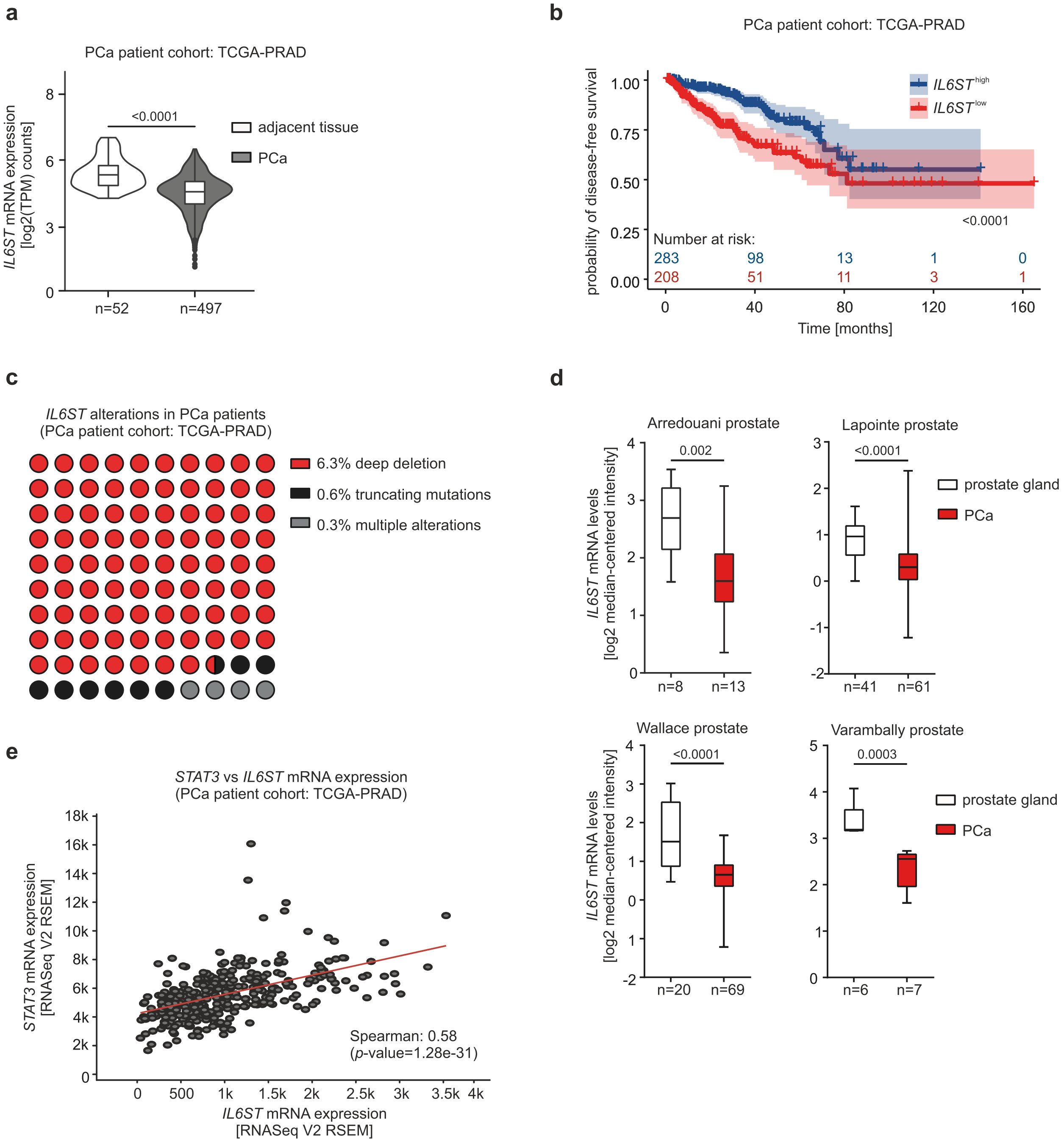

Fig. 3 High *IL6ST* expression is significantly associated with low-risk groups and better recurrence-free survival in human PCa. **a** *IL6ST* gene expression in adjacent ($n = 52$) and PCa ($n = 497$) tissue in TCGA-PRAD data set. Statistical analysis of the two risk groups was determined by using the Mann–Whitney test. **b** Kaplan–Meier plot showing time of disease-free survival in months for *IL6ST*^{low} and *IL6ST*^{high} risk groups of the TCGA-PRAD data set. Groups were assessed based on the maximally selected rank statistics. blue: high *IL6ST* expressing group, red: low *IL6ST* expressing group. The blue and red numbers above horizontal axis represent the number of patients. **c** Proportion of *IL6ST* alterations in the TCGA-PRAD data set. Mutation types: deep deletion ($n = 21$; red), truncating mutations ($n = 2$; black) and multiple alterations ($n = 1$; grey). One patient has simultaneous mutations. The data originate from cBioPortal. **d** *IL6ST* mRNA expression levels of four different data sets of PCa patient samples compared to healthy prostate sample control. Normalized data and statistical analyses were extracted from the Oncomine Platform. The respective prostate data set and n-numbers are indicated. Representation: boxes as interquartile range, horizontal line as the mean, whiskers as lower and upper limits. **e** Spearman-correlation analysis of *IL6ST* and *STAT3* expression in TCGA-PRAD data set using cBioPortal analysis tool

sets, the downregulated HALLMARK gene set “Androgen response” (Fig. 4a) points to less androgen receptor signaling in *Pten*$^{\mathrm{pe}\Delta/\Delta}$;*L-gp130*$^{\mathrm{peKI/KI}}$ mice, which is in line with its crucial role in PCa development [46] and the observed reduction in cancer aggressiveness in our *Pten*$^{\mathrm{pe}\Delta/\Delta}$;*L-gp130*$^{\mathrm{peKI/KI}}$ mice. The two HALLMARK gene sets showing the most pronounced downregulation were “Oxidative phosphorylation” and “Fatty acid metabolism”. This observation is noteworthy as we have previously demonstrated an inverse association between the regulation of oxidative phosphorylation and the TCA cycle with STAT3 expression [47, 48]. This downregulation is also seen in the corresponding KEGG and Biological Processes from Gene Ontology pathways (GO-BP) gene sets (Supplementary Fig. 4b, Additional File 5). Given that the downregulation of these pathways has previously been shown to rely on STAT3 signaling, it underscores the importance of active STAT3 signaling in the context of this study. Surprisingly, the two most prominent upregulated gene sets are the proliferation-associated “MYC targets V1” and “MYC targets V2” (Fig. 4a). We also observed an upregulation of MYC target genes in the comparison of *L-gp130*$^{\mathrm{peKI/KI}}$ and wild type (Supplementary Fig. 4a, Additional File 5). As *MYC* gene expression is regulated by IL6ST/STAT3 [49], this might contribute to the observed upregulation of MYC target genes in both comparisons (*Pten*$^{\mathrm{pe}\Delta/\Delta}$;*L-gp130*$^{\mathrm{peKI/KI}}$ versus *Pten*$^{\mathrm{pe}\Delta/\Delta}$ and *L-gp130*$^{\mathrm{peKI/KI}}$ versus wild type). Additionally, the cell cycle-related gene sets “E2F targets” and “G2M checkpoint” were significantly upregulated. Considering the reported potential of the IL-6/STAT3 axis to drive rather than inhibit tumor cell proliferation [50], we investigated proliferation. We did not observe a significant difference in Ki67 assessed by IHC staining (Fig. 4b-c). Another gene set that was observed to be significantly upregulated is the “P53 pathway”, which is known to mediate oncogene-induced senescence in prostate tumorigenesis [51, 52] and in the *Pten*-deficient PCa context [8]. Therefore we hypothesized that the induction of senescence in *Pten*$^{\mathrm{pe}\Delta/\Delta}$;*L-gp130*$^{\mathrm{peKI/KI}}$ compared to *Pten*$^{\mathrm{pe}\Delta/\Delta}$ mice causes the smaller tumors observed in *Pten*$^{\mathrm{pe}\Delta/\Delta}$;*L-gp130*$^{\mathrm{peKI/KI}}$ mice. Senescence is often accompanied by the upregulation of promyelocytic leukemia protein (PML) [53]. Indeed, we observed increased numbers of PML nuclear bodies in our *Pten*$^{\mathrm{pe}\Delta/\Delta}$;*L-gp130*$^{\mathrm{peKI/KI}}$ mice (Fig. 4d-e). An additional defining characteristic of senescent cells is the release of inflammatory cytokines and signaling molecules referred to as SASP [17]. To investigate the alteration of SASP-related genes in *Pten*$^{\mathrm{pe}\Delta/\Delta}$;*L-gp130*$^{\mathrm{peKI/KI}}$ prostate epithelial cells, we performed fGSEA using the “Core SASP of Pten-loss induced cellular senescence (PICS)” [54] gene set, previously described to be induced upon PICS, and found it to be significantly upregulated in *Pten*$^{\mathrm{pe}\Delta/\Delta}$;*L-gp130*$^{\mathrm{peKI/KI}}$ mice compared to *Pten*$^{\mathrm{pe}\Delta/\Delta}$ mice (Supplementary Fig. 4c, Additional File 5).

Upon closer examination of the molecular players involved in senescence induction, we found that the p19$^{\mathrm{ARF}}$/p53-dependent pathway was activated. We observed significantly enhanced expression of *Cdkn2a* mRNA, which encodes both *p16*^{INK4A} and *p19*^{ARF} (Fig. 4f) [55]. Using *p19*^{ARF} specific primers revealed a significant upregulation of this previously described STAT3 target gene [8] (Fig. 4g). We observed a significant increase in p53 protein abundance (Fig. 4h-i). In line with this, we also noted that gene sets representing transcriptional p53 activity were significantly upregulated in our fGSEA of GO-BP gene sets derived from MSigDB (Supplementary Fig. 4d, Additional File 5). Based on our data, we thus propose a model of IL6ST signaling-induced senescence in PCa, in which STAT3, activated by L-gp130, upregulates *p19*^{ARF} mRNA expression, followed by increased p53 expression and induction of senescence as seen by elevated PML expression (Fig. 4j).

(See figure on next page.)

Fig. 4 Expression of L-gp130 induces p19$^{\mathrm{ARF}}$-p53-driven senescence in *Pten*-deficient PCa. **a** Fast pre-ranked gene set enrichment analysis (fGSEA) of significantly enriched HALLMARK gene sets with genes regulated in *Pten*$^{\mathrm{pe}\Delta/\Delta}$;*L-gp130*$^{\mathrm{peKI/KI}}$ compared to *Pten*$^{\mathrm{pe}\Delta/\Delta}$ prostate epithelial cells. Dotted line: adj. p-value (-log10(0.05)), blue: downregulated, red: upregulated; **b** Representative pictures of immunohistochemistry (IHC) staining of mouse prostates from the indicated genotypes stained for the proliferation marker Ki67. Scale bar: 40 µm. **c** Semi-quantitative analysis of Ki67^{+} prostate epithelial cells in the indicated genotypes ($n=7$) shown in b). **d** Representative pictures of IHC staining of PML of *Pten*$^{\mathrm{pe}\Delta/\Delta}$ and *Pten*$^{\mathrm{pe}\Delta/\Delta}$;*L-gp130*$^{\mathrm{peKI/KI}}$ prostates. Scale bar: 40 µm. **e** Quantification of PML nuclear bodies per high power field (HPF) shown in d) ($n \geq 5$). **f** *Cdkn2a* mRNA expression levels based on normalized counts from RNA-Seq analysis of *Pten*$^{\mathrm{pe}\Delta/\Delta}$ and *Pten*$^{\mathrm{pe}\Delta/\Delta}$;*L-gp130*$^{\mathrm{peKI/KI}}$ prostates ($n \geq 5$). **g** qRT-PCR mRNA expression analysis of *p19*^{ARF} in mouse prostate tissue of *Pten*$^{\mathrm{pe}\Delta/\Delta}$ and *Pten*$^{\mathrm{pe}\Delta/\Delta}$;*L-gp130*$^{\mathrm{peKI/KI}}$ mice ($n \geq 5$). Signals are relative to the geometric mean of housekeeping genes. **h** Western Blot analysis of prostate protein lysates of *Pten*$^{\mathrm{pe}\Delta/\Delta}$ and *Pten*$^{\mathrm{pe}\Delta/\Delta}$;*L-gp130*$^{\mathrm{peKI/K}}$ mice ($n=5$) for p53 expression. β-ACTIN (β-ACT) served as loading control. **i** Quantification of p53 protein levels shown in h) normalized to loading control. **j** Proposed model of IL6ST signaling induced senescence. L-gp130 activated STAT3 binds to its binding sites in Cdkn2a promoter, followed by upregulation of p19$^{\mathrm{ARF}}$ and p53 expression promoting senescence in PCa. **c**,**e**–**g**,**i** Individual biological replicates are shown (e–g,i). Data are plotted as the means ± SD and p-values were determined by Mann–Whitney test (c,f), unpaired two-tailed Student’s t-tests (e,g,i)

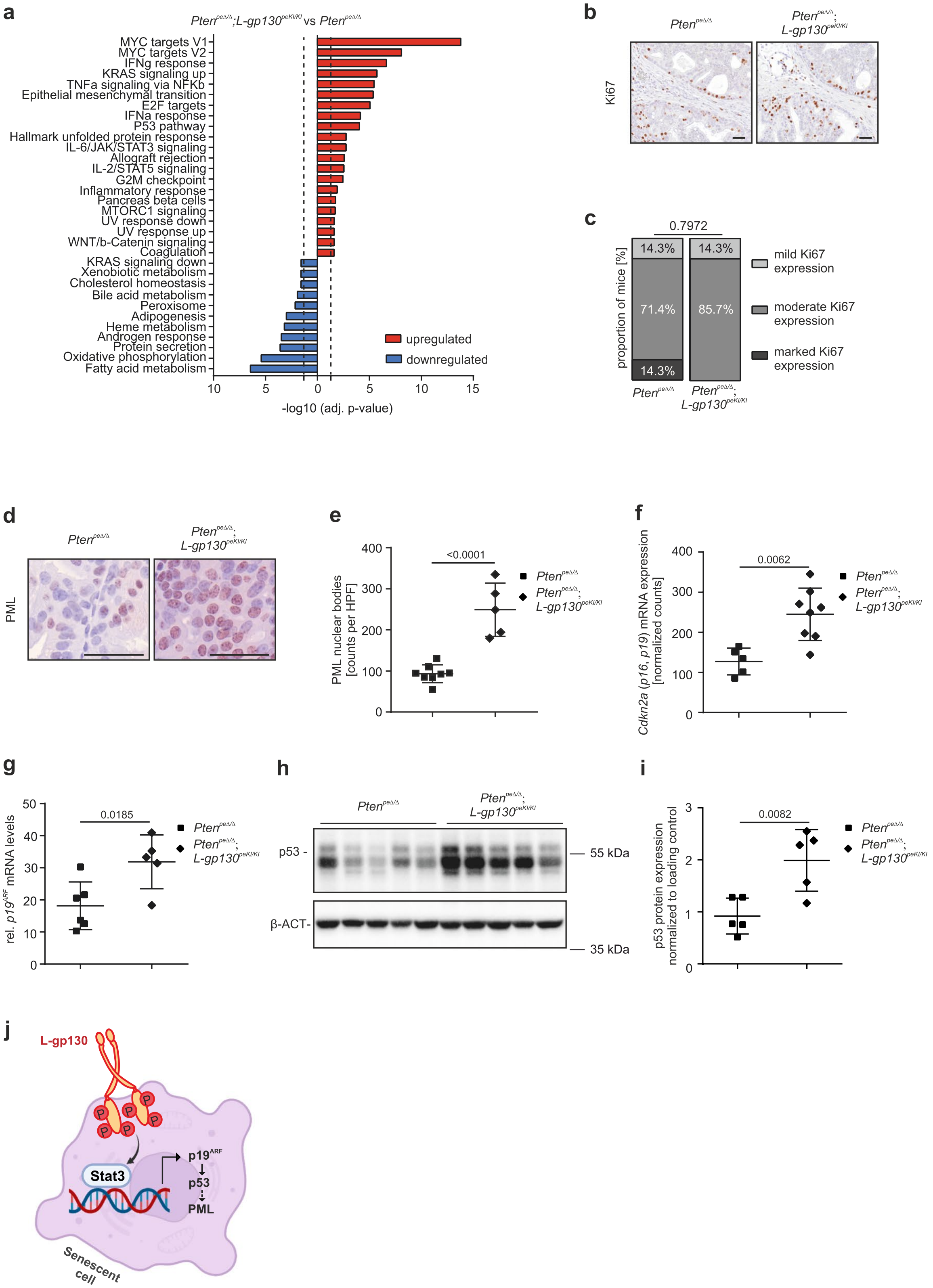

Fig. 4 (See legend on previous page.)

IL6ST signaling recruits anti-tumor infiltrating immune cells

Senescence is closely connected to the TME, known to be immune-cold in PCa [19]. Consequently, we focused our examination on the impact of constitutively active IL6ST on the TME. Indeed, upon analysis of H&E stained prostate sections we detected high-grade immune cell infiltration in 66.7% of *Pten*$^{\mathrm{pe}\Delta/\Delta}$;*L-gp130*$^{\mathrm{peKI/KI}}$ mice compared to 36.4% of *Pten*$^{\mathrm{pe}\Delta/\Delta}$ mice (Fig. 5a). Only few immune cells were seen in wild type and *L-gp130*$^{\mathrm{peKI/KI}}$ prostates (Supplementary Fig. 5a, Additional File 5). IF analysis allowed us to examine the infiltrating immune cell subtypes and their distribution and revealed a significantly higher number of CD45$^+$ cells in *Pten*$^{\mathrm{pe}\Delta/\Delta}$;*L-gp130*$^{\mathrm{peKI/KI}}$ mice compared to *Pten*$^{\mathrm{pe}\Delta/\Delta}$ mice and the occurrence of minimal CD45$^+$ cells in wild type and *L-gp130*$^{\mathrm{peKI/KI}}$ mice (Fig. 5b-c and Supplementary Fig. 5b-c, Additional File 5).

A more detailed characterization showed that L-gp130 expression did not affect B-cell (CD79b) involvement in immune cell infiltration (Supplementary Fig. 5d-e, Additional File 5). Importantly, CD3$^+$ cells were significantly increased in the prostate epithelium of *Pten*$^{\mathrm{pe}\Delta/\Delta}$;*L-gp130*$^{\mathrm{peKI/KI}}$ mice (Supplementary Fig. 5f-g, Additional File 5), whereas, in the adjacent stroma, the CD3$^+$ cell levels did not exhibit a significant difference compared to *Pten*$^{\mathrm{pe}\Delta/\Delta}$ mice (Supplementary Fig. 5h, Additional File 5). Notably, a substantial proportion of these cells were CD3$^+$;CD8$^+$ positive (Fig. 5d and Supplementary Fig. 5i-j, Additional File 5), which are considered major drivers of anti-tumor immunity [56]. We also noted a significant difference in the ability of CD3$^+$;CD8$^+$ cells to migrate into the epithelium between *Pten*$^{\mathrm{pe}\Delta/\Delta}$ and *Pten*$^{\mathrm{pe}\Delta/\Delta}$;*L-gp130*$^{\mathrm{peKI/KI}}$ mice (Fig. 5e), whereas their proportion in the stroma was unaffected by L-gp130 expression (Supplementary Fig. 5k, Additional File 5). Concurrently, our findings indicated that CD3$^+$;CD4$^+$ T-cells did not play a significant role in anti-tumor infiltration in our mouse model (Supplementary Fig. 5l-n, Additional File 5).

Next, we examined neutrophils and macrophages to understand their potential contributions to the immune response within the prostate epithelium and the TME. IHC stainings for the neutrophil marker NimpR14 and macrophage marker F4/80 revealed a significant increase in the epithelial fraction of *Pten*$^{\mathrm{pe}\Delta/\Delta}$;*L-gp130*$^{\mathrm{peKI/KI}}$ compared to *Pten*$^{\mathrm{pe}\Delta/\Delta}$ prostates (Fig. 5f-h), but no change in stroma or in the comparison of wild type and *L-gp130*$^{\mathrm{peKI/KI}}$ mice (Supplementary Fig. 5o-t, Additional File 5), reflecting innate immune cell tumor infiltration upon constitutive IL6ST signaling activation in *Pten*$^{\mathrm{pe}\Delta/\Delta}$;*L-gp130*$^{\mathrm{peKI/KI}}$ mice. To characterize and distinguish M1 and M2 macrophages, we performed flow cytometry using CD86 and MHC class II for M1, and CD206 for M2. Results indicated a proinflammatory and tumor-suppressive M1-like phenotype in *Pten*$^{\mathrm{pe}\Delta/\Delta}$;*L-gp130*$^{\mathrm{peKI/KI}}$ prostates, evidenced by significantly downregulated CD206 expression and a tendency towards upregulated CD86 and MHC class II compared to *Pten*$^{\mathrm{pe}\Delta/\Delta}$ prostates (Fig. 5i-j). Interestingly, selected adaptive and innate immune system-related gene sets associated with chemotaxis, migration, regulation, and activation of immune cells were significantly upregulated when comparing *Pten*$^{\mathrm{pe}\Delta/\Delta}$;*L-gp130*$^{\mathrm{peKI/KI}}$ with *Pten*$^{\mathrm{pe}\Delta/\Delta}$ samples (Supplementary Fig. 5u, Additional File 5), further substantiating the importance of infiltrating immune cells, specifically T-cells, neutrophils and macrophages, in our mouse model of PCa.

Given the importance of inflammatory cytokines in regulating the recruitment and activation of T-cells, neutrophils, and macrophages, we screened the significantly deregulated HALLMARK gene sets for related genes sets. Indeed, the gene set "Inflammatory response"

(See figure on next page.)

Fig. 5 Expression of L-gp130 in *Pten*$^{\mathrm{pe}\Delta/\Delta}$ mice increases infiltration of immune cells mediating anti-tumor defense. **a** Representative pictures of hematoxylin & eosin (H&E) stains (upper panel) showing immune infiltrate and quantification of histopathological analysis (lower panel) of prostate tissue from *Pten*$^{\mathrm{pe}\Delta/\Delta}$ ($n=11$) and *Pten*$^{\mathrm{pe}\Delta/\Delta}$;*L-gp130*$^{\mathrm{peKI/KI}}$ ($n=9$) mice in regards of infiltration (low-grade (grey) and high-grade (red)). Scale bar: 60 µm. **b** Representative pictures of immunofluorescence (IF) staining of CD45 (red) and DAPI (blue) of mouse prostates with indicated genotypes. DAPI is used as a nuclear stain. Scale bar: 20 µm. **c** Quantification of CD45$^+$ cells of IF stainings shown in b) ($n=5$). The percentage of positive cells relative to *Pten*$^{\mathrm{pe}\Delta/\Delta}$ was calculated. **d** Representative pictures of immunofluorescence (IF) staining of CD3 (yellow), CD8 (green) and DAPI (blue) of mouse prostates with indicated genotypes. DAPI is used as a nuclear stain. Scale bar: 20 µm. **e** Quantification of CD3$^+$;CD8$^+$ cells in the epithelium of IF stainings shown in d) ($n=5$). The percentage of positive cells in the prostate epithelium relative to *Pten*$^{\mathrm{pe}\Delta/\Delta}$ was calculated. **f** Representative pictures of immunohistochemistry (IHC) staining of NimpR14 (higher panel) and F4/80 (lower panel) of mouse prostates with indicated genotypes. Scale bar: 40 µm. **g**-**h**) Quantification of NimpR14$^+$ (g) and F4/80$^+$ (h) cells in the prostate epithelium of IHC stainings shown in f) ($n \geq 6$). The percentage of positive cells in the prostate epithelium relative to *Pten*$^{\mathrm{pe}\Delta/\Delta}$ was calculated. **i)** Flow cytometry data showing mean fluorescence intensity (MFI) of F4/80$^+$;Cd11b$^+$ macrophages in *Pten*$^{\mathrm{pe}\Delta/\Delta}$ and *Pten*$^{\mathrm{pe}\Delta/\Delta}$;*L-gp130*$^{\mathrm{peKI/KI}}$ prostate tissue ($n \geq 3$) for CD86, MHC class II, and CD206. **j** Representative flow cytomentry blots of data shown in i. **k** Representative pictures of IHC staining of CD3, NimpR14 and F4/80 (in presented order) of *Pten*$^{\mathrm{pe}\Delta/\Delta}$ and *Pten*$^{\mathrm{pe}\Delta/\Delta}$;Stat3$^{\mathrm{pe}\Delta/\Delta}$ prostates. Scale bar: 40 µm. **l** Semi-quantitative analysis of CD3, NimpR14 and F4/80 IHC stainings shown in k) ($n \geq 3$). **c, e, g-i, l** Individual biological replicates are shown (c,e,g-i). Data are plotted as the means ± SD and p-values were determined by unpaired two-tailed Student's t-tests (c,e,g-i) or Mann–Whitney test (l)

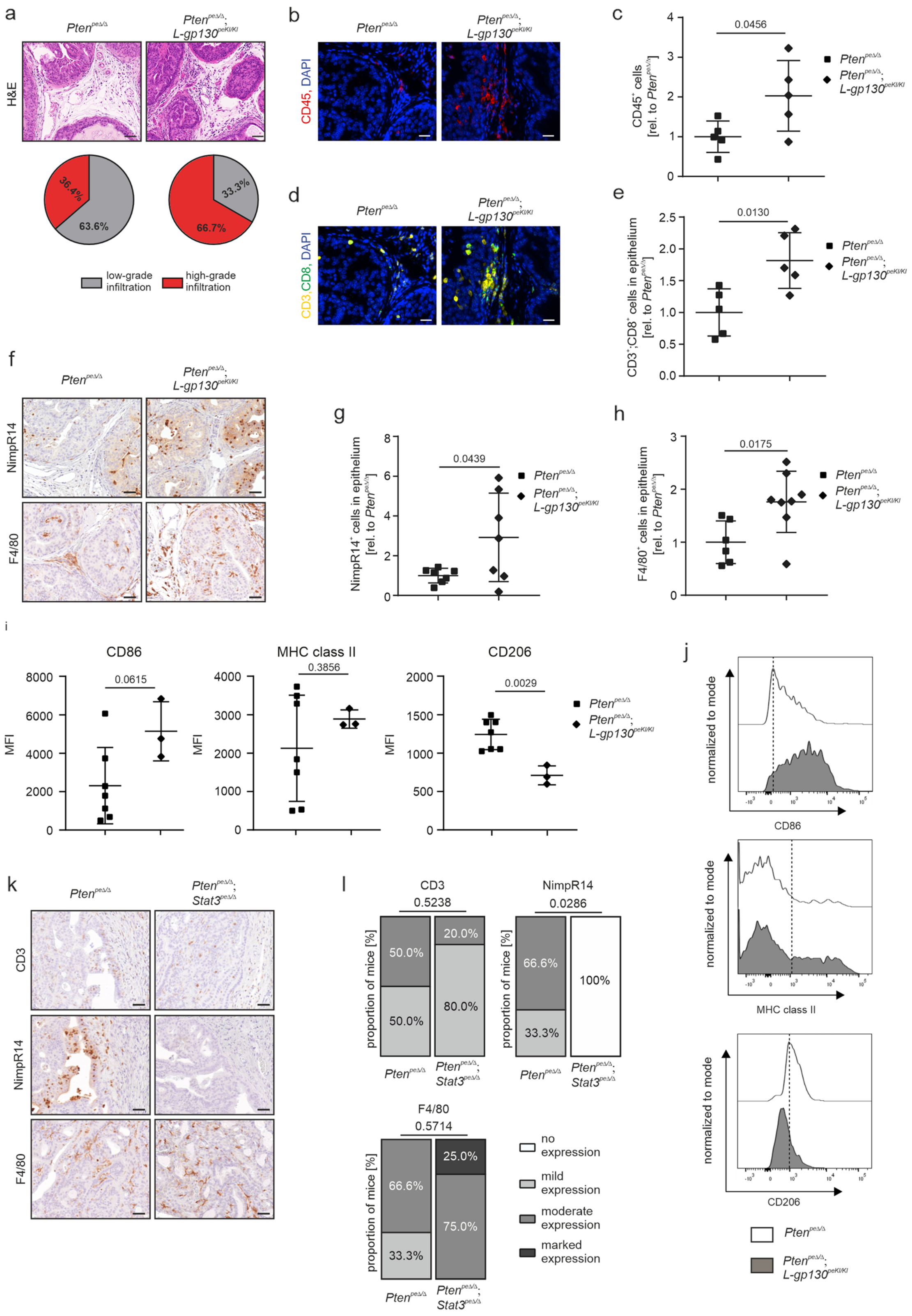

Fig. 5 (See legend on previous page.)

and signaling of the effector molecules IFNy and TNFα, which are secreted by cytotoxic T-cells and affect tumor cells [57, 58], were significantly upregulated in our RNA-Seq data set (Fig. 4a). In order to delineate the cytokine profile more comprehensively, we analyzed serum samples obtained from the PCa mouse model. We specifically assessed the expression levels of various cytokines, chemokines, and receptors, including VEGF, CCL5, TNFα, IL-1α, IL-2R, IL-12p70, CXCL1, CXCL5, CXCL10, CD27, G-CSF. The multiplex immunobead assay analysis revealed a significant alteration in the cytokine profile, characterized by a significant upregulation of the expression of inflammatory cytokines in the serum of $Pten^{pe\Delta/\Delta}$;$L\text{-}gp130^{peKI/KI}$ mice compared to the $Pten^{pe\Delta/\Delta}$ group (Supplementary Fig. 5v, Additional File 5). Taken together, these findings provide evidence that constitutively active IL6ST signaling in prostate epithelial cells, possibly through modifying the chemokine/cytokine profile, promotes the recruitment of T-cells, neutrophils, and macrophages and reshapes the TME towards higher infiltration susceptibility.

To provide mechanistic evidence that these alterations depend on STAT3 signaling, we utilized a previously established PCa mouse model featuring $Pten^{pe\Delta/\Delta}$ with an additional prostate epithelium-specific deletion of *Stat3* ($Pten^{pe\Delta/\Delta}$;$Stat3^{pe\Delta/\Delta}$). These mice exhibit rapid tumor proliferation, metastasis, and an early death, in contrast to the slow, localized tumor progression seen in $Pten^{pe\Delta/\Delta}$ mice [8]. Interestingly, several immune response-related pathways are downregulated in $Pten^{pe\Delta/\Delta}$;$Stat3^{pe\Delta/\Delta}$ compared to $Pten^{pe\Delta/\Delta}$ prostates [47]. Consistent with these findings and our data in $Pten^{pe\Delta/\Delta}$;$L\text{-}gp130^{peKI/KI}$ mice, $Pten^{pe\Delta/\Delta}$;$Stat3^{pe\Delta/\Delta}$ prostates showed no increase in the infiltration of $CD3^+$ T-cells and $F4/80^+$ macrophages, and a significant decrease in $NimpR14^+$ neutrophils compared to $Pten^{pe\Delta/\Delta}$ mice (Fig. 5k-l) highlighting the importance of STAT3 in immune cell infiltration in *Pten*-deficient PCa mice with concomitant active IL6ST signaling.

IL6ST signaling in PCa patients promotes STAT3 activation, senescence upregulation, elevated immune scores, and T-cell mediated cytotoxicity

To address the human relevance of our findings concerning the involvement of senescence and anti-tumor immunity in the proposed tumor-suppressive role of IL6ST/STAT3 signaling, we refined our analysis of the TCGA-PRAD patient data set by distinguishing $IL6ST^{high}$ and $IL6ST^{low}$ groups based on *IL6ST* mRNA expression levels (Fig. 3b). The fGSEA of HALLMARK gene sets revealed that “IL-6/JAK/STAT3 signaling” was upregulated in $IL6ST^{high}$ compared with $IL6ST^{low}$ patients (Fig. 6a), as evidenced by increased STAT3 target genes expression (Supplementary Fig. 6a, Additional File 5). The observed downregulation of “Oxidative phosphorylation” is in accordance with the inverse association with STAT3 [47] and the corresponding KEGG gene set (Supplementary Fig. 6b, Additional File 5).

As we depicted alterations in senescence and cell cycle regulators in our in vivo mouse model, we performed fGSEA excluding any patients with *TP53* mutations (Supplementary Table 4, Additional File 1). Analysis of senescence-related gene sets (previously published “Core SASP of PICS (Guccini)” [54] and “Fridman senescence up” taken from curated gene sets, class chemical and genetic perturbations (CGP)) revealed their significant upregulation in $IL6ST^{high}$ PCa patients (Fig. 6b), providing a possible explanation for their improved survival (Fig. 3b). These patients also exhibited downregulation of cell cycle gene sets (“REACTOME: Cell cycle” and “REACTOME: G1/S transition”) and upregulation of p53 signaling (“WikiPathways (WP): p53 transcriptional gene network”) (Fig. 6c).

Using ESTIMATE (Estimation of STromal and Immune cells in MAlignant Tumor tissues using Expression data), a tool for predicting tumor purity, and the presence of infiltrating stromal/immune cells in tumor tissues based on gene expression data [32], we confirmed that the majority of PCa patients can be considered immune-cold

(See figure on next page.)

Fig. 6 IL6ST signaling in PCa patients actives STAT3 signaling and upregulates senescence, immune score and cytotoxicity. **a** Fast pre-ranked gene set enrichment analysis (fGSEA) of significantly enriched HALLMARK gene sets with genes regulated in $IL6ST^{high}$ compared to $IL6ST^{low}$ expressing patients from the TCGA-PRAD data set. Dotted line: adj. p-value (-log10(0.05)), blue: downregulated, red: upregulated; **b** fGSEA of the previously described core SASP gene signature upon PICS “Core SASP of PICS (Guccini)” (upper panel) and the curated gene set, class chemical and genetic perturbations (CGP) “CGP: Fridman senescence up” (lower panel) with genes regulated in $IL6ST^{high}$ compared to $IL6ST^{low}$ expressing patients from the TCGA-PRAD data set. Genes sorted based on their Wald statistics are represented as vertical lines on the x-axis. NES: normalized enrichment score. **c** fGSEA of WikiPathways (WP) gene sets “REACTOME: Cell cycle”, “REACTOME: G1/S transition” and “WP: p53 transcriptional gene network” with genes regulated in $IL6ST^{high}$ compared to $IL6ST^{low}$ expressing patients from the TCGA-PRAD data set. Genes sorted based on their Wald statistics are represented as vertical lines on the x-axis. NES: normalized enrichment score. **d** Immune score from the ESTIMATE method for $IL6ST^{low}$ (red, $n = 208$) and $IL6ST^{high}$ (blue, $n = 283$) patients from the TCGA-PRAD data set, compared with Mann–Whitney test. **e** fGSEA of the top 20 T-cell-, neutrophil-, and macrophage-associated Biological Processes from Gene Ontology pathways (GO-BP) gene sets with genes significantly regulated in $IL6ST^{high}$ compared to $IL6ST^{low}$ expressing patients from the TCGA-PRAD data set. Dotted line: adj. p-value (-log10(0.05)), red: upregulated;

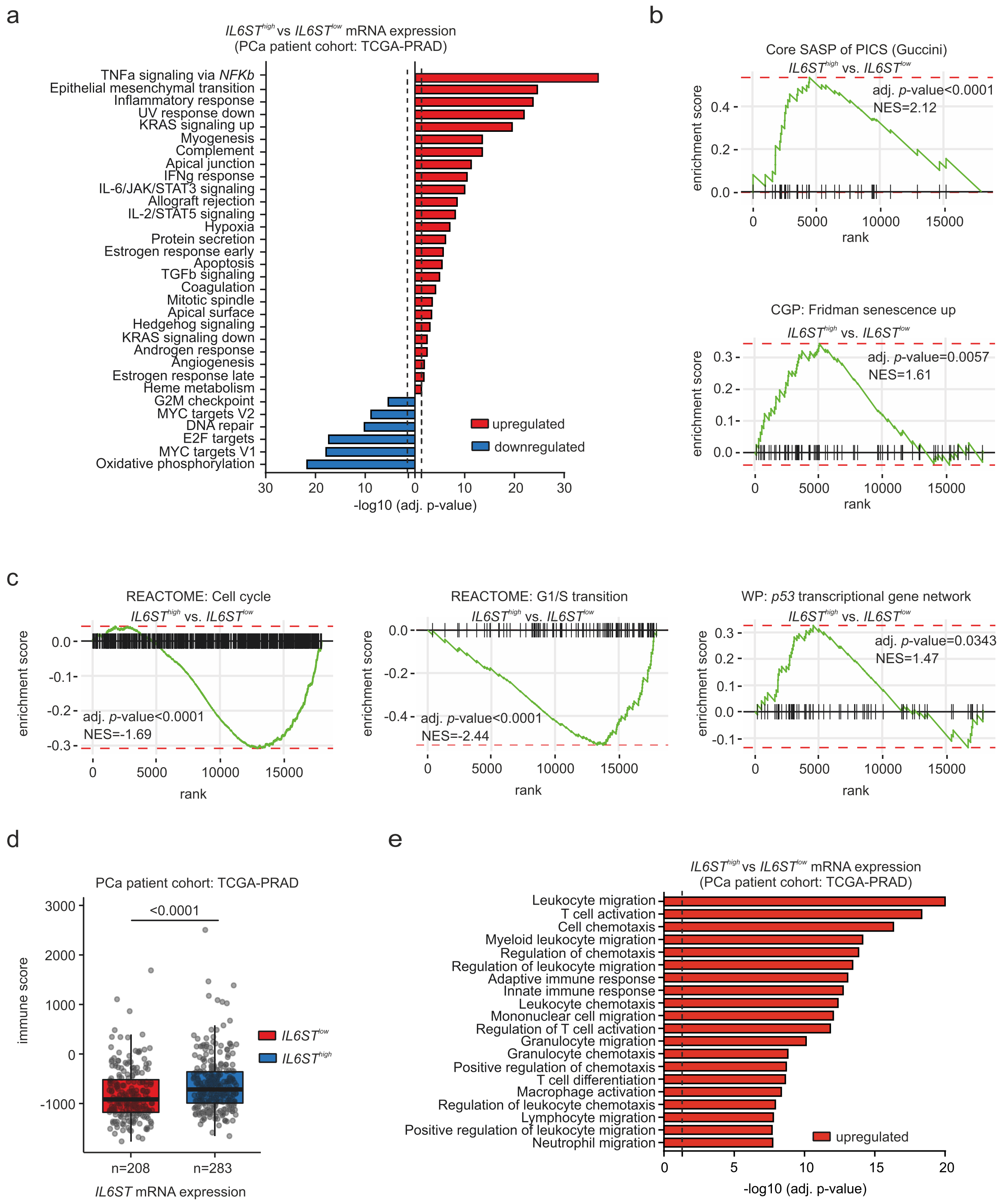

Fig. 6 (See legend on previous page.)

due to their low immune scores (Supplementary Fig. 6c, Additional File 5). Notably, higher immune scores have been associated with longer survival rates in PCa patients [59]. In our patient cohort, *IL6ST*^{high} patients showed significantly higher immune scores compared to *IL6ST*-^{low} patients (Fig. 6d), correlating with the upregulation

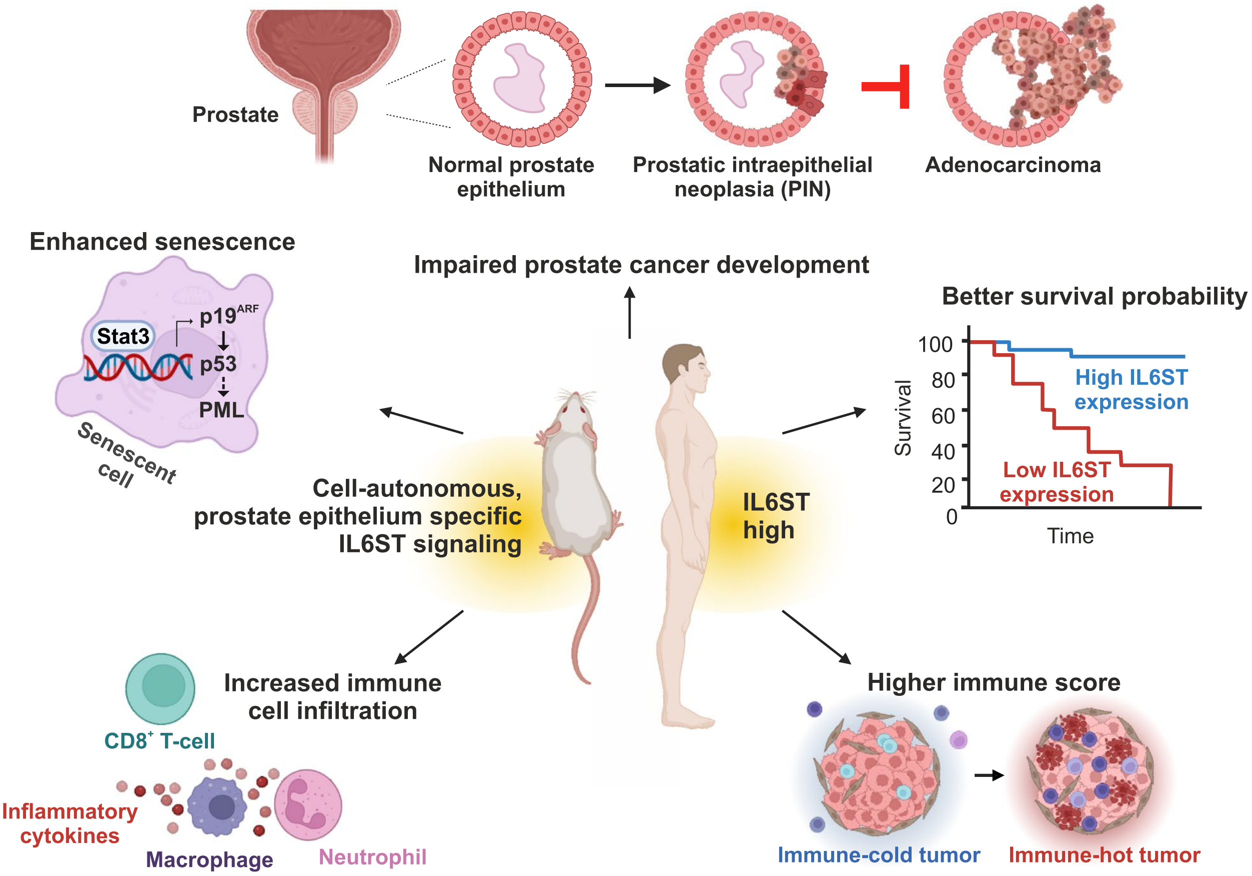

Fig. 7 Proposed roles of active IL6ST signaling in prostate tumorigenesis. Using the genetic mouse model, we showed that cell-autonomous, prostate epithelium-specific and constitutively active IL6ST signaling reduces *Pten*-deficient tumor growth, enhances the STAT3/p19^{ARF}/p53-driven senescence and recruits tumor-infiltrating immune cells (T-cells, neutrophils, and macrophages). In human PCa, high *IL6ST* expression causes active STAT3 signaling, correlates with better survival and is associated with higher level of immune infiltrates

of immune response-related gene sets (Fig. 6a). Furthermore, the top 20 GO-BP gene sets associated with T-cell activation and cytotoxicity, neutrophils and macrophages were upregulated in *IL6ST*^{high} compared to *IL6ST*^{low} expressing patients from the TCGA-PRAD data set, emphasizing the relevance of T-cell, neutrophil and macrophage mediated tumor-defense in PCa patients with high *IL6ST* expression (Fig. 6e). In summary, our data reveal that PCa patients with high *IL6ST* expression exhibit increased senescence, reduced cell cycle activity, and enhanced immune cell infiltration, which likely contribute to their improved survival outcomes.

Discussion

In this study, we show that in a *Pten*-deficient PCa mouse model engineered to constitutively activate IL6ST signaling, STAT3 activation was increased, STAT3 target gene signature was amplified and PCa tumor growth was significantly reduced compared to mice only deficient in *Pten*. The proposed roles of active IL6ST signaling in PCa observed in this study are summarized in Fig. 7. We found that enhanced STAT3 signaling was associated with more pronounced p19^{ARF}/p53 mediated cellular senescence in the tumor tissue. These findings complement previous data showing that inducing a *Stat3* knock out (KO) in PCa mice resulted in larger tumor sizes mediated by loss of senescence [7, 8]. The STAT3 signaling axis thus appears to regulate tumor growth in PCa by primarily inhibiting tumor progression rather than initiation. This is evidenced by the majority of *Pten*$^{pe\Delta/\Delta}$;*L-gp130*$^{peKI/KI}$ mice displaying PINs and not PCa, as was predominantly found in *Pten*$^{pe\Delta/\Delta}$ mice.

The data presented here provide substantial validation and significantly broaden the scope of our previously posited hypotheses [8], that 1) the STAT3/p19^{ARF} axis acts as a safeguard mechanism against malignant progression in PCa, 2) expression levels of constituents of the IL6ST/STAT3 signaling axis could act as key markers to stratify PCa cases into low- and high-risk groups, and

3) strategies aimed at manipulating this signaling pathway could serve as a novel therapeutic approach for PCa treatment.

The tumor-suppressive role of STAT3 signaling in PCa contrasts with the oncogenic function in numerous cancers, where it is often hyperactivated [4, 60]. However, accumulating evidence suggests that it may also function as tumor suppressor depending on signaling context and tumor type [61, 62]. For example, *Stat3* deletion resulted in increased astrocyte tumor formation in SCID mice in the absence but not in the presence of PTEN [63]. Additionally, in a mouse model of colorectal cancer crossed with *Stat3* conditional KO mice, *Stat3* KO in intestinal cells revealed an oncogenic role, whereas a KO during tumor progression enhanced tumor invasiveness, reflecting a tumor suppressive role [64]. In a more specific example, a mouse model of drug-induced cancer demonstrated that STAT3 expression appeared to suppress tumor formation in the presence of a toxicant causing chronic liver injury, inflammation, and fibrosis, whereas it enhanced tumor formation induced by a DNA damaging agent [65]. Further examples have been reported for lung cancer, thyroid cancer and head and neck squamous cell cancers [62], additionally supporting the notion that STAT3 signaling has a dual role, rather than a strictly oncogenic one.

As a possible molecular mechanism underlying this ambiguous behavior, activity of the STAT3β isoform has been suggested. This isoform lacks the C-terminal transactivation domain and was shown to inhibit proliferation and stimulate cell death, possibly through heterodimerizing with STAT3α, thereby preventing it from activating its target genes [61]. In contrast, our data suggest that a different mechanism mediates the tumor suppressive activity of STAT3 signaling in prostate cells with constitutively activated IL6ST. This assumption is based on the observed clear upregulation of transcription in both the absence and presence of PTEN (*Pten*$^{\mathrm{pe}\Delta/\Delta}$;*L-gp130*$^{\mathrm{peKI/KI}}$ and *L-gp130*$^{\mathrm{peKI/KI}}$ mice), as determined from differential gene expression analyses. Another aspect where context dependency seems to be decisive is senescence and its associated SASP. Both have nuanced roles in PCa, with outcomes potentially shaped by context and genetic backgrounds [66]. Examining the transcriptome upon constitutively active IL6ST signaling in greater detail, we identified a significant upregulation of the senescence-associated p19$^{\mathrm{ARF}}$/p53 pathway and PICS. Targeting senescence in this context has been suggested to potentially hold significant promise in cancer therapy [52, 67, 68]. However, a tumor-promoting effect linked to increased SASP in a PCa mouse model with additional KO of *Stat3* has been reported [69]. One possible factor contributing to this divergence in outcomes might be influenced by the specific *Stat3* KO approach that targets only the tyrosine phosphorylation site of *Stat3* and not the DNA-binding domain [70]. Variations in STAT3 expression, such as dominant-negative STAT3, can have profound implications on disease outcomes [71]. Our studies, spanning four independent mouse model systems addressing the IL-6/IL6ST/JAK2/STAT3 signaling axis, consistently indicate a tumor-suppressive effect of STAT3 activation [7, 8]. Specifically, our genetic PCa mouse model with KO of *Stat3*, in which the DNA-binding domain of *Stat3* is targeted [72], leads to aggressive PCa growth [8]. Additionally, we have previously shown that the KO of *Il6*, the activator of the IL6ST/STAT3 signaling, enhances PCa development [8]. By using an independent mouse model, our current study additionally emphasizes a tumor-suppressive role for constitutively active IL6ST/STAT3 signaling and its associated elevated SASP. This divergence in findings highlights the need to consider context- and patient-specific factors, further challenging the current discussion on the therapeutic advantages or hazards of IL-6/STAT3 inhibition.

To assess the potential clinical relevance of our murine findings, we analyzed several PCa patient cohorts. We discovered that in the overall patient population *IL6ST* expression was significantly reduced in the prostate tumor tissue compared to surrounding non-cancerous tissue. However, when we separated these patients into a high and a low *IL6ST* expressing group, we detected that higher *IL6ST* expression correlated with higher *STAT3* expression and, more importantly, with prolonged survival of these patients. Therefore, based on the hypothesis that enhanced IL6ST signaling, as observed in our mouse model, helps restrain cancer progression, we propose that *IL6ST* expression levels, possibly along with *STAT3* and *ARF* levels, could serve as indicators for low- and high-risk PCa groups. However, it must be considered that the chosen RNA analysis methods can impact the outcome [73]. Therefore, further analyses are needed to validate IL6ST expression as a prognostic marker in PCa, including protein-level analysis, robust biomarker models, and functional studies. This could help prevent overtreatment and unnecessary reductions in quality of life for PCa patients [74].

A further important potential lead for future treatment of PCa patients derived from our study is the observation that enhanced IL6ST signaling was associated with high-grade immune cell infiltration at the tumor site. This infiltration included CD3^{+};CD8^{+} T-cells, neutrophils, and M1-like macrophages that are considered major drivers of anti-tumor immunity [56, 75], and was accompanied by an upregulation of adaptive and innate immune system-related gene sets. In general, PCa cells and those comprising its microenvironment are known to express and secrete molecules mediating immunosuppression, rendering PCa immune-cold [19] and thus not a good target for otherwise highly efficient immune-based therapies [76]. PCa is also associated with low mutational burden and low immunogenicity [77], and thus little responsiveness to therapies based on immune checkpoint inhibitors [78]. Consequently, the potential to enhance immunogenicity by manipulating IL6ST signaling could present a novel therapeutic approach in PCa therapy.

Our analysis of human patient data sets supports this idea, confirming that, while most PCa patients examined must be regarded as immune-cold (as determined by the ESTIMATE tool [32]) those with high *IL6ST* expression exhibited a better immune score. These patients also showed upregulated gene sets associated with T-cells, neutrophils, and macrophages and, noteworthy, increased senescence-related gene sets. As to the latter, it remains to be shown whether immune cell infiltration is the direct consequence of enhanced IL6ST signaling and the associated senescence induction or its cause [66, 79]. In either case, there is evidence suggesting that a higher number of tumor infiltrating lymphocytes in PCa is associated with better patient outcomes [80]. Considering the immense potential of novel approaches, such as the induction of synthetic cytokine signaling circuits allowing immune cells to overcome immunosuppressive microenvironments and infiltrate immune-excluded solid tumors [81], it appears conceivable that strategies mediating prostate-specific, active IL6ST signaling have potential to effectively attack tumor cells.

Altogether, the present study reveals that increased IL6ST signaling is linked with suppressed tumor growth and amplified STAT3 target gene signatures. Contrary to its oncogenic role in many cancers, IL6ST/STAT3 signaling demonstrated tumor-suppressive activity in the context of PCa, potentially through the upregulation of the senescence-associated $p19^{ARF}/p53$ pathway. Additionally, elevated IL6ST signaling in tumors was linked to increased immune cell infiltration, implying that enhancing IL6ST signaling might be a promising therapeutic strategy for boosting anti-tumor immunity in PCa. Clinical analysis of PCa patients showed a positive correlation between high *IL6ST* expression and longer recurrence-free survival, suggesting that *IL6ST* expression levels could aid in risk stratification.

Conclusions

In conclusion, our study redefines the role of IL6ST/STAT3 signaling in PCa, uncovering its tumor-suppressive effects through senescence and immune cell recruitment. This challenges the traditional view of STAT3 as an oncogene and questions the strategy of inhibiting this pathway for PCa treatment. Advocating for IL6ST activation as a novel therapeutic strategy, we pave the way for innovative cancer therapies that leverage immune system engagement to combat tumors. Our findings position active IL6ST signaling as a crucial element in developing more effective treatments for PCa, highlighting its potential to transform PCa therapy.

Abbreviations

adj. p-value	Adjusted p-value
ARF	Alternative reading frame
AL	Anterior lobe
CAG	Synthetic CMV-Actin-Globin composite promoter
CGP	Chemical and genetic perturbations
CL	Caudal lobe
DE	Differentially expressed
EpCAM	Epithelial cell adhesion molecule
ERK	Extracellular signal-regulated kinase
ESTIMATE	Estimation of STromal and Immune cells in MAlignant Tumor tissues using Expression data
fGSEA	Fast pre-ranked gene set enrichment analysis
fl	Floxed
FFPE	Formalin-fixed paraffin-embedded
FWHM	Full width at half maximum
GP130	Glycoprotein 130 kDa = IL6ST
GO-BP	Gene Ontology Biological Process
H&E	Hematoxylin & eosin
IF	Immunofluorescence
IHC	Immunohistochemistry
IL-6	Interleukin-6
IL-6R	Interleukin-6 receptor
IL6ST	Interleukin-6 cytokine family signal transducer = GP130
JAK	Janus kinase
KEGG	Kyoto Encyclopedia of Genes and Genomes
KI	Knock in
KO	Knock out
L-gp130	Leucine-gp130
MAPK	Mitogen-activated protein kinase
MFI	Mean fluorescence intensity
NES	Normalized enrichment score
OIS	Oncogene-induced senescence
P	Phospho
PB	Probasin
PCa	Prostate cancer
PCR	Polymerase chain reaction
Pe	Prostate epithelium
PICS	PTEN-loss induced cellular senescence
PIN	Prostatic intraepithelial neoplasia
PI3K	Phosphatidylinositol 3-kinase
PML	Promyelocytic leukemia protein
PTEN	Phosphatase and tensin homolog
qRT-PCR	Quantitative reverse transcription-polymerase chain reaction
RNA-Seq	RNA sequencing
SASP	Senescence-associated secretory phenotype
SD	Standard deviation
SHP2	Src homology 2 domain-containing tyrosine phosphatase-2
ssGSVA	Single sample gene set variation analysis
STAT3	Signal transducer and activator of transcription 3
T	Total
TCGA-PRAD	The Cancer Genome Atlas-PRostate ADenocarcinoma
TME	Tumor microenvironment
VST	Variance stabilizing transformation
WP	WikiPathways
ZSGreen	Zoanthus sp. green fluorescent protein

Supplementary Information

The online version contains supplementary material available at https://doi.org/10.1186/s12943-024-02114-8.

Additional File 1: Supplementary tables.

Additional File 2: Detailed histopathological analysis of mouse prostate lobes 1.

Additional File 3: Detailed histopathological analysis of mouse prostate lobes 2.

Additional File 4: Supplementary methods.

Additional File 5: Supplementary figures and figure legend.

Additional File 6: Flow cytometry gating strategy.

Acknowledgements

We acknowledge the Core Facility Bioinformatics supported by the NCMG research infrastructure (LM2023067 funded by MEYS CR) for their support with the bioinformatic analysis of the RNA sequencing data presented in this paper. This research was supported using resources of the VetCore Facility (VetImaging) of the University of Veterinary Medicine Vienna. The authors are grateful to Dr. Natalie Bordag (Medical University of Graz) for providing help with R programming and bioinformatic analysis, and to Anton Jäger (Medical University of Vienna) for his assistance in generating macroscopic pictures and graphical illustrations. Scientific coaching to C.S. was provided by Gerhard Krumschnabel (medical-writing.at) and was funded by University of Veterinary Medicine Vienna. We acknowledge the use of BioRender.com for creating Fig. 1a, Fig. 4j and Fig. 7.

Authors' contributions

Conceptualization and design: C.S., S.R.-J., L.K.; Development of methodology: C.S., M.R., T.L., K.T., J.K., D.Z., M.O., F.S., S.H., S.L., S.R.-J.; Acquisition of data: C.S., M.R., T.L., K.T., D.L., M.S., R.Z., J.K., S.S., S.D., D.Z., H.A.N., M.O., T.R., F.S.; Technical assistance: M.S., P.K., J.Y., B.T., M.T., N.S.H., S.T.; Project administration: C.S., S.R.-J., L.K.; Formal analysis: C.S., M.R., K.T., V.H., F.S.; Analysis and interpretation of data: C.S., T.L., H.A.N., F.S., S.H., S.L., S.R.-J., L.K.; Resources: C.S., J.P., V.B., J.L.P., G.E., S.P., R.E., P.W., S.R.-J., L.K.; Study supervision: S.R.-J., L.K.; Funding acquisition: S.R.-J., L.K.; Writing—original draft: C.S.; Figure preparation: C.S., M.R., M.S., F.S.; Writing—review & editing: C.S., M.R., T.L., K.T., H.A.N., S.S., S.D., M.O., T.R., P.W., F.S., S.H., S.L., S.R.-J., L.K.; All authors read and approved the final manuscript.

Authors' information

Not applicable.

Funding

This study was financially supported by grant Nr. 70112589 from the Deutsche Krebshilfe, Bonn, Germany to S.R.-J. L.K. acknowledges the support from MicroONE, a COMET Modul under the lead of CBmed GmbH, which is funded by the federal ministries BMK and BMDW, the provinces of Styria and Vienna, and managed by the Austrian Research Promotion Agency (FFG) within the COMET-Competence Centers for Excellent Technologies-program. Financial support was also received from the Austrian Federal Ministry of Science, Research and Economy, the National Foundation for Research, Technology and Development, the Christian Doppler Research Association and Siemens Healthineers. L.K. was also supported by European Union Horizon 2020 Marie Sklodowska-Curie Doctoral Network grants (ALKATRAS, n. 675712; FANTOM, n. P101072735 and eRaDicate, n. 101119427) as well as BM Fonds (n. 15142), the Margaretha Hehberger Stiftung (n. 15142), the Christian Doppler Lab for Applied Metabolomics (CDL-AM), and the Austrian Science Fund (FWF) P26011, P29251 and P34781. This work was also supported by the Austrian Science Fund (FWF) W1241 to P.W., the Austrian Science Fund (FWF) DOC 59–833 "International PhD Program in Translational Oncology – IPPTO" to R.E. and L.K., the Austrian Science Fund (FWF) P35069-B "CDHR5 in Intestinal Barrier Function and Inflammation" to R.E. and the Austrian Science Fund (FWF) P32771 to J.K. and G.E. Additionally, this research was funded by the Vienna Science and Technology Fund (WWTF), grant number LS19-018. L.K. is a member of the European Research Initiative for ALK-Related Malignancies (www.erialcl.net). The National Institute for Cancer Research (Programme EXCELES, No. LX22NPO5102) funded by Next Generation EU is gratefully acknowledged for funding.

Availability of data and materials

The RNA-Seq data set supporting the conclusions of this article is publicly available in the GEO repository with the accession number GSE277063. The following publicly available data sets were used: TCGA-PRAD [28], MSKCC Prostate GSE21032 [44], SMD GSE40272 [45] and data sets provided by the Oncomine™ Research Premium Edition database [42] and by MSigDB [35].

Declarations

Ethics approval and consent to participate

Animal experiments and care were conducted in accordance with the guidelines of institutional authorities and approved by the Federal Ministry of Austria for Education, Science and Research (BMWFW-66.009/0307-WF/V/3b/2017 and the associated amendments).

Consent for publication

Not applicable.

Competing interests

The authors declare no competing interests.

Author details

[1]Department of Pathology, Medical University of Vienna, Vienna, Austria. [2]Biochemical Institute, University of Kiel, Kiel, Germany. [3]Unit of Laboratory Animal Pathology, University of Veterinary Medicine Vienna, Vienna, Austria. [4]Department of Biomedical Imaging and Image-Guided Therapy, Division of Nuclear Medicine, Medical University of Vienna, Vienna, Austria. [5]Center for Biomarker Research in Medicine GmbH (CBmed), Graz, Styria, Austria. [6]Central European Institute of Technology, Masaryk University, Brno, Czech Republic. [7]Christian Doppler Laboratory for Applied Metabolomics, Medical University of Vienna, Vienna, Austria. [8]Department of Dermatology and Venereology, Medical University of Graz, Graz, Austria. [9]Center for Cancer Research, Medical University of Vienna & Comprehensive Cancer Center, Vienna, Austria. [10]Institute of Animal Breeding and Genetics, University of Veterinary Medicine Vienna, Vienna, Austria. [11]Department of Molecular Biology, Umeå University, Umeå, Sweden. [12]Department of Biomedical Sciences, Malmö Universitet, Malmö, Sweden. [13]Comprehensive Cancer Center, Medical University of Vienna, Vienna, Austria. [14]BioTechMed Graz, Graz, Austria. [15]Department of Nutritional Sciences, Faculty of Life Sciences, University of Vienna, Vienna, Austria. [16]Department of Biological Sciences and Pathobiology, Physiology and Biophysics, University of Veterinary Medicine Vienna, Vienna, Austria. [17]Department of Cell Biology, Charles University, Prague, Czech Republic and Biotechnology and Biomedicine Centre of the Academy of Sciences and Charles University (BIOCEV), Vestec u Prahy, Czech Republic. [18]Institute of Medical Biochemistry, University of Veterinary Medicine Vienna, Vienna, Austria.

Received: 17 March 2024 Accepted: 5 September 2024

References

1. Wang L, Lu B, He M, Wang Y, Wang Z, Du L. Prostate Cancer Incidence and Mortality: Global Status and Temporal Trends in 89 Countries From 2000 to 2019. Front Public Health. 2022;10:176.
2. del Pino-Sedeño T, Infante-Ventura D, de Armas CA, de Pablos-Rodríguez P, Rueda-Domínguez A, Serrano-Aguilar P, Trujillo-Martín MM. Molecular Biomarkers for the Detection of Clinically Significant Prostate Cancer: A Systematic Review and Meta-analysis. Eur Urol Open Sci. 2022;46:105–27.
3. Scherger AK, Al-Maarri M, Maurer HC, et al. Activated gp130 signaling selectively targets B cell differentiation to induce mature lymphoma and plasmacytoma. JCI Insight. 2019;4:e128435–e128435.
4. Golus M, Bugajski P, Chorbińska J, Krajewski W, Lemiński A, Saczko J, Kulbacka J, Szydełko T, Małkiewicz B. STAT3 and Its Pathways' Dysregulation-Underestimated Role in Urological Tumors. Cells. 2022;11:3024.

5. Mora LB, Buettner R, Seigne J, et al. Constitutive activation of Stat3 in human prostate tumors and cell lines: Direct inhibition of Stat3 signaling induces apoptosis of prostate cancer cells. Cancer Res. 2002;62:6659–66.
6. Lee H, Jeong AJ, Ye SK. Highlighted STAT3 as a potential drug target for cancer therapy. BMB Rep. 2019;52:415–23.
7. Pencik J, Philippe C, Schlederer M, et al. STAT3/LKB1 controls metastatic prostate cancer by regulating mTORC1/CREB pathway. Mol Cancer. 2023;22:133.
8. Pencik J, Schlederer M, Gruber W, et al. STAT3 regulated ARF expression suppresses prostate cancer metastasis. Nat Commun. 2015;6:7736–8802.
9. Schaper F, Rose-John S. Interleukin-6: Biology, signaling and strategies of blockade. Cytokine Growth Factor Rev. 2015;26:475–87.
10. Liu Z, Zhao Y, Fang J, Cui R, Xiao Y, Xu Q. SHP2 negatively regulates HLA-ABC and PD-L1 expression via STAT1 phosphorylation in prostate cancer cells. Oncotarget. 2017;8:53518–30.
11. Chen H, Zhou L, Wu X, Li R, Wen J, Sha J, Wen X. The PI3K/AKT pathway in the pathogenesis of prostate cancer. Front Biosci - Landmark. 2016;21:1084–91.
12. Sheng X, Bin LW, Wang DL, Chen KH, Cao JJ, Luo Z, He J, Li MC, Liu WJ, Yu C. YAP is closely correlated with castration-resistant prostate cancer, and downregulation of YAP reduces proliferation and induces apoptosis of PC-3 cells. Mol Med Rep. 2015;12:4867–76.
13. Jamaspishvili T, Berman DM, Ross AE, Scher HI, De Marzo AM, Squire JA. Lotan TL (2018) Clinical implications of PTEN loss in prostate cancer. Nat Rev Urol. 2018;15(4):222–34.
14. Choudhury AD. PTEN-PI3K pathway alterations in advanced prostate cancer and clinical implications. Prostate. 2022;82(Suppl 1):S60–72.
15. Chen Z, Trotman LC, Shaffer D, et al. Crucial role of p53-dependent cellular senescence in suppression of Pten-deficient tumorigenesis. Nature. 2005;436:725–30.
16. Parisotto M, Grelet E, El Bizri R, Metzger D. Senescence controls prostatic neoplasia driven by Pten loss. Mol Cell Oncol. 2019;6:1511205.
17. Young ARJ, Narita M. SASP reflects senescence. EMBO Rep. 2009;10:228–30.
18. Huang W, Hickson LTJ, Eirin A, Kirkland JL, Lerman LO. Cellular senescence: the good, the bad and the unknown. Nat Rev Nephrol. 2022;18:611–27.
19. Stultz J, Fong L. How to turn up the heat on the cold immune microenvironment of metastatic prostate cancer. Prostate Cancer Prostatic Dis. 2021;24:697–717.
20. Suzuki A, Yamaguchi MT, Ohteki T, et al. T cell-specific loss of Pten leads to defects in central and peripheral tolerance. Immunity. 2001;14:523–34.
21. Wu X, Wu J, Huang J, Powell WC, Zhang JF, Matusik RJ, Sangiorgi FO, Maxson RE, Sucov HM, Roy-Burman P. Generation of a prostate epithelial cell-specific Cre transgenic mouse model for tissue-specific gene ablation. Mech Dev. 2001;101:61–9.
22. Limberger T, Schlederer M, Trachtová K, et al. KMT2C methyltransferase domain regulated INK4A expression suppresses prostate cancer metastasis. Mol Cancer. 2022;21:1–19.
23. Birbach A, Eisenbarth D, Kozakowski N, Ladenhauf E, Schmidt-Supprian M, Schmid JA. Persistent inflammation leads to proliferative neoplasia and loss of smooth muscle cells in a prostate tumor model. Neoplasia. 2011;13:692–703.
24. Redmer T, Raigel M, Sternberg C, et al. JUN mediates the senescence associated secretory phenotype and immune cell recruitment to prevent prostate cancer progression. Mol Cancer. 2024;23:114.
25. Schmidt U, Weigert M, Broaddus C, Myers G (2018) Cell Detection with Star-Convex Polygons. In: Frangi A., Schnabel J., Davatzikos C., Alberola-López C., Fichtinger G. (eds) Medical Image Computing and Computer Assisted Intervention – MICCAI 2018. Lecture Notes in Computer Science, vol 11071. Springer, Cham. p. 265–273. https://link.springer.com/chapter/10.1007/978-3-030-00934-2_30.
26. Ding Z, Wu CJ, Chu GC, et al. SMAD4-dependent barrier constrains prostate cancer growth and metastatic progression. Nature. 2011;470:269–76.
27. Drost J, Karthaus WR, Gao D, Driehuis E, Sawyers CL, Chen Y, Clevers H. Organoid culture systems for prostate epithelial and cancer tissue. Nat Protoc. 2016;11:347–58.
28. Abeshouse A, Ahn J, Akbani R, et al. The Molecular Taxonomy of Primary Prostate Cancer. Cell. 2015;163:1011–25.
29. Gao J, Aksoy BA, Dogrusoz U, et al. Integrative analysis of complex cancer genomics and clinical profiles using the cBioPortal. Sci Signal. 2013;6:1.
30. Cerami E, Gao J, Dogrusoz U, et al. The cBio cancer genomics portal: an open platform for exploring multidimensional cancer genomics data. Cancer Discov. 2012;2:401–4.
31. CRAN - Package survminer. https://cran.r-project.org/web/packages/survminer/index.html. Accessed 9 Feb 2023.
32. Yoshihara K, Shahmoradgoli M, Martínez E, et al. Inferring tumour purity and stromal and immune cell admixture from expression data. Nat Commun. 2013;4:2612.
33. Stuhlmann-Laeisz C, Lang S, Chalaris A, et al. Forced dimerization of gp130 leads to constitutive STAT3 activation, cytokine-independent growth, and blockade of differentiation of embryonic stem cells. Mol Biol Cell. 2006;17:2986–95.
34. Wang S, Gao J, Lei Q, et al. Prostate-specific deletion of the murine Pten tumor suppressor gene leads to metastatic prostate cancer. Cancer Cell. 2003;4(3):209–21.
35. Subramanian A, Tamayo P, Mootha VK, et al. Gene set enrichment analysis: A knowledge-based approach for interpreting genome-wide expression profiles. Proc Natl Acad Sci U S A. 2005;102:15545–50.
36. Liberzon A, Birger C, Thorvaldsdóttir H, Ghandi M, Mesirov JP, Tamayo P. The Molecular Signatures Database (MSigDB) hallmark gene set collection. Cell Syst. 2015;1:417.
37. Swoboda A, Soukup R, Eckel O, et al. STAT3 promotes melanoma metastasis by CEBP-induced repression of the MITF pathway. Oncogene. 2021;40:1091–105.
38. Azare J, Leslie K, Al-Ahmadie H, Gerald W, Weinreb PH, Violette SM, Bromberg J. Constitutively activated Stat3 induces tumorigenesis and enhances cell motility of prostate epithelial cells through integrin beta 6. Mol Cell Biol. 2007;27:4444–53.
39. Carpenter RL, Lo HW. STAT3 Target Genes Relevant to Human Cancers. Cancers (Basel). 2014;6:897–925.
40. Darnell JE. Kerr Ian M, Stark GR (1994) Jak-STAT Pathways and Transcriptional Activation in Response to IFNs and Other Extracellular Signaling Proteins. Science. 1979;264:1415–21.
41. Wen Z, Zhong Z, Darnell JE. Maximal Activation of Transcription by Statl and Stat3 Requires Both Tyrosine and Serine Phosphorylation. Cell. 1995;82:241–50.
42. Rhodes DR, Yu J, Shanker K, Deshpande N, Varambally R, Ghosh D, Barrette T, Pandey A, Chinnaiyan AM. ONCOMINE: a cancer microarray database and integrated data-mining platform. Neoplasia. 2004;6:1–6.
43. Aguirre-Gamboa R, Gomez-Rueda H, Martínez-Ledesma E, Martínez-Torteya A, Chacolla-Huaringa R, Rodriguez-Barrientos A, Tamez-Peña JG, Treviño V. SurvExpress: an online biomarker validation tool and database for cancer gene expression data using survival analysis. PLoS ONE. 2013;8:e74250.
44. Taylor BS, Schultz N, Hieronymus H, et al. Integrative Genomic Profiling of Human Prostate Cancer. Cancer Cell. 2010;18:11–22.
45. Gulzar ZG, Mckenney JK, Brooks JD. Increased expression of NuSAP in recurrent prostate cancer is mediated by E2F1. Oncogene. 2013;32:70–7.
46. Tan MH, Li J, Xu HE, Melcher K, Yong EL. Androgen receptor: structure, role in prostate cancer and drug discovery. Acta Pharmacol Sin. 2015;36:3–23. https://doi.org/10.1038/aps.2014.18. https://www.nature.com/articles/aps201418#citeas.
47. Oberhuber M, Pecoraro M, Rusz M, et al (2020) STAT3-dependent analysis reveals PDK4 as independent predictor of recurrence in prostate cancer. Mol Syst Biol. https://doi.org/10.15252/MSB.20199247
48. Wiebringhaus R, Pecoraro M, Neubauer HA, et al. Proteomic analysis identifies ndufs1 and atp5o as novel markers for survival outcome in prostate cancer. Cancers (Basel). 2021;13:6036.
49. Kiuchi N, Nakajima K, Ichiba M, Fukada T, Narimatsu M, Mizuno K, Hibi M, Hirano T. STAT3 Is Required for the gp130-mediated Full Activation of the c-myc Gene. J Exp Med. 1999;189:63–73.
50. Johnson DE, O'Keefe RA, Grandis JR. Targeting the IL-6/JAK/STAT3 signalling axis in cancer. Nat Rev Clin Oncol. 2018;15(4):234–48.
51. Hanahan D. Hallmarks of Cancer: New Dimensions. Cancer Discov. 2022;12:31–46.
52. Alimonti A, Nardella C, Chen Z, et al. A novel type of cellular senescence that can be enhanced in mouse models and human tumor xenografts to suppress prostate tumorigenesis. J Clin Invest. 2010;120:681–93.
53. Bischof O, Kirsh O, Pearson M, Itahana K, Pelicci PG, Dejean A. Deconstructing PML-induced premature senescence. EMBO J. 2002;21:3358–69.

54. Guccini I, Revandkar A, D'Ambrosio M, et al. Senescence Reprogramming by TIMP1 Deficiency Promotes Prostate Cancer Metastasis. Cancer Cell. 2021;39:68–82.e9.
55. Ouelle DE, Zindy F, Ashmun RA, Sherr CJ. Alternative reading frames of the INK4a tumor suppressor gene encode two unrelated proteins capable of inducing cell cycle arrest. Cell. 1995;83:993–1000.
56. Reiser J, Banerjee A. Effector, Memory, and Dysfunctional CD8(+) T Cell Fates in the Antitumor Immune Response. J Immunol Res. 2016. https://doi.org/10.1155/2016/8941260.
57. Jorgovanovic D, Song M, Wang L, Zhang Y. Roles of IFN-γ in tumor progression and regression: a review. Biomark Res. 2020;8:49. https://doi.org/10.1186/s40364-020-00228-x.
58. Farhood B, Najafi M, Mortezaee K. CD8+ cytotoxic T lymphocytes in cancer immunotherapy: A review. J Cell Physiol. 2019;234:8509–21.
59. Sun W, Shi H, Yuan Z, Xia L, Xiang X, Quan X, Shi W, Jiang L. Prognostic Value of Genes and Immune Infiltration in Prostate Tumor Microenvironment. Front Oncol. 2020. https://doi.org/10.3389/FONC.2020.584055/FULL.
60. Tošić I, Frank DA. STAT3 as a mediator of oncogenic cellular metabolism: Pathogenic and therapeutic implications. Neoplasia. 2021;23:1167–78.
61. Zhang HF, Lai R. STAT3 in cancer-friend or foe? Cancers (Basel). 2014;6:1408–40.
62. Tolomeo M, Cascio A. The Multifaced Role of STAT3 in Cancer and Its Implication for Anticancer Therapy. Int J Mol Sci. 2021;22:603.
63. De La Iglesia N, Konopka G, Puram SV, Chan JA, Bachoo RM, You MJ, Levy DE, DePinho RA, Bonni A. Identification of a PTEN-regulated STAT3 brain tumor suppressor pathway. Genes Dev. 2008;22:449–62.
64. Musteanu M, Blaas L, Mair M, et al. Stat3 is a negative regulator of intestinal tumor progression in Apc(Min) mice. Gastroenterology. 2010. https://doi.org/10.1053/J.GASTRO.2009.11.049.
65. Wang H, Lafdil F, Wang L, Park O, Yin S, Niu J, Miller AM, Sun Z, Gao B. Hepatoprotective versus oncogenic functions of STAT3 in liver tumorigenesis. Am J Pathol. 2011;179:714–24.
66. Schmitt CA, Wang B, Demaria M. Senescence and cancer — role and therapeutic opportunities. Nat Rev Clin Oncol. 2022;19:619–36.
67. Rufini A, Tucci P, Celardo I, Melino G. Senescence and aging: the critical roles of p53. Oncogene. 2013;32:5129–43. https://doi.org/10.1038/onc.2012.640.
68. Bousset L, Gil J. Targeting senescence as an anticancer therapy. Mol Oncol. 2022;16:3855–80.
69. Toso A, Revandkar A, DiMitri D, et al. Enhancing chemotherapy efficacy in Pten-deficient prostate tumors by activating the senescence-associated antitumor immunity. Cell Rep. 2014;9:75–89.
70. Takeda K, Kaisho T, Yoshida N, Takeda J, Kishimoto T, Akira S. Stat3 activation is responsible for IL-6-dependent T cell proliferation through preventing apoptosis: generation and characterization of T cell-specific Stat3-deficient mice. J Immunol. 1998;161(9):4652–60. Erratum in: J Immunol. 2015;194(7):3526. https://doi.org/10.4049/jimmunol.1500168. https://pubmed.ncbi.nlm.nih.gov/9794394/.
71. Minegishi Y, Saito M, Tsuchiya S, et al. Dominant-negative mutations in the DNA-binding domain of STAT3 cause hyper-IgE syndrome. Nature. 2007;448:1058–62.
72. Alonzi T, Maritano D, Gorgoni B, Rizzuto G, Libert C, Poli V. Essential Role of STAT3 in the Control of the Acute-Phase Response as Revealed by Inducible Gene Activation in the Liver. Mol Cell Biol. 2001;21:1621–32.
73. Kremer A, Kremer T, Kristiansen G, Tolkach Y. Where is the limit of prostate cancer biomarker research? Systematic investigation of potential prognostic and diagnostic biomarkers. BMC Urol. 2019;19:46.
74. Loeb S, Bjurlin MA, Nicholson J, Tammela TL, Penson DF, Carter HB, Carroll P, Etzioni R. Overdiagnosis and overtreatment of prostate cancer. Eur Urol. 2014;65:1046–55.
75. Russo M, Nastasi C. Targeting the Tumor Microenvironment: A Close Up of Tumor-Associated Macrophages and Neutrophils. Front Oncol. 2022. https://doi.org/10.3389/fonc.2022.871513.
76. Strasner A, Karin M. Immune infiltration and prostate cancer. Front Oncol. 2015;5:128.
77. Wang L, Pan S, Zhu B, Yu Z, Wang W. Comprehensive analysis of tumour mutational burden and its clinical significance in prostate cancer. BMC Urol. 2021;21:1–10.
78. Maleki Vareki S. High and low mutational burden tumors versus immunologically hot and cold tumors and response to immune checkpoint inhibitors. J Immunother Cancer. 2018;6:157.
79. Reimann M, Schrezenmeier J, Richter-Pechanska P, et al. Adaptive T-cell immunity controls senescence-prone MyD88- or CARD11-mutant B-cell lymphomas. Blood. 2021;137:2785–99.
80. Miyake M, Hori S, Owari T, Oda Y, Tatsumi Y, Nakai Y, Fujii T, Fujimoto K. Clinical Impact of Tumor-Infiltrating Lymphocytes and PD-L1-Positive Cells as Prognostic and Predictive Biomarkers in Urological Malignancies and Retroperitoneal Sarcoma. Cancers (Basel). 2020;12:1–28.
81. Allen GM, Frankel NW, Reddy NR, Bhargava HK, Yoshida MA, Stark SR, Purl M, Lee J, Yee JL, Yu W, Li AW, Garcia KC, El-Samad H, Roybal KT, Spitzer MH, Lim WA. Synthetic cytokine circuits that drive T cells into immune-excluded tumors. Science. 2022;378(6625):eaba1624. https://doi.org/10.1126/science.aba1624.

Publisher's Note

IVYSPRING
INTERNATIONAL PUBLISHER

Theranostics

2024; 14(12): 4570-4581. doi: 10.7150/thno.96921

Research Paper

A novel assessment of whole-mount Gleason grading in prostate cancer to identify candidates for radical prostatectomy: a machine learning-based multiomics study

Jing Ning*[1,2,3], Clemens P. Spielvogel*[1,2], David Haberl[1,2], Karolina Trachtova[1,4], Stefan Stoiber[1,2], Sazan Rasul[2], Vojtech Bystry[4], Gabriel Wasinger[3], Pascal Baltzer[5], Elisabeth Gurnhofer[3], Gerald Timelthaler[6], Michaela Schlederer[3], Laszlo Papp[7], Helga Schachner[3], Thomas Helbich[5], Markus Hartenbach[2], Bernhard Grubmüller[8,9], Shahrokh F Shariat[10,11,12,13], Marcus Hacker[2], Alexander Haug[1,2], Lukas Kenner[1,3,14,15,16]✉

1. Christian Doppler Laboratory for Applied Metabolomics, Medical University of Vienna, 1090 Vienna, Austria.
2. Division of Nuclear Medicine, Department of Biomedical Imaging and Image-Guided Therapy, Medical University of Vienna, 1090 Vienna, Austria.
3. Department of Pathology, Medical University of Vienna, 1090 Vienna, Austria
4. Central European Institute of Technology, Masaryk University, Brno 62500, Czech Republic.
5. Department of Biomedical Imaging and Image-guided Therapy, Medical University of Vienna, 1090 Vienna, Austria.
6. Center for Cancer Research, Medical University of Vienna, 1090 Vienna, Austria.
7. Center for Medical Physics and Biomedical Engineering, Medical University of Vienna, Vienna, Austria.
8. Working Group of Diagnostic Imaging in Urology, Austrian Society of Urology, Vienna, Austria.
9. Department of Urology and Andrology, University Hospital Krems, Karl Landsteiner University of Health Sciences, Krems, Austria.
10. Department of Urology, Comprehensive Cancer Center, Medical University of Vienna, Vienna, Austria.
11. Department of Urology, Weill Cornell Medical College, New York, New York.
12. Department of Urology, University of Texas Southwestern, Dallas, Texas, USA
13. Hourani Center for Applied Scientific Research, Al-Ahliyya Amman University, Amman, Jordan.
14. Unit of Laboratory Animal Pathology, University of Veterinary Medicine Vienna, 1210 Vienna, Austria.
15. Comprehensive Cancer Center, Medical University Vienna, Vienna, Austria.
16. Center for Biomarker Research in Medicine (CBmed), Graz, Styria, Austria.

*First authors contributed equally.

✉ Corresponding author: Lukas Kenner, Address: Währinger Gürtel 18-20 1Q, 1090 Vienna, Austria; E-mail: lukas.kenner@meduniwien.ac.at; Tel.: +43 1 40400 3659.

Received: 2024.04.03; Accepted: 2024.07.10; Published: 2024.08.01

Abstract

Purpose: This study aims to assess whole-mount Gleason grading (GG) in prostate cancer (PCa) accurately using a multiomics machine learning (ML) model and to compare its performance with biopsy-proven GG (bxGG) assessment.

Materials and Methods: A total of 146 patients with PCa recruited in a pilot study of a prospective clinical trial (NCT02659527) were retrospectively included in the side study, all of whom underwent ^{68}Ga-PSMA-11 integrated positron emission tomography (PET) / magnetic resonance (MR) before radical prostatectomy (RP) between May 2014 and April 2020. To establish a multiomics ML model, we quantified PET radiomics features, pathway-level genomics features from whole exome sequencing, and pathomics features derived from immunohistochemical staining of 11 biomarkers. Based on the multiomics dataset, five ML models were established and validated using 100-fold Monte Carlo cross-validation.

Results: Among five ML models, the random forest (RF) model performed best in terms of the area under the curve (AUC). Compared to bxGG assessment alone, the RF model was superior in terms of AUC (0.87 vs 0.75), specificity (0.72 vs 0.61), positive predictive value (0.79 vs 0.75), and accuracy (0.78 vs 0.77) and showed slightly decreased sensitivity (0.83 vs 0.89) and negative predictive value (0.80 vs 0.81). Among the feature categories, bxGG was identified as the most important feature, followed by pathomics, clinical, radiomics and genomics features. The three important individual features were bxGG, PSA staining and one intensity-related radiomics feature.

Conclusion: The findings demonstrate a superior assessment of the developed multiomics-based ML model in whole-mount GG compared to the current clinical baseline of bxGG. This enables personalized patient management by identifying high-risk PCa patients for RP.

Keywords: prostate cancer, PSMA, Gleason grading, machine learning, multiomics

Introduction

Prostate cancer (PCa) is the second leading cancer-related death in men, with an incidence of nearly 20% worldwide [1]. PCa has the highest five-year survival rate (98%) for all stages combined among different tumor types [2]. As first-line therapy, radical prostatectomy (RP) has substantially contributed to this phenomenon [3]. However, as a consequence of RP, around 31% of patients suffer from urinary incontinence [4], and about 90% suffer from erectile dysfunction [5]. Hence, precise identification of individuals who experience minimal clinical advantages but encounter substantial adverse effects in RP is of utmost importance. Currently, the decision on whether to perform RP is mainly determined by biopsy-proven Gleason score (bxGS)[6]. Despite its important role in identifying PCa type, stage, differentiation, and the resulting influence on treatment modality [7], several studies have revealed a strong discrepancy between bxGS and whole-mount GS after RP [8–10]. Since whole-mount GS holds a strong association with clinical outcomes [11–13], a more reliable method to assess whole-mount Gleason grading (GG) is needed to accurately identify candidates for RP.

Multiomics provides urologists with comprehensive insights into various aspects of PCa [14], including genetic signatures from genomics, molecular heterogeneity from radiomics, and protein expression from pathomics. Genetic tests of PCa biopsy samples are currently available to predict subsequent disease progression after RP [15]. While genomics is nowadays part of the standard repertoire of cancer research approaches, the full prospects of pathomics and positron emission tomography (PET)-based radiomics yet remain to be explored. Radiomics is an emerging field where imaging features are extracted for objective and quantitative tumor characterization [16]. Radiomics application on prostate-specific membrane antigen (PSMA) PET scans has shifted clinical PCa research towards a personalized direction [17,18]. Recent studies have showcased the capability of pathomics, an approach for the extraction of quantitative features from pathological images, in PCa characterization [19–21]. However, no studies have yet leveraged the potential of combining genomics, radiomics, and pathomics. Machine learning (ML) can serve as an ideal platform for the integration of high-dimensional multiomics data.

In this study, we aimed to assess whole-mount GG in PCa accurately using a novel ML approach to identify appropriate candidates for RP and to compare it with biopsy-proven GG (bxGG).

Materials and Methods

Study Design

A total of 146 patients with histologically-confirmed PCa from the pilot study of a prospective clinical trial (clinicaltrials.gov NCT02659527) were retrospectively enrolled, all of whom underwent ^{68}Ga-PSMA-11 PET/MR scans before RP between May 2014 to April 2020 at the Division of Nuclear Medicine in the Vienna General Hospital. This clinical trial complied with the Helsinki Declaration and its amendments. The inclusion and exclusion criteria were listed in **Supplementary Method M1**. The primary aim of this prospective trial was to improve the detection rate of primary localized PCa using non-invasive PSMA PET/MR in comparison with conventional biopsy. Our study, in contrast to previous work, incorporates radiomics, pathomics and genomics data, offering a more comprehensive analysis while predicting whole-mount Gleason grading rather than the improvement of detection rate. The study was approved by the ethics committee of the Vienna General Hospital (ID: 1649/2016). Each subject gave prior written informed consent.

Clinical Data Acquisition

Clinical parameters, including age, weight, height, body mass index (BMI), and pre-operative prostate-specific antigen (PSA) levels in serum were collected from the documentation of the clinical trial.

Based on ^{68}Ga-PSMA PET/MR images, two nuclear medicine physicians (S.R. and A.H.) with more than 10 years of experience, blinded to the outcome of each patient, assessed six parameters: (1) lesion involvement: whether the tumor affected one or two lobes or was diffusely spread throughout the prostate; (2) lesion position in the anatomy zone: whether the tumor was located in the central zone (CZ), transition zone (TZ), peripheral zone (PZ), anterior fibromuscular stroma (AFS), or it was diffusely distributed (i.e., tumor lesions involving at least two anatomical zones or the whole prostate; (3) extracapsular extension: whether the tumor exceeded the prostate capsule; (4) contact with neurovascular bundles: whether the tumor infiltrated adjacent neurovascular bundles; (5) lymph node (LN) infiltration: whether the tumor infiltrated the pelvic or distant LNs; (6) bone metastasis: whether tumor metastasized to bones.

Genomics Data Acquisition

Formalin-fixed paraffin-embedded (FFPE) tissue sections (3×10 µm) were obtained from RP samples and DNA extraction was performed. Genomic libraries were prepared and the raw sequencing data were processed. Somatic small variants were identified from paired samples of the tumor and corresponding normal tissue using the SomaticSeq variant caller [22].

Identified variants were annotated using Ensembl's Variant Effect Predictor (VEP) tool. Pathogenicity scores from the evolutionary model of variant effect (EVE) [23], Combined Annotation-Dependent Depletion (CADD) [24], and PolyPhen [25] were annotated and combined into a final pathogenicity metascore for each identified variant after normalization. Pathogenic genetic disruption was computed as the sum of combined pathogenicity scores of all variants in the given gene. Pathway genetic disruption was subsequently computed as the sum of the pathogenicity scores of all genes in each pathway based on the Kyoto Encyclopedia of Genes and Genomes (KEGG).

The tumor mutational burden (TMB) for each sample was computed as the number of identified somatic variants per million base pairs of the sequence region. Copy number variants (CNVs) were called using the CNVkit tool [26] with the set of paired normal samples used as a panel of “normals" in the computation. CNV burden was computed as the ratio of CNV sum size to the sum size of all sequenced regions. More details are described in **Supplementary Method M2 and Supplementary Figure S1**.

Radiomics Data Acquisition

The imaging protocol was described in a previously published study [27]. ^{68}Ga-PSMA-11 PET/MR images were acquired and volumes of interest (VOIs) were delineated on PET images with the T2-weighted imaging (T2WI) as anatomical reference. The delineations were performed manually by two nuclear medicine physicians (S.R and A.H) with more than 10 years of diagnostic experience in a slice-by-slice fashion. In instances of differing viewpoints, the physicians reached a consensus through discussion, ensuring precise and accurate identification of the VOIs. PET image intensities were converted to standardized uptake values (SUV) normalized to body weight, and conventional SUV metrics were extracted from VOIs, including SUVmin, SUVmax, SUVmean, SUVpeak, PSMA-tumor volume (PSMA-TV) and total lesion-PSMA (TL-PSMA) [28].

Radiomics features were computed using PyRadiomics 3.0.1 [29]. All extracted features were compliant with the international biomarker standardization initiative (IBSI) [30]. PET images were resampled to an isotropic voxel size of 2x2x2 mm^3 using B-spline interpolation and bin width was set to 0.3 SUV units. The workflow is shown in **Supplementary Figure S2**.

Pathomics Data Acquisition

Tissue samples were obtained from FFPE specimens. Tumor areas and normal areas from each sample were delineated on hematoxylin and eosin (H&E)-stained slides by an uro-pathologist with over 30 years of diagnostic experience (L.K.). Three cylindrical cores (diameter: 2.2 mm) were punched from annotated tumor areas and three from normal areas. These cores were transferred to a recipient paraffin block to create an array of tissue samples. The recipient block was sectioned into 2-5 µm thick sections and TMA slides were prepared. The tumor cores were specifically chosen from areas within the RP specimens that presented the most aggressive features upon pathological morphology in order to be most representative of the PCa tissue aggressiveness.

H&E and IHC staining were performed on the TMA slides. PSMA[31], androgen receptor (AR) [31], Ki-67[32], PSA[31], NK3 homeobox 1 (NKX3.1) [31], cyclin-dependent kinase 2 (CDK2) [33,34], cluster of differentiation 3 (CD3) [35], signal transducer and activator of transcription 3 (STAT3) [36], fatty acid synthase (FASN) [31], thyroid hormone receptor beta (TRβ) [37] and interleukin-6 signal transducer (IL6ST)[38] were selected as targets. The antibodies for IHC staining were listed in **Supplementary Method M3**.

The uro-pathologist (L.K.), blinded to the clinical data, evaluated the GS of each core based on H&E-stained TMA slides. As the punching process effectively mimics the targeted biopsy in clinical routines [39,40], the GS from each core was considered as bxGS to eliminate any time discrepancy. Moreover, the pathologist determined the percentages of strongly, moderately, or weakly stained cells of each core on IHC slides using the modified H-score [41], which was calculated using the formula: ([% of weak staining] × 1) or ([% of moderate staining] × 2) or ([% of strong staining] × 3), yielding a range from 0 to 300 [42,43]. The average and maximum H-score values from tumor cores were considered representative indicators of different targets' expression levels. The workflow is shown in **Supplementary Figure S3**.

Reference Standard

As binary ML prediction target, the post-operative International Society of Urological Pathology (ISUP) grading derived from whole-mount samples was split into low-risk (ISUP < 3) and high-risk (ISUP ≥ 3) [44]. This aligns with a previous large multicenter study indicating that the best prognostic stratification can be achieved at the threshold of grade three [45]. The ISUP grading system allows for better interpretation of morphological patterns and more accurate GG stratification [46,47].

Machine Learning

The resulting 203 input features included 13 clinical features, 113 radiomics-wide features (107 radiomics features and 6 conventional SUV metrics), 53 genomics features, 23 pathomics features, and 1 feature, namely biopsy-proven ISUP (bxISUP). All the features are listed in **Supplementary Table S1**.

ML was conducted using five classification algorithms, namely k-nearest neighbors (kNN), random forest (RF), extreme gradient boosting (XGB), support vector machine (SVM) and logistic regression (LGR). Robust performance evaluation was performed using 100-fold stratified Monte Carlo cross-validation with 70% of samples in the training set and 30% in the test set. The test set was exclusively used for testing, while a subset of the training data was employed for preprocessing and hyperparameter tuning. Features with more than 30% missing values were excluded. Any remaining missing values were imputed using k-nearest neighbor imputation with distance weighting [48]. Features were normalized using z-score. Feature selection was performed using minimum redundancy and maximum relevance (mRMR) [49]. Hyperparameter tuning was performed using random search. All procedures, including imputation, normalization, feature selection, and hyperparameter tuning, were performed separately for each fold while fitting on the training set and performing corresponding transformations on the test set to avoid any data leakage. Probability calibration was performed using an isotonic regression.

To ensure maximum transparency of the ML models and to enable the interpretation of decisions made by the applied algorithms, a set of explainable artificial intelligence (XAI) methods were employed, Shapley additive explanations (SHAP), permutation feature importance, and surrogate models. Permutation and SHAP importance both show feature importance, but the calculation of importance values differs [50]. Surrogate models are post-hoc explainable artificial intelligence techniques that aim to estimate the predictions of black-box models using a simple and interpretable model. In this study, we extracted this description from the RF model to create a simplified diagnostic workflow (decision tree). Further details on ML are described in **Supplementary Method M4**.

Statistical Analysis

The Python 3 package-scipy package 1.11.4 was used for statistical analysis. Quantitative metrics were calculated as mean ± standard deviation (SD), and categorical variables as percentages. Mann-Whitney test was used for comparison between quantitative variables. The chi-square test was used for comparison between categorical variables. All p values were tested as two-tailed. P values less than 0.05 were regarded as statistically significant.

Results

Data Overview

A total of 65 PCa patients (age: 64 ± 7.6) with clinical, genomics, radiomics, and pathomics data were included for final analysis following the cohort flow chart in **Figure 1**. Of these patients, 28 (43%) patients (age: 62.4 ± 7.9) were categorized as low risk (ISUP < 3) and 37 (57%) patients (age: 65.2 ± 7.1) as high risk (ISUP ≥ 3). Clinical and imaging parameters of both groups are shown in **Table 1**.

Based on the KEGG database, a total of 10,305 genes were identified in the exome of DNA. The overall mutation frequency was low, with only 29 genes mutated in ≥10% of patients (**Supplementary Figure S4**). No significant correlation (p ≥0.05) was found between any of the gene mutations and TMB, CNV burden, or whole-mount ISUP. Due to the sparse distribution of gene mutations, only pathway-level genomics features were employed for the subsequent ML analysis (Figure 2). Among 341 pathways annotated in the KEGG database, 51 pathways were selected due to their association with PCa tumorigenesis, aggressiveness, progression, or metastasis. The literature is listed in **Supplementary Table S2** to show the predictive potential of 51 pathways.

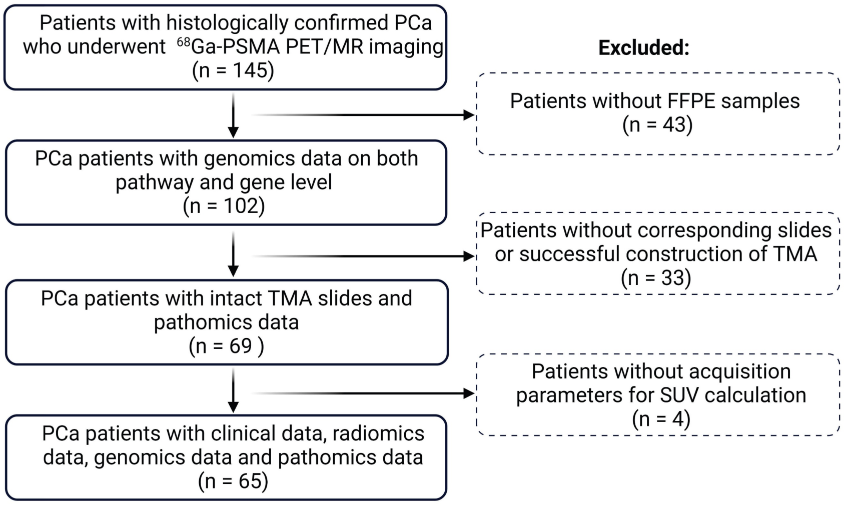

Figure 1. Flowchart of the study cohort. PCa: prostate cancer; TMA: tumor microarray; FFPE: formalin-fixed paraffin-embedded; SUV: standardized uptake value.

Table 1. Comparison of clinical and imaging parameters between the ISUP low (ISUP<3) group and ISUP high (ISUP≥3) group. Continuous data are expressed as mean ± standard deviation (SD); categorical variables are presented as numbers and percentages.

Parameters		Low risk (ISUP < 3)	High risk (ISUP ≥ 3)	*p* value
Clinical Parameters				
Age (years)		62.4 (7.9)	65.2 (7.1)	0.14
Weight (kg)		80.5 (10.9)	86.7 (11.1)	0.01
Height (m)		1.8 (0.1)	1.8 (0.1)	0.25
BMI (kg/m^2)		25.8 (2.8)	27.4 (3.3)	0.05
PSA-pre OP (μg/l)		9.4 (8.0)	55.4 (135.0)	<0.001
Pre-OP therapy	*No*	27 (96.43%)	30 (81.08%)	0.21
	Yes	1 (3.57%)	5 (13.51%)	
	NA	0 (0%)	2 (5.41%)	
Image-based Parameters				
Lesion involvement	*One lobe*	13 (46.43%)	20 (54.05%)	0.23
	Two lobes	5 (17.86%)	3 (8.11%)	
	Whole prostate	0 (0%)	2 (5.41%)	
	NA	10 (35.71%)	12 (32.43%)	
Lesion position in anatomy zone*	*CZ*	1 (3.57%)	0 (0%)	0.49
	TZ	2 (7.14%)	1 (2.7%)	
	PZ	12 (42.86%)	18 (48.65%)	
	AFS	0 (0%)	1 (2.7%)	
	Diffusion	2 (7.14%)	5 (13.51%)	
	NA	11 (39.29%)	12 (32.43%)	
Extracapsular extension	*No*	17 (60.71%)	11 (29.73%)	<0.001
	Yes	1 (3.57%)	14 (37.84%)	
	NA	10 (35.71%)	12 (32.43%)	
Contact to neurovascular bundles	*No*	18 (64.29%)	20 (54.05%)	0.06
	Yes	0 (0%)	5 (13.51%)	
	NA	10 (35.71%)	12 (32.43%)	
Lymph node infiltration	*No*	17 (60.71%)	17 (45.95%)	0.03
	Yes	1 (3.57%)	9 (24.32%)	
	NA	10 (35.71%)	11 (29.73%)	
Bone metastasis	*No*	17 (60.71%)	21 (56.76%)	0.38
	Yes	1 (3.57%)	4 (10.81%)	
	NA	10 (35.71%)	12 (32.43%)	
Clinical T staging	*cT2a*	3 (10.71%)	4 (10.81%)	0.03
	cT2b	5 (17.86%)	2 (5.41%)	
	cT2c	8 (28.57%)	4 (10.81%)	
	cT3a	1 (3.57%)	3 (8.11%)	
	cT3b	1 (3.57%)	12 (32.43%)	
	cT3a+b	0 (0%)	1 (2.7%)	
	cT4	0 (0%)	1 (2.7%)	
	NA	10 (35.71%)	10 (27.03%)	

Value in the bracket is standard deviation for numeric data and percentage for categorical data

*CZ: central zone; TZ: transition zone; PZ: peripheral zone; AFS: anterior fibromuscular stroma; Diffusion means PCa lesions involve any two/three anatomy zones or the whole prostate; NA: not applicable.

In total, 107 radiomics features were extracted and categorized into shape (n=14), histogram (n=18), and texture (n=75) features. Texture features included 24 gray level co-occurrence matrix (GLCM), 16 gray level run length matrix (GLRLM), 16 gray level size zone matrix (GLSZM), 14 gray level dependence matrix (GLDM) and 5 neighboring gray-tone difference matrix (NGTDM) features. Features are categorized in **Supplementary Table S3**.

ISUP grading was determined by H&E-staining with morphological details depicted in **Figure 3A**. Representative images of PSA expression between ISUP high and low groups are shown in **Figure 3B**. After statistical analysis of the whole cohort, we found that the maximum H-score of PSA was the most distinguished biomarker, and its value in high-risk PCa was lower than that of the low-risk group.

Machine Learning Performance

The five ML models (KNN, RF, SVM, LGR, XGB) were compared based on area under the curve (AUC), accuracy (ACC), sensitivity (SNS), specificity (SPC), positive predictive value (PPV) and negative predictive value (NPV), as depicted in **Figure 4A**. In terms of AUC, the RF model achieved the highest performance (**Supplementary Table S4**). The AUC, ACC, SNS, SPC, PPV, and NPV of the RF model were 0.87 (95%confidence interval ([CI], 0.85-0.89), 0.78 (95%CI, 0.76-0.80), 0.83 (95%CI, 0.80-0.86), 0.72 (95%CI, 0.68-0.76), 0.79 (95%CI, 0.77-0.81) and 0.80 (95%CI, 0.77-0.83) respectively.

The performance metrics of needle biopsy AUC, ACC, SNS, SPC, PPV, and NPV were 0.75, 0.77, 0.83, 0.61, 0.75, and 0.80 respectively. In comparison, the performance of RF showed an increase in AUC, ACC, SNS, and NPV by 12%, 1%, 11%, and 1%, respectively while SNS and PPV decreased by 6% and 4% (**Figure 4B. 4C**).

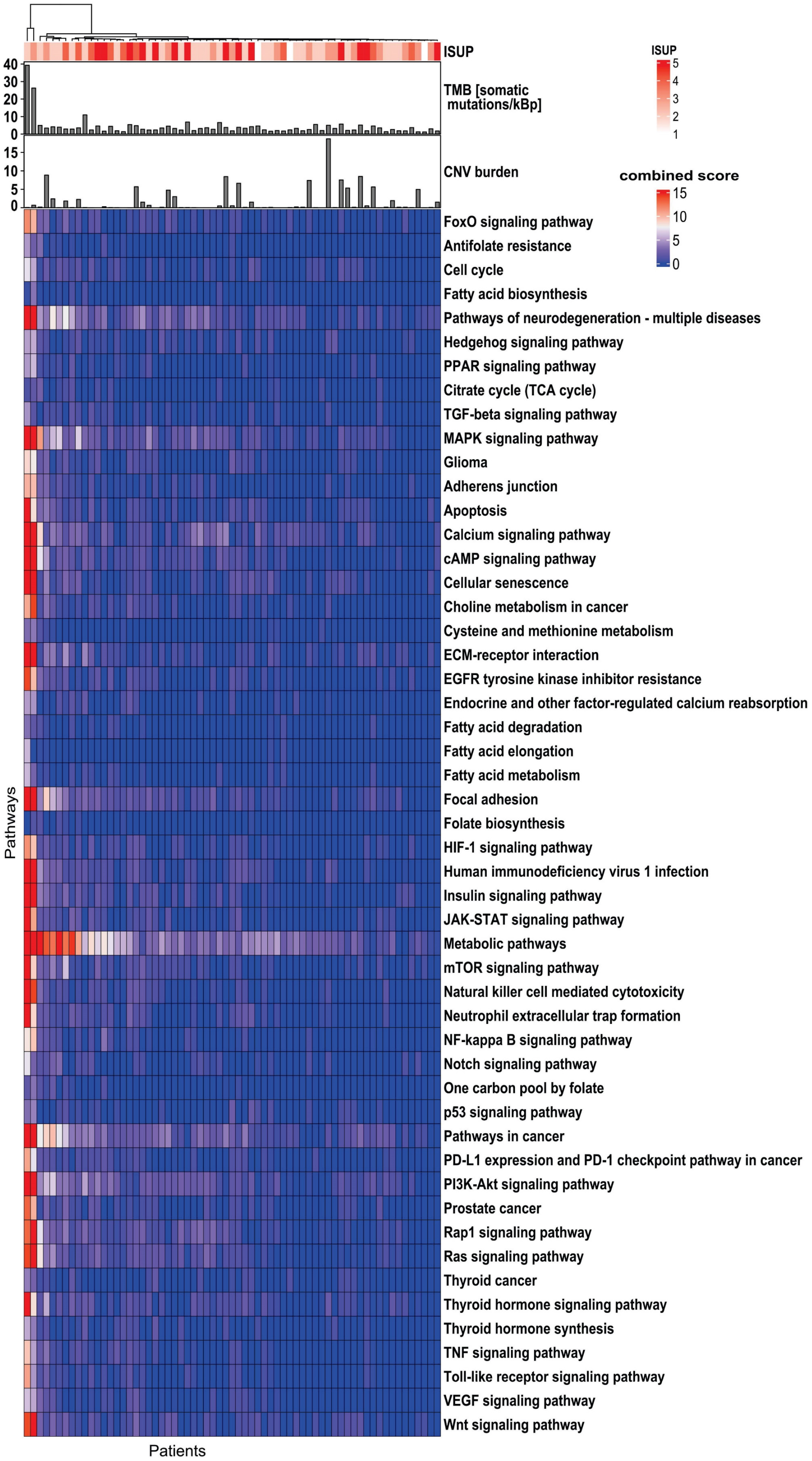

Figure 2. Genomics profile indicates the heterogeneity of the 51 investigated biological pathways in 65 PCa patients. The top bar shows TMB and CNV burden distribution. The top panel shows the correlation of genes/pathways mutation profile with ISUP groups. The top dendrogram shows the clustering patterns of genes/pathways based on their mutation profiles. TMB: tumor mutational burden; CNV: copy number variant; ISUP: International Society of Urological Pathology; PCa: prostate cancer.

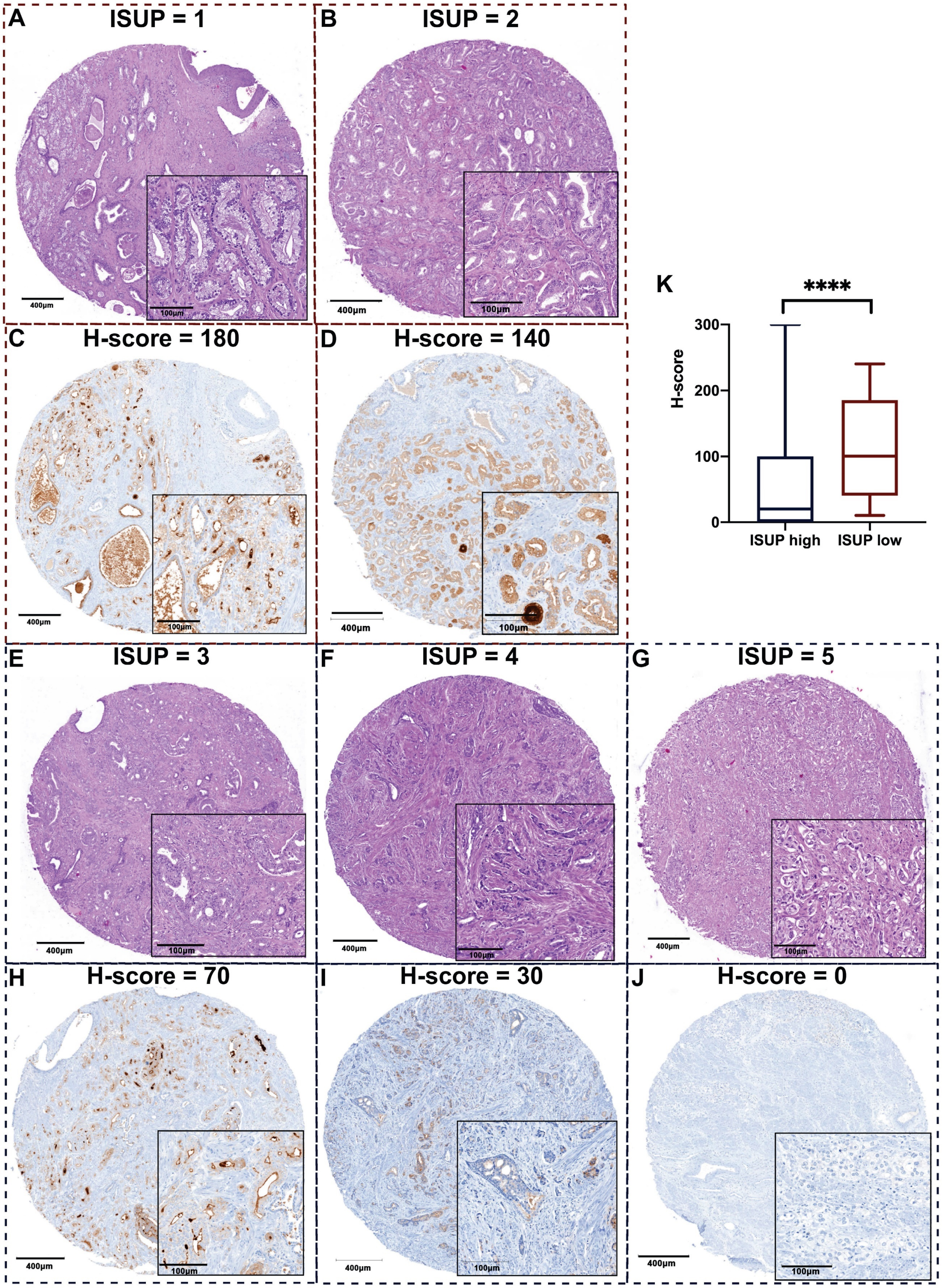

Figure 3. Representative images of H&E staining and PSA staining on TMA slides revealing less PSA expression when PCa tissue is more aggressive. A. Representative images of H&E staining for each ISUP grade: a. Patient 1, GS 6 (3+3); b. Patient 2, GS 7 (3+4); c. Patient 3, GS 7 (4+3); d. Patient 4, GS 8 (4+4); e. Patient 5, GS 9 (4+5); according to ISUP consensus 2019. B. Representative images of PSA expression in each ISUP grade core. a. Patient 1, high PSA expression; b. Patient 2, relatively high PSA expression; c. Patient 3, moderate PSA expression; d. Patient 4, relatively low PSA expression; d. Patient 5, negative PSA expression. The corresponding H&E core and PSA core are from the same cylinder of the same patient. The scale bars of the overview core and enlarged details are 400 µm and 100 µm respectively. C. The maximum H-score of PSA is significantly different between ISUP high and low groups (p < 0.0001). TMA: tumor microarray; PSA: prostate-specific antigen; ISUP: International Society of Urological Pathology; GS: Gleason score.

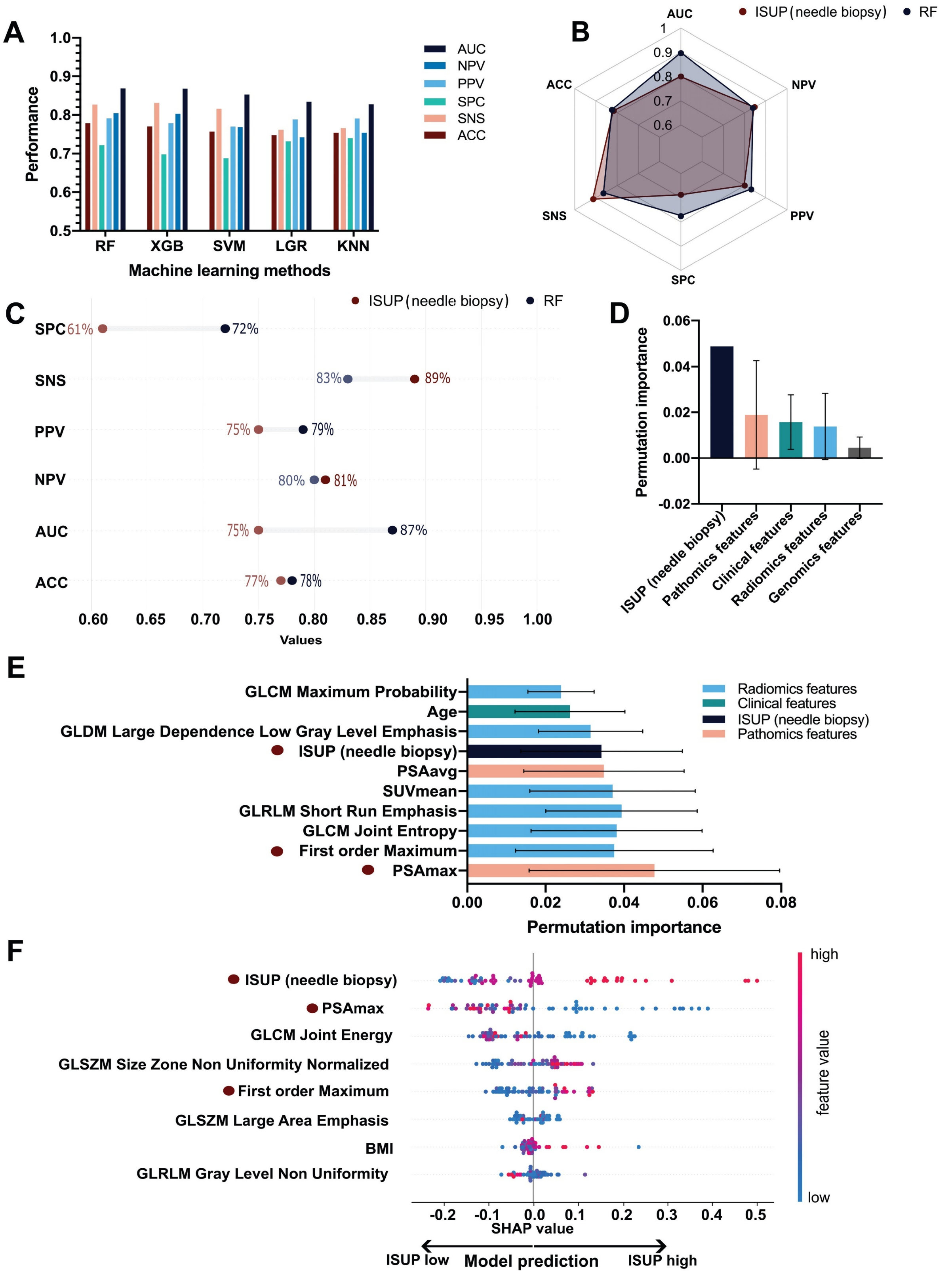

Figure 4. ML Performance of the ISUP prediction in PCa. A. Performance comparison of the five ML algorithms (KNN, RF, SVM, LGR, XGB). Ranked by AUC, the RF model had the best performance. B. Overall comparison of different performance metrics between the RF model and ISUP derived from needle biopsy. C. Comparison of the mean permutation importance between different types of features. D. Detailed comparison of different performance metrics between the RF model and ISUP derived from needle biopsy. E. The top 10 performing features in ISUP prediction based on permutation importance over all cross-validation folds. F. SHAP importance of the eight features included in the final RF model trained on the entire dataset. Each dot represents a single patient and higher feature values are labeled as red while lower values are blue. The increasing positive SHAP values are indicative of the model's tendency to predict high ISUP while decreasing SHAP values indicate the tendency of the model to predict low ISUP. KNN: k-nearest neighbors; RF: random forest; XGB: extreme gradient boosting; SVM: support vector machine; LGR: logistic regression; AUC: area under the curve; ACC: accuracy; SNS: sensitivity, SPC: specificity; PPV: positive predictive value; NPV: negative predictive value; ML: machine learning; SUVmean: mean standardized uptake value; PSAmax: maximum H-score of PSA expression on three cores of TMA slides; PSAavg: average H-score of PSA expression on three cores of TMA slides.

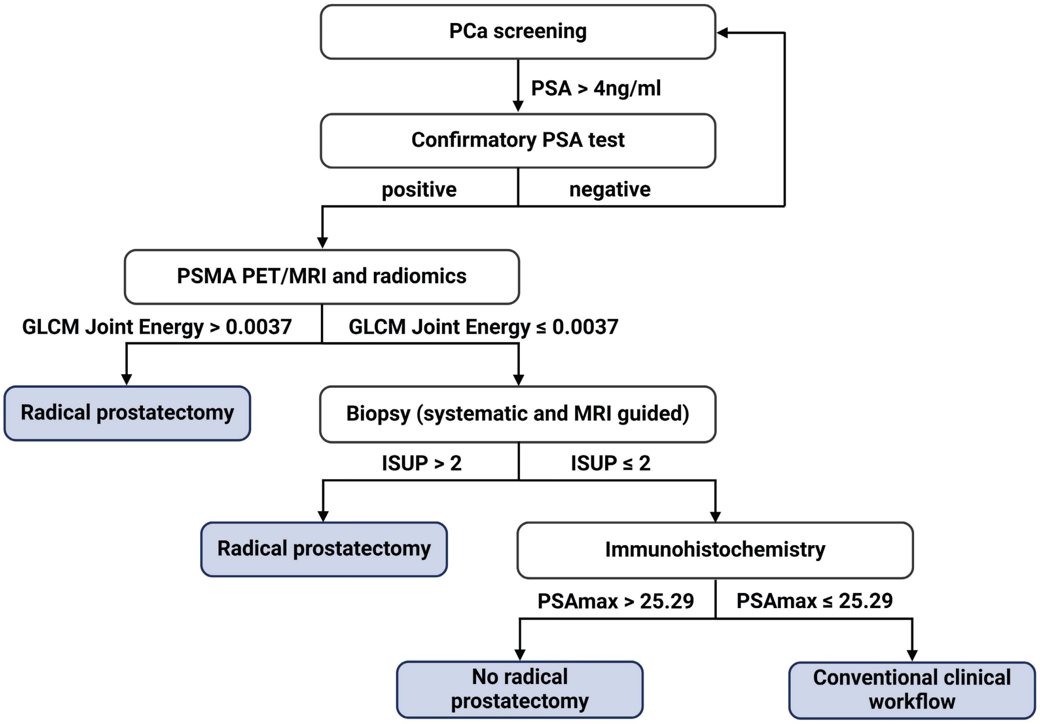

Figure 5. Proposed diagnostic flowchart for prostate cancer (PCa) management. PSAmax: maximum H-score of PSA expression on three cores of TMA slides; PSA: prostate-specific antigen.

Table 2. Performance for different input feature type combinations.

Feature types	ACC	SNS	SPC	PPV	NPV	BACC	AUC
Genomics and pathomics	0.805	0.830	0.775	0.822	0.820	0.803	0.893
Radiomics and genomics	0.727	0.743	0.708	0.770	0.716	0.726	0.835
Radiomics and pathomics	0.781	0.820	0.735	0.795	0.803	0.778	0.874
Radiomics, genomics and pathomics	0.779	0.827	0.722	0.791	0.804	0.774	0.869

ACC: accuracy; SNS: sensitivity; SPC: specificity; PPV: Positive predictive value; NPV: Negative predictive value; BACC: Balanced accuracy; AUC: Area under the receiver operating characteristic curve.

A total of 73 features were selected in the validation procedure, consisting of 1 feature, namely bxISUP, 5 clinical features, 12 gene-level genomics features, 43 radiomics-wide features and 13 pathomics features. After comparison of the mean permutation importance of different types of features, bxISUP was identified as the most attributable feature, followed by pathomics, clinical, radiomics, and genomics features (**Figure 4D**). Ranked by permutation importance value, the ten most important features included six radiomics features, three pathomics features, one clinical feature, and biopsy-derived ISUP (**Figure 4E**). More details were described in **Supplementary Results R1-3**.

SHAP importance revealed bxISUP as the most predictive feature, followed by maximum H-score of PSA, and texture/histogram-based radiomics features. **Figure 4F** shows the top 8 features and their SHAP importance values between high and low ISUP groups. In the ISUP high group, ISUP derived from needle biopsy tends to be higher, PSA is less expressed on IHC slides and GLCM Joint Energy values are lower compared to the ISUP low group.

A surrogate model was established to provide a simplified diagnostic workflow describing the more complex ML model (RF). The resulting simplified diagnostic workflow included three features, which were GLCM_Joint Energy, PSAmax_IHC, and bxISUP, which achieved a performance of AUC 0.89 in estimating the output of the complex ML model (**Supplementary Figure S5**). Based on the surrogate model, the ML-based workflow is incorporated in the clinical diagnostic scheme (**Figure 5**). We further performed three analyses, each using a combination of two feature types, including genomics, pathomics, and radiomics as input. AUC values ranged between 0.84 and 0.89 with the full performance metrics for the individual analyses shown in **Table 2**.

Discussion

In this study, we integrated clinical, imaging, pathomics, and genomics data for the ML-based GG prediction in PCa and demonstrated the superiority of the ML approach over the clinical standard of bxGG assessment. Furthermore, we developed a simplistic and interpretable diagnostic workflow, enabling a software-independent step-by-step procedure for the identification of high-risk patients instead of running the ML software. This makes validation and integration of the presented findings substantially easier since the repeatability and adaptability of ML models are major hurdles for the translation of ML-based software into clinical settings [51,52].

Numerous published multiomics studies in PCa aimed to guide clinical decision-making by directly inferring clinically relevant outcomes and parameters [53–56]. However, most of them focused on predictors from genomics, epigenomics, transcriptomics, and proteomics, omitting image-based predictors, which is problematic given that imaging features have been shown to be important for GS prediction [57–59]. This study addresses this gap by integrating not only PSMA PET radiomics with genomics features but also additional pathomics and clinical features. Thus, by leveraging diverse data sources, the ML model capitalized on comprehensive and complementary underlying information, facilitating more accurate GG assessment.

Despite the slight decrease in SNS and NPV, the AUC, ACC, SPC, and PPV of the ML model were superior to those of needle biopsy. The increased specificity, in comparison with the current clinical standard, indicates that the ML model has the ability to identify low ISUP patients accurately, which is aligned with our goal to avoid unnecessary interventions. Also, the high PPV is indicative of our study's reliability in identifying high-risk patients to provide timely and appropriate treatment.

Despite a discrepancy between bxGG and whole-mount GG, bxISUP was among the most important features in our analysis. Especially when combining needle biopsy with additional features such as PSA, ML outperformed the current clinical standard of bxGG substantially. Additionally, our findings unveil that PSAmax as the most important feature in predicting whole-mount GG based on two importance measurement algorithms. PSAmax represents the maximum H-score of the tumor tissue in needle biopsy and our results denote the more aggressive PCa is, the less PSA the tumor tissue expresses. This is consistent with the study that also explored the correlation between PSA H-scores and GG using TMA slides [60]. In line with other investigations [61], our study identified the first-order radiomics feature Maximum as an important feature in GG prediction. This is because this histogram-based feature, similar to the conventional SUVmax, manifests the highest uptake of ^{68}Ga-PSMA-11.

Of note, our ML model provides a simplified surrogate diagnostic workflow by combining the radiomics feature GLCM_Joint Energy, PSAmax_IHC, and ISUP in needle biopsy. Following the corresponding decision tree, urologists can select appropriate candidates for RP, which has the potential to revolutionize the diagnostic workflow of PCa. In addition to the two previously mentioned common features, the decision tree also includes GLCM_Joint Energy, a radiomics feature indicative of homogeneous patterns within PCa lesions. The lower Energy value means more heterogeneity within the tumor. Our results demonstrate that PCa with higher GG is more heterogeneous, as previously suggested by a study that identified the transcriptomic heterogeneity of GG 5 groups in a large dataset [62].

Despite the promising results, our study still has several limitations. First, due to its design as a retrospective multiomics study, not all the required parameters were available in some patients, resulting in a relatively small number of subjects for analysis. Second, due to the complexity and unique nature of our study, incorporating an independent validation cohort from another center poses significant challenges, particularly in the retrospective collection of high-dimensional datasets that are consistent with the ones used in our study. However, to ensure the robustness and validity of our findings, employed a rigorous 100-fold Monte Carlo cross-validation scheme, which enhanced the robustness, generalizability, and reduced bias of our study. Third, ML models in medical imaging, specifically in nuclear medicine, are known to suffer from center-specific variabilities, reducing the reproducibility of radiomics features [63–65]. Consequently, external validation is needed to verify the reliability of the developed approach in the future.

In conclusion, the presented multiomics ML model poses a promising advance in GG assessment for the improved stratification of PCa patients for RP. Our findings have the potential to substantially impact clinical decision-making and personalized management of PCa patients.

Supplementary Material

Supplementary materials, figures and tables. https://www.thno.org/v14p4570s1.pdf

Acknowledgements

The financial support by the Austrian Federal Ministry for Digital and Economic Affairs, the National Foundation for Research, Technology and Development, and the Christian Doppler Research Association is gratefully acknowledged. We thank Siemens Healthineers for the financial and scientific support. We would like to thank the Chinese

Scholarship Council for the financial support. We thank Central European Institute of Technology for scientific support. We thank Chun Li and Daniel Frigo for their insightful comments and constructive suggestions. We thank Boris Tichý, Leonhard Müllauer, Brigitte Hantusch, Christina Sternberg, Martin Raigel, Josef Yu and David Iommi for their contribution to this study. L.K. acknowledges the support from MicroONE, CBmed GmbH, the Austrian Research Promotion Agency (FFG), the European Union Horizon 2020 Marie Sklodowska-Curie Doctoral Network grants, the Margaretha Hehberger Stiftung and the Vienna Science and Technology Fund (WWTF).

Author contributions

JN and CPS conceived and conducted the study. JN, CPS, EG, SS and SR participated in gathering and cleaning the raw data. JN, LK and GW performed data annotation. DH, VB, SS and KT were involved in feature extraction from raw data and visualization. EG, GT, MS and HS provided technical support for histological data. JN and CPS conducted the experiment and analysis, developed the associated software and performed the validation. JN and CPS performed the statistical analysis. LK, AH, LP and MH provided either clinical or technical expertise. JN and CPS designed the figures and wrote the manuscript. All authors reviewed the manuscript and provided critical feedback.

Competing Interests

The authors have declared that no competing interest exists.

References

1. McGuire S. World Cancer Report 2014. Geneva, Switzerland: World Health Organization, International Agency for Research on Cancer, WHO Press, 2015. Adv Nutr. 2016; 7: 418–9.
2. Siegel RL, Miller KD, Fuchs HE, Jemal A. Cancer statistics, 2022. CA Cancer J Clin. 2022; 72: 7–33.
3. Bill-Axelson A, Holmberg L, Garmo H, et al. Radical Prostatectomy or Watchful Waiting in Prostate Cancer - 29-Year Follow-up. N Engl J Med. 2018; 379: 2319–29.
4. Castellan P, Ferretti S, Litterio G, Marchioni M, Schips L. Management of Urinary Incontinence Following Radical Prostatectomy: Challenges and Solutions. Ther Clin Risk Manag. 2023; 19: 43–56.
5. Bratu O, Oprea I, Marcu D, et al. Erectile dysfunction post-radical prostatectomy - a challenge for both patient and physician. J Med Life. 2017; 10: 13–8.
6. Costello AJ. Considering the role of radical prostatectomy in 21st century prostate cancer care. Nat Rev Urol. 2020; 17: 177–88.
7. Mottet N, van den Bergh RCN, Briers E, et al. EAU-EANM-ESTRO-ESUR-SIOG Guidelines on Prostate Cancer-2020 Update. Part 1: Screening, Diagnosis, and Local Treatment with Curative Intent. Eur Urol. 2021; 79: 243–62.
8. Yeldir N, Yildiz E, Dündar G. Gleason Score Correlation Between Prostate Needle Biopsy and Radical Prostatectomy Materials. Turk Patoloji Derg. 2019; 35: 185–92.
9. Mansouri N, Msakni I, Gargouri F, Khiari R, Bouziani A, Laabidi B. Evaluation of concordance of Gleason score between prostate biopsy and radical prostatectomy. Tunis Med. 2018; 96: 430–6.
10. Abedi AR, Basiri A, Shakhssalim N, et al. The Discrepancy between Needle Biopsy and Radical Prostatectomy Gleason Score in Patients with Prostate Cancer. Urol J. 2020; 18: 395–9.
11. Li QK, Lih T-SM, Wang Y, et al. Improving the detection of aggressive prostate cancer using immunohistochemical staining of protein marker panels. Am J Cancer Res. 2022; 12: 1323–36.
12. Swanson GP, Trevathan S, Hammonds KAP, Speights VO, Hermans MR. Gleason score evolution and the effect on prostate cancer outcomes. Am J Clin Pathol. 2021; 155: 711–7.
13. Vollmer RT. Gleason grading, biochemical failure, and prostate cancer–specific death. Am J Clin Pathol. 2017; 147: 273–7.
14. Canzler S, Schor J, Busch W, et al. Prospects and challenges of multi-omics data integration in toxicology. Arch Toxicol. 2020; 94: 371–88.
15. Loeb S, Ross AE. Genomic testing for localized prostate cancer: where do we go from here? Curr Opin Urol. 2017; 27: 495–9.
16. Yip SSF, Aerts HJWL. Applications and limitations of radiomics. Phys Med Biol. 2016; 61: R150-66.
17. Norris JM, Simpson BS, Parry MA, et al. Genetic Landscape of Prostate Cancer Conspicuity on Multiparametric Magnetic Resonance Imaging: A Systematic Review and Bioinformatic Analysis. Eur Urol Open Sci. 2020; 20: 37–47.
18. Ferro M, de Cobelli O, Vartolomei MD, et al. Prostate Cancer Radiogenomics-From Imaging to Molecular Characterization. Int J Mol Sci [Internet]. 2021; 22. Available at: http://dx.doi.org/10.3390/ijms22189971
19. Gupta R, Kurc T, Sharma A, Almeida JS, Saltz J. The Emergence of Pathomics. Curr Pathobiol Rep. 2019; 7: 73–84.
20. Schuettfort VM, Pradere B, Rink M, Comperat E, Shariat SF. Pathomics in urology. Curr Opin Urol. 2020; 30: 823–31.
21. McGarry SD, Hurrell SL, Iczkowski KA, et al. Radio-pathomic Maps of Epithelium and Lumen Density Predict the Location of High-Grade Prostate Cancer. Int J Radiat Oncol Biol Phys. 2018; 101: 1179–87.
22. Fang LT. SomaticSeq: An Ensemble and Machine Learning Method to Detect Somatic Mutations. In: Boegel S, Ed. Bioinformatics for Cancer Immunotherapy: Methods and Protocols. New York, NY: Springer US; 2020: 47–70.
23. Frazer J, Notin P, Dias M, et al. Disease variant prediction with deep generative models of evolutionary data. Nature. 2021; 599: 91–5.
24. Rentzsch P, Witten D, Cooper GM, Shendure J, Kircher M. CADD: predicting the deleteriousness of variants throughout the human genome. Nucleic Acids Res. 2019; 47: D886–94.
25. Adzhubei I, Jordan DM, Sunyaev SR. Predicting functional effect of human missense mutations using PolyPhen-2. Curr Protoc Hum Genet. 2013; Chapter 7: Unit7.20.
26. Talevich E, Shain AH, Botton T, Bastian BC. CNVkit: Genome-Wide Copy Number Detection and Visualization from Targeted DNA Sequencing. PLoS Comput Biol. 2016; 12: e1004873.
27. Grubmüller B, Baltzer P, Hartenbach S, et al. PSMA Ligand PET/MRI for Primary Prostate Cancer: Staging Performance and Clinical Impact. Clin Cancer Res. 2018; 24: 6300–7.
28. Schmuck S, von Klot CA, Henkenberens C, et al. Initial Experience with Volumetric 68Ga-PSMA I&T PET/CT for Assessment of Whole-Body Tumor Burden as a Quantitative Imaging Biomarker in Patients with Prostate Cancer. J Nucl Med. 2017; 58: 1962–8.
29. van Griethuysen JJM, Fedorov A, Parmar C, et al. Computational Radiomics System to Decode the Radiographic Phenotype. Cancer Res. 2017; 77: e104–7.
30. Zwanenburg A, Vallières M, Abdalah MA, et al. The Image Biomarker Standardization Initiative: Standardized Quantitative Radiomics for High-Throughput Image-based Phenotyping. Radiology. 2020; 295: 328–38.
31. Kristiansen G, Epstein JI. IHC Prostate Pathology [Internet]. [cited July 18, 2023]. Available at: https://www.patologi.com/DAKO%20immun%20-prostate-pathology.pdf
32. Maia R, Santos GADOS, Reis S, et al. Can we use Ki67 expression to predict prostate cancer aggressiveness? Revista do Colégio Brasileiro de Cirurgiões [Internet]. 2022; 49. Available at: https://www.scielo.br/j/rcbc/a/pYjPndLW69VXczN94GMrwqk/?format=pdf&lang=en
33. Zhang J, Gan Y, Li H, et al. Inhibition of the CDK2 and Cyclin A complex leads to autophagic degradation of CDK2 in cancer cells. Nat Commun. 2022; 13: 1–16.
34. Yin X, Yu J, Zhou Y, et al. Identification of CDK2 as a novel target in treatment of prostate cancer. Future Oncol. 2018; 14: 709–18.
35. Glud EN, Rasmussen M, Zhang Y, et al. Identification of a high-risk immunogenic prostate cancer patient subset as candidates for T-cell engager immunotherapy and the introduction of a novel albumin-fused anti-CD3 × anti-PSMA bispecific design. Br J Cancer. 2022; 127: 2186–97.
36. Pencik J, Schlederer M, Gruber W, et al. STAT3 regulated ARF expression suppresses prostate cancer metastasis. Nat Commun. 2015; 6: 7736.
37. Aksoy O, Pencik J, Hartenbach M, et al. Thyroid and androgen receptor signaling are antagonized by μ-Crystallin in prostate cancer. Int J Cancer. 2021; 148: 731–47.
38. Shariat SF, Chromecki TF, Hoefer J, et al. Soluble gp130 regulates prostate cancer invasion and progression in an interleukin-6 dependent and independent manner. J Urol. 2011; 186: 2107–14.
39. Glinsmann-Gibson B, Wisner L, Stanton M, Larsen B, Rimsza L, Maguire A. Recommendations for Tissue Microarray Construction and Quality Assurance. Appl Immunohistochem Mol Morphol. 2020; 28: 325–30.
40. Das CJ, Netaji A, Razik A, Verma S. MRI-Targeted Prostate Biopsy: What Radiologists Should Know. Korean J Radiol. 2020; 21: 1087–94.

41. Purdie CA, Quinlan P, Jordan LB, et al. Progesterone receptor expression is an independent prognostic variable in early breast cancer: a population-based study. Br J Cancer. 2014; 110: 565–72.
42. Detre S, Saclani Jotti G, Dowsett M. A "quickscore" method for immunohistochemical semiquantitation: validation for oestrogen receptor in breast carcinomas. J Clin Pathol. 1995; 48: 876–8.
43. Sowalsky AG, Figueiredo I, Lis RT, et al. Assessment of Androgen Receptor Splice Variant-7 as a Biomarker of Clinical Response in Castration-Sensitive Prostate Cancer. Clin Cancer Res. 2022; 28: 3509–25.
44. Epstein JI, Egevad L, Amin MB, et al. The 2014 International Society of Urological Pathology (ISUP) Consensus Conference on Gleason Grading of Prostatic Carcinoma: Definition of Grading Patterns and Proposal for a New Grading System. Am J Surg Pathol. 2016; 40: 244–52.
45. Epstein JI, Zelefsky MJ, Sjoberg DD, et al. A Contemporary Prostate Cancer Grading System: A Validated Alternative to the Gleason Score. Eur Urol. 2016; 69: 428–35.
46. van Leenders GJLH, van der Kwast TH, Grignon DJ, et al. The 2019 International Society of Urological Pathology (ISUP) Consensus Conference on Grading of Prostatic Carcinoma. Am J Surg Pathol. 2020; 44: e87–99.
47. Zelic R, Giunchi F, Fridfeldt J, et al. Prognostic Utility of the Gleason Grading System Revisions and Histopathological Factors Beyond Gleason Grade. Clin Epidemiol. 2022; 14: 59–70.
48. Beretta L, Santaniello A. Nearest neighbor imputation algorithms: a critical evaluation. BMC Med Inform Decis Mak [Internet]. 2016; 16. Available at: http://dx.doi.org/10.1186/s12911-016-0318-z
49. Peng H, Long F, Ding C. Feature selection based on mutual information: criteria of max-dependency, max-relevance, and min-redundancy. IEEE Trans Pattern Anal Mach Intell. 2005; 27: 1226–38.
50. Altmann A, Toloşi L, Sander O, Lengauer T. Permutation importance: a corrected feature importance measure. Bioinformatics. 2010; 26: 1340–7.
51. Pumplun L, Fecho M, Wahl N, Peters F, Buxmann P. Adoption of Machine Learning Systems for Medical Diagnostics in Clinics: Qualitative Interview Study. J Med Internet Res. 2021; 23: e29301.
52. Sandhu S, Lin AL, Brajer N, et al. Integrating a Machine Learning System Into Clinical Workflows: Qualitative Study. J Med Internet Res. 2020; 22: e22421.
53. Gómez-Cebrián N, Poveda JL, Pineda-Lucena A, Puchades-Carrasco L. Metabolic Phenotyping in Prostate Cancer Using Multi-Omics Approaches. Cancers [Internet]. 2022; 14. Available at: http://dx.doi.org/10.3390/cancers14030596
54. Wei Z, Han D, Zhang C, et al. Deep Learning-Based Multi-Omics Integration Robustly Predicts Relapse in Prostate Cancer. Front Oncol. 2022; 12: 893424.
55. Wu L, Yang Y, Guo X, et al. An integrative multi-omics analysis to identify candidate DNA methylation biomarkers related to prostate cancer risk. Nat Commun. 2020; 11: 3905.
56. Kiebish MA, Cullen J, Mishra P, et al. Multi-omic serum biomarkers for prognosis of disease progression in prostate cancer. J Transl Med. 2020; 18: 10.
57. Abdollahi H, Mofid B, Shiri I, et al. Machine learning-based radiomic models to predict intensity-modulated radiation therapy response, Gleason score and stage in prostate cancer. Radiol Med. 2019; 124: 555–67.
58. Chaddad A, Kucharczyk MJ, Niazi T. Multimodal Radiomic Features for the Predicting Gleason Score of Prostate Cancer. Cancers [Internet]. 2018; 10. Available at: http://dx.doi.org/10.3390/cancers10080249
59. Papp L, Spielvogel CP, Grubmüller B, et al. Supervised machine learning enables non-invasive lesion characterization in primary prostate cancer with [68Ga]Ga-PSMA-11 PET/MRI. Eur J Nucl Med Mol Imaging. 2021; 48: 1795–805.
60. Bonk S, Kluth M, Hube-Magg C, et al. Prognostic and diagnostic role of PSA immunohistochemistry: A tissue microarray study on 21,000 normal and cancerous tissues. Oncotarget. 2019; 10: 5439–53.
61. Zschaeck S, Andela SB, Amthauer H, et al. Correlation Between Quantitative PSMA PET Parameters and Clinical Risk Factors in Non-Metastatic Primary Prostate Cancer Patients. Front Oncol. 2022; 12: 879089.
62. Kishan AU, Romero T, Alshalalfa M, et al. Transcriptomic Heterogeneity of Gleason Grade Group 5 Prostate Cancer. Eur Urol. 2020; 78: 327–32.
63. Leithner D, Schöder H, Haug A, et al. Impact of ComBat Harmonization on PET Radiomics-Based Tissue Classification: A Dual-Center PET/MRI and PET/CT Study. J Nucl Med. 2022; 63: 1611–6.
64. Da-Ano R, Visvikis D, Hatt M. Harmonization strategies for multicenter radiomics investigations. Phys Med Biol. 2020; 65: 24TR02.
65. Orlhac F, Frouin F, Nioche C, Ayache N, Buvat I. Validation of A Method to Compensate Multicenter Effects Affecting CT Radiomics. Radiology. 2019; 291: 53–9.

European Journal of Nuclear Medicine and Molecular Imaging (2023) 50:546–558
https://doi.org/10.1007/s00259-022-05973-9

ORIGINAL ARTICLE

Radiogenomic markers enable risk stratification and inference of mutational pathway states in head and neck cancer

Clemens P. Spielvogel[1,2] · **Stefan Stoiber**[1,3] · **Laszlo Papp**[4] · **Denis Krajnc**[4] · **Marko Grahovac**[2] · **Elisabeth Gurnhofer**[3] · **Karolina Trachtova**[1,2,5] · **Vojtech Bystry**[5] · **Asha Leisser**[2] · **Bernhard Jank**[6] · **Julia Schnoell**[6] · **Lorenz Kadletz**[6] · **Gregor Heiduschka**[6] · **Thomas Beyer**[4] · **Marcus Hacker**[2] · **Lukas Kenner**[1,3] · **Alexander R. Haug**[1,2]

Received: 26 April 2022 / Accepted: 15 September 2022 / Published online: 26 September 2022

Abstract

Purpose Head and neck squamous cell carcinomas (HNSCCs) are a molecularly, histologically, and clinically heterogeneous set of tumors originating from the mucosal epithelium of the oral cavity, pharynx, and larynx. This heterogeneous nature of HNSCC is one of the main contributing factors to the lack of prognostic markers for personalized treatment. The aim of this study was to develop and identify multi-omics markers capable of improved risk stratification in this highly heterogeneous patient population.

Methods In this retrospective study, we approached this issue by establishing radiogenomics markers to identify high-risk individuals in a cohort of 127 HNSCC patients. Hybrid *in vivo* imaging and whole-exome sequencing were employed to identify quantitative imaging markers as well as genetic markers on pathway-level prognostic in HNSCC. We investigated the deductibility of the prognostic genetic markers using anatomical and metabolic imaging using positron emission tomography combined with computed tomography. Moreover, we used statistical and machine learning modeling to investigate whether a multi-omics approach can be used to derive prognostic markers for HNSCC.

Results Radiogenomic analysis revealed a significant influence of genetic pathway alterations on imaging markers. A highly prognostic radiogenomic marker based on cellular senescence was identified. Furthermore, the radiogenomic biomarkers designed in this study vastly outperformed the prognostic value of markers derived from genetics and imaging alone.

Conclusion Using the identified markers, a clinically meaningful stratification of patients is possible, guiding the identification of high-risk patients and potentially aiding in the development of effective targeted therapies.

Keywords Head and neck cancer · Biomarkers · Radiomics · Machine learning · Artificial intelligence · Cancer genomics

Background

Worldwide, head and neck cancer accounts for more than 430,000 annual deaths and over 830,000 individuals are diagnosed with head and neck cancer every year [1]. Head and neck squamous cell carcinoma (HNSCC) accounts

---

This article is part of the Topical Collection on Oncology - Head and Neck.

✉ Lukas Kenner
lukas.kenner@meduniwien.ac.at

[1] Christian Doppler Laboratory for Applied Metabolomics, Vienna, Austria

[2] Department of Biomedical Imaging and Image-Guided Therapy, Division of Nuclear Medicine, Medical University of Vienna, Vienna, Austria

[3] Clinical Institute of Pathology, Medical University of Vienna, Vienna, Austria

[4] Center for Medical Physics and Biomedical Engineering, Medical University of Vienna, Vienna, Austria

[5] Centre for Molecular Medicine, Central European Institute of Technology, Brno, Czech Republic

[6] Department of Otorhinolaryngology, Head and Neck Surgery, Medical University of Vienna, Vienna, Austria

for approximately 90% of all head and neck cancers [2]. HNSCC originates from the epithelial cells outlining the mucosa of various cavities in the head and neck area. The anatomical, clinical, histological, and molecular heterogeneity of HNSCC has been a limiting factor for the development of personalized treatments. Today, PD-L1 expression and human papilloma virus (HPV) infection status are the only considered biomarkers for personalized clinical management of HNSCC patients [3, 4]. Consequently, further markers are urgently needed for the stratification of clinically meaningful groups to better tailor the management of these patients to their individual characteristics.

Metabolic *in vivo* imaging provided by technologies such as positron emission tomography combined with computed tomography (PET/CT) is a non-invasive way to capture information about biological processes on a whole-body scale. *In vivo* imaging further enables the high-throughput acquisition of quantitative imaging features, referred to as radiomics. Radiomics has been deployed to describe tumor characteristics, such as shape and heterogeneity on a quantitative level, which have been shown to deliver prognostic information in various settings [5, 6].

In parallel to the advancements of diagnostic imaging modalities driven by clinical research, mechanistic cancer research has been capitalizing on the revolution in sequencing technologies. Today, genomics provides crucial diagnostic information to advance toward personalized cancer medicine. Tissue-based DNA biomarkers comprise some of the most important prognostic factors in HNSCC [7]. These prognostic markers can be useful for the monitoring and selection of patients for a specific treatment [6, 8]. In contrast to these gene-level markers, pathway-level biomarkers are largely unexplored. Still, since mutations are only one of several ways to inactivate tumor suppressors or activate oncogenes [9], genetic analysis inherently provides an important but only partial view of the cancer phenotype. Radiomic features, on the other hand, have the potential to provide functional information on the activity of oncogenic drivers at a holistic level. Thus, an approach combining the strength of both technologies which is referred to as radiogenomics has the potential to raise currently underexplored synergies to advance the personalized management of cancer patients.

The aim of the present study was therefore threefold (Fig. 1): (1) the identification of quantitative and prognostic [^{18}F]FDG PET/CT imaging and genetic markers in HNSCC; (2) the assessment of the association of previously identified imaging markers with pathways related to cell proliferation and energy metabolism; (3) to investigate if complementary information within imaging and genetic patterns can be used to create combined radiogenomic markers with improved prognostic value over imaging or genetic markers only.

Materials and methods

Patient data

One hundred and twenty-seven (127) patients diagnosed with HNSCC between June 8, 2006 and July 31, 2015 with whole-body [^{18}F]FDG PET/CT scans at the General Hospital Vienna were retrospectively enrolled into the study. CT was acquired using contrast enhancement with 100 ml Iomeron 400 mg/ml. Overall, 2 patients were excluded due to lesion sizes below 64 voxels [11], 4 due to a second primary tumor, and 59 due to missing or insufficient tumor tissue for DNA extraction, resulting in 62 patients for further analysis. The clinical annotation was acquired by the head-and-neck surgeon taking the tissue biopsies and included overall survival (OS) starting from the date of histologically confirmed diagnosis. An overview of patient characteristics is provided in Table 1. All biopsies originated from histologically confirmed head and neck squamous cell carcinomas. The study was approved by the institutional review board with ethics ID 1649/2016 at the General Hospital of Vienna.

DNA extraction, whole-exome sequencing, and sequencing data analysis

DNA was extracted from formalin-fixed paraffin-embedded samples and sequenced using whole-exome sequencing (WES). Details on DNA extraction and WES analysis can be found in Supplement section 1 under "DNA extraction and whole exome sequencing."

DNA sequencing analysis

Raw reads were mapped to the genomic reference GRCh38 using the Burrows–Wheeler Alignment (BWA) tool [12]. Small variants were detected using Strelka2 [13] and VarDict [14] variant callers independently, and the resulting variants were merged. Variants were annotated with the Variant Effect Predictor (VEP) tool from Ensemble [15] including the annotation of CADD scores [10, 16, 17]. Resulting annotated variants were joined across the cohort and germline variants were filtered. The discrimination of somatic and germline variants was based on a somatic tumor variant filtering strategy from Sukhai et al. [18], with additional filters added and parameters adjusted in order to minimize the ratio of known germline variants resulting from a set of 15 paired normal tissues. The final somatic variant filtering was performed as follows. Only variants present in less than 10% of samples were kept. Variants called by both Strelka2 and VarDict with

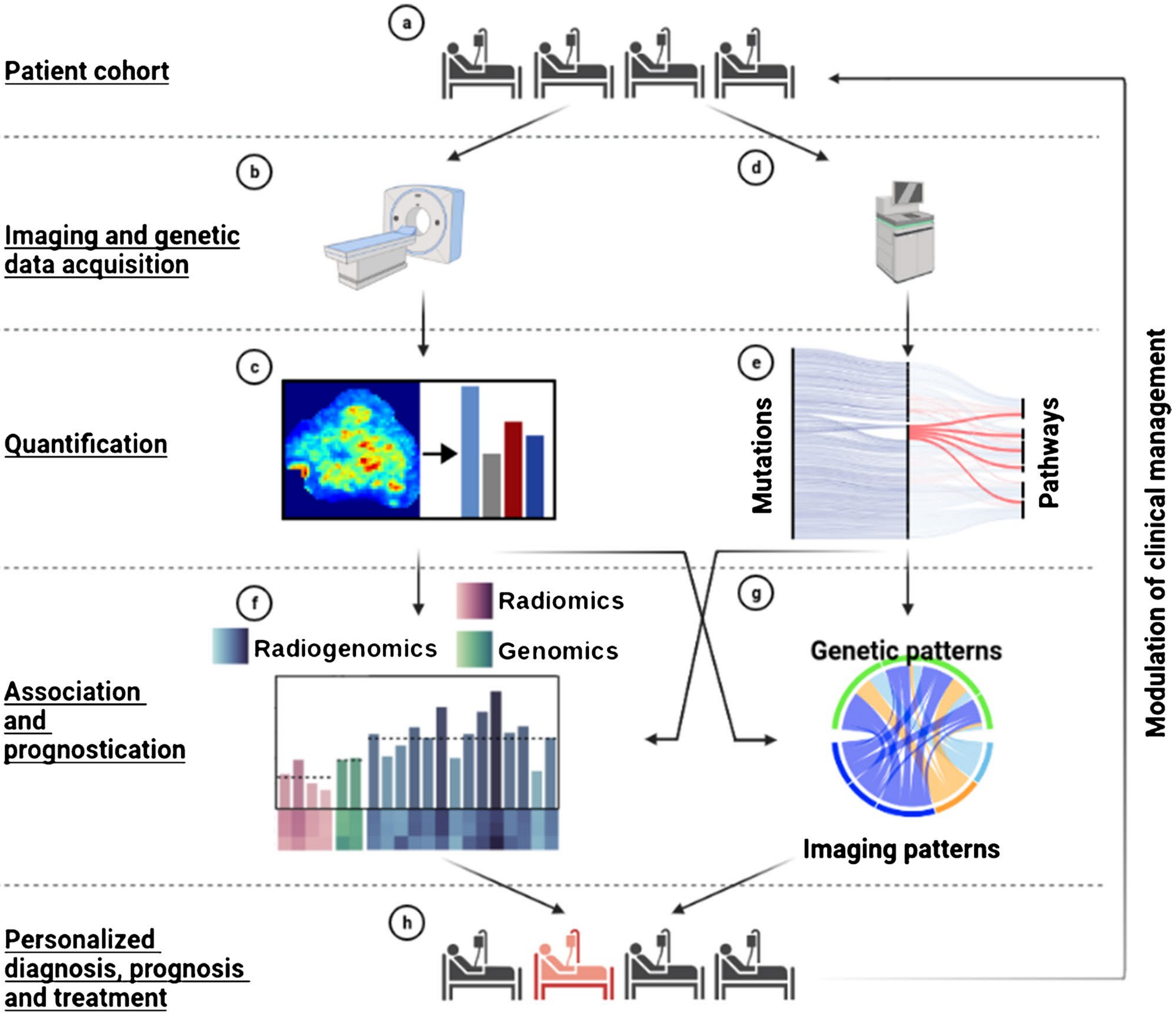

Fig. 1 Workflow diagram of the study. **a** Primary tumor tissue from 62 patients with HNSCC was acquired through surgical biopsy. **b** Image data acquisition using [.^{18}F]FDG PET/CT. **c** Quantification of tumor characteristics based on imaging data using radiomics. **d** DNA extraction from solid tumor tissue and subsequent whole exome sequencing. **e** Quantification of genetically disrupted pathways related to cell growth and death as well as energy metabolism using combined annotation dependent depletion (CADD) scores [10]. **f** Identification and evaluation of prognostic radiomic, genomic, and radiogenomic features using statistical and machine learning approaches. **g** Statistical assessment of the association and complementary information of pathway-level genetic features and non-redundant radiomic features. **h** Patient-tailored diagnosis, prognosis, and treatment based on the detected radiogenomic markers and associated risk assessment. This figure was created using BioRender (biorender.com)

a number of variant reads above 10 and variants called by only one variant caller with a number of variant reads above 20 were kept. Three population variant databases were used for variant filtering including 1000 genome [19], Gnomad [20], and the NHLBI Exome Sequencing Project [21]. Variants with a minor allele frequency below 1% for the non-Finnish European group in all three databases were kept. Variants with a record in ClinVar database [22] with significance “benign” or “likely benign” were removed.

Pathway-level disruption scores and pathway selection

Mutation-level combined annotation dependent depletion (CADD) scores [10] were summed over all variants in associated genes to derive gene-level CADD scores indicating the functional disruption of each gene. The KEGG pathway

Table 1 Characteristics of the 62 patients included for analysis

Patient characteristics	
Median age, years (range)	57 (35–83)
Median overall survival, months (range)	25 (0–130)
Male, n (%)	45 (73)
Female, n (%)	17 (27)
Treatment naive at tissue acquisition, n (%)	52 (84)
Clinical stage, n (%)	
I	4 (6)
II	5 (8)
III	4 (6)
IVA	38 (61)
IVB	3 (5)
IVC	7 (11)
Not reported	1 (2)
Localization, n (%)	
Oral cavity	35 (56)
Oropharynx	16 (26)
Hypopharynx	6 (10)
Larynx	4 (6)
Nasal sinuses	1 (2)

database [23] was used to assign genes to corresponding pathways. Pathway CADD scores were computed as sum of gene-level CADD scores for all genes in the respective pathway. Pathways were considered for the analysis if they were either annotated as related to energy metabolism or to cell growth and death based on the KEGG pathway database. Pathways were excluded if they do not exist in humans or were irrelevant for somatic tissue (Supplementary Table 6).

Gene-level CADD score cutoffs were unlikely to be accurately determined by setting a uniform cutoff [24]. Therefore, we used the prognostically relevant cutoffs as determined by the survival analysis for the dichotomization of each pathway's score individually. By doing so, we derived prognostically relevant binary states, functional or disrupted, for each pathway (Supplementary Fig. 8). The binary pathway states were used for the associated with imaging patterns and the derivation of radiogenomic markers.

Delineation

Two board-registered nuclear medicine specialists at the Division of Nuclear Medicine at the Medical University of Vienna performed tumor boundary delineation to derive volumes of interest (VOIs) from the whole-body images. For each patient, one delineation was created based on the agreement of the two nuclear medicine specialists. Delineation of lesions and background tissue were performed utilizing semi-automated iso-count VOI tools from the commercially available Hybrid 3D software version 4.0.0 (Hermes Medical Solutions AB, Stockholm, Sweden). If required, a slice-by-slice modification was performed [25, 26]. Delineation in PET/CT images was guided by the PET image. VOIs were dilated by 5 voxels into every spatial dimension.

Radiomic feature extraction and preprocessing

The SUV maps of the VOIs were normalized using a standardized reference region before performing interpolation to 2 and 4 mm. Radiomic features were extracted from the resulting VOIs using an IBSI-conform in-house framework. Overall, 104 Imaging Biomarker Standardization Initiative (IBSI)-conform radiomic features were extracted, 52 from the background-normalized PET and the corresponding CT each. Details on the extraction and preprocessing of image biomarkers are outlined in Supplemental section 1 under "Radiomic feature extraction and preprocessing."

Development of radiogenomic markers

Radiogenomic features were created by combining the most prognostic pathways ($p < 0.05$) with the most prognostic radiomic features ($p < 0.05$). Each radiogenomic feature consists of a radiomic–genomic feature pair with one radiomic and one pathway feature. For each radiomic–genomic feature pair, four binary radiogenomic features were created (pathway-disrupted and radiomic-high, pathway-disrupted and radiomic-low, pathway-functional and radiomic-high, pathway-disrupted and radiomic-low). For example, the radiogenomic feature *cellular senescence (functional)-CT ih.kurt (high)* was defined to be "present" for a patient if the patient has a functional cellular senescence pathway and a high value (above threshold determined by survival analysis) for the CT radiomic feature *ih.kurt*. In all other cases, the radiogenomic feature value was defined as "absent." From the total of 84 radiogenomic markers, only those with sufficiently large subgroups for survival analysis (at least 15% samples in each group) were considered, leaving 49 radiogenomic markers for further analysis.

Statistical analysis

Survival analysis was conducted using two-sided logrank tests with an optimized cutoff and OS. Logrank tests, two-sided Cox proportional hazard models, and plotting for Kaplan–Meier curves were performed using the lifelines Python package. No survival analysis was performed if one of the groups contained less than 15% samples. The association between radiomic features and pathway-level scores was performed using the non-parametric, two-sided Mann–Whitney *U* test implementation of the SciPy Python package. Bonferroni correction was applied for all statistical analyses to account for multiple testing.

Machine learning classification

Binary machine learning (ML) classification models were built using Dedicaid AutoML version 1.1 (Dedicaid GmbH, Vienna, Austria) via a stacked and mixed ensemble approach. Algorithms used in the ensemble included random forest, support vector machine, and a multi-Gaussian genetic algorithm. Preprocessing included standardization of input features and removal of redundant features. In case of label imbalance, oversampling was employed on the training data via the synthetic minority oversampling technique (SMOTE) [27]. A total of 20 genomic, radiomic, and radiogenomic features were included which were identified to be prognostic in the preceding univariate analyses. Prediction target labels were generated by dichotomization of the continuous OS information. Three binary classification models were created for OS greater 24 months, OS greater median (25 months) and OS greater 36 months. Results were validated using 100-fold Monte Carlo cross-validation with a training-to-test sample ratio of 80:20. Details on the ML analysis can be found in Supplement section 2.

Feature importance measurement

Feature importance measurement was based on R-squared ranking [28]. R-squared ranks were determined on the binary target labels for each of the ML models, leading to one feature importance ranking per model. The final importance was calculated as the average feature importance across all 100 Monte Carlo cross-validation folds. The importance metrics were further normalized to a sum of 100 (%) per model.

Code and visualization tools

All analyses were conducted using Python 3. Packages used included pandas 1.0.3, numpy 1.19.2, and scikit-learn 0.23.2. For the survival analysis and plotting of associated Kaplan–Meier curves, lifelines 0.24.13 was used. For any other statistical analysis, we used SciPy 1.4.1. Visualizations were created using Matplotlib 3.2.1 and Seaborn 0.11.1. For the creation of rain cloud plots, we used the package Ptprince 0.2. For the creation of sankey diagrams, Plotly 4.4.1 was used. The graphical abstract was created using BioRender (biorender.com).

Results

Processing and analysis of the radiomic features

IBSI-conform radiomic features were extracted from [^{18}F]FDG PET/CT images of primary lesions from 62 patients with HNSCC [29]. After redundancy removal [26, 30], 4 PET-based and 10 CT-based features remained for further analysis (Supplemental Fig. 1). Independent assessment of PET and CT features identified two texture CT features, *szm.lzhge* (p 6.4 * 10^{-5}) and *szm.z.perc* (p 0.0016), one morphological feature, *morph.vol* (p 0.0021), and one intensity-related PET feature, *stat.sum* (p 0.0013), to be prognostic (Fig. 2a).

On visual inspection of tumors, lesions with high PET-based *stat.sum* were associated with large volumes (Fig. 2b). Since PET-based metabolic tumor volume (MTV) has been proposed as a prognostic marker for multiple cancers, including HNSCC [31], we further investigated the association between *stat.sum* and MTV. The analysis confirmed a strong correlation ($p < 0.0001$) (Fig. 2c). CT-based morph.vol was the only additional feature correlated with MTV, indicating no systematic effect of volume on the radiomic features. Furthermore, *stat.sum* was associated with a slightly improved prognostic value over MTV (p 0.0013 vs. 0.0040) (Fig. 2d, e).

None of the SUV-based features, SUVmax, SUVmin, SUVmean, SUVpeak, and SUV total lesion glycolysis (TLG), were significantly prognostic after Bonferroni correction ($p < 0.01$) (Supplementary Table 1 and Supplementary Figs. 2–6), indicating a higher prognostic value of radiomic features over SUV metrics in this study cohort.

Processing of genetic data and creation of pathway disruption scores

Solid tissue from primary tumors of 62 patients was acquired and WES was performed. A total of 15,689 mutations in 8502 genes was detected across all patients. The most mutated genes included MUC4 (66%), TTN (35%), TP53 (27%), MUC12 (24%), and CSMD3 (23%). The relation of mutation-, gene-, and pathway-level CADD scores for the six selected cell growth and death-related pathways and three energy metabolism–related pathways is visualized in two interactive CADD score diagrams (representatively shown in Fig. 3). Of the nine pathways, survival analysis identified cellular senescence and apoptosis to be significantly prognostic ($p < 0.008$).

The proliferation-related CADD composition diagram (Fig. 3a) suggested a major role of the *TP53* gene in deriving the pathway-level CADD score for p53 signaling, cellular senescence, ferroptosis, cell cycle, and apoptosis. However, survival analysis revealed that *TP53* alone has no prognostic value (p 0.18) (Supplementary Fig. 7). Since mutation frequencies in 8486 of 8502 mutated genes was below 15%, no additional analyses on single gene level were carried out.

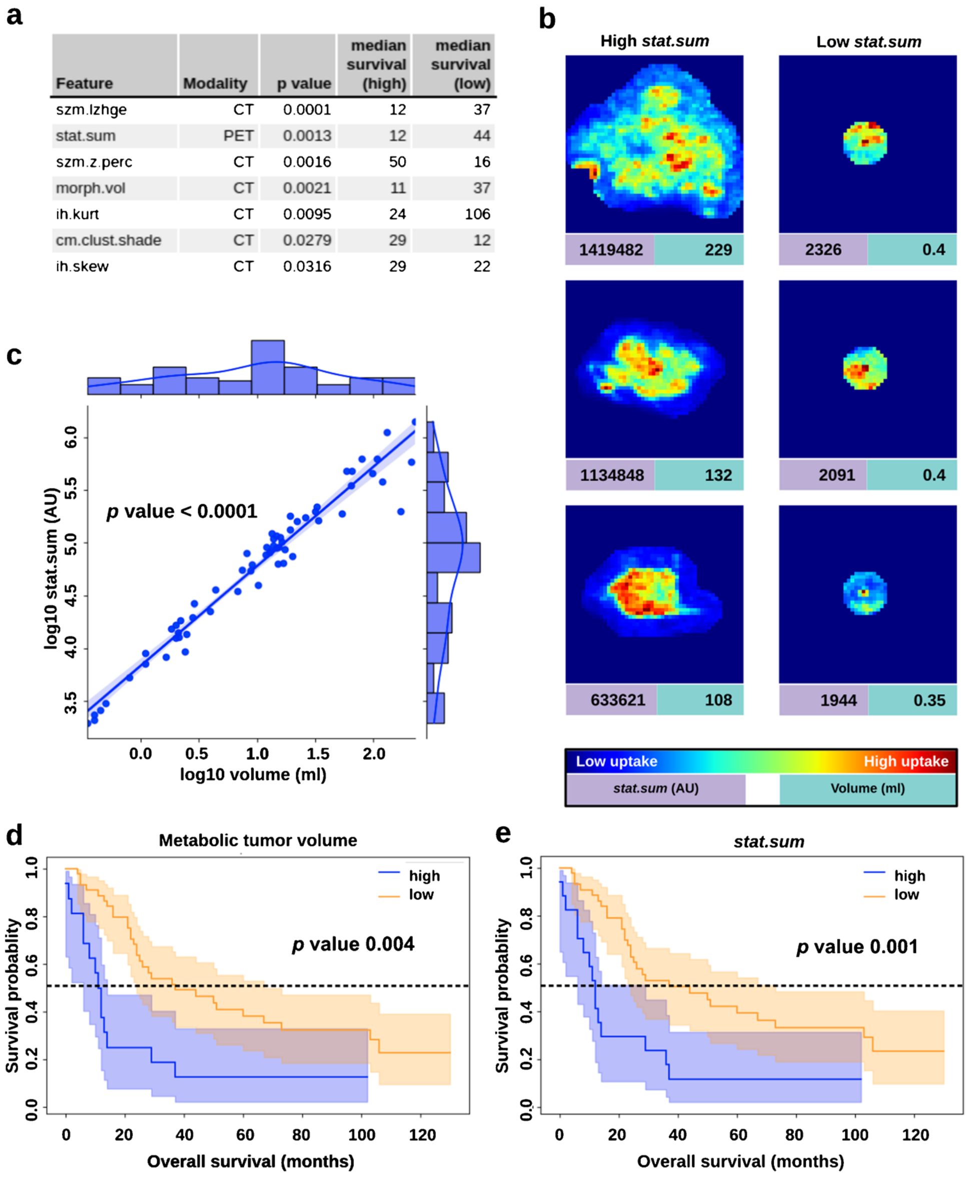

Feature	Modality	p value	median survival (high)	median survival (low)
szm.lzhge	CT	0.0001	12	37
stat.sum	PET	0.0013	12	44
szm.z.perc	CT	0.0016	50	16
morph.vol	CT	0.0021	11	37
ih.kurt	CT	0.0095	24	106
cm.clust.shade	CT	0.0279	29	12
ih.skew	CT	0.0316	29	22

Fig. 2 *stat.sum* captures information of metabolic tumor volume (MTV) and improves prognostic stratification. **a** Most prognostic radiomic features ($p < 0.05$) with associated modalities and respective survival analysis results. Ordered by *p* value. **b** Coronal maximum intensity projections (MIPs) of the PET images for the three lesions with the highest *stat.sum* (left column) and lowest *stat.sum* (right column). Red values indicate a high [.^{18}F]FDG uptake while blue values indicate a low or no uptake. **c** Pearson correlation between MTV and *stat.sum* after applying log transformation. **d** Kaplan–Meier curve for MTV. **e** Kaplan–Meier curve for *stat.sum*. Radiomic feature values are shown in arbitrary units (AU)

Association of radiomics and pathway disruption scores

Significant associations between four radiomic-pathway pairs were identified ($p < 0.05$) (Fig. 4a). A significant association was found between p53 signaling and PET-based *ih.kurt* ($p < 0.002$) (Fig. 4). The overlap of radiomic feature distributions for both functional pathway states identified *ih.kurt* as indicator but not as an error-free predictor of the pathway states (Fig. 4b). Multiple other radiomic-pathway combinations are potentially associated, but did not reach significance (Fig. 4c, d). A full list of association results is shown in Supplementary Table 2.

Prognostic value of radiogenomic markers

Since the preceding analysis indicated pathway states cannot be predicted solely from imaging markers (Fig. 4b), the incorporation of complementary information via combining radiomic and pathway features to radiogenomic features was investigated. Of the 49 radiogenomic markers (Supplementary Table 3), 14 were significantly prognostic ($p < 0.001$). Seven radiogenomic markers were more prognostic than the most prognostic univariate marker *szm.lzhge* ($p < 0.0001$). The best performing radiogenomic marker was *cellular senescence (functional)-CT ih.kurt (high)* indicating a worse prognosis (p 5.5 * 10^{-8}).

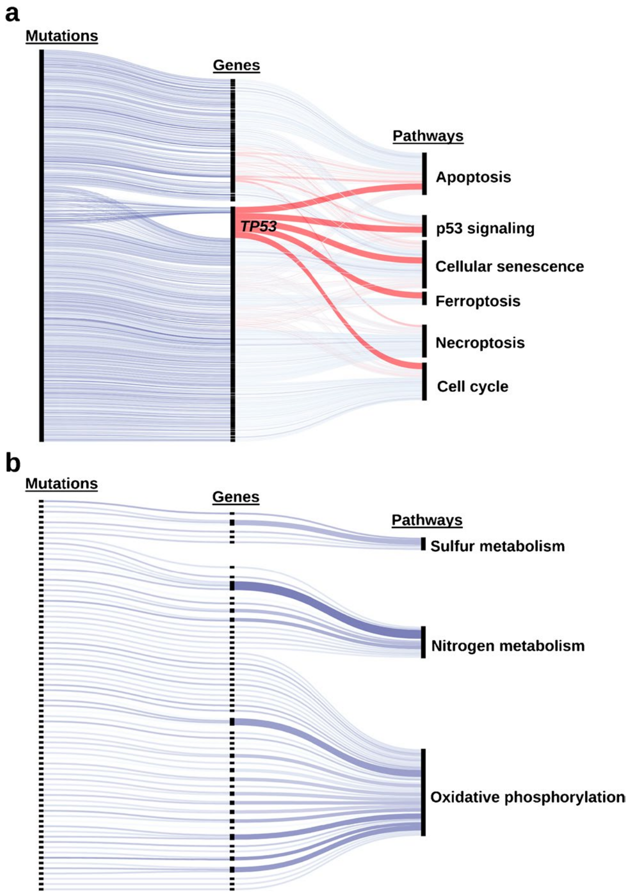

Fig. 3 Composition of pathway CADD scores from gene- and mutation-level scores for KEGG pathways associated with cell growth and death (**a**) and energy metabolism (**b**). Links of genes influencing multiple pathways are shown in red. The color intensity of links indicates the CADD score of mutations and sums of CADD scores over all mutations for mutations and genes, respectively. Hence, darker blue or red indicate a higher CADD score (disrupted) while a lighter color indicates a low CADD score (functional). The width of links between genes and pathways indicates the number of mutations in a gene over all patients in our cohort. The fully annotated, interactive version of this figure is available at https://cspielvogel.github.io/cadd-diagram/cadd_composition_cell_growth_and_death.html and https://cspielvogel.github.io/cadd-diagram/cadd_composition_energy_metabolism.html for cell growth and death or energy metabolism, respectively

Multiple cox regression with *cellular senescence (functional)-CT ih.kurt (high)* indicated a strong prognostic value of the radiogenomic marker ($p < 0.0001$, HR 2.41) (Fig. 5d, e). Covariates included age at diagnosis ($p < 0.01$, HR 0.04), SUVmax (p 0.08, HR -0.01), and stage IVc (p 0.02, HR 1.06). None of the demographic factors age and gender as well as stage IVc were significantly prognostic in the independent univariate analysis (Supplementary Figs. 10–12).

Machine learning classification

To assess the performance of models integrating complex interactions between multiple genomic, radiomic, and radiogenomic features, a ML approach was employed to establish and cross-validate three binary classifications. Prediction targets were OS greater than 24 months, OS greater than the median OS, and OS greater than 36 months. The cross-validation revealed an area under the receiver operating characteristic curve (AUC) of 0.72 for both the 24-months-OS and the median-OS model. For the 36-months-OS model, a cross-validated AUC of 0.75 was observed. Additional performance metrics are shown in Fig. 6a. Feature importance ranking further indicated the clinical relevance of radiogenomic features, which were the most important attributes in all three models, outperforming genetic as well as radiomic features (Fig. 6b). Over all models, radiomic features had the lowest prognostic value with an average importance of 2.5%, genomic features were associated with an average importance of 4.0%, and radiogenomic features were most important (5.5%).

Discussion

In our study, we analyzed the association of radiomic with genomic data in HNSCC patients. Our results show a strong influence of the genetic status on quantitative imaging markers in a cohort of HNSCC patients following radiomic and genomic data analysis. By using complementary information from imaging and genetic patterns, we were able to demonstrate that combining radiomic and pathway-level genomic features to radiogenomic markers improves prognostic performance significantly. Furthermore, we identified cellular senescence-derived radiogenomic markers essential for prognostic stratification of HNSCC patients.

In the association analysis of radiomic and genetic traits at the pathway level, we found that higher levels of the PET-based histogram feature *ih.kurt* can be associated with an impaired state of p53 signaling and nitrogen metabolism (Fig. 4). One plausible explanation for the observed association of p53 signaling is the heterogeneous uptake of [^{18}F]FDG indicated by *ih.kurt*. The genetic and phenotypic heterogeneity of clonal populations in tumors are the result of an increased number of proliferation cycles, which results in increased mutation rates given the fast growth of tumor tissue [32]. This genetic heterogeneity in clonal populations could be caused by impaired p53 signaling causing genome instability [33]. Genome instability has previously been shown to promote intratumoral heterogeneity detectable on PET via epigenetic mechanisms [34]. Targeting p53 signaling has been shown to be a successful treatment strategy and is currently evaluated in clinical trials using

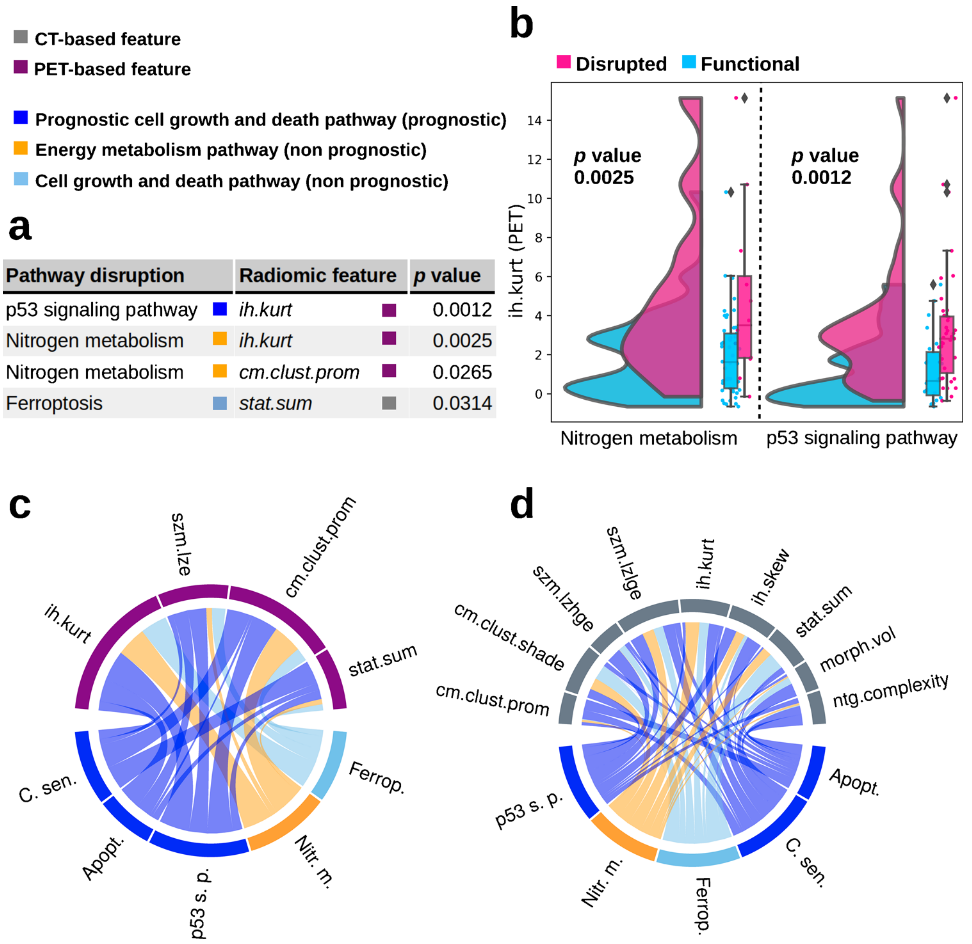

Pathway disruption		Radiomic feature		p value
p53 signaling pathway	🟦	*ih.kurt*	🟪	0.0012
Nitrogen metabolism	🟧	*ih.kurt*	🟪	0.0025
Nitrogen metabolism	🟧	*cm.clust.prom*	🟪	0.0265
Ferroptosis	🟦	*stat.sum*	◼	0.0314

Fig. 4 Association of PET- and CT-based radiomic features with pathways related to cell growth and death as well as energy metabolism. **a** Pathways and linked radiomic features with *p* values below 0.05. **b** Distribution of the two most significant associations: PET-based radiomic histogram feature excess discretized intensity kurtosis (*ih.kurt*) depending on the functional state of two pathways, nitrogen metabolism (left) and p53 signaling (right). For each pathway, the distribution of the radiomic feature *ih.kurt* (PET) is visualized for patients with functional (blue) and disrupted (pink) genetic status via kernel density estimation. A higher width of the curve area at a given radiomic feature value on the *y*-axis indicates a higher probability of a patient to have the respective radiomic feature value as estimated by the kernel density estimation. Furthermore, for each pathway, two boxplots indicate the distribution of the radiomic feature for patients with functional and disrupted genetic status. Radiomic features are displayed in arbitrary units. **c** Associations between PET radiomic features and pathways. **d** Associations between CT radiomic features and pathways. The width of the links indicates the inverse *p* value within each of the chord plots. Pathways include cellular senescence (C. sen.), apoptosis (Apopt.), p53 signaling pathway (p53 s. p.), nitrogen metabolism (Nitr. m.), and ferroptosis (Ferrop.)

multiple strategies for treating various cancers, including HNSCC [35]. In the association of nitrogen metabolism and the increased metabolism indicated by PET imaging, the amino acid glutamine might play a crucial role. Many cancer cells are reliant on glutamine as main anaplerotic metabolite to fuel the citric acid cycle through a series of biochemical reactions termed glutaminolysis [36]. Therefore, nitrogen metabolism plays an essential role in cells proliferation via anabolic processes such as the biosynthesis of amino acids, nucleotides, and polyamines. Similar to p53 signaling, targeting nitrogen metabolism in proliferating cancer cells has been suggested to be a promising therapeutic approach in clinical studies [37–39]. Considering these aspects, exploring *ih.kurt* as a novel imaging-based marker to determine patients benefitting from these therapeutic approaches is highly promising.

Currently, SUV-based metrics dominate clinical image analysis, given their ease of use and compatibility with conventional PET/CT acquisition protocols. SUV-based metrics have shown prognostic value in a meta-analysis [40]. However, we were not able to reproduce this finding in this study's cohort. Still, our results identify PET- and CT-derived radiomic features that have prognostic value (Fig. 2a), even where SUV-based metrics did not provide prognostic information in this study's cohort. Moreover, we identify specific tumor characteristics, which reflect

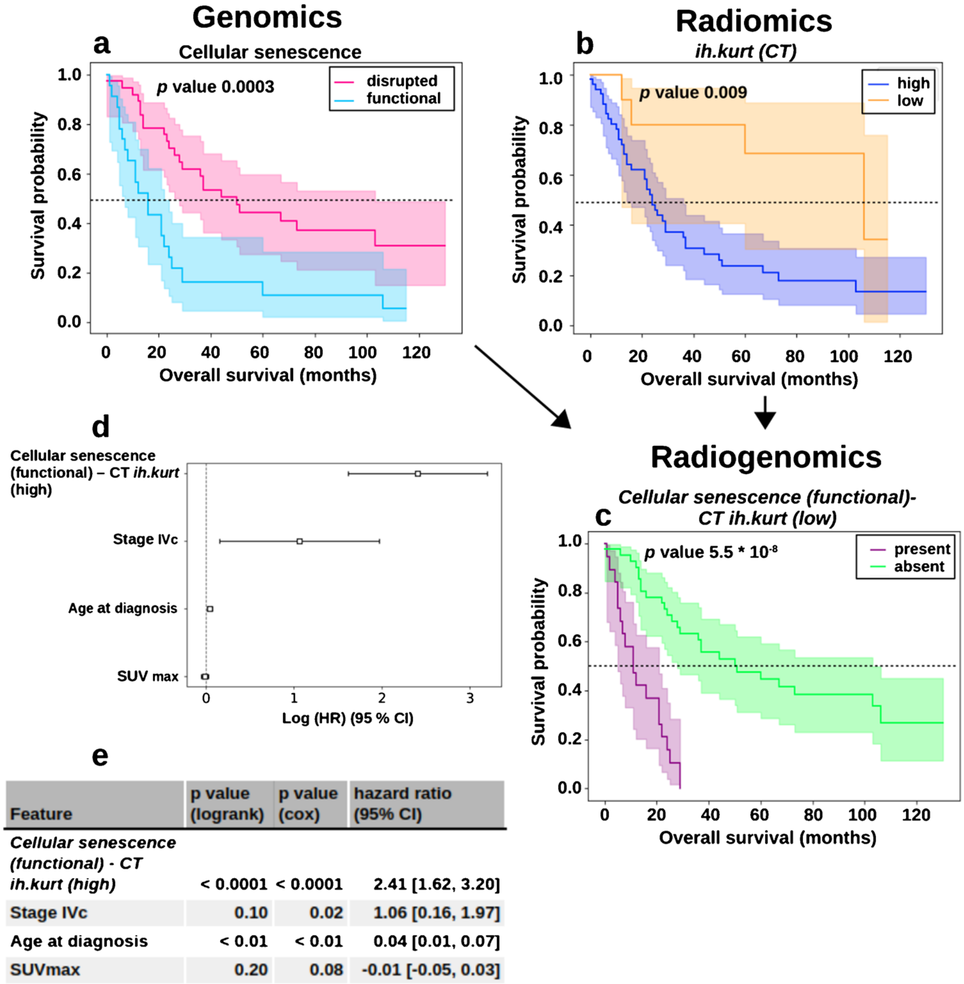

Feature	p value (logrank)	p value (cox)	hazard ratio (95% CI)
Cellular senescence (functional) - CT ih.kurt (high)	< 0.0001	< 0.0001	2.41 [1.62, 3.20]
Stage IVc	0.10	0.02	1.06 [0.16, 1.97]
Age at diagnosis	< 0.01	< 0.01	0.04 [0.01, 0.07]
SUVmax	0.20	0.08	-0.01 [-0.05, 0.03]

Fig. 5 Kaplan–Meier curves for the most prognostic radiogenomic marker and the corresponding univariate markers. Kaplan–Meier curves associated with univariate markers include cellular senescence (**a**) and the CT-based radiomic feature *ih.kurt* (**b**). The Kaplan–Meier curve of the combined radiogenomic marker clearly indicates an improved prognostic stratification (**c**). The radiogenomic marker was defined to be "present" if cellular senescence was functional and the ih.kurt (CT) was low. In all other cases, the radiogenomic marker is "absent." The forest plot shows the hazard ratios derived using Cox regression (**d**). A summary of the univariate analysis (logrank) and multivariate (cox) analysis with a set of covariates are shown in (**e**)

these radiomic features. PET-derived *stat.sum* captures the information of MTV (Fig. 2b, c). This can be explained by PET-derived *stat.sum* indicating the summed activity throughout the entire lesion and consequently is subject to a strong volume-confounding effect [41]. Since *stat.sum* is related to MTV and therefore to the T stage of the tumor, a relation with prognosis is not surprising and presents an expected finding. However, *stat.sum* was slightly more prognostic than MTV, indicating additional prognostic information being captured by the radiomic feature compared to volume alone (Fig. 2d, e). Overall, despite the association of volume-related radiomic features such as *stat.sum* and *morph.vol* with T stage, the investigation of these features is potentially valuable. On the one hand, some of these features provide a fine-grained resolution of the tumor volume itself due to their continuous nature. This makes volume-related radiomic features not only better parameters for automated analysis but also allows for finding optimal thresholds to stratify patients. On the other hand, some volume-related radiomic features such as *stat.sum* incorporate additional information to tumor volume and therefore provide a different viewpoint of the tumor.

The genetically functional state of cellular senescence was significantly associated with reduced survival rates and comprised the most prognostic markers when combined with radiomic features, in the statistical and ML analysis (Figs. 5 and 6). Senescence is known to induce a stable cell cycle arrest triggered by p53 and was therefore proposed as a prevention mechanism for tumorigenesis [42]. However, recent studies have shown that senescent cells can function as tumor promoters, partly due to the proinflammatory and growth-stimulating effects of the senescence-associated secretory phenotype [43].

Since none of the extracted imaging features had a strong association with senescence (Fig. 4), we hypothesized that the identified prognostic imaging markers contain complementary information relevant for prognosis. The ML analysis confirmed the added value of combined radiogenomic features over their univariate counterparts (Fig. 6). Furthermore, the ML analysis demonstrated the capabilities

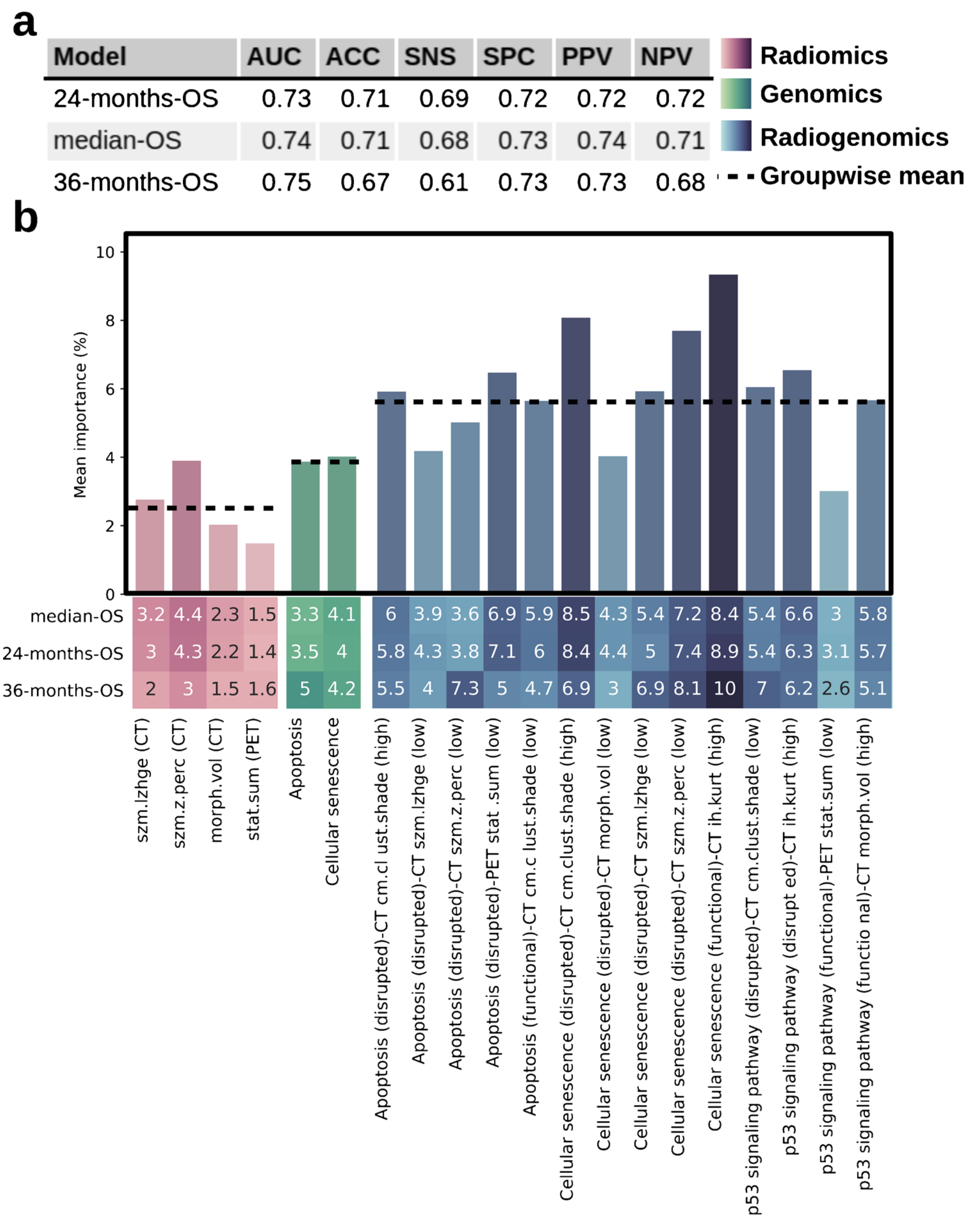

Model	AUC	ACC	SNS	SPC	PPV	NPV
24-months-OS	0.73	0.71	0.69	0.72	0.72	0.72
median-OS	0.74	0.71	0.68	0.73	0.74	0.71
36-months-OS	0.75	0.67	0.61	0.73	0.73	0.68

	szm.lzhge (CT)	szm.z.perc (CT)	morph.vol (CT)	stat.sum (PET)	Apoptosis	Cellular senescence	Apoptosis (disrupted)-CT cm.cl ust.shade (high)	Apoptosis (disrupted)-CT szm.lzhge (low)	Apoptosis (disrupted)-CT szm.z.perc (low)	Apoptosis (disrupted)-PET stat .sum (low)	Apoptosis (functional)-CT cm.c lust.shade (low)	Cellular senescence (disrupted)-CT cm.clust.shade (high)	Cellular senescence (disrupted)-CT morph.vol (low)	Cellular senescence (disrupted)-CT szm.lzhge (low)	Cellular senescence (disrupted)-CT szm.z.perc (low)	Cellular senescence (functional)-CT ih.kurt (high)	p53 signaling pathway (disrupted)-CT cm.clust.shade (low)	p53 signaling pathway (disrupt ed)-CT ih.kurt (high)	p53 signaling pathway (functional)-PET stat.sum (low)	p53 signaling pathway (functio nal)-CT morph.vol (high)
median-OS	3.2	4.4	2.3	1.5	3.3	4.1	6	3.9	3.6	6.9	5.9	8.5	4.3	5.4	7.2	8.4	5.4	6.6	3	5.8
24-months-OS	3	4.3	2.2	1.4	3.5	4	5.8	4.3	3.8	7.1	6	8.4	4.4	5	7.4	8.9	5.4	6.3	3.1	5.7
36-months-OS	2	3	1.5	1.6	5	4.2	5.5	4	7.3	5	4.7	6.9	3	6.9	8.1	10	7	6.2	2.6	5.1

Fig. 6 Machine learning–derived feature ranking (% importance) for the three classification models. **a** Performance metrics for the classification models include area under the receiver operating characteristic curve (AUC), accuracy (ACC), sensitivity (SNS), specificity (SPC), positive predictive value (PPV), and negative predictive value (NPV). **b** The heatmap shows the feature contribution for each model. The bar chart shows the importance of each feature as mean over the models. Darker colors indicate higher values. The dashed lines indicate the mean importance over all features belonging to one of the three feature categories, radiomics, genomics, and radiogenomics. Feature importance was calculated based on R-squared ranking

of highly multivariate prediction models as prognostic biomarker (Fig. 5).

Our findings encourage the utilization of senescence-derived radiogenomic markers for the prognostic stratification of HNSCC patients into clinically meaningful groups. Prognosis is certainly one of the most important, yet most difficult issues to address in clinical oncology, not only for the patients but also for their relatives. Prognostic markers, like the ones presented in the present study, can play a vital role in clinical decision-making. They allow for an accurate estimation of prognosis, enabling physicians to anticipate disease progression and, thus, aiding the selection of the most suitable treatment and follow-up scheme and allowing for an optimized allocation of healthcare resources. In addition, the prognostic markers identified in this study provide a primer for research into the mechanistic causes of the survival differences depending on the state of radiogenomic markers.

In our study, mutational tumor DNA was used, delivering a stable and easily reproducible ground truth compared to transcriptomics data deployed in similar radiogenomic studies [44, 45]. In addition, pathway-level genetic markers were used not only integrating information about multiple genes but also deriving information closer to the functional state of the cell. Furthermore, most studies used CT imaging alone [44, 45] while in this study, anatomical information from CT and metabolic information from [^{18}F]FDG PET were integrated.

Since we used genetic data derived from solid biopsies, subclonal populations of the tumor cells may not be adequately reflected. To overcome this issue and avoid the drawbacks of surgical interventions, future radiogenomic studies may therefore focus on the use of cell-free DNA (cfDNA) from liquid biopsies to obtain genetic data. Follow-up studies involving DNA sequencing could be greatly simplified, accelerated, and cheapened since panel sequencing focusing on senescence and nitrogen metabolism signaling pathways would be sufficient.

Our study is based on a limited cohort size, which restricted the ML approach to features selected based on the prognostic value in the overall cohort. Since the semi-automated segmentation procedure led to only one segmentation, we were not able to assess the segmentation's reliability. Furthermore, we were not able to validate our findings using public data since we did not find [^{18}F]FDG PET/CT and matched WES data available online. The cohort used in this study is highly heterogeneous, including different clinical subtypes and tumors from multiple locations and stages. Together, this presents a limitation for the translation to clinics since not all findings might be true for all subgroups. The cohort is derived from a single center, requiring an independent, multi-centric validation to account for center-specific biases introduced, for example, through different imaging protocols. Next to imaging protocols, radiomic features are generally sensitive to variations in segmentation protocols and scanner types, creating a challenge when applying radiomic features to other centers.

Conclusions

In this work, we compared and correlated radiomic with genomic data from HNSCC patients using classical statistics as well as machine learning and were able to find a significant impact of genomic alterations on the corresponding radiomic imaging markers. We demonstrate that combining and unifying PET/CT radiomic and pathway-level genomic features into radiogenomic markers radically improves prognostic performance. In addition, our experiments have revealed the essential role of cellular senescence and derived radiogenomic markers in patient outcome, which may be essential for prognostic stratification of HNSCC patients in the future. Future studies can potentially validate our approach by induction of the presented genetic patterns in preclinical models to investigate the resulting imaging patterns found to be associated with genetic patterns. More research is needed focusing on the investigation of additional data types such as proteomic, epigenomic, and microscopy data to further add to a holistic, personalized picture of cancer patients and improve prognostic biomarkers.

Abbreviations HNSCC: Head and neck squamous cell carcinoma; OS: Overall survival; WES: Whole-exome sequencing; CADD: Combined annotation dependent depletion; VOI: Volume of interest; ML: Machine learning; MTV: Metabolic tumor volume; SUV: Standard uptake value; AUC: Area under the receiver operating characteristic curve

Supplementary Information The online version contains supplementary material available at https://doi.org/10.1007/s00259-022-05973-9.

Acknowledgements The Core Facility Genomics and Core Facility Bioinformatics of CEITEC Masaryk University are gratefully acknowledged for the DNA sequencing and associated analysis. The financial support by the Austrian Federal Ministry for Digital and Economic Affairs, the National Foundation for Research, Technology and Development, and the Christian Doppler Research Association is gratefully acknowledged. The financial and scientific support from Siemens Healthineers is gratefully acknowledged. We thank Stefan Grünert for the critical review of the text and the exceptional support in writing the manuscript. We thank Jing Ning for the critical review and support in writing the manuscript. We thank Eva Sauer for her support in the data extraction and preprocessing procedure.

Author contributions C.P.S. performed the radiomic feature extraction, planning, and execution of experiments including statistical and ML, result interpretation, data visualization, and figure design as well as the lead in writing the manuscript. C.P.S., L.P., L.Kenner, S.S., A.R.H., and M.H. were involved in the study design. S.S., A.L., B.J., J.S., and L.Kadletz contributed to the acquisition of tumor tissue and clinical annotation. M.G. and A.L. contributed to the image data acquisition. L.Kenner and S.S. performed the inspection and annotation of tumor tissue eligible for sequencing. E.G. and S.S. performed the tissue sample preparation and DNA extraction. C.P.S., D.K., and L.P. contributed to the development of the radiomic feature extraction and ML software. K.T. and V.B. performed the sequencing data analysis. S.S., V.B., T.B., M.H., L.P., L.Kenner, and A.H. contributed to the writing. All authors reviewed the manuscript and provided feedback.

Funding Open access funding provided by Medical University of Vienna. This work was supported by the Austrian Federal Ministry for Digital and Economic Affairs, the National Foundation for Research, Technology and Development, Siemens Healthineers, and the Christian Doppler Research Association.

Data availability The pathway-level genetic, radiomic, standard uptake value (SUV) features and clinical annotation data is publicly available at https://osf.io/rbuqa/.

Declarations

Ethics approval The study was approved by the institutional review board with ethics ID 1649/2016 at the General Hospital of Vienna.

Consent to participate Informed consent was obtained from all individual participants included in the study.

Consent to publish All individuals participating in the study provided informed consent for publication.

Conflict of interest M.H., L.P., and T.B. are co-founders of Dedicaid GmbH, Austria. No other potential conflicts of interest relevant to this article exist.

References

1. Cramer JD, Burtness B, Le QT, Ferris RL. The changing therapeutic landscape of head and neck cancer. Nat Rev Clin Oncol. 2019;16(11):669–83.
2. Pfister DG, Spencer S, Adelstein D, et al. Head and Neck Cancers, Version 2.2020, NCCN Clinical Practice Guidelines in Oncology. J Natl Compr Cancer Netw. 2020;18(7):873–98.
3. Leemans CR, Snijders PJF, Brakenhoff RH. The molecular landscape of head and neck cancer. Nat Rev Cancer. 2018;18(5):269–82.
4. Machiels JP, René Leemans C, Golusinski W, Grau C, Licitra L, Gregoire V. Squamous cell carcinoma of the oral cavity, larynx, oropharynx and hypopharynx: EHNS–ESMO–ESTRO Clinical Practice Guidelines for diagnosis, treatment and follow-up. Ann Oncol. 2020;31(11):1462–1475.
5. Lambin P, Leijenaar RTH, Deist TM, et al. Radiomics: the bridge between medical imaging and personalized medicine. Nat Rev Clin Oncol. 2017;14(12):749–62.
6. Budach V, Tinhofer I. Novel prognostic clinical factors and biomarkers for outcome prediction in head and neck cancer: a systematic review. Lancet Oncol. 2019;20(6):e313–26.
7. Hsieh JC, Wang H, Wu M, et al. Review of emerging biomarkers in head and neck squamous cell carcinoma in the era of immunotherapy and targeted therapy. Head Neck. 2019;41(S1):19–45.
8. Oldenhuis CNAM, Oosting SF, Gietema JA, de Vries EGE. Prognostic versus predictive value of biomarkers in oncology. Eur J Cancer. 2008;44(7):946–53.
9. Wong CC, Qian Y, Yu J. Interplay between epigenetics and metabolism in oncogenesis: mechanisms and therapeutic approaches. Oncogene. 2017;36(24):3359–74.
10. Rentzsch P, Witten D, Cooper GM, Shendure J, Kircher M. CADD: predicting the deleteriousness of variants throughout the human genome. Nucleic Acids Res. 2019;47(D1):D886–94.
11. Orlhac F, Frouin F, Nioche C, Ayache N, Buvat I. Validation of a method to compensate multicenter effects affecting CT Radiomics. Radiology. 2019;291(1):53–9.
12. Li H, Durbin R. Fast and accurate short read alignment with Burrows-Wheeler transform. Bioinformatics. 2009;25(14):1754–60.
13. Kim S, Scheffler K, Halpern AL, et al. Strelka2: fast and accurate calling of germline and somatic variants. Nat Methods. 2018;15(8):591–4.
14. Lai Z, Markovets A, Ahdesmaki M, et al. VarDict: a novel and versatile variant caller for next-generation sequencing in cancer research. Nucleic Acids Res. 2016;44(11):e108–e108.
15. McLaren W, Gil L, Hunt SE, et al. The Ensembl Variant Effect Predictor. Genome Biol. 2016;17(1):122.
16. Kircher M, Witten DM, Jain P, O'Roak BJ, Cooper GM, Shendure J. A general framework for estimating the relative pathogenicity of human genetic variants. Nat Genet. 2014;46(3):310–5.
17. Rentzsch P, Schubach M, Shendure J, Kircher M. CADD-Splice—improving genome-wide variant effect prediction using deep learning-derived splice scores. Genome Med. 2021;13(1):31.
18. Sukhai MA, Misyura M, Thomas M, et al. Somatic tumor variant filtration strategies to optimize tumor-only molecular profiling using targeted next-generation sequencing panels. J Mol Diagnostics. 2019;21(2):261–73.
19. Auton A, Abecasis GR, Altshuler DM, et al. A global reference for human genetic variation. Nature. 2015;526(7571):68–74.
20. Karczewski KJ, Francioli LC, Tiao G, et al. The mutational constraint spectrum quantified from variation in 141,456 humans. Nature. 2020;581(7809):434–43.
21. Auer PL, Johnsen JM, Johnson AD, et al. Imputation of exome sequence variants into population-based samples and blood-cell-trait-associated loci in African Americans: NHLBI GO Exome Sequencing Project. Am J Hum Genet. 2012;91(5):794–808.
22. Landrum MJ, Chitipiralla S, Brown GR, et al. ClinVar: improvements to accessing data. Nucleic Acids Res. 2020;48(D1):D835–44.
23. Kanehisa M, Goto S. KEGG: kyoto encyclopedia of genes and genomes. Nucleic Acids Res. 2000;28(1):27–30.
24. Itan Y, Shang L, Boisson B, et al. The mutation significance cutoff: gene-level thresholds for variant predictions. Nat Methods. 2016;13(2):109–10.
25. Papp L, Pötsch N, Grahovac M, et al. Glioma survival prediction with combined analysis of in vivo 11C-MET PET features, ex vivo features, and patient features by supervised machine learning. J Nucl Med. 2018;59(6):892–9.
26. Papp L, Spielvogel CP, Grubmüller B, et al. Supervised machine learning enables non-invasive lesion characterization in primary prostate cancer with [68Ga]Ga-PSMA-11 PET/MRI. Eur J Nucl Med Mol Imaging. 2021;48(6):1795–805.
27. Chawla NV, Bowyer KW, Hall LO, Kegelmeyer WP. SMOTE: synthetic minority over-sampling technique. J Artif Intell Res. 2002;16:321–57.
28. Chicco D, Warrens MJ, Jurman G. The coefficient of determination R-squared is more informative than SMAPE, MAE, MAPE, MSE and RMSE in regression analysis evaluation. PeerJ Comput Sci. 2021;7:e623.
29. Zwanenburg A, Leger S, Vallières M, Löck S. Image biomarker standardisation initiative. *arXiv Prepr arXiv161207003*. Published online 2016.
30. Van Griethuysen JJM, Fedorov A, Parmar C, et al. Computational radiomics system to decode the radiographic phenotype. Cancer Res. 2017;77(21):e104–7.
31. Cottereau AS, Versari A, Loft A, et al. Prognostic value of baseline metabolic tumor volume in early-stage Hodgkin lymphoma in the standard arm of the H10 trial. Blood. 2018;131(13):1456–63.
32. Marusyk A, Polyak K. Tumor heterogeneity: causes and consequences. Biochim Biophys Acta - Rev Cancer. 2010;1805(1):105–17.
33. Levine AJ, Ting DT, Greenbaum BD. P53 and the defenses against genome instability caused by transposons and repetitive elements. BioEssays. 2016;38(6):508–13.
34. Pisanic TR, Athamanolap P, Wang TH. Defining, distinguishing and detecting the contribution of heterogeneous methylation to cancer heterogeneity. Semin Cell Dev Biol. 2017;64:5–17.
35. Huang J. Current developments of targeting the p53 signaling pathway for cancer treatment. Pharmacol Ther. 2021;220:107720.
36. Hensley CT, Wasti AT, DeBerardinis RJ. Glutamine and cancer: cell biology, physiology, and clinical opportunities. J Clin Invest. 2013;123(9):3678–84.

37. Casero RA, Murray Stewart T, Pegg AE. Polyamine metabolism and cancer: treatments, challenges and opportunities. Nat Rev Cancer. 2018;18(11):681–95.
38. Ananieva E. Targeting amino acid metabolism in cancer growth and anti-tumor immune response. World J Biol Chem. 2015;6(4):281.
39. Kurmi K, Haigis MC. Nitrogen metabolism in cancer and immunity. Trends Cell Biol. 2020;30(5):408–24.
40. Pak K, Cheon GJ, Nam HY, et al. Prognostic value of metabolic tumor volume and total lesion glycolysis in head and neck cancer: a systematic review and meta-analysis. J Nucl Med. 2014;55(6):884–90.
41. Traverso A, Kazmierski M, Zhovannik I, et al. Machine learning helps identifying volume-confounding effects in radiomics. Phys Medica. 2020;71:24–30.
42. Calcinotto A, Kohli J, Zagato E, Pellegrini L, Demaria M, Alimonti A. Cellular senescence: aging, cancer, and injury. Physiol Rev. 2019;99(2):1047–78.
43. Alimirah F, Pulido T, Valdovinos A, et al. Cellular senescence promotes skin carcinogenesis through p38MAPK and p44/42MAPK signaling. Cancer Res. 2020;80(17):3606–19.

44 Grossmann P, Stringfield O, El-Hachem N, et al. Defining the biological basis of radiomic phenotypes in lung cancer. Elife. 2017;6:e23421.

45. Aerts HJWL, Velazquez ER, Leijenaar RTH, et al. Decoding tumour phenotype by noninvasive imaging using a quantitative radiomics approach. Nat Commun. 2014;5(1):4006.

Lab Invest 104 (2024) 102161

LABORATORY INVESTIGATION

journal homepage: https://laboratoryinvestigation.org/

USCAP UNITED STATES AND CANADIAN ACADEMY OF PATHOLOGY
Creating a Better Pathologist

Research Article

Real-World Performance of Integrative Clinical Genomics in Pediatric Precision Oncology

Petra Pokorna[a,b,c,d], Hana Palova[a,b], Sona Adamcova[a,b], Robin Jugas[a,b], Dagmar Al Tukmachi[a,b,c], Michal Kyr[e], Dana Knoflickova[a], Katerina Kozelkova[a,b], Vojtech Bystry[a], Sona Mejstrikova[a,f], Tomas Merta[e], Karolina Trachtova[a,b], Eliska Podlipna[a,b], Peter Mudry[e], Zdenek Pavelka[e], Viera Bajciova[e], Pavel Tinka[e], Marie Jarosova[f], Tina Catela Ivkovic[a], Sibylle Madlener[g], Karol Pal[a], Natalia Stepien[g], Lisa Mayr[g], Boris Tichy[a], Klara Drabova[e], Marta Jezova[h], Sarka Kozakova[i,j], Jitka Vanackova[a], Lenka Radova[a], Karin Steininger[g], Christine Haberler[k], Johannes Gojo[g], Jaroslav Sterba[d,e,*], Ondrej Slaby[a,b,d,h,*]

[a] *Central European Institute of Technology, Masaryk University, Brno, Czech Republic;* [b] *Department of Biology, Faculty of Medicine, Masaryk University, Brno, Czech Republic;* [c] *Department of Biochemistry, Faculty of Science, Masaryk University, Brno, Czech Republic;* [d] *Center for Precision Medicine, University Hospital Brno, Brno, Czech Republic;* [e] *Department of Pediatric Oncology, University Hospital Brno and Faculty of Medicine, Masaryk University, Brno, Czech Republic;* [f] *Department of Internal Medicine, Hematology and Oncology, University Hospital Brno and Faculty of Medicine, Masaryk University, Brno, Czech Republic;* [g] *Department of Pediatrics and Adolescent Medicine, Comprehensive Center for Pediatrics and Comprehensive Cancer Center, Medical University of Vienna, Vienna, Austria;* [h] *Department of Pathology, University Hospital Brno and Faculty of Medicine, Masaryk University, Brno, Czech Republic;* [i] *Department of Pharmacology, Faculty of Medicine, Masaryk University, Brno, Czech Republic;* [j] *Department of Pharmacy, University Hospital Brno, Brno, Czech Republic;* [k] *Division of Neuropathology and Neurochemistry, Department of Neurology, Medical University of Vienna, Vienna, Austria*

ARTICLE INFO

Article history:
Received 26 June 2024
Revised 16 September 2024
Accepted 15 October 2024
Available online 21 October 2024

Keywords:
next-generation sequencing
pediatric oncology
precision medicine

ABSTRACT

Despite significant improvement in the survival of pediatric patients with cancer, treatment outcomes for high-risk, relapsed, and refractory cancers remain unsatisfactory. Moreover, prolonged survival is frequently associated with long-term adverse effects due to intensive multimodal treatments. Accelerating the progress of pediatric oncology requires both therapeutic advances and strategies to mitigate the long-term cytotoxic side effects, potentially through targeting specific molecular drivers of pediatric malignancies. In this report, we present the results of integrative genomic and transcriptomic profiling of 230 patients with malignant solid tumors (the "primary cohort") and 18 patients with recurrent or otherwise difficult-to-treat nonmalignant conditions (the "secondary cohort"). The integrative workflow for the primary cohort enabled the identification of clinically significant single nucleotide variants, small insertions/deletions, and fusion genes, which were found in 55% and 28% of patients, respectively. For 38% of patients, molecularly informed treatment recommendations were made. In the secondary cohort, known or potentially driving alteration was detected in 89% of cases, including a suspected novel causal gene for patients with inclusion body infantile digital fibromatosis. Furthermore, 47% of findings also brought therapeutic implications for subsequent management. Across both cohorts, changes or refinements to the original histopathological diagnoses were achieved in 4% of cases. Our study demonstrates the efficacy of integrating advanced genomic and transcriptomic analyses to identify therapeutic targets, refine diagnoses, and optimize treatment strategies for challenging pediatric

---

* Corresponding authors.
E-mail addresses: oslaby@med.muni.cz (O. Slaby), sterba.jaroslav@fnbrno.cz) (J. Sterba).

https://doi.org/10.1016/j.labinv.2024.102161

and young adult malignancies and underscores the need for broad implementation of precision oncology in clinical settings.

Introduction

Over the past several decades, we have observed a significant increase in the overall survival rates for pediatric patients with cancer, now reaching up to 85% within 5 years from diagnosis.[1] Despite these encouraging results, the pace of progress in treatment outcomes for specific groups of patients, consisting of relapsed, refractory, or high-risk primary tumors, has slowed down, and their clinical management remains challenging. The expanding understanding of the molecular mechanisms underlying carcinogenesis, combined with advancements in sequencing and bioinformatics, now allows for detailed molecular characterization of a patient's tumor tissue and the host itself under the paradigm of precision oncology.

Precision oncology is an evolving field that not only aims to enhance survival rates but also to develop or facilitate access to more effective and less-toxic treatment options. In pediatric precision oncology, implementing comprehensive high-throughput techniques, such as whole-exome, whole-genome, and RNA sequencing, is particularly crucial, as these methods offer more thorough analysis, addressing the unique molecular characteristics of pediatric tumors. Several initiatives have explored the feasibility of this approach and demonstrated significant, although varied, success rates in identifying actionable mutations in pediatric tumors, as well as treatment outcomes upon administration of targeted treatment.[2-10] Here, we present the molecular findings obtained by implementing comprehensive molecular profiling in a mixed cohort of pediatric and young adult patients with solid tumors within a real-world clinical setting.

Material and Methods

Patient Cohort

Between August 2016 and June 2023, 248 pediatric and young adult patients with relapsed, refractory, or high-risk primary solid tumors, as well as secondary malignancies (hereafter referred to as the "primary cohort"), were prospectively enrolled in the Pediatric Precision Oncology Program at the Department of Pediatric Oncology at University Hospital Brno to undergo comprehensive molecular profiling. Two hundred twenty-four patients were referred for testing directly from the Department of Pediatric Oncology at University Hospital Brno, and 24 patients were referred through a collaboration with the Department of Pediatrics and Adolescent Medicine at the Medical University of Vienna. In addition to the primary cohort, 18 patients with benign recurrent tumors or other difficult-to-treat nonmalignant conditions enrolled at the Department of Pediatric Oncology at University Hospital Brno were included as well (subsequently referred to as the "secondary cohort"). Basic demographic and clinicopathological information for both cohorts is summarized in the Table.

In this study, the primary cohort was subdivided into 3 diagnostic categories. Central nervous system (CNS) tumors constituted the largest subgroup, representing 41% of the cases. This was closely followed by sarcomas, which accounted for 34%, and a heterogeneous group of other solid tumors comprising 25%.

The secondary cohort predominantly consisted of patients with fibroblastic and myofibroblastic tumors, making up 67% of this group. This subgroup comprised tumors diagnosed as desmoid fibromatosis (n = 4), infantile fibromatosis/lipofibromatosis (n = 3), infantile myofibromatosis (n = 2), inclusion body infantile digital fibromatosis (n = 2), and plantar fibromatosis (n = 1). Additional conditions in this cohort included histiocytic neoplasms, schwannoma, hemangioendothelioma, and myxoma.

Table

Demographic and clinicopathological overview of primary and secondary cohorts.

Primary cohort	n
Total no. of enrolled patients	248
Age range (y)	0-36
Sex	
Women	108
Men	140
Disease status	
High-risk primary tumor	135
Relapsed/refractory tumor	109
Secondary malignancy	4
Diagnosis	
CNS	101
Diffuse pediatric-type high-grade gliomas	38
Circumscribed astrocytic gliomas	14
Ependymal tumors	14
Medulloblastoma	12
Atypical teratoid/rhabdoid tumor	7
Others	16
Sarcoma	84
Ewing sarcoma	24
Osteosarcoma	13
Alveolar rhabdomyosarcoma	11
Embryonal rhabdomyosarcoma	9
Undifferentiated small round cell sarcoma (Ewing sarcoma excluded)	5
Synovial sarcoma	4
Others	18
Other solid tumor	63
Peripheral neuroblastic tumors	18
Hematolymphoid disorders (lymphomas)	16
Nephroblastoma	8
Epithelial liver tumors	6
Others	15
Secondary cohort	
Total no. of enrolled patients	18
Age range (y)	0-25
Sex	
Women	7
Men	11
Diagnosis	
Fibroblastic and myofibroblastic tumors	12
Histiocytic and dendritic cell neoplasms	3
Other benign tumors	3

Whole-Exome Sequencing

For whole-exome sequencing, DNA from peripheral blood was extracted using QIAamp DNA Micro Kit (Qiagen). Matched tumor samples were extracted from either formalin-fixed paraffin-embedded (FFPE) or frozen tissues using either the QIAmp FFPE Tissue Kit or DNeasy Blood & Tissue Kit (Qiagen). Sequencing libraries were prepared using the TruSeq DNA Exome (Illumina) for 233 cases and the KAPA HyperExome (Roche) for 33 cases. Sequencing was performed using NextSeq 500/550 Mid Output Kit (150 cycles) on the NextSeq 500 (Illumina) platform in a paired-end setting with read lengths of 2 × 75 bp. Obtained reads were aligned to the GRCh37 reference genome for libraries prepared with the TruSeq DNA Exome kit and to GRCh38 for libraries prepared with the KAPA HyperExome panel, using the BWA-MEM (v0.7.17) algorithm[11] with default settings. PCR duplicates were removed using Picard tools (v2.27.1).[12] Aligned BAM files were sorted and processed using SAMtools (v1.12).[13] The alignment quality was assessed using Qualimap (v2.2.2)[14] and Picard tools (v2.27.1).[12] The codes for DNA alignment and alignment quality control can be found within the repository at https://github.com/orgs/BioIT-CEITEC/repositories. Apart from the mean coverage metric, quality assessment focused on the percentage of the target regions with at least the given depth of coverage as per the Cumulative genome coverage feature of the Qualimap tool, aiming for over 90% of the captured regions to achieve at least ×20 coverage. Germline variant calling involved an integrative approach using 3 variant callers: GATK HaplotypeCaller (v4.2.4.0),[15] VarDict (v1.8.3),[16] and Strelka (v2.9.10).[17] The default settings for variant detection were used with defined targeted regions. The detected variants were normalized using the bcftools norm command.[13] The variants' VCF files were merged using GATK MergeVcfs[18] and annotated with Ensemble Variant Effect Predictor (v95).[19] The code is available at https://github.com/BioIT-CEITEC/germline_small_var_call. For somatic variant calling, the SomaticSeq (v3.6.2) pipeline[20] was employed, with the use of VarDict (v1.8.3),[16] Strelka (v2.9.10),[17] GATK Mutect2 (v4.2.4.0),[21] Lofreq (v2.1.5),[22] and VarScan (v2.4.4).[23] Similar to germline variant calling, the defined targeted regions were used for somatic variant calling as well. The following additional parameters were used for the respective variant callers: lofreq (–call-indels), MuSE (-D -E), GATK Mutect2 (default), Strelka (–disableEVS -exome), varscan (–strand-filter 0 –*P* value .95 –min-var-freq 0.05). The variants were merged within the SomaticSeq pipeline with arguments (–minimum-num-callers 0.4 paired). The code is available at https://github.com/BioIT-CEITEC/somatic_small_var_call. Identified variants were initially filtered to include only nonsynonymous single nucleotide variants (SNVs), insertions, and deletions in coding and adjacent noncoding regions with a population frequency of <1%, as per the gnomAD database.[24] Subsequent analysis was specifically focused on variants within 354 cancer-related genes for germline exome and 780 cancer-related genes with a variant allele frequency exceeding 5% for the somatic exome. Manual inspection to exclude false-positive variant calls was performed using Integrative Genomics Viewer (IGV) software.[25] Germline variants were classified according to the American College of Medical Genetics guidelines,[26] and their significance was assessed using the HGMD database[27] and ClinVar.[28] Somatic variants were deemed clinically significant and were reported if they were annotated in databases of genetic variants (including the OncoKB database,[29] The Clinical Knowledgebase by Jackson's Laboratory,[30] MD Anderson's Personalized Cancer Therapy Knowledgebase,[31] and COSMIC[32]), described in scientific literature, resulted in the truncation of a tumor suppressor gene or altered a recurrently mutated residue even if the variant itself was not thoroughly characterized. Tumor mutational burden (TMB) was calculated from somatic SNVs found in coding sequences as previously described.[33] Synonymous variants and variants with <5% VAF were filtered out. Small insertions and deletions were not included in the calculations because they tend to be called with high false-positive rates and could potentially lead to TMB overestimation. The sum of the remaining SNVs was then divided by the size of the capture panel in megabases. The code is available at https://github.com/BioIT-CEITEC/somatic-tumor-mutational-burden.

Targeted RNA Sequencing

RNA was extracted from either frozen or FFPE tissue using miRVana miRNA Isolation Kit (ThermoFisher Scientific) and subsequently treated with the DNA-free DNA Removal Kit (ThermoFisher Scientific). Sequencing libraries were prepared using TruSight RNA Pan-Cancer Panel covering 1358 cancer-associated genes, loaded onto NextSeq 500/550 Mid Output Kit (150 cycles), and sequenced on the NextSeq 500 platform in a paired-end setting with read lengths of 2 × 75 bp. Sequencing reads were aligned to the GRCh38 reference genome using STAR aligner (v2.7.3a),[34] with parameters set to allow the detection of fusion genes. The alignment quality was assessed using Qualimap (v2.2.2)[14] and Picard tools (v2.25.6).[12] Fusion calling was performed using the Arriba (v2.1.0)[35] and STARfusion (v1.10.0)[36] tools, and manual verification of identified fusions was conducted using the IGV software.[25] If at least 3 soft-clipped reads were present, fusion genes were reported as true positives. The code for fusion genes detection is available at https://github.com/BioIT-CEITEC/fusion_genes_detection. Fusion genes were deemed clinically significant and reported if they were annotated in previously listed databases of genetic variants or the scientific literature. Moreover, novel in-frame fusions involving recognized cancer-related genes were also considered to hold clinical significance. In such cases, an independent verification was performed using RT-PCR.

Whole-Transcriptome Profiling

In 117 cases, whole-transcriptome profiling was performed using a microarray-based approach. Subsequently, this approach was replaced by RNA sequencing, which was performed in 81 cases. For both techniques, RNA was extracted from frozen tissue samples using the miRVana miRNA Isolation Kit (ThermoFisher Scientific) and treated with the DNA-free DNA Removal Kit (ThermoFisher Scientific).

For microarray profiling, RNA samples were processed with the GeneChip WT PLUS Reagent Kit and hybridized onto the GeneChip Human Gene 1.0 ST Array (ThermoFisher Scientific). GeneChips with hybridized and labeled cDNA fragments were placed in the GeneChip Fluidics Station 450 (ThermoFisher Scientific) and washed. Scanning was performed with GeneChip Scanner 3000 7G (ThermoFisher Scientific). After a quality control check, array data from each patient were combined with control array data composed of a heterogeneous sample of 408 nondisease tissues obtained from the ArrayExpress database,[37] which composed a control background set. Combined data were processed using a robust multichip average algorithm implemented in the R package oligo (version 1.62.2).[38] Fold changes of genes from the patient sample against the control background set were computed along with one sample *t* test and displayed using volcano plots. A region of interest for overexpressed genes was considered beyond the 95th percentile of the gene's fold change. In patients with medulloblastoma, microarray data were used to predict 1 of 4 molecular subtypes defined by the 4th edition of the WHO Classification of CNS Tumors.[39] Gene expression data published by Northcott et al[40] were used to create a regression model, which was subsequently used for subgroup prediction in a total of 7 patients.

For RNA sequencing, messenger RNA was purified using the NEBNext Poly(A) mRNA Magnetic Isolation Module (New England Biolabs). Sequencing libraries from the polyA-selected mRNA were prepared using NEBNext Ultra II Directional RNA Library Prep Kit (New England Biolabs) and sequenced on the NextSeq 500 platform using NextSeq 500/550 Mid Output Kit (75 cycles) (Illumina) in a single-end setting with a read length of 75 bp. Raw sequencing reads were quality checked with FastQC and then aligned against the GRCh37 reference genome using the R package Rsubread (v2.12.2)[41] and annotated using Gencode (v19) definitions.[42] A random set of 498 nondisease tissue-specific samples (v6) from the GTEx database[43] was generated and used as a control background. Read counts from the patient sample and the control background set were combined, then normalized using the trimmed mean of M-values method, and fold changes of genes were calculated along with 1-sample *t* tests. Overexpressed genes were generally considered those beyond the 95th percentile of their fold change value, similar to GeneChip data. The code for differential expression is available at https://github.com/robinjugas/transcriptome_analysis.

Copy Number Variation Analysis

Copy number variation (CNV) analysis was initially performed in only selected cases and was eventually integrated into the workflow in 2019. CNV detection was primarily conducted using array comparative genomic hybridization (aCGH), which was performed in 113 cases. In 34 cases, multiplex ligation-dependent probe amplification (MLPA) was employed. The remaining 5 cases were analyzed through low-coverage whole-genome sequencing (lcWGS). For aCGH and lcWGS, DNA was isolated from frozen tissue using the DNeasy Blood & Tissue Kit (Qiagen). For MLPA, DNA was isolated either from frozen or FFPE tissue using the DNeasy Blood & Tissue Kit and the QIAmp FFPE Tissue Kit (Qiagen), respectively.

Oligonucleotide aCGH was performed using the SurePrint G3 Cancer CGH + SNP Microarray Kit, 4×180K (Agilent). Sample DNA and sex-matched control DNA (Human Genomic DNA, Agilent) were restricted, labeled, and purified with the SureTag Complete DNA Labeling Kit according to the manufacturer's protocol (Agilent). The quality of DNA was assessed using a NanoDrop 2000c Spectrophotometer (ThermoFisher Scientific) to ensure that it was within an optimal range for both the patient and reference sample. Hybridization was performed with Oligo aCGH/ChIP-Chip Hybridization Kit (Agilent) according to the manufacturer's protocol and conducted for 24 hours at 67°C. Arrays were scanned using the SureScan High Resolution Microarray Scanner (Agilent). Data were imported using the Feature Extraction V.5.0.2.1 software, and results were analyzed using CytoGenomics Analysis software v5.1.2.1 (Agilent). All genomic coordinates were established using the human reference genome GRCh38.

MLPA was performed using SALSA MLPA Probemix P175-B1 Tumour Gain and SALSA MLPA Probemix P294-C1 Tumour Loss, in conjunction with FAM-labeled SALSA MLPA Reagent Kit (MRC). Capillary electrophoresis was carried out on the ABI 3130XL device (Applied Biosystems). Data were evaluated using the Coffalyser.Net software.

Libraries for lcWGS were prepared using the TruSeq DNA PCR-Free kit (Illumina) and quantified with the KAPA Library Quantification Kit (Roche). Sequencing was performed using the NextSeq 500/550 Mid Output Kit (300 cycles) on the NextSeq 500 (Illumina) platform in a paired-end setting with read lengths of 2 × 150 bp, aiming at a ×3 mean coverage. Obtained reads were aligned to the GRCh38 reference genome using the BWA-MEM (v0.7.17)[11] algorithm with default parameters and subsequently processed by SAMtools (v1.12).[13] CNVs were called using the ControlFREEC (v11.6) tool[44] with parameters set to almost default settings (window = 50,000, ploidy = 2, breakPointThreshold = 0.8). The code for the analysis is available at https://github.com/BioIT-CEITEC/cnv_analysis.

Expert Evaluation of the Molecular Findings

All findings from individual cases were routinely reviewed by a multidisciplinary panel of experts, the molecular tumor board, at the Department of Pediatric Oncology of University Hospital Brno, Czech Republic. Actionable findings were defined as specific genetic changes with clinical or preclinical evidence indicating their potential as predictive biomarkers for response to regulatory-approved targeted inhibitors or alterations resulting in analogous effects on protein function.

Methylation Profiling

Methylation profiling was introduced toward the end of 2022 and, for the cohort discussed in this manuscript, was applied retrospectively as an additional method in 18 cases. DNA was extracted from frozen tissue samples using the DNeasy Blood & Tissue Kit (Qiagen) and then subjected to bisulfite conversion with the EZ DNA Methylation Kit (Zymo Research). Subsequently, samples were processed using the Infinium Methylation EPIC BeadChip Kit and loaded onto MethylationEPIC v1.0 BeadChip (Illumina). BeadChips were scanned using the NextSeq 550 device (Illumina), and generated IDAT files were uploaded and processed through the MolecularNeuropathology.org brain tumor classifier version 12.5.[45]

Results

In the primary cohort, 18 subjects were excluded due to either insufficient cancer cell content in the tumor samples (n = 6) or inadequate sequencing data quality (n = 12). Consequently, whole-exome sequencing (WES) was successfully completed in 230 patients. During the program's duration, 1 patient afflicted with hereditary cancer-predisposing syndrome developed a secondary malignancy, augmenting the total number of successfully analyzed tumors to 231 across the cohort of 230 patients. Additionally, targeted RNA sequencing focused on fusion transcript detection was performed in 220 cases (95%), whole-transcriptome profiling in 198 cases (86%), and CNV analysis in 152 cases (66%) (see Fig. 1A and Supplementary Table S1). The application of these methodologies largely depended on the availability of suitable tumor tissue material and the integrity of the nucleic acids necessary for successful library preparation. Selected demographic data for patients from the primary cohort are

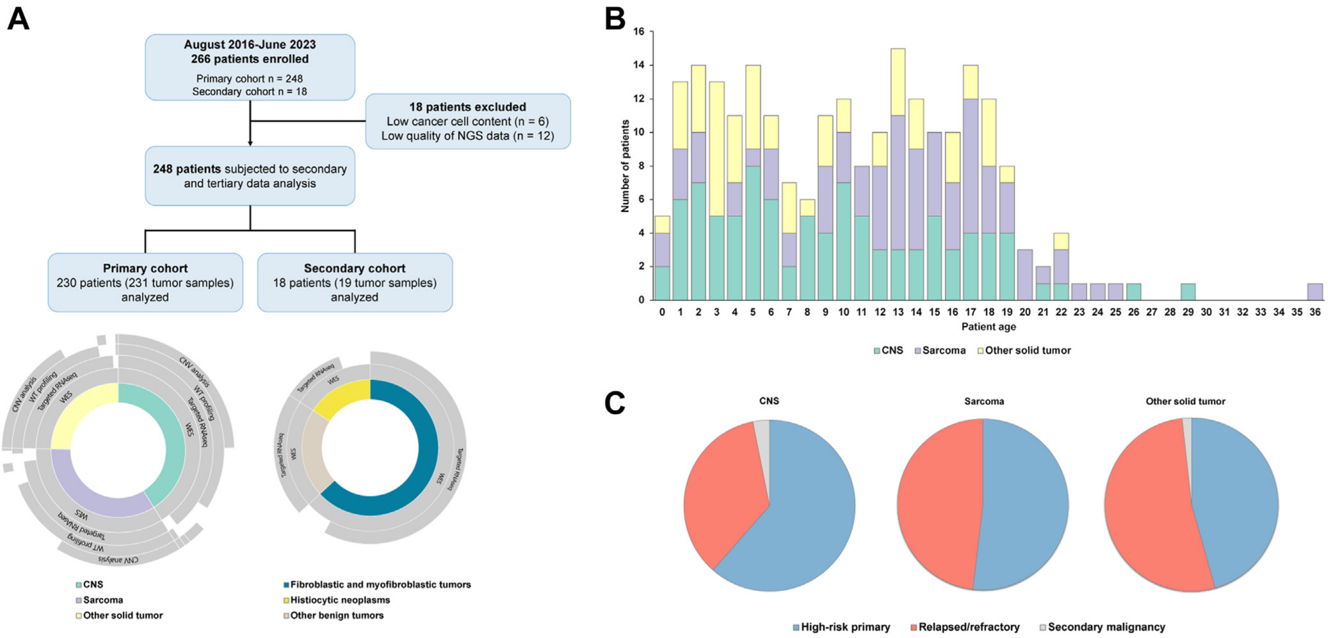

Figure 1.
(A) Cohort flow chart illustrating patient enrollment along with a visualization of performed molecular analyses. (B) Histogram showing the distribution of patient ages and their categorization into diagnostic groups within each age bracket. (C) Pie chart depicting the stage of disease at the time of enrollment in the respective diagnostic groups.

presented in Fig. 1B, C. In the secondary cohort, WES was conducted on all samples, with targeted RNA sequencing additionally performed in 16 individuals (see Fig. 1A and Supplementary Table S2). Notably, 1 patient initially enrolled with hemangioendothelioma developed a juxtaglomerular cell tumor over the course of the study, increasing the total number of analyzed samples to 19.

Molecular Findings in the Primary Cohort

Based on the results of somatic WES, 302 variants with known or potential clinical significance in cancer-associated genes were reported in 55% of cases (n = 128, see Supplementary Table S3). Among these, *TP53* variants were the most prevalent and were found in over 38% of cases. Other commonly observed alterations were found in genes encoding for proteins involved in epigenetic regulation or chromatin remodeling (*H3-3A* or other genes encoding for H3 isoforms, *ATRX*, *BCOR*, *ARID1A*, *CREBBP*, *SMARCB1*), members of the Ras/MAPK pathway (*NF1*, *NRAS*, *KRAS*, and *BRAF*), receptor kinases (*FGFR1*, *PDGFRA*, and *ACVR1*), and PI3K/Akt/mTOR pathway members (*PIK3CA* and *PIK3R1*). Genes altered in at least 2 patients are summarized in Figure 2, whereas comprehensive results are presented in Supplementary Figure S1. Consistent with previous studies indicating low TMB in pediatric tumors,[46] the median TMB was 0.62 (range, 0-263.64, see Supplementary Table S4). Four patients had a TMB exceeding 10 mut/Mb, including 2 siblings with constitutional mismatch repair (MMR) deficiency syndrome, who exhibited particularly high TMB.[47] In the other 2 cases, no germline predisposition was identified. However, MMR deficiency was assessed using immunohistochemistry staining for MMR proteins, revealing an absence of MSH2 expression and abnormal MSH6 expression in one case. In the other case, due to poor cancer cell viability, the tissue was considered unsuitable for assessment.

Germline predisposition analysis was carried out using WES data; therefore, only SNVs, insertions, or deletions (InDels) were evaluated. Pathogenic or likely pathogenic variants in zygosity consistent with the mode of inheritance of the associated germline predisposition syndromes were identified in 11% of patients (n = 26, see Supplementary Table S5). Additionally, 10% of patients (n = 24) carried pathogenic or likely pathogenic variants in genes linked to cancer predisposition syndromes inherited in an autosomal recessive manner. Three patients harbored pathogenic or likely pathogenic variants in recognized susceptibility genes for breast and ovarian cancer, including *PALB2*, *RAD51D*, and *BRIP1*. All patients with confirmed germline findings and their families received genetic counseling.

Clinically relevant fusion genes or structural variants were identified in 28% of analyzed cases (n = 61), with the vast majority having primarily diagnostic relevance (see Fig. 3A and Supplementary Table S6). Fusion gene status was preferentially evaluated using targeted RNA sequencing data. However, certain rearrangements, such as *CIC*::*DUX4*, highlighted limitations in this method as the targeted RNA panel did not adequately cover the fusion breakpoint, resulting in false-negative results. Additionally, the detection of specific lymphoma-associated fusions such as *IGH*::*MYC* was constrained by this approach, necessitating their assessment through DNA-based detection methods outside of this study. Notably, several novel translocations involving recognized fusion partners were identified, including a *DVL3*::*TFE3* fusion in a patient with renal cell carcinoma (Fig. 3B) and *SRGAP3*::*NTRK2* fusion in a patient with neuroblastoma (Fig. 3C).

Aberrant gene expression levels were primarily used as supporting evidence for concurrent genomic events (eg, gene amplifications) or to indicate the expression of specific gene sets, including those related to immune checkpoints. Additionally, increased expression of genes encoding for targetable kinases exceeding a fold change of 0.5 was reported. However, kinase overexpression without corresponding genomic alteration, or

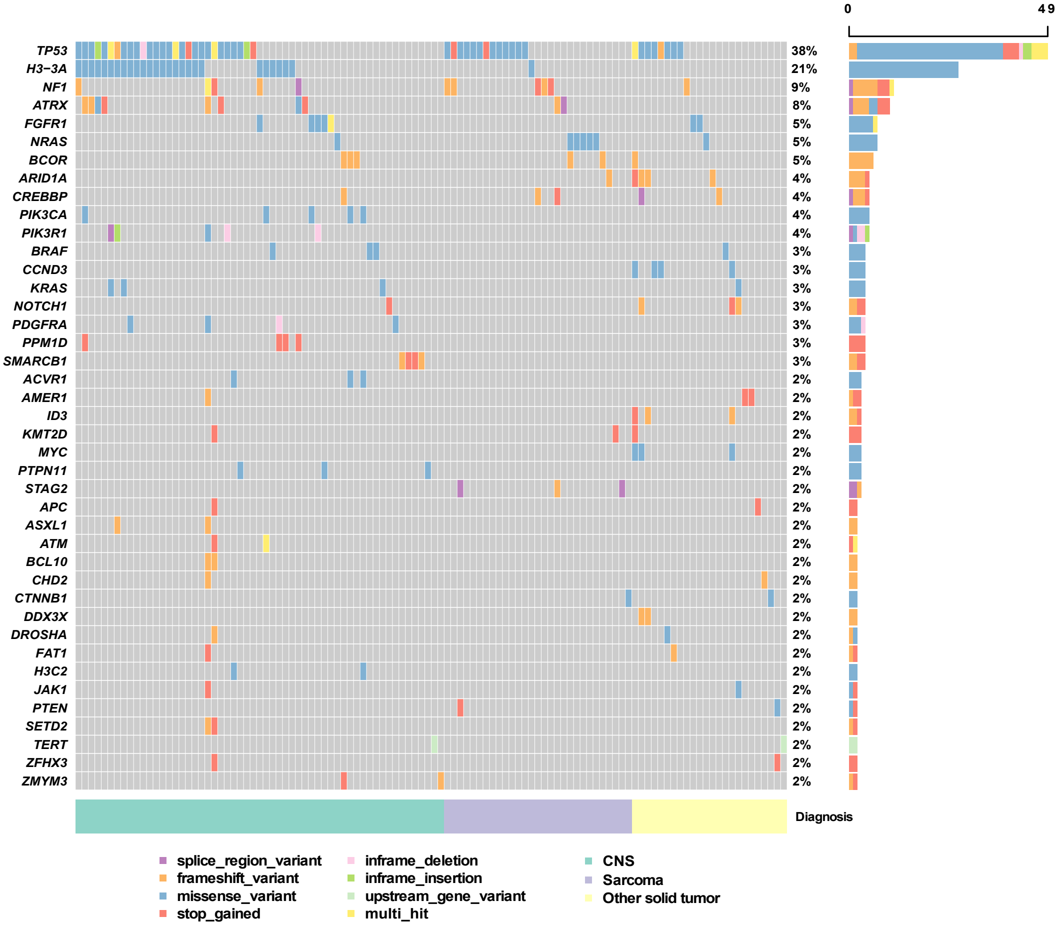

Figure 2.

Oncoplot displaying genes with clinically relevant SNVs, insertions, and deletions identified across the primary cohort. Only genes altered in at least 2 patients are shown here, whereas the complete version can be found in Supplementary Figure S1. SNV, single nucleotide variant.

generally any specific gene expression that could not be verified at the protein level, was approached as having a low level of evidence for therapeutic planning and was deemed insufficient for subsequent clinical decision making. Therefore, such findings are not further reflected within the diagnostic yield of this manuscript. Moreover, transcriptomic microarray profiling was employed to differentiate among the 4 subtypes of medulloblastoma as defined by the 4th edition of the WHO classification of CNS tumors.[39] Since the end of 2022, this approach has been replaced with methylation profiling.[45]

Copy number changes were detected in 85% of analyzed cases (n = 129). The majority (n = 110) presented with complex karyotypes characterized by whole-chromosomal or segmental gains and losses across multiple chromosomes. Sixteen patients showed changes involving only a single chromosome, and a polyploid genome was identified in 3 patients. Given their significant clinical implications, the analysis of CNVs focused particularly on oncogene amplifications, defined as 5 or more copies of the respective genes, and biallelic deletions of tumor suppressor genes. Although the majority of identified chromosomal aberrations involved single-copy changes, 19 patients exhibited amplifications, some of which affected critical oncogenes such as *MYCN*, *MYC*, *CDK4*, *MDM2*, *PDGFRA*, *KIT*, *MET*, or *SMO*. Additionally, 10 patients harbored biallelic tumor suppressor deletions, 5 of which included the *CDKN2A/B* locus (see Supplementary Table S7).

A multidisciplinary panel of experts routinely reviewed all findings from individual cases, and actionable findings were found in 38% of patients (n = 87, see Supplementary Table S8). The prevalence of actionable findings varied across diagnostic groups, with CNS tumors showing the highest rate at 53%, followed by other solid tumors at 37% and sarcomas at 20%. The most common actionable alterations were SNVs and InDels, found in 61 patients either as isolated events or in combination with other events, such as copy number loss or loss of heterozygosity that inactivated the second allele. Gene fusions or other structural variants were the second most common actionable finding (n = 11), followed by CNVs as standalone events (n = 7) and high TMB (n = 4). In 4 additional cases, a concurrent presence of SNV or InDel with a CNV in different genes was identified. Overall, WES was proven as the most effective approach for generating actionable findings across most diagnostic units in our cohort, with the exception of astrocytic gliomas exhibiting predominantly actionable gene fusions (see Fig. 4A). Therapeutic recommendations based on these findings included MEK inhibitors (n = 26), receptor tyrosine kinase inhibitors (n = 15), EZH2 inhibitors (n = 13), combinations of various agents (n = 11), PI3K inhibitors (n = 6), and other treatments (n = 16) (see Fig. 4B, C).

Sequential Tumor Samples

Over the stipulated study interval, 31 subjects from the cohort underwent multiple biopsies due to relapse or progression of the disease, with the total number of consecutive biopsy samples

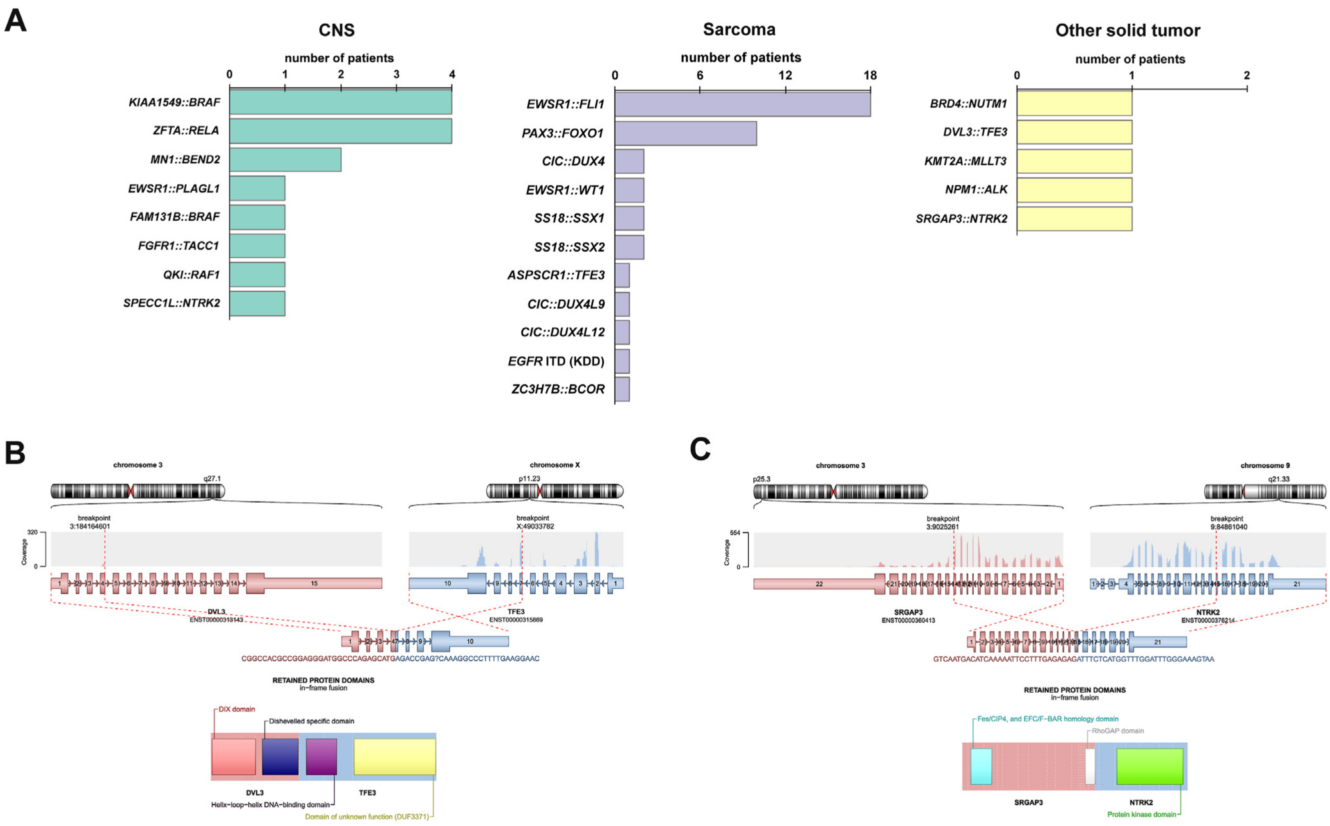

Figure 3.

(A) Results of fusion gene analysis showing the respective findings in each disease category. The analysis yielded several newly identified rearrangements with known fusion partners, including *DVL3*::*TFE3* (B) in a patient diagnosed with renal cell carcinoma and *SRGAP3*::*NTRK2* (C) in a patient diagnosed with neuroblastoma.

ranging from 2 to 5 (2 biopsies: n = 25, 3 biopsies: n = 3, 4 biopsies: n = 2, 5 biopsies: n = 1). For 2 patients, prior biopsy specimens were additionally analyzed to track the evolution of the tumor. Of these 33 patients, 15 were diagnosed with sarcomas, 14 with CNS tumors, and the remainder with other solid tumors.

In cases with 2 consecutive biopsies, the proportion of shared SNVs and InDels varied between 2% and 66% (see Fig. 5A). For patients with 3 or more biopsies, the number of consistent variants across all samples ranged from 1 to 52, with an additional 1 to 25 variants shared between various biopsy time points (see Fig. 5B). Similarly, qualitative differences in the spectrum of chromosomal aberrations were observed in cases with available CNV data, with the exception of 2 cases where no chromosomal aberrations were detected in any of the analyzed samples. The median change in TMB was an increase of +0.34 mut/Mb from the previous biopsy, with changes ranging from −2.19 to +85.95 mut/Mb (visualized in Fig. 5C). Despite the low observed overlap, most patients with tumors characterized by a single or few driver alterations retained these alterations in subsequent biopsies (see Supplementary Table S9). This suggests that the changes may have primarily impacted passenger variants. Moreover, 10 of these patients harbored additional known or potentially significant SNVs or InDels, indicating that some of these newly acquired variants may also contribute to tumor evolution or treatment resistance.

A key point of interest was whether tumor evolution might reveal new therapeutic opportunities. Initially, 11 patients presented with therapeutically actionable genomic alterations. In 9 of these cases, the alteration was retained in subsequent biopsies. In 1 patient, the initially detected targetable alteration in the *PIK3CA* gene was no longer detectable after targeted therapy and was replaced by a mutation in a different gene within the same signaling pathway, namely, *PIK3R1*. In another, a targetable *KRAS* alteration was absent at relapse despite not being previously targeted for treatment. Among patients who initially lacked actionable alterations, only 2 later developed potentially targetable changes; one involved a *CDKN2A/B* deletion, potentially undetected in earlier biopsies due to the absence of CNV data, and the other a splicing variant in the *ATR* gene at disease progression. In the remaining patients, no new predictive biomarkers were identified.

Molecular Findings in the Secondary Cohort

Patients in the secondary cohort presented with diverse conditions, which are often driven by a single molecular alteration. In 19 analyzed samples, a well-established or suspected driving alteration was identified in 89% of cases (n = 17). The results and information on whether their presence holds potential therapeutic implications are summarized in Figure 6A and Supplementary Table S10. The identified alterations were therapeutically actionable in 47% of cases (n = 9), leading to recommendations for matched targeted treatments (see Fig. 6B, C).

In the subgroup of fibroblastic and myofibroblastic tumors, common *CTNNB1* variants affecting codons Thr41 and Ser45 were found in patients with desmoid and plantar fibromatosis. In infantile fibromatosis/lipofibromatosis cases, molecular findings were more varied, revealing somatic findings of *EGFR* exon 20 in-frame insertion and *NTRK1* fusion, as well as germline variant in the *ACVR1* gene. The identification of the

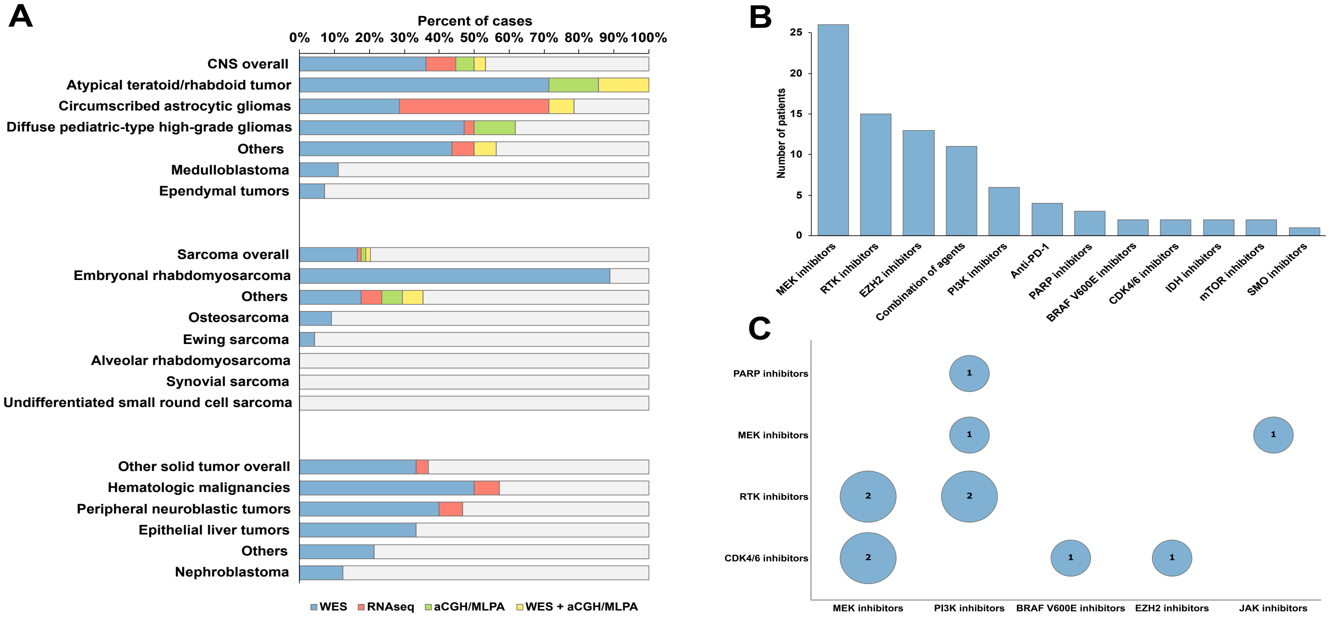

Figure 4.

(A) The overall rate of therapeutically actionable findings across different diagnostic categories, as well as specific diagnostic units within each category. The positive cases are divided based on the method of detection. (B) The frequency of recommendations for various classes of targeted therapeutic agents. (C) Depiction of recommended drug combinations with the respective frequencies.

ACVR1 variant subsequently had an impact on diagnosis assessment, as discussed in the following section of the manuscript. The 2 patients with infantile myofibromatosis were siblings who harbored a pathogenic *PDGFRB* variant with an additional somatic mutation in the Asn666 residue, as detailed in a separate case report.[49] Notably, in 2 cases of inclusion body infantile digital fibromatosis, identical somatic mutations in the *FLNA* gene, *FLNA*(NM_001110556.2):c.2326G>A p.(Gly776Ser), were found (see Fig. 6D). Patients with histiocytic neoplasms presented alterations in the Ras/MAPK pathway, including 2 *BRAF* variants and 1 *MAP2K1* variant. Additionally, an *IDH2* variant was detected in a case of hemangioendothelioma, and concurrent inactivating variants in *SMARCB1* and *NF2* were found in a patient with schwannoma.

Refinements of Original Histopathological Diagnoses Based on Molecular Findings

In the primary cohort, the use of WES and RNA sequencing resulted in refinements to the initial histopathological diagnoses in 4% of cases (n = 10) (see Supplementary Table S11), largely due to emerging updates introduced in either the fourth or the fifth edition of the WHO classification of CNS tumors. In 9 of 10 cases, identified alterations informed diagnostic evaluation and treatment decision making prospectively. The remaining case was reclassified 3 years after the discovery of a previously unknown *EWSR1*::*PLAGL1* fusion gene, which was later established by Sievers et al[50] as a hallmark alteration for a newly identified entity known as *PLAGL1* fusion-driven neuroepithelial tumor. Toward

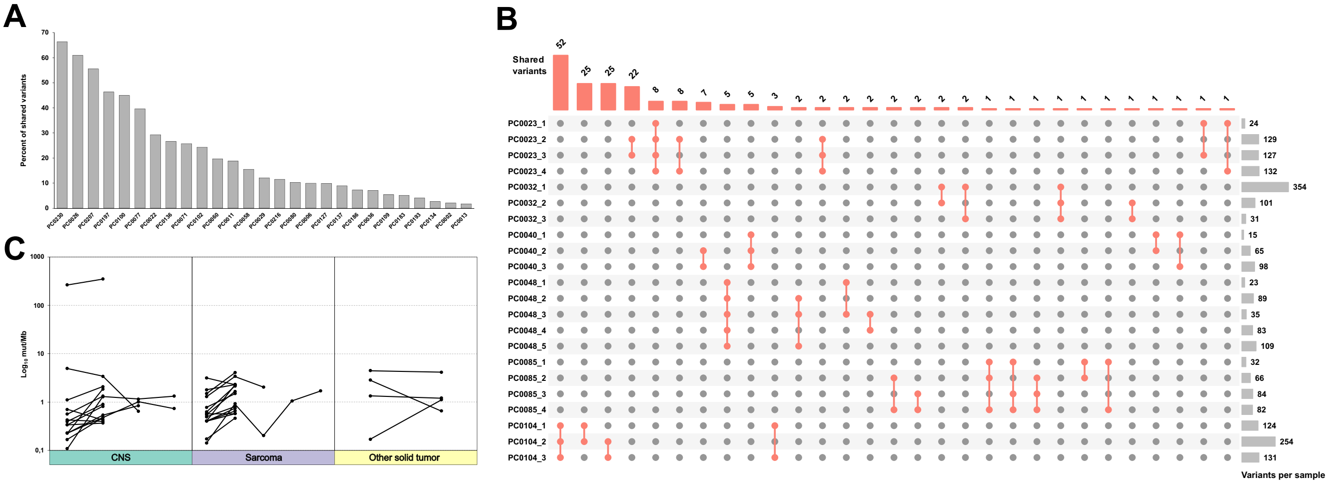

Figure 5.

(A) Percent of shared variants in patients with 2 consecutive biopsies. (B) Upset plot visualizing an overlap between the respective samples in patients with 3 or more consecutive biopsies. (C) Dynamics in TMB values visualized separately for each diagnostic category. TMB, tumor mutational burden.

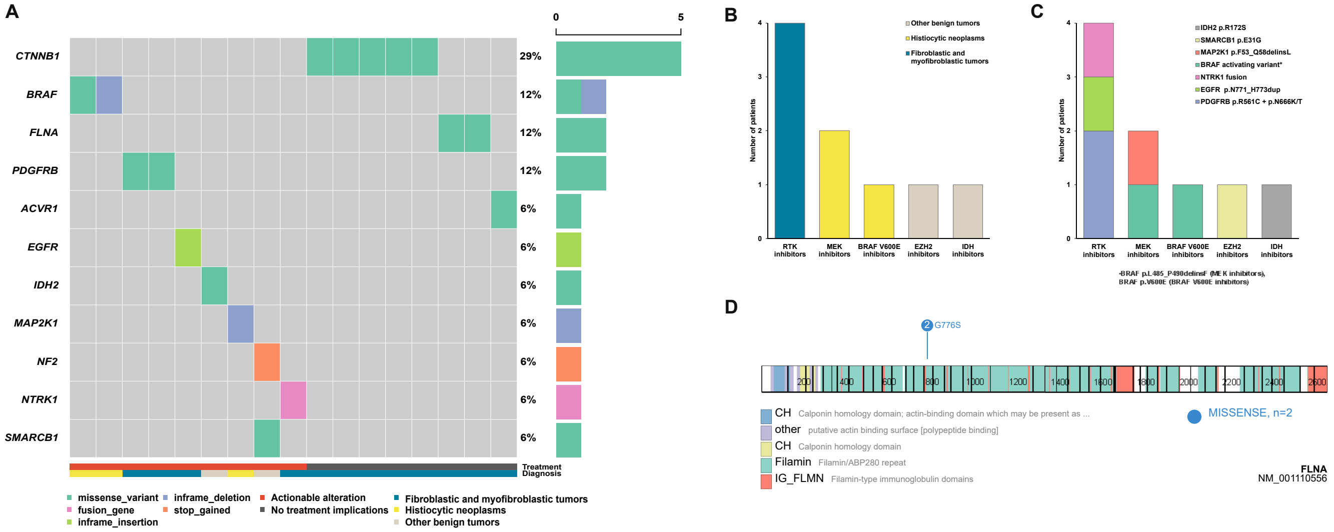

Figure 6.

(A) Oncoplot illustrating known or potentially significant germline and somatic alterations identified in the secondary cohort, along with an indication of whether the identified alteration holds implications for subsequent therapeutic planning. (B, C) Therapeutic recommendations derived from findings in the secondary cohort, categorized by (B) diagnostic group and (C) identified predictive biomarkers. (D) Depiction of the *FLNA* p.(Gly776Ser) variant found in inclusion body infantile digital fibromatosis patients created using ProteinPaint.[48]

the end of the study period detailed in this manuscript, the incorporation of methylation profiling enabled the retrospective refinement of diagnoses for 2 additional patients and confirmed the initial diagnosis reassessment based on WES or RNA sequencing in 4 cases. In the secondary cohort, there was only 1 case for which the diagnosis was subsequently refined. In this case, the diagnosis was changed upon the detection of an *ACVR1* germline variant from infantile fibromatosis to fibrodysplasia ossificans progressiva, which, in its early stage, morphologically resembled infantile fibromatosis.[51]

Furthermore, methods utilized within the study helped in assessing molecularly defined subgroups of various tumor types, including embryonal and ependymal tumors. As already mentioned, whole-transcriptome microarray profiling was used to predict molecular subtypes of medulloblastoma, and targeted RNA sequencing enabled the classification of prognostically distinct fusion-driven subgroups of supratentorial ependymoma. After the introduction of methylation profiling to the study workflow, the method was applied retrospectively to confirm or categorize subgroups in 7 cases of posterior fossa ependymomas and 5 cases of atypical teratoid/rhabdoid tumors (see Supplementary Table S11).

Discussion

In this report, we detailed our experience with comprehensive genomic and transcriptomic profiling of pediatric and young adult patients within our precision oncology program. Over nearly 7 years since its initiation, we have analyzed ~250 patients with various malignant and benign neoplasms, contributing to the broader literature on this topic.

Our primary methodological approach combined WES, RNA sequencing, and various means of CNV analysis, especially aCGH. The methodological portfolio was chosen to include methods that allow gaining thorough clinical insights even from FFPE tissue samples, given the routine availability of FFPE tissues and the logistical challenges associated with parallel frozen tissue biobanking, particularly for tumors situated in complex anatomical locations. However, it is important to acknowledge certain limitations inherent to this methodology. Although comprehensive, it does not match the capabilities of workflows that integrate WGS and RNA sequencing, which are more efficient in detecting intergenic and intrachromosomal structural variations and assessing mutational signatures.[52] The practicality of WGS/RNA sequencing, however, may be hindered by the need for substantial representative tumor tissue and the high demands for DNA input, sequencing capacity, computational resources, and storage capacity, which can limit its broader application.

The increasing prevalence of large scale profiling in research and clinical settings underscores the shift toward methods such as WES or WGS. However, many diagnostic laboratories currently favor multigene sequencing panels, which, if not customized, may not be ideally suited for pediatric populations due to the focus of commercially available solutions on alterations observed in adult malignancies. Given the real-world setting of this study, the transferability of its findings to clinical practice holds significant importance for all authors involved, and recent discoveries of key molecular alterations in pediatric tumors, some of which became critical for accurate diagnosis,[53] underscores the urgent need for broader implementation of pediatric molecular diagnostics and either the development of tailored multigene testing panels that effectively capture clinically relevant information for this demographic, or utilization of WES/WGS approach. Enhancing accessibility to large scale genomic techniques necessitates continuous improvements in bioinformatics, data analysis, interpretation, and standardization. Additionally, establishing robust financial reimbursement systems is essential to support these advancements.

Nonetheless, the advantages of large scale approaches remain undeniable, particularly in the identification of novel hallmark drivers. In our study, this was exemplified in patients with inclusion body infantile digital fibromatosis, where identical missense mutations in the *FLNA* gene were observed. Inclusion body infantile digital fibromatosis currently has no reported hallmark somatic alterations. When of germline origin, *FLNA* variants are associated with a range of X-linked conditions, including terminal osseous dysplasia characterized by recurrent digital fibromas during infancy.[54] This finding suggests a possible causal relationship with sporadic fibroma development in our patients. Further investigation is warranted to validate the presence of *FLNA* alterations in a broader cohort and to elucidate their role in disease pathogenesis.

In assessing the primary outcome of this program, the attainment of therapeutically actionable findings, we achieved an overall yield of 38% in the primary cohort. This rate is comparable with rates reported in international studies such as INFORM (43% rate when considering genetically altered actionable targets)[5] and Pediatric MATCH (31.5% rate).[9] However, our findings align with the lower spectrum of published data, where some studies have reported yields as high as 54% to 82%.[3,6-8,10] Variations in these outcomes can be attributed to several factors, including the composition of the primary cohort and the specific challenges associated with pediatric oncology, such as the scarcity of matched targeted treatments tailored to the unique molecular profiles of pediatric tumors. These challenges are particularly pronounced in cases where hallmark alterations may be either poorly understood or considered nontargetable. Interestingly, several promising approaches[55,56] are emerging to address these challenges, and new investigational medicinal products are entering early-phase clinical trials.[57,58] Nevertheless, investigational medicinal products were not included in our therapeutic recommendations.

Furthermore, the criteria for defining the "actionability" of genomic alterations vary significantly, which influences the overall rate of actionable findings. For example, alterations that were considered only prognostic within our study, such as *TP53* variants or *MYC* and *MYCN* amplifications, have been explored for their potential as predictive biomarkers for specific novel inhibitors[59-61] and were therefore utilized by other programs for treatment recommendations.[6,8] In some studies, expanding the scope of actionability to consider significantly overexpressed genes dramatically increased the proportion of actionable findings, as observed in the INFORM study,[5] where actionable targets increased from 43% to 85.9% when such criteria were included. This discrepancy in the assessment of actionability highlights the ongoing debate and lack of consensus among experts, which is further complicated by varying target prioritization algorithms and differing expert opinions across studies.

In the secondary cohort, a slightly higher yield of therapeutically actionable findings was achieved, reaching 47%. Typically, the conditions within this cohort are managed either conservatively, by surgery, or by other means of standard treatment. However, for cases exhibiting aggressive behavior, recurrence, or resistance to conventional treatments, targeted therapies might offer a considerable advantage.[48,62,63] The decision to use targeted therapies in these conditions always depends on individual patient factors, including the genetic profile of the tumor and the availability of targeted therapeutic options. Nevertheless, as clinical research advances, we might see more definitive roles for these therapies in standard therapeutic guidelines.

Germline predisposition to cancer development was detected in 11% of patients, which falls within the previously reported range of 7.5% to 22%.[4-8,10] Notably, several germline findings included variants in genes that are not typically associated with pediatric tumors but can serve as predictive markers in various adult tumors. This ultimately requires cautious interpretations in regard to further therapeutic planning. For instance, *BRCA1/2* variants were found in 7 patients, but only 1 exhibited a loss of the second allele, indicating possible homologous recombination deficiency (HRD) in the tumor. Overall, among patients identified with likely pathogenic or pathogenic heterozygous germline variants in homologous recombination repair genes, only 2 exhibited a second somatic hit that led to the inactivation of protein function. Recently, the KiCS study authors demonstrated that individuals with such germline predisposition might show HRD-specific mutational signature 3 despite lacking the second somatic hit, pointing to potential epigenetic or other mechanisms leading to HRD.[10] Because our study did not employ WGS, we could not provide the necessary rationale for PARP inhibitors administration and therefore discounted those findings as therapeutically actionable.

One of the key aspects of molecular profiling, frequently highlighted in precision oncology studies, is the ability to revise original histopathological diagnoses based on molecular findings. For this purpose, methylation profiling has proven effective in reclassifying broad diagnostic groups, including CNS tumors and sarcomas.[45,64] Although methylation profiling was not incorporated until later in the project, our comprehensive workflow still enabled refinements to the initial histopathological diagnoses in 4% of cases, which aligns with the rates published within other studies.[5-8,10] Many adjustments trace back to the project's early stages when the 4th edition of the WHO Classification of CNS Tumors[39] introduced new molecular markers as hallmarks of specific tumor types. Although those will not be discussed further here, several notable examples underscore the importance of this approach. These include, for instance, a case morphologically appearing as papillary ependymoma that was reclassified as astroblastoma, *MN1*-altered based on the presence of the *MN1*::*BEND2* fusion. Another case included a tumor histologically assessed as a diffuse leptomeningeal glioneuronal tumor that harbored *FGFR1* and *PTPN11* mutations instead of the hallmark *KIAA1549*::*BRAF* fusion and 1p deletion. Although the 2 detected alterations are rather common for dysembryoplastic neuroepithelial tumors (DNET), the lack of common DNET-associated morphologic features led to a provisional diagnosis of a low-grade glioneuronal tumor with *FGFR1* alteration. This reinforces the necessity for integrating molecular analyses with histopathology and immunohistochemistry to establish accurate diagnosis. Such integration, emphasized in the 5th edition of the WHO Classification of CNS Tumors[53] and the newly published WHO Classification of Pediatric Tumors,[65] exemplifies the transformative role of molecular profiling in modern pathology.

Similarly, the benefit of integrating comprehensive profiling also applies to the discovery of previously unpublished driving alterations in selected solid tumors. Despite data from various studies[2-10] and extensive pan-cancer pediatric cohorts,[46,66] rare patient subsets within specific diagnostic groups may still be underrepresented. A striking example is the identification of the *SRGAP3*::*NTRK2* fusion gene in a neuroblastoma case, a rare instance where this tumor is driven by *NTRK2* rearrangements. Although the expression of Trk receptor kinase isoforms has been linked to various clinical outcomes in these patients,[67] this is the first report on the presence of NTRK genomic rearrangements in neuroblastoma patients to our knowledge.

In summary, the integration of advanced genomic and transcriptomic technologies has enabled the personalization of the treatment of diverse malignancies. As we work to translate these advances into broad clinical applications, it is essential to foster collaborative efforts among researchers, clinicians, and policymakers, which are necessary to unlock the full potential of pediatric precision oncology and ensure its successful implementation across health care settings.

Acknowledgments

The authors acknowledge the Core Facility Bioinformatics and the Core Facility Genomics, supported by the NCMG research infrastructure (LM2023067 funded by MEYS CR) of CEITEC Masaryk University, for their support in obtaining the scientific data presented in this paper. The project was generated within the European Reference Network on Paediatric Cancer (ERN PaedCan).

Author Contributions

P.P. contributed to methodology, investigation, data curation, visualization, and writing – original draft. H.P., S.A., S.M., and T.C.I. were involved in methodology, investigation, and data curation. R.J. performed formal analysis, visualization, and software. D.A.T., M.K., V.By., K.T., K.P., and L.R. performed formal analysis and software. D.K., K.K., E.P., M.Ja., B.T., and J.V. contributed methodology and investigation. T.M., P.M., Z.P., V.Ba., P.T., N.S., L.M., K.D., M.Je., S.K., K.S., C.H., and J.G. were involved investigation, resources. J.S. and O.S. performed conceptualization, supervision, and funding acquisition. All authors contributed to writing – reviewing and editing. All authors read and approved the final version of the paper.

Data Availability

The data that support the findings of this study are available on request from the corresponding author.

Funding

Supported by the Ministry of Health of the Czech Republic, grant nr. NU20-03-00240. All rights reserved. Supported by the project National Institute for Cancer Research (Programme EXCELES, ID Project No. LX22NPO5102) – Funded by the European Union – Next Generation EU. Supported by the project National Institute for Neurological Research (Programme EXCELES, ID Project No. LX22NPO5107) – Funded by the European Union – Next Generation EU. Supported by Ministry of Health of the Czech Republic – conceptual development of research organization (FNBr, 65269705). Supported by the Specific University Research provided by the Ministry of Education, Youth and Sports of the Czech Republic (MUNI/A/1625/2023). Supported by the project CREATIC funded from European Union's Horizon Europe Coordination and Support Action under the Grant agreement number 101059788.

Declaration of Competing Interest

None.

Ethics Approval and Consent to Participate

All subjects gave their informed consent for inclusion before they participated in the study. The study was conducted in accordance with the Declaration of Helsinki and was approved by the Ethics Committee of University Hospital Brno (16-120619/EK), the Ethics Committee of the Faculty of Medicine of Masaryk University (26/2019), and the Ethics Committee of the Medical University of Vienna (1244/2026, 1484/2021).

Supplementary Material

The online version contains supplementary material available at https://doi.org/10.1016/j.labinv.2024.102161.

References

1. Krejci D, Zapletalova M, Svobodova I, et al. Childhood cancer epidemiology in the Czech Republic (1994–2016). *Cancer Epidemiol*. 2020;69:101848. https://doi.org/10.1016/j.canep.2020.101848
2. Harris MH, DuBois SG, Glade Bender JL, et al. Multicenter feasibility study of tumor molecular profiling to inform therapeutic decisions in advanced pediatric solid tumors: the individualized cancer therapy (iCat) study. *JAMA Oncol*. 2016;2(5):608–615. https://doi.org/10.1001/jamaoncol.2015.5689
3. Wong M, Mayoh C, Lau LMS, et al. Whole genome, transcriptome and methylome profiling enhances actionable target discovery in high-risk pediatric cancer. *Nat Med*. 2020;26(11):1742–1753. https://doi.org/10.1038/s41591-020-1072-4
4. Newman S, Nakitandwe J, Kesserwan CA, et al. Genomes for kids: the scope of pathogenic mutations in pediatric cancer revealed by comprehensive DNA and RNA sequencing. *Cancer Discov*. 2021;11(12):3008–3027. https://doi.org/10.1158/2159-8290.CD-20-1631
5. van Tilburg CM, Pfaff E, Pajtler KW, et al. The pediatric precision oncology INFORM registry: clinical outcome and benefit for patients with very high-evidence targets. *Cancer Discov*. 2021;11(11):2764–2779. https://doi.org/10.1158/2159-8290.CD-21-0094
6. Langenberg KPS, Looze EJ, Molenaar JJ. The landscape of pediatric precision oncology: program design, actionable alterations, and clinical trial development. *Cancers*. 2021;13(17):4324. https://doi.org/10.3390/cancers13174324
7. Berlanga P, Pierron G, Lacroix L, et al. The European MAPPYACTS trial: precision medicine program in pediatric and adolescent patients with recurrent malignancies. *Cancer Discov*. 2022;12(5):1266–1281. https://doi.org/10.1158/2159-8290.CD-21-1136
8. Church AJ, Corson LB, Kao PC, et al. Molecular profiling identifies targeted therapy opportunities in pediatric solid cancer. *Nat Med*. 2022;28(8): 1581–1589. https://doi.org/10.1038/s41591-022-01856-6
9. Parsons DW, Janeway KA, Patton DR, et al. Actionable tumor alterations and treatment protocol enrollment of pediatric and young adult patients with refractory cancers in the National Cancer Institute–Children's Oncology Group Pediatric MATCH trial. *J Clin Oncol*. 40(20):2224-2234. https://doi.org/10.1200/JCO.21.02838
10. Villani A, Davidson S, Kanwar N, et al. The clinical utility of integrative genomics in childhood cancer extends beyond targetable mutations. *Nat Cancer*. 2023;4(2):203–221. https://doi.org/10.1038/s43018-022-00474-y
11. Li H. Aligning sequence reads, clone sequences and assembly contigs with BWA-MEM. Preprint. *bioRxiv*. Published online May 26, 2013;1303:3997. https://doi.org/10.48550/arXiv.1303.3997
12. Picard Tools – By Broad Institute. Accessed August 20, 2024. https://broadinstitute.github.io/picard/
13. Danecek P, Bonfield JK, Liddle J, et al. Twelve years of SAMtools and BCFtools. *GigaScience*. 2021;10(2):giab008. https://doi.org/10.1093/gigascience/giab008
14. Okonechnikov K, Conesa A, García-Alcalde F. Qualimap 2: advanced multi-sample quality control for high-throughput sequencing data. *Bioinformatics*. 2016;32(2):292–294. https://doi.org/10.1093/bioinformatics/btv566
15. Poplin R, Ruano-Rubio V, DePristo MA, et al. Scaling accurate genetic variant discovery to tens of thousands of samples. *Preprint*. Published online July 24, 2018. https://doi.org/10.1101/201178. bioRxiv 201178.
16. Lai Z, Markovets A, Ahdesmaki M, et al. VarDict: a novel and versatile variant caller for next-generation sequencing in cancer research. *Nucleic Acids Res*. 2016;44(11):e108. https://doi.org/10.1093/nar/gkw227
17. Saunders CT, Wong WSW, Swamy S, Becq J, Murray LJ, Cheetham RK. Strelka: accurate somatic small-variant calling from sequenced tumor-normal sample pairs. *Bioinformatics*. 2012;28(14):1811–1817. https://doi.org/10.1093/bioinformatics/bts271
18. Auwera G van der, O'Connor BD. *Genomics in the Cloud: Using Docker, GATK, and WDL in Terra*. First edition. O'Reilly Media; 2020.
19. McLaren W, Gil L, Hunt SE, et al. The ensembl variant effect predictor. *Genome Biol*. 2016;17(1):122. https://doi.org/10.1186/s13059-016-0974-4
20. Fang LT, Afshar PT, Chhibber A, et al. An ensemble approach to accurately detect somatic mutations using SomaticSeq. *Genome Biol*. 2015;16(1):197. https://doi.org/10.1186/s13059-015-0758-2
21. Benjamin D, Sato T, Cibulskis K, Getz G, Stewart C, Lichtenstein L. Calling somatic SNVs and indels with Mutect2. *Preprint*. Published online December 2, 2019. BioRxiv 861054. https://doi.org/10.1101/861054
22. Wilm A, Aw PPK, Bertrand D, et al. LoFreq: a sequence-quality aware, ultra-sensitive variant caller for uncovering cell-population heterogeneity from high-throughput sequencing datasets. *Nucleic Acids Res*. 2012;40(22): 11189–11201. https://doi.org/10.1093/nar/gks918

23. Koboldt DC, Chen K, Wylie T, et al. VarScan: variant detection in massively parallel sequencing of individual and pooled samples. *Bioinformatics*. 2009;25(17):2283–2285. https://doi.org/10.1093/bioinformatics/btp373
24. Karczewski KJ, Francioli LC, Tiao G, et al. The mutational constraint spectrum quantified from variation in 141,456 humans. *Nature*. 2020;581(7809): 434–443. https://doi.org/10.1038/s41586-020-2308-7
25. Robinson JT, Thorvaldsdóttir H, Winckler W, et al. Integrative genomics viewer. *Nat Biotechnol*. 2011;29(1):24–26. https://doi.org/10.1038/nbt.1754
26. Richards S, Aziz N, Bale S, et al. Standards and guidelines for the interpretation of sequence variants: a joint consensus recommendation of the American College of Medical Genetics and Genomics and the Association for Molecular Pathology. *Genet Med*. 2015;17(5):405–424. https://doi.org/10.1038/gim.2015.30
27. Stenson PD, Mort M, Ball EV, Shaw K, Phillips A, Cooper DN. The human gene mutation database: building a comprehensive mutation repository for clinical and molecular genetics, diagnostic testing and personalized genomic medicine. *Hum Genet*. 2014;133(1):1–9. https://doi.org/10.1007/s00439-013-1358-4
28. Landrum MJ, Lee JM, Riley GR, et al. ClinVar: public archive of relationships among sequence variation and human phenotype. *Nucleic Acids Res*. 2014;42(Database issue):D980–D985. https://doi.org/10.1093/nar/gkt1113
29. Chakravarty D, Gao J, Phillips SM, et al. OncoKB: a precision oncology knowledge base. *JCO Precis Oncol*. 2017;2017:PO.17.00011. https://doi.org/10.1200/PO.17.00011
30. Patterson SE, Statz CM, Yin T, Mockus SM. Utility of the JAX clinical knowledgebase in capture and assessment of complex genomic cancer data. *NPJ Precis Oncol*. 2019;3(2). https://doi.org/10.1038/s41698-018-0073-y
31. Dumbrava EI, Meric-Bernstam F. Personalized cancer therapy-leveraging a knowledge base for clinical decision-making. *Cold Spring Harb Mol Case Stud*. 2018;4(2):a001578. https://doi.org/10.1101/mcs.a001578
32. Tate JG, Bamford S, Jubb HC, et al. COSMIC: the catalogue of somatic mutations in cancer. *Nucleic Acids Res*. 2019;47(D1):D941–D947. https://doi.org/10.1093/nar/gky1015
33. Noskova H, Kyr M, Pal K, et al. Assessment of tumor mutational burden in pediatric tumors by real-life whole-exome sequencing and in silico simulation of targeted gene panels: how the choice of method could affect the clinical decision? *Cancers*. 2020;12(1):230. https://doi.org/10.3390/cancers12010230
34. Dobin A, Davis CA, Schlesinger F, et al. STAR: ultrafast universal RNA-seq aligner. *Bioinformatics*. 2013;29(1):15–21. https://doi.org/10.1093/bioinformatics/bts635
35. Uhrig S, Ellermann J, Walther T, et al. Accurate and efficient detection of gene fusions from RNA sequencing data. *Genome Res*. 2021;31(3):448–460. https://doi.org/10.1101/gr.257246.119
36. Haas BJ, Dobin A, Stransky N, et al. STAR-Fusion: fast and accurate fusion transcript detection from RNA-Seq. *Preprint*. Posted online March 24, 2017: 120295. https://doi.org/10.1101/120295. bioRxiv.
37. Parkinson H, Kapushesky M, Shojatalab M, et al. ArrayExpress—a public database of microarray experiments and gene expression profiles. *Nucleic Acids Res*. 2007;35(Database issue):D747–D750. https://doi.org/10.1093/nar/gkl995
38. Carvalho BS, Irizarry RA. A framework for oligonucleotide microarray preprocessing. *Bioinformatics*. 2010;26(19):2363–2367. https://doi.org/10.1093/bioinformatics/btq431
39. Louis DN, Perry A, Reifenberger G, et al. The 2016 World Health Organization classification of tumors of the central nervous system: a summary. *Acta Neuropathol*. 2016;131(6):803–820. https://doi.org/10.1007/s00401-016-1545-1
40. Northcott PA, Shih DJH, Remke M, et al. Rapid, reliable, and reproducible molecular sub-grouping of clinical medulloblastoma samples. *Acta Neuropathol*. 2012;123(4):615–626. https://doi.org/10.1007/s00401-011-0899-7
41. Liao Y, Smyth GK, Shi W. The R package Rsubread is easier, faster, cheaper and better for alignment and quantification of RNA sequencing reads. *Nucleic Acids Res*. 2019;47(8):e47. https://doi.org/10.1093/nar/gkz114
42. Frankish A, Diekhans M, Ferreira AM, et al. GENCODE reference annotation for the human and mouse genomes. *Nucleic Acids Res*. 2019;47(D1): D766–D773. https://doi.org/10.1093/nar/gky955
43. GTEx Consortium. The genotype-tissue expression (GTEx) project. *Nat Genet*. 2013;45(6):580–585. https://doi.org/10.1038/ng.2653
44. Boeva V, Popova T, Bleakley K, et al. Control-FREEC: a tool for assessing copy number and allelic content using next-generation sequencing data. *Bioinformatics*. 2012;28(3):423–425. https://doi.org/10.1093/bioinformatics/btr670
45. Capper D, Jones DTW, Sill M, et al. DNA methylation-based classification of central nervous system tumours. *Nature*. 2018;555(7697):469–474. https://doi.org/10.1038/nature26000
46. Gröbner SN, Worst BC, Weischenfeldt J, et al. The landscape of genomic alterations across childhood cancers. *Nature*. 2018;555(7696):321–327. https://doi.org/10.1038/nature25480
47. Palova H, Das A, Pokorna P, et al. Precision immuno-oncology approach for four malignant tumors in siblings with constitutional mismatch repair deficiency syndrome. *NPJ Precis Oncol*. 2024;8(1):110. https://doi.org/10.1038/s41698-024-00597-8
48. Zhou X, Edmonson MN, Wilkinson MR, et al. Exploring genomic alteration in pediatric cancer using ProteinPaint. *Nat Genet*. 2016;48(1):4–6. https://doi.org/10.1038/ng.3466
49. Mudry P, Slaby O, Neradil J, et al. Case report: rapid and durable response to PDGFR targeted therapy in a child with refractory multiple infantile myofibromatosis and a heterozygous germline mutation of the PDGFRB gene. *BMC Cancer*. 2017;17(1):119. https://doi.org/10.1186/s12885-017-3115-x
50. Sievers P, Henneken SC, Blume C, et al. Recurrent fusions in PLAGL1 define a distinct subset of pediatric-type supratentorial neuroepithelial tumors. *Acta Neuropathol*. 2021;142(5):827–839. https://doi.org/10.1007/s00401-021-02356-6
51. Rohleder O, Mudry P, Neradil J, Noskova H, Slaby O, Sterba J. Letter to editor: F.S. Kaplan, et al., Early clinical observations on the use of imatinibmesylate in FOP: a report of seven cases, Bone (2017). *Bone*. 2018;116:171. https://doi.org/10.1016/j.bone.2018.08.003
52. Bagger FO, Borgwardt L, Jespersen AS, et al. Whole genome sequencing in clinical practice. *BMC Med Genomics*. 2024;17(1):39. https://doi.org/10.1186/s12920-024-01795-w
53. Louis DN, Perry A, Wesseling P, et al. The 2021 WHO classification of tumors of the central nervous system: a summary. *Neuro-Oncol*. 2021;23(8): 1231–1251. https://doi.org/10.1093/neuonc/noab106
54. Sun Y, Almomani R, Aten E, et al. Terminal osseous dysplasia is caused by a single recurrent mutation in the FLNA gene. *Am J Hum Genet*. 2010;87(1): 146–153. https://doi.org/10.1016/j.ajhg.2010.06.008
55. Brien GL, Remillard D, Shi J, et al. Targeted degradation of BRD9 reverses oncogenic gene expression in synovial sarcoma. *eLife*. 2018;7:e41305. https://doi.org/10.7554/eLife.41305
56. Dharia NV, Kugener G, Guenther LM, et al. A first-generation pediatric cancer dependency map. *Nat Genet*. 2021;53(4):529–538. https://doi.org/10.1038/s41588-021-00819-w
57. Shulman DS. Phase 1 Study of the Dual MDM2/MDMX Inhibitor ALRN-6924 in Pediatric Cancer. clinicaltrials.gov. 2023. Accessed January 1, 2024. https://clinicaltrials.gov/study/NCT03654716
58. Shanghai Pharmaceuticals Holding Co., Ltd. The Efficacy and Safety of TK216 in Subjects With Relapsed or Refractory Ewing's Sarcoma: a Phase II Clinical Trial in China. clinicaltrials.gov. 2024. Accessed January 1, 2024. https://clinicaltrials.gov/study/NCT05046314
59. Rajeshkumar NV, De Oliveira E, Ottenhof N, et al. MK-1775, a potent Wee1 inhibitor, synergizes with gemcitabine to achieve tumor regressions, selectively in p53-deficient pancreatic cancer xenografts. *Clin Cancer Res*. 2011;17(9):2799–2806. https://doi.org/10.1158/1078-0432.CCR-10-2580
60. Puissant A, Frumm SM, Alexe G, et al. Targeting MYCN in neuroblastoma by BET bromodomain inhibition. *Cancer Discov*. 2013;3(3):308–323. https://doi.org/10.1158/2159-8290.CD-12-0418
61. Bandopadhayay P, Bergthold G, Nguyen B, et al. BET bromodomain inhibition of MYC-amplified medulloblastoma. *Clin Cancer Res Off J Am Assoc Cancer Res*. 2014;20(4):912–925. https://doi.org/10.1158/1078-0432.CCR-13-2281
62. Laetsch TW, DuBois SG, Mascarenhas L, et al. Larotrectinib for paediatric solid tumours harbouring NTRK gene fusions: a multicentre, open-label, phase 1 study. *Lancet Oncol*. 2018;19(5):705–714. https://doi.org/10.1016/S1470-2045(18)30119-0
63. Cournoyer E, Ferrell J, Sharp S, et al. Dabrafenib and trametinib in Langerhans cell histiocytosis and other histiocytic disorders. *Haematologica*. 2024;109(4): 1137–1148. https://doi.org/10.3324/haematol.2023.283295
64. Koelsche C, Schrimpf D, Stichel D, et al. Sarcoma classification by DNA methylation profiling. *Nat Commun*. 2021;12(1):498. https://doi.org/10.1038/s41467-020-20603-4
65. Pfister SM, Reyes-Múgica M, Chan JKC, et al. A summary of the inaugural WHO classification of pediatric tumors: transitioning from the optical into the molecular era. *Cancer Discov*. 2022;12(2):331–355. https://doi.org/10.1158/2159-8290.CD-21-1094
66. Ma X, Liu Y, Liu Y, et al. Pan-cancer genome and transcriptome analyses of 1,699 pediatric leukemias and solid tumors. *Nature*. 2018;555(7696): 371–376. https://doi.org/10.1038/nature25795
67. Brodeur GM, Minturn JE, Ho R, et al. Trk receptor expression and inhibition in neuroblastomas. *Clin Cancer Res*. 2009;15(10):3244–3250. https://doi.org/10.1158/1078-0432.CCR-08-1815